Spring 1-1-2011

Toward Regular Arrays of Surface-Mounted Molecular Rotors

Lukas Kobr
University of Colorado at Boulder, kobr@eefus.colorado.edu

Toward Regular Arrays of Surface-Mounted Molecular Rotors

by

Lukáš Kobr

M.S., Universita Karlova v Praze, 2003

A thesis submitted to the

Faculty of the Graduate School of the

University of Colorado in partial fulfillment

of the requirements for the degree of

Doctor of Philosophy

Department of Chemistry and Biochemistry

2011

This thesis entitled:
Toward Regular Arrays of Surface-Mounted Molecular Rotors
written by Lukáš Kobr
has been approved for the Department of Chemistry and Biochemistry

_____

Josef Michl

_____

Dr. Richard K. Shoemaker

Date _____

The final copy of this thesis has been examined by the signatories, and we find that both the content and the form meet acceptable presentation standards of scholarly work in the above mentioned discipline.

Kobr, Lukáš (Ph.D., Chemistry)

Toward Regular Arrays of Surface-Mounted Molecular Rotors

Thesis directed by Prof. Josef Michl

Molecular rotors, motors, or in broader sense, functional nanostructures belong among the few areas of fundamental science and applied technology that bring together a broad spectrum of scientists from different backgrounds, such as chemists, physicists, engineers and biologists. There are two basic approaches to these molecular machines: one is based on observing biological systems that developed over billions of years, studying them, mimicking them and modifying them. The second approach is based on the design of new artificial materials. The design of artificial molecular machines involves synthetic and computational strategies to learn how to control the degrees of freedom of the system by covalent bonds, intramolecular interactions and self-assembly in order to the achieve the desired molecular function. Further challenge is to translate the function of small molecules into a change in some observable property in order to construct potentially useful materials. One way among many possibilities to achieve a change in macroscopic properties is to control the motion of not only one rotor, but the motion of the whole array of interacting rotors in a correlated fashion. Such materials with controllable average orientation of the rotors can have many useful optical and dielectric properties with applications in display technologies, field effect transistors, signal filtering etc. This work explores two novel approaches to surface mounted two-dimensional arrays of dipolar molecular rotors: arrays of dipolar molecular rotors via surface inclusion compounds and arrays of dipolar molecular rotors via self-assembled Langmuir-Blodgett films.

Acknowledgements

Richard K. Shoemaker

Ke Zhao

Charles Rogers

Joe Ryerson

Thomas Magnera

Jaroslav Vacek

Dominik Horinek

Jin Wen

Katka Polívková

Doug Caskey

Subhadeep Roy

Deb Casher

Mary Beth Mulcahy

Tarek Sammakia

Zdeněk Havlas

Andy Phillips

Eric Buchanan

John Downing

Pierro Sozzani

Barney Ellison

David Walba

Rob Horansky

Josef Michl

Postdocs, Graduate and Undergraduate Students in the Michl Lab

Matthew MacLeod

Contents

Chapter

Tables

Table

Figures

Figure

Chapter 1

Introduction

Molecular rotors, motors, or in broader sense, functional nanostructures belong among the few areas of fundamental science and applied technology that bring together a broad spectrum of scientists from different backgrounds, such as chemists, physicists, engineers and biologists. There are two basic approaches to these molecular machines: one is based on observing biological systems that developed over billions of years, studying them, mimicking them and modifying them.[2] The second approach is based on the design of new artificial materials.

The design of artificial molecular machines involves synthetic and computational strategies to learn how to control the degrees of freedom of the system by covalent bonds, intramolecular interactions and self-assembly in order to the achieve the desired molecular function. Further challenge is to translate the function of small molecules into a change in some observable property in order to construct potentially useful materials.

One way among many possibilities[3–7] to achieve a change in macroscopic properties[3–7] is to control the motion of not only one rotor, but the motion of the whole array of interacting rotors in a correlated fashion. Such materials with controllable average orientation of the rotors can have many useful optical and dielectric properties with applications in display technologies, field effect transistors, signal filtering etc.[4,8–11]

This work explores two novel approaches to surface mounted two-dimensional arrays of dipolar molecular rotors: arrays of dipolar molecular rotors via surface inclusion compounds

and arrays of dipolar molecular rotors via self-assembled Langmuir-Blodgett films.

This introduction will first give an overview of the work on surface mounted molecular rotors and then an overview of the literature about rotor arrays. Each chapter then gives an introduction that is specific to its subject matter.

1.1 Surface Mounted Molecular Rotors

The understanding of the collective interactions between surface mounted molecular rotors and with the surfaces is the key step necessary for engineering useful materials.[12] Rotors as well as more complex machinery are employed at nature's interfaces. Surface mounted rotors mimic nature's design and therefore represent a simplified approach to such devices. Many tools of the diverse field of surface science are deployed. Scanning tunneling microscopy (STM), atomic force microscopy (AFM), IR and UV spectroscopies are the most commonly employed techniques for studying surface mounted rotors.

The earliest studies of rotations of a single molecule were done on porhyrin based systems.[13] Other non-porphyrin based studies included work on halogenated thiophenol molecules on Cu{111} surfaces by Bartels and coworkers.[14] These researchers found that these molecules can rotate freely until temperatures dropped below 15 K, when the S-H bond cleavage occured due to increased electron tunneling rates.[14] The first report on collective unidirectional movement in came from early motor-dopped liquid crystal studies.[15] The unidirectional rotation was photo-driven and was determined to occurr at maximimum frequencies of 3MHz.[15]

Molecular switching of oligophenylene ethylene molecules embedded in alkane thiolate forests (matrices) mounted on gold surfaces has been measured with STM methods.[16] These measurements are done on the millisecond timescale. The nature of the switching observed in the STM measurements has been attributed to changes in hybridization of the oligophenylene ethylene molecules at the Au{111} surface interface, although this is largely spectulation. Switching in terms of photoisomerism has been looked at by multiple research

groups.[16,17] Interestingly, photoisomerism rates were reduced compared to those in solution. Explanations in terms of steric hindrance and excitation coupling were given.

The design of high frequency artifical rotors which can rotate at frequencies on the GHz timescale is based on constructing the rotors from simple building functional blocks,[18] the rotator, the axle and the stand. The stand contains the surface mounting groups and it holds the rotator, the rotating part, above the surface. The axle connects the rotator to the stand.

Two types of surface mounted molecular rotors can be recognized: the ones with the axis of rotation perpendicular to the surface (azimuthal rotors)[19] and the ones with the axis of rotation parallel to the surface (altitudinal rotors).

Surface mounted altitudinal rotors have been synthesized and studied on Au{111} surfaces. It has been shown that the thiol groups of the linker moiety easily undergo oxidation with air, but the additional Hg atoms, still present in the linker moiety function are capable of binding the rotor to the gold surface.[20] Recent investigations of surface mounted rotors on Cu{111} surfaces has been carried out and vibrational modes for torsional motion were studied.[21]

Additional work by Tierny et al. on gold surfaces has determined the energy barrier of rotations for a series of thioethers.[22] These barriers increase as a function of chain length but quickly saturated for chain lengths above two. The smallest thioether measured, dimethyl sulfide, yielded rotational barriers of 0.5 kJ/mol when measured with STM techniques. Dibutyl sulfide has a larger barrier of 1.2 kJ/mol under similar conditions. The saturation of the barrier size was attributed to the flexibility of longer chains which allowed for one site in the molecule to interact strongly with the surface, allowing the remaining part of the molecule to move more freely, effectively removing chain length dependence at an early stage. This interpretation came largely from molecular dynamics simulation results.[22]

Self-assembly is a promising route to simpler synthesis of complex molecules.[23] The self-assembly of molecular rotors designed to be mounted on surfaces has been investigated,[24,25]

but the the stability of self-assembled structures possesses a problem. The development of new methodologies for covalent stabilization of the self-assebled structures is underway[a] and represents a possible solution.

1.2 Approaches to Rotor Arrays

1.2.1 Designed Crystals

These rotors are usually composed of two bulky stators that serve as shielding groups for the rotator (Figure 1.1). The rotator is shown in red and the stator groups that interlock in the crystal and remain largely immobilized are shown in black. The crystalline solids of compounds with highly mobile and rigid parts in the solid state are often referred to as amphidynamic crystals.

The rotational freedom in the crystals is affected by several factors. One of them is the intrinsic rotational barrier of the rotor, caused by the steric bulk around the rotator, dipolar and van der Waals interactions between the rotator and the stator, and by conjugation and conformation effects. These effects can be manipulated by the choice of the functional groups, proper spacer groups, symmetry of the rotator, etc.[26]

The second important factor that affects rotational barriers in solid materials is the packing in the crystal, characterized by the packing coefficient C_k (a ratio of the van der Waals volume of the molecules in a unit cell and the unit cell volume). Voids in the crystal are necessary for unhindered rotation of the rotator, and crystals with a small packing coefficient exhibit rapid rotator rotations. This is illustrated by a series of rotors shown in Figure 1.1.[27]

Low packing densities often come at a price: such crystals tend to commonly crystallize with solvent molecules inside and when the solvent is removed, they often become unstable, easily collapse and form amorphous powders, which was the case for the rotor **3**. This problem can be solved by including strongly interacting groups, such as *m*-terphenyl,[27,28]

[a] Olive A., Parkan, K., Michl J., unpublished results

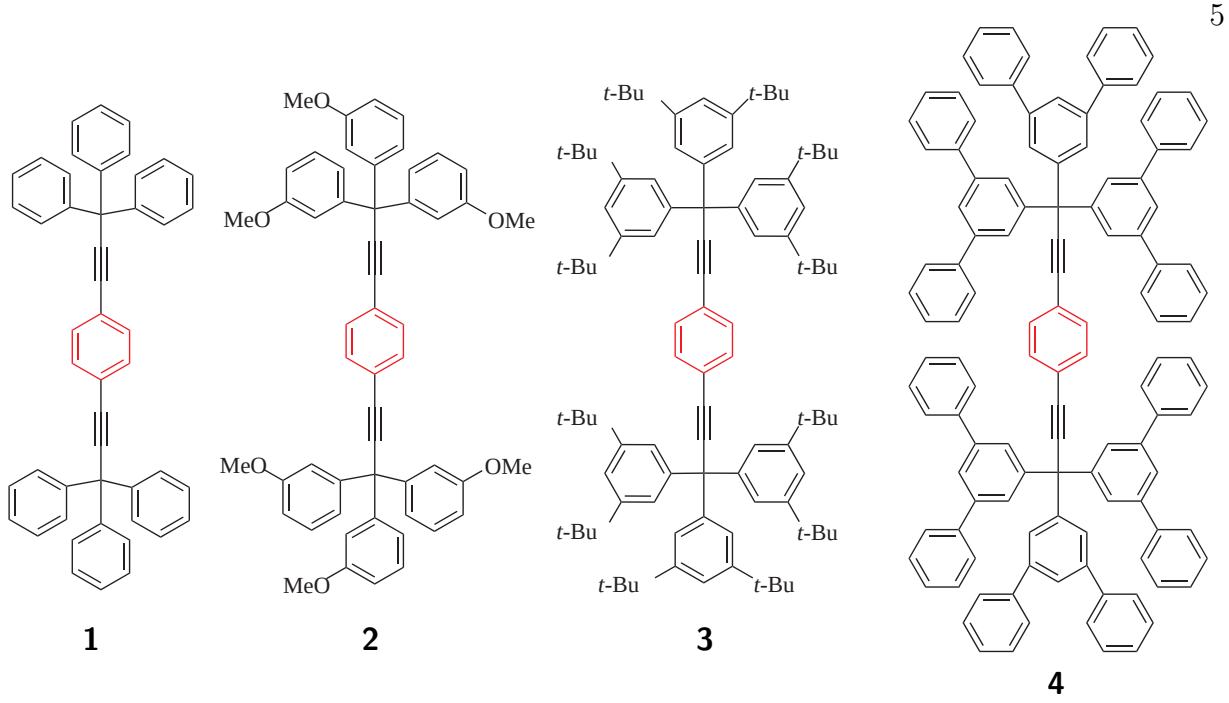

k_r [s^{-1}]	5 x 10^3	1.1 x 10^5	>1.0 x 10^8	5 x 10^5, >1 x 10^8
E_a [kcal/mol]	12.8	11.7	<5	7.0, <5.0
C_k	0.73	0.73	0.68	0.68

Figure 1.1: Rotors: effects of packing on the rotational barrier.

large aromatic systems,[29–31] groups for halogen bonding[32] and other groups[30,31] in the rotor design.

The rotation rates are usually determined from solid-state NMR. One of the widely used methods is coalescence analysis in ^{13}C CP MAS NMR at variable temperature.[33,34] The method is based on crystallographic non-equivalence of chemically equivalent carbons related by rotation that is hindered in the crystal. With varying temperature, the signals exchange and the line shapes are analyzed in terms of exchange rates. The signals need to be spectrally resolved for this analysis.

Another method employs quadrupolar echo solid-state deuterium NMR.[35] The method

relies on the orientational dependence of the quadrupolar coupling and its modulation by molecular motion, which is temperature dependent. The line shapes depend on the motion rate and type of motion.[36–38] This is a very versatile method that covers a large dynamic range of rotational frequencies (10^4 to 10^8 s^{-1}).

The initial efforts involved the rotor structures **1**,[39–43] **5**,[44] **6**[45] and **7**,[43] (Figure 1.2, the rotator is shown in red).

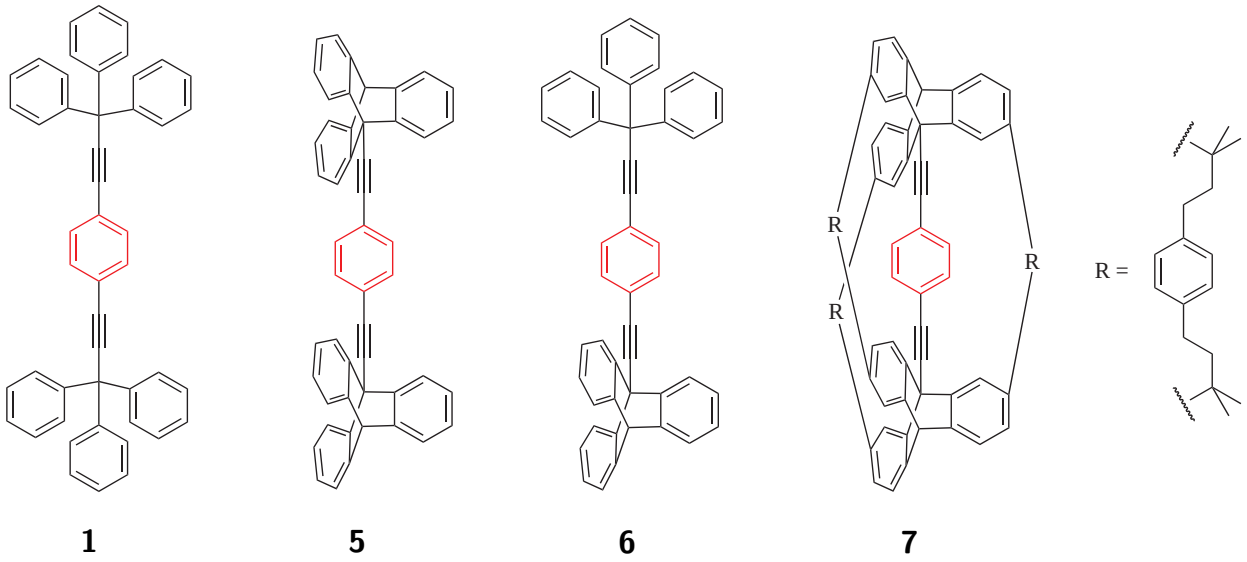

Figure 1.2: Initial trityl and triptycene based rotors.

The rotor **1** crystallizes in several crystallographic forms.[39,40] The rotational barriers of the rotor **1** with perdeuterated rotator were measured using wide-line deuterium NMR.[39,40] The solvent-free form displayed rotational barrier of 12.8 kcal/mol and the benzene clathrate barrier of 14.6 kcal/mol for the phenylene flip.[39] The crystal packing of the two forms are shown in Figure 1.3.

Rotational barrier measurements with the rotor **1** with perdeuterated stator using the coalescence analysis in ^{13}C CP MAS NMR at variable temperature yielded lower rotational barriers, 11.3 kcal/mol, for both the solvent-free form and the benzene clathrate.[40] The differences were attributed to higher experimental error of the broad line deuterium NMR method and to different vibrational amplitudes of protons and deuteriums, giving different

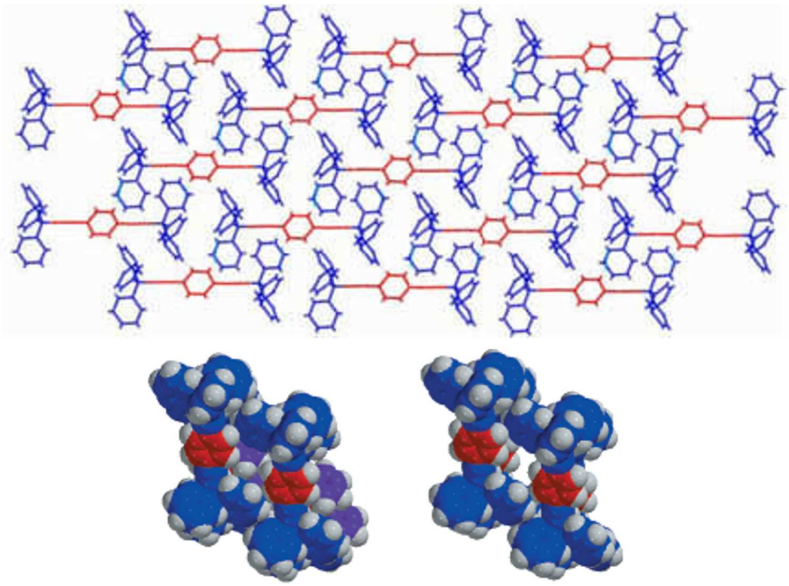

Figure 1.3: Rotor **1** crystal packing. Top and bottom right: solvent-free form, bottom left: clathrate with benzene (benzenes in purple).

effective sizes to C-H and C-D bonds.

The high rotational barriers are caused by steric hindrance of the rotator with the stator in the solvent-free form (Figure 1.3). The rotor **5** displays similar crystal packing properties to the rotor **1** and therefore a similar high rotational barrier.[44]

Interestingly, the cross between structures **1** and **5**, the rotor **6**, displays a different mode of crystal packing without the interlocking of the stator by the rotator, and a lower barrier to rotation of the phenylene rotator, about 7.9 kcal/mol for the solvent-free form, determined for the rotor **6** with perdeuterated rotator by broad line solid-state deuterium NMR at variable temperature.[45]

Other variations of the rotor **1** have been prepared and studied. These were rotors with apolar rotators[46] **8**, **9**, **10**, **11** (Figure 1.4) and most notably rotors with dipolar rotators, **12**,[9,47] **13**,[48] **14**,[48] **15**,[48–50] **16**[48] and **17**.[49]

The rotational barrier analysis of *o*-xylene clathrate of the rotor **10** with perdeuterated rotator using broad line solid-state deuterium NMR at variable temperature showed a

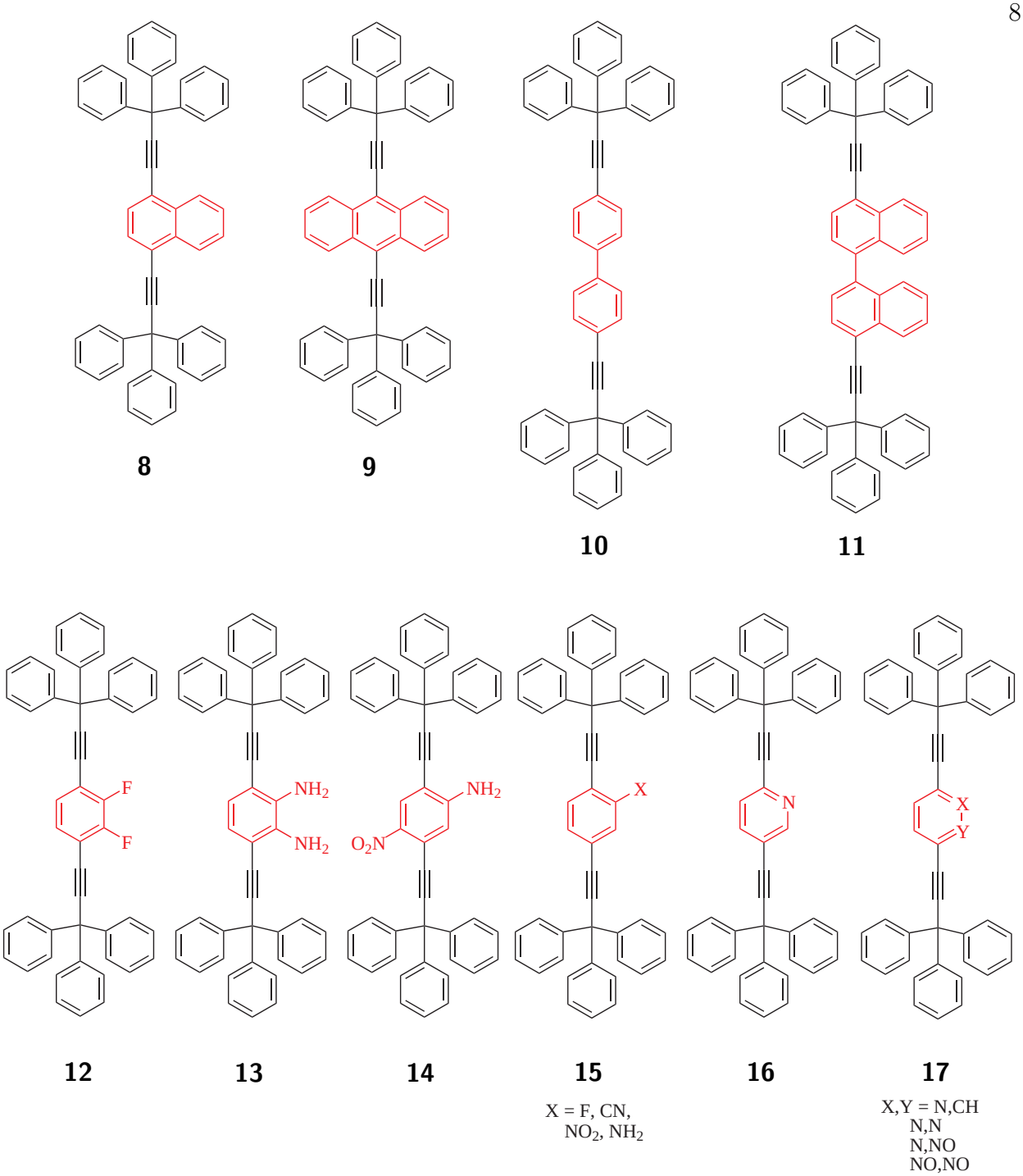

Figure 1.4: More trityl based rotors.

remarkably low rotational barrier of 7.4 kcal/mol.[46] The crystal structure of the rotor **10** *o*-xylene clathrate shows a different packing from the crystal of the rotor **1** (Figure 1.5).

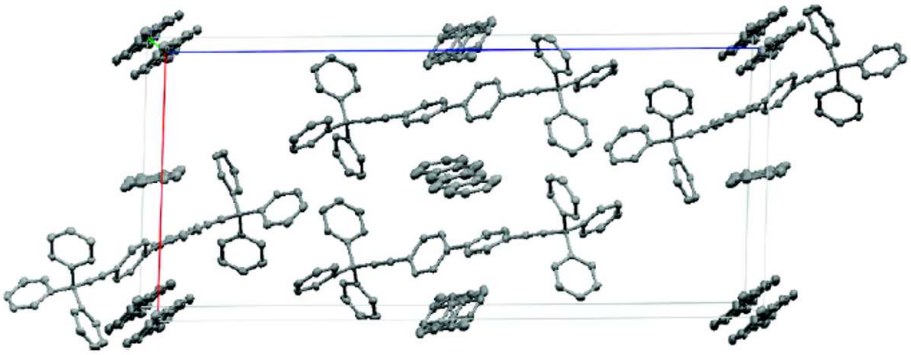

Figure 1.5: X-ray structure of the rotor **10** *o*-xylene clathrate.

The crystals of the rotor **12** were studied by dielectric spectroscopy.[9] The rotational barrier was measured to be 14-15 kcal/mol and evidence for dipolar interactions was found. The rotational potential showed an asymmetry of 0.9 kcal/mol. The X-ray structure is shown in Figure 1.6.

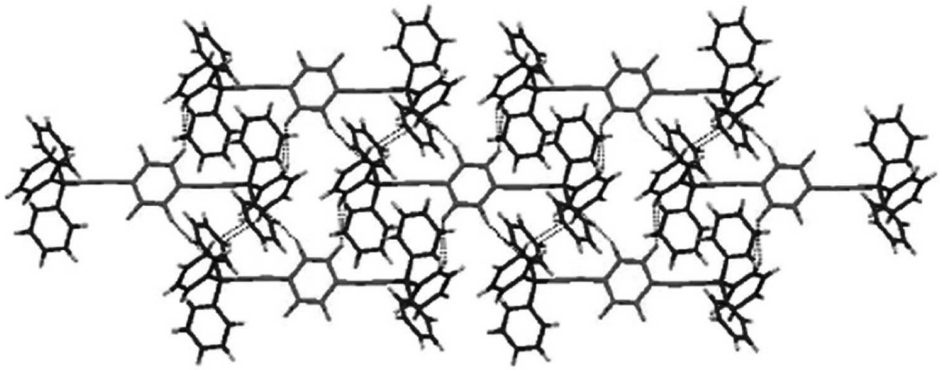

Figure 1.6: X-ray structure of the rotor **12** crystal.

Crystals of the rotors **15**F (X = F) and **16** were obtained in sufficient quality for X-ray crystallography and to determine the rotational barriers; the solid-state NMR spectra were resolved enough to permit a determination of rotational barriers for the rotator rotations.[49] The solvent-free crystals of the rotor **15**F exhibited a rotational barrier of 13.7 kcal/mol, while the solvent-free crystals of the rotor **16** showed a rotational barrier of 8.5 kcal/mol for flipping of the less bulky pyridine rotator. The rotors exhibit similar packing to the rotor **1**.

The X-ray and NMR data showed a weak preference for ordering of the dipoles.

The rotors **2**,[51,52] **3**[53] and **4**[27] have additional steric bulk on the stator in order to increase the void space for the rotator and decrease the rotational barriers. The approach was successful and the rotor **2** displays a rotational barrier of about 11.6 kcal/mol and a rich polymorphogenic behavior.[51,52] The rotor **3** exhibited two rotational barriers over 7 kcal/mol and less than 5 kcal/mol that were attributed to two crystal phases in the sample due to poor crystallinity.[53]

The rotor **4** exhibited better crystal stability than the rotor **3**, and again two different frequencies of the phenylene rotator rotations were found, one associated with a barrier of less than 5 kcal/mol and the other with a barrier of over 7 kcal/mol. The existence of the two rotational barriers was attributed to two different crystallographic orientations of the rotor in the crystal.[27]

Other successful structural modifications to the rotor **1** structure motif were made[54–56] and improved structural analogs of **5** were prepared.[57,58] The symmetry of the rotator as well as the symmetry of the surroundings also plays a significant role in the magnitude of the rotational barrier (Figure 1.7). The effect of the rotator symmetry was illustrated on a series of rotors **18**, **19**, **20**, **21** (Figure 1.8).[26]

The phenylene rotator in **18** has C_{2v} symmetry and it exhibits a rotational barrier of 8.5 kcal/mol. This is significantly lower compared to the trityl analog **1** and the difference is due to the larger atomic radius of the silicon atom and the increased length of the Si-C bond relative to the C-C bond. The bicyclo[2.2.2]octane rotator with its C_3 axis displayed a remarkably low rotational barrier of 3.5 kcal/mol in the rotor **19**. The *p*-carborane based rotor **127** had the lowest rotational barrier in the series, 3.0 kcal/mol, for the rotation of the *p*-carborane with its C_5 symmetry axis.

The cubane based rotor **20** showed a rather high rotational barrier of 12.6 kcal/mol, despite the high C_3 symmetry axis of the cubane rotator. The unusually high rotational barrier value was attributed to a difference in crystal packing in solid **20** compared to crystals

of **18**, **19**, and **21**. The comparison of the packing modes in the rotors **18**, **19**, **20**, and **21** is shown in Figure 1.9.

Also other rotors with highly symmetric rotators were prepared and studied, and they showed lower rotational barriers than their phenylene analog.[32,59,60]

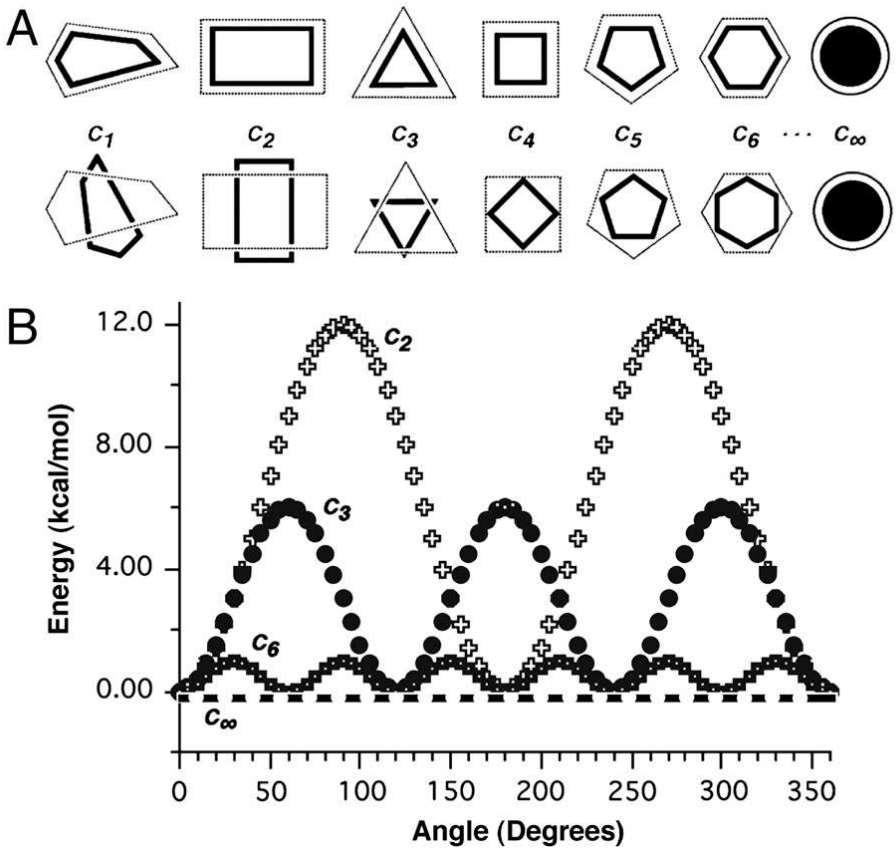

Figure 1.7: The effect of symmetry on the rotational barrier (calculated values in an idealized potential).

1.2.2 Metal Organic Frameworks

Metal-Organic frameworks (MOFs) are periodic polymeric crystalline materials of polydentate organic ligands and metals or metal clusters.[61–64] They are one of the lowest density materials known, and hold promise for many potential applications. They were also studied for potential applications for constructing rotor arrays.

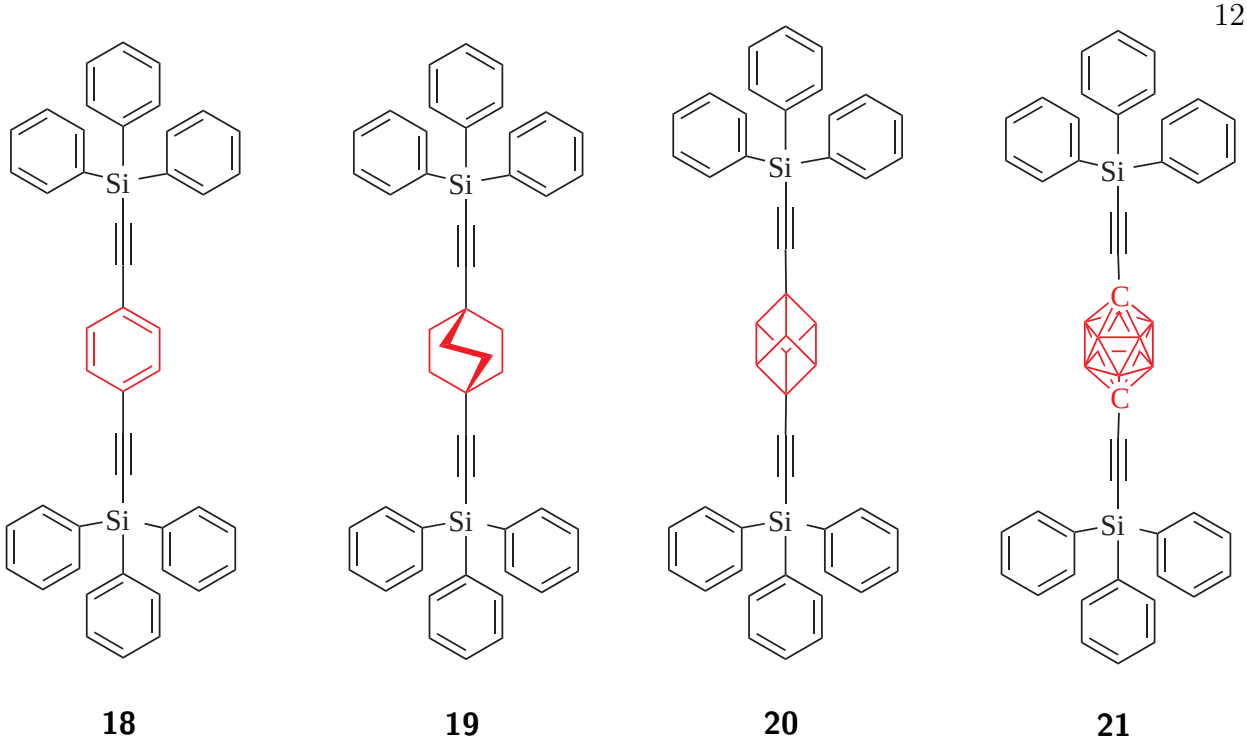

Figure 1.8: The structures studied for effect of symmetry on the rotational barrier.

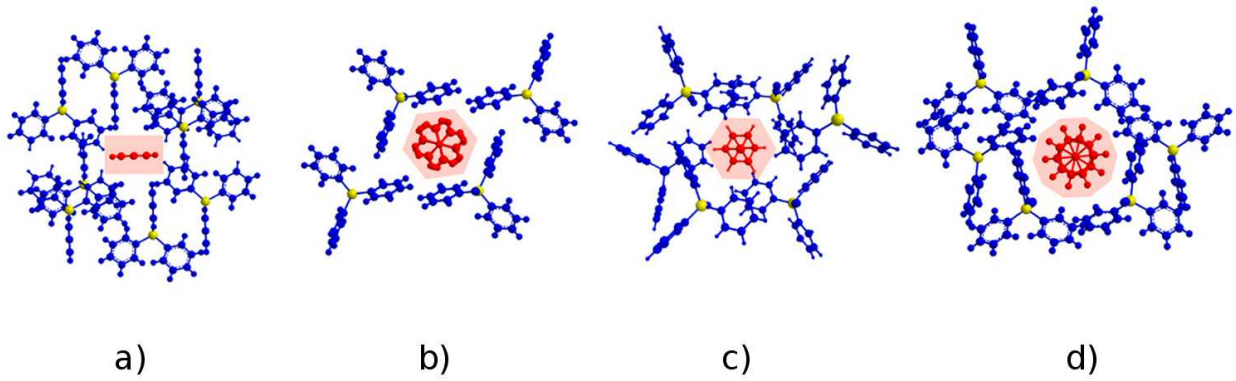

Figure 1.9: The crystal structures of the rotors **18** (a), **19** (b), **20** (c) and **21** (d).

The metal-organic frameworks of octahedral Zn_4O clusters connected into cubic cell with twelve molecules of terphtalic-d_4 acid (MOF **22**, Figure 1.10)[65] or with 2-bromoterphtalic acid (MOF **23**)[66] were studied with dielectric spectroscopy and with variable temperature broad line solid-state deuterium NMR as well as computationally.[65–67]

The rotational barrier for the rotation of 2-bromophenylene in MOF **23** was determined

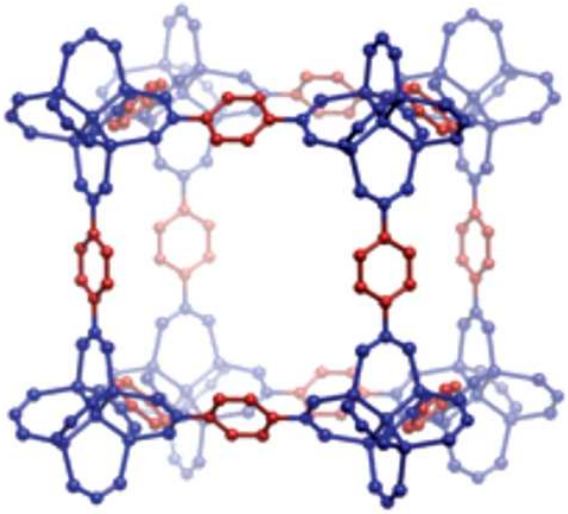

Figure 1.10: Metal organic framework **128**.

to be about 7.3 kcal/mol using dielectric spectroscopy and fitting the data into the two-minimum potential model.[68] The value showed a good agreement with the rotational barrier of 2-bromophenylene in a model structure shown in Figure 1.11, calculated to be 7.5 kcal/mol using B3LYP/SDD calculations,[66] The X-ray structure of MOF **23** showed disorder of the bromine in 2,3,5 and 6 positions of the aromatic ring of 2-bromoterephtalic acid, which further indicates the rotation of 2-bromophenylene, and it also indicates not strong enough dipolar interactions for polar ordering. The dipolar interaction energy was determined as about 0.14 kcal/mol which was less than the experimental uncertainty of the measurements.

The barrier for rotation of phenylene-d_4 in MOF **22** was determined to be about 11.3 kcal/mol using variable temperature broad-line deuterium NMR.[65] The experimental value is lower than the computed value of 14 kcal/mol using B3LYP/DGDZVP,[67] but it is in relatively good agreement with the computed value of 12.2 kcal/mol using BP86/TZVP(P).[66] The high rotational barrier of phenylene-d_4 in MOF **22** was attributed to the conjugation with the carboxylates, and it was recognized that MOFs derived from compounds with substitution in positions 2,3,5 and 6 of the terephtalate benzene ring hold promise not only

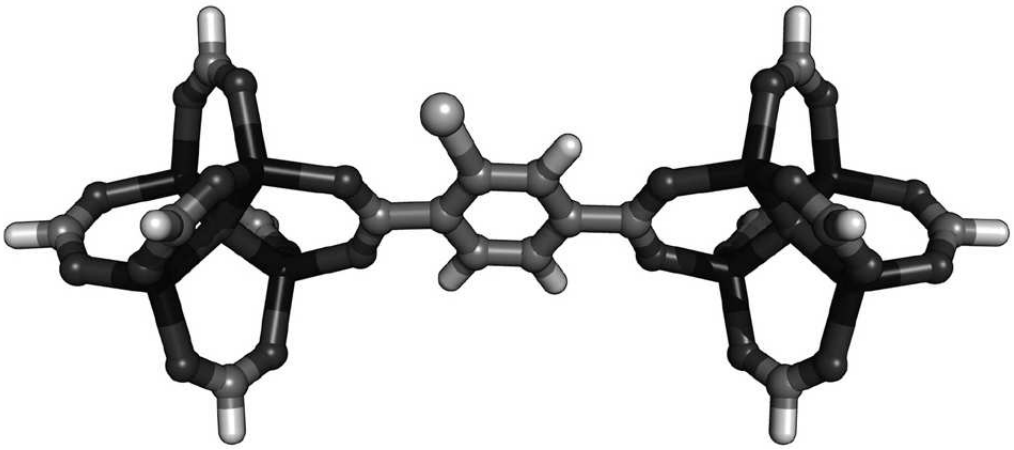

Figure 1.11: Model structure used for computation of the rotationa barrier in MOF **23**.

for structures with low rotational barrier, but also for improved dipolar interactions.

Further challenge that needs to be addressed in the future is also the stability of empty metal-organic frameworks as they tend not to be stable when the solvents are removed from the crystal lattice.[66,b]

[b] Kobr L., Meng H., Michl J., unpublished results.

Chapter 2

Toward Rotor Arrays Using Surface Inclusion Compounds

2.1 Introduction

2.1.1 Project Overview and Goals

This project explores a new approach to ordered regular arrays of dipolar azimuthal molecular rotors. Two-dimensional lattices of interacting dipoles are predicted to display order states,[69] including ferroelectric states for triangular arrays. Such new states of matter open up opportunities for many applications, such as frequency filters for RF signal processing, fast light modulation, data storage, field-effect transistors, etc.

The rotor attachment is achieved through non-covalent interactions during a self-assembly process. The mount points consist of parallel channels in a planar crystal surface. The channel axes are perpendicular to the surface of the crystal. Each rotor possesses a tail with affinity for the channel (Figure 2.1). The tail is attached to a bulky group, the stopper, which carries a bulky rotator connected via an axle. The stopper and the rotator should be bulky enough not to fit into the channel. The insertion of such rotor into the channel should yield a surface inclusion compound with the rotor tails inserted inside the channel and the stoppers with the rotators protruding above the surface, forming a two-dimensional array of dipolar rotors.

The ordered states of a regular two-dimensional array of dipoles depend on the lattice parameters. In simple lattices described by two lattice vectors, there are two limiting cases: the square lattice ($\alpha = 90°$, Figure 2.2a), and the trigonal lattice $\alpha = 60°$, Figure 2.2b). The

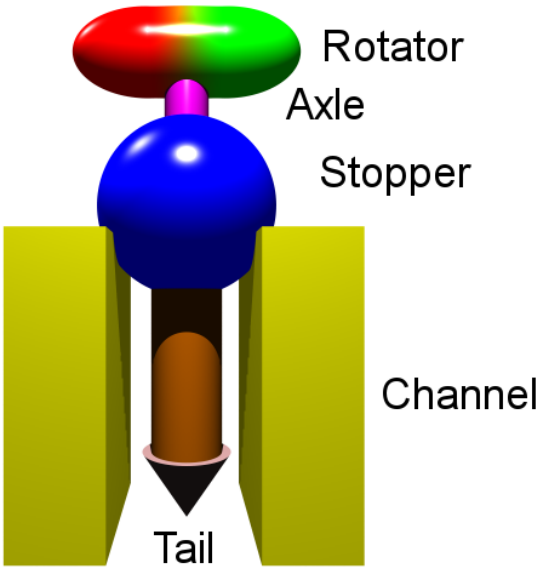

Figure 2.1: Rotor design: the rotor possesses a rotator, an axle, a stopper and a tail with affinity for the channel.

ground state of the square lattice is antiferroelectric, while the ground state of the trigonal lattice is ferroelectric.

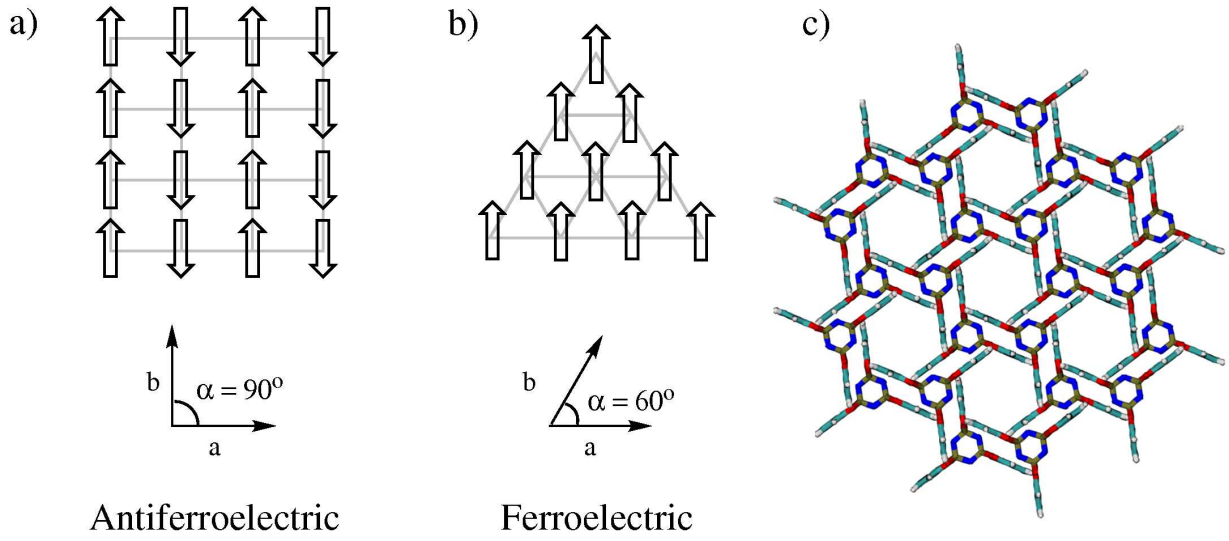

Figure 2.2: a) square lattice (antiferroelectric ground state); b) trigonal lattice (ferroelectric ground state); c) TPP lattice (top view).

A number of hexagonal lattices with channels are known. Of these, spirocyclotriphosp-

hazines seem to be the most suitable host system for our purpose due to their rich inclusion behavior, availability, presence of several NMR-active nuclei, and the possible variation of the lattice parameters with the structure of the spirocyclotriphosphazine. We have chosen tris(o-phenylenedioxy)cyclotriphosphazine (TPP, **24**, Figure 2.3) as the host system. The TPP structure with the channels arranged in a trigonal fashion is shown in Figure 2.2c.

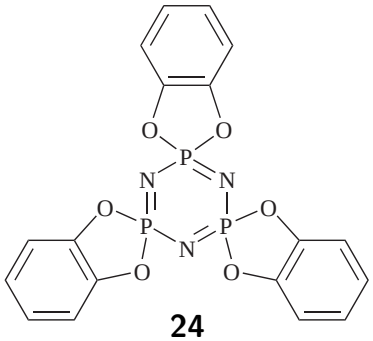

24

Figure 2.3: The structure of TPP.

The goal of this work is to find suitable systems for surface inclusion compounds and to develop the methods for their characterization. One of the first challenges is to find a suitable stopper, as the host channels are expandable to some extent. Several candidates (*p*-carborane, durene, B-substituted *p*-carborane, and triptycene) were considered and some of them explored in this work. Furthermore, the success of the self-assembly process depends on the thermodynamic stability of the inclusion compound. It needs to be thermodynamicaly more stable than the neat materials, which is difficult to predict. The rotor needs to have a sufficient dipole moment and a low enough rotational barrier for ferroelectric ordering to take place. And finally, an inclusion compound preparation method that yields large flat surfaces covered with the rotors needs to be developed.

2.1.2 Cyclotriphosphazines and their Inclusion Compounds

Inclusion compounds are non-covalent complexes of a porous host and guest molecules trapped inside the host lattice. They offer many interesting applications, such as means

of studying stable or highly reactive molecules (*e.g.* radicals)[70] in a confined well defined environment, separations of mixtures,[71,72] selective absorption of target species, such as removal of radioactive iodine from the environment,[73] stereoregular polymerizations that lead to highly crystalline polymers,[74,75] hydrogen storage,[72], etc.

Many host systems have been studied.[76] The inclusion compounds of urea, thiourea, cyclodextrins, perhydrotriphenylene, cyclotriphosphazines and others belong among the most studied systems.

A number of cyclotriphosphazines are known to form inclusion compounds (discussed in detail further in this section). The variation of cyclotriphosphazine structure determines the type of inclusion compound formed, and correlates with channel spacing in the channel-forming inclusion compounds. These properties together with high mechanical and thermal stability of the inclusion compounds and the presence of several nuclei (^{13}C , ^{31}P , ^{1}H) suitable for NMR spectroscopy, make cyclotriphosphazines the most suitable host systems for our purpose and this introduction will therefore only focus on them. Our host system of choice is TPP (**24**,[77] Scheme 2.1) for the smallest known channel spacing among the cyclotriphosphazines.

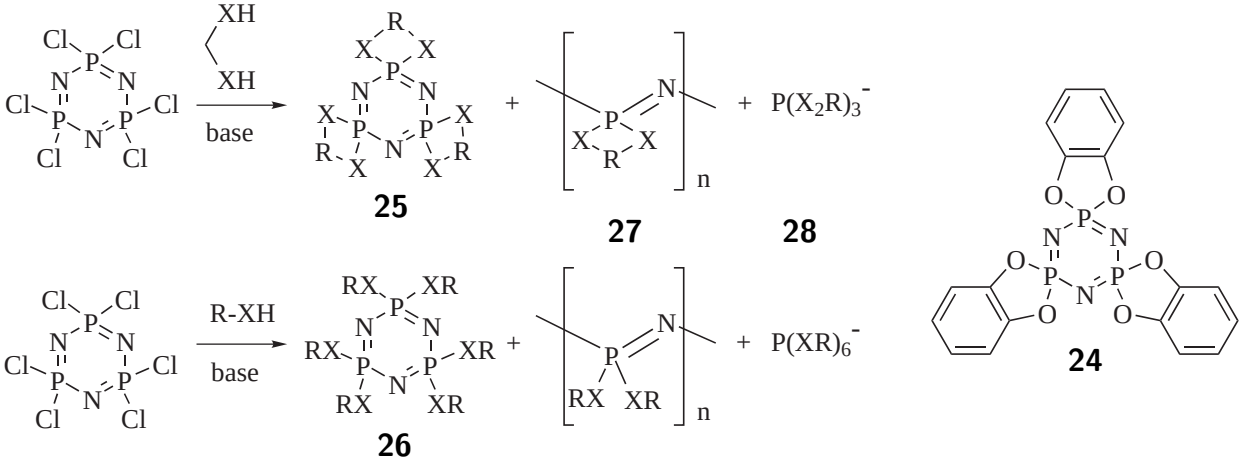

Scheme 2.1: Some examples of cyclotriphosphazine structures, their synthesis, and common side products.

Cyclotriphosphazines (Scheme 2.1) can be divided into several classes, depending on the character of the side groups attached to the phosphorus atoms via heteroatoms. Cyclotriphosphazines with aliphatic side groups generally do not form inclusion compounds.[78,79] A number of cyclotriphosphazines with aromatic side groups are known to form inclusion compounds, especially spirocyclotriphosphazines (**25**, Scheme 2.1).

Cyclotriphosphazines (**25** and **26**, Scheme 2.1) are usually prepared by the reaction of hexachlorocyclotriphosphazine with phenols, amines, thiols, etc, in presence of a base, such as triethylamine.[80] Moderate amounts of polyphosphazines (**27**, Scheme 2.1) and phosphates (**28**, Scheme 2.1) are formed as side-products during the reaction.

TPP and its inclusion compounds. TPP is the simplest known spirocyclotriphosphazine that can form the tunnel structure. It is a white crystalline solid with a melting point of 244-245 °C,[81] it is sparingly soluble in most organic solvents, and it occurs in two crystalline modification: monoclinic and hexagonal.[71]

The monoclinic modification can be obtained by sublimation, and the hexagonal modification is generally favored if a suitable guest molecule can be clathrated in the lattice. Inclusion compounds of monoclinic TPP are not known.

All the known inclusion compounds of TPP are hexagonal, regardless of the guest compound, and they can be prepared by crystallization of TPP from organic solvents, exposure of the monoclinic or empty hexagonal TPP to a liquid organic solvent or its vapors, grinding neat TPP and the guest together, or by exchange of guests from a TPP inclusion compounds of another solvent. During the guest exchange, smaller solvents generally replace bulkier solvents.

TPP can accommodate a large variety of guests of different sizes and properties (tetralin,[71] norbornadiene,[71] isooctane,[71] *trans*-decalin,[71] *p*-xylene,[82] cumene,[71] cyclohexane,[71] n-alkanes,[71] styrene,[71] ethyl acetate,[71] carbon tetrachloride,[71] tetrahydrofuran,[71] chloroform,[71] methyl methacrylate,[71] diethyl ether,[71] benzene,[71] acetone,[71] carbon disulfide,[71] acrylonitrile,[71] ethanol,[71] methanol,[71] water,[83] polyethylene,[84] poly(ethylene oxide),[84] carbon dioxide,[72]

methane,[72] argon,[72] hydrogen,[72] nitrogen,[72] oxygen,[72] *cis*−1,4-polybutadiene,[85] *trans*−1,4-polyisoprene,[85] polytetrahydrofuran,[85] oligothiophenes,[86,87] various alkanes,[88,89] polyconjugated olefines,[87] azo dyes,[87] etc). There seems to be no correlation between the ease of formation of the inclusion and polarity, π-character or hydrogen-bonding properties of the guest molecule, and van der Waals interactions seem to be the dominant stabilizing force for the formation of hexagonal inclusion compounds. All the inclusion compounds have similar lattice constants (a = 11.7 Å, c = 10 Å) with approximately 2 % variation.

The hexagonal TPP structure ($P6_3/m$ space group) requires the molecules to retain mean three-fold symmetry axis.[71] It is thus composed of TPP molecules in paddle-wheel like arrangement as determined by polarized infrared spectroscopy. The crystals are formed by an alternating sequence of two layers separated by about 5 Å($c/2$). This distance is too small for guests to be sandwiched between the layers. The two layers are identical but they are rotated by 180° with respect to each other (Figure 2.4). Each layer is composed of equivalent host molecules in a hexagonal arrangement, with the planes of the cyclotriphosphazine rings in the plane of a-vectors. The planes of the catechol side groups are parallel to the plane of c-vectors. The bilayers stack with no relative displacement, *i.e.* the molecules of equivalent layers lie on the same symmetry axis. This arrangement gives rise to hexagonal channels that extend over the entire crystal as shown by polymerization inside the channels,[85,90,91] diffusion studies through the channels,[92] and solid-state NMR studies with hyperpolarized xenon inside the channels.[93] The channels are approximately 4.5 Å wide, and each single layer forms a triangular cavity about 7.0 Å across.

Hexagonal TPP and its inclusions exhibit a single resonance in ^{31}P solid-state NMR (with residual dipolar coupling to ^{14}N) corresponding to all equivalent phosphorus atoms (Figure 2.5a) and three singlets for three sets of equivalent carbons in ^{13}C solid-state NMR (Figure 2.5c).[82]

Monoclinic TPP contains molecules of TPP with twisted cyclotriphosphazine ring and benzodioxaphosphazole groups in order to improve crystal packing. The crystal packing

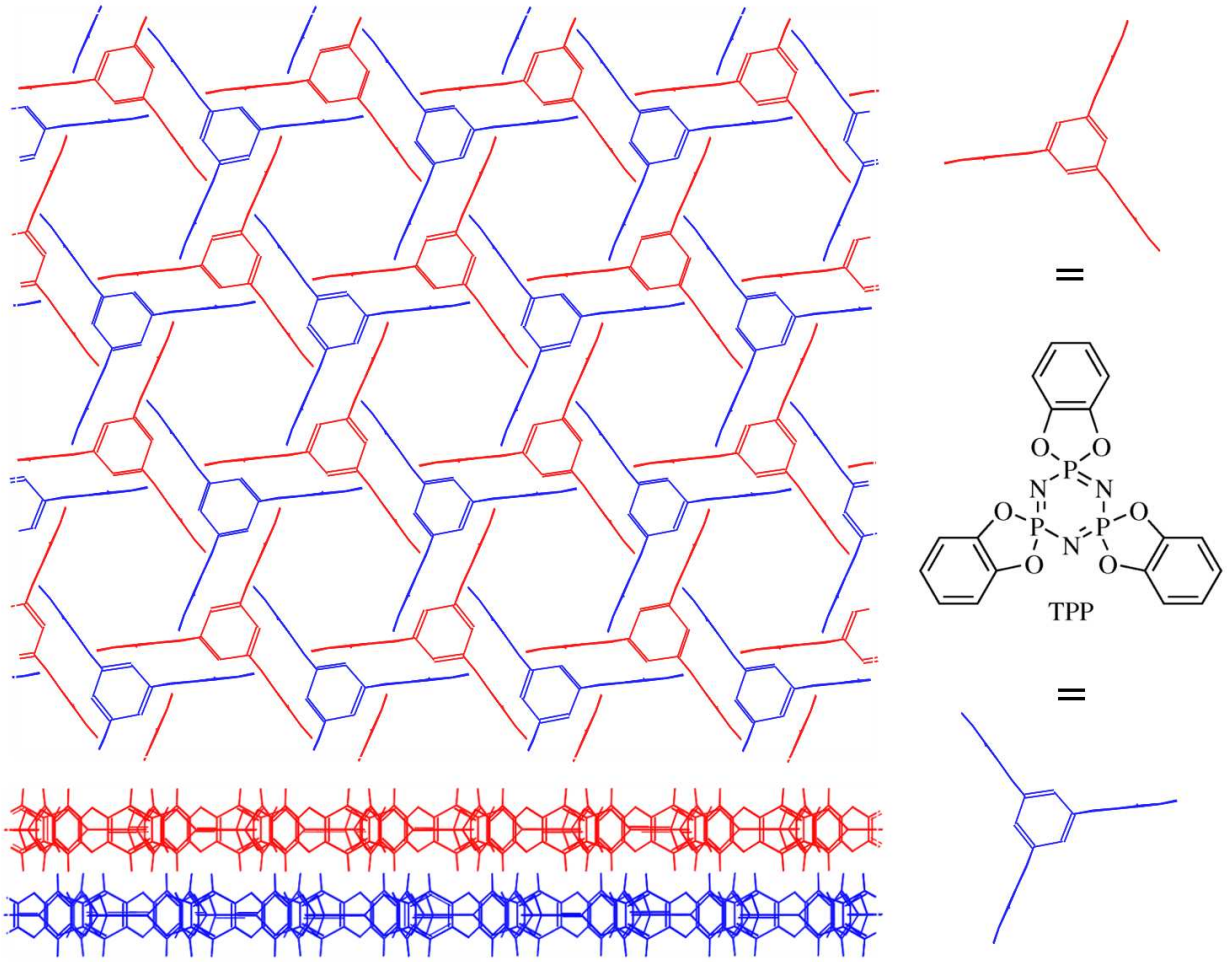

Figure 2.4: Hexagonal TPP structure: the hexagonal TPP channel is formed by the trigonal-shaped cavities rotated by 180° with respect to each other. Above: top view of the hexagonal TPP structure; below: side view of hexagonal TPP structure.

remains inefficient, the structure contains relatively large percentage of void space, and it is believed to be the reason for the ease of transformation into the hexagonal structure upon contact with a guest. The solid-state ^{31}P NMR of monoclinic TPP shows three broad peaks, which is consistent with three inequivalent phosphorus atoms (Figure 2.5b)[82]. The broadening is most likely caused by ^{31}P -^{31}P J-coupling, not fully suppressed by magic angle spinning. The ^{13}C solid-state NMR spectrum of monoclinic TPP displays three multiplets (Figure 2.5d).[82]

The reorganization of monoclinic TPP into the hexagonal form occurs upon contact

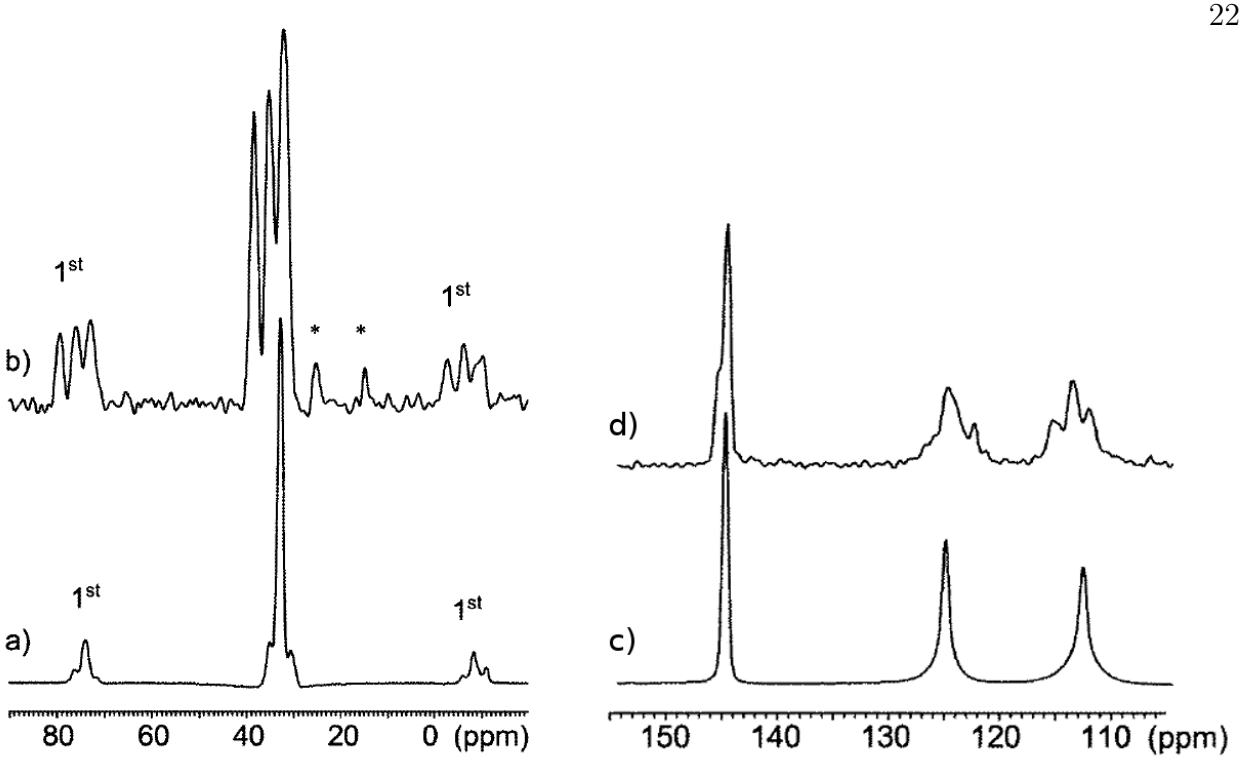

Figure 2.5: TPP solid state NMR: a) empty hexagonal TPP ^{31}P CP MAS; b) monoclinic TPP ^{31}P CP MAS; c) empty hexagonal TPP ^{13}C CP MAS; d) monoclinic TPP ^{13}C CP MAS.[82]

with a suitable solvent or its vapors. The solvent forms an inclusion compound with TPP, the process is exothermic, and it is associated with rapid swelling and disintegration of the crystals due to a large volume increase (23% for the benzene TPP inclusion). The inclusions obtained by crystallization or solvent absorption exhibit the same X-ray powder patterns. The crystallization provides larger crystals, and solvent absorption by the monoclinic TPP forms microcrystallites of quite uniform size and morphology.[83]

The transformation of monoclinic to hexagonal modification is thought to occur in a stepwise fashion via initial filling of voids in the monoclinic TPP that does not stack efficiently because of the unusual shape of the molecule. This is followed by molecular reorganization into the hexagonal form to improve the space utilization. A channel is formed and more guest molecules diffuse through the channel to the monoclinic crystal underneath, causing

further modification change. It is not likely that the process takes place by recrystallization as it can also be observed when monoclinic TPP is exposed to solvent vapors and it is not likely that the reorganization of the crystal happens all simultaneously.[71,83]

When monoclinic TPP is heated above 170 °C it undergoes partial spontaneous transition into hexagonal TPP. Both forms coexist above this temperature as determined from X-ray powder patterns.[71] Many TPP inclusion compounds expel their guests around this temperature. The spontaneous transition of monoclinic TPP into hexagonal form and the guest expulsion are likely due to vigorous vibrations and librations of the TPP phhenylene rings at elevated temperature and thus larger sterical demands of TPP molecules.[71]

The remarkable property of TPP inclusion compounds with volatile guests is that the guest can be removed while maintaining the hexagonal structure.[83] This behavior is rare, since usually the framework rearranges into a non-porous form upon guest removal, and it is not even observed in frameworks stabilized by hydrogen bonding.[76]

The DSC trace of TPP - benzene inclusion compound shows three endoterms and an exotherm (Figure 2.6a).[82] The low-temperature endotherm is very broad, it ranges from from 30 to 150 °C, and it is due to loss of included benzene. The broad exotherm centered around 150 °C is due to a first order transition of empty hexagonal into the monoclinic form. The empty hexagonal TPP is hence metastable at low temperatures. The endotherm around 225 °C corresponds to another first order transition (monoclinic to hexagonal), and the high temperature endotherm corresponds to melting. The phase above 170 °C contains both hexagonal and monoclinic forms.

The DSC trace of empty hexagonal TPP (Figure 2.6b) is similar to the trace of the TPP-benzene inclusion compound, but it is missing the broad endotherm that corresponds to the loss of the guest. It shows two endoterms and an exotherm that are identical the peaks found in the DSC trace of the TPP - benzene inclusion compound.

The DSC trace of monoclinic TPP (Figure 2.6c) shows only the two high-temperature endoterms, identical to those of empty hexagonal TPP.

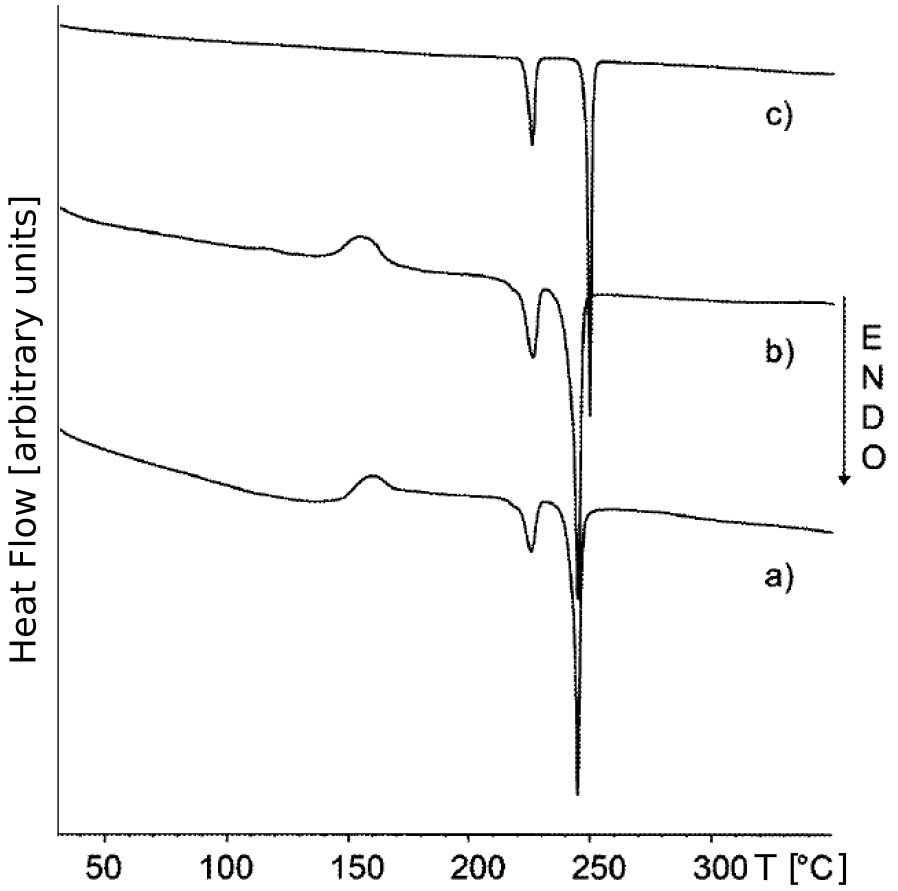

Figure 2.6: TPP DSC traces (downward-pointing peaks are associated with endothermic processes): a) TPP - benzene inclusion; b) empty hexagonal TPP; c) monoclinic form.[82]

Heating of inclusion compounds typically leads to expulsion of the guest from the channels below the melting temperature of TPP. There are exceptions - long alkanes and polymers form inclusion compounds with melting temperatures well above the meting temperature of pure TPP.[84,85,88]

Solid-state NMR of TPP inclusion compounds shows a very strong shielding effect throughout the entire TPP channel. The chemical shifts of the guest inside the channel change by 0.5 - 5 ppm upfield with respect to the NMR shifts of the neat guest.[86–89,94,95] This strong effect on the chemical shift is a useful indication that an inclusion compound is present. The chemical shifts of the TPP carbons are usually not very strongly affected by

the guest. The largest changes are observed for the catechol α-carbons of TPP as they are usually closest to the guest.

Relaxation times of the guest and the host atoms provide useful insight into the dynamics of the motion inside the channels. The T_1 relaxation times of ^{13}C atoms in rigid solids are usually on the order of hundreds of seconds.[86] The T_1 relaxation times in the TPP - benzene inclusion are on the order of 300 s for the TPP carbons while benzene carbons exhibit a T_1 relaxation time of 24 s.[82] The T_1 relaxation times of carbons in empty hexagonal TPP are around 200 s for the tertiary carbons and on the order of 1000 s for the quaternary carbon.[82] The results indicate a rapid motion of benzene inside the channels. Benzene hinders the motion of the TPP lattice which relaxes mainly through the motion of the guest. Empty hexagonal TPP molecules experience large librations of the *o*-phenylenedioxy paddles, and this motion provides an efficient relaxation mechanism.

The motion rates of various guests have been measured using T_1 relaxation times as a function of temperature,[86] by analysis of line shapes in deuterium solid-state NMR,[96,97] and by analyses of cross-polarization build-up rates.[94] The results show rapid hopping motion in the 10^8 to 10^{11} Hz range at room temperature for a wide variety of aromatic compounds. Surprisingly, alkanes experience smaller freedom of motion inside the channel (10^7 to 10^8 Hz at room temperature).[86] This result is rationalized by CH-π interactions.

The mobilities of alkanes in the nanochannels can also be probed by the dependence of their chemical shift on conformation.[88,95] Long *n*-alkanes confined in small nanochanels are constrained to anti conformations. However, a small number of them explore gauche conformations as shown by the drift of the ^{13}C chemical shift with temperature and with channel width. The chemical shift of *n*-alkanes is greatly dependent on the conformation and the γ-gauche interaction accounts for a 5 ppm upfield change.[98] The small number of gauche conformations average into the chemical shift of the inner methylenes, causing the temperature and channel diameter dependence of the chemical shift. The probability of the gauche defects decreases with increasing chain length.

Other cyclotriphosphazines and their inclusion behavior. Various other cyclotriphosphazine derivatives have been prepared and their inclusion behavior was studied (Figure 2.7). The cyclotriphosphazines **29**, **30** and **31** are known to form inclusion compounds with channel structures. The derivative **32** does not form inclusion compounds,[80] and **33** forms inclusion compounds without channel structure with some guests capable of hydrogen bonding.[80]

The structure of inclusion compounds of **29** resembles that of TPP. The inclusion compounds of **29** form a hexagonal lattice with an a-axis parameter of 15.75 Å, which is significantly larger than for TPP, and a lattice c-axis parameter similar to TPP, 10.19 Å.[80] The molecule of **29** is paddle-wheel shaped (with approximately D_{3h} symmetry) with planar cyclotriphosphazine ring and three 2,3-naphtalenedioxy groups perpendicular to the plane of the cyclotriphosphazine ring.[99,100] The TNP tunnels are about 9 to 10 Å wide.[101] The TNP inclusion compounds of volatile guests are significantly less stable than corresponding TPP inclusion compounds. Unlike TPP inclusion compounds, the loss of guest from those of **29** occurs quickly at atmospheric pressure and room temperature. Empty hexagonal lattice of **29** is not known and the guest-free form is monoclinic.[102]

The compound **29** exhibits very high affinity for p-substituted benzenes, and absorbs the p-isomers in presence of o- and m-isomers with high selectivity for many different disubstituted benzenes.[103] The inclusion compounds of **29** with p-substituted benzenes usually do not form the channel structure, but cage-like orthorhombic structures.[100,103,104]

Inclusion compounds of the cyclotriphosphazine **30** form a channel structure that is different from TPP, with a triclinic unit cell[105] and approximately rectangular tunnels 5.2 and 7.0 Å wide.[101] The inclusion compounds of **30** are more stable than the corresponding inclusion compounds of TPP and the guests experience much less motion of freedom as determined by variable temperature broad-line ^{1}H solid-state NMR.

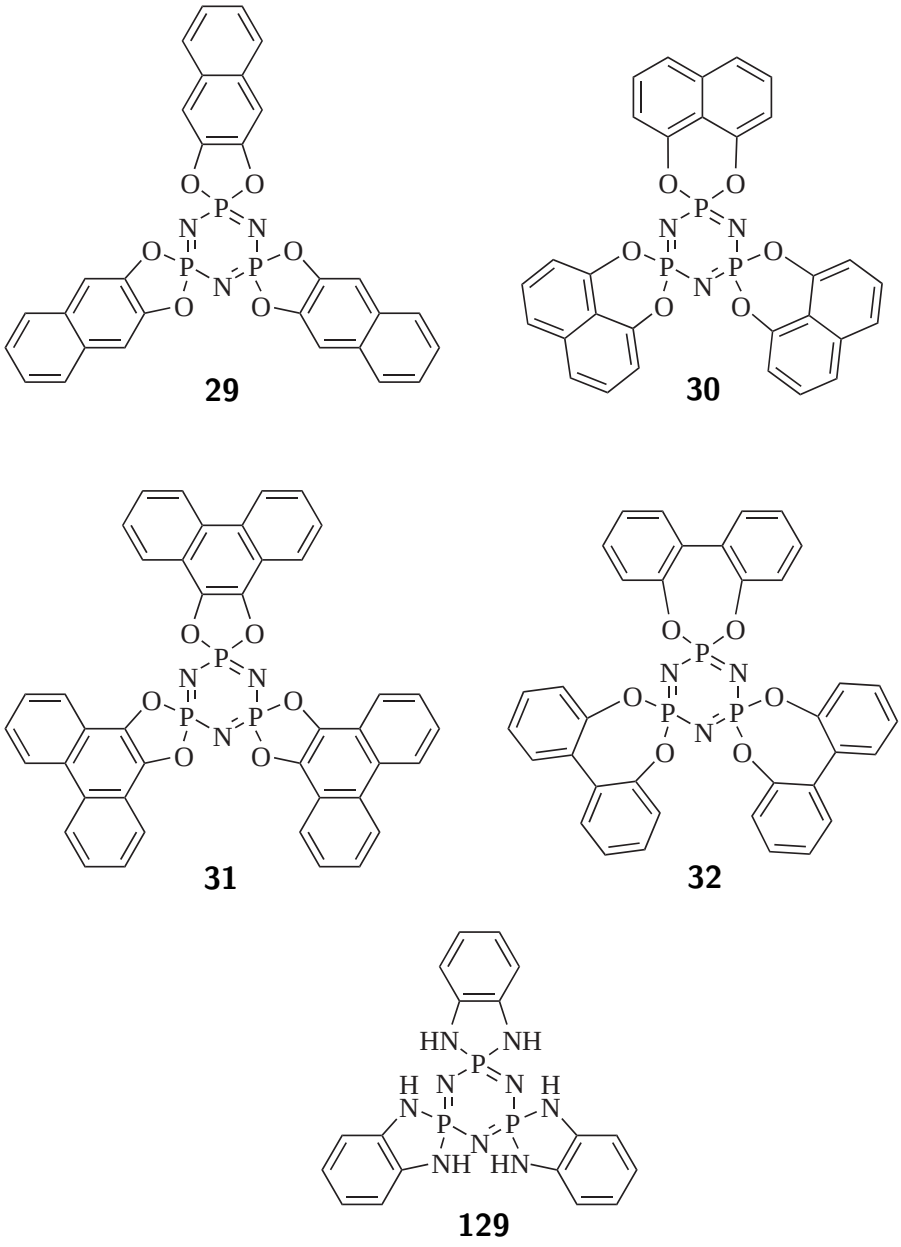

Figure 2.7: Examples of other cyclotriphosphazines.

2.1.3 Dielectrics[1]

Dielectrics are materials which do not conduct electricity. However, if a dielectric material is inserted between the electrodes of a capacitor and it fills up all the available space, the capacitance increases by a factor of ϵ_r, the relative dielectric constant. The relative dielectric constant depends only on the nature of the material and the temperature,

and it is unity for vacuum. The capacitance is given by:

$$C = \frac{\epsilon_r \epsilon_0 A}{d} = \frac{Q}{U}, \tag{2.1}$$

where ϵ_0 is the dielectric constant of vacuum, A is the area of the capacitor plate, d is the distance between the plates, Q is the charge on the capacitor, and U is the voltage on the capacitor. Since the voltage remains the same, the dielectric reduces the charge on the capacitor for eq. (2.1) to hold. This is because charges are induced in the dielectric, and dipoles, if present, orient in the dielectric to oppose the electric field of the capacitor.

The electric field E inside the dielectric will be the difference between the surface charge density σ_0 on the capacitor and the induced surface charge density on the dielectric, also called the polarization P of the dielectric. Assuming small electric fields, the polarization P is linear and depends on the electric field E:

$$E = \frac{\sigma_0 - P}{\epsilon_0}, \quad P = \chi \epsilon_0 E, \tag{2.2}$$

where χ is the electric susceptibility of the dielectric. Combining the equations eq. (2.1) and eq. (2.2) yields:

$$\epsilon_r = 1 + \chi. \tag{2.3}$$

In oscillating electric field E, in the simplest case, the rate of change of polarization is proportional to the induced polarization P:

$$\frac{dP}{dt} = \frac{1}{\tau}(P_E - P), \tag{2.4}$$

where P_E is the equilibrium value of polarization at electric field $E(t)$, and τ is the proportionality constant that relates to how quickly the material can respond to electric field. In harmonic electric field $E(t)$, the solution of eq. (2.4) is:

$$P(t) = \frac{1}{1 + i\omega\tau} P_E + P_0 e^{-t/\tau}, \tag{2.5}$$

where P_0 is the initial polarization. The second term describes the decay toward the steady state. Equation (2.5) can also be written in terms of permittivity ϵ_{ac} (using eq. (2.2)):

$$\epsilon_{ac} = \epsilon_0 + \frac{\epsilon - \epsilon_0}{1 + i\omega\tau}, \tag{2.6}$$

where ϵ is the static (zero frequency) permittivity of the material. The permittivity ϵ_{ac} is complex and it can be separated into the real $\epsilon^{'}$ and the imaginary $\epsilon^{''}$ component, $\epsilon_{ac} = \epsilon^{'} + i\epsilon^{''}$, where:

$$\epsilon^{'} = \epsilon_0 + \frac{\epsilon_s - \epsilon_0}{1 + \omega^2\tau^2}, \tag{2.7}$$

and:

$$\epsilon^{''} = \frac{(\epsilon_s - \epsilon_0)\omega\tau}{1 + \omega^2\tau^2}. \tag{2.8}$$

The equations eq. (2.6), eq. (2.7), and eq. (2.8) are generally known as Debye equations.[106] The real and the imaginary components to the Debye response are shown in Figure 2.8[a] ($\kappa = \epsilon_{ac}/\epsilon_0$). The interpretation of the response is that if the relaxation time is much greater than the period of electric field oscillation, the dielectric contributes to the capacitance minimally, and the same applies when the electric field oscillations are too slow. If the field moves in resonance with the dielectric, the contribution of the dielectric to the capacitance is maximal, and the dielectric absorbs maximal energy.

The energy absorbed by the dielectric has to do with inner friction in the sample and it is converted into heat. The ratio of the energy dissipated to the heat stored is defined by the dissipation factor, or loss tangent:

$$\tan\delta = -\frac{\epsilon^{''}}{\epsilon^{'}} \tag{2.9}$$

[a] Figure adapted from PhD thesis by Erick Winston (2008, University of Colorado at Boulder)

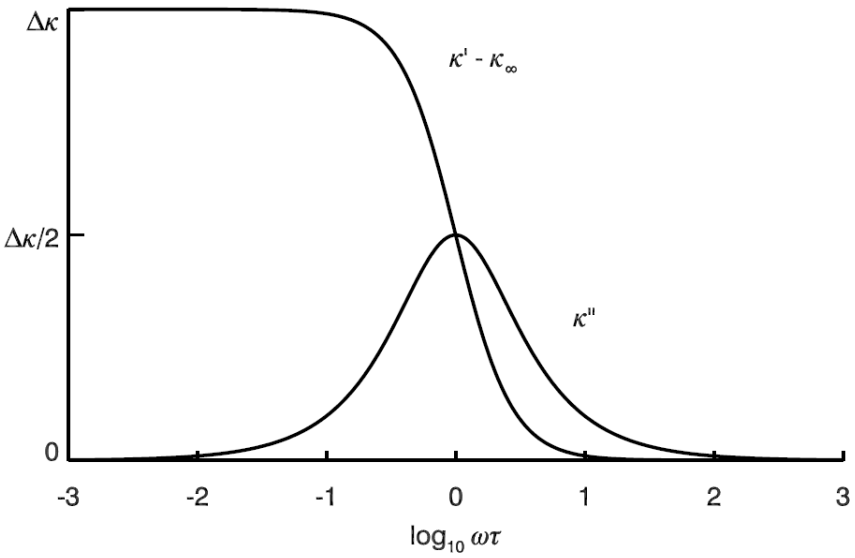

Figure 2.8: Debye response ($\kappa = \epsilon_{ac}/\epsilon_0$).

The macroscopic behavior of dielectrics has its microscopic origins. The polarization can be explained in terms of several microscopic phenomena: electronic, atomic/molecular, orientational, interfacial and ferroelectric polarization.

Electronic polarization. Electric field causes electronic polarization of the material which is proportional to the field for small electric fields. The behavior of the center of charge of the electrons in electric field oscillating at frequency ω can classically be described as a harmonic oscillator by:

$$m\frac{d^2x}{dt^2} + m\omega_0^2 x = q_e E, \tag{2.10}$$

with the solution:

$$x = \frac{q_e E}{m(\omega_0^2 - \omega^2)}. \tag{2.11}$$

In static field, the polarization p (the induced dipole) is defined as:

$$p = q_e x = \frac{q_e E}{m\omega_0^2} = \alpha\epsilon_0 E, \tag{2.12}$$

where α is called the polarizability. The polarizability tends to be inversely related to the electronegativity, and therefore related to the atomic radius r: $\alpha \cong 4\pi r^3$.

The electronic polarization response is a resonant phenomenon, and the response generally shows in ultraviolet to visible frequencies.

Atomic/molecular polarization. External electric field applied to molecules causes changes in the positions of nuclei. As this response is due to movement of nuclei which are heavier than electrons, the response due to molecular polarization is slower. It is also a resonant phenomenon and the resonance generally occurs at frequencies of the external electric field that correspond to the infrared part of the spectrum.

Nuclear polarization can be described by similar equations as the electronic polarization.

Orientation polarization. A collection of freely movable, weakly interacting dipolar molecules (such as dipolar molecules in the gas phase) contains random orientations of the dipoles in the absence of electric field, and the overall dipole moment is zero. If an electric field is applied, the molecules will partially align, producing non-zero net dipole moment.

At frequencies at which the effect of electronic polarization can be neglected, the potential energy U of the dipole moment p in an electric field E is given by:

$$U = -pEcos\theta, \tag{2.13}$$

where θ is the angle between the electric field E and the dipole. As the fraction of molecules with energy U is proportional to $e^{-U/kT}$ in a system under thermal equilibrium, the fraction of molecules $N(\theta)$ at angle θ is given by:

$$N(\theta) = N_0 e^{+pEcos\theta/kT} \cong N_0 \left(1 + \frac{pEcos\theta}{kT}\right), \tag{2.14}$$

where N_0 is the total number of molecules, and the right-hand expression is approximately true for small values of the exponent.

The net dipole moment is the sum over all the dipole moments, and it can be evaluated by integration:

$$P = \sum pcos\theta = \int_0^{\pi} N(\theta)pcos\theta 2\pi sin\theta d\theta = \frac{Np^2E}{3kT} \tag{2.15}$$

The polarization is proportional to the electric field E, and inversely proportional to the temperature as higher temperature produces more disorder. The inverse dependence on temperature is called Curie's law. Combining equations 2.2, eq. (2.3), and eq. (2.15) yields following expression for the relative dielectric constant:

$$\epsilon_r = \frac{P}{\epsilon_r E_0} + 1 = \frac{Np^2}{3\epsilon kT} + 1. \tag{2.16}$$

The first term in the expansion for the dielectric constant also shows inverse dependence on temperature.

In oscillating electric field, the dielectric constant also depends on the frequency of the field. It takes some time for the molecules to adjust to the field due to their moment of inertia, and if the frequency is too high, the dielectric polarization is small because the molecules cannot follow.

In the presence of a barrier to orientation of the molecule, eq. (2.14) becomes:

$$P = \int N(\theta)pcos\theta e^{-U_i/kT} sin\theta d\theta, \tag{2.17}$$

where $U_i = U_s + U_E$ is the orientational potential of i^{th} dipole, the term U_s describes the steric interactions and U_E described the interaction with the external electric field. Several approximations were taken: the dependence of the barrier on the electric field, and the induced electronic polarization were neglected.

This equation is more general, and it can be also used for the description of interacting

dipoles by including the interaction energy U_{p-p} in U_i. This will be discussed in more detail in the section dealing with ferroelectric polarization.

If the potential is dominated by a steric barrier, the dielectric polarization can be described as being driven by thermal hopping: the rotor oscillates in its potential minimum and occasionally it receives enough thermal energy to move to one of the neighboring minima.[107] The analytical solution to this problem is very challenging and the information about the time scales is usually obtained from molecular dynamics, but this can only be done for reasonably short time scales. Reasonable results can also be obtained from the Eyring transition state theory, and using equilibrium populations dictated by the Boltzmann distribution.[108]

Interfacial polarization. The materials containing mobile ions exhibit this type of polarization. The electric field causes the ions to move through the dielectric until they reach the boundary. This polarization can be very strong, usually stronger than other types of dielectric polarizations, and the time scale of this process can be very long, such as minutes or even hours.

The interfacial polarization is usually described using a model capacitor with two dielectric layers each with their own permittivity ϵ and conductivity σ (Figure 2.9a). Such model can be described as a circuit with a pair of a capacitor and a resistor connected in series (Figure 2.9b). The impedance of a such circuit is given by:

$$Z = \frac{R_1}{1 + i\omega R_1 C_1} + \frac{R_2}{1 + i\omega R_2 C_2}. \tag{2.18}$$

The solution of eq. (2.18) yields eq. (2.7) for the real component of permittivity, and eq. (2.8) $+1/\omega C_0(R_1 + R_2)$ for the imaginary component, where C_0 is the capacitance of the duplex layer capacitor (Figure 2.9a).[b] This additional term is often referred to as the conductivity term.

Ferroelectric Polarization. The dielectric polarizations discussed so far only included non-interacting systems of N components i described by a simple N-body partition

[b] Figure adapted from PhD thesis by Erick Winston (2008, University of Colorado at Boulder)

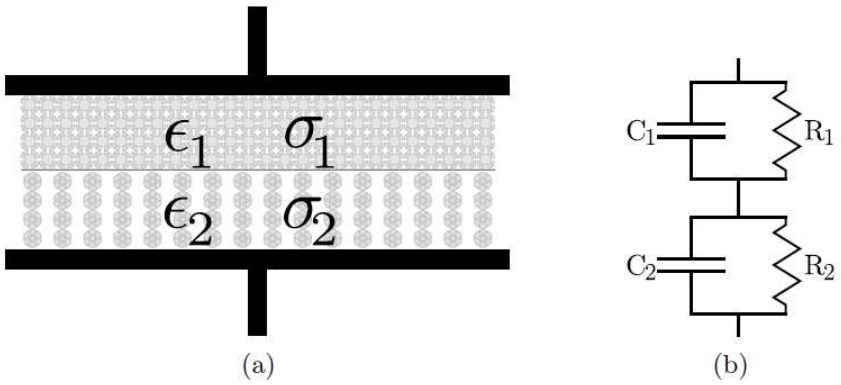

Figure 2.9: Interfacial polarization. (a) Two-layer dielectric capacitor model. (b) Circuit equivalent to (a).

function $Z_n = Z_i^N$. Systems of interacting dipoles can be described by eq. (2.17) when the dipolar interactions U_{p-p} is added to the potential energy term U_i. The dipolar interactions are strong in certain types of materials, such as ferroelectric (materials with permanent electric polarization), antiferroelectric (materials with several permanent polarizations that cancel each other), pyroelectric (materials that exhibit electric dipole change with thermal expansion), and piezoelectric materials (they show electric dipole change when compressed or stretched). In such materials, $Z_n \neq Z_i^N$, and finding the solutions becomes a more complex many-body problem.

An approximate solution to this problem for a one-component regular system was developed by Landau.[109] This method assumes that the polarization P near the second order phase transition is small, and the thermodynamic potential can therefore be expanded in terms of polarization:

$$G = G_0 + \frac{1}{2}\alpha P^2 + \frac{1}{4}\beta P^4 + \ldots, \tag{2.19}$$

where only even powers are non-zero for a crystal with a center of symmetry. As the polarization also depends on temperature, there is a certain temperature T_c (Curie temperature),

where the spontaneous polarization turns on, the coefficients ($\alpha,\ \beta\dots$) can be expanded in temperature:

$$\alpha = \alpha_0 + \alpha_1(T - T_c)\dots, \tag{2.20}$$

and:

$$\beta = \beta_0 + \beta_1(T - T_c)\dots \tag{2.21}$$

At minima:

$$\frac{\partial G}{\partial P} \cong \alpha P + \beta P^3 = 0 \tag{2.22}$$

and:

$$\frac{\partial^2 G}{\partial P^2} \cong \alpha + 3\beta P^2 > 0. \tag{2.23}$$

The solution of eq. (2.22) is $P = 0$, or $P = \sqrt{-\alpha/\beta}$. Equation 2.23 requires $\alpha > 0$ for $P = 0$, and $\alpha < 0,\ \beta > 0$ for $P = \sqrt{-\alpha/\beta}$. Thus, right when the polarization becomes non-zero, $\alpha = 0$, which implies, using eq. (2.20), that $\alpha_0 = 0$, and eq. (2.19) becomes (using only the first significant term from equations 2.22 and 2.23):

$$G = G_0 + \frac{1}{2}\alpha_1(T - T_c)P^2 + \frac{1}{4}\beta_0 P^4 + \dots \tag{2.24}$$

This shows that above the Curie temperature T_c, the system will have zero polarization, but below this temperature, there will be net polarization given by:

$$P = \sqrt{-\frac{\alpha_1(T - T_c)}{\beta_0}} \tag{2.25}$$

This behavior is depicted in Figure 2.10,[c] and it is apparent from the picture that the system

[c] Figure adapted from PhD thesis by Erick Winston (2008, University of Colorado at Boulder)

is equally likely to develop polarization of $-P$ as $+P$. At the temperatures below the Curie temperature T_c, but close to it, the energy cost to switch the polarization is low.

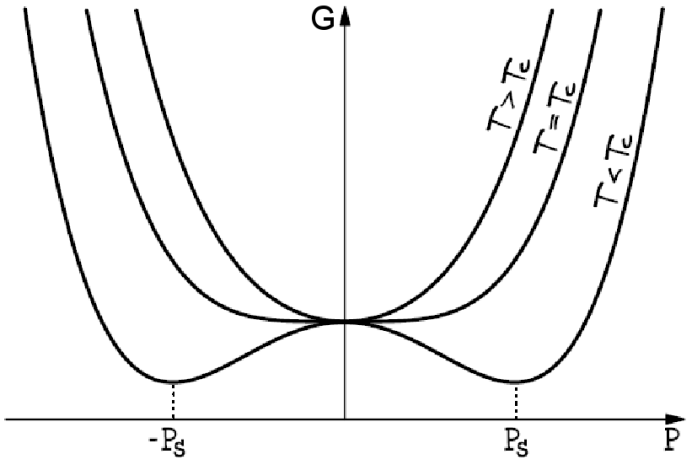

Figure 2.10: Gibbs free energy G near ferroelectric transition.

In presence of an external electric field E, eq. (2.24) becomes:

$$G = G_0 + \frac{1}{2}\alpha_1(T - T_c)P^2 + \frac{1}{4}\beta_0 P^4 - EP, \tag{2.26}$$

and at small fields:

$$\frac{\partial G}{\partial P} = \alpha_1 P + \beta_0 P^3 - E \cong 0, \tag{2.27}$$

which reduces if $P << E$, using eq. (2.2), the dielectric susceptibility is given by:

$$\chi \cong \frac{1}{\epsilon_0 \alpha_1 (T - T_c)} \tag{2.28}$$

near the phase transition. This dependence is known as the Curie-Weiss law.

Spontaneous polarization is usually characterized by measuring the permittivity in weak oscillating electric field. Near the phase transition, Curie-Weiss behavior is usually observed. At the second order transition, the Curie-Weiss constant ($C = 1/\epsilon_0\alpha_1$) in the

ferroelectric phase should be about twice its value in the paraelectric phase. Near the transition, also dielectric loss shows its maximum.

The polarization relaxation in strongly interacting regular systems can be fitted with an exponential with a single time constant.

Dielectrics spectroscopy of dipolar rotor samples. Dielectric spectroscopy measures dielectric properties as a function of the frequency of the applied oscillating electric field and/or the temperature. In a perfect capacitor the current through the capacitor I_C is 90° out of phase with the applied voltage, and energy can be stored indefinitely. The current through a perfect resistor I_R is in the phase with the voltage, and no energy can be stored.

The current through a real dielectric I_D (Figure 2.11)[d] is complex with a real and imaginary part, due to conversion of part of the energy into heat. The phase difference δ between the current through the capacitor loaded with the dielectric I_D and the imaginary component I_C is a measure of the fraction of energy converted into heat, and its tangent (the dielectric loss $\tan\delta$) is related to dielectric constant by eq. (2.9).

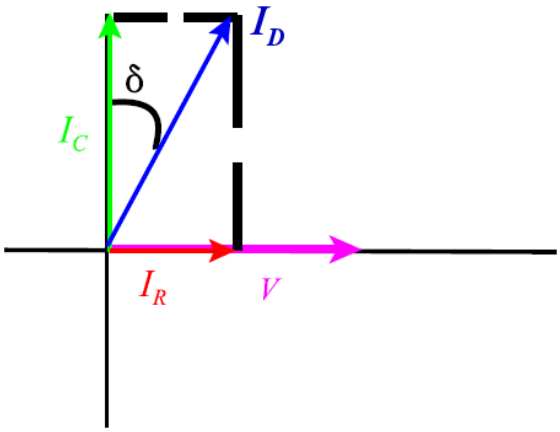

Figure 2.11: Phase diagram of the voltage and the current through a capacitor filled with dielectric.

In a dielectric that is an ensemble of dipolar molecular rotors, the dissipation loss is mainly caused by the orientation of rotors with the electric field. There are two limiting

[d] Figure adapted from PhD thesis by Mary Beth Mulcahy (2006, University of Colorado at Boulder)

cases of such systems in a weak electric field, both described by eq. (2.17).

If the system is composed of strongly interacting dipolar molecular rotors, the dielectric behavior in a weak electric field is dominated by the dipolar interaction, and for the systems of our interest by ferroelectric polarization, which was discussed in detail earlier in this section. The temperature dependence of the dielectric behavior ϵ near the Curie temperature T_c is described by eq. (2.28).

In a system of weakly interacting dipolar rotors in a weak electric field ($\mu E < kT << E_{rb}$, where μE is the coupling with the electric field and E_{rb} is the barrier to rotation),[108] the dielectric behavior mainly depends on the barrier to rotation. The resulting polarization is paraelectric, and it can be described by eq. (2.17) if the rotational potential is known.[68]

2.2 General Considerations for Rotators

A series of calculations for different rotators have been conducted as a means to select good candidates.

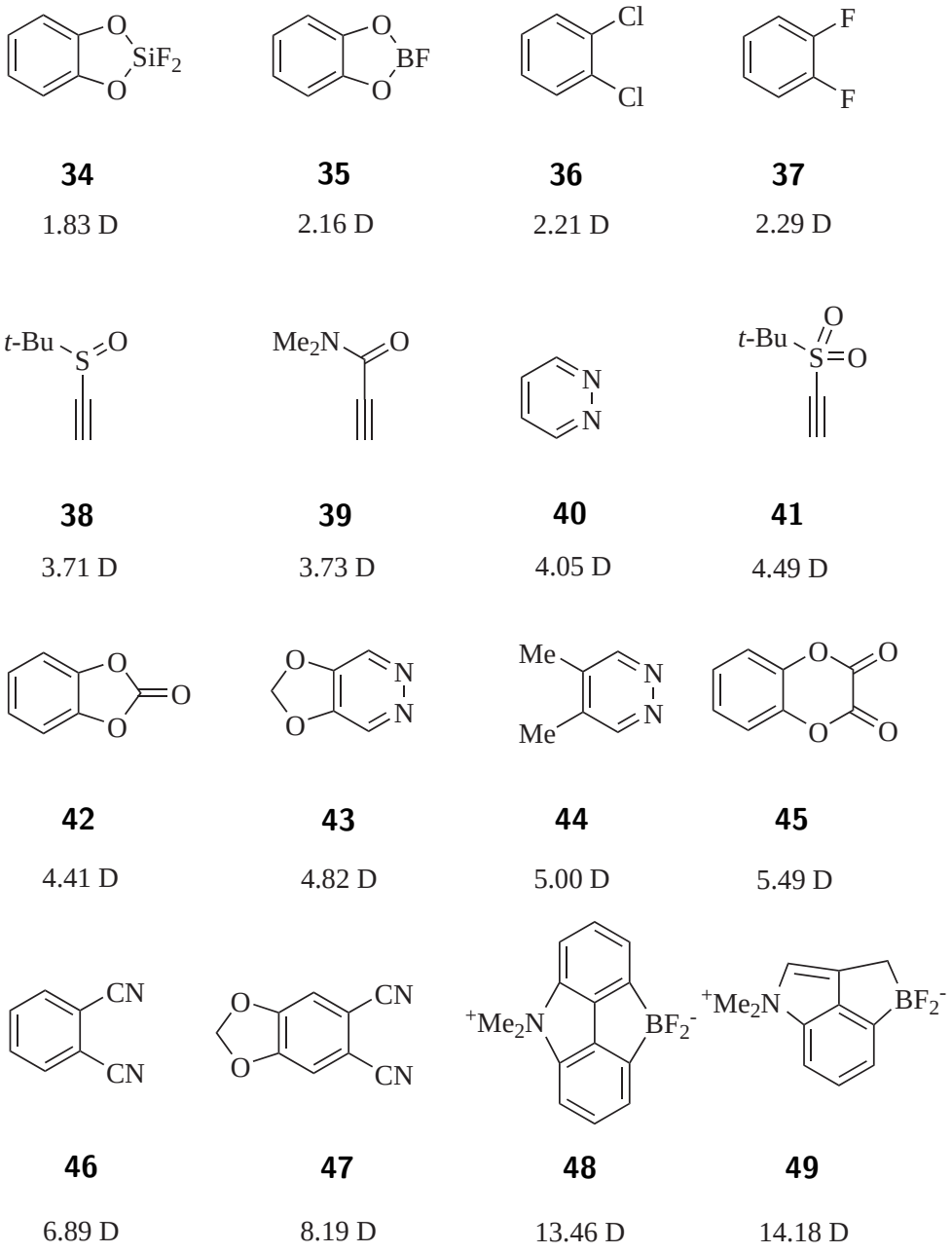

Figure 2.12: Computed dipole moments (B3LYP/SVP) for various possible rotators.

In order to form ferroelectric two-dimensional arrays of dipolar rotors, the dipolar interactions between the rotators need to be strong, and the barrier to rotation of the rotator must be sufficiently low. To the first approximation, a good measure of the strength of dipolar interactions is the rotator's dipole moment.

Geometry optimizations for each structure were performed at B3LYP level of theory with SVP basis set, and the dipole moments are given for each optimized structure in increasing order (Figure 2.12). The structures are drawn such that the negative part of the dipole points to the right and the positive part of the dipole points to the left.

The attachment point of the rotator to the axle needs to be made such that the dipole moment of the rotator is orthogonal to the axis of rotation in order to maximize the dipolar interaction of the rotators in the rotor array.

The dipole moment of the rotators without a plane of symmetry (**38**, **39**, **41**, **49** in Figure 2.12) is oriented at least 90 % orthogonal to the expected axis of rotation.

Another important consideration for the choice of a suitable rotator also are the stabilizing interactions in the crystal of the neat rotor. These are difficult to predict, but generally, large aromatic systems without bulky groups or systems with large dipoles without steric bulk around them tend to form stable crystals of the neat material that can be favored over the inclusion compound. Adding sterically demanding groups and decreasing the symmetry can help to circumvent this problem.

This work primarily focuses on rotors with smaller dipole moments as they form inclusion compounds more readily. As the phenomenon of surface inclusion compounds is a step into an unexplored territory, the preparation and the characterization of surface inclusion compounds need to be established first on simpler systems. Once this is accomplished, systems with larger dipole moments, that will likely introduce additional complexities, can be attempted.

2.3 First Generation Rotor

The first rotor **50** (Scheme 2.2) uses an *n*-hexadecyl chain as the tail, *p*-carborane (*closo*-1,12-dicarbadodecaborane) as the stopper, and a 2,3-difluorophenyl rotator connected to the *p*-carborane stopper via a *p*-ethynylphenyl axle.

The long axle should keep the rotator well above the surface, and introduce a low rotational barrier. The choice of *n*-hexadecyl chain was made based on the fact that long *n*-alkanes are known to form very stable inclusion compounds readily.[88] The *p*-carborane stopper was chosen for its large van der Waals radius, 6.9 Å (B3LYP/SVP optimized structure), which is much larger than the diameter of the TPP channel in the narrowest point - 4.5 to 5.0 Å in a wide variety of inclusion compounds.

The feasibility of the above design was first tested on a simplified version of **50**, the compound **51**.

2.3.1 Results

Synthesis. The rotor **50** was synthesized by the following sequence of reactions (Scheme 2.2): 1,2-difluorobenzene was ortho-lithiated with *n*-BuLi according to a known literature procedure,[110] and the *o*-lithio compound was treated with iodine to yield **52** (56 % yield). Sonogashira coupling of **52** with trimethylsilylacetylene yielded **53** (99 % yield). The deprotection of **53** with TBAF yielded a very volatile compound **54** that was not isolated, but instead, it was used *in situ*.

Attempts to monosubstitute *p*-carborane carbon usually yield small amounts of disubstituted compound which is often difficult to separate. Thus, *p*-carborane was first protected with the triphenylsilyl group,[111] then deprotonated with *n*-BuLi and the lithium salt was alkylated with *n*-hexadecyl bromide to prepare **56** in 90 % yield. The deprotection of **56** with TBAF gave **57** in 92 % yield.

Compound **58** was prepared by deprotonation of **57** with *n*-BuLi, transmetallation with

cuprous chloride, and palladium catalyzed coupling of the product with *p*-bromoiodobenzene in 72 % yield. Sonogashira coupling of **54**, prepared *in situ* (from **53** by deprotection with TBAF), and **58** yielded the rotor **50** (85 % yield).

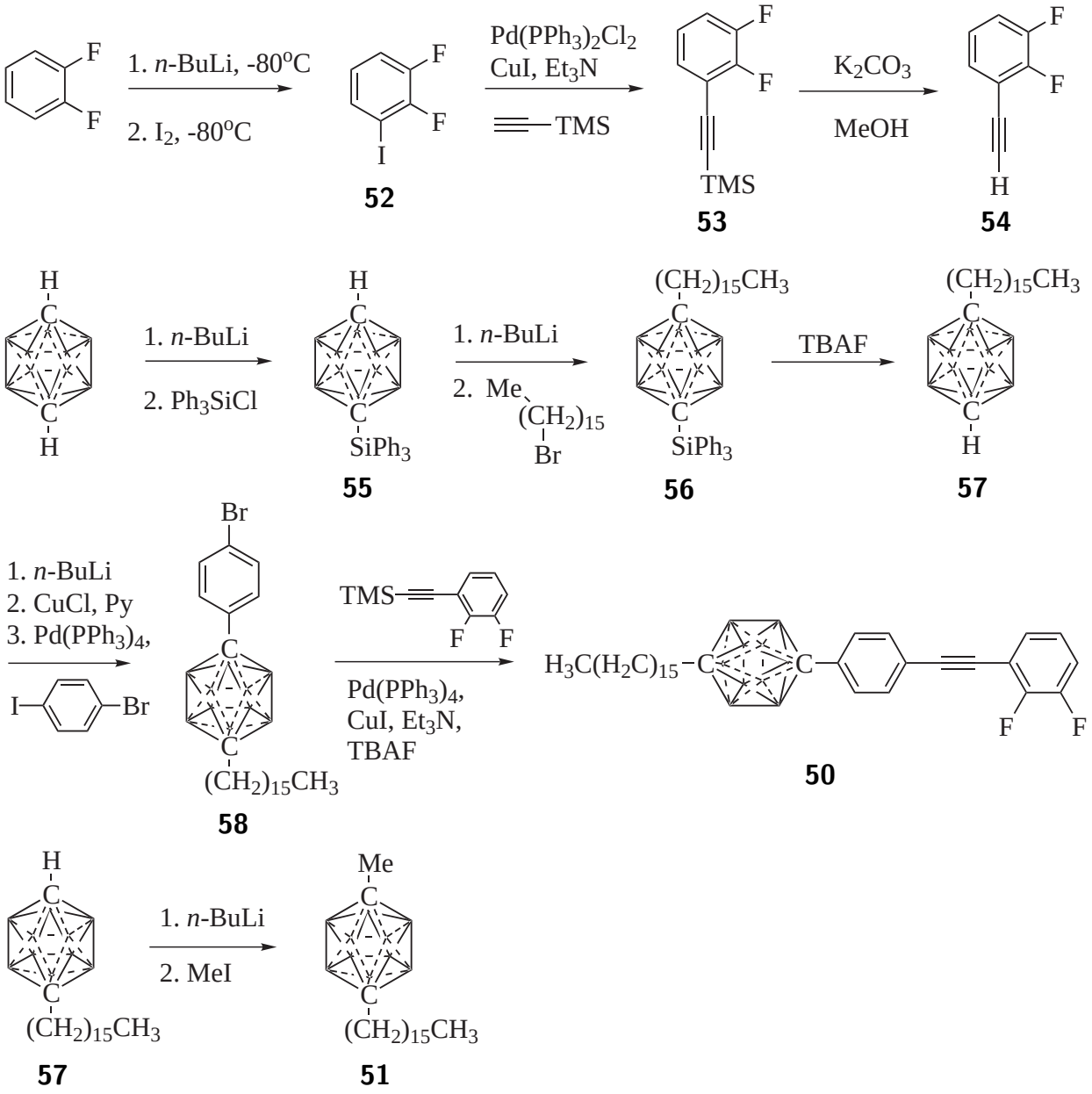

Scheme 2.2: Synthesis of compounds **50** and **51**.

The test compound **51** was prepared by deprotonation of **57** with *n*-BuLi, and methylation of the resulting lithium salt with methyl iodide (97 % yield).

NMR. A solution ^{13}C NMR and DEPT-135 with assignments are shown in Figure 2.13. The peaks were assigned based on their chemical shifts and the phase in the DEPT-135 spectrum: carbons C_a and C_b show chemical shifts characteristic for a terminal ethyl of a long *n*-alkyl chain, carbons C_c and C_d exhibit chemical shifts usual for primary and secondary carbons connected to *p*-carborane. The assignment of carbon C_c was confirmed by its phase in the DEPT-135 spectrum. The *p*-carborane carbons C_e and C_f were identified by their chemical shift and the characteristic broadening due to coupling with ^{11}B nuclei. The carbon C_f shows more downfield resonance than the carbon C_e as it is connected to the secondary carbon C_d, while carbon C_e is substituted with a primary carbon C_c.

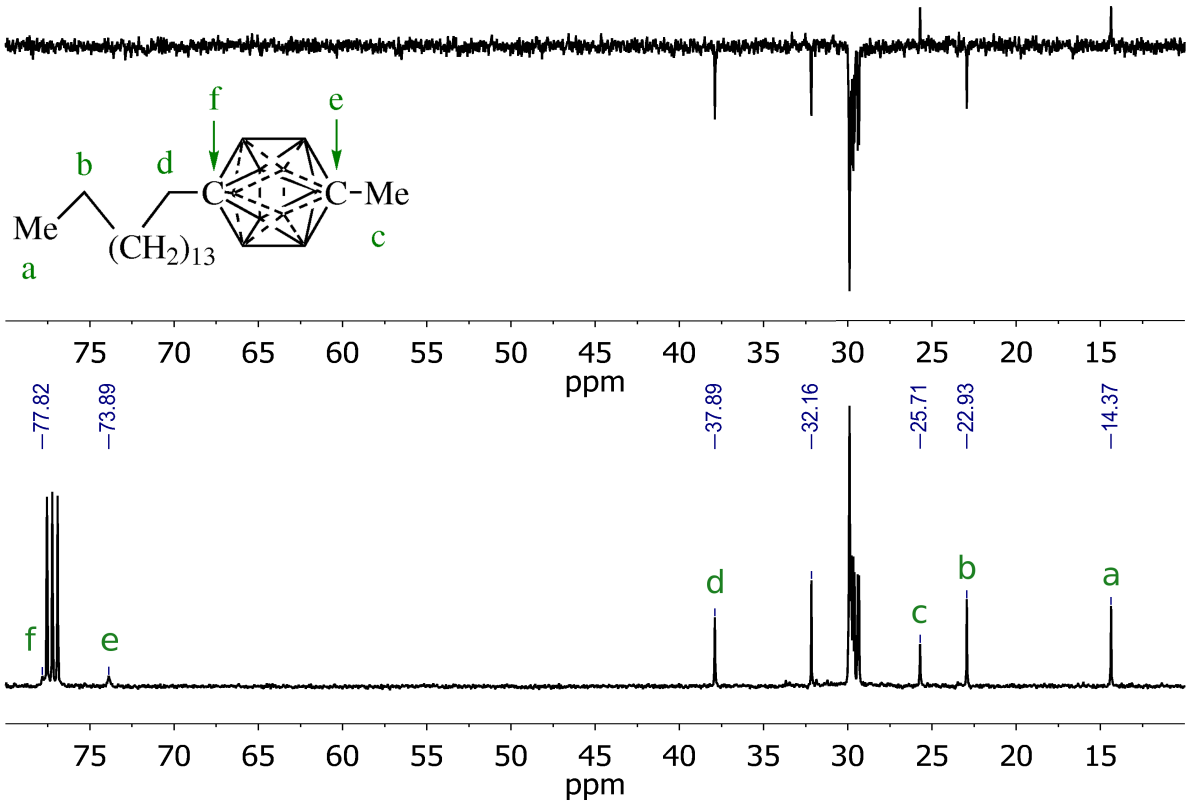

Figure 2.13: Solution ^{13}C NMR spectra of **51** in chloroform-*d*. Top: DEPT-135, bottom: ^{13}C NMR.

An inclusion compound of **51** (3 mol %) in TPP (**51**@TPP) was prepared by grinding

the neat powders and ^{13}C CP MAS solid-state NMR spectra of both neat **51** and the inclusion compound **51**@TPP were recorded using 5 ms contact time (Figure 2.14).

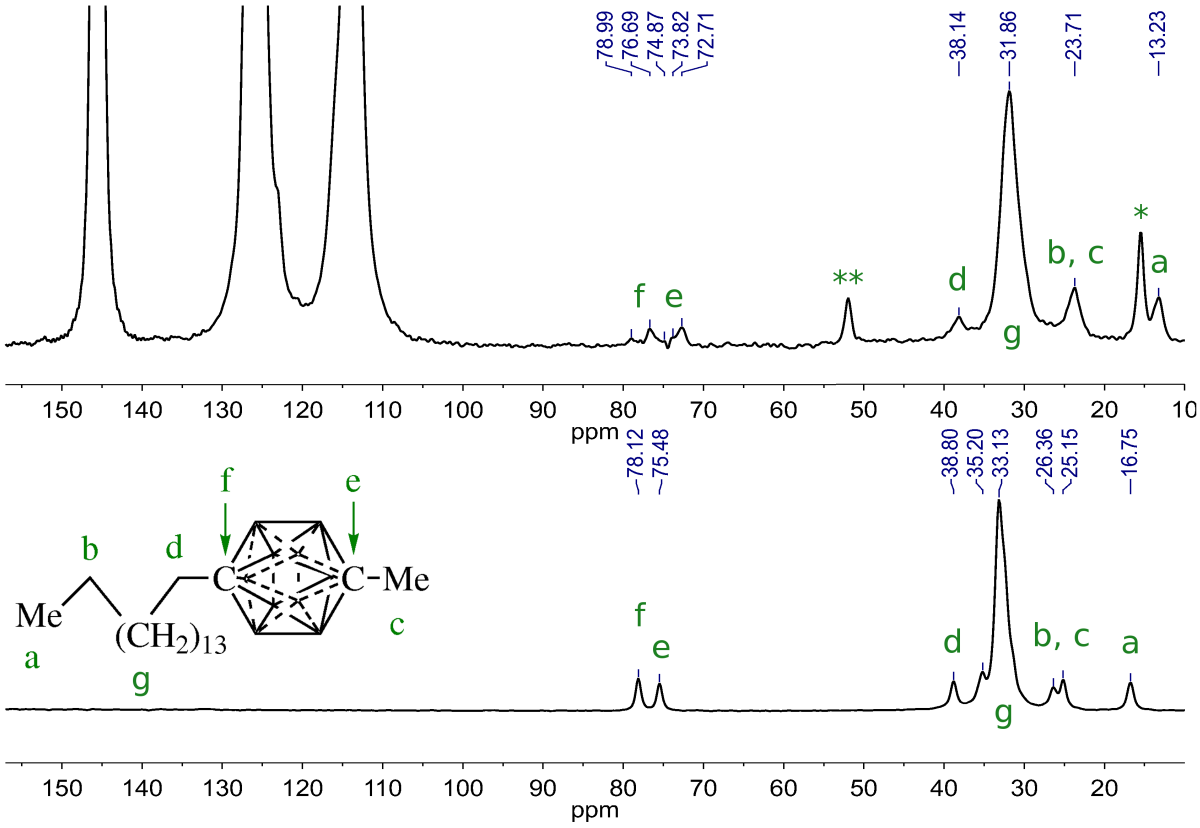

Figure 2.14: Solid-state ^{13}C CP MAS NMR spectra of **51**. Top: **51**@TPP, bottom: **51**.
* spinning sideband.
** contamination with dichloromethane.

The ^{13}C CP MAS solid-state NMR spectrum of the neat compound **51** spectrum (Figure 2.14 bottom) contains a single resonance for each carborane carbon C_e and C_f. The peaks are about 1-2 ppm upfield compared to the solution spectrum (Figure 2.13). All the aliphatic carbon signals in the solid-state spectrum of neat **51** are moved downfield by about 1-3 ppm compared to the solution spectrum. The carbons C_a, C_b, C_c and C_d are all resolved, but the carbons C_b and C_c are close and they cannot be assigned with confidence by simple comparison to the compound **51** solution spectrum. The remaining aliphatic carbons

show a single large peak C_g.

The spectrum of inclusion compound **51**@TPP (Figure 2.14 top) displays three singlet resonances characteristic for hexagonal TPP[82] in the aromatic region.

The carborane region contains at least two resolved sets of signals for each carborane carbon. One of the carbon C_f signals in the inclusion **51**@TPP NMR is moved downfield, the other is moved upfield with respect to the neat **51** solid-state NMR spectrum (Figure 2.14 bottom). The carborane carbon C_e has two resonances that are upfield with respect to the neat **51** spectrum. If there are any peaks downfield with respect to neat **51**, they overlap with C_f.

The signals of aliphatic carbons in the solid-state NMR spectrum of the inclusion compound **51**@TPPare broader than in the spectrum of the neat compound **51**. The carbon C_d displays a small upfield change in chemical shift with respect to the neat **51** (0.66 ppm), and it has an upfield shoulder. The C_g signal exhibits an upfield change in chemical shift (1.27 ppm) with respect to neat **51** and the signals of C_b and C_c show a single resonance shifted upfield with respect to neat **51**. The methyl carbon C_a is moved upfield by 3.52 ppm compared to neat **51**.

The solid-state ^{13}C NMR of the inclusion compound **51**@TPP does not change appreciably upon further grinding. The proton and carbon signals in compound **50** were assigned using boron-decoupled gHMBC (Figure 2.15), $\{^1H, ^{13}C\}$ gHMBC (Figure 2.16), boron-decoupled ^1H NMR, ^{13}C NMR and DEPT-135.

The *p*-carborane carbons C_m and C_n were identified using boron-decoupled $\{^1H, ^{13}C\}$ gHMBC (Figure 2.15). The carbon C_m and proton H_k were identified by their cross-peak in the $\{^1H, ^{13}C\}$ gHMBC spectrum (Figure 2.16a).

The proton H_j was identified by the coupling constant with H_k in the ^1H NMR spectrum. The cross-peaks between C_i (quaternary), C_k (protonated), C_h (4 bond coupling) and H_k in the gHMBC spectrum were used to assign atoms C_i, C_k and C_h, considering typical chemical shift for acetylenic carbon C_h. The cross-peaks between H_j with C_g (quaternary),

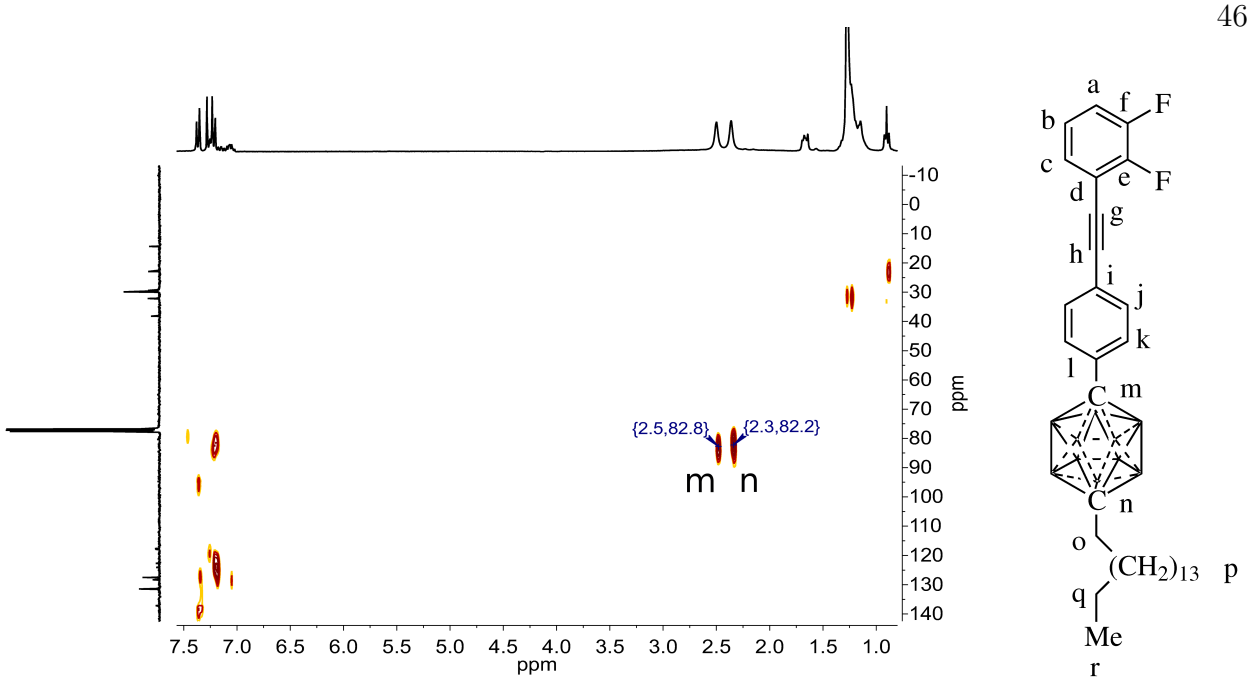

Figure 2.15: Boron-decoupled gHMBC spectrum of compound **50** (J = 8 Hz).

C_j (protonated), and C_l (quaternary) in the gHMBC spectrum identified the carbons C_g, C_j and C_l while taking into account the usual chemical shifts for C_g type carbon.

The protons H_a, H_b and H_c were assigned based on the multiplicity of the signal and the chemical shift in the ^{1}H NMR spectrum. The protonated carbons C_a, C_b and C_c were identified by their cross-peak with H_a in the gHMBC spectrum (Figure 2.16b). The quaternary carbons C_e and C_f were assigned by their chemical shift and the cross-peak with H_a, H_b and H_c in the gHMBC spectrum. The carbon C_d was identified based on the chemical shift and the cross-peak with H_d in the gHMBC spectrum.

The *p*-carborane carbon C_n and proton H_o were assigned based on their cross-peak in the gHMBC spectrum, and by their chemical shift. The protons H_q, H_r and the carbons C_q and C_r were assigned by their chemical shift.

The assignments are summarized in Table 2.1.

Some of the carbons of the neat compound **50** display two signals close together for one carbon in the solid-state ^{13}C CP MAS NMR spectrum (Figure 2.17 bottom, peaks a, b, c at

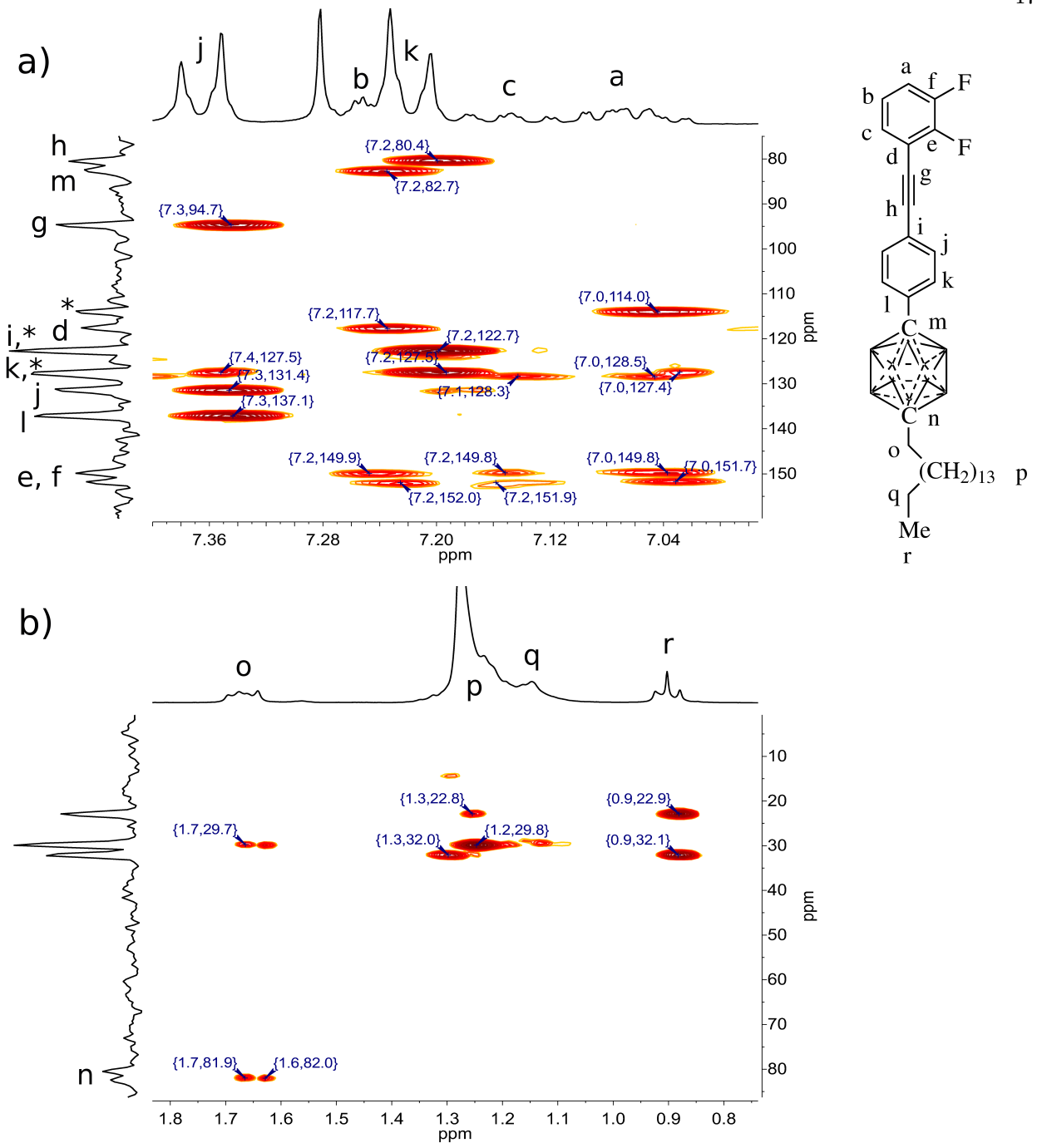

Figure 2.16: The gHMBC spectrai of compound **50** (J = 8 Hz): a) aromatic region; b) aliphatic region.

113.6 ppm, peaks d, h, m, o and q). This is commonly seen in samples where the molecule occurs in two inequivalent crystallographic orientations or in imperfectly crystalline solids.

The signals in the spectrum of neat **50** were tentatively assigned based on the comparison with the solution ^{13}C NMR spectrum, and some of the signals were reassigned based on peak intensity (peaks a, b, c at 126.3 ppm and 133.74 ppm, peaks j and k). The results are summarized in Table 2.1.

Table 2.1: Summary of NMR assignments for the compound **50**.

Atom	^{1}H solution NMR δ [ppm]	^{13}C solution NMR δ [ppm]	^{13}C CP MAS NMR δ [ppm]
a	7.04	114.0/127.4/128.3	113.6/126.3/133.7
b	7.22	114.0/127.4/128.3	113.6/126.3/133.7
c	7.13	114.0/127.4/128.3	113.6/126.3/133.7
d	-	117.7	120.0
e	-	149.8/151.9	150.4/152.6
f	-	149.8/151.9	150.4/152.6
g	-	94.7	94.5
h	-	80.4	79.7
i	-	122.7	122.9
j	7.34	131.5	132.0
k	7.20	127.5	127.6
l	-	137.1	137.6
m	-	82.8	83.5
n	-	82.1	81.1
o	1.65	46.7	39.8
p	1.03-1.36	31.4 - 40.7	28.8-36.5
q	1.03-1.36	22.9	25.3
r	0.88	14.3	15.3

The inclusion compound of **50** (5 mol %) in TPP (**50**@TPP) was prepared using the neat powders grinding method. The solid-state ^{13}C CP MAS NMR spectrum was recorded using 5 ms contact time (Figure 2.17 top).

The solid-state spectrum of the inclusion compound **50**@TPP contains three very intense singlet resonances at 145.5, 125.7 and 114.1 ppm that are characteristic of TPP in hexagonal form. These peaks overlap with most of the aromatic signals of the guest compound **50**. The resolved resonances are peaks belonging to carbons C_e, C_f, C_l and C_j.

The peaks of the carbons C_e and C_f display a downfield change in the chemical shift

of about 2 ppm with respect to the solid-state ^{13}C NMR spectrum of neat **50**. The signal of carbon C_l appears to split into a peak with a downfield change in the chemical shift by 1.45 ppm, and into a peak with a small upfield change in the chemical shift by 0.27 ppm compared to the solid-state ^{13}C NMR spectrum of the neat compound **50** . The carbon C_j partially overlaps with the middle TPP signal, but there is an apparent signal with downfield change in the chemical shift by 1.22 ppm with respect to neat **50**.

The acetylenic carbon C_g is moved downfield by 1.54 ppm in the inclusion compound relative to the solid-state ^{13}C NMR of neat **50**. There is an apparent shoulder with approximately the same chemical shift as the neat compound **50**.

The remaining acetylenic carbon and the *p*-carborane carbons overlap in the solid-state ^{13}C NMR spectrum of **50**@TPP. The carbon C_m forms two apparent peaks, both shifted downfield (0.97 and 1.79 ppm) compared to solid-state ^{13}C NMR spectrum of the neat rotor **50**. The signals for C_n and C_h are broadened and they overlap but they are overall shifted by about 1 ppm downfield relative to the solid-state ^{13}C NMR of neat **50**.

The signals belonging to C_o and C_p are broadened and they have both components moved downfield and upfield with respect to the solid-state ^{13}C NMR of the neat rotor **50**. The signals C_q and C_r both display upfield change in chemical shift with respect to the neat rotor **50** (C_q: 1.45 ppm, C_r: 1.42 ppm). The solid-state ^{13}C NMR of the inclusion compound **50**@TPP does not change appreciably upon further grinding.

Calculations. The calculations were performed using the universal force-field (UFF)[112] and the program Tink.[113] Since the force-field parameters for the unique phosphorus found in cyclotriphosphazines were not described previously, they had to be developed.

Several cyclotriphosphazines, TPP (**24**, Figure 2.3), **59**, and **60** (Figure 2.18) were optimized at the B3LYP level of theory with the cc-pVTZ basis set using Turbomole 6.0.[114] The resulting structures were fitted to UFF-optimized geometries using trial parameters that were based on phosphorus P_3+5 force field.[112] In order to fully describe the force field of cyclotriphosphazine phosphorus, including the dihedral angles with the phosphorus of the

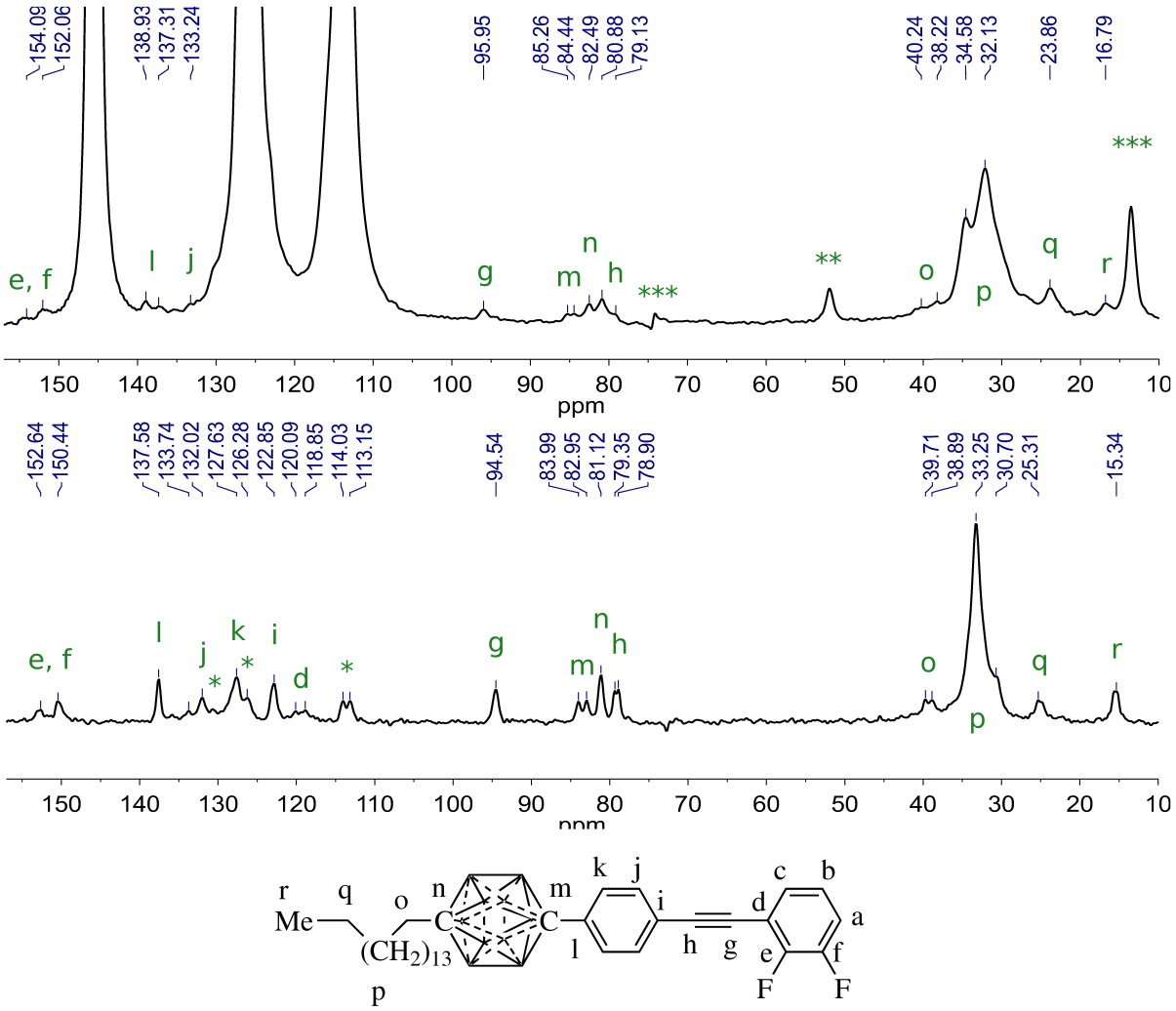

Figure 2.17: Solid-state ^{13}C CP MAS NMR spectra of **50** and its inclusion compound. Top: inclusion compound **50**@TPP, bottom: neat **50**.

* peaks a, b and c

** contamination with dichloromethane

*** spinning sideband or folded-in spinning sideband

spirocyclotriphosphazine structure, additional explicit terms to the force field are needed.[112] As this could be a very tedious task, the explicit terms were not included and the values of the dihedral angles generated with the force field without the explicit terms were corrected in the connectivity file. The correct values were obtained from a single cyclotriphosphazine molecule geometry optimization using B3LYP/cc-pVTZ. For more complicated structures

with hundreds of the dihedral angles this task was automated by a shell script. The optimum force field parameters[113] in standard format[112] are given in Table 2.2.

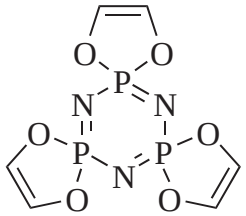

59

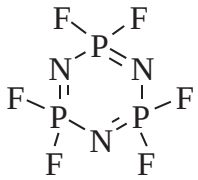

60

Figure 2.18: Model structures for force field development for phosphorus in cyclotriphosphazines.

Table 2.2: Optimum force field parameters for cyclotriphosphazine phosphorus.

Force field	r_I [Å]	θ_0 [°]	x_I [Å]	D_I [a]	ζ	Z_I [a]	T_3	E_D, $H_{at.}$ [a]	b_m	H, Co
P_R+5	1.009	110.0	4.147	0.305	13.072	2.945	0.00	100.0	4	3

[a] [kcal/mol]

The deviation of the phosphorus bond length between the UFF-optimized geometry and B3LYP/cc-pVTZ optimized geometry for phosphorus in TPP, **59** and **60** was less than ±0.075 Å, the deviation in valence angles was within ±2.5°, except for the F-P-F valence angle in **60**, where the deviation was −5.4°, and it was insensitive to variation of the phosphorus force field parameters.

The quality of the new UFF parameters was checked by comparison of the UFF optimized geometry of the TPP - *n*-alkane inclusion compound with known[84] TPP - polyethylene inclusion compound X-ray structure. The comparison is shown in Figure 2.19.

A geometry optimization using UFF with simulated annealing (500 K to 0 K in 500,000 one-femtosecond steps) was performed on a structure with seven channels filled with rotors. The TPP lattice was constrained at the lattice parameters of the polyethylene - TPP inclusion compound known from the X-ray structure.[84] Without the constraint, the hexagonal TPP structure collapses during the calculation at high temperatures.

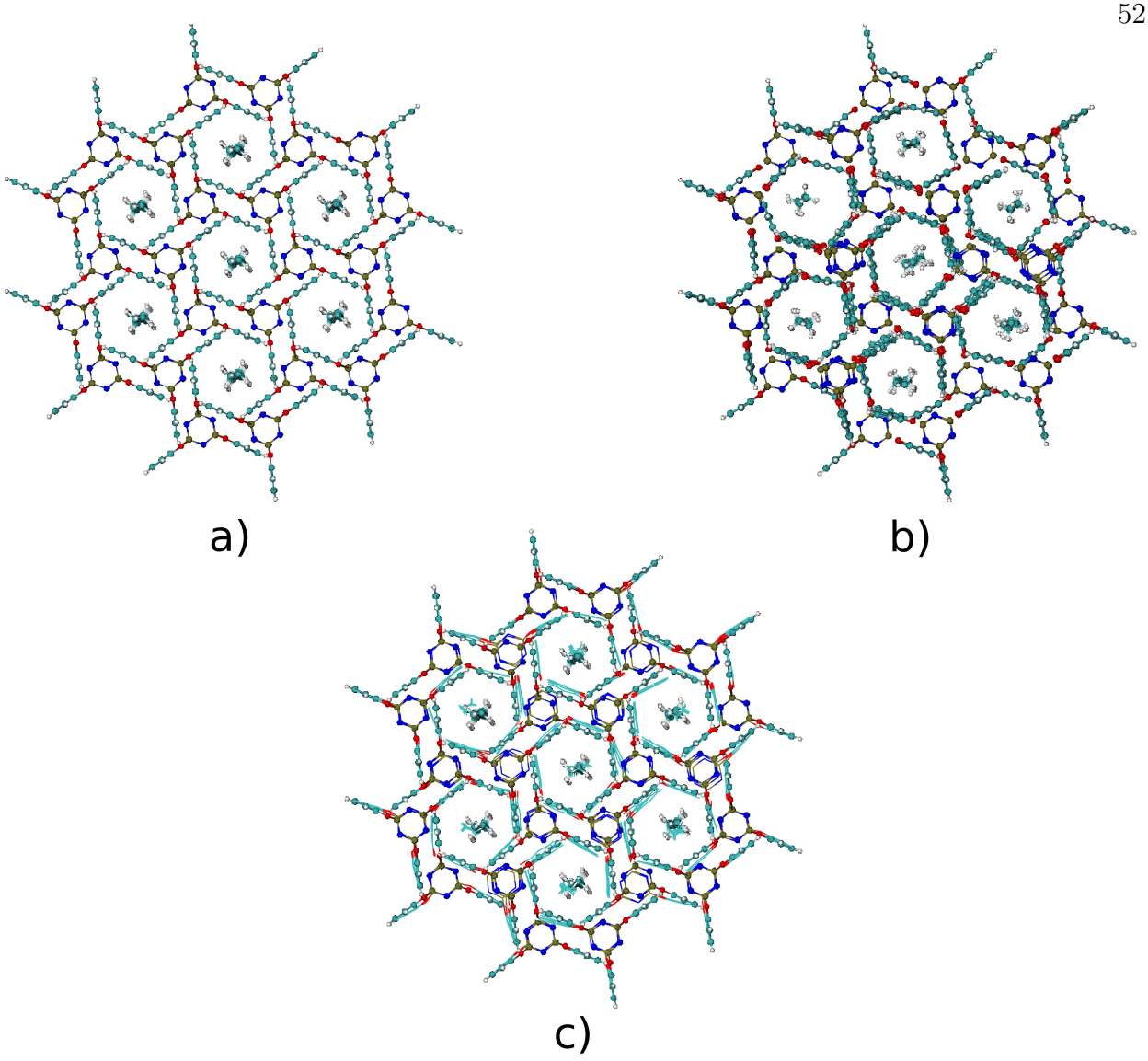

Figure 2.19: Comparison of the X-ray structure of the polyethylene - TPP inclusion compound and the UFF-optimized geometry of TPP - *n*-alkane inclusion compound: a) polyethylene - TPP X-ray structure, b) TPP - *n*-alkane (UFF optimized); c) overlayed structures a) and b).

The lowest energy geometry found (Figure 2.20) shows rotors with *n*-hexadecyl chains inserted in the channels, *p*-carboranes outside the channels and the axles with rotators π-stacking together.

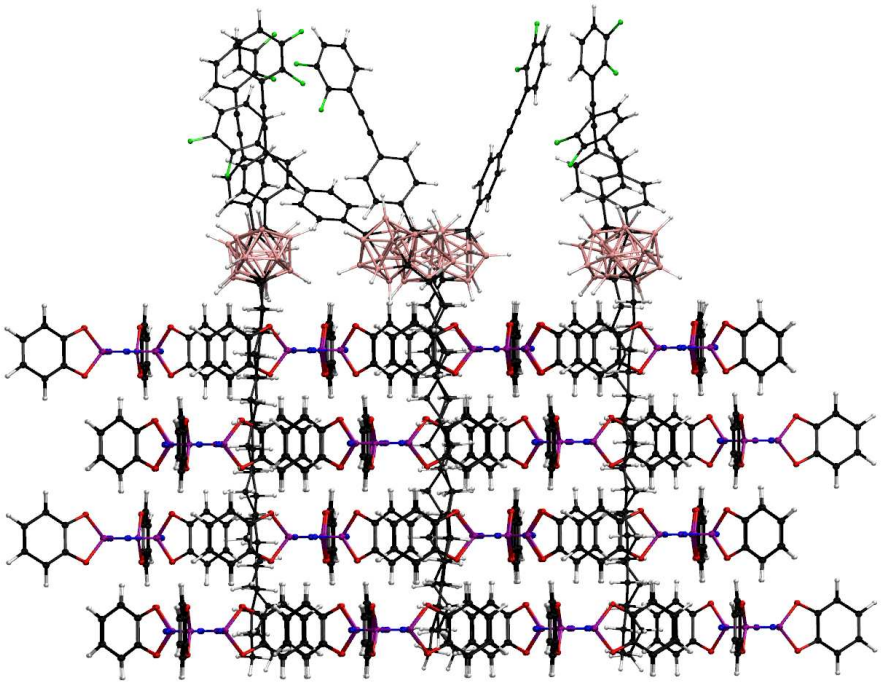

Figure 2.20: UFF simulated annealing optimized geometry of **50** in TPP.

2.3.2 Discussion

The solid-state ^{13}C CP MAS NMR result for the inclusion compound **51**@TPP (Figure 2.14) shows that the inclusion compound was formed, but it is heterogeneous. The high upfield shift of the carbons C_a (3.52 ppm) and C_b (about 2 or 3 ppm) relative to the neat compound **51**, and only a small, if any, residual intensity corresponding to the chemical shift od C_b as the neat solid suggest that almost all **51** in the sample is in the form of the inclusion compound.

The inner methylene carbon signal C_g is broader than in the neat **51** solid which could be partially caused by the heterogeneity of the sample, and partially by the conformational freedom and the presence of the gauche conformers with their chemical shifts averaged into the observed chemical shift (the γ-gauche arrangement displays chemical shift displaced upfield by about 5 ppm with respect to the anti conformation).[98]

The carbon C_d is broadened in the inclusion compound **51**@TPP compared to neat **51** solid-state ^{13}C NMR spectrum, which is indicative of heterogeneity of the sample.

Both *p*-carborane carbons C_e and C_f in the solid-state ^{13}C spectrum of the inclusion compound **51**@TPP exhibit upfield change in the chemical shift relative to neat **51** which suggests that they are inserted in the channel. As TPP forms triangular cavities in each layer (6.8 - 7.5 Å wide) and a hexagonal channel with the limiting van der Waals diameter of 4.5 - 5.0 Å in the narrowest point, the insertion of *p*-carborane (van der Waals radius of 6.9 Å) into the first layer was expected.

Part of the C_f signal and possibly also C_e exhibit downfield change in chemical shift relative to neat **51**. Whether C_e also contains a downfield peak could not be determined due to signal overlap with C_f. The upfield signal suggests that the carbon experiences deshielding. As the channels only impose strong shielding effect, part of the carborane has to be on the surface, in the deshielding zone of the TPP benzene rings.

It is not possible to tell with confidence from the inclusion spectrum whether the *p*-carborane is only inserted in the first layer or deeper into the channel. The carbon C_c of the carborane attached methyl could provide the necessary information if it did not overlap with other signals. In case of surface inclusion (*p*-carborane only in the top layer of TPP), the methyl should be in the deshielding zone of TPP phenyls. If so, the signal is buried in peak C_g. In case the methyl is inserted inside the channel, it should experience shielding by the channel. The presence of a downfield-shifted signal for C_c would not necessarily indicate that *p*-carborane does not function as a stopper as part of the *n*-hexadecyl chain could be inserted in one channel, and *p*-carborane could be with its methyl down into one of the neighboring channels. The uninserted segment of the *n*-alkyl tail may not be observed due to the signal broadness.

As the attempts to obtain the inclusion compound **51**@TPP in a homogeneous form failed, and because of the uncertainty in interpretation of its spectra, no further investigation of this inclusion compound was pursued.

The assignments of carbons in the solid-state ^{13}C CP MAS NMR spectrum of neat **50** (Figure 2.17) were based on a comparison with the solution spectrum. This is a common practice, but it should be noted that there is some amount of uncertainty in assignments made this way, as the local magnetic susceptibility can be very different in a solution than it is in a crystal due to packing in the solids, conformation effects, and solvent effects.

Nevertheless, the solid-state ^{13}C NMR of neat **50** closely resembles the solution spectrum which gives us some confidence in the assignments, especially for the aliphatic carbons, as *n*-alkanes in TPP were well studied by others before,[88] and for the carbons that are well separated from the rest of the spectrum, such as C_e, C_f, and C_g. Most of this discussion will therefore focus on these signals.

The aliphatic carbons of the *n*-hexadecyl chain in the inclusion compound all display upfield change in the chemical shifts relative to neat **50**. This result is consistent with the alkyl chain being inserted inside the channel. The signal of inner methylene carbons is broad, broader than in the inclusion compound **51**@TPP which indicates higher heterogeneity in the inclusion compound **50**@TPP, and a lesser extent of insertion of the alkyl chain. This can be best seen on the chemical shift of C_o that is very broad and it even has a downfield component.

The *p*-carborane signals C_m and C_n are close to the acetylenic carbon C_h in the solid-state ^{13}C CP MAS NMR spectrum of the inclusion compound **50**@TPP and the neat compound **50**. There is no apparent upfield change in the chemical shifts of the *p*-carborane carbons, although it could be lost in overlaps. As the signals C_m, C_n and C_h overall move downfield, most if not all of them are not inserted inside the TPP channels.

As all the resolved aromatic carbons (C_e, C_f, C_i and C_j) and the acetylenic carbon C_g show mostly downfield shifts in the inclusion compound **50**@TPP solid-state ^{13}C NMR spectrum, relative to the spectrum of neat **50**, it is concluded that the axle and the rotator are not inserted inside the channel.

Simulated annealing using universal force field is in good agreement with the conclu-

sions drawn from the NMR data. The calculations predict that only the *n*-hexadecyl chains insert into the TPP channel, and they show that the axle with the rotator π-stack. The stabilizing π-stacking interactions likely prevent the *p*-carborane from insertion as the insertion of *p*-carborane would limit the ability of the axle with rotator to tilt toward each other and form π-stacks.

Dielectric spectroscopy on the inclusion compound **50**@TPP did not show any Debye peaks characteristic for free rotatable dipoles,[e] and it further supports the hypothesis that the rotors form π-stacks on the surface of TPP.

In order to improve the design of these rotors to prevent the undesired π-stacking interactions between the rotators, the axle should be shortened. It is still likely that the design with flexible *n*-alkyl tail will not be able to support rotators with large dipoles. For such rotators, a stiff tail such as *p*-oligophenylene may be needed.

2.3.3 Conclusions

NMR spectroscopy showed that the rotor **50** formed a surface inclusion compound with TPP where only the *n*-hexadecyl chains were inserted. The inclusion was heterogeneous, and some *n*-hexadecyl chains did not insert completely. The rotators and the axles engaged in π-stacking interactions on the surface. The NMR data were supported by results obtained from calculations and dielectric spectroscopy, which were in good agreement with each other.

Improvements to the rotor design were proposed based on the results with the inclusion compound **50**@TPP. For rotors with small rotators possessing small dipole moments, it may be sufficient to shorten the axle in order to reduce the possibility of π-stacking interactions (**61**, Section 2.5). Rotors with dipolar rotators bearing larger dipoles or for larger aromatic systems, a stiffer tail (**62**, Section 2.5), such as *p*-oligophenylene, may be necessary.

The new designs will be further developed, explored and discussed in more detail in the next sections.

[e] Ke Zhao, unpublished results.

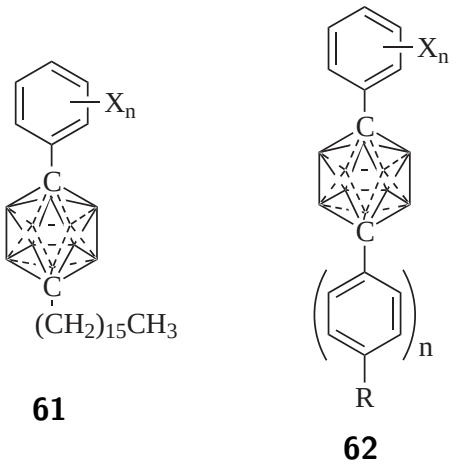

Figure 2.21: Improved first generation rotor designs.

2.4 Second Generation Rotor

The second generation rotor **63** (Figure 2.22) is based on the improved design **62** (Section 2.5). The tail used in this rotor is a biphenyl with an *n*-pentyl group added for better solubility and easier synthetic work, *p*-carborane is the stopper and 2,3-dichlorophenyl is used as the rotator. The dichlorophenyl is attached to *p*-carborane directly, and no axle is used.

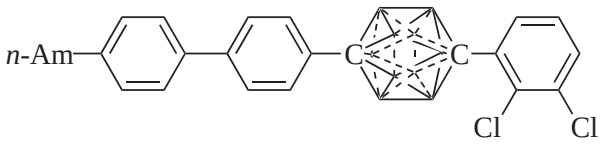

63

Figure 2.22: Second generation rotor.

Preliminary work. Before the work on the rotor **63** was started, it was checked that the parent biphenyl can form inclusion compound with TPP.

The inclusion compound of biphenyl in TPP was prepared by grinding neat powders. The solid-state ^{13}C CP MAS NMR spectrum of the biphenyl inclusion compound (Figure 2.23, top) and neat biphenyl (Figure 2.23, bottom) were recorded using 5 ms contact time.

The spectrum of the biphenyl inclusion compound shows three large singlet peaks characteristic for TPP in hexagonal form. The carbons C_a and C_b belong to the included biphenyl, they are both moved downfield relative to the spectrum of neat biphenyl, and they became sharper. The TPP channel creates strongly shielding environment, and the downfield change in the chemical shift for included biphenyl compared to the neat solid is undoubtedly caused by the shielding in biphenyl solid being even stronger than in the TPP channel.

The different chemical shift and the decreased peak width in the inclusion sample strongly indicate that biphenyl forms an inclusion with TPP. Thus, the compound **63** appeared as a feasible candidate for a new rotor.

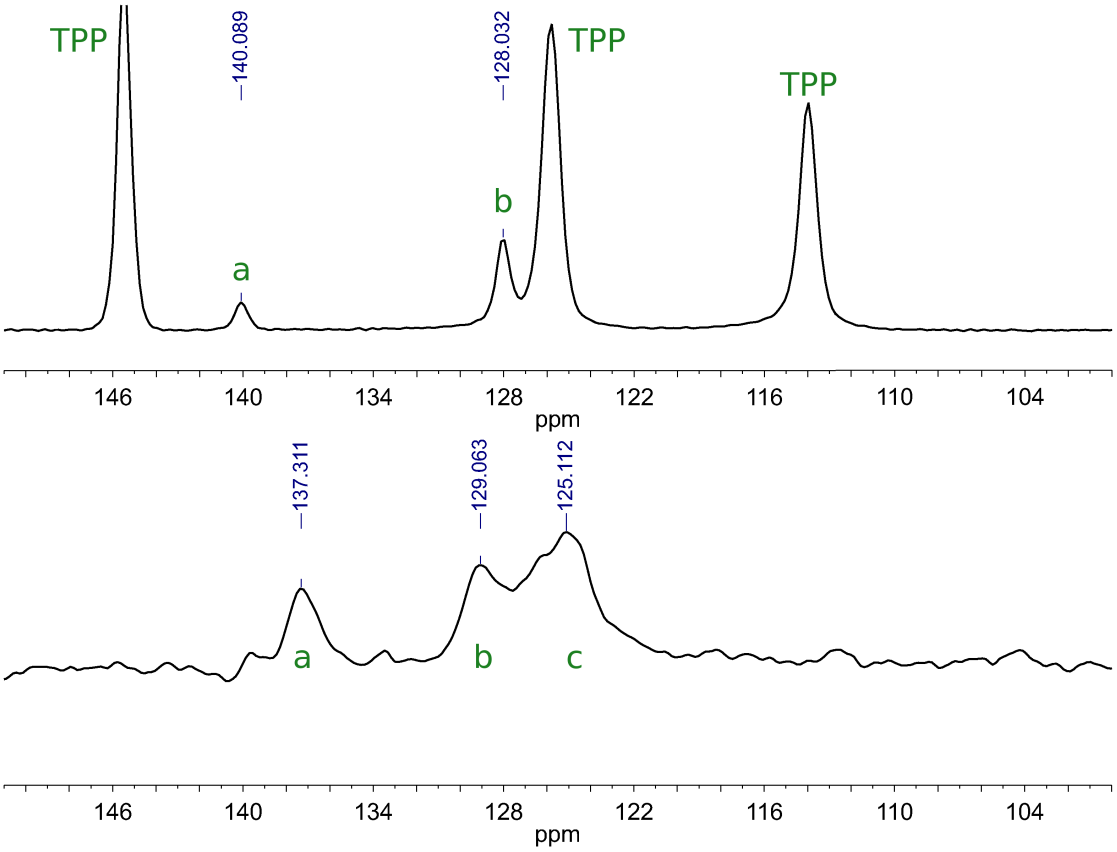

Figure 2.23: Biphenyl (bottom) and its inclusion compound in TPP (top) solid-state ^{13}C CP MAS NMR.

2.4.1 Results

Synthesis. The rotor **63** was synthesized by a sequence of reactions shown in Scheme 2.3. An organozinc reagent was prepared by lithiation of *p*-*n*-pentylbromobenzene and transmetallation with zinc chloride. Subsequent Negishi coupling with *p*-iodonitrobenzene gave **64** in 84 % yield. The nitro derivative **64** was then reduced to **65** with tin in hydrochloric acid in 94 % yield. The diazotatization of **65** with aqueous sodium nitrite in presence of diluted aqueous sulfuric acid, followed by Sandmayer reaction with potassium iodide, gave **66** in 84 % yield.

The compound **67** was prepared by Ulmann coupling of **66** and cuprous *p*-carborane (92 % yield), formed by deprotonation of *p*-carborane with *n*-butyllithium and transmetallation

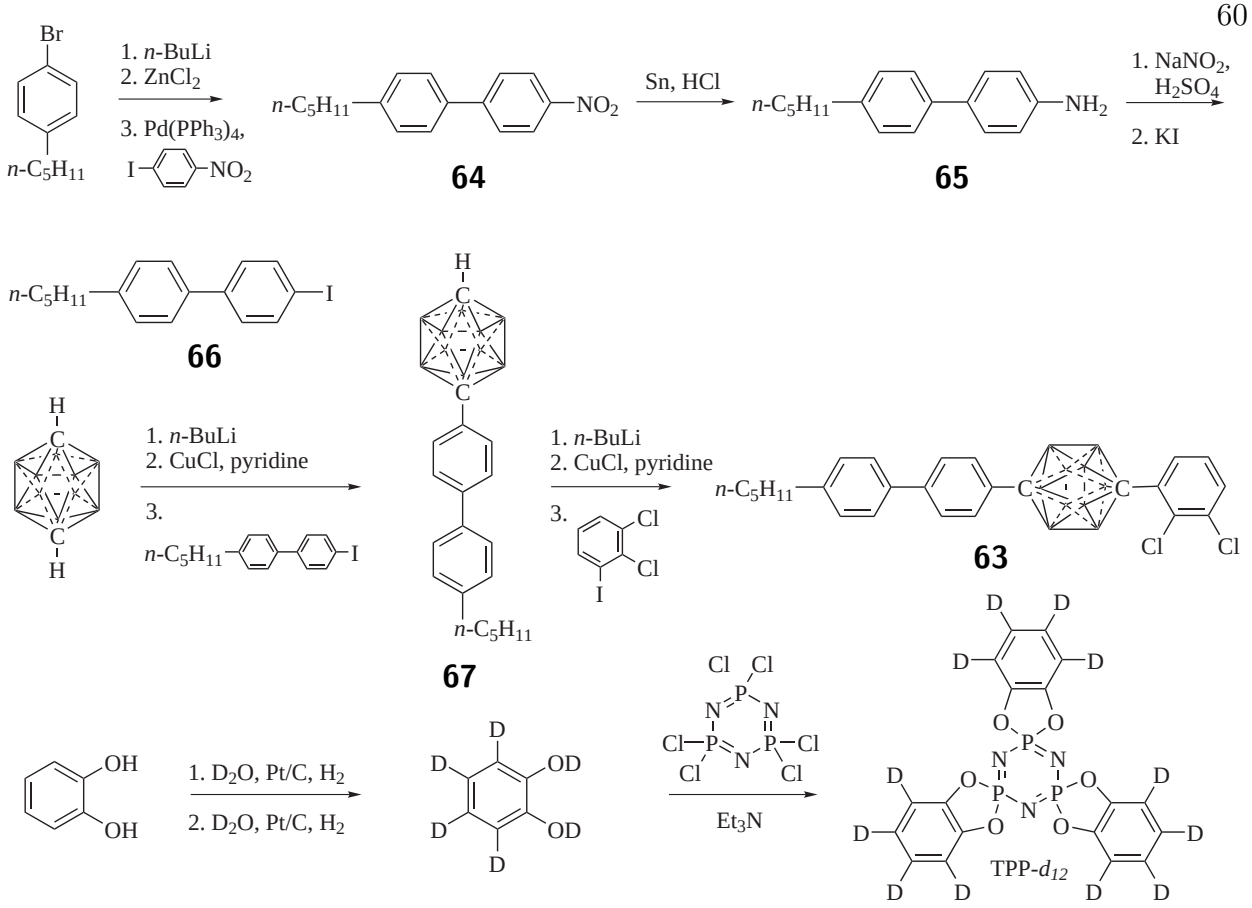

Scheme 2.3: Second generation rotor synthesis.

with cuprous chloride. A small amount of the disubstituted product was formed. When the reaction was tried with palladium catalysts, tetrakis(triphenylphosphino)palladium and bis(*o*-tolylphosphino)palladium the yield of **67** was low, and large quantities of *p*-*n*-pentylbiphenyl were formed as a side-product. Addition of triethylamine to the reaction improved the yield of **67**, but the Ulmann conditions gave superior results.

The compound **67** was deprotonated with *n*-butyllithium, transmetallated with cuprous chloride and coupled with 1,2-dichloro-3-iodobenzene. Ulmann-type conditions were superior (87 % yield) to palladium catalyzed coupling (with tetrakis(triphenylphosphino)palladium).

Perdeuterated TPP was synthesized from known catechol-d_6[115] according to the usual procedure.[81] The literature procedure for the deuteration of catechol was modified in order to improve the incorporation of deuterium. The deuteration was performed twice, and

purification by chromatography on silica gel was avoided as proton-deuterium exchange on the hydroxyl and on the α-carbon occurred on silica gel. The incorporation of deuterium by the improved procedure was better than 99.8 %, as measured by NMR.

NMR Assignments. The carbons and protons in the compound **63** were assigned using ^{1}H NMR, ^{13}C NMR, ^{1}H -^{1}H gCOSY (Figure 2.24, top), ^{1}H -^{13}C gHSQC (Figure 2.24, bottom), ^{1}H -^{13}C gHMBC, (Figure 2.25, top), and boron decoupled ^{1}H -^{13}C gHMBC (Figure 2.25, bottom). The carbons C_q, C_r, C_s, C_t, C_u and the protons H_q, H_r, H_s, H_t, H_u were assigned based on their chemical shift, and the assignments were confirmed by gCOSY, gHSQC and gHMBC spectra.

The carbon C_p was identified by its cross-peak with H_q in the gHMBC spectrum. The correlation between C_p and H_n in the gHMBC spectrum was used to assign atoms H_n and C_n, with the help of the gHSQC spectrum. The cross-peak between H_n and H_o in the gCOSY spectrum helped with the identification of H_o. The carbons C_l and C_m were assigned by their cross-peaks with H_n and H_o, respectively, in the gHMBC spectrum.

The cross-peaks of C_l with H_n and C_m with H_k in the gHMBC spectrum were used for the identification of H_n and H_k. The assignment was confirmed by the correlation between H_n and H_k in the gCOSY spectrum. The carbons C_n and C_k were identified by their cross-peaks with H_n and H_k in the gHSQC spectrum. The carbon C_i was assigned by its cross-peak with H_k in the gHMBC spectrum and by its cross-peak with carborane protons in the boron-decoupled gHMBC spectrum.

The correlations of H_j with C_h and H_c with C_g helped with the identification of C_h, H_c, C_c and C_g. The proton H_b was found by its cross-peak with H_c in the gCOSY spectrum. The correlation between H_b and H_a in the gCOSY spectrum identified the proton H_a. The carbons C_b and C_a were assigned using a gHSQC spectrum. The carbon C_d was assigned by its cross-peak with the carborane protons and with H_b in the boron-decoupled gHMBC spectrum.

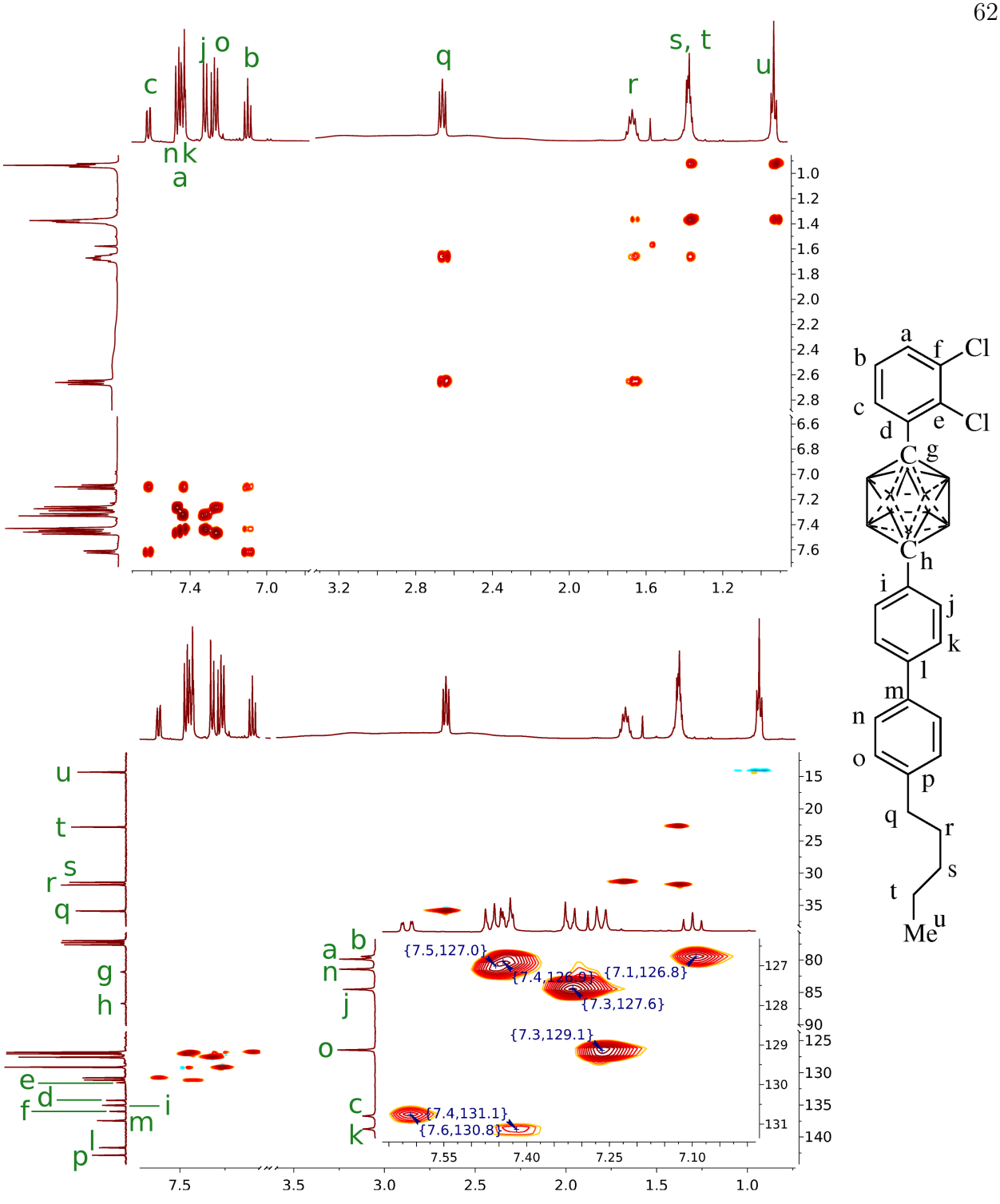

Figure 2.24: 2D NMR spectra of **63**. Top: ^{1}H -^{1}H gCOSY, bottom: ^{1}H -^{13}C gHSQC.

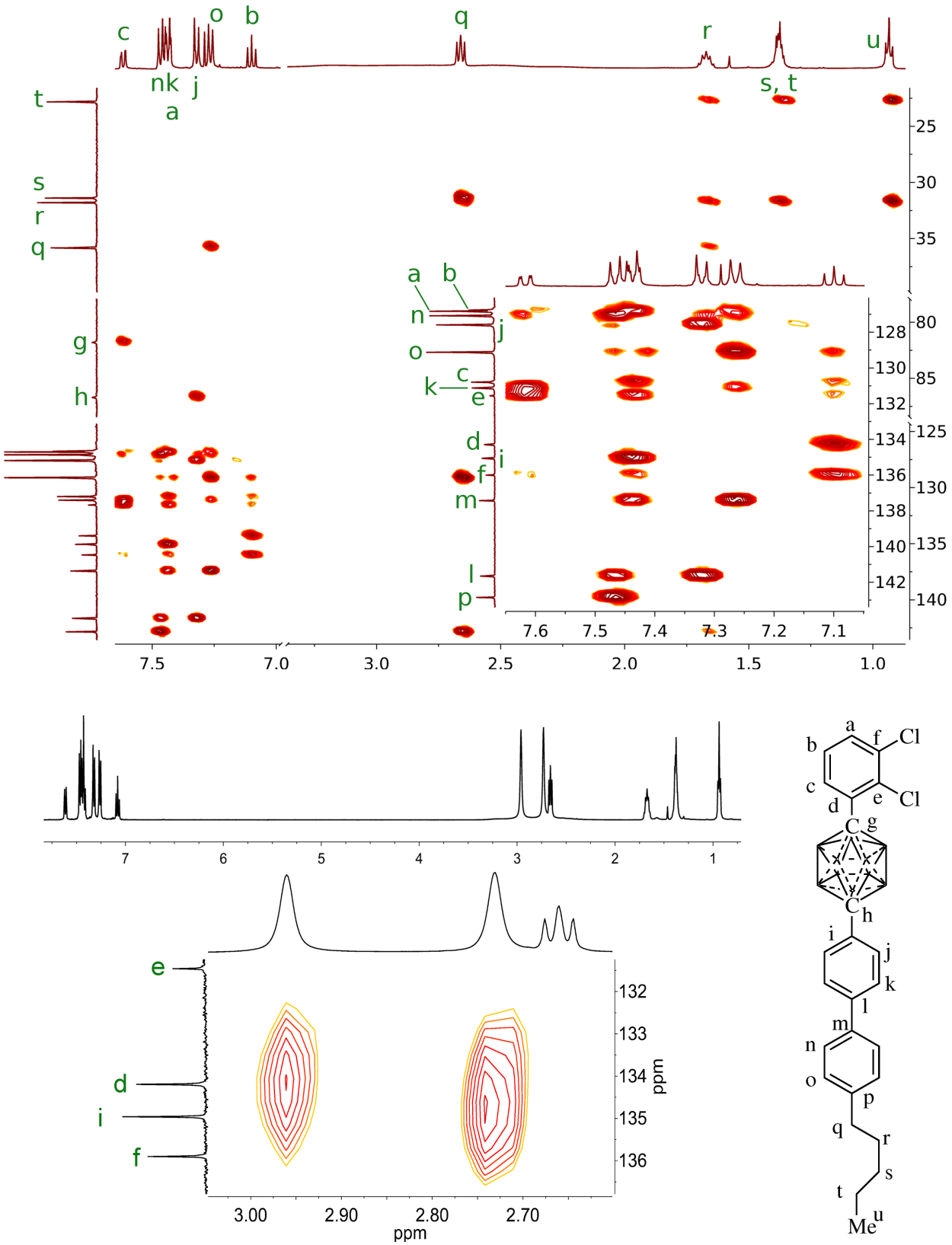

Figure 2.25: NMR spectra of **63**. Top: ^{1}H -^{13}C gHMBC (J = 8 Hz), middle: boron-decoupled ^{1}H , bottom: boron decoupled ^{1}H -^{13}C gHMBC (J = 12 Hz).

The carbon C_f was assigned by its strong three-bond coupling to H_b in the gHMBC spectrum. The remaining carbon C_i was identified by its correlations with protons H_a and H_c in the gHMBC spectrum. The assignments are summarized in Table 2.3.

Table 2.3: Rotor **63**. Summary of the ^{1}H and ^{13}C assignments.

Atom	^{1}H δ [ppm]	^{13}C δ [ppm]	Atom	^{1}H δ [ppm]	^{13}C δ [ppm]	Atom	^{1}H δ [ppm]	^{13}C δ [ppm]
a	7.41*	131.02	h	-	86.60	o	7.24	129.02
b	7.08	126.66	i	-	134.96	p	-	142.75
c	7.59	130.69	j	7.30	127.49	q	2.64	35.73
d	-	134.19	k	7.41*	126.73	r	1.65	31.70
e	-	131.46	l	-	141.55	s	1.36*	31.29
f	-	135.90	m	-	137.32	t	1.36*	22.71
g	-	81.70	n	7.44	126.98	u	0.91	14.20

* An approximate value of the chemical shift (overlapping signal).

Solid-state NMR. The inclusion compound of the rotor **63** (5 mol %) in TPP (5%**63**@TPP) was prepared by the grinding technique. The solid-state ^{13}C CP MAS NMR spectrum of the neat rotor **63** (Figure 2.26, middle) and the inclusion compound 5%**63**@TPP (Figure 2.26, top) were recorded using 5 ms contact time.

The solid-state ^{13}C CP MAS NMR spectrum of neat **63** shows values of the chemical shifts and a pattern that are similar to the ^{13}C solution spectrum. Some signals in the neat **63** split into two peaks which is usually an indication of two inequivalent crystallographic orientations in the crystal.

The ^{13}C CP MAS NMR spectrum of the inclusion compound 5%**63**@TPP solid-state displays three large resonances in the aromatic region that belong to TPP. It also shows a pattern for the resolved guest peaks that is more similar to the solution ^{13}C spectrum with most of the peaks shifted upfield with respect to both the solution ^{13}C NMR of compound **63** and its neat ^{13}C CP MAS NMR spectrum.

Most signals in the solid-state ^{13}C CP MAS NMR spectrum of the inclusion com-

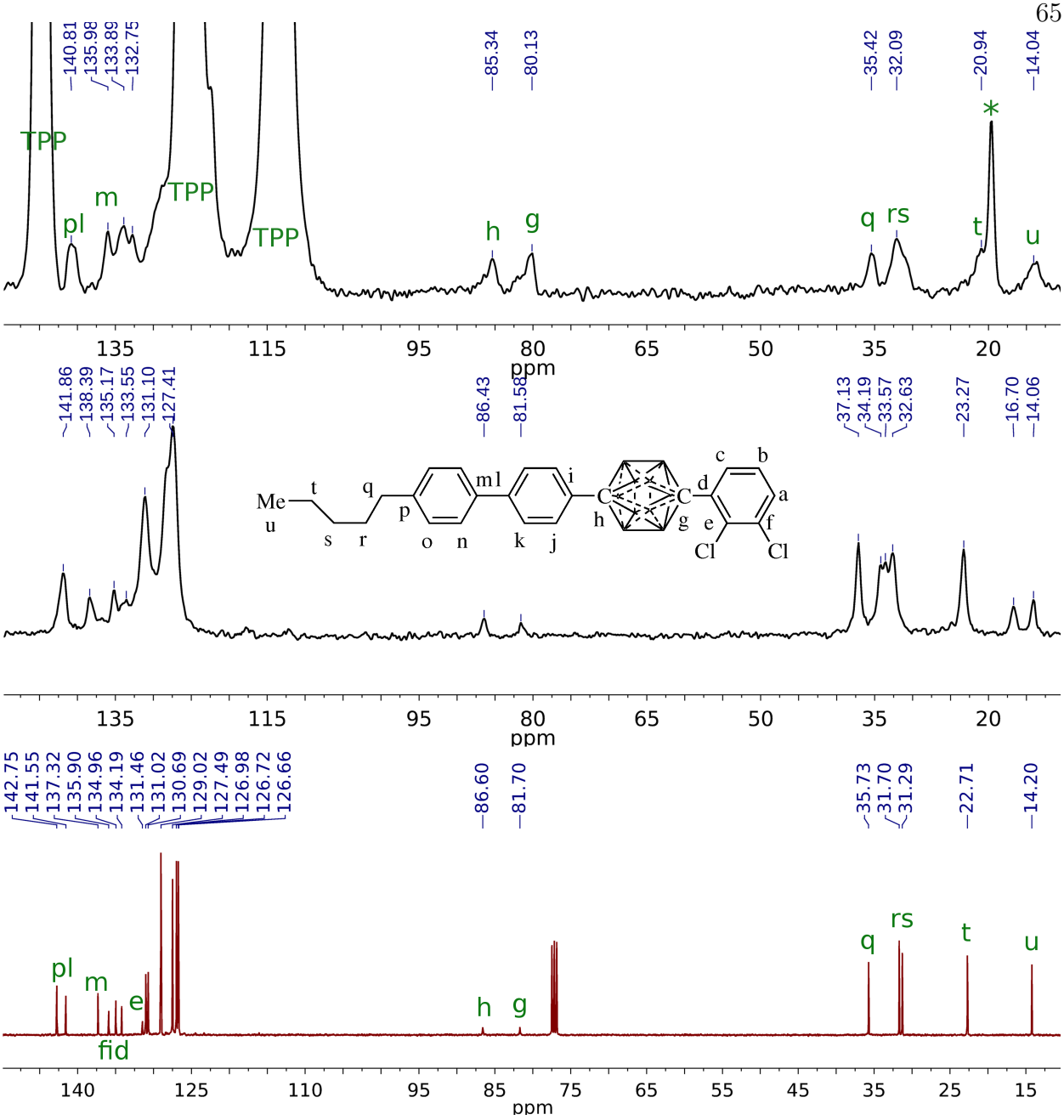

Figure 2.26: Solid-state ^{13}C CP MAS and solution ^{13}C NMR spectra of compound **63**. Top: solid inclusion compound 5%**63**@TPP, middle: neat solid **63**, bottom: **63** solution in $CDCl_3$. * Spinning sideband.

pound 5%**63**@TPP overlap with the middle TPP signal. When the inclusion compound 5%**63**@TPP was annealed, the NMR signals became sharper. A comparison of the spectra of the unannealed and annealed inclusion compounds is shown in Figure 2.27.

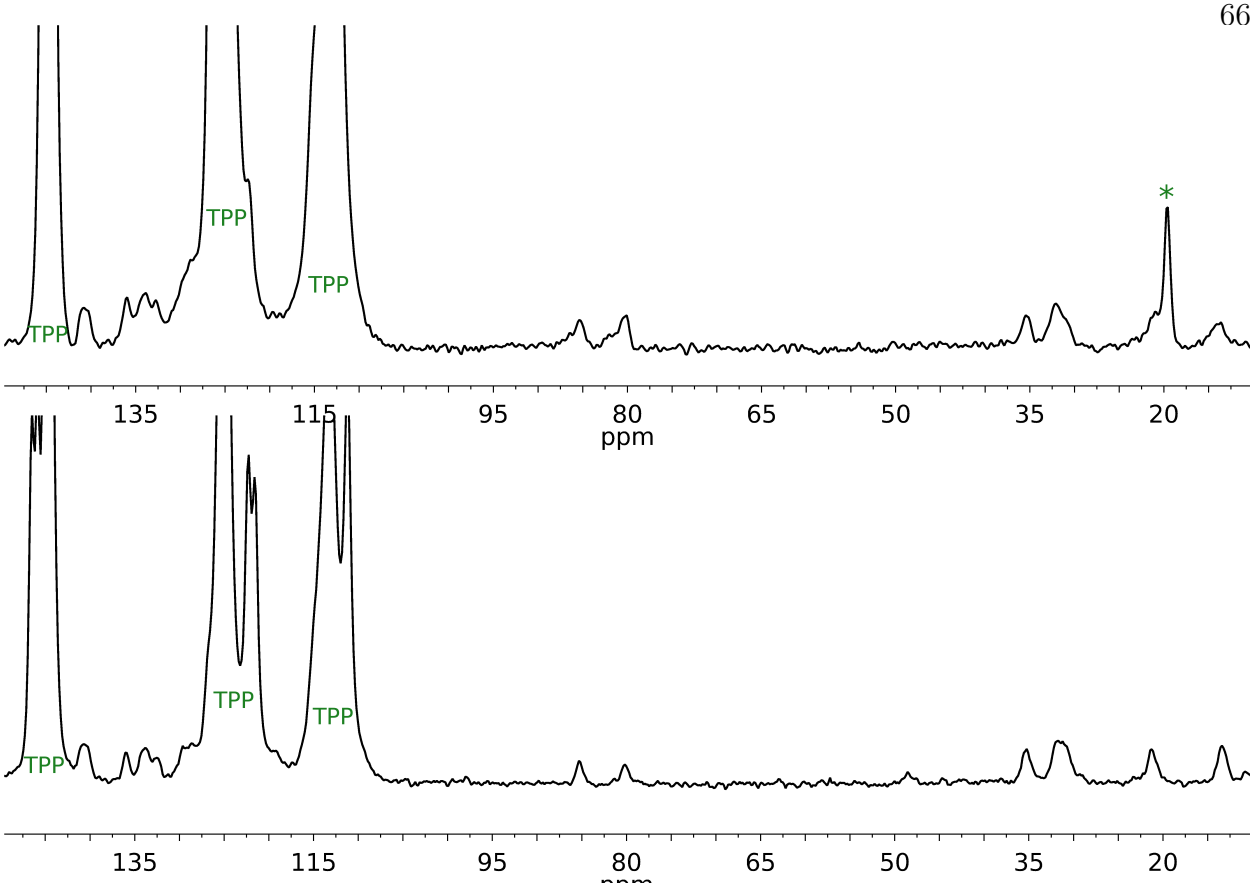

Figure 2.27: Solid-state ^{13}C CP MAS NMR spectra of the inclusion compound 5%**63**@TPP. Top: not annealed, bottom: annealed.
* Spinning sideband.

The signals of TPP in the annealed inclusion compound 5%**63**@TPP split into several signals. Some belong to filled hexagonal TPP of the inclusion, and the rest correspond to empty TPP that collapsed into monoclinic form during the annealing process.

The inclusion compound 15%**63**@TPP-d_{12} (15 mol % **63** in TPP-d_{12}) was prepared by the ball milling/annealing method described in detail in the experimental section. The solid-state ^{31}P SPE MAS NMR spectrum of the inclusion compound 15%**63**@TPP-d_{12} (Figure 2.28) was recorded. The spectrum shows a singlet resonance at 34.1 ppm and a few small signals around 0 ppm.

The solid-state ^{13}C CP MAS NMR spectra of the obtained inclusion compound 15%**63**@TPP-d_{12} were recorded using two different contact times (0.2 ms, Figure 2.29d, and 5 ms, Figure

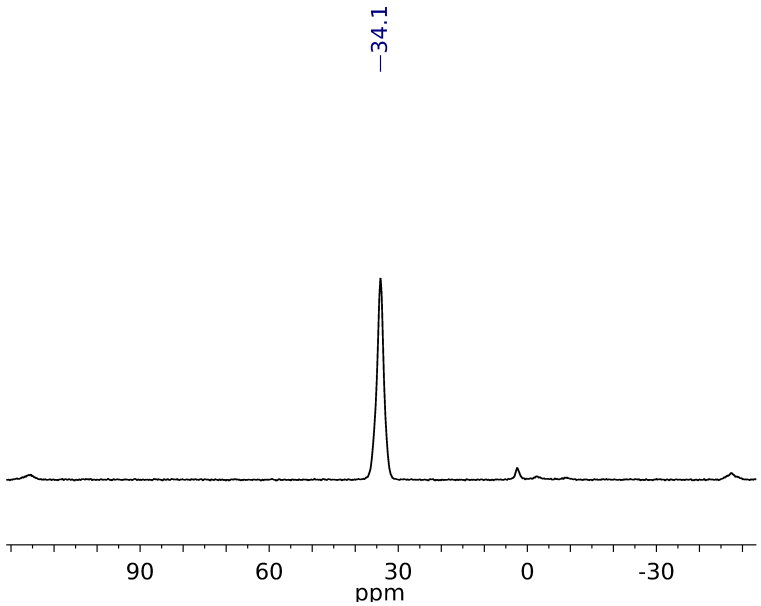

Figure 2.28: Solid-state ^{31}P SPE MAS NMR spectrum of inclusion compound 15%**63**@TPP-d_{12}.

2.29a). The solid-state ^{13}C spectra of the inclusion compound 15%**63**@TPP-d_{12} are different from those of neat **63** (Figure 2.29b).

The long-contact time spectrum shows three intense singlet aromatic resonances that belong to TPP-d_{12}. The short contact time spectrum displays protonated carbon signals enhanced relative to the quaternary signals. The comparison of the two spectra shows that the signals C_p, C_l, C_m, C_f, C_i, C_d, C_e, C_h and C_g belong to quaternary carbons, while the signals X, Y, Z, C_q, C_r, C_s, C_t and C_u belong to the protonated carbons.

The signals C_p, C_l, C_m, C_f, C_i, C_d, C_e, C_h, C_q, C_r, C_s, C_t and C_u in the solid-state ^{13}C NMR spectrum of the inclusion compound 15%**63**@TPP-d_{12} were tentatively assigned by comparison with the solution ^{13}C NMR spectrum of **63**.

The inspection of the chemical shifts of the solid-state ^{13}C NMR spectrum of the inclusion compound 15%**63**@TPP-d_{12} and the solution ^{13}C spectrum of **63** shows upfield displacements in the chemical shifts in the inclusion compound relative to the solution spectrum.

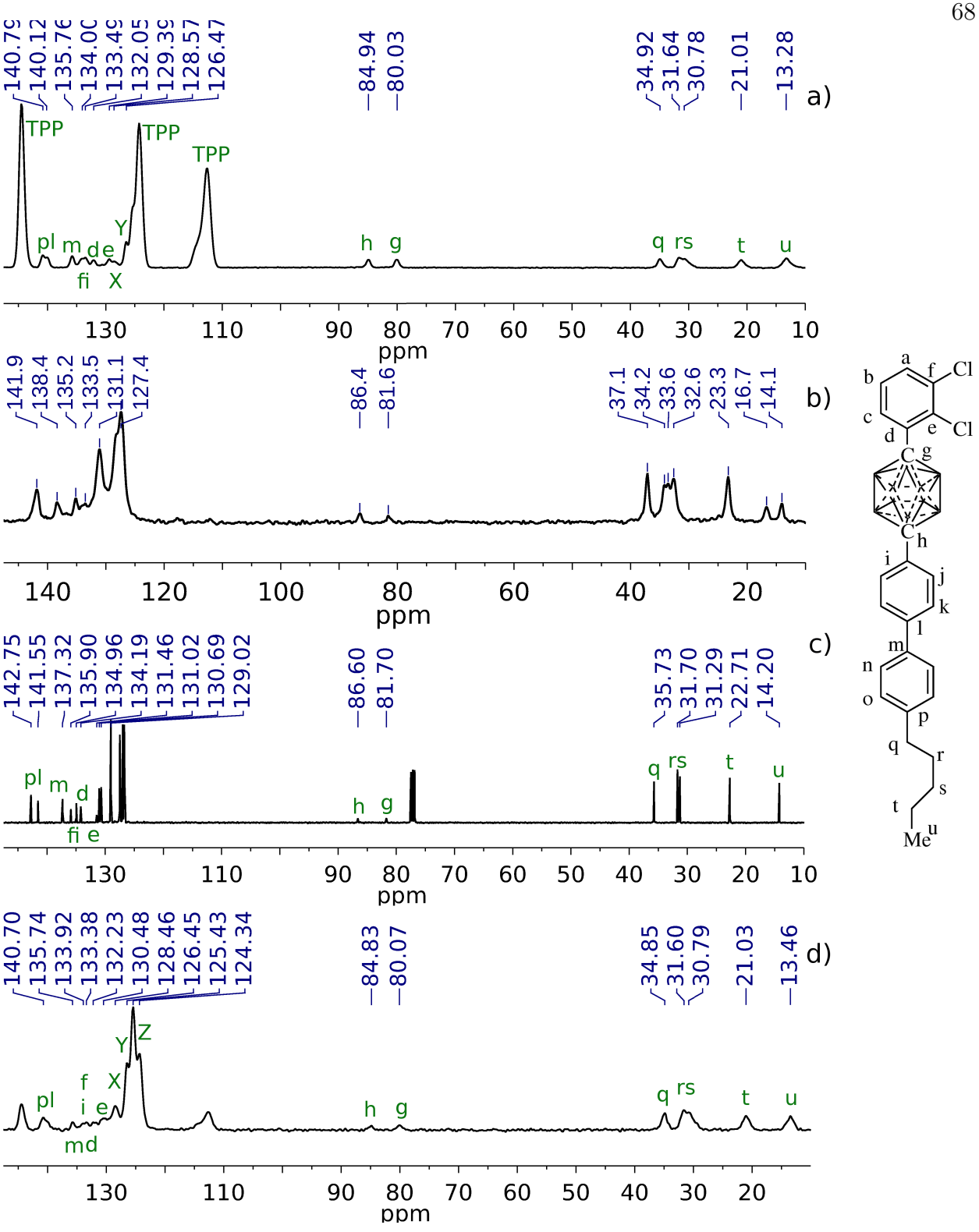

Figure 2.29: **63** and 15%**63**@TPP-d_{12} NMR: a) 15%**63**@TPP-d_{12} ^{13}C CP MAS (5 ms), b) neat **63** ^{13}C CP MAS, c) **63** solution ($CDCl_3$), d) 15%**63**@TPP-d_{12} ^{13}C CP MAS (0.2 ms).

The chemical shift changes for the resolved carbons are summarized in Table 2.4. The protonated aromatic carbons are not fully resolved, but they all display an upfield change in the chemical shift.

Table 2.4: Differences in the chemical shifts the inclusion compound 15%**63**@TPP-d_{12} relative to the solution spectrum of **63**.

Carbon	$\Delta\delta$ [ppm]	Carbon	$\Delta\delta$ [ppm]	Carbon	$\Delta\delta$ [ppm]	Carbon	$\Delta\delta$ [ppm]
d	-2.1	h	-1.7	p	-2.0	t	-0.7
e	-1.1	i	-1.5	q	-1.8	u	-0.9
f	-1.9	l	-1.4	r	-0.1		
g	-1.7	m	-1.7	s	-0.5		

Differential scanning calorimetry. The differential scanning calorimetry traces are shown in Figure 2.30. The rotor **63** shows a single endotherm at 152 °C. The inclusion compound 15%**63**@TPP-d_{12} shows two very broad exotherms at 100 °C and 210 °C, and two endoterms at 251 °C and 282 °C.

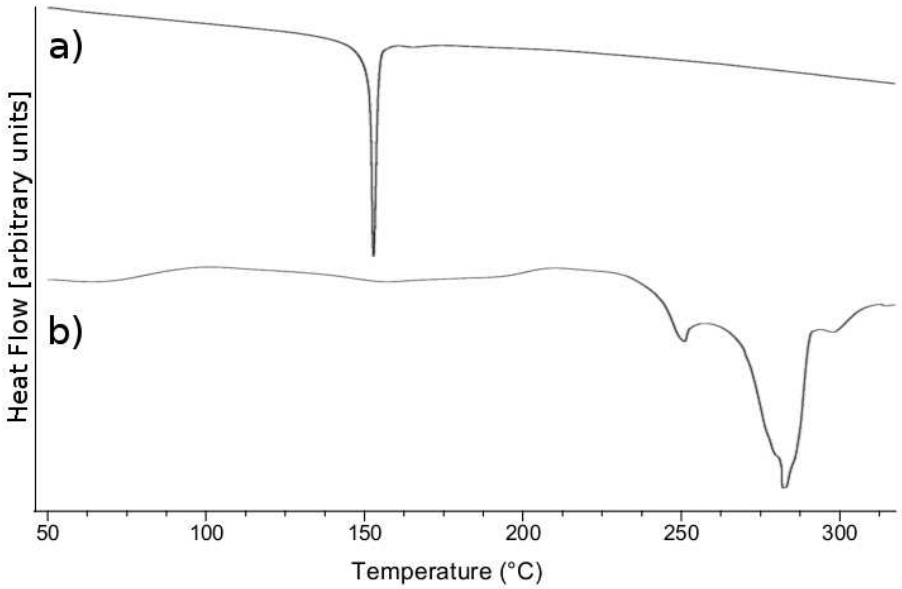

Figure 2.30: Differential scanning calorimetry: a) **63**, b) 15%**63**@TPP-d_{12}.

2.4.2 Discussion

Synthesis. The troublesome palladium catalyzed coupling of halogen derivatives with cuprous *p*-carborane derivatives is most likely caused by a slow transmetallation of cuprous *p*-carborane derivatives with arylpalladium halides (**68**, Scheme 2.4). The arylpalladium halide **68** can also undergo reduction to *p*-*n*-pentylbiphenyl by the solvent or trace impurities in the solvent. This hypothesis is supported by the fact that when solvents capable of reducing **68**, such as THF, are avoided, the reduction is partially suppressed. The addition of ligands to activate the copper in *p*-carborane for transmetallation, such as triethylamine, also suppresses the formation of *p*-*n*-pentylbiphenyl.

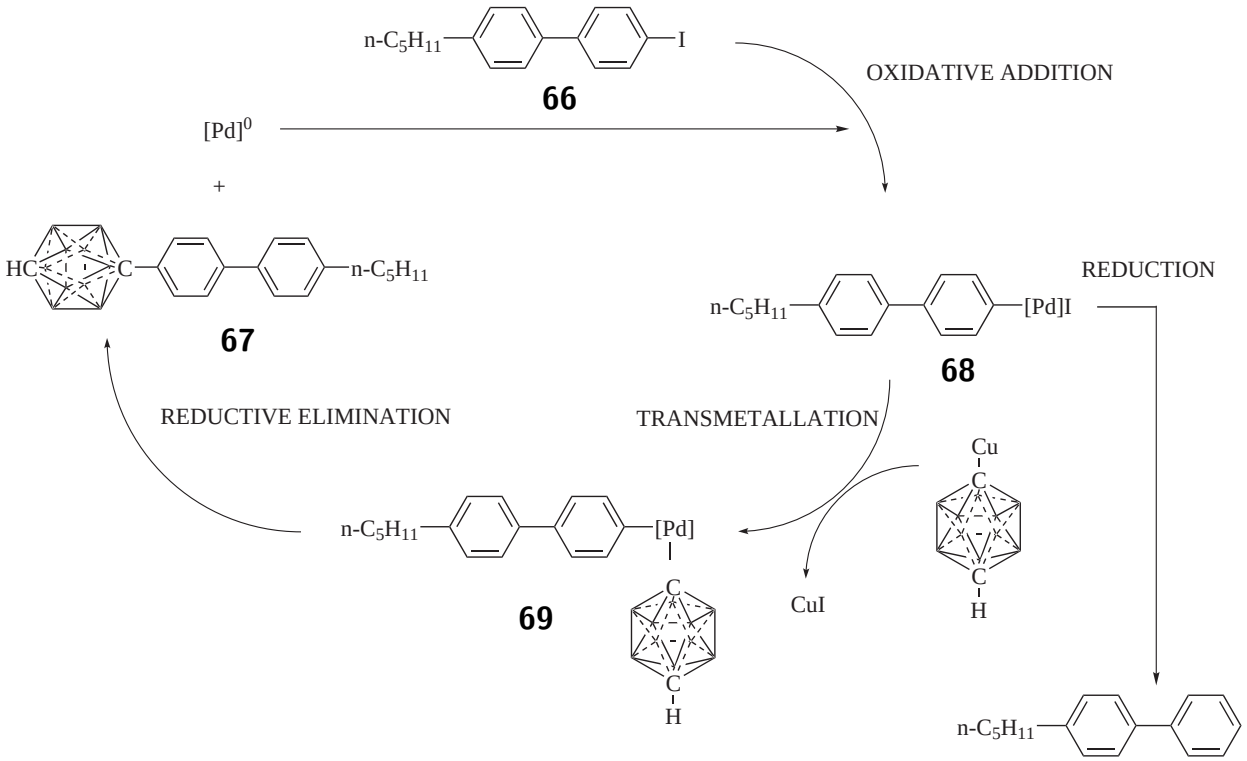

Scheme 2.4: Side pathway in palladium-catalyzed coupling reactions of cuprous *p*-carborane derivatives with aryl halides.

The hydrogen-deuterium exchange in perdeuterated catechol on silica gel occurs mainly on the OH-group and in the α-position[115] due to acidity of the hydroxyl groups. Keto-enol tautomerization provides the means for hydrogen-deuterium exchange in the α-position of

the catechol. The hydrogen-deuterium exchange in the β-position is less likely as another tautomerization is required for this exchange.

Differential scanning calorimetry. The rotor **63** shows a single endotherm at 152 °C that corresponds to melting (Figure 2.30). The two broad exotherms in the DSC trace of the inclusion compound 15%**63**@TPP-d_{12} are associated with the first order transition of hexagonal TPP-d_{12} into its monoclinic form (100 °C) and further insertion of the guest rotors into TPP-d_{12} (210 °C). The endoterms are due to melting TPP-d_{12} (251 °C) and melting the inclusion compound (282 °C). The origin of the small endotherm at 298 °C is unknown.

Solid-state NMR. The aromatic carbon assignments in neat **63** could not be reliably made by comparison with the solution spectrum as the aromatic chemical shifts in the rotor **63** have very similar values. The solution spectra contain a signal that is averaged over all the accessible conformations while there is little conformational freedom in the solid state. The effect of conformation on the chemical shift can be very strong for both aromatic and aliphatic compounds, and it is larger than the signal separation in the aromatic region of the ^{13}C NMR spectra ofcompound **63**. The resolved aliphatic and *p*-carborane signals display sufficient signal separation for the assignments by comparison of solution spectra with the solid-state spectra to be made with a high level of confidence.

In the inclusion compound, the guest experiences a large conformational freedom, and the motion of the guests similar to the systems studied in this work at room temperature is much faster than the NMR time scale.[86,94,94,96,97] The solid-state NMR spectra of the inclusion compounds are therefore averaged over the accessible conformations, although the relative contribution of a particular conformation to the resulting chemical shift is likely different than in solution as the conformational potential energy surface for a molecule in the solution and in the channel are undoubtedly different.

The NMR spectra of the inclusion compounds display the same signal pattern as the solution spectra. Thus, the assumption that the conformational effects are similar in the solution and in the channel seems justified. With this assumption in mind, the resolved

aromatic signals in the ^{13}C solid-state spectra of the inclusion compounds of the rotor **63** were assigned by comparison with the solution spectrum. The differences in the chemical shifts are assumed to be due to the differences in the local magnetic susceptibilities of the environment, *i.e.* to the shielding and the deshielding effects.

In the solid-state NMR spectra of the inclusion compound 5%**63**@TPP (Figure 2.26 and Figure 2.27), the aromatic signals of the guest compound **63** largely overlap with the TPP signals. The spectra showed the need for reducing the TPP signal in order to be able to interpret the results. A simple way to reduce the TPP signal in the CP NMR experiments without using a different guest system is to use perdeuterated TPP in place of TPP. The use of TPP-d_{12} also has the advantage of permitting a quick determination whether the inclusion compound was formed. A mixture of a protonated compound with TPP-d_{12} containing no guests inside the channels does not give rise to any ^{13}C or ^{31}P NMR signal in the CP MAS experiment unless the contact times are very long. If the guest molecule is inserted into the channel, the ^{13}C or ^{31}P atoms get cross-polarized by the guest protons, providing evidence that the inclusion compound formed and information on the local crystallographic structure of TPP-d_{12}.

The comparison of the unannealed 5%**63**@TPPa and annealed 5%**63**@TPP (Figure 2.27) shows that the annealing process greatly improves the homogeneity of the inclusion compound.

The solid-state ^{31}P SPE MAS NMR of the inclusion compound 15%**63**@TPP-d_{12} (Figure 2.28) shows a singlet peak for the TPP-d_{12} phosphorus. This indicates TPP-d_{12} in hexagonal form. The small signals around 0 ppm, a value of chemical shift typical for phosphates,[116] were assigned to oxidation impurities of TPP-d_{12} formed during the annealing process.

The three singlet resonances for the TPP-d_{12} carbons in the solid-state ^{13}C CP MAS NMR spectrum of the inclusion compound 15%**63**@TPP-d_{12} (Figure 2.29) and the difference from that of neat **63** (Figure 2.29) provide additional evidence for the formation of the

inclusion compound. The carbon assignments for the inclusion compound 15%**63**@TPP-d_{12} by comparison with the solution ^{13}C NMR spectrum of **63** are in agreement with the short contact time experiment that distinguished protonated and quaternary carbons.

The upfield changes in the ^{13}C chemical shifts of the tail, the stopper and the rotator in the 15%**63**@TPP-d_{12} solid-state ^{13}C spectrum relative to the **63** ^{13}C solution spectrum indicate that all the rotor parts are inserted inside the channel.

The upfield changes in the chemical shifts of the aliphatic carbons in 15%**63**@TPP-d_{12} are smaller compared to those of remaining carbons. This is due to the presence of other chain conformations than anti in the solution and the averaging of their chemical shift into the observed value.[98] The aliphatic chains inside TPP are largely constrained to anti conformation.[88,95]

2.4.3 Conclusions

The inclusion compounds of the rotor **63** were successfully prepared as indicated by solid-state NMR spectroscopy. The importance of annealing in the inclusion compound preparation was demonstrated. It was shown to be critical to use TPP-d_{12} in place of TPP in order to characterize the inclusion compounds.

The inclusion compounds of the rotor **63** were shown to insert completely into TPP channels. Thus, the combination of *p*-oligophenylenes with *p*-carborane stopper is not suitable for obtaining surface inclusion compounds.

2.5 Improved First Generation Rotor

The improved first generation rotor **70** (Figure 2.31) is based on the design **61** (Section 2.3). The *n*-hexadecyl tail and *p*-carborane stopper are still used, but the axle is only a bond connecting the *p*-carborane stopper to the 2,3-dichlorophenyl rotator, in order to minimize the aggregation observed for the original first generation rotor **50**.

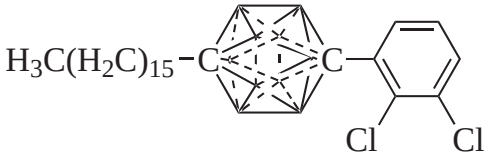

70

Figure 2.31: Improved first generation rotor **70**.

2.5.1 Results

Synthesis. The rotor **70** was synthesized (Scheme 2.5) by deprotonation of **57** (its synthesis was described in Section 2.3) with *n*-butyllithium, transmetallation with cuprous chloride and Ulmann coupling of the resulting cuprous *p*-carborane derivative with 1,2-dichloro-3-iodobenzene (92 % yield).

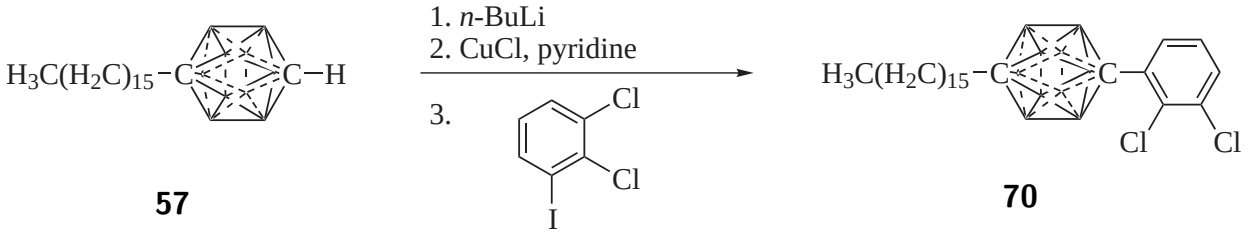

57 **70**

Scheme 2.5: Rotor **70** synthesis.

NMR assignments. The NMR signals of compound **70** were assigned using ^{1}H -^{1}H gCOSY (Figure 2.32, top), ^{1}H -^{13}C gHSQC (Figure 2.32, bottom), ^{1}H NMR, boron-decoupled ^{1}H -^{13}C gHMBC NMR (J = 8 Hz: Figure 2.33 top, J = 18 Hz: Figure 2.33 bottom), ^{13}C NMR(Figure 2.34a), and DEPT-135 (Figure 2.34b).

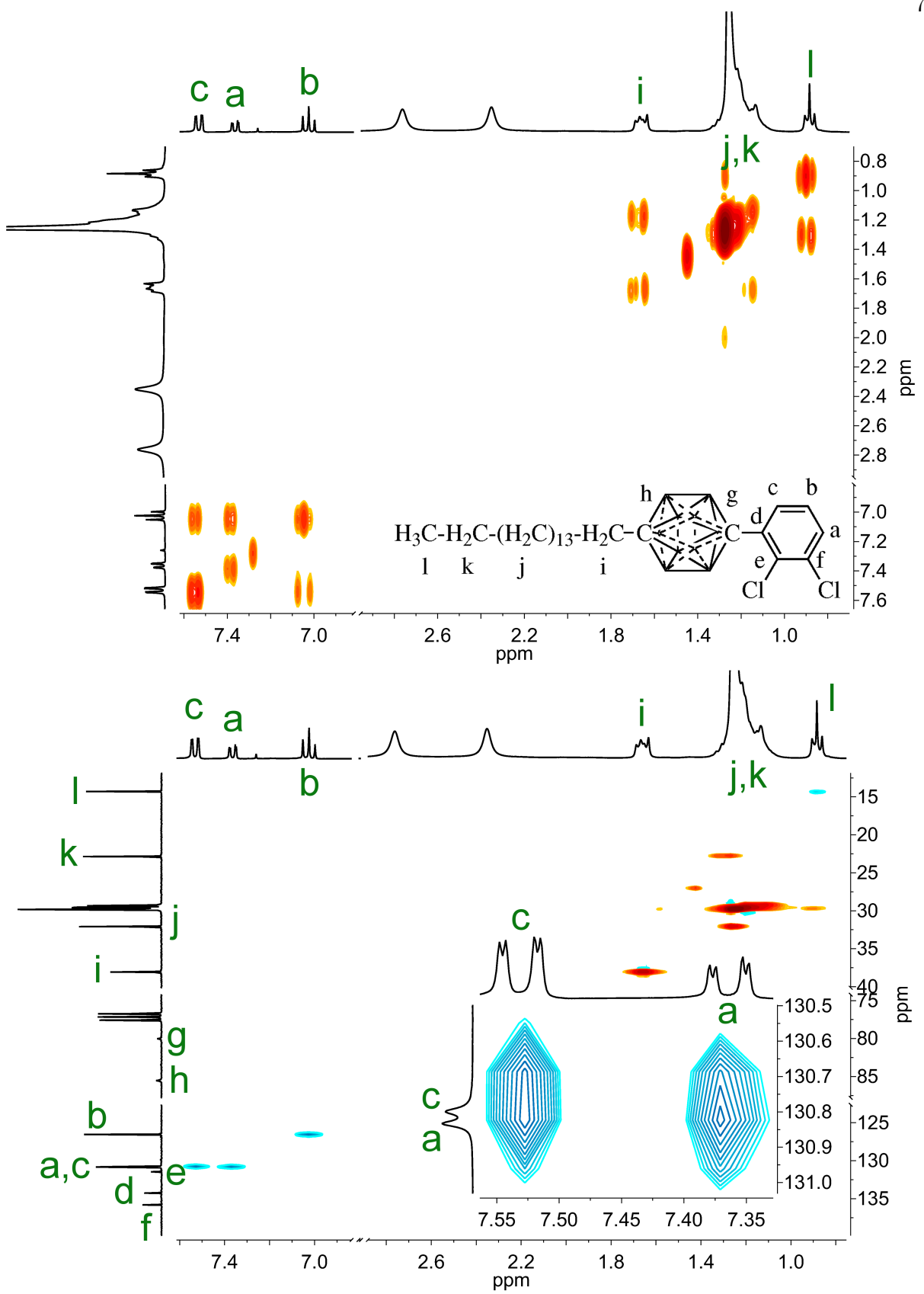

Figure 2.32: Rotor **70** 2D solution NMR. Top: ^{1}H -^{1}H gCOSY, bottom: ^{1}H -^{13}C gHSQC.

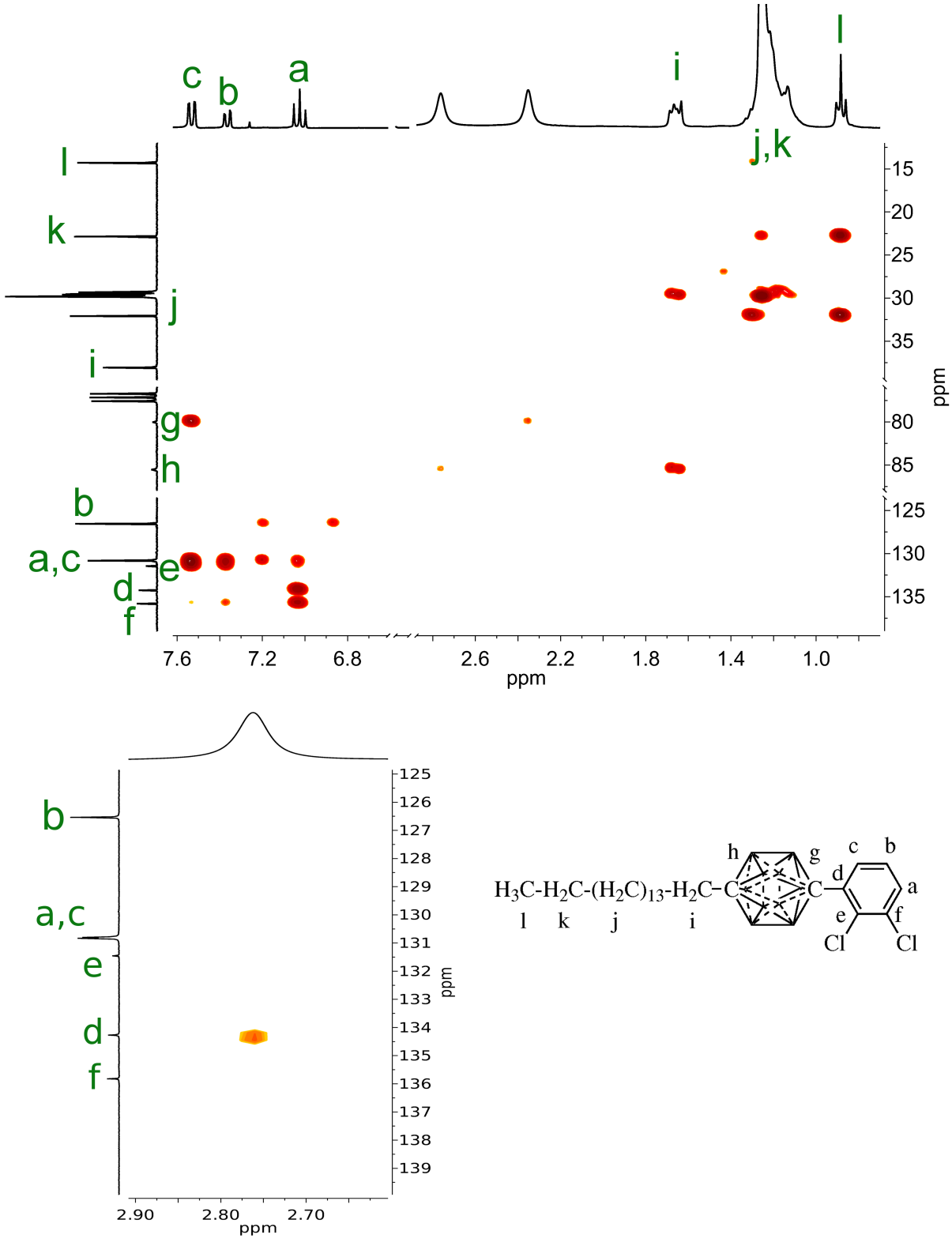

Figure 2.33: Boron-decoupled ^{1}H -^{13}C gHMBC NMR spectra of the rotor **70**. Top: $J = 8$ Hz, bottom: $J = 18$ Hz.

The carbon C_d was assigned based on its cross-peak with the *p*-carborane protons in the boron-decoupled gHMBC spectrum (Figure 2.33 bottom). The correlation between the carbon C_g and the proton H_c in the boron-decoupled gHMBC spectrum (Figure 2.33 top) was used to assign C_g and H_c. The carbon C_c was identified by its correlation with H_c in the gHSQC spectrum.

The correlations of H_c with H_b, H_b with H_a in the gCOSY spectrum, and H_b with C_b, H_a with C_a in the gHSQC spectrum were used for the assignment of the atoms H_b, H_a, C_b and C_a. The cross-peak between H_b and C_f in the boron-decoupled gHMBC spectrum (Figure 2.33 bottom) was used for the assignment of the carbons C_f and H_e, while also taking into account the usual values of the chemical shifts in this type of compound.

The *p*-carborane carbon C_h and the aliphatic carbon C_i were assigned based on their chemical shift and by the correlation between them in the boron-decoupled gHMBC spectrum (Figure 2.33 top). The remaining atoms C_j, C_k, C_l, H_j, H_k and H_l were assigned by their chemical shifts and by the cross-peaks in the gCOSY and gHSQC spectra. The assignments are summarized in Table 2.5.

Table 2.5: Summary of the NMR assignments for compound **70**.

Atom	^{1}H δ [ppm]	^{13}C δ [ppm]	Atom	^{1}H δ [ppm]	^{13}C δ [ppm]	Atom	^{1}H δ [ppm]	^{13}C δ [ppm]
a	7.02	130.83	e	-	131.46	i	1.66	30.08
b	7.36	126.54	f	-	135.82	j	1.08-1.31	29.27-32.10
c	7.53	130.80	g	-	80.03	k	1.08-1.31	22.87
d	-	134.27	h	-	85.54	l	0.88	14.29

Solid-state NMR. The solid-state ^{13}C CP MAS NMR spectrum of the rotor **70** obtained with a long contact time t_C (5 ms, Figure 2.34c) displays several aromatic resonances (A, B and C) that are not fully resolved. The aromatic signals are in a range of the chemical shifts that is similar to the solution ^{13}C NMR spectrum (Figure 2.34a and b). The chemical shifts of the aromatic carbons in the compound **70** are very similar, and it is therefore not

possible to assign these signals with confidence by comparison to the solution spectrum.

The most downfield signal, C, in the solid-state spectrum of the rotor **70** (Figure 2.34c) is the only fully resolved aromatic signal and it displays a chemical shift that is displaced by about +1.9 ppm from the most downfield peak in the solution ^{13}C NMR spectrum of the rotor **70**.

The signals of the quaternary carbons are significantly reduced in the solid-state ^{13}C CP MAS NMR spectrum of the rotor **70** obtained with a short contact time (0.2 ms, Figure 2.34d). Thus, the signals B and C belong to quaternary aromatic carbons C_d, C_e and C_f and the signal A belongs to the protonated aromatic carbons C_a, C_b and C_c.

The remaining carbon resonances in **70** are well separated and display similar chemical shifts in the solution and solid-state ^{13}C NMR spectra. They were therefore assigned in the solid-state spectrum by comparison to the solution spectrum. The aliphatic signals C_i, C_j and C_k display a large upfield change in the chemical shift (about 2-3 ppm) in the solid-state ^{13}C NMR spectrum relative to the solution ^{13}C NMR spectrum.

The inclusion compound of **70** (10 mol%) in TPP-d_{12}(10%**70**@TPP-d_{12}) was prepared by the ball milling/annealing technique described in the experimental section, and its solid-state ^{13}C CP MAS NMR spectra were recorded using 5 ms contact time (Figure 2.35a) and using 0.2 ms contact time (Figure 2.35b). The ^{13}C CP MAS NMR spectra of the inclusion compound are dominated by three aromatic singlet resonances associated with the hexagonal TPP-d_{12} carbons that are cross-polarized by the guest molecule protons. The spectrum with a short contact time shows resonances from quaternary carbons decreased in intensity relative to the protonated carbons, and was therefore used to distinguish between them. A comparison of the two spectra reveals that the signals C_d, C_e and C_f belong to the quaternary aromatic carbons, and signals C_a, C_b and C_c to the protonated aromatic carbons.

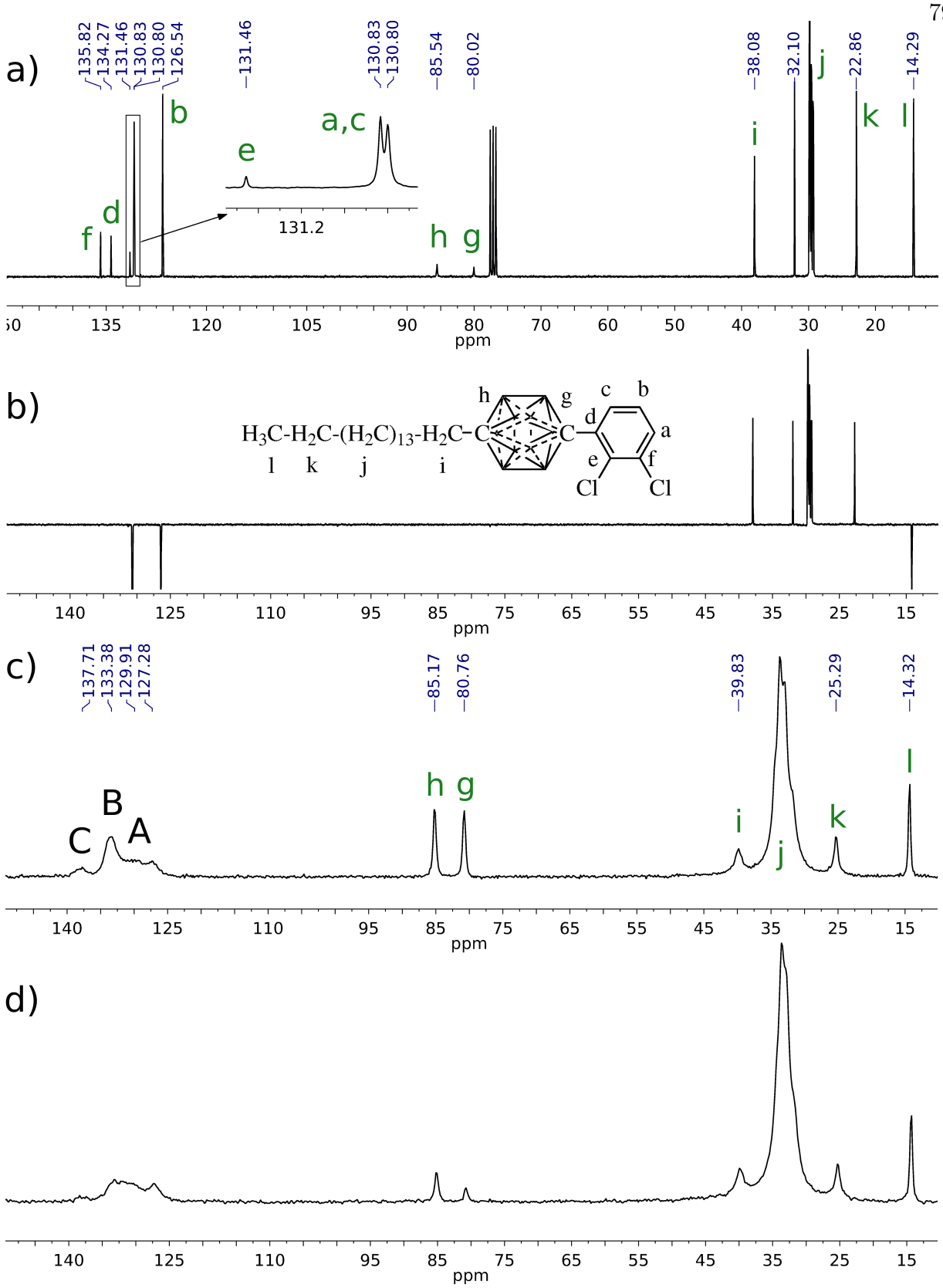

Figure 2.34: Rotor **70** NMR: a) $CDCl_3$ solution ^{13}C NMR, b) $CDCl_3$ solution DEPT-135, c) solid-state ^{13}C CP MAS NMR ($t_C = 5$ ms), solid-state ^{13}C CP MAS NMR ($t_C = 0.2$ ms).

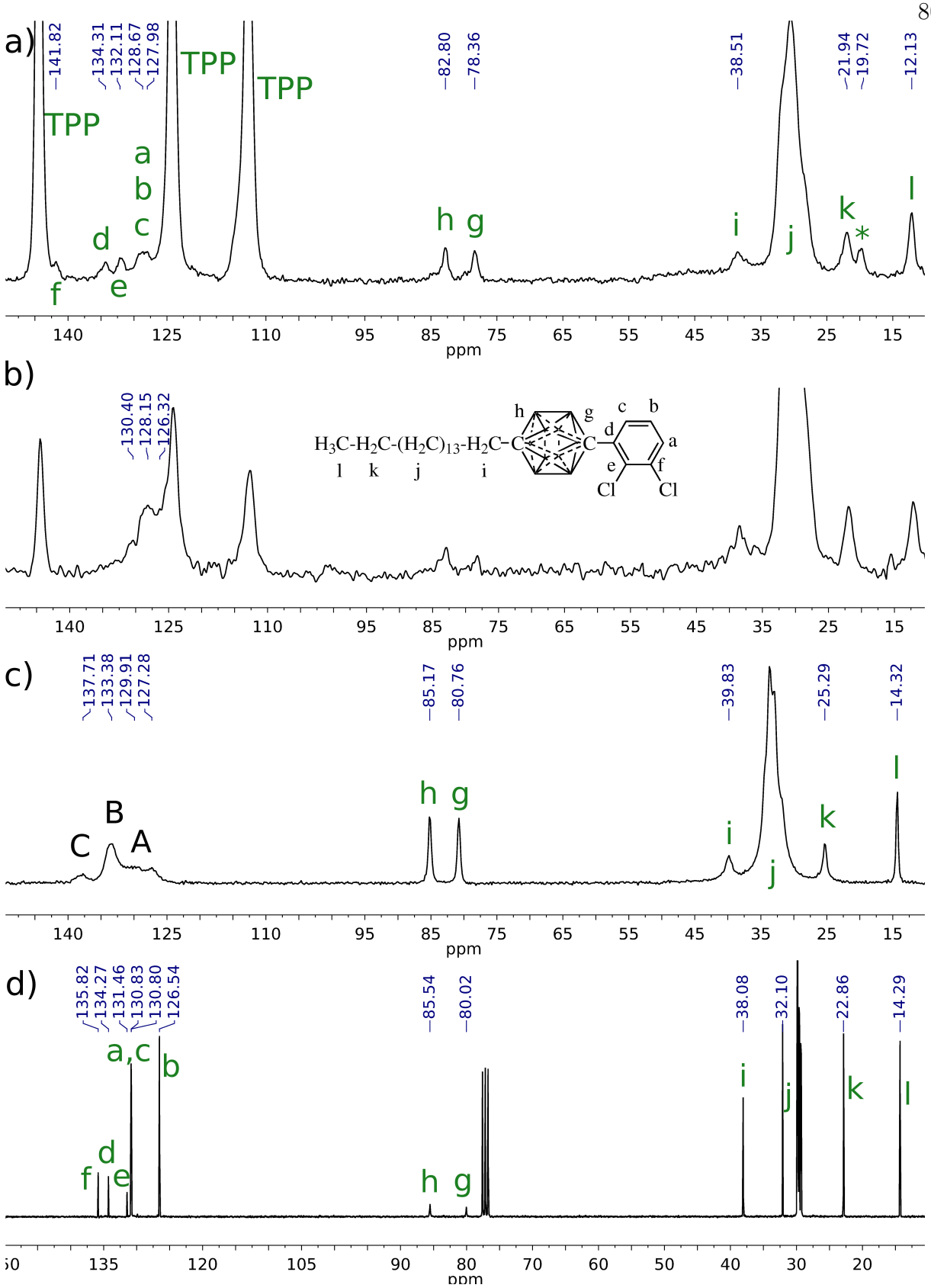

Figure 2.35: **70** and 10%**70**@TPP-d_{12} ^{13}C NMR: a) **70**@TPP-d_{12} CPMAS (t_C = 5 ms), b) **70**@TPP-d_{12} CPMAS (t_C = 0.2 ms), c) **70** CPMAS (t_C = 5 ms), d) ^{13}C NMR in $CDCl_3$.

The aromatic signals of the rotor **70** were tentatively assigned based on a comparison with the solution ^{13}C NMR spectrum (Figure 2.35d). The quaternary carbons C_d, C_e and C_f are fully resolved in the inclusion compound 10%**70**@TPP-d_{12}, whereas the signals of the protonated carbons overlap with each other and partially with the middle TPP-d_{12} signal.

The carbon C_f displays a downfield change in the chemical shift of 4.1 ppm relative to the signal C in the solid-state ^{13}C CP MAS NMR spectrum of neat **70** (Figure 2.35c), and a downfield change in the chemical shift of 6.0 ppm relative to the solution ^{13}C NMR spectrum. The carbon signal B in the solid-state ^{13}C NMR spectrum of neat **70** gives rise to two resolved resonances, C_d and C_e, in spectrum of the inclusion compound 10%**70**@TPP-d_{12}. The signal C_d in the spectrum of the inclusion compound 10%**70**@TPP-d_{12} is 0.9 ppm downfield from the peak C in the solid-state ^{13}C NMR spectrum of neat **70**, while the signal C_e appears 1.27 ppm upfield from the peak C in the solid-state ^{13}C NMR spectrum of neat **70**.

The carbon C_d displays only a small +0.04 ppm change in the chemical shift relative to the solution ^{13}C NMR spectrum of **70**, which is within the resolution error of the solid-state ^{13}C NMR spectrum of the inclusion compound 10%**70**@TPP-d_{12}. The carbon C_e also displays a small change in the chemical shift by -0.7 ppm relative to the solution ^{13}C spectrum of **70**.

The protonated aromatic aromatic carbons C_a, C_b and C_c are resolved in the solid-state ^{13}C NMR spectra of neither the neat **70** nor the inclusion compound 10%**70**@TPP-d_{12} and it is not possible to tell whether one of carbons in the solid-state ^{13}C NMR spectrum of the inclusion compound 10%**70**@TPP-d_{12} lies beneath the middle TPP-d_{12} carbon signal. They display chemical shifts similar to those in the solid-state ^{13}C NMR spectrum of neat **70**, and their chemical shifts are also similar to the solution ^{13}C NMR spectrum of **70**.

The *p*-carborane carbon signals C_g and C_h in the solid-state ^{13}C NMR spectrum of the inclusion compound 10%**70**@TPP-d_{12} display upfield changes in the chemical shift, relative both to the solution ^{13}C NMR spectrum of **70** (C_g: 1.7 ppm, C_h: 2.7 ppm) and to the solid-

state ^{13}C NMR spectrum of the compound **70** (C_g: 2.4 ppm, C_h: 2.4 ppm). Both *p*-carborane carbons in the solid-state ^{13}C NMR spectrum of the inclusion compound 10%**70**@TPP-d_{12} display small downfield shoulders with chemical shifts that are similar to those in the ^{13}C NMR spectra of **70** as a solid and in solution.

The aliphatic carbons C_i, C_j, C_k and C_l in the solid-state ^{13}C NMR spectrum of the inclusion compound 10%**70**@TPP-d_{12} all show an upfield change in the chemical shift by 1.3 to 3.3 ppm relative to the solid-state ^{13}C NMR spectrum of neat **70**. A comparison of the solid-state ^{13}C NMR spectrum of the inclusion compound 10%**70**@TPP-d_{12} with the solution ^{13}C NMR spectrum of **70** shows an upfield change in the chemical shifts in the inclusion compound spectrum for the carbons C_k (0.9 ppm), C_l (2.1 ppm), and a small downfield change in the inclusion compound spectrum for the carbons C_i (0.4 ppm) and for C_j (1.0 ppm).

Another inclusion compound of **70** (15 mol%) in TPP-d_{12}(15%**70**@TPP-d_{12}) was prepared by the ball milling/annealing technique, and its solid-state ^{13}C CP MAS NMR with 5 ms contact time (Figure 2.36b) and solid-state ^{13}C SPE MAS NMR with a short relaxation delay (3 s) were recorded (Figure 2.36c).

A comparison with the solid-state ^{13}C CP MAS NMR spectrum of 10%**70**@TPP-d_{12} (Figure 2.36a) shows that the resolved quaternary carbon C_d, C_e and the protonated carbons C_a, C_b and C_c have similar chemical shifts in both inclusions. The signals in the inclusion compound 15%**70**@TPP-d_{12} are broader. It is not obvious if one of the carbon signals C_a, C_b and C_c in the inclusion compound solid-state ^{13}C NMR spectra overlaps with the middle TPP-d_{12} carbon peak. The signal of carbon C_f has changed in the solid-state ^{13}C NMR spectrum of the inclusion compound 15%**70**@TPP-d_{12}, and it is not resolved any more.

The *p*-carborane and the aliphatic region of the solid-state ^{13}C NMR spectra of the inclusion compound 10%**70**@TPP-d_{12} and 15%**70**@TPP-d_{12} are very similar with only a small chemical shifts variation. The downfield shoulders of the *p*-carborane carbons C_g and

C_h are larger in intensity relative to their upfield components in the spectrum of the inclusion compound 15%**70**@TPP-d_{12}. The signal of carbon C_i is broader and the carbon C_k coincides with a spinning sideband in the spectrum of the inclusion compound 15%**70**@TPP-d_{12}.

The solid-state ^{13}C SPE MAS NMR spectrum of the inclusion compound 15%**70**@TPP-d_{12} enhances the signals of fast relaxing carbons. All of the guest molecule **70** carbon signals are enhanced relative to the TPP-d_{12} signals, and a new signal C_f is apparent in the spectrum.

In order to test the reliability of the inclusion compound preparation method, a new inclusion compound of **70** (8 mol%) in TPP-d_{12}(8%**70**@TPP-d_{12}) was prepared by the ball milling/annealing technique. The solid-state ^{13}C CP MAS NMR spectra were recorded using 5 ms contact time (Figure 2.36c).

The solid-state ^{13}C NMR spectra of the inclusion compounds 8%**70**@TPP-d_{12} and 10%**70**@TPP-d_{12} show nearly identical sets of peaks, with only very small variations of the chemical shift due to noise. The variation of the chemical shift is within 0.1 ppm except for carbons C_h, C_g and C_i where the difference is -0.7 ppm for C_h, C_g and +0.3 ppm for carbon C_i.

The solid-state ^{31}P SPE and CP MAS NMR spectra of the inclusion compound 10%**70**@TPP-d_{12} (Figure 2.38a,b) and the inclusion compound 15%**70**@TPP-d_{12} (Figure 2.38c,d) were recorded. All the spectra show a single resonance at 34.2 ppm.

Differential scanning calorimetry. Differential scanning calorimetry traces are shown in Figure 2.39. The rotor **70** shows a single endotherm at 62 °C. The inclusion compound 10%**70**@TPP-d_{12} shows a small exotherm at 178 °C, and two endotherms at 255 °C and 275 °C. The DSC trace of the inclusion compound 15%**70**@TPP-d_{12} shows a single endotherm at 284 °C.

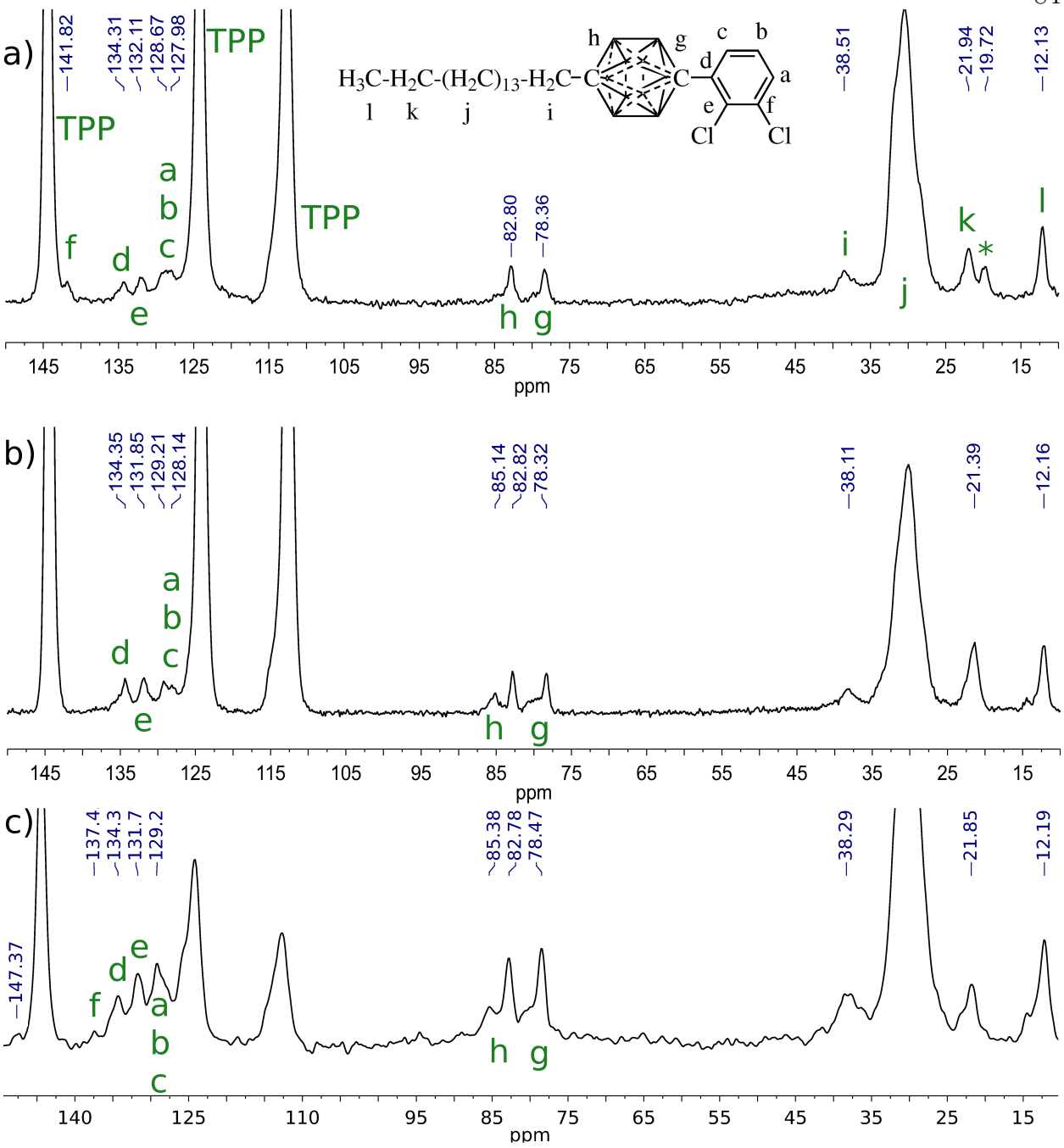

Figure 2.36: ^{13}C NMR of the inclusion compounds of **70** in TPP-d_{12}: a) 10%**70**@TPP-d_{12} ^{13}C CP MAS, b) 15%**70**@TPP-d_{12} ^{13}C CP MAS, c) 15%**70**@TPP-d_{12} ^{13}C SPE MAS.
* Spinning sideband.

2.5.2 Discussion

The aromatic carbon signals in the neat solid **70** are not likely to be affected much by conformation effects (rotation about the C_g-C_d bond), but they are dominated by the

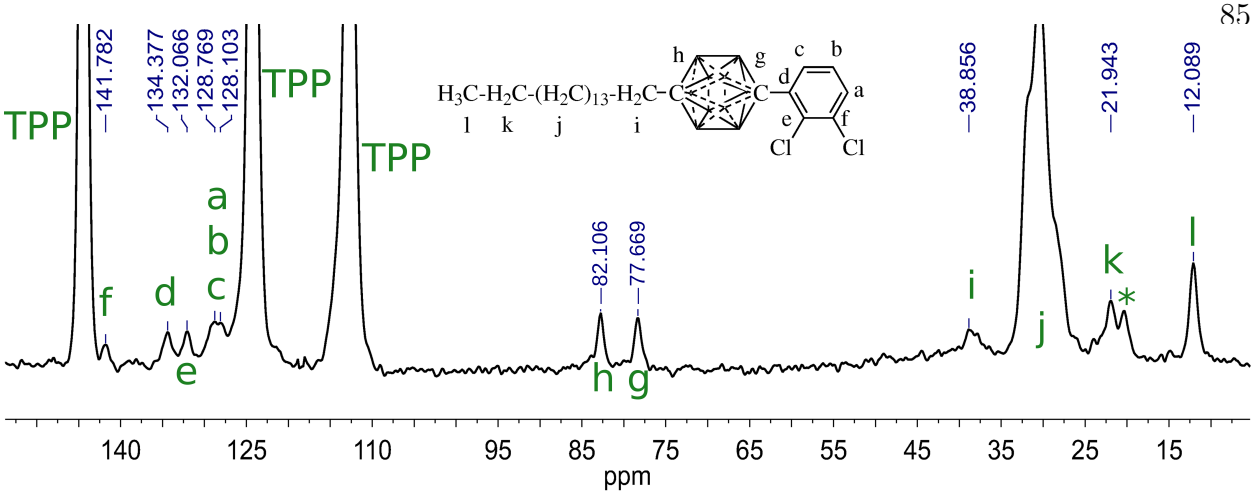

Figure 2.37: Solid-state ^{13}C CP MAS NMR of the inclusion compound 8%**70**@TPP-d_{12}. * Spinning sideband.

local shielding and deshielding effects due to the π-stacking interactions in the crystal. These effects cannot be elucidated without the knowledge of crystal packing. The comparison of the solution ^{13}C NMR spectrum of **70** (Figure 2.34d) with its solid-state ^{13}C spectrum (Figure 2.34a) shows that these effects on the chemical shifts of the aromatic carbons are comparable to the peak separation of the aromatic carbons. Thus, the aromatic carbon assignments in neat **70** could not be reliably made based on the solution spectrum chemical shifts.

The solution spectra in weakly interacting solvents contain signals that are averaged over all the accessible conformations in the averaged environment of the solvent. In the inclusion compound, the guest also experiences some conformational freedom, and the motion of the guests similar to the systems studied in this work at room temperature is much faster than the NMR time scale.[86,94,96,97] The TPP channel forms a defined, well studied strongly shielding environment inside the channel and strongly deshielding environment at the channel end. It is therefore feasible to compare the solution ^{13}C NMR spectra of **70** with its solid-state ^{13}C inclusion compound spectra, and to attribute the differences in the chemical shifts between the two to different shielding environments. As the shielding/deshielding effect at the channel end is sensitive to the position of the atom it is possible to determine the extent

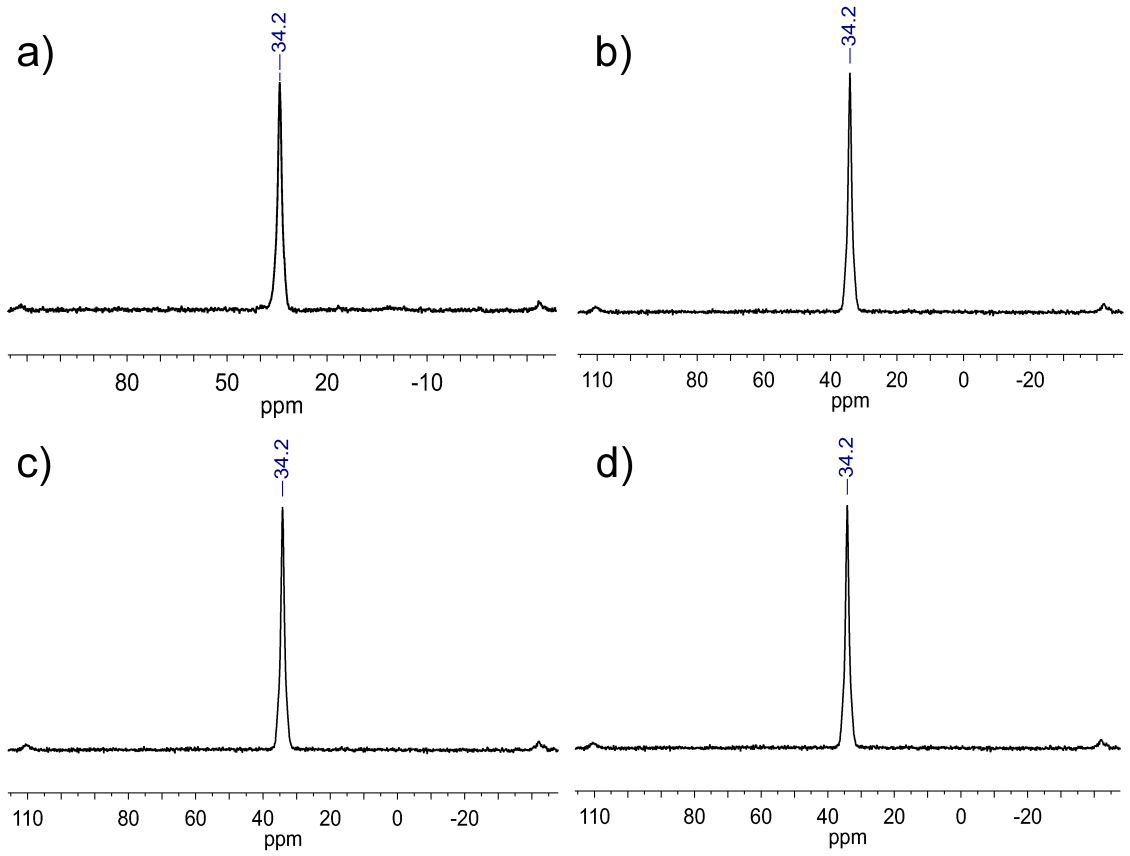

Figure 2.38: Solid-state ^{31}P NMR of **70** inclusion compounds: a) ^{31}P SPE MAS NMR spectrum of 10%**70**@TPP-d_{12}, b) ^{31}P CP MAS NMR spectrum of 10%**70**@TPP-d_{12}, c) ^{31}P SPE MAS NMR spectrum of 15%**70**@TPP-d_{12}, d) ^{31}P CP MAS NMR spectrum of 15%**70**@TPP-d_{12}; (the small downfield and upfield peaks are spinning sidebands).

of insertion of the rotor into the channel. Because the effect of magnetic anisotropy can be greater than the peak separation in the ^{13}C NMR spectra of **70**, there is always some uncertainty involved, and the conclusions drawn from the solid-state NMR results were checked with the measurements of rotational barriers using dielectric spectroscopy.

The remarkable similarity of the pattern of the resolved aromatic signals in the solid-state ^{13}C NMR of the inclusion compound **70** and those in the solution ^{13}C NMR spectrum of **70** supports the notion that a comparison between the ^{13}C NMR spectrum of **70** in solution and those of the solid inclusion compounds of **70** is valid, and the aromatic signal assignments were made under this assumption. The short contact time solid-state ^{13}C CP MAS NMR

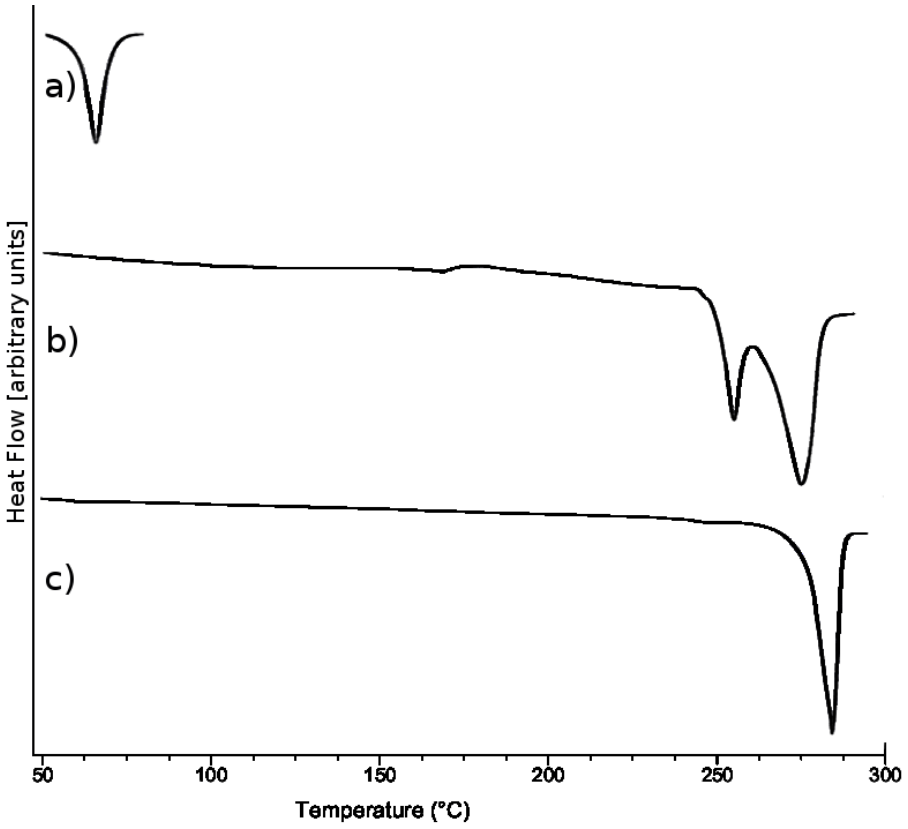

Figure 2.39: Differential scanning calorimetry: a) **70**, b) 10%**70**@TPP-d_{12}, c) 15%**70**@TPP-d_{12}.

spectrum of the inclusion compound 10%**70**@TPP-d_{12} (Figure 2.35b), which discriminates between the protonated and quaternary carbons, is in agreement with the assignments.

The resolved aliphatic and *p*-carborane carbon signals display sufficient signal separation for the assignments by comparison of solution spectra with the solid-state spectra to be made with a high level of confidence.

The solid-state ^{13}C CP MAS NMR spectra of the inclusion compounds 10%**70**@TPP-d_{12} (Figure 2.35), 15%**70**@TPP-d_{12}(Figure 2.36) and 8%**70**@TPP-d_{12} (Figure 2.37) are dominated by three aromatic singlet resonances that belong to TPP-d_{12}. This result shows that TPP-d_{12} is in the hexagonal form, and the fact that the TPP-d_{12} carbons are being cross-polarized shows that the guest compound **70** is inserted inside the channel. The solid-state ^{31}P CP MAS NMR spectra (Figure 2.38) give supporting evidence for the hexagonal struc-

ture and for the insertion of the guest compound **70**. These spectra reveal the local TPP-d_{12} structure around the guest compound **70**, but any TPP-d_{12} molecules that are not in proximity of the molecules of **70** do not give rise to any NMR signal in the CP MAS experiments. The solid-state ^{31}P SPE MAS NMR spectra of the inclusion compounds 10%**70**@TPP-d_{12} and 15%**70**@TPP-d_{12}(Figure 2.38) reveal the structure in the entire sample, and it is also hexagonal.

The upfield change in the chemical shifts of aliphatic carbons C_i, C_j, C_k and C_l in the solid-state ^{13}C NMR spectra of the inclusion compounds of the rotor **70** provides strong evidence of the inclusion behavior of the aliphatic chain. The smaller changes in the chemical shifts relative to the solution spectrum are caused by higher conformational freedom of the aliphatic chain in the solution. The chemical shift in aliphatic chains is conformation sensitive. The prevalent conformation conformation of *n*-alkanes confined inside the TPP channel is anti.[88,95] The difference between the chemical shifts in the solids and in the solution are due to higher conformational freedom in the solution, and by the contribution of these other conformations to the observed chemical shift.[98]

Both *p*-carborane carbons exhibit an upfield change in the chemical shift in the inclusion compounds of the rotor **70**, and they are therefore inserted in the channel. A small fraction of the *p*-carborane stoppers in the sample is not inserted, which is demonstrated by the downfield shoulder in the signal of these two carbons. The shoulder increases with higher loading of the rotor **70** in TPP-d_{12}.

The remarkable downfield change in the carbon C_f chemical shift of 4.1 ppm relative to the spectrum of neat **70**, and 6.0 ppm relative to the solution spectrum of **70**, provides strong evidence that the rotator protrudes above the channel in the inclusion compounds 8%**70**@TPP-d_{12} and 10%**70**@TPP-d_{12}. The inside of the channel only imposes shielding environment.[86–89,94,95] The protonated carbon C_b should find itself in a similar deshielding environment, but this is not seen due to the signal overlap.

The above conclusion holds even if the signal C_f does not belong to the carbon C_f.

This possibility needs to be addressed as there is uncertainty in the way the signals were assigned. In such a case, the downfield change in the chemical shift would be even greater.

Almost no change in the chemical shift for the carbon C_d suggests that it is at the boundary of shielding and deshielding zone, and the downfield change in the chemical shift by 0.7 ppm for the carbon C_e gives further evidence for the rotator protruding above the channel. The gradual change of the magnetic anisotropy of these carbons is in good agreement with the signal assignments. A qualitative picture of the the extent of insertion of the rotor **70** is provided in Figure 2.40.

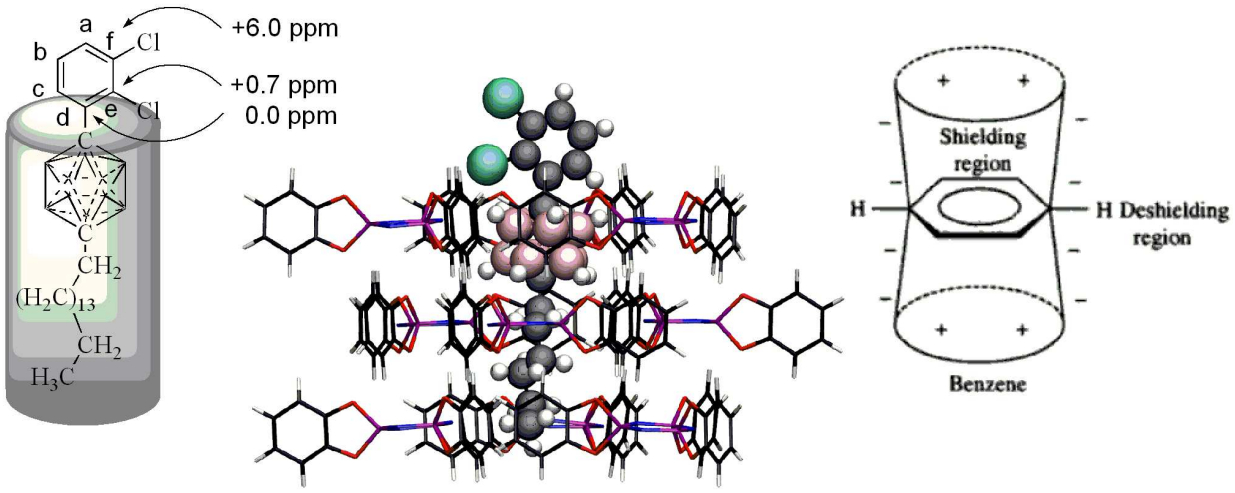

Figure 2.40: Qualitative picture of the extent of insertion of the rotor **70** in TPP.

The inclusion compound 15%**70**@TPP-d_{12} shows similar changes in the chemical shifts of the aliphatic and *p*-carborane carbons in the solid-state ^{13}C NMR spectra as the inclusion compounds 8%**70**@TPP-d_{12} and 10%**70**@TPP-d_{12}. It shows more heterogeneity, as judged by the larger downfield shoulders of the *p*-carborane carbons C_g and C_h.

The aromatic region in the solid-state ^{13}C NMR spectra of the inclusion compound 15%**70**@TPP-d_{12} is different from those of the other two inclusion compounds. The main difference is the absence of the signal of carbon C_f seen in the inclusion compounds 8%**70**@TPP-d_{12} and 10%**70**@TPP-d_{12}. This could be caused by the heterogeneity of the sample. Figure

2.40 shows that a small displacement in the vertical position of the guest causes a large change in the chemical shift close to the channel end. As the channels in the inclusion compound 15%**70**@TPP-d_{12} are saturated, it is likely that many different extents of insertion exist in the 15%**70**@TPP-d_{12}sample.

It is unlikely that the carbon C_f experiences deshielding strong enough to move the C_f signal in the solid-state ^{13}C NMR spectrum of 15%**70**@TPP-d_{12} beneath the most downfield TPP signal.

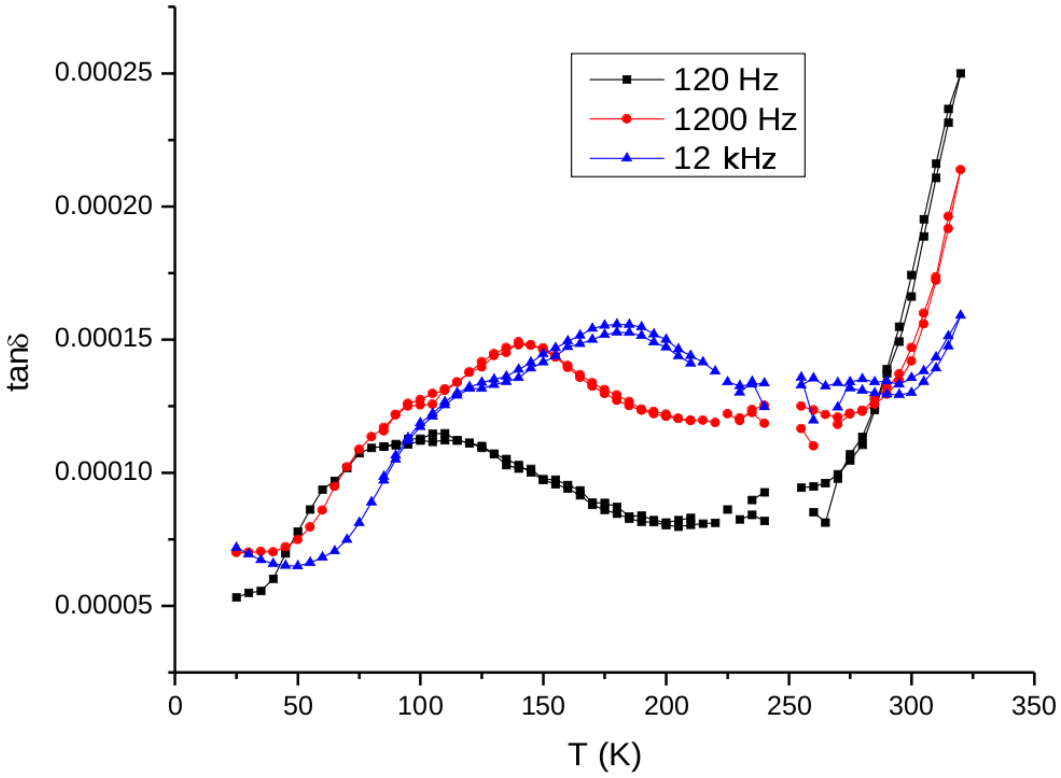

Figure 2.41: Inclusion compound 15%**70**@TPP-d_{12}: dielectric loss dependence on temperature (Ke Zhao, unpublished results).

The dielectric loss versus temperature curve for the inclusion compound 15%**70**@TPP-d_{12} (Figure 2.41, measured at three different frequencies of the oscillating electric field (120 Hz, 1200 Hz and 12 kHz),[f] shows two broad dissipation peaks associated with a rotation of a dipole with two rotational barriers: 1.9 kcal/mol and 2.4 kcal/mol (calculated for the

[f] Ke Zhao, unpublished results.

peak maxima). The broadness of the signal is associated with a high dispersity of the values, which it is in agreement with the heterogeneity of the sample observed by solid-state ^{13}C NMR.

The computed rotational barrier for the rotation of 2,3-dichlorophenyl in 1-(2,3-dichlorophenyl)-*p*-carborane (**71**) is 1.56 kcal/mol (Section 2.6). The measured rotational barrier for the rotation of 2,3-dichlorophenyl in 1,12-bis(2,3-dichlorophenyl)-*p*-carborane (**72**), fully included in TPP, is 6.7 to 9.3 kcal/mol (Section 2.6).

the conclusion that the rotator in the inclusion compound 15%**70**@TPP-d_{12} protrudes above the surface.

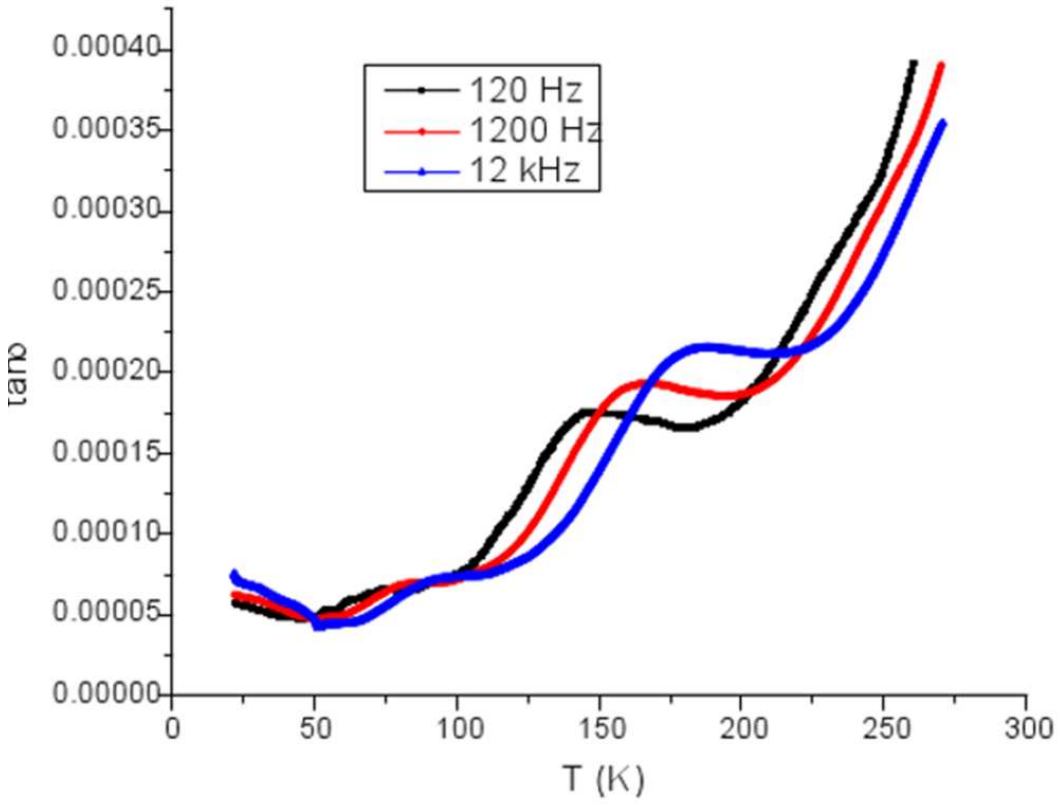

Figure 2.42: Dielectric measurements for 10%**63**@TPP-d_{12} (Ke Zhao, unpublished results).

The low rotational barrier values provide further support for The inclusion compound 10%**63**@TPP-d_{12} (Figure 2.42) shows two peaks for each frequency of the oscillating electric

field. The small low temperature peak is associated with a rotational barrier of 3 kcal/mol, whereas the high temperature peak yields a rotational barrier of 7.3 kcal/mol.

The existence of two barriers is in agreement with the solid-state NMR results. The downfield location of the *p*-carborane signals suggested that a small fraction of the rotors is inserted with only the *n*-hexadecyl chain and the majority of the sample contains the rotors inserted with both the *n*-hexadecyl chain and the *p*-carborane stopper inside the channel. However, the magnitude of the rotational barriers for the inclusion compound 10%**63**@TPP-d_{12} is not understood. A barrier of 7.3 kcal/mol would correspond to the rotator fully included inside the channel (Section 2.6, Discussion, Dielectric results for **72**) which is in contradiction with the solid-state NMR results. The high rotational barrier could be due to a tilting of the rotors or due to presence of molecules on the surface (such as water), but this remains to be shown by detailed analysis of the dielectric results and by further dielectric experiments.

Differential scanning calorimetry. The single endotherm (62 °C) in the DSC trace of the rotor **70** (Figure 2.39) corresponds to melting. The inclusion compound 10%**63**@TPP-d_{12} shows a small exotherm at 178 °C due to additional insertion of the rotor into the channel and two endotherms for melting TPP-d_{12} (255 °C) and melting the inclusion compound (275 °C). The DSC trace of the inclusion compound 15%**63**@TPP-d_{12} shows a single endotherm at 284 °C due to the melting of the inclusion compound.

X-ray powder diffraction. All the inclusion compounds of the rotor **70** show the same lattice parameters in the plane of *a*-vectors as empty hexagonal TPP-d_{12}.[g]

2.5.3 Conclusions

The solid-state ^{13}C and ^{31}P NMR results showed that the rotor **70** forms surface inclusion compounds, with the *n*-hexadecyl chain and *p*-carborane inserted in the channel and the 2,3-dichlorophenyl rotator protruding above the surface of the crystal. The supporting mea-

[g] Yongquiang S., Rogers C. T., unpublished results.

surements of the rotational barriers using dielectric spectroscopy for the inclusion compound 15%**63**@TPP-d_{12} are in good agreement with the NMR results. However, the rotational barrier measurements for the 10%**63**@TPP-d_{12} show a high rotational barrier, whose origin is not understood. It is possibly caused by the orientation of the rotator at a tilt angle, but this remains to be confirmed by further analysis of the dielectric results.

The X-ray powder diffraction data also support the conclusion that surface inclusion compounds were formed. The X-ray data show a-lattice parameter identical to empty hexagonal TPP-d_{12} (compare to bulk inclusion compounds of the third generation rotors with 5 % expansion in a-vector plane, Section 2.6, Discussion) The inclusion compounds show some heterogeneity which is higher with greater loadings of the rotor **70** in TPP-d_{12}.

However, the conclusion from the computational results (Section 2.3) is that this system is not suitable for rotators with larger dipole moments due to large flexibility of the n-hexadecyl chain, and the risk of aggregation of the rotators on the TPP surface as observed for the rotor **50**. The search for a better system therefore continues...

2.6 Third Generation Rotors

The third generation rotors are based on the design **62** (Section 2.3). The stopper employed in these rotors is *p*-carborane, *p*-terphenyl serves as the tail (Figure 2.43) and four different rotators are used in the new rotors **72**, **73**, **74**, **75**, and **76** (Figure 2.43). The rotators are either connected directly via a single bond to the *p*-carborane carbon, or via an acetylene axle. The stiff tail in the third generation rotors should prevent aggregation that was observed in the inclusion compound of the rotor **50**.

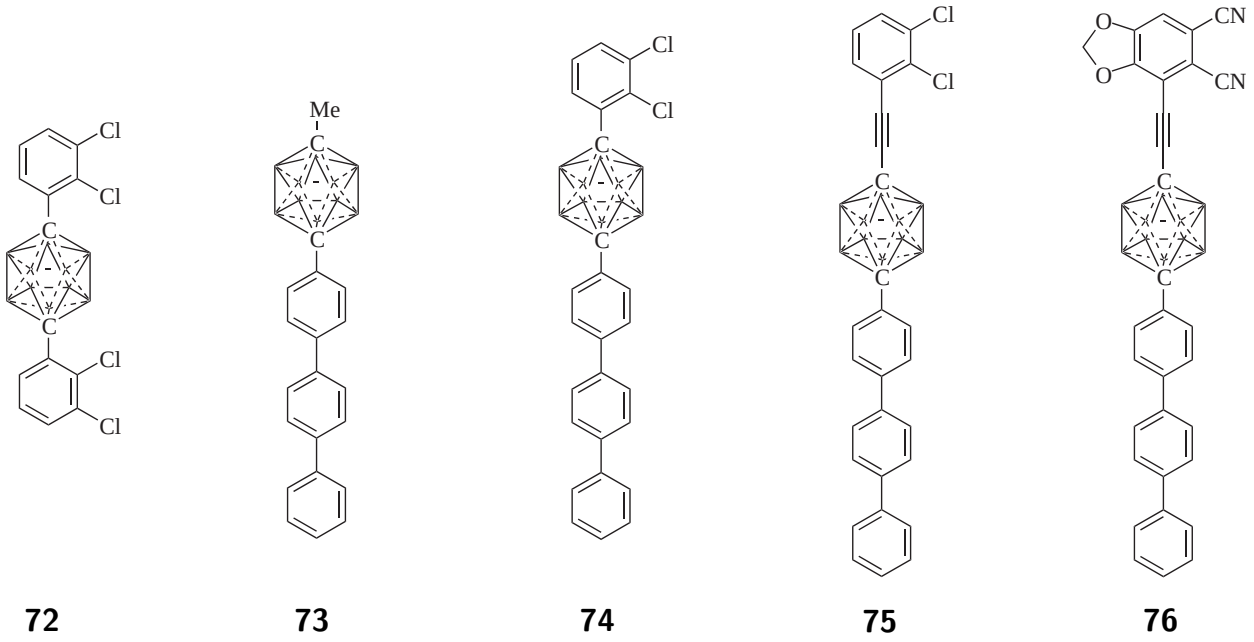

Figure 2.43: Third generation rotor structures.

Preliminary work. As a test whether *p*-terphenyl derivatives form inclusion compounds, preliminary experiments with *p*-terphenyl and 4-nitro-*p*-terphenyl were performed.

The inclusion compounds of *p*-terphenyl (5 mol %) and 4-nitro-*p*-terphenyl (5 mol %) in TPP were made by the grinding method. The solid-state ^{13}C CP MAS NMR spectra of the neat guests and their inclusion compounds were recorded using 5 ms contact time (Figure 2.44).

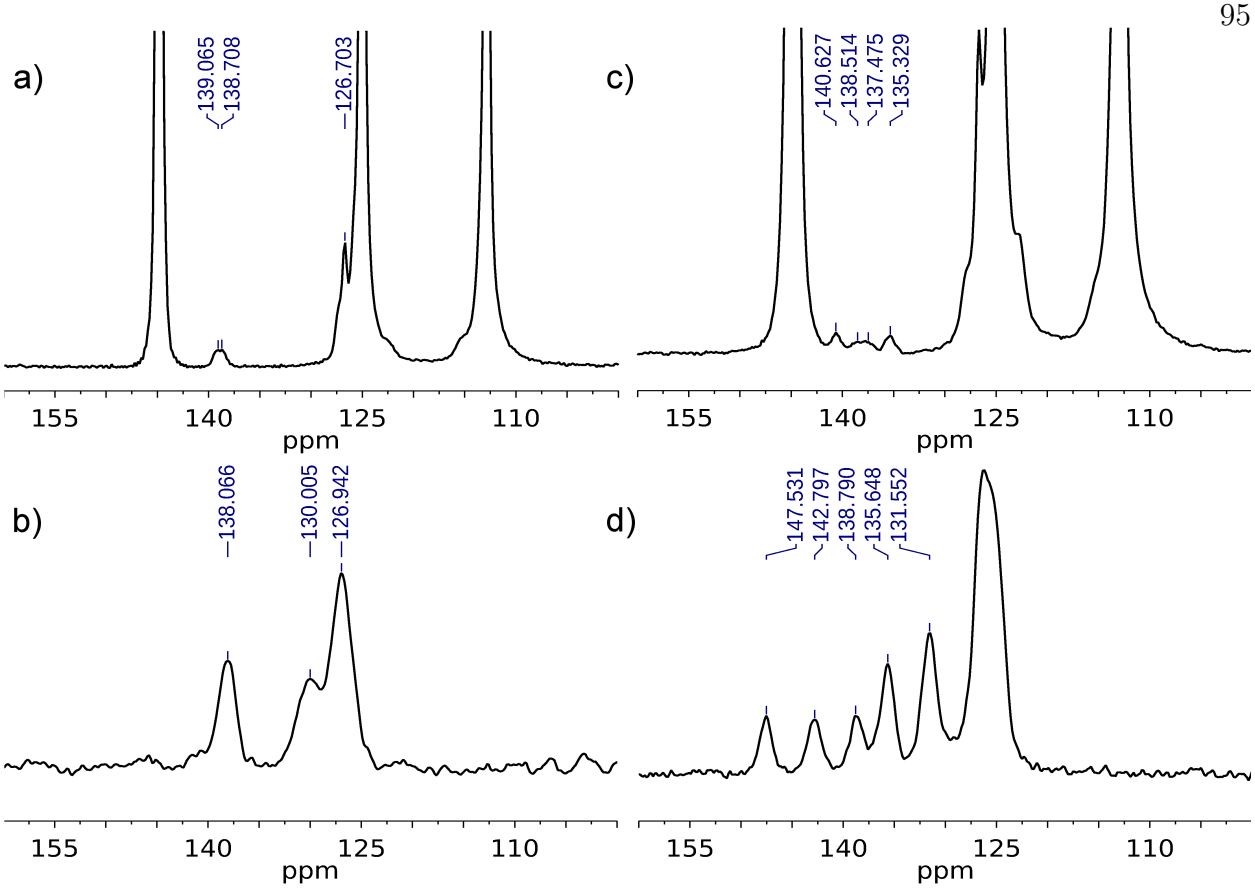

Figure 2.44: Inclusion compound solid-state ^{13}C CP MAS NMR spectra: a) *p*-terphenyl in TPP, b) neat *p*-terphenyl, c) 4-nitro-*p*-terphenyl in TPP, d) neat 4-nitro-*p*-terphenyl.

The solid-state spectra of the inclusion compounds both display three singlet resonances, characteristic for hexagonal TPP. The pattern of the guest signals is different in the inclusion compounds and in the neat guest solids, which suggests that both guest compounds formed inclusion compounds.

2.6.1 Results

2.6.1.1 Synthesis

The rotors were synthesized as shown in Scheme 2.6. The coupling reactions on the *p*-carborane carbon were performed using the Ulmann conditions. Attempts to perform these couplings at lower temperatures with various palladium catalysts resulted in partial reduction

of the iodo derivative besides the formation of the desired coupling products (Section 2.4). The use of Ulmann coupling completely suppressed the formation of the reduction products.

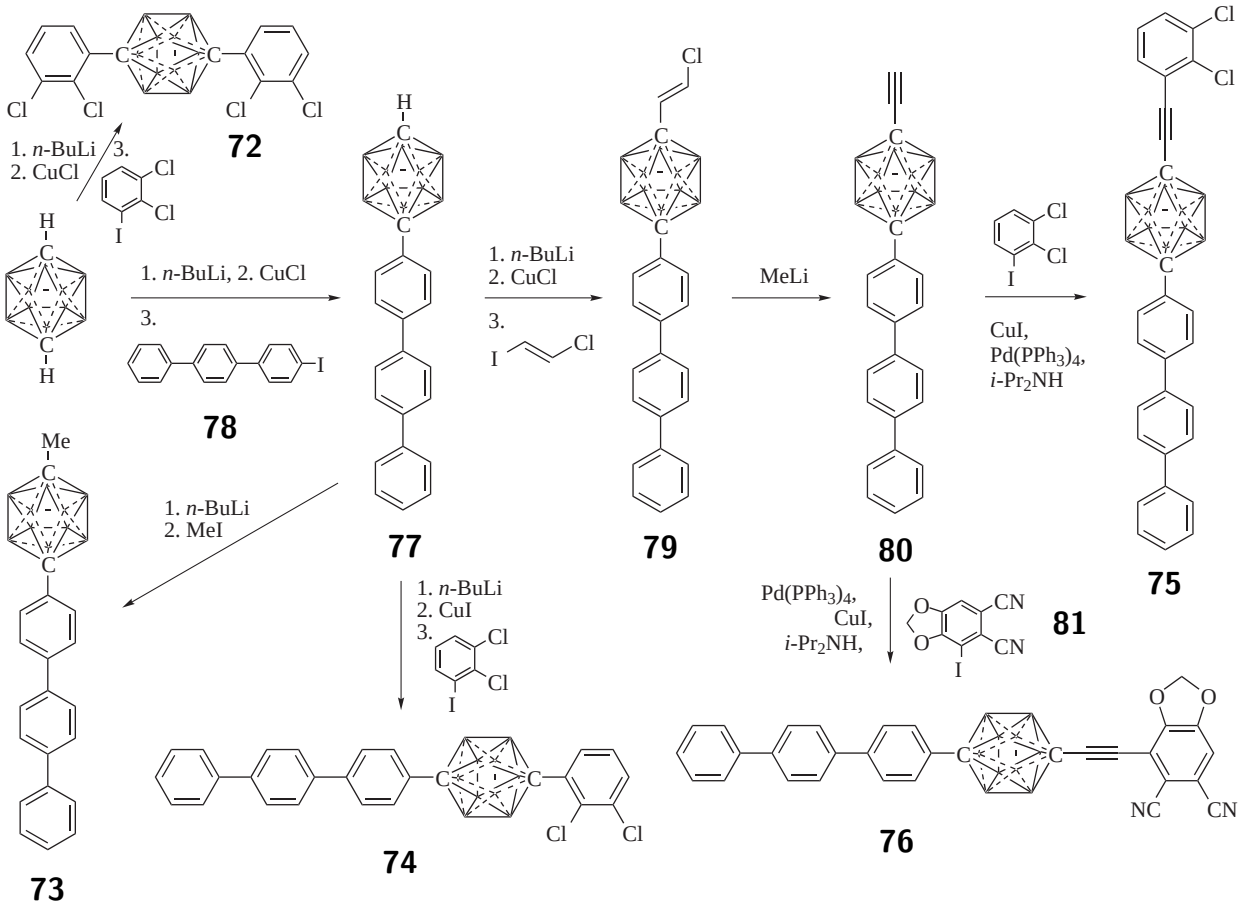

Scheme 2.6: Synthesis of the third generation rotors.

The compound **77** was made from *p*-carborane by the deprotonation with one equivalent of *n*-BuLi, and transmetallation with cuprous chloride, followed by the Ulmann coupling with **78** (81 % yield). The compound **78** was prepared by a modified literature iodination procedure from *p*-terphenyl using iodine, periodic acid and sulfuric acid in acetic acid (94 % yield).[117] The rotor **73** was prepared by the deprotonation of **77** with *n*-BuLi followed by methylation with methyl iodide (79 % yield).

The deprotonation of **77** with *n*-BuLi, transmetallation with cuprous chloride and the Ulmann coupling of the resulting organo-copper species with 1,2-dichloro-3-iodobenzene

leads to **74** (96 % yield), while the coupling with 2-iodo vinylchloride[118] provides **79** (76 % yield). The compound **79** was dehydrohalogenated with methyllithium to yield **80** (99 % yield). The product **80** was then coupled with 1,2-dichloro-3-iodobenzene using Sonogashira coupling to yield **75** (92 % yield).

The compound **72** was prepared by deprotonation of *p*-carborane with two equivalents of *n*-BuLi, and subsequent transmetallation with cuprous chloride and Ulmann coupling of the product with an excess 1,2-dichloro-3-iodobenzene (76 % yield). The Sonogashira coupling of **80** with **81**[119] yielded the rotor **76** (83 % yield).

The partially deuterated rotor **82** (Scheme 2.7) was prepared from **78**-d_{13} by the same sequence of reactions as the rotor **74**. The compound **78**-d_{13} was synthesized from *p*-terphenyl-d_{14} by iodination with iodine and silver nitrate (65 % yield).

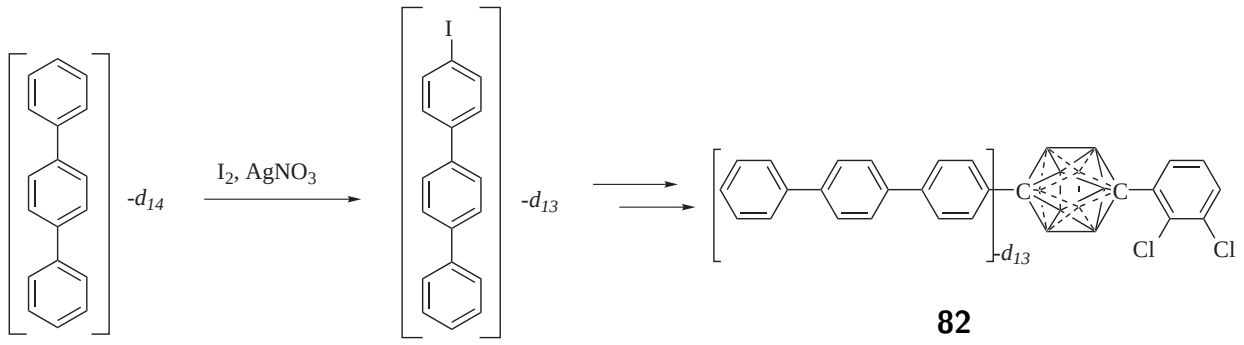

Scheme 2.7: Synthesis of the rotor **82**.

2.6.1.2 NMR Assignments

Rotor 74. The carbon atoms in the compound **74** were assigned using ^{1}H NMR, ^{1}H -^{1}H gCOSY (Figure 2.45), ^{1}H -^{13}C gHSQC (Figure 2.45), ^{1}H -^{13}C gHMBC (Figure 2.46a, b), and boron-decoupled ^{1}H -^{13}C gHMBC (Figure 2.46c), while keeping in mind that two-bond ^{1}H -^{13}C coupling constants are usually small and two-bond couplings are thus often not observed in the gHMBC spectra of aromatic compounds.

The proton H_e in the compound **74** was identified by its multiplicity in the ^{1}H NMR

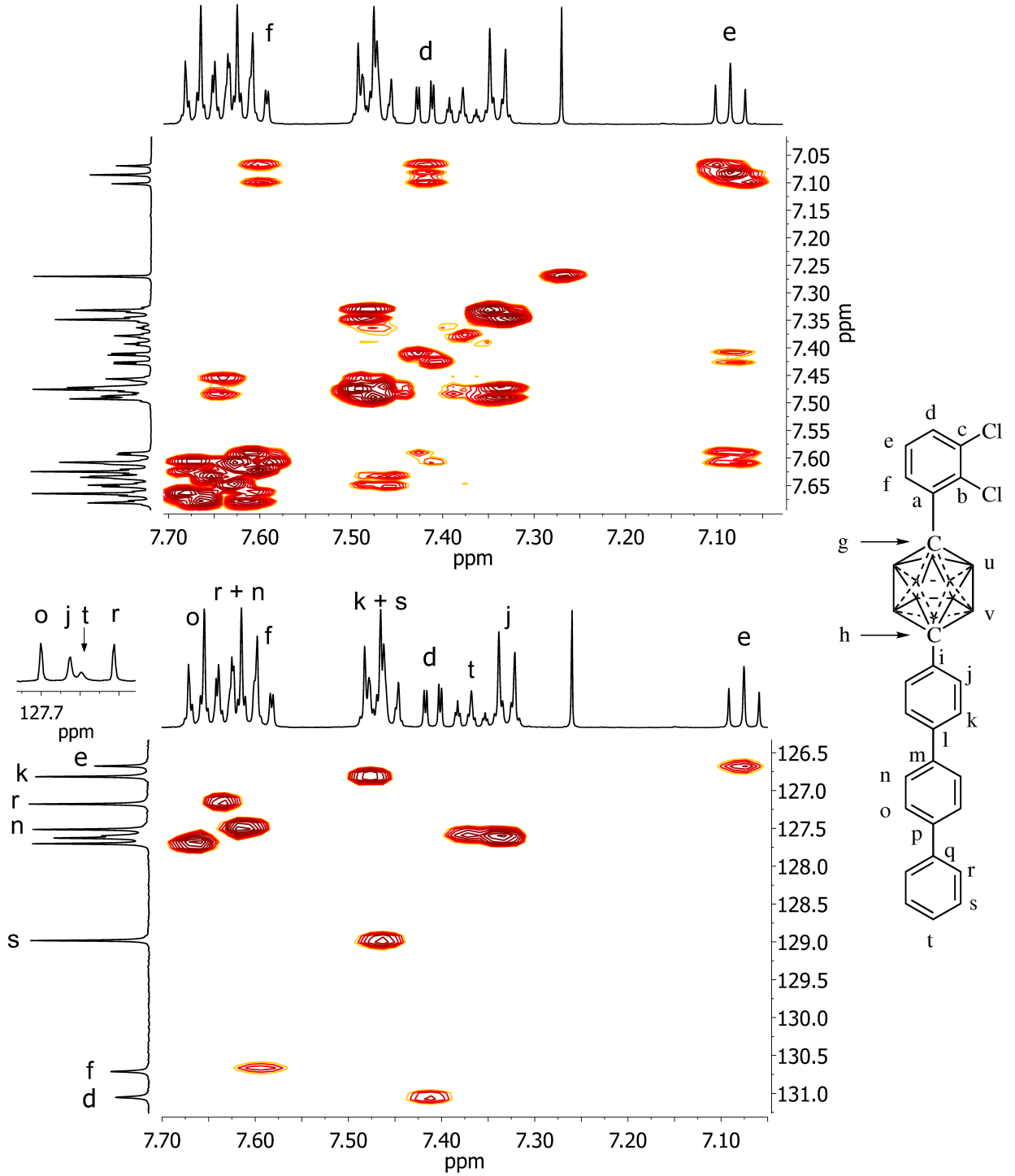

Figure 2.45: Compound **74** signal assignments: top: ^{1}H -^{1}H gCOSY; bottom: ^{1}H -^{13}C gHSQC.

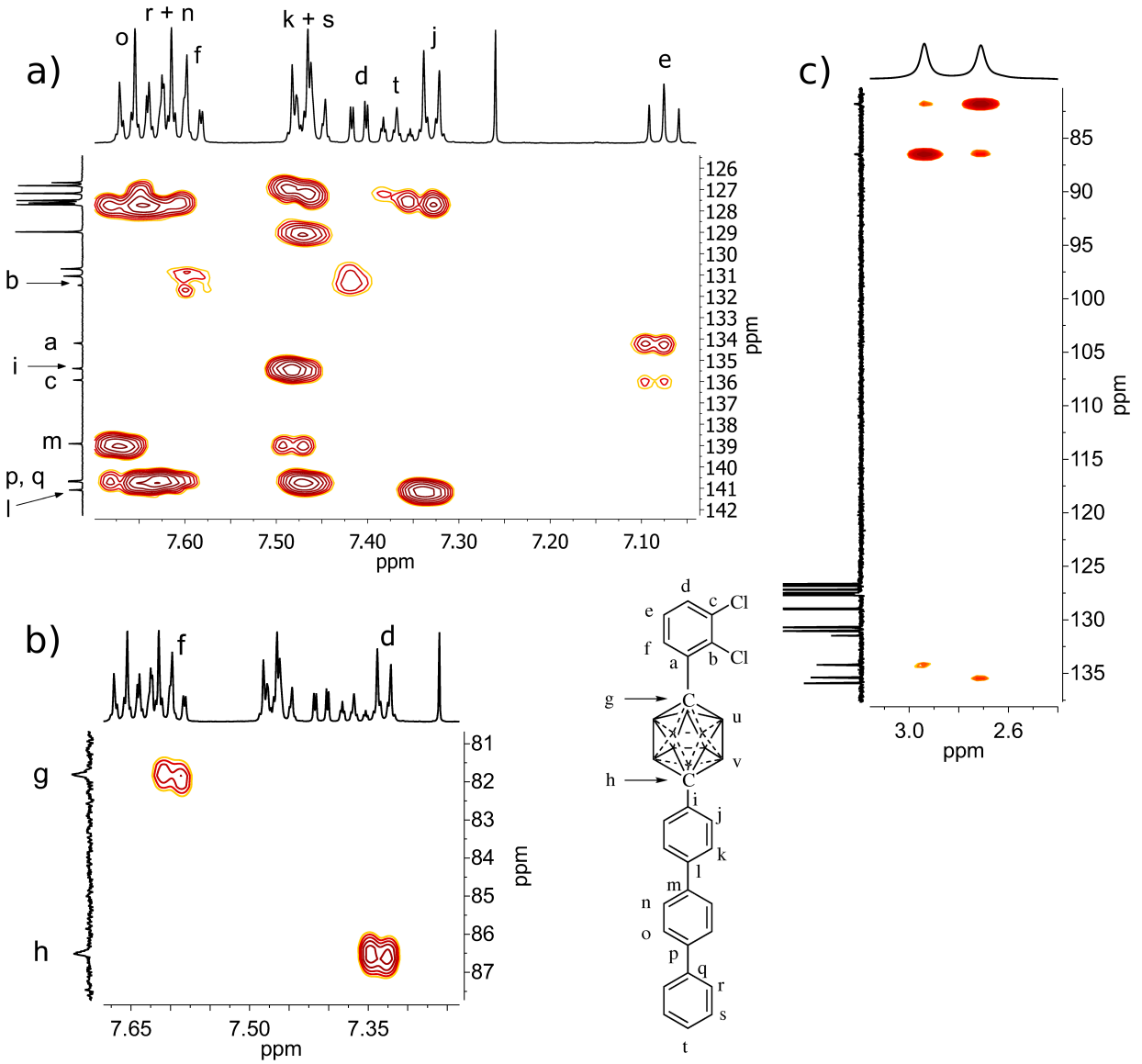

Figure 2.46: Compound **74** signal assignments: a) ^{1}H -^{13}C gHMBC (J = 8 Hz), b) ^{1}H -^{13}C gHMBC (J = 8 Hz, expansion), c) boron-decoupled ^{1}H -^{13}C gHMBC.

spectrum. The cross-peaks with H_d and H_f in the gCOSY spectrum identify the remaining protons of the 2,3-dichlorophenyl fragment in **74**. The coupling of H_f with carborane carbon C_g in the gHMBC spectrum helps to assign H_f, H_d, C_g, and C_h. The carbon C_b was identified by the cross-peaks with H_f and H_d in the gHMBC spectrum, and the carbons C_a and C_c were assigned based on the cross-peak of C_a with H_u in the boron-decoupled gHMBC spectrum.

The inspection of the gHSQC spectrum reveals the carbons C_d, C_e and C_f.

The cross-peak between C_h and H_j in the gHMBC spectrum identifies H_j, and the coupling of H_j to H_k in the gCOSY spectrum reveals the hydrogen H_k. The carbon C_i was identified by its coupling to H_k in the gHMBC spectrum, and by coupling to H_v in the boron-decoupled gHMBC spectrum.

The cross-peaks between H_j and C_l, H_k and C_m, C_m and H_o in the gHMBC spectrum assign C_l, C_m, and H_o. The coupling between H_o and H_n in the gCOSY spectrum helps to assign the proton H_n. The cross-peaks (unresolved in the carbon dimension) between H_o and C_q, C_p and H_r, C_q and H_s in the gHMBC spectrum help with the assignment of the C_p, C_q, H_r, and H_s signals, while taking into account reasonable proton chemical shift for the oligophenylene system. The couplings of H_r with H_s and H_s with H_t confirm the H_r, and H_s proton assignments and identify the remaining proton H_t. The missing carbons or protons were identified from the gHSQC spectrum. The results are summarized in Table 2.6.

Table 2.6: NMR assignments for **74**.

Atom	Solution ^{13}C NMR δ [ppm]	Solution ^{1}H NMR δ [ppm]	Atom	Solution ^{13}C NMR δ [ppm]	Solution ^{1}H NMR δ [ppm]
a	134.20	-	k	126.82	7.48*
b	131.48	-	l	141.08	-
c	135.93	-	m	138.91	-
d	131.05	7.41	n	127.51	7.62*
e	126.68	7.08	o	127.70	7.66*
f	130.71	7.60*	p, q	140.66,140.69	-
g	81.80	-	r	127.18	7.64*
h	86.52	-	s	128.98	7.46*
i	135.39	-	t	127.60	7.37
j	127.63	7.33			

* Approximate chemical shift. Accurate value could not be determined due to signal overlap.

Rotor 75. The proton H_e in **75** was identified by its multiplicity in the ^{1}H NMR spectrum. The other protons of the 2,3-dichlorophenyl ring (H_d and H_f) were found based

on their cross-peaks with H_e in the ^1H -^1H gCOSY spectrum (Figure 2.47). Protons H_f and H_d were identified by the cross-peak between H_f and the carbon C_w in the ^1H -^{13}C gHMBC spectrum (Figure 2.48a). The chemical shift of C_w was also taken into account for the assignment. The carbons C_d, C_e and C_f were assigned based on their cross-peaks with protons H_d, H_e and H_f in the ^1H -^{13}C gHSQC spectrum (Figure 2.47).

The cross-peak between the carbon C_a and proton H_e in the gHMBC spectrum reveals C_a, taking into account the value of the chemical shift. The carbons C_c and C_b were assigned based on their cross-peaks with H_e and H_di, respectively, in the gHMBC spectrum. The determinations of the *p*-carborane carbon chemical shift C_g, C_h and acetylenic carbon C_x were made based on the value of the chemical shift and on the cross-peaks with H_u and H_v in the boron-decoupled gHMBC spectrum (Figure 2.48c).

The cross-peak between C_h and H_j in the gHMBC spectrum reveals the proton H_j, and the cross-peak between H_v and C_i in the boron decoupled gHMBC spectrum assigns the signals of C_i, H_u, H_v. The proton H_k was assigned based on its cross-peak with H_j in the gCOSY spectrum, and its cross-peak with H_i in the gHMBC spectrum. The carbon C_l was identified by its cross-peak with the proton H_j in the gHMBC spectrum. The carbon C_m was identified by its cross-peak with H_k in the gHMBC spectrum.

The proton H_t was assigned based on its multiplicity in the ^1H NMR spectrum. The atoms H_r, H_s, C_r, C_s, C_p and C_q were assigned based on the cross-peak between H_t, H_s, and H_r in the gCOSY spectrum, and the cross-peaks between H_t and C_r, H_s and C_q, H_s and C_s in the gHMBC spectrum.

The assignments of atoms H_n, H_o, C_n, and C_o are based on the cross-peak between H_o with C_m and C_q, the cross-peak between H_n and C_p in the gHMBC spectrum, and the cross-peak between H_n and H_o in the gCOSY spectrum. The remaining carbons and protons were assigned using the gHSQC spectrum. The results are summarized in Table 2.7.

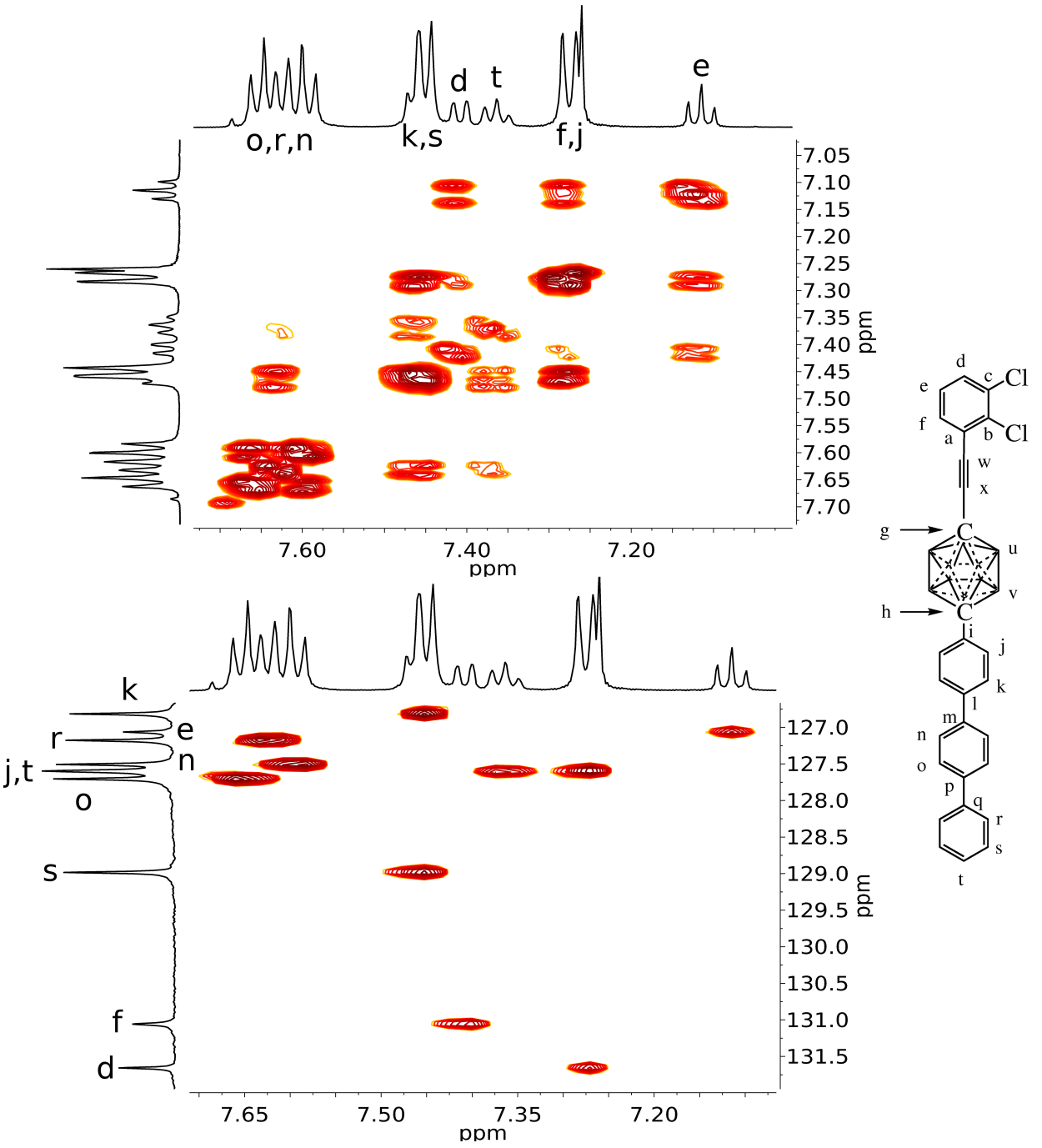

Figure 2.47: Compound **75** signal assignments. Top: ^{1}H -^{1}H gCOSY, bottom: ^{1}H -^{13}C gHSQC.

2.6.1.3 Inclusion Compound Preparation

The homogeneous inclusion compounds were prepared by ball milling of empty hexagonal TPP-d_{12} with the neat rotor followed by annealing at 70 to 75 °C and repetition of the

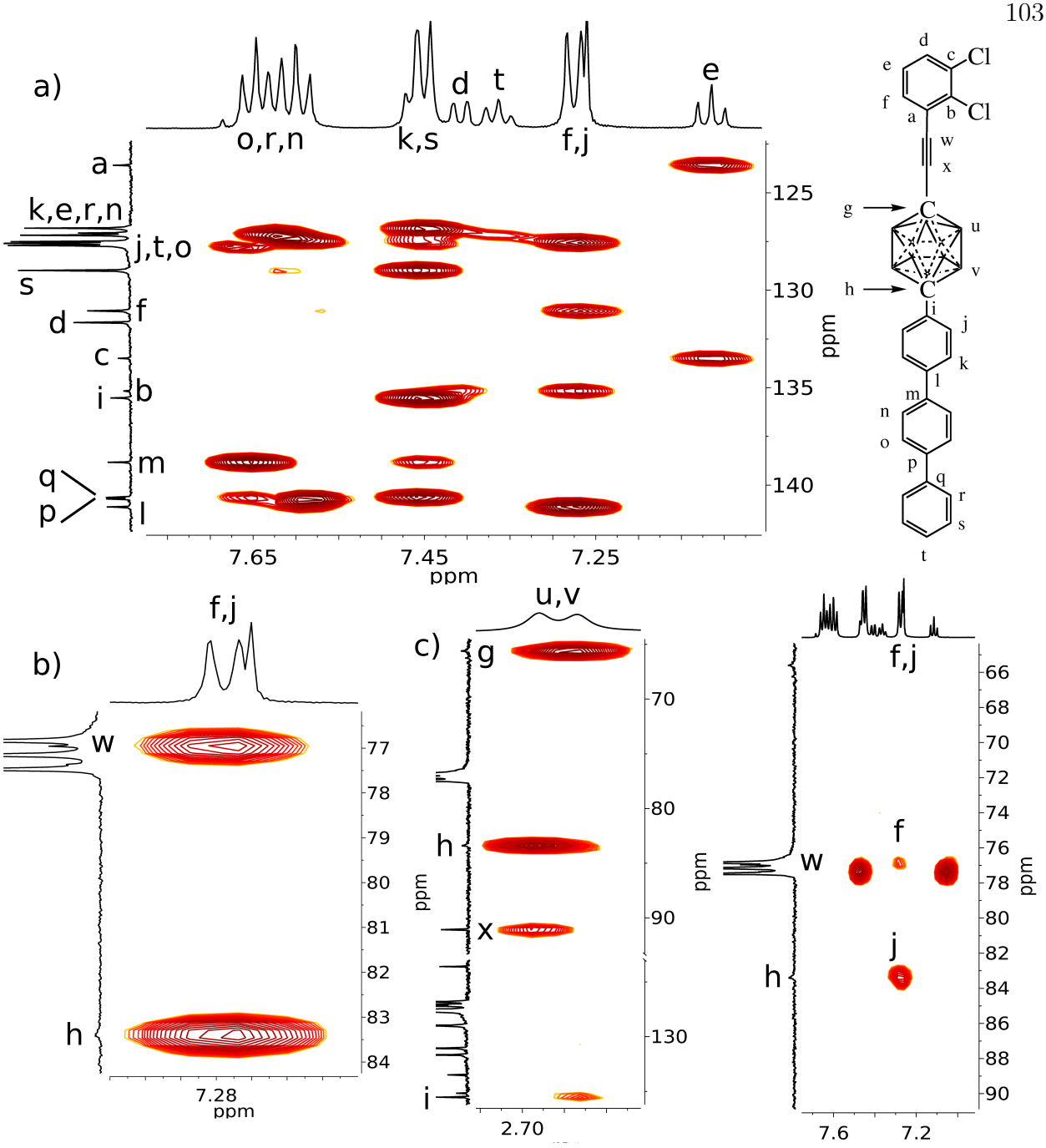

Figure 2.48: Compound **75** signal assignments: a) and b) ^{1}H -^{13}C gHMBC (J = 8 Hz), c) boron-decoupled ^{1}H -^{13}C gHMBC (J = 18 Hz).

two steps. The heterogeneous inclusion compounds were prepared by ball milling the neat rotor and empty hexagonal TPP-d_{12} without the annealing step.

Table 2.7: NMR assignments for **75**.

Atom	Solution ^{13}C NMR δ [ppm]	Solution ^{1}H NMR δ [ppm]	Atom	Solution ^{13}C NMR δ [ppm]	Solution ^{1}H NMR δ [ppm]
a	123.59	-	m	138.83	-
b	135.17	-	n	127.51	7.59*
c	133.50	-	o	127.71	7.66*
d	131.66	7.41	p	140.71	-
e	127.06	7.12	q	140.63	-
f	131.06	7.28*	r	127.18	7.63*
g	65.62 1	-	s	128.98	7.45*
h	83.39	-	t	127.61	7.37*
i	135.53	-	u	-	2.68
j	127.60	7.28*	v	-	2.64
k	126.82	7.47*	w	76.96	-
l	141.12	-	x	91.08	-

* Approximate chemical shift (signal overlap).

2.6.1.4 Solid-State NMR

Rotor 73 and its Inclusion Compound. The ^{31}P CP MAS (Figure 2.49d), and ^{31}P SPE MAS solid-state NMR (Figure 2.49e) spectra of the inclusion compound 15%**73**@TPP-d_{12} (15 mol. % **73** in TPP-d_{12}) both show a single resonance at 34.0 ppm.

Figure 2.49a,b shows the ^{13}C NMR spectra of **73**. The solid-state ^{13}C CP MAS NMR of neat **73** (5 ms contact time, Figure 2.49a) shows five resolved quaternary aromatic carbons between 133 and 140 ppm, unresolved protonated aromatic signals between 123 and 130 ppm, a peak for each carborane carbon (76.2 and 79.5 ppm), and a peak of the methyl (26.4 ppm).

The solution ^{13}C NMR spectrum of **73** in deuterated chloroform (Figure 2.49b) shows all the signals resolved. The CP MAS solid-state NMR spectrum of the inclusion compound 15%**73**@TPP-d_{12} obtained with 5 ms contact time, dipolar dephasing (DPD) and total side-band suppression (TOSS) (Figure 2.49c) displays only non-protonated carbon signals, while the ^{13}C CP MAS solid-state NMR spectrum of the inclusion compound 15%**73**@TPP-d_{12}

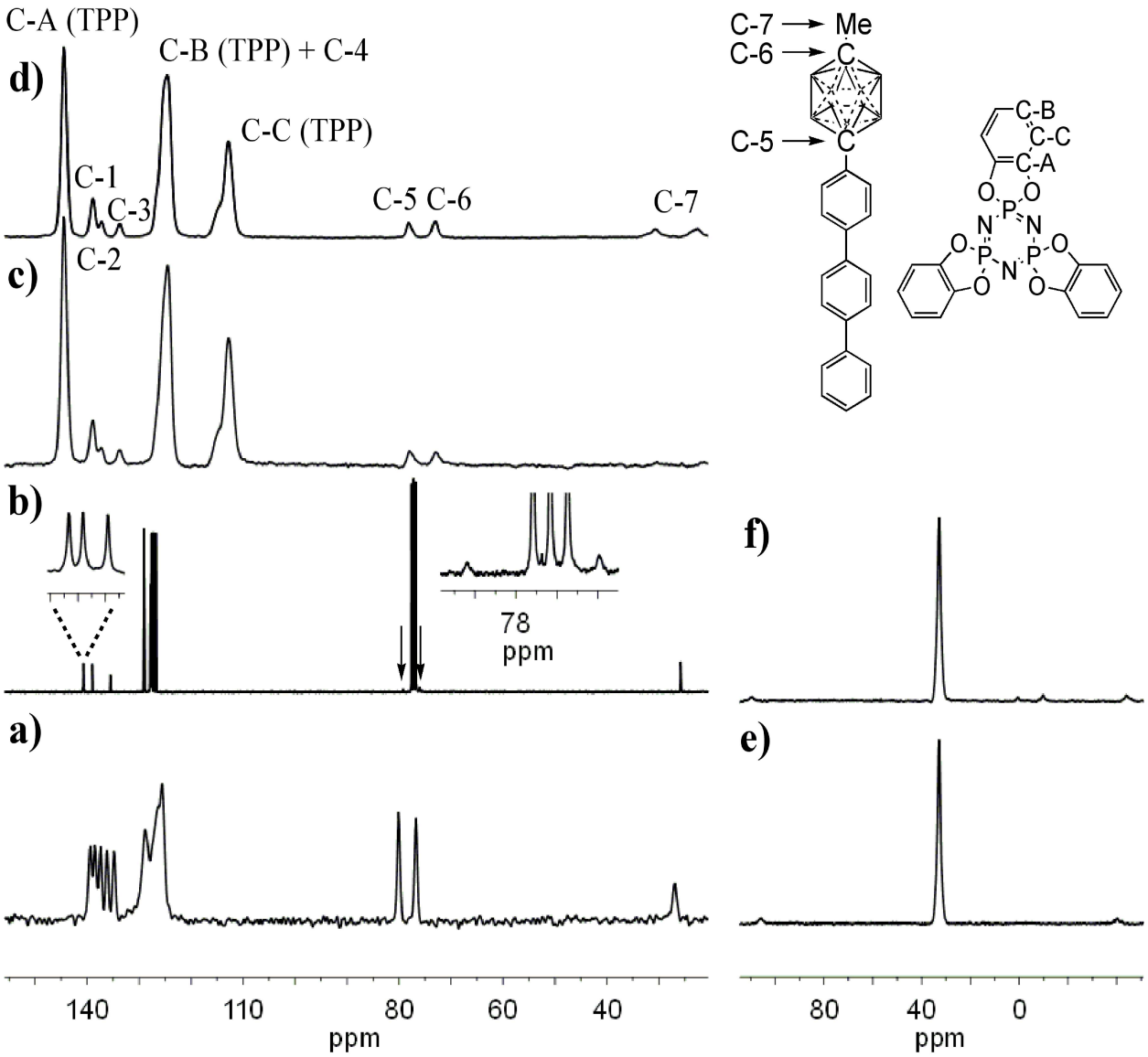

Figure 2.49: Compound **73** NMR spectra: a) ^{13}C CP MAS solid-state NMR spectrum of neat **73**; b) solution ^{13}C NMR in $CDCl_3$; c) ^{13}C CP MAS with DPD and TOSS of the inclusion compound 15%**73**@TPP-d_{12}; d) ^{13}C CP MAS NMR of 15%**73**@TPP-d_{12}; e) ^{31}P CP MAS solid-state NMR spectrum of 15%**73**@TPP-d_{12}; f) ^{31}P SPE MAS solid-state NMR spectrum of 15%**73**@TPP-d_{12}.

obtained with 5 ms contact time (Figure 2.49d) shows both protonated and non-protonated carbons.

The five quaternary aromatic carbons in the compound **73** give rise to three peaks

in the spectra of the inclusion compound 15%**73**@TPP-d_{12} (C-1, C-2, and C-3, Figure 2.49 spectra c) and d). The carborane carbons give rise to two peaks (C-5 and C-6) in all spectra. All the aromatic and carborane signals in the ^{13}C solid-state NMR spectra of the inclusion compound 15%**73**@TPP-d_{12} show a strong upfield shift of about 1.0 to 1.9 ppm relative to the solution spectrum (Table 2.8b). The protonated aromatic carbons of the inclusion compound 15%**73**@TPP-d_{12} also exhibit a strong upfield shift, and they overlap with C-B of TPP-d_{12}. The methyl signal in the inclusion compound 15%**73**@TPP-d_{12} exhibits two separate broad peaks. One of them is shifted upfield, and the other one downfield with respect to the solution spectrum of **73**.

Table 2.8: NMR signal assignments for **73**.

	C-1	C-2	C-3	C-4	C-5	C-6	C-7
73 in $CDCl_3$ δ [ppm]	140.73 to 140.59	139.00	135.49	128.97 to 126.70	79.20	75.96	25.83
15%**73**@TPP-d_{12} δ [ppm]	138.88	137.26	133.70	124.58	78.15	73.03	22.62, 30.64

Rotor 72 and its inclusion compound. The solid-state ^{13}C CP MAS NMR spectrum of **72** (Figure 2.50b) and of the inclusion compound 15%**72**@TPP-d_{12} (Figure 2.50a, 15 mol % **72** in TPP-d_{12}, prepared by the ball milling/annealing procedure) was recorded using 5 ms contact time.

The inclusion compound spectrum is different from the neat **72** solid-state ^{13}C spectrum, and shows three intense aromatic resonances that belong to TPP-d_{12}, and signals A, B, C and D that belong to the guest compound **72**. The upfield TPP-d_{12} signal is split into two signals.

The solid-state ^{13}C CP MAS NMR spectrum of **72** (Figure 2.50d) with dipolar dephasing only shows non-protonated signals, while the solid-state ^{13}C CP MAS NMR spectrum of **72** with a short contact time (0.2 ms, Figure 2.50e) displays protonated carbon signals en-

hanced relative to non-protonated ones. The comparison of the two spectra reveals that the signals A and B belong to quaternary aromatic carbons, and signal C contains protonated and non-protonated carbon signals. The short contact time experiment shows an additional protonated carbon, D.

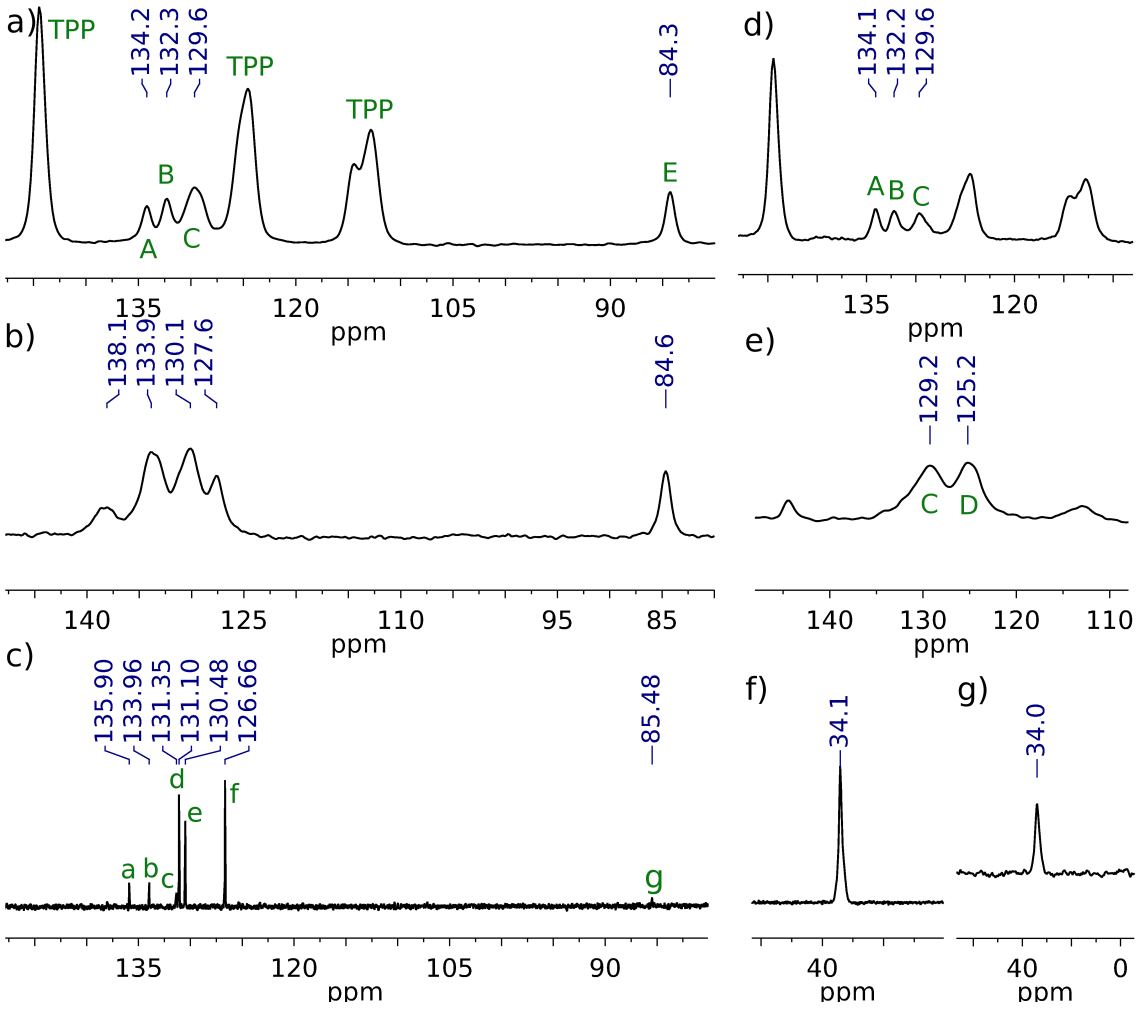

Figure 2.50: **72** and 15%**72**@TPP-d_{12} NMR: a) 15%**72**@TPP-d_{12} ^{13}C CP MAS, b) neat **72** ^{13}C CP MAS, c) **72** solution ^{13}C ($CDCl_3$), d) 15%**72**@TPP-d_{12} ^{13}C CP MAS with DPD, e) 15%**72**@TPP-d_{12} ^{13}C CP MAS with short contact time, f) 15%**72**@TPP-d_{12} ^{31}P SPE MAS, 15%**72**@TPP-d_{12} ^{31}P CP MAS.

The solution ^{13}C NMR spectrum of the rotor **72** (Figure 2.50c) displays six resolved

aromatic signals. The signals C_a, C_b and C_c belong to the quaternary carbons of the 2,3-dichlorophenyl rotator, and the signals C_d, C_e and C_f correspond to the protonated aromatic carbons of the rotator. The signal C_g belongs to the *p*-carborane carbons.

The comparison of the solid-state ^{13}C NMR spectrum to the **72** solution spectrum suggests that the carbon C_a gives rise to the signal A in the inclusion compound solid-state spectrum, the carbon C_b is equivalent to signal B and a part of the signal C belongs to the carbon C_c. The remaining intensity of the signal C and the signal D belong to the protonated carbons C_d, C_e and C_f. The signal E belongs to the *p*-carborane carbons C_g. All the aromatic signals of **72** in 15%**72**@TPP-d_{12} are shifted upfield relative to the solution ^{13}C NMR spectrum of **72**, and the *p*-carborane carbons are shifted upfield by 1.2 ppm.

The solid-state ^{31}P SPE MAS NMR (Figure 2.50f) and ^{31}P CP MAS NMR (Figure 2.50g) both show a single resonance at 34.1 and 34.0 ppm, respectively.

Rotor 74 and its inclusion compounds. The ^{31}P CP MAS solid-state NMR (Figure 2.52f) and ^{31}P SPE MAS solid-state NMR (Figure 2.52e) of the inclusion compound 15%**74**@TPP-d_{12} (15 mol. % of the rotor**74** in TPP-d_{12}) both show a single resonance at 34.0 ppm.

The ^{13}C NMR spectra of **74** are shown in Figure 2.51. The ^{13}C CP MAS solid-state NMR spectrum of neat **74** (Figure 2.51a) was recorded using 5 ms contact time and it shows a series of broad largely overlapping peaks in the aromatic region, and a distinct peak for each *p*-carborane carbon at 82.7 and 87.5 ppm.

The solution ^{13}C NMR spectrum of **74** shows all the peaks resolved and the *p*-terphenyl resonances show nearly identical chemical shifts as the solution ^{13}C NMR spectrum of **73**.

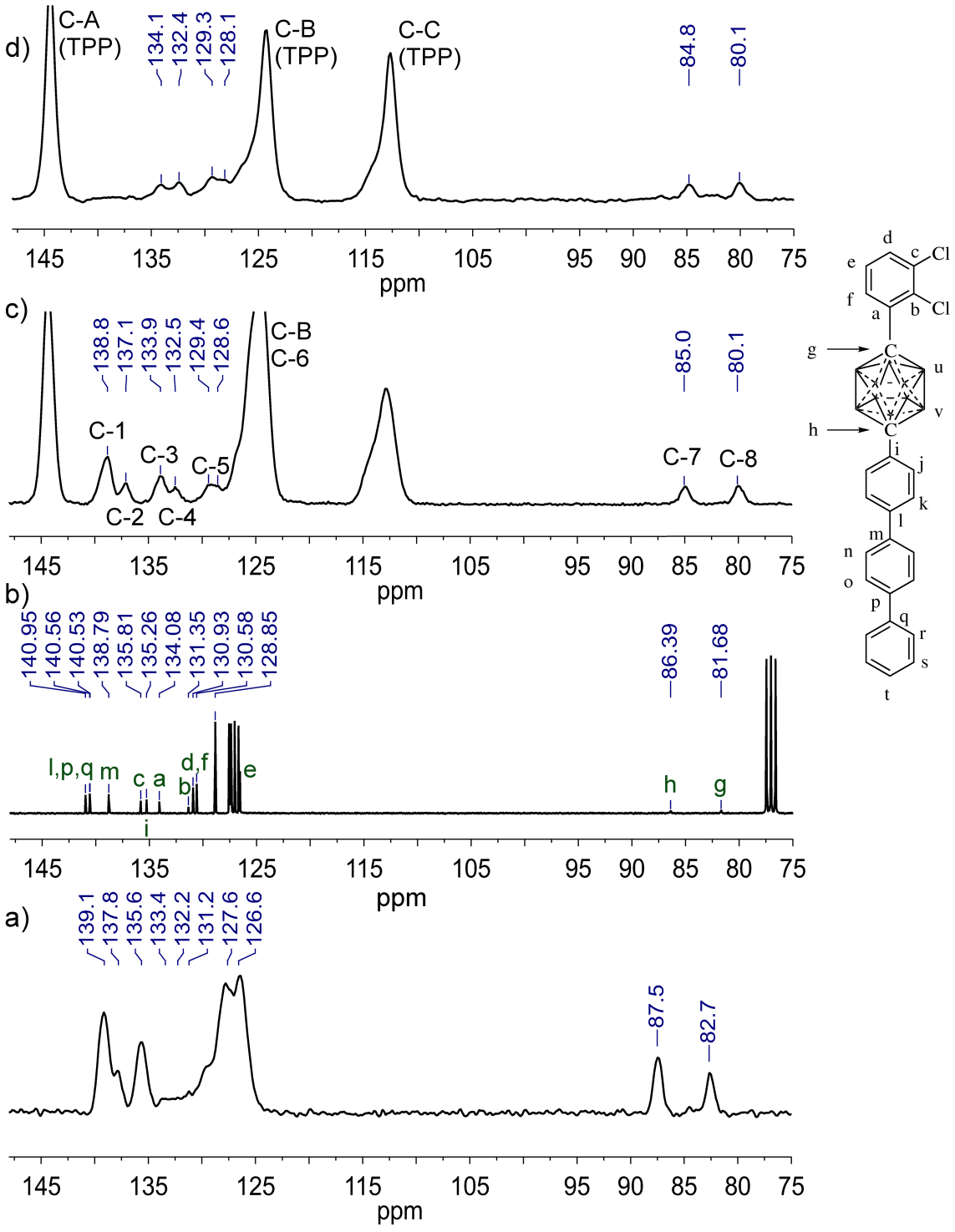

Figure 2.51: a) ^{13}C solid-state NMR of neat **74**, b) **70** solution ^{13}C NMR in $CDCl_3$, c) ^{13}C CP MAS solid-state NMR of 15%**74**@TPP-d_{12}, d) ^{13}C CP MAS solid-state NMR of 9%**82**@TPP-d_{12} .

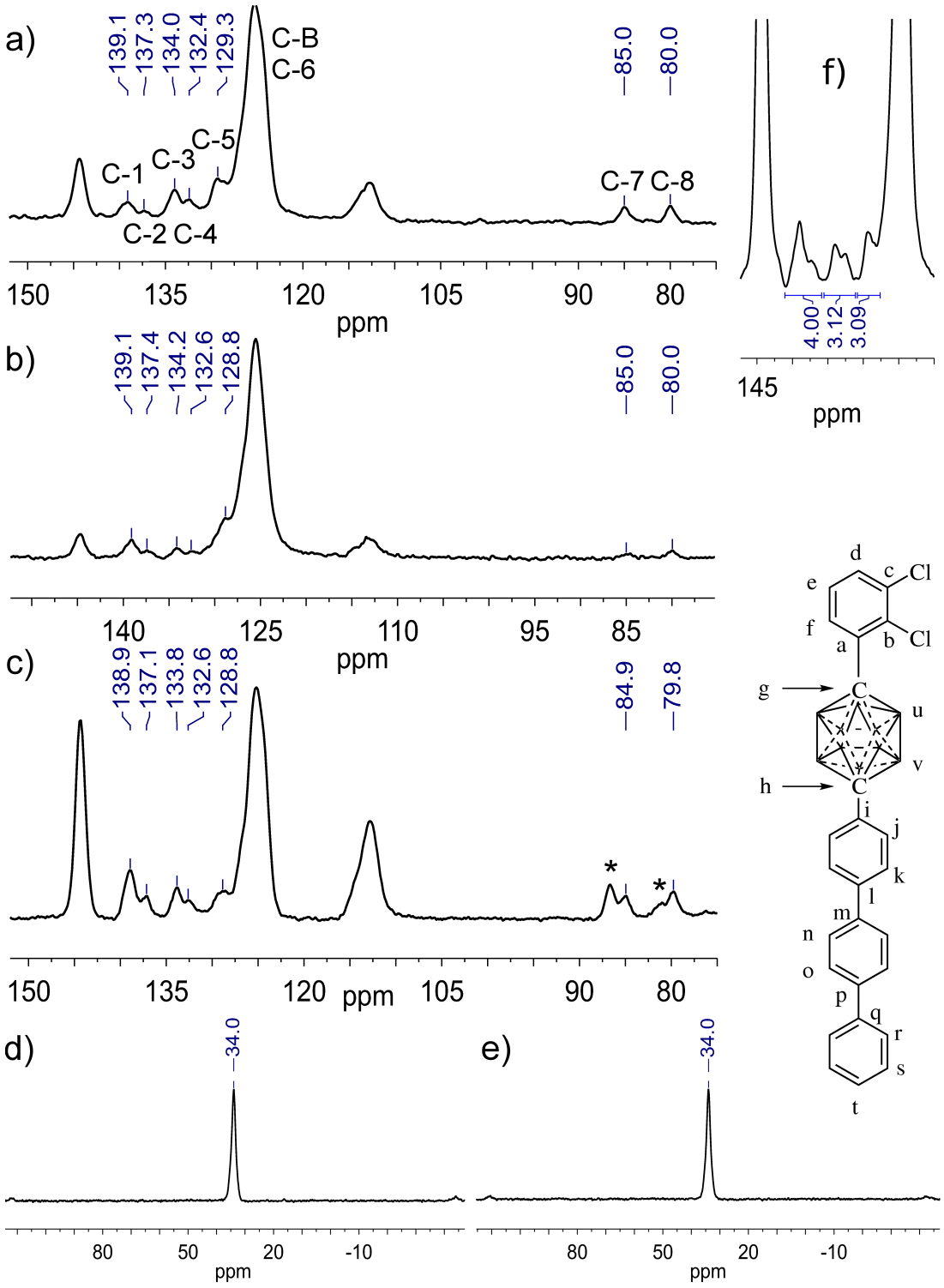

Figure 2.52: solid-state NMR of 15%**74**@TPP-d_{12} a), f) ^{13}C SPE MAS with a short (a) and long (f) relaxation delay, b) ^{13}C CP MAS with a short contact time, c) ^{13}C CP MAS with DPD; d) ^{31}P SPE MAS, e) ^{31}P CP MAS solid-state NMR. (* spinning sidebands)

The solid-state ^{13}C CP MAS NMR spectrum of the inclusion compound 15%**74**@TPP-d_{12} (Figure 2.51c) displays three intense aromatic singlet resonances associated with hexagonal TPP and a series of aromatic and two resolved *p*-carborane resonances, associated with the guest rotor. The spectrum shows a similar pattern of signals as the solid-state ^{13}C spectrum of neat **74**, but the spectra are distinctly different. The signals in the spectrum of the inclusion compound 15%**74**@TPP-d_{12} are better resolved and they are shifted upfield by 1-2 ppm relative to the ^{13}C CP MAS solid-state spectrum of neat **74**.

In order to assign the aromatic signals, several additional solid-state spectra were recorded for the inclusion compound 15%**74**@TPP-d_{12}: ^{13}C SPE MAS with a short (Figure 2.52a) and long (Figure 2.52f) relaxation delay, ^{13}C CP MAS NMR with a short contact time (0.2 ms) (Figure 2.52c), and ^{13}C CP MAS NMR spectrum with DPD using 5 ms contact time (Figure 2.52c)

The ^{13}C CP MAS solid-state NMR spectrum of the inclusion compound 15%**74**@TPP-d_{12} obtained with DPD shows only non-protonated carbons, while the ^{13}C CP MAS solid-state NMR spectrum of the inclusion compound 15%**74**@TPP-d_{12} obtained with a short contact time (0.2 ms, Figure 2.52b), shows protonated carbon signals enhanced relative to quaternary carbons. The two experiments reveal that the peaks C-1 and C-2 belong to quaternary carbons. The same peaks with identical chemical shifts are also found in the solid-state ^{13}C NMR spectrum of the inclusion compound 15%**73**@TPP-d_{12} (C-1 and C-2, Figure 2.49c), and they therefore belong to the four *p*-terphenyl carbons. The fifth signal of the *p*-terphenyl carbon, C-3, in the inclusion compound 15%**74**@TPP-d_{12} overlaps with that of another quaternary carbon that belongs to the 2,3-dichlorophenyl fragment. The carbons C-4 and C-5 contain signals from the two quaternary carbons of 2,3-dichlorophenyl fragment, and the peak C-5 contains at least one of the three protonated carbons of the 2,3-dichlorophenyl fragment.

The quantitative solid-state ^{13}C SPE MAS NMR spectrum of 15%**74**@TPP-d_{12} (long relaxation delay, Figure 2.52b) shows that the peaks C-1 and C-2 contain four carbons, peaks

C-3 and C-4 integrate to three and peak C-5 to three. The integration of the signal C-5 is not accurate due to an overlap with a TPP signal.

The solid-state ^{13}C CP MAS NMR spectrum of an inclusion compound 9%**82**@TPP-d_{12} (9 mol % **82** in TPP-d_{12}, Figure 2.51d) only contains the signals of the 2,3-dichlorophenyl fragment as the deuterated *p*-terphenyl carbons in TPP-d_{12} channels do not get significantly cross-polarized by the protons in the sample, and they are missing in the spectrum. The comparison with the 15%**74**@TPP-d_{12} ^{13}C CP MAS solid-state NMR spectrum confirms the assignment of the carbons C-1, C-2 and part of C-3 to *p*-terphenyl and C-4, C-5 and part of C-3 to 2,3-dichlorophenyl.

The C-B peak in the spectrum of the inclusion compound 9%**82**@TPP-d_{12} is sharper than the C-B signal in the solid-state spectra of the inclusion compound 15%**74**@TPP-d_{12} ^{13}C , which has a downfield shoulder. This indicates that a significant portion of the signal from the protonated carbons of the *p*-terphenyl lies in this shoulder. The remaining aromatic signals (C-4, C5, and part of C-3) belong to the 2,3-dichlorophenyl fragment.

The comparison with the solution ^{13}C NMR spectrum of compound **74** suggests that the signal C-1 corresponds to the carbons C_l, C_p and C_q, while the signal C-2 to C_m and a part of signal C-3 belong to C_i. Most of the protonated carbon signals are not resolved (C-6) and they overlap with the TPP peak C-B. The remaining part of peak C-3 belongs to the carbon C_a, C-4 to the carbon C_c, and a part of the peak C-5 corresponds to the carbon C_b. All the quaternary and protonated carbons are shifted upfield with respect to the solution ^{13}C NMR spectrum.

All the aromatic and *p*-carborane carbons in the solid-state ^{13}C NMR spectra of the inclusion compound 15%**74**@TPP-d_{12} display a large upfield shift with respect to solution ^{13}C NMR spectrum of **74**. The assignments and changes in the chemical shift relative to the solution spectrum are summarized in Table 2.9.

Table 2.9: Summary of solid-state NMR assignments and the displacements in the chemical shift (15%**74**@TPP-d_{12} ^{13}C CP MAS solid-state NMR relative to **74** solution ^{13}C NMR).

Solid-state signal	Corresponding solution NMR signal	$\Delta\delta$ [ppm]	Solid-state signal	Corresponding solution signal	$\Delta\delta$ [ppm]
C-1	l, p, q	-1.7 to -2.2	C-5	b, d, f (?)	-2 to -3 (?)
C-2	m	-1.7	C-6	j, k, n, o, r, s, t	?
C-3	c, i	-1.4 to -1.9	C-7	h	-1.6
C-4	a	-1.5	C-8	g	-1.6

The ^{13}C CP MAS solid-state NMR spectrum of the heterogeneous inclusion compound (het-5%**74**@TPP-d_{12}) is shown in Figure 2.53d. The spectrum was recorded using a 5 ms contact time. It shows multiple sets of signals that are not fully resolved. The first set is more intense and it is identical to the signals of the homogeneous inclusion compound 15%**74**@TPP-d_{12}. The new sets of signals are different from ^{13}C CP MAS solid-state NMR spectra of both neat **74** and of the inclusion compound 15%**74**@TPP-d_{12} (Figure 2.53a,c).

The C-1 and C-2 signals are not as well resolved as in the homogeneous inclusion compound 15%**74**@TPP-d_{12} (Figure 2.53c), but they are better resolved than in the spectrum of the neat compound **74**. Both these signals exhibit upfield shift relative to the solution ^{13}C NMR spectrum of compound **74**. The signals corresponding to the peaks C-3 and C-4 in the inclusion compound 15%**74**@TPP-d_{12} are not resolved in the spectrum of the inclusion compound het-5%**74**@TPP-d_{12} due to presence of downfield shoulders for each of the peaks. These shoulders have similar chemical shifts as the signals of C_a, C_i and C_c in the solution ^{13}C NMR spectrum of compound **74**. The peak C-5 in the spectrum of the heterogeneous inclusion compound het-5%**74**@TPP-d_{12} also shows a small downfield shoulder relative to the homogeneous inclusion 15%**74**@TPP-d_{12}. This shoulder overlaps with signals of C_b, C_d and C_f. The peak C-6 in the spectrum of the heterogeneous inclusion compound het-

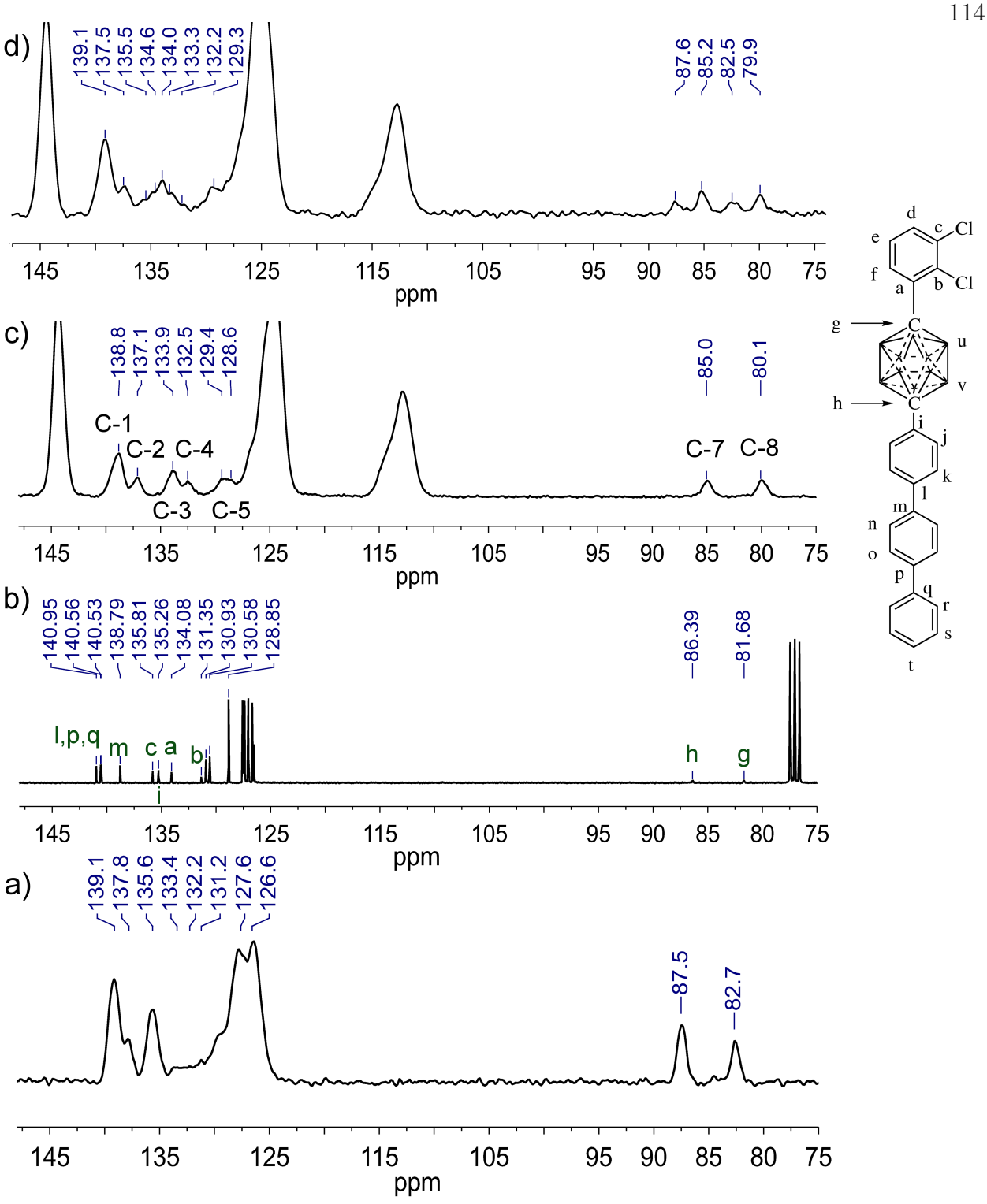

Figure 2.53: a) solution ^{13}C NMR of **74** in $CDCl_3$; b) neat **74** ^{13}C CP MAS solid-state NMR; c) ^{13}C CP MAS solid-state NMR of 15%**74**@TPP-d_{12}; d) ^{13}C CP MAS solid-state NMR het-5%**74**@TPP-d_{12}.

5%**74**@TPP-d_{12} overlaps with the TPP-d_{12} C-B signal, and it shows downfield shift relative to the homogeneous inclusion 15%**74**@TPP-d_{12} as well, but it is upfield relative to the solid-state spectrum of neat compound **74**. Each carborane carbon (C-7 and C-8) shows a few signals. One set is identical to the inclusion compound 15%**74**@TPP-d_{12}, and the other sets exhibit chemical shifts similar to those of the neat rotor **74**.

If the heterogeneous inclusion compound het-5%**74**@TPP-d_{12} is heated at 70 °C for about one day, it turns into the homogeneous inclusion compound with solid-state ^{13}C NMR spectra that closely resemble the 15%**74**@TPP-d_{12} solid-state ^{13}C NMR spectra. On the other hand, a mixture of finely ground compound **74** and TPP-d_{12} heated together under the same conditions does not form an inclusion compound.

Rotor 75 and its Inclusion Compounds. Both ^{31}P CP MAS (Figure 2.55d) and ^{31}P SPE MAS (Figure 2.55e) solid-state NMR spectra of the inclusion compound TPP-d_{12} (15%**75**@TPP-d_{12} (15 mol % **75** in TPP-d_{12}) show a single resonance at 34.1 ppm.

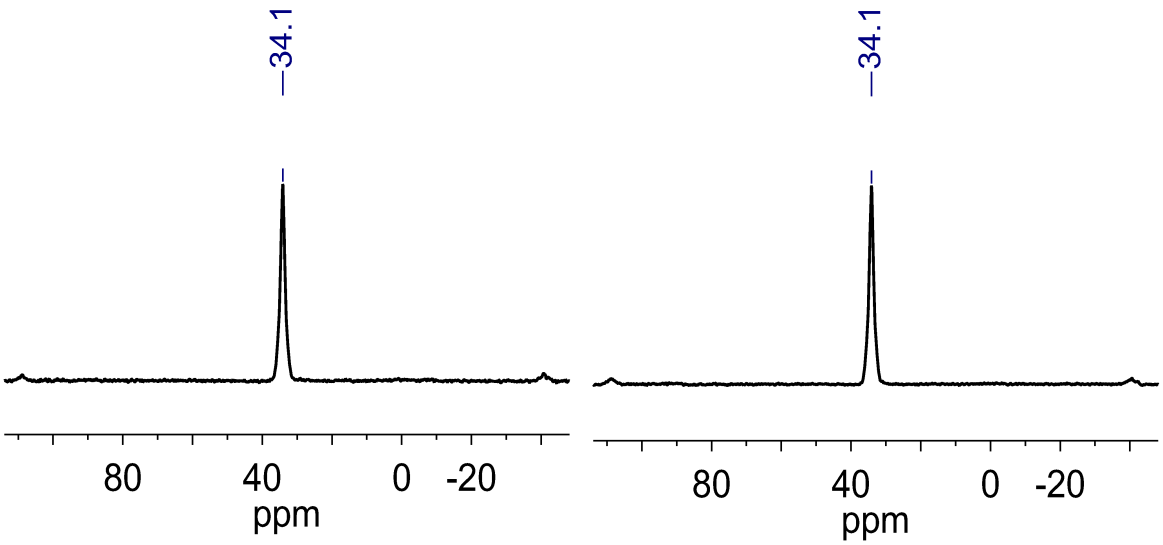

Figure 2.54: Solid-state ^{31}P NMR of 15%**75**@TPP-d_{12}: left: SPE MAS, right: CP MAS (the upfield and downfield small signals are spinning sidebands.

The solid-state ^{13}C CP MAS NMR spectrum of neat **75** (Figure 2.55a) was recorded

using a 5 ms contact time. It contains a series of aromatic resonances that are not fully resolved, and well separated resonances for each *p*-carborane and acetylene carbon.

The solid-state ^{13}C CP MAS NMR spectrum of the inclusion compound 15%**75**@TPP-d_{12} (Figure 2.55c) was recorded using a 5 ms contact time. The spectrum contains three intense aromatic signals (C-A, C-B and C-C) that belong to TPP-d_{12}. The signal C-B also contains protonated carbons (C-6) of the *p*-terphenyl substituent. The ^{13}C CP MAS solid-state NMR spectrum of the inclusion compound 15%**75**@TPP-d_{12} shows different chemical shifts from the neat compound **75** ^{13}C CP MAS solid-state NMR. The signals in the spectrum of the inclusion compound 15%**75**@TPP-d_{12} are better resolved and separated. The biggest difference in the carbon chemical shifts is exhibited by the protonated carbons (C-6, over 2 ppm upfield). In the inclusion compound 15%**75**@TPP-d_{12}, the quaternary *p*-terphenyl aromatic carbons display a small downfield (0.2 ppm) change in the chemical shift, and the signal C-3 is shifted by 1.2 ppm upfield. The signal of carbon C-7 partially overlaps with the signal C-B. The acetylenic and *p*-carborane carbons in the ^{13}C solid-state NMR spectrum of the inclusion compound display changes in the chemical shift relative to the solid-state spectrum of neat **74** (C-8: +0.1 ppm, C-9: -1.8 ppm, C-10: -4.7 ppm, C-11: +0.4 ppm).

The downfield part of the aromatic region shows a pattern (C-1, C-2 and C-3) similar to the solid-state ^{13}C NMR spectra of compound **73** and the inclusion compounds of **74** (Figure 2.49c and Figure 2.51c), and these signals likewise belong to the quaternary *p*-terphenyl carbons.

The signal C-5 in the inclusion compound ^{13}C CP MAS solid-state NMR spectrum of 15%**75**@TPP-d_{12} survives both dipolar dephasing (Figure 2.56c) and application of a short contact time (0.2 ms, Figure 2.56d), which indicates that it contains both protonated and quaternary carbon signals.

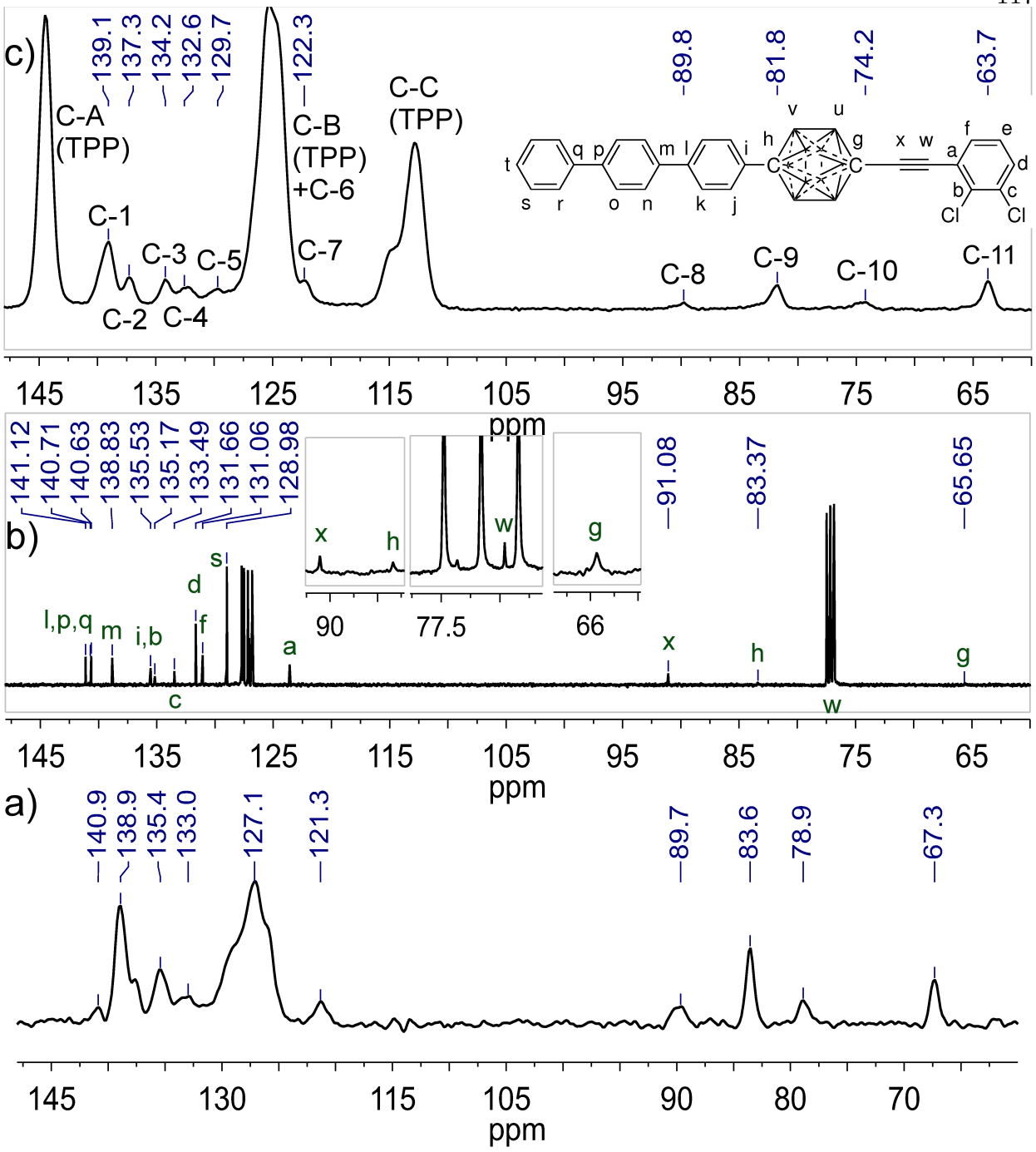

Figure 2.55: ^{13}C NMR of **75** and 15%**75**@TPP-d_{12} a) neat **75** CP MAS NMR, b) solution ^{13}C NMR in $CDCl_3$, c) 15%**75**@TPP-d_{12} CP MAS.

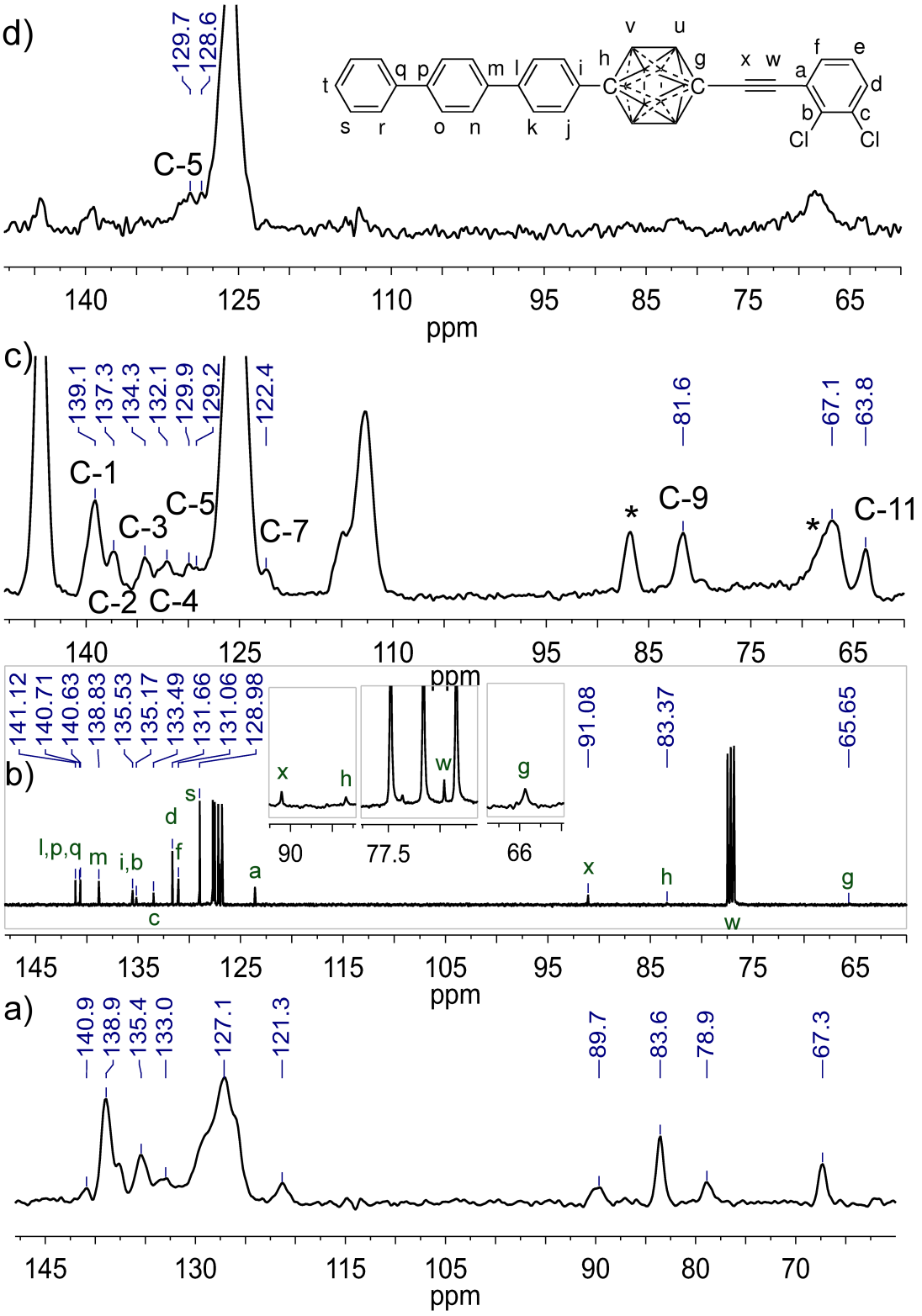

Figure 2.56: ^{13}C NMR of **75** and 15%**75**@TPP-d_{12}a) neat **75** CP MAS NMR, b) solution ^{13}C NMR in $CDCl_3$, c) 15%**75**@TPP-d_{12} CP MAS with DPD, d) 15%**75**@TPP-d_{12} CP MAS with short contact time. (* spinning sidebands)

The signal C-B in the ^{13}C CP MAS solid-state NMR spectrum of the inclusion compound 15%**75**@TPP-d_{12} obatained with a short contact time mostly consists of the protonated aromatic carbons. The comparison of its chemical shift with the solution spectrum of **75** shows an average upfield change in the chemical shift by more than 2 ppm.

The comparison of the solid-state ^{13}C spectra of the inclusion compound 15%**75**@TPP-d_{12} with solution ^{13}C NMR spectrum of **75** (Figure 2.55b) suggests that the signal C-1 belongs to carbons C_l, C_p and C_q, the signal C-2 belongs to the carbon C_m, and the signal C-3 corresponds to C_i. All the quaternary *p*-terphenyl carbon signals display upfield shifts of 1-2 ppm in the ^{13}C CP MAS NMR spectrum of the inclusion compound 15%**75**@TPP-d_{12} compared to the solution ^{13}C NMR spectrum of **75**.

The signals C-4, C-5 and C-7 belong to the 2,3-dichlorophenyl rotator. The signal C-4 represents the carbon C_b, and it is shifted upfield by 1 ppm with respect to the solution spectrum of **75**. The signal C-5 partially belongs to the carbon C_c, and again, it shows an upfield shift with respect to the solution spectrum **75**. The signal C-7 in the solid-state ^{13}C CP MAS NMR spectrum of the inclusion compound 15%**75**@TPP-d_{12} (Figure 2.55c) corresponds to the carbon C_a and it shows upfield change in the chemical shift by 1.3 ppm with respect to the solution ^{13}C NMR spectrum of **75**.

The signal C-8, C-9, C-10 and C-11 in the solid-state ^{13}C CP MAS NMR spectrum of the inclusion compound 15%**75**@TPP-d_{12} (Figure 2.55c) belong to the carbons C_w, C_h, C_x and C_g respectively, and they all display an upfield change in the chemical shift with respect to the solution ^{13}C NMR spectrum of **75** (C_w by 1.4 ppm, C_h: 2.8 ppm, C_x: 1.3 ppm, C_g: 1.9 ppm). Except for C-8, they all also show upfield change in chemical shift with respect to the solid-state ^{13}C CP MAS NMR spectrum of the neat compound **75** (Figure 2.55a, C_h: 1.8 ppm, C_w: 4.8 ppm, C_g: 3.6 ppm).

The solid-state ^{13}C CP MAS NMR spectra and ^{31}P SPE NMR of the inclusion compound 15%**75**@TPP-d_{12} annealed at 200 to 210 °C are shown in Figure 2.57.

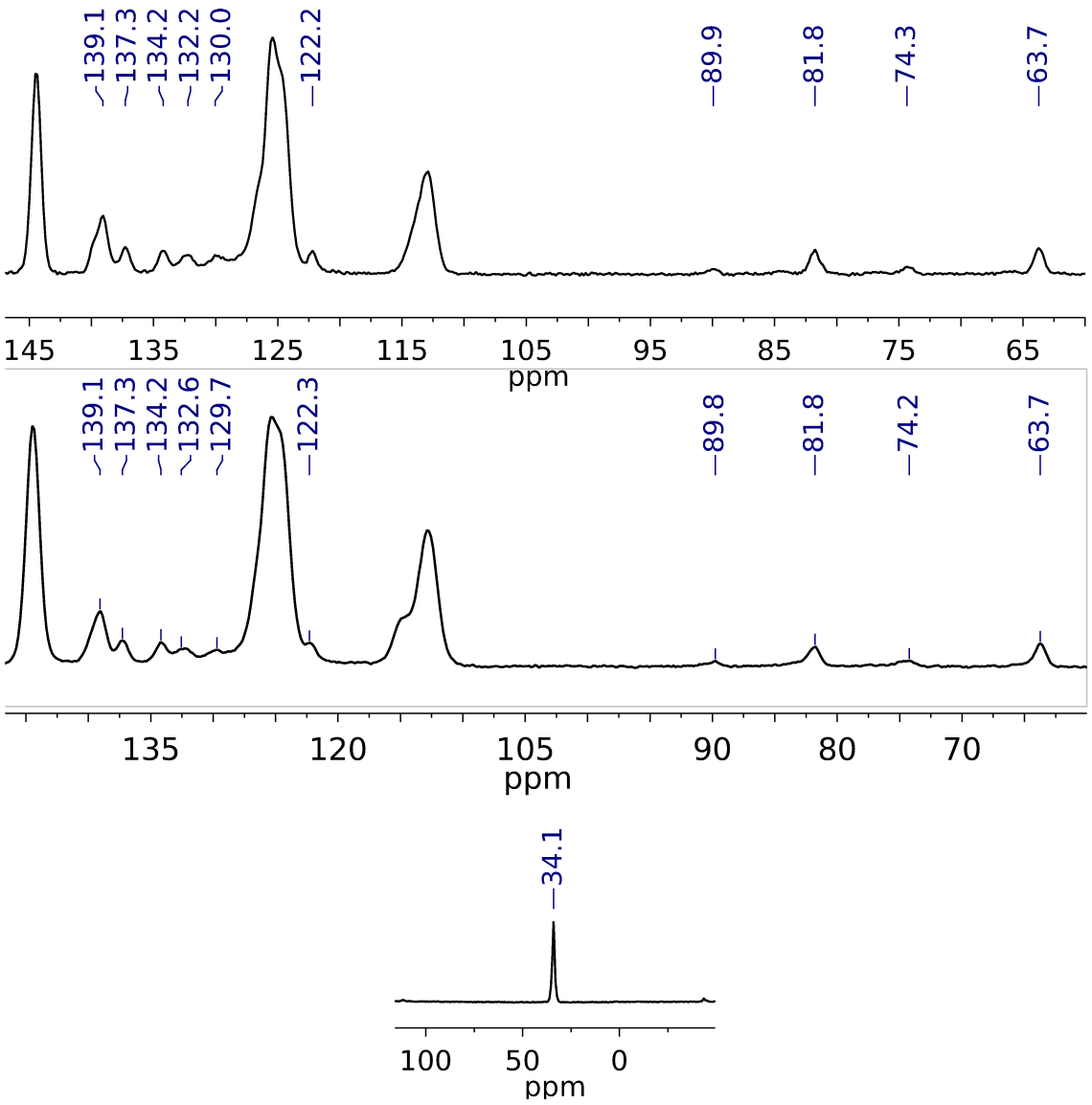

Figure 2.57: solid-state NMR of 15%**75**@TPP-d_{12}. Top: annealed at 200°C, ^{13}C NMR, middle: annealed at 70°C, ^{13}C NMR, bottom: annealed at 200°C, ^{31}P NMR.

The ^{13}C spectrum shows sharper and better resolved peaks than the spectrum of the inclusion compound 15%**75**@TPP-d_{12} that was annealed at 70 °C. The upfield shoulder of the upfield TPP-d_{12} carbons in the spectrum of the inclusion compound 15%**75**@TPP-d_{12} annealed at 70 °C is missing in the spectrum of 15%**75**@TPP-d_{12} annealed at 200 to 210 °C. The chemical shifts in both inclusion compounds remain similar, and small variations are due to better resolved signals in 15%**75**@TPP-d_{12} annealed at the higher temperature.

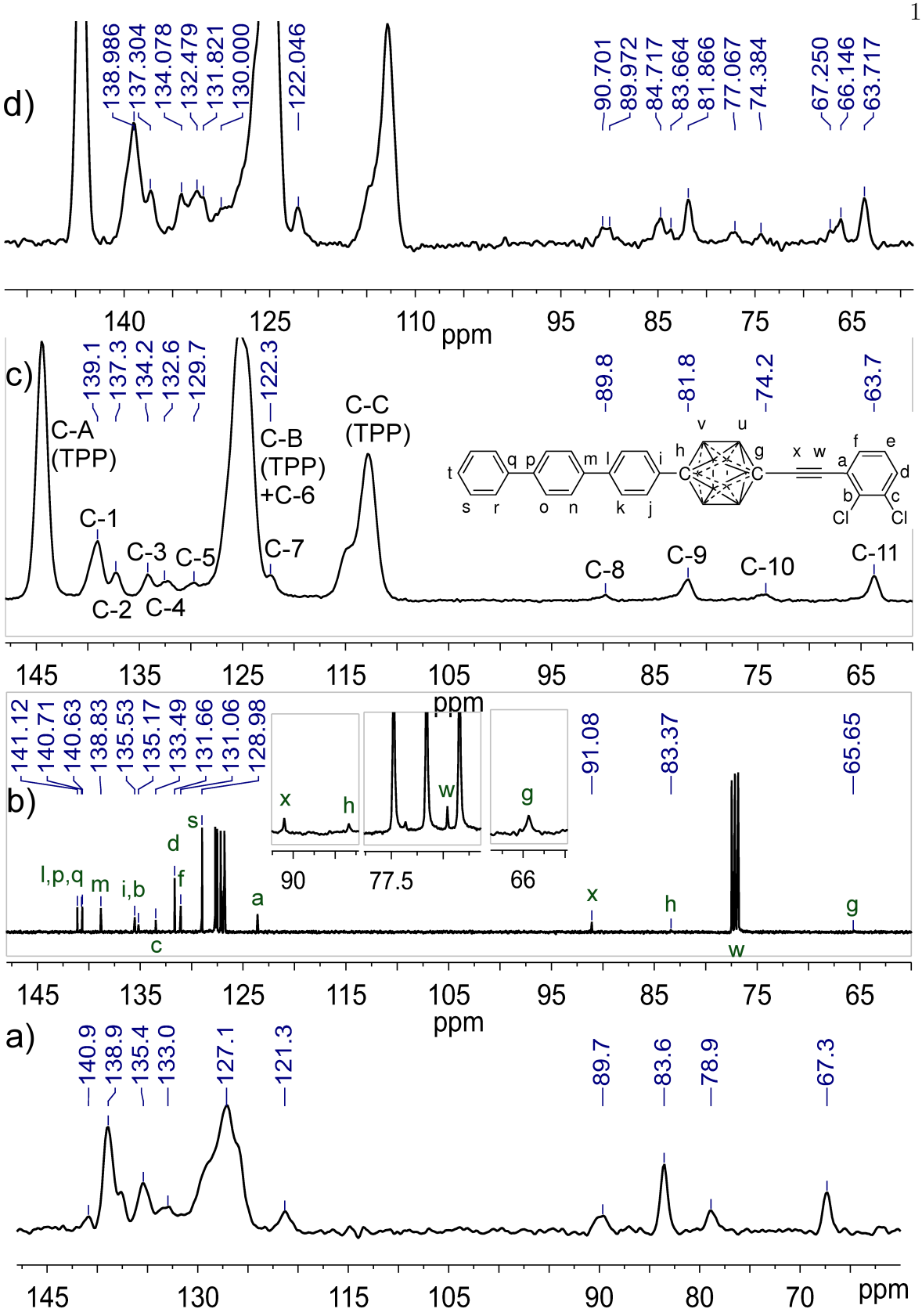

Figure 2.58: solid-state ^{13}C NMR of **75** and 15%**75**@TPP-d_{12}: a) neat **75** CP MAS, b) solution ^{13}C NMR in $CDCl_3$; c) 15%**75**@TPP-d_{12} CP MAS, d) het-22%**75**@TPP-d_{12} CP MAS.

The ^{13}C CP MAS solid-state NMR spectrum of the heterogeneous inclusion compound het-22%**75**@TPP-d_{12} (Figure 2.58d) was recorded using a 5 ms contact time. It shows several incompletely resolved sets of signals. The most intense set is identical to the set of signals found in the spectrum of the homogeneous inclusion compound 15%**75**@TPP-d_{12}. The new sets of signals are different from both ^{13}C CP MAS solid-state NMR spectra of neat **75** and of the inclusion compound 15%**75**@TPP-d_{12} (Figure 2.58b,c).

The C-1 and C-2 signals in the ^{13}C CP MAS solid-state NMR spectrum of the inclusion compound het-22%**75**@TPP-d_{12} are better resolved than in the CP MAS spectrum of neat compound **75**, but they are not quite as well resolved as in the ^{13}C CP MAS solid-state NMR spectrum of the homogeneous inclusion compound 15%**75**@TPP-d_{12} (Figure 2.58c). The signals of both C-1 and C-2 are shifted upfield relative to the ^{13}C NMR of compound **75** in solution (Figure 2.58b).

The C-3, C-4 and C-5 signals in the inclusion compound 15%**75**@TPP-d_{12} are less resolved in the spectrum of the inclusion compound het-22%**75**@TPP-d_{12} due to the presence of additional unresolved shoulders downfield of each peak. The downfield shoulders exhibit chemical shifts close to the **75** solution ^{13}C spectrum.

The carborane carbons (C-9 and C-11) show several new sets of signals in addition to the set of peaks that are identical to those in the homogeneous inclusion compound 15%**75**@TPP-d_{12}. One of the new sets of signals exhibits similar chemical shifts as the neat rotor **75** in solution and as the neat solid, whereas the other peaks are shifted both upfield and downfield relative to those of **75** in solution and neat solid.

The acetylenic carbons (C-8 and C-10) are relatively broad and they are barely resolved above the noise. The carbon C-8 shows almost identical chemical shift in the heterogeneous inclusion compound het-22%**75**@TPP-d_{12}, in the homogeneous inclusion compound 15%**75**@TPP-d_{12} and as neat solid **75**. The signal C-10 splits into a peak identical to the one found in the homogeneous inclusion compound 15%**75**@TPP-d_{12}, and another peak with a chemical shift close to C_w carbon signal of **75** in solution or neat solid.

Rotor 76 and its inclusion behavior. The solid-state ^{13}C CP MAS NMR of **76** (Figure 2.59 bottom) and its inclusion compound 15%**76**@TPP-d_{12} (Figure 2.59 top, 15 mol % **76** in TPP-d_{12}) were recorded using a 5 ms contact time.

The inclusion compound spectrum displays three aromatic carbons of TPP-d_{12} that are less intense than in the other inclusion compounds. It shows chemical shifts of the carbons of **76** that are almost identical to those in the spectrum of neat **76**.

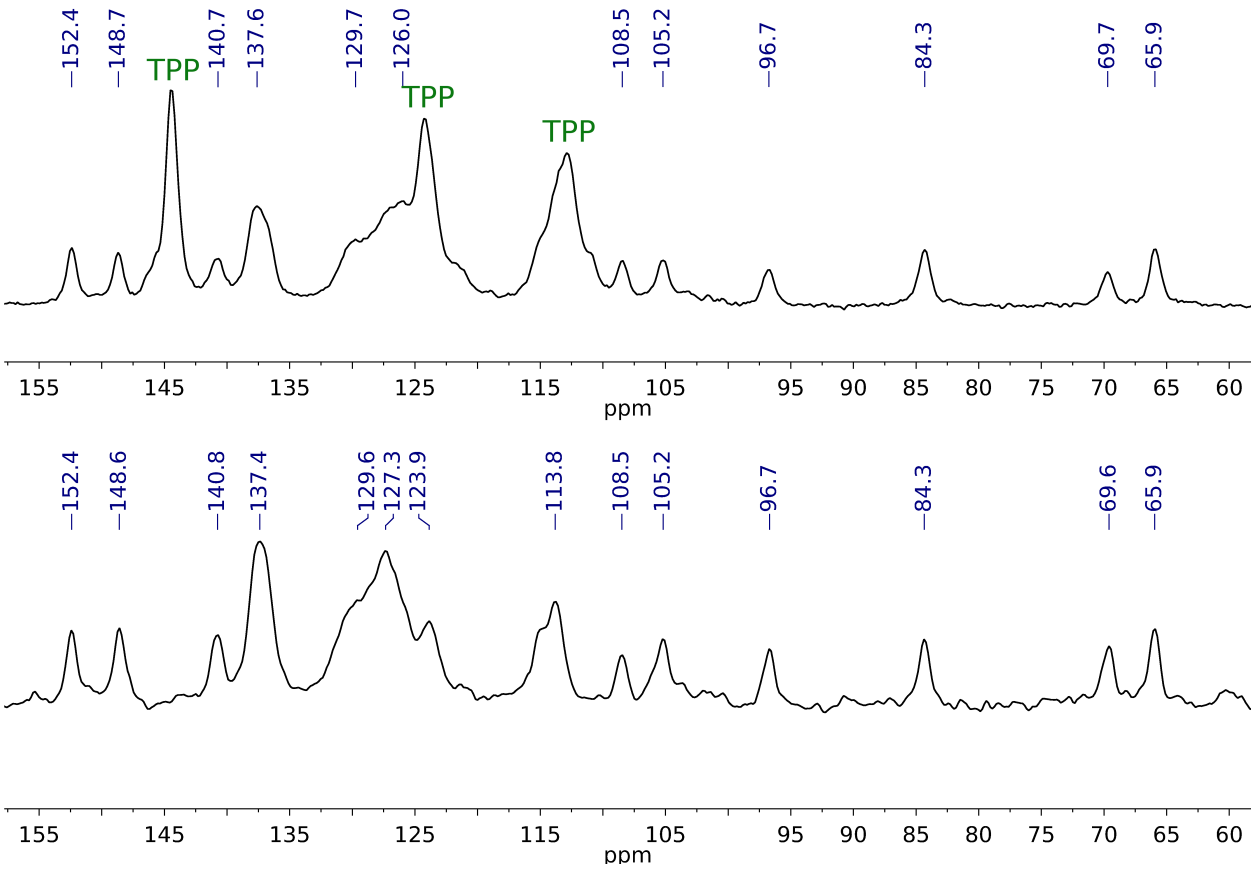

Figure 2.59: Solid-state ^{13}C CP MAS NMR: inclusion compound 15%**76**@TPP-d_{12} (top) and neat **76**.

Compound 77 and its inclusion compound. The inclusion compound 15%**77**@TPP-d_{12} (15 mol % **77** in TPP-d_{12}) was prepared by the ball milling/annealing method and the solid-state ^{13}C NMR spectrum was recorded using a 5 ms contact time (Figure 2.60).

The solid-state spectrum of the inclusion compound is dominated by the three TPP-d_{12}

singlet resonances. It displays identical chemical shifts for the aromatic quaternary carbons as the inclusion compound 15%**73**@TPP-d_{12}. The protonated aromatic carbons also overlap with the middle TPP-d_{12} signal. The *p*-carborane carbon region (60 to 90 ppm) only shows a single broad peak.

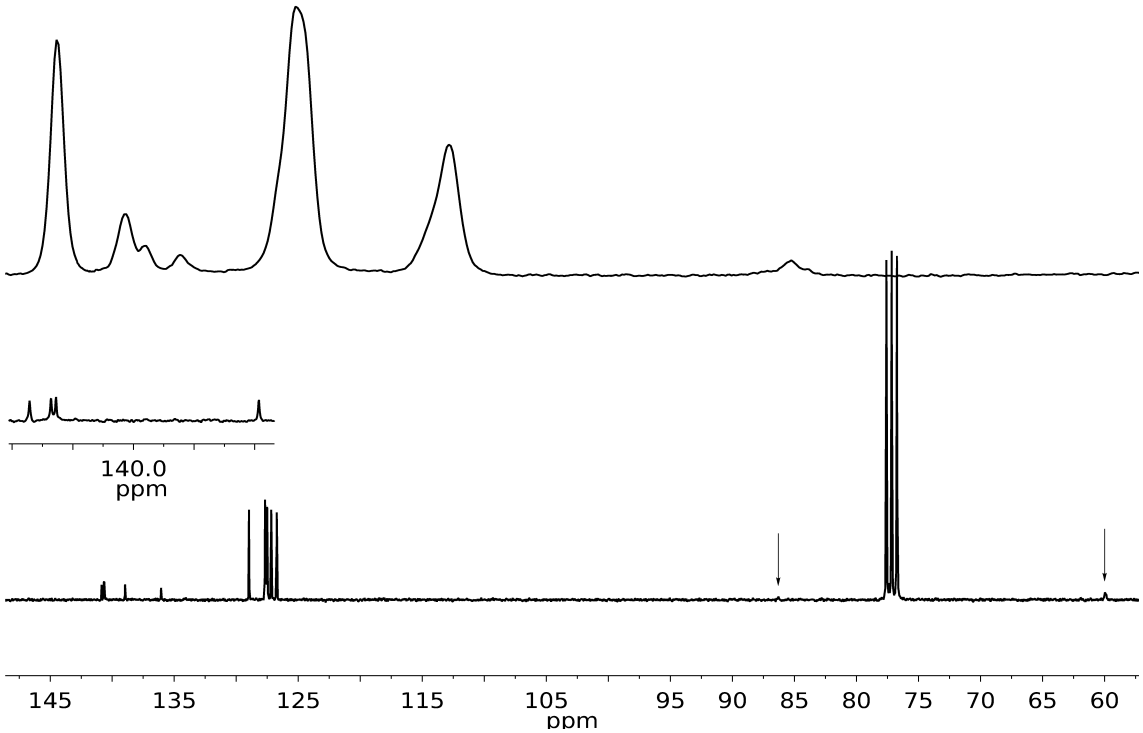

Figure 2.60: Solid-state ^{13}C CP MAS NMR spectrum of the inclusion compound 15%**77**@TPP-d_{12} (top) and ^{13}C NMR spectrum of **77** in $CDCl_3$ (bottom).

2.6.1.5 Differential Scanning Calorimetry

The differential scanning calorimetry traces of the rotor **74** and **75** inclusion complexes and the neat rotors **74** and **75** are shown in Figure 2.61. The DSC of hexagonal TPP is known in the literature,[82] and the DSC trace of hexagonal TPP-d_{12} (Figure 2.61a) closely resembles it: a broad exotherm centered around 148 °C and endoterms at 222 °C and 252 °C. Both the rotor **74** (Figure 2.61b) and **75** (Figure 2.61e) show single endoterms at 234

°C and 276 °C respectively. The inclusion compounds 15%**74**@TPP-d_{12} (Figure 2.61c) and het-5%**74**@TPP-d_{12} (Figure 2.61d) each show a broad exotherm (15%**74**@TPP-d_{12}: 236 °C, het-5%**74**@TPP-d_{12}: 176 °C), and an endotherm (15%**74**@TPP-d_{12}: 286 °C, het-5%**74**@TPP-d_{12}: 252 °C) in their DSC trace. The inclusion compounds 15%**75**@TPP-d_{12} (Figure 2.61f) and het-22%**75**@TPP-d_{12} (Figure 2.61g) each show more complicated series of the same endoterms (252 °C, 263 °C, 272 °C) and an exotherm (15%**75**@TPP-d_{12}: 203 °C, het-22%**75**@TPP-d_{12}: 233 °C).

The DSC traces of the compounds **73**, **77** and **72** and their inclusion compounds are shown in Figure 2.62. The neat compounds **73**, **77** (Figure 2.62c) and **72** (Figure 2.62e) all show a single endotherm at 262°C, 255°C and 265°C, respectively. The inclusion compound 15%**73**@TPP-d_{12} shows two endoterms at 233°C and 275°C and a sharp exotherm at 235°C. The inclusion compound 15%**77**@TPP-d_{12} displays three endoterms (232°C, 252°C and 261°C, Figure 2.62d) in the DSC measurement. The inclusion compound 15%**72**@TPP-d_{12} also exhibits three endoterms (232°C, 240°C and 246°C, Figure 2.62f) in the DSC.

2.6.1.6 Calculations

The dipole moment of 2,3-dichlorobenzene was calculated to be 2.64 D using the B3LYP level of theory and the TZVP basis set.

The rotational barriers were calculated using the B3LYP level of theory and the TZVP basis set. The barrier was computed as the difference between the energy of the lowest minimum and the energy of the transition state along the rotational coordinate.

The rotational barrier of 2,3-dichlorophenyl in 1-(2,3-dichlorophenyl)-*p*-carborane was found to be 1.56 kcal/mol, and the rotational barrier of 2,3-dichlorophenyl in 1-(2,3-dichlorophenylethynyl)-*p*-carborane was found to be 0.15 kcal/mol.

The geometry of a single channel composed of four layers of TPP with a guest molecule **74** (Figure 2.63) was optimized using BLYP with dispersion and the 3-21G basis set using Terachem 1.5.[120] The channel was only partially constrained during the optimization to

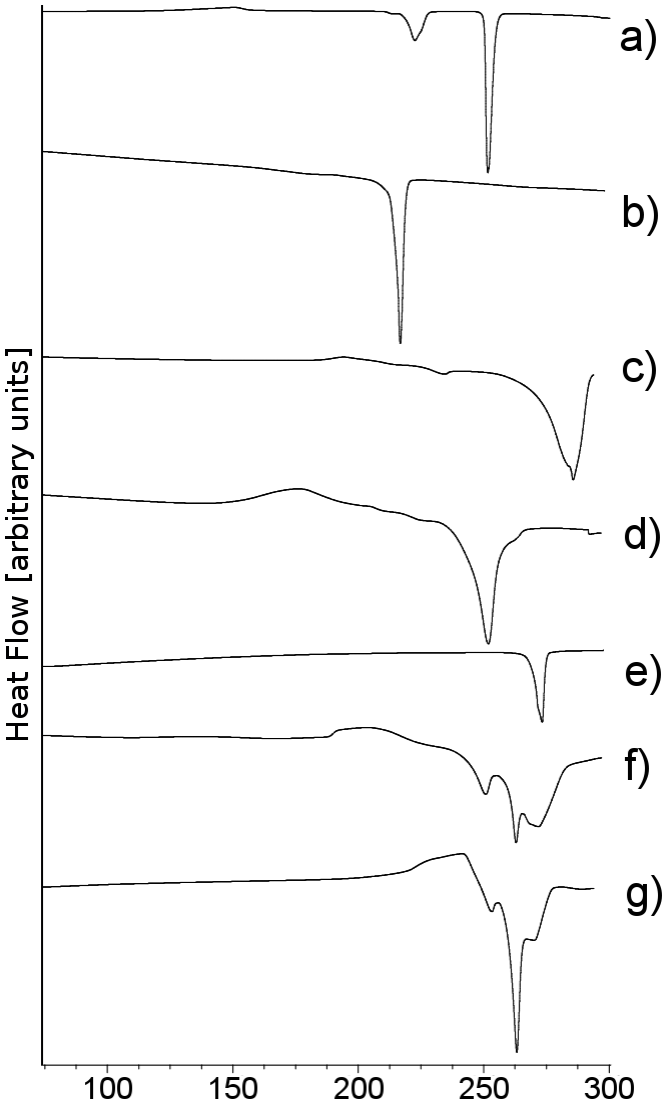

Figure 2.61: Differential scanning calorimetry traces: a) hexagonal TPP-d_{12}; b) **74**; c) 15%**74**@TPP-d_{12}; d) het-5%**74**@TPP-d_{12}; e) **75**; f) 15%**75**@TPP-d_{12}; g) het-22%**75**@TPP-d_{12}.

allow for expansion or contraction. The initial geometries were generated from the R=0 Å geometry (Figure 2.63) by moving the guest by multiples of an Angstroem inside or outside the channel along the axis of the channel, and by optimizing the resulting geometry into the nearest local minimum.

The lowest minimum obtained by this method shows most of the guest molecule **74** contained inside the channel, except for a small part of the dichlorophenyl rotator (Figure

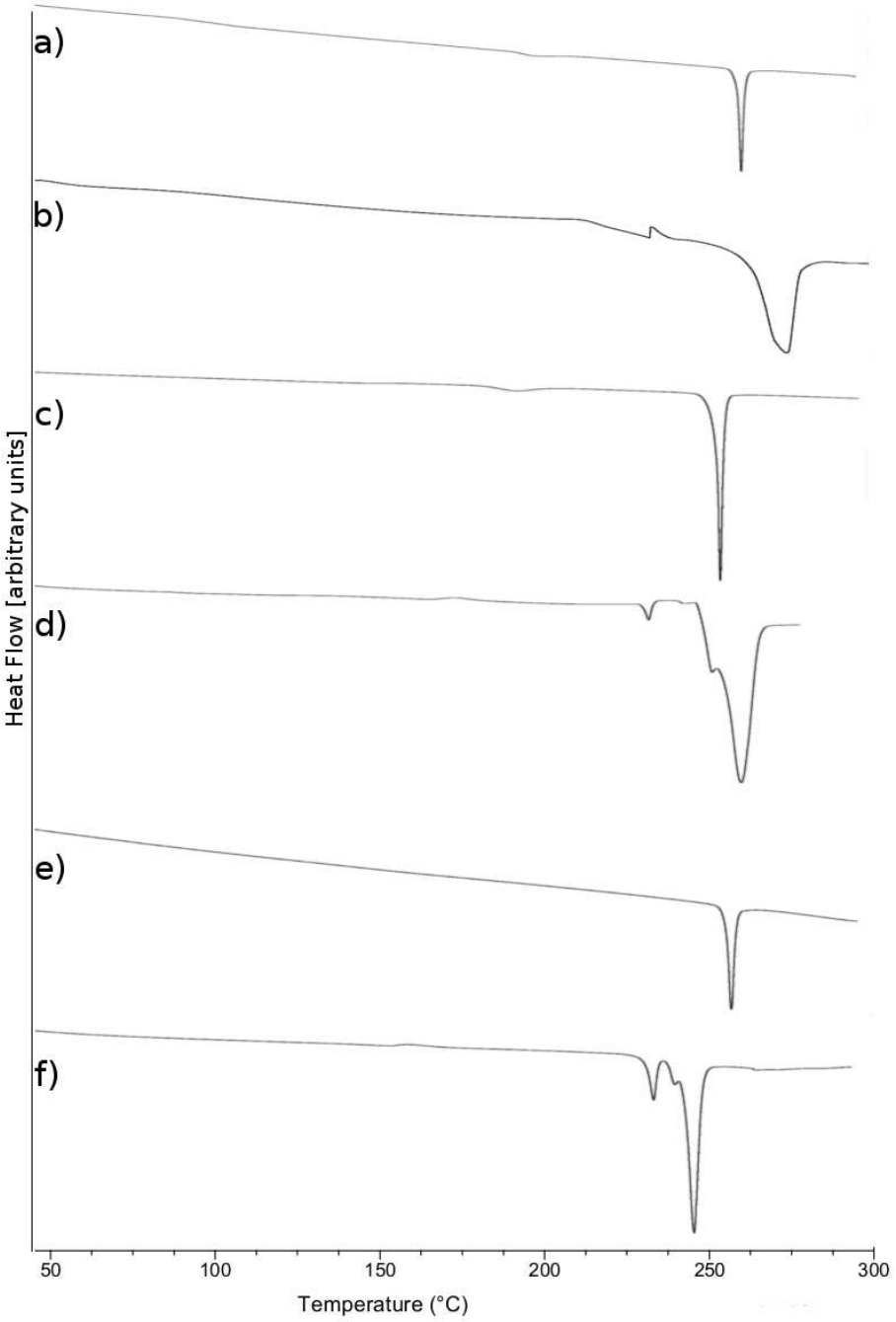

Figure 2.62: Differential scanning calorimetry traces: a) neat **73**, b) 15%**73**@TPP-d_{12}, c) neat **77**, d) 15%**77**@TPP-d_{12}, e) neat **72**, f) 15%**72**@TPP-d_{12}.

2.63).

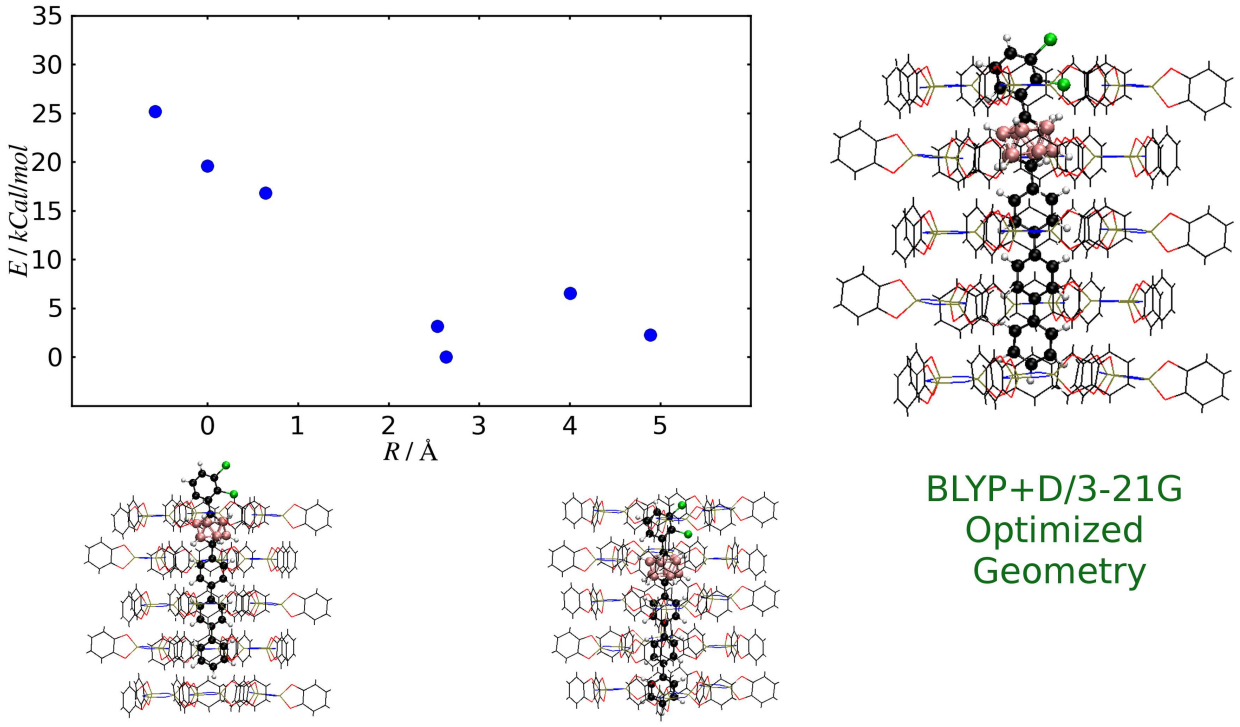

Figure 2.63: BLYP+D/3-21G geometry optimization of a single TPP channel with compound **74** inside. The x-axis is the displacement of **74** into (R>0) or outside (R<0) the channel along the axis of the channel.

2.6.2 Discussion

The data for all three compounds **73**, **74** and **75** show different spectra for the neat rotors and for the inclusions.

The ^{31}P CP MAS solid-state NMR data for all the inclusion compounds show a single phosphorus signal for the TPP-d_{12} molecules that surround the guest. This is a result of cross-polarization between the guests protons and the phosphorus atoms of the TPP-d_{12} lattice. In absence of a guest with protons, TPP-d_{12} shows no signal in the ^{31}P SPE MAS solid-state NMR experiment. The single phosphorus signal is an indication of inclusion compound of a hexagonal structure filled with guest molecules.

The local hexagonal structure in proximity of the guest compound is further confirmed by the ^{13}C CP MAS solid-state NMR experiments on all the inclusion compound samples.

The C-A, C-B and C-C TPP-d_{12} carbons get cross-polarized by the protons from the guest molecules, and three singlets for three sets of equivalent TPP-d_{12} carbons indicate hexagonal lattice. The ^{31}P SPE MAS solid-state NMR reveals the structure of the entire sample. The single peaks in the inclusion compound spectra show hexagonal lattices throughout the entire sample.

Differential scanning calorimetry. The DSC trace (Figure 2.61) of TPP-d_{12} is analogous to the DSC trace of TPP.[82] It shows two endoterms and an exotherm. The exotherm is broad and it is associated with the first-order transition of hexagonal TPP-d_{12} into its monoclinic form. The low temperature endotherm is associated with the first-order transition of monoclinic TPP-d_{12} into hexagonal TPP-d_{12}, and the high temperature endotherm corresponds to melting TPP-d_{12}.

The DSC traces of the inclusion compounds all contain a small endotherm associated with melting TPP-d_{12}. This endotherm is most pronounced for the inclusion compound 5%**75** that has only small loading of the rotor. The endotherm is broad and it corresponds to melting both TPP-d_{12} and the inclusion compound.

The remaining endoterms in the DSC traces of the rotor **74** correspond to the melting of the inclusion compounds. The inclusion sample 15%**74**@TPP-d_{12} shows a higher melting point than the inclusion het-5%**74**@TPP-d_{12} because het-5%**74**@TPP-d_{12} contains excess amount of TPP-d_{12} as an impurity that lowers the melting point. The DSC traces of the inclusion compounds of the rotor **75** contain another endotherm at a temperature close to the melting temperature of the neat rotor. This is most likely due to expulsion of the guest from the channel, a behavior usual for a number of inclusion compounds.[121]

The exotherms observed in the DSC traces of the rotors **74** and **75** are associated with insertion of the rotor into TPP-d_{12}. This is confirmed by solid-state NMR spectrum of the 15%**75**@TPP-d_{12} annealed at 200 to 210 °C (Figure 2.57). The NMR spectrum shows the same features as the spectrum of the sample that was not annealed, but the peaks are sharper. The C-C TPP-d_{12} signal in the solid-state ^{13}C NMR spectrum of the inclusion

compound 15%**75**@TPP-d_{12} annealed at high temperature does not display a downfield shoulder associated with unfilled TPP-d_{12}. Also the X-ray powder diffraction pattern[h] (Figure 2.64) shows sharper features for the sample annealed at 200 to 210 °C compared to the sample that was only annealed at 70 °C. The inclusion compound annealed at the high temperature does not show the exotherms in its DSC trace.

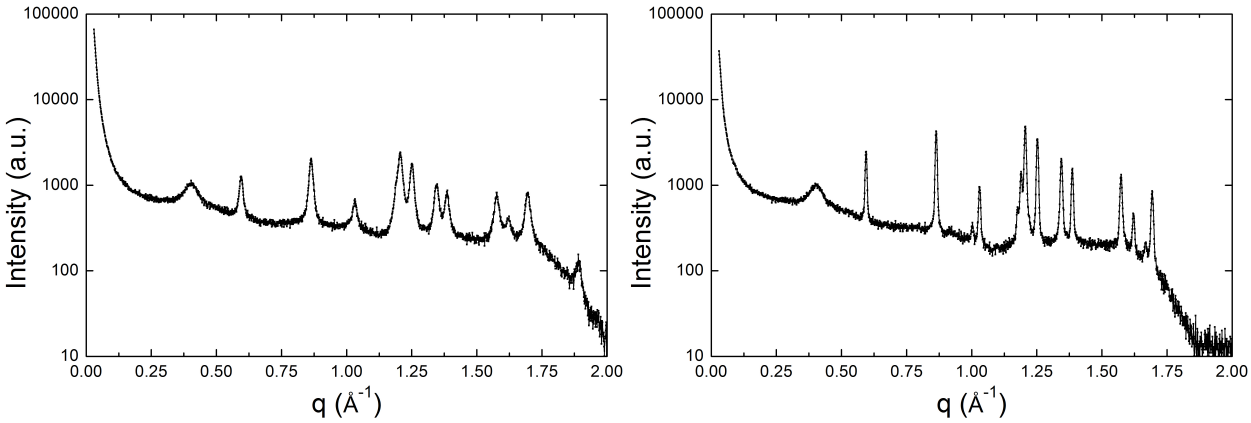

Figure 2.64: X-ray powder diffraction patterns. Left 15%**75**@TPP-d_{12} annealed at 70 °C, right 15%**75**@TPP-d_{12} annealed at 200 to 210 °C (Rogers C. T., Yongqiang S., unpublished results).

The differential scanning calorimetry trace of 15%**73**@TPP-d_{12} shows one endotherm at 233 °C that is associated with the first order transition of monoclinic TPP-d_{12} into its hexagonal form and a high temperature endotherm (275 °C) that corresponds to melting the inclusion compound. The DSC trace of the inclusion compound 15%**77**@TPP-d_{12}displays two endotherms associated with TPP-d_{12} and one that corresponds to the melting of the inclusion compound.

The DSC trace of the inclusion compound 15%**72**@TPP-d_{12} shows the first endotherm that corresponds to the first order transition of monoclinic to hexagonal TPP-d_{12} and evidence for guest compound **72** expulsion. The two high temperature phase transition are associated with melting TPP-d_{12} and **72** at temperatures lower than the pure components,

[h] Rogers C. T., Yongqiang S., unpublished results.

due to the mixture effect.

NMR assignments. In the inclusion compound, the guest experiences large conformational freedom. The motion of guests similar to the systems studied in this work was shown to be much faster than the NMR time scale at room temperature.[86,94,94,96,97] The solid-state NMR spectra of the inclusion compounds are therefore averaged over the accessible conformations, although the relative contribution of a particular conformation to the resulting chemical shift is likely different than in the solution as the conformational potential energy surface for a molecule in the solution and in the channel are undoubtedly different.

The solid-state ^{13}C NMR spectra of the inclusion compound show the same signal pattern as the solution spectra and the changes in the chemical shifts in the inclusion compounds relative to the solution spectra are much more consistent than comparisons to the neat rotor spectra. Thus, the assumption that the conformational effects are similar in the solution and in the channel seems justified. With this assumption in mind, the resolved aromatic signals in the inclusion compound ^{13}C solid-state spectra were assigned by comparison with the solution spectrum in a weakly interacting solvent. The differences in the chemical shifts are assumed to be due to the differences in the local magnetic anisotropy of the environment, *i.e.* by the shielding and the deshielding effects.

As the assignment of the carbon signals made by the comparison with the solution ^{13}C NMR spectra can easily be incorrect for carbons with a small peak separation, the assignments were further examined by short-contact time solid-state experiments and solid-state experiments with dipolar dephasing. The chemical shifts of heterogeneous inclusion compounds that contain only partially inserted rotors display chemical shifts of some carbons similar to the solution spectrum which gives some ground for determination of the extent of insertion.

The chemical shifts were also compared to inclusion compounds of similar guests or to inclusion compounds of a partially deuterated version of the guest. Measurements of the rotational barriers and calculations were used to lend greater support to the conclusions

drawn from the NMR data.

The X-ray powder diffraction data for all the inclusion compounds of third generation rotors showed lattice expanded by about 5 % in the plane of *a*-vectors relative to empty hexagonal TPP-d_{12}.[i]

Rotor 73. The solid-state ^{13}C spectra of the inclusion compound 15%**73**@TPP-d_{12} display three aromatic singlet resonances characteristic for hexagonal TPP. This is strong evidence that the inclusion compound was formed.

The ^{13}C CP MAS solid-state NMR spectra of the inclusion compound 15%**73**@TPP-d_{12} (Figure 2.49c,d) show an upfield change in the chemical shift of the *p*-terphenyl carbons and *p*-carborane carbons with respect to the solution spectrum (Figure 2.49b). This indicates that both *p*-terphenyl and *p*-carborane are inserted into the TPP-d_{12} channel.

The methyl carbon signal splits into two peaks in the ^{13}C CP MAS solid-state NMR spectra of the inclusion compound 15%**73**@TPP-d_{12}, one is downfield by 4.8 ppm, and the other is upfield by 3.2 ppm with respect to the ^{13}C NMR spectrum of the compound **73** in solution. The upfield signal clearly belongs to the methyl included inside the channel.

The molecules of compound **73** can possibly fill the channel with three different relative orientations shown in Figure 2.65b,c,d. It is unlikely that the remarkable 4.8 ppm downfield change in the chemical shift of the methyl carbon is due to deshielding by the terminal *p*-terphenyl phenyl of the neighboring rotor **73** inside the channel (Figure 2.65c). A number of solid-state ^{13}C NMR spectra of bulk inclusion compounds are known in the literature,[82,86,87,87] and no such strong effect on the chemical shift has been observed. The downfield change in the chemical shift of the methyl is more consistent with the methyl protruding above the surface in the deshielding zone of the channel (Figure 2.65a).

Compound 72. The solid-state ^{13}C CP MAS NMR spectra of the inclusion compound 15%**72**@TPP-d_{12} (Figure 2.50) show three intense TPP-d_{12} resonances, providing strong evidence for inclusion compound formation. The splitting of the most upfield TPP-d_{12} signal

[i] Yongquiang S., Rogers, C. T., unpublished results

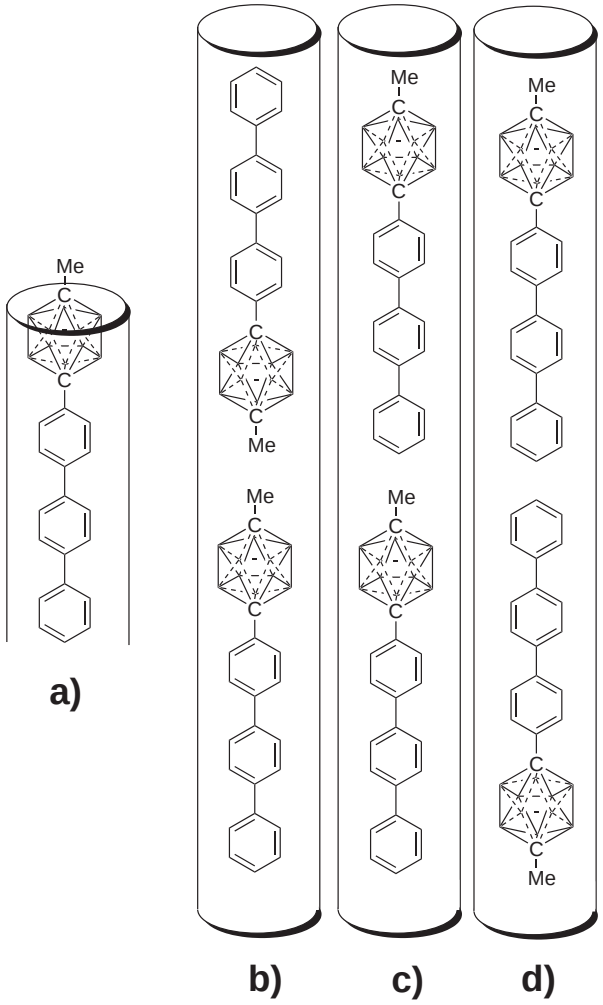

Figure 2.65: Possible relative orientations of compound **73** in the TPP-d_{12} channel.

into two peaks is due to TPP-d_{12} molecules of the filled channel and TPP-d_{12} molecules of unfilled or only partially filled channels. The TPP-d_{12} molecules of the unfilled or partially filled channels are still in the proximity of the guest molecules **72** as the TPP-d_{12} carbons are cross-polarized.

The solid-state ^{31}P SPE MAS NMR spectrum of 15%**72**@TPP-d_{12} shows that all the TPP-d_{12} is in its hexagonal form, and the solid-state ^{31}P CP MAS NMR spectrum confirms that the inclusion compound was formed.

The whole rotor **72** is inserted inside the TPP-d_{12} channels as all the carbons of **72** display a strong upfield change in the chemical shift relative to the solution ^{13}C spectrum.

The inclusion compound 15%**72**@TPP-d_{12} is a bulk inclusion compound.

The results of dielectric spectroscopy measurements of the rotational barriers are shown in Figure 2.66.[j] The three peaks for each frequency correspond to three rotational barriers: 5.4 kcal/mol, 6.7 kcal/mol and 9.25 kcal/mol. The lowest rotational barrier is thought to be due to rotators at the channel end, but fully included in the channel. The two high energy barriers are interpreted as being due to rotator rotations in the bulk. The lower energy barrier corresponds to the rotation of one rotator of a rotator pair that has dipole moments aligned in the same direction. The high energy rotational barrier is attributed to the rotation of one rotator of a rotator pair that has dipole moments pointing in opposite directions.

Rotor 74. The three singlet aromatic TPP-d_{12} resonances in the solid-state ^{13}C NMR spectra of the inclusion compounds of **74** (Figures 2.51, 2.52 and 2.53) indicate TPP-d_{12} in hexagonal form with guest molecules inserted inside the channel.

The carbon signal assignments were based on a comparison with the solution spectrum (Figure 2.51). The assignments were further examined by comparison with the short contact time solid-state ^{13}C CP MAS NMR, solid-state ^{13}C CP MAS NMR with dipolar dephasing, solid-state ^{13}C SPE MAS NMR with a short and a long relaxation delay, the solid-state ^{13}C NMR of the inclusion compound 9%**82**@TPP-d_{12} (Figure 2.52), and the solid-state ^{13}C spectrum of the inclusion compound 15%**73**@TPP-d_{12} (Figure 2.49).

The short contact time solid-state ^{13}C CP MAS NMR spectrum shows signals of protonated carbons enhanced relative to the quaternary carbons, the dipolar dephasing suppresses protonated carbon signals, and the long relaxation delay solid-state ^{13}C SPE MAS NMR provides accurate integration. The results of these experiments were in agreement with the assignments based on comparison with the solution ^{13}C NMR spectrum.

Compounds **73**, **74** and **75** exhibit remarkably similar carbon chemical shifts of the *p*-terphenyl carbons. Also the inclusion compound 15%**73**@TPP-d_{12} shows the same chemical shifts for the *p*-terphenyl carbons as the inclusion compound 15%**74**@TPP-d_{12}.

[j] Ke Zhao, unpublished results

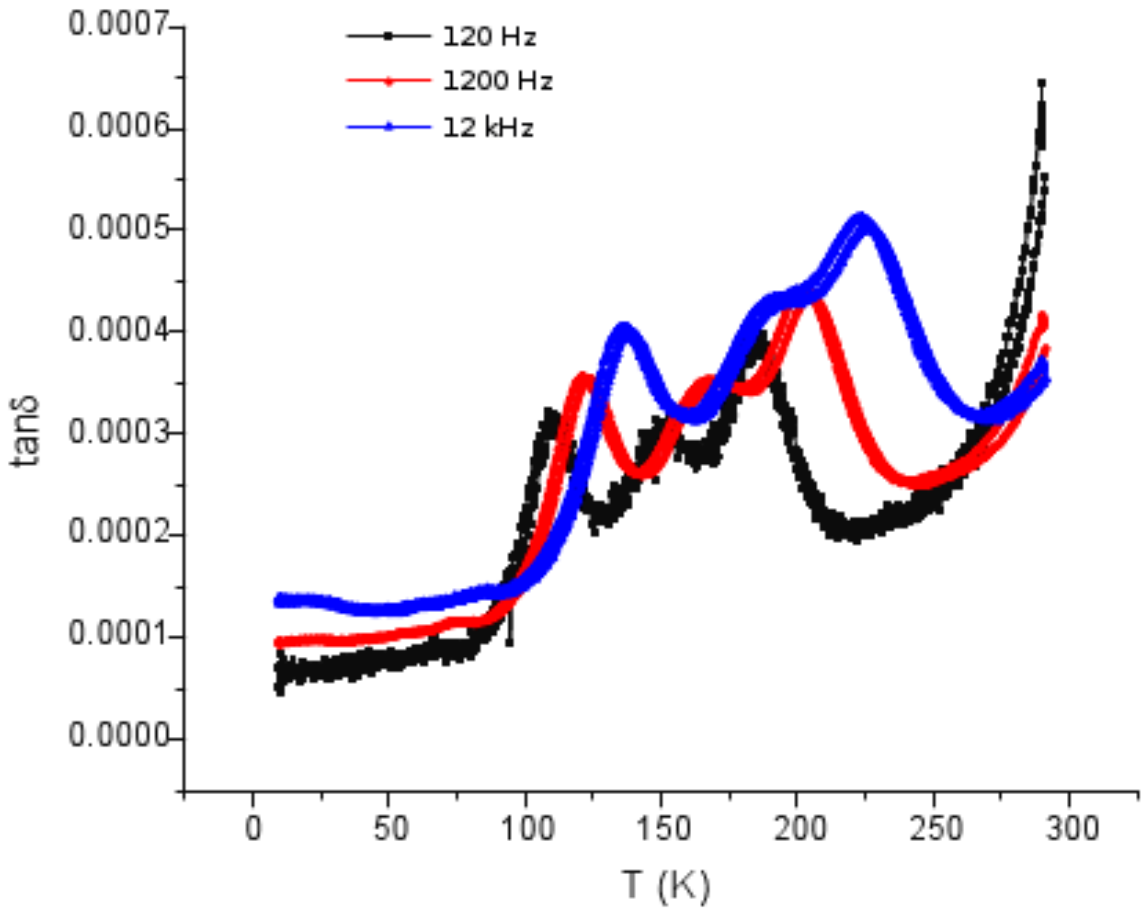

Figure 2.66: Dielectric spectroscopy results with 15%**72**@TPP-d_{12} (Ke Zhao, unpublished results).

The solid-state ^{13}C CP MAS NMR spectra of the inclusion compound 15%**74**@TPP-d_{12} (Figure 2.51c,d and Figure 2.55c) display an upfield change in the chemical shift relative to the solid-state ^{13}C NMR spectrum of neat **74** and to the solution spectrum of **74** for all the resolved carbons and therefore indicate that all parts of **74** are inserted in the TPP-d_{12} channel.

The solid-state ^{13}C SPE MAS NMR spectrum of the inclusion compound 15%**74**@TPP-d_{12} with short relaxation delays enhances the signal of fast relaxing carbons. Highly mobile parts of the molecule exhibit fast relaxations. As there is no greater enhancement in the signal of the 2,3-dichlorophenyl rotator compared to the rest of the rotor, this result also

suggests that the rotator is inserted in the channel.

The solid-state ^{13}C CP MAS NMR spectrum of the inclusion compound 9%**82**@TPP-d_{12} contains only the rotor signals of the 2,3-dichlorophenyl in the aromatic region. Thus, it permits an inspection of the chemical shifts of the 2,3-dichlorophenyl without interference from the signals from the rest of the rotor molecule. The solid-state ^{13}C CP MAS NMR spectrum only displays upfield changes in the chemical shifts relative to the solution ^{13}C NMR spectrum, and therefore confirms insertion of the 2,3-dichlorophenyl rotator inside the TPP-d_{12} channel.

The insertion of all the rotor parts including the rotator is likely due to the stabilizing π-stacking interactions of 2,3-dichlorophenyls with an expanded TPP-d_{12} channel. Such interactions are absent in case of the methyl in compound **73**. Thus, there is not a strong preference for the methyl to be included in the channel.

The results of calculations suggest the optimum geometry contains the rotor **74** mostly but not completely inserted, although a calculation with a longer channel was not performed due to the excessive system size. This case would likely not be easily distinguishable by solid-state NMR from the bulk inclusion compound. The plot (Figure 2.63) indicates that the interaction of the guest molecule with the channel is described by a complicated potential where only a few modes of insertion are favored.

The dielectric spectroscopy trace for the inclusion compound 15%**74**@TPP-d_{12} is shown in Figure 2.67.[k] It contains a single peak for each frequency of the oscillating electric field. This corresponds to the rotational barrier of 6.98 kcal/mol. The barrier is similar to the rotor 15%**72**@TPP-d_{12} fully included in the channel (6.7 kcal/mol), which is evidence for 15%**74**@TPP-d_{12} being a bulk inclusion compound, although only one rotational barrier is seen, and it would be expected to see several rotational barriers for the bulk inclusion compound, as in the case of 15%**72**@TPP-d_{12}.

The four downfield quaternary *p*-terphenyl carbons signals C-1 and C-2 C_q in the solid-

[k] Ke Zhao, unpublished results.

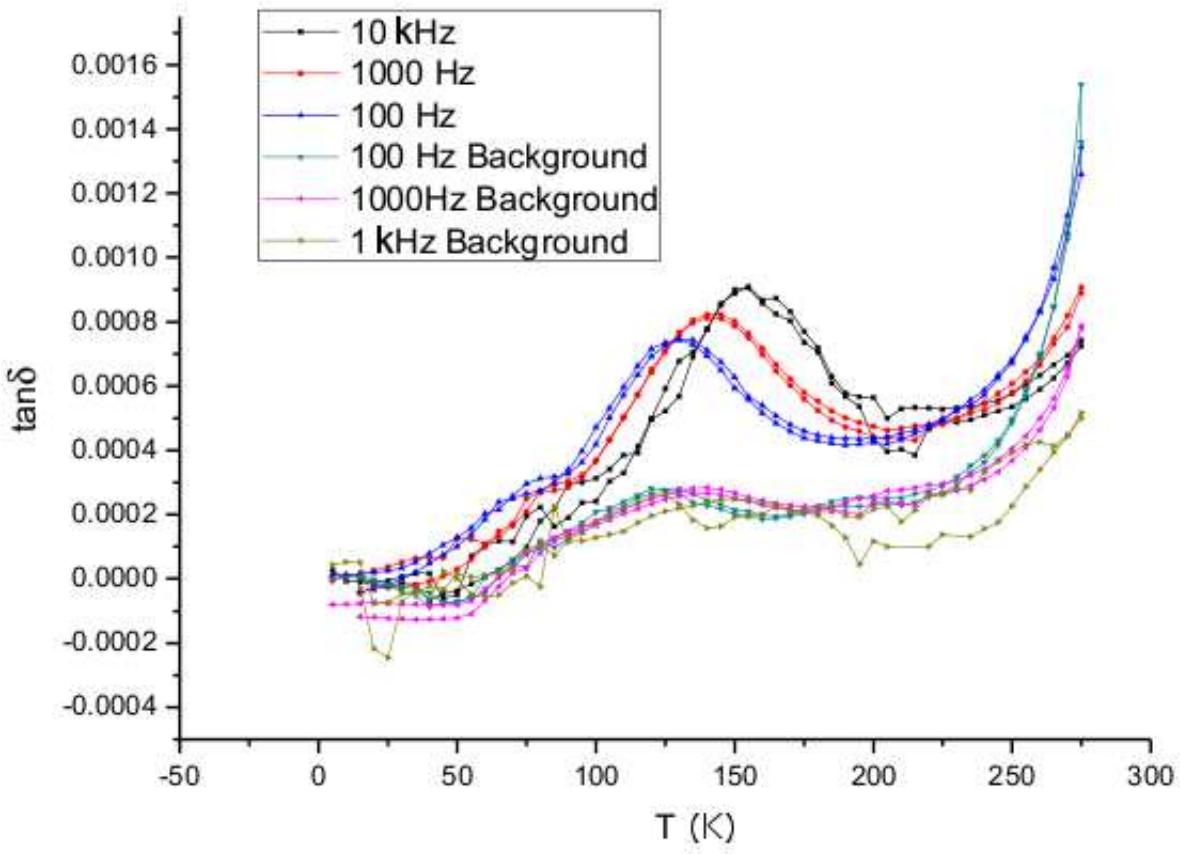

Figure 2.67: Dielectric spectroscopy results with 15%**74**@TPP-d_{12} (Ke Zhao, unpublished results).

state ^{13}C CP MAS NMR spectrum of the inclusion compound het-5%**74**@TPP-d_{12} (Figures 2.58d and 2.53d) all show an upfield change in the chemical shifts relative to the solution ^{13}C spectrum of **74** (C_l, C_m, C_p and C_q, Figure 2.53b). The change in the chemical shift of the remaining *p*-terphenyl carbon, C_i, cannot be determined due to signal overlap. Comparison with the solid-state ^{13}C spectrum of neat **74** (Figure 2.53a) shows no change in the chemical shift for the carbon C-1 and a small change (-0.3 ppm) for the carbon C-2.

However, the protonated aromatic carbon signals that show two intense signals at 127.6 ppm and 126.6 ppm in the solid-state spectrum of **74**@TPP-d_{12} are shifted upfield in the solid-state NMR spectrum of the inclusion compound het-5%**74**@TPP-d_{12}, and they overlap with the TPP-d_{12} carbon at 125 ppm. This is a strong indication that all the *p*-terphenyl or

most of it is inserted inside the channel.

The inclusion compound het-5%**74**@TPP-d_{12} therefore contains a collection of rotors, some with the *p*-terphenyl tail mostly or fully inserted, and some completely inserted into the channel, including the *p*-carborane. Heating the inclusion compound het-5%**74**@TPP-d_{12} results in an inclusion compound with the same sets of the ^{13}C signals as 15%**74**@TPP-d_{12}, while heating of a mixture of finely ground **74** and TPP-d_{12} does not yield an inclusion compound. This suggests that the inclusion compound het-5%**74**@TPP-d_{12} is not contminated with detectable amounts of the neat rotor **74**. The heterogeneous inclusion compound het-5%**74**@TPP-d_{12} is a mixture of surface inclusion compounds, and the inclusion compound is of the same type as 15%**74**@TPP-d_{12}.

The dielectric spectroscopy trace for the inclusion compound het-5%**74**@TPP-d_{12} is shown in Figure 2.67.[1] It shows two peaks for each frequency of the oscillating electric field. The peaks correspond to the rotational barriers of 3.39 kcal/mol and 6.98 kcal/mol. The high energy barrier is identical to the rotational barrier measured for 2,3-dichlorophenyl rotation in 15%**74**@TPP-d_{12} and it is also similar to the barrier observed for the rotor in 15%**72**@TPP-d_{12}, fully included in the channel (6.7 kcal/mol). The low energy barrier is much lower and it supports the conclusion from the solid-state ^{13}C NMR data, that the sample contains a fraction of a surface inclusion compound, besides the bulk inclusion compound found in 15%**72**@TPP-d_{12}.

Rotor 75. The three singlet aromatic resonances of TPP-d_{12} in the solid-state ^{13}C NMR spectra of inclusion compounds of **75** (Figures 2.55, 2.56, 2.58 and 2.57) indicate that TPP-d_{12} is present in hexagonal form with guest molecules inserted inside the channel.

Judging by the solid-state NMR spectra, the inclusion compound 15%**75**@TPP-d_{12} exhibits similar behavior as the inclusion compound 15%**74**@TPP-d_{12}, and much of the discussion for 15%**74**@TPP-d_{12} also applies to 15%**75**@TPP-d_{12}. The upfield changes in the chemical shifts of all the aromatic, *p*-carborane and acetylenic carbons in the solid-state

[1] Ke Zhao, unpublished results.

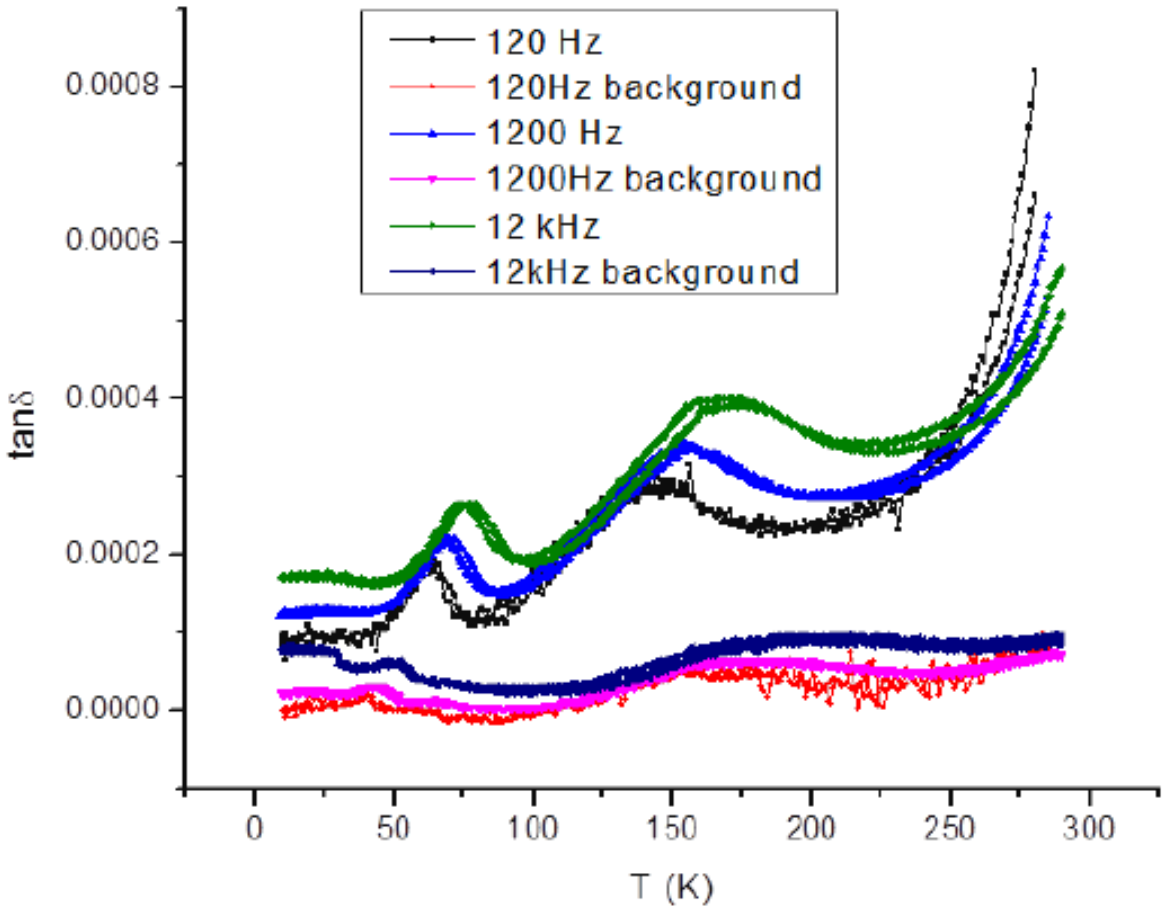

Figure 2.68: Dielectric spectroscopy results with het-5%**74**@TPP-d_{12} (Ke Zhao, unpublished results).

^{13}C NMR spectrum of the inclusion compound 15%**75**@TPP-d_{12} relative to the solution spectrum of **75** (Figure 2.55) indicate insertion of the whole rotor.

The dielectric data for the rotor **75** are not available, but it is likely that 15%**75**@TPP-d_{12} is a bulk inclusion compound. Calculations similar to the rotor **74** in a single TPP channel could not be performed due to an excessive system size.

The inclusion compound het-22%**75**@TPP-d_{12} (Figure 2.58) is a mixture of the inclusion compound of the same type as 15%**75**@TPP-d_{12}, and surface inclusion compounds with parts of the rotor uninserted. The solid-state ^{13}C CP MAS NMR spectrum of the inclusion compound het-22%**75**@TPP-d_{12} shows a large upfield change in the chemical shift

of the protonated *p*-terphenyl carbons, indicating that most of the sample contains the rotor with *p*-terphenyl tail partially or fully inserted. The downfield shoulders of the rotator aromatic signals, and downfield *p*-carborane and acetylenic signals indicate that some of the *p*-carboranes with the rotators are not inserted inside the channels, and experience strong deshielding by the TPP benzene rings at the channel terminus.

Rotor 76 and its inclusion behavior. The sample 15%**76**@TPP-d_{12} exhibits the same chemical shifts as neat **76** (Figure 2.59). Thus, no inclusion compound was formed. The small intensity from TPP-d_{12} carbons that indicates the presence of hexagonal TPP-d_{12} filled with protonated guests is most likely due to absorption of water from the air.

As no inclusion compound was formed by any usual method of inclusion compound preparation, it is likely that the interactions in the crystal of neat **76** are more favorable than in the inclusion compound.

Compound 77. The inclusion compound 15%**77**@TPP-d_{12} was prepared as a background sample for dielectric measurements.

The solid-state ^{13}C CP MAS NMR spectrum of the inclusion compound 15%**77**@TPP-d_{12} (Figure 2.60) shows three singlet resonances of TPP-d_{12}, which is an indication of TPP-d_{12} in its hexagonal form, and evidence for inclusion compound formation. The spectrum shows similar changes in the chemical shift as 15%**73**@TPP-d_{12}. It only shows one signal of *p*-carborane carbon shifted upfield with respect to **77** solution NMR spectrum, and the protonated *p*-carborane signal is missing due to fast relaxation. All the carbon signals indicate full insertion.

2.6.3 Conclusions

The inclusion compounds of the rotors **73**, **74**, **75** and **72** were successfully prepared, characterized by solid-state NMR, differential scanning calorimetry, dielectric spectroscopy, and X-ray powder diffraction.

The bulk inclusion compound 15%**72**@TPP-d_{12} served as a comparison of the magni-

tude of the rotational barrier of 2,3-dichlorophenyl fully inserted inside the channel. The inclusion compound 15%**77**@TPP-d_{12} was used as the background in dielectric measurements of the rotational barriers.

The inclusion compounds prepared by the ball milling/annealing technique are more homogeneous, but they are most likely bulk inclusion compounds, with the exception of 15%**73**@TPP-d_{12} which is a mixture of the bulk inclusion compound and a surface inclusion compound. This is despite the same loading levels with the guest molecules, and it is because methyl is too small to significantly interact with the channel and thus there is not much preference for its insertion. The 2,3-dichlorophenyl rotator on the other hand has stabilizing interactions with the channel and it therefore inserts.

The inclusion compounds of **74** and **75** that were not annealed are more heterogeneous and they contain a fraction of surface inclusion compounds.

The rotor **76** did not form inclusion compounds with TPP-d_{12}.

The combination of *p*-oligophenylene tails and *p*-carborane stopper proved to be unsuitable for surface inclusion compounds.

2.7 Fourth Generation Rotors

The fourth generation rotors use durene as the stopper because *p*-carborane attached to *p*-oligophenylenes was shown to have too small a van der Waals radius (6.9 Å) to act as a stopper. The van der Waals radius of durene was calculated to be 9.0 Å (UFF optimized geometry).

The new rotors are shown in Figure 2.69. The tail used in the new design is *p*-*t*-butylbiphenyl. The *t*-butyl group was added for better solubility in the synthetic work and to prevent too strong π-stacking interactions in the neat rotor crystal and thus to favor inclusion formation. The rotators employed in the new rotor structures are 2,3-dichlorophenyl (**83**), N,N-dimethylcarbamoyl (**84**) and N,N-diisopropylcarbamoyl (**85**).

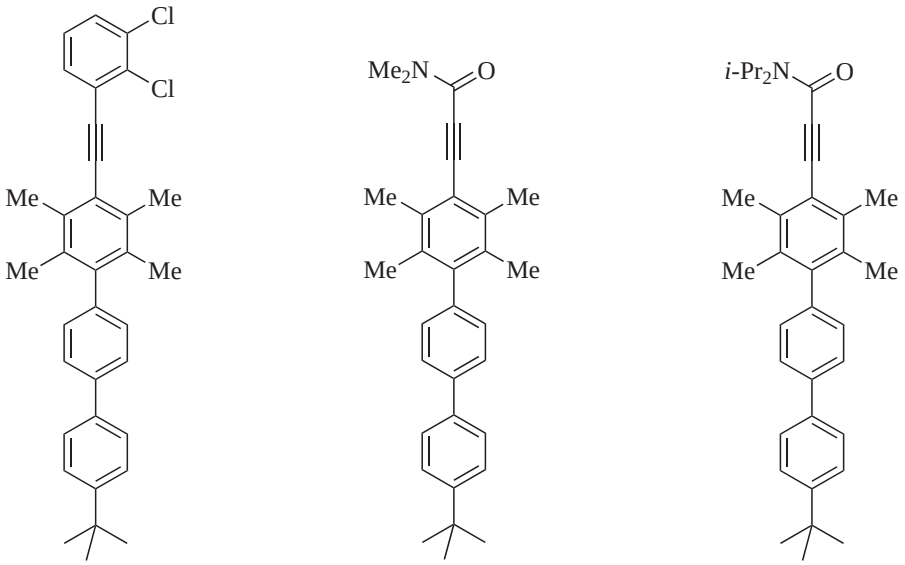

83 **84** **85**

Figure 2.69: Fourth generation rotor structures.

Preliminary results. In order to examine the suitability of the new tail-stopper systems, several preliminary experiments were performed. An inclusion behavior of hexamethylbenzene as a model system for the stopper and of p,p'-di-*t*-butylbiphenyl as a model system for the tail was examined.

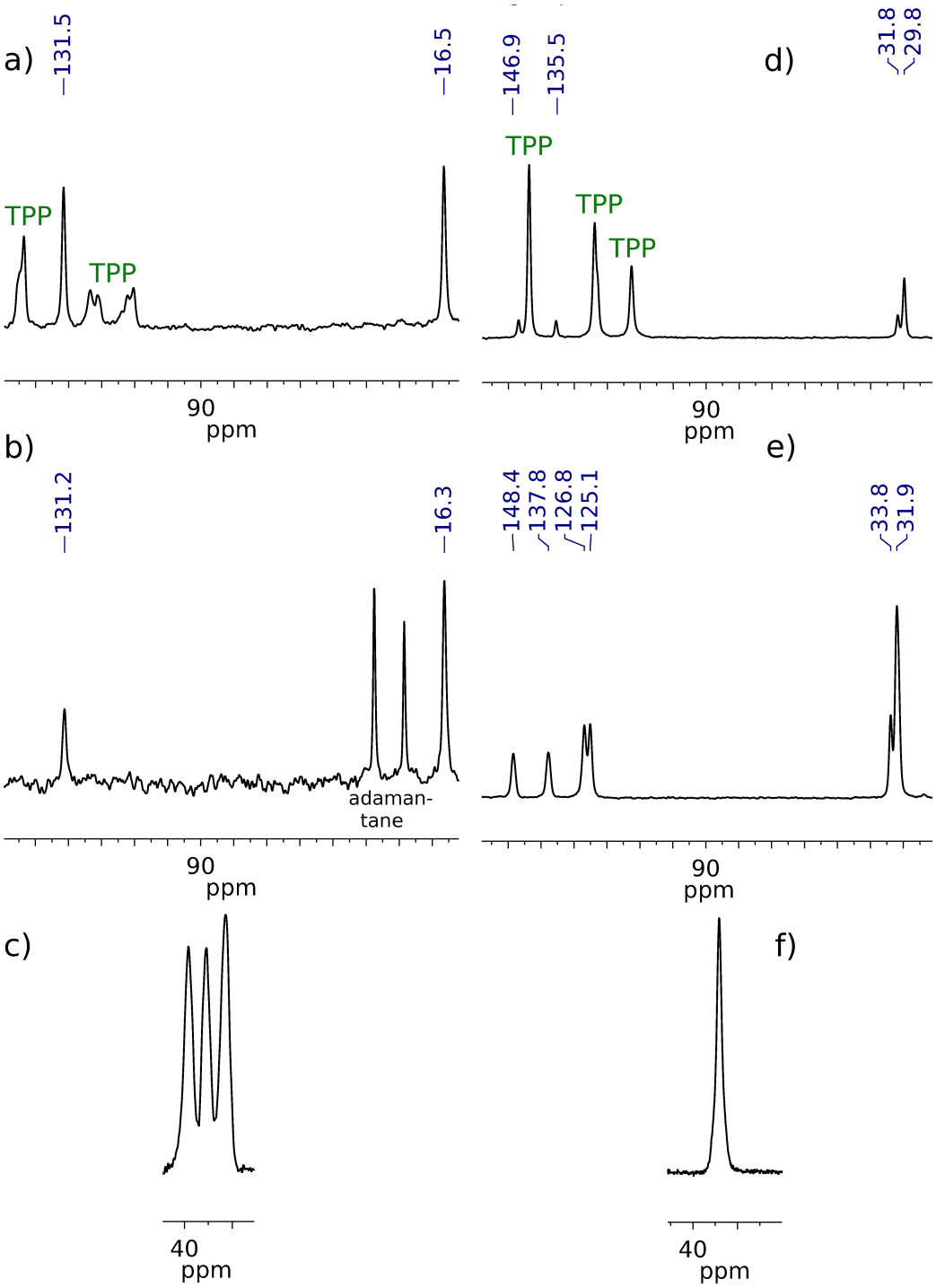

Figure 2.70: Preliminary tests of inclusion behavior of the new rotor building blocks: a) hexamethylbenzene-TPP solid-state ^{13}C CP MAS, b) hexamethylbenzene-adamantane solid-state ^{13}C CP MAS, c) hexamethylbenzene-TPP solid-state ^{31}P SPE MAS, d) p,p'-di-*t*-butylbiphenyl-TPP solid-state ^{13}C CP MAS, e) p,p'-di-*t*-butylbiphenyl solid-state ^{13}C CP MAS, f) p,p'-di-*t*-butylbiphenyl-TPP solid-state ^{31}P SPE MAS.

The solid-state ^{13}C CP MAS NMR spectra of hexamethylbenzene with TPP (prepared by the ball milling/annealing procedure described in the experimental section, 40 mol % of hexamethylbenzene in TPP) (Figure 2.70a) and hexamethylbenzene with adamantane (an NMR standard that was on hand, Figure 2.70b) were recorded using 5 ms contact time. The comparison of the two spectra shows only minor changes in the chemical shifts of hexamethylbenzene carbons, due to different magnetic susceptibilities of the two samples. The TPP signals do not show singlets, which is an indication of monoclinic structure. The solid-state ^{31}P SPE MAS NMR of the hexamethylbenzene TPP mixture (Figure 2.70c) confirms the monoclinic crystal structure. Thus, no inclusion compound was formed and durene should be a good stopper candidate.

The inclusion compound of p,p'-di-t-butylbiphenyl (20 mol %) in TPP was prepared by the ball milling/annealing procedure. Figure 2.70 shows its solid-state ^{13}C CP MAS NMR spectrum (5 ms contact time, d) and its solid-state ^{31}P SPE MAS NMR spectrum (f). Both spectra show singlet peaks for the carbon and phosphorus atoms which is an indication of hexagonal structure. The chemical shifts of the guest carbons are different in the inclusion than in the neat p,p'-di-t-butylbiphenyl solid (Figure 2.70e), and they are shifted downfield in the inclusion compound spectrum. Thus, p,p'-di-t-butylbiphenyl forms inclusion compound with TPP and p-t-butylbiphenyl should be a good candidate for the tail.

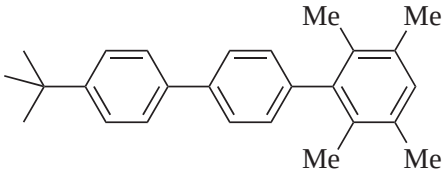

86

Figure 2.71: Solid-state NMR of **86** and its inclusion: a) ^{13}C CP MAS NMR of 20%**86**@TPP-d_{12}, b) ^{31}P SPE MAS NMR of 20%**86**@TPP-d_{12}, c) ^{13}C CP MAS NMR of neat **86**.

Next, the compound **86** (Figure 2.71) was synthesized and its inclusion behavior was

tested. The inclusion compound 20%**86**@TPP-d_{12} was prepared by the ball milling/annealing method and its solid-state ^{13}C CP MAS (5 ms contact time, Figure 2.72a) and ^{31}P SPE MAS NMR (Figure 2.72b) spectrum were recorded.

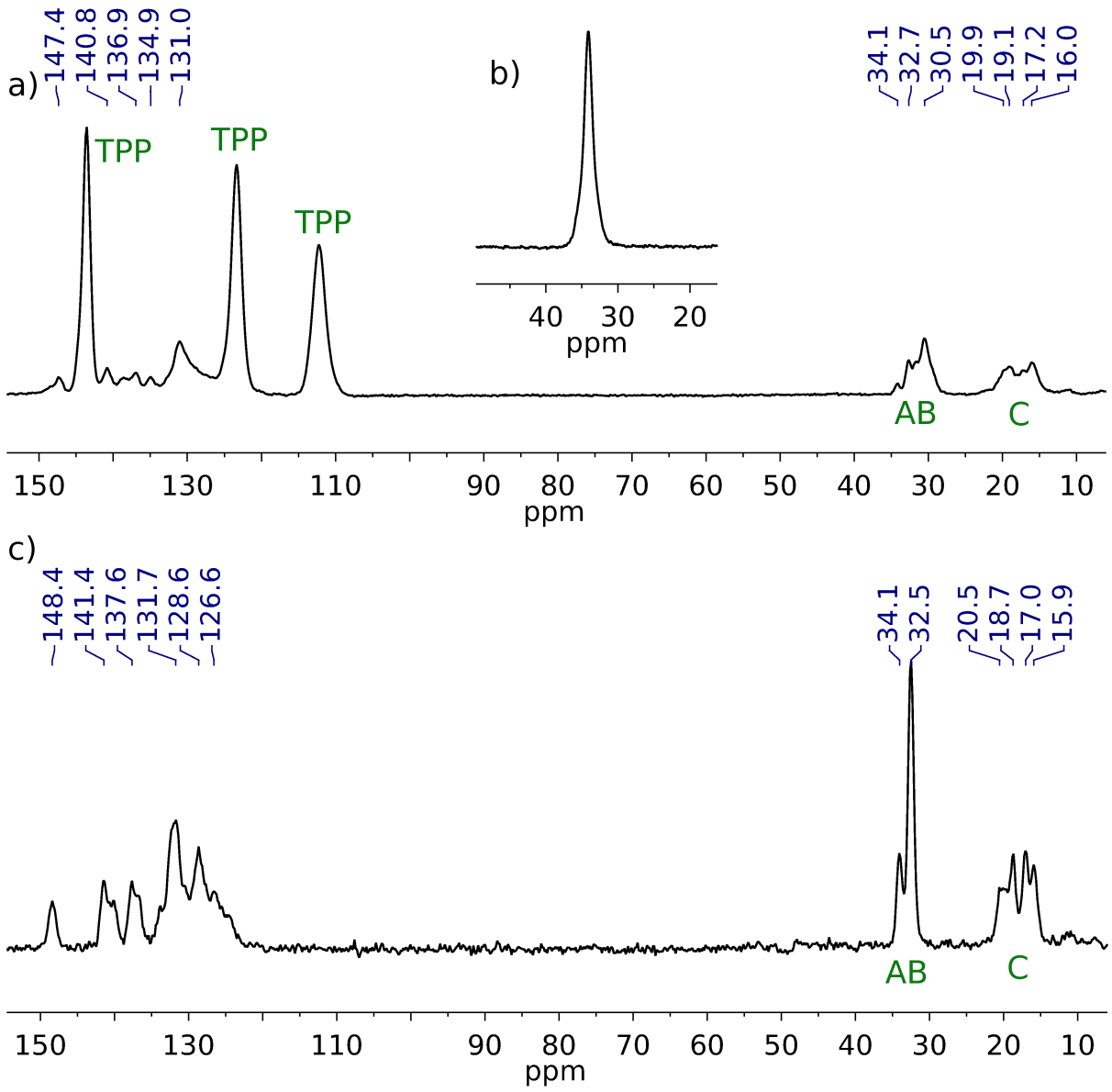

Figure 2.72: Rotor test compound.

A quick comparison (without the need for full signal assignments) of the solid-state ^{13}C NMR spectrum of the inclusion compound with the neat **86** solid-state ^{13}C spectrum reveals that the signals A (quaternary *t*-butyl carbon) and B (*t*-butyl methyl signals) move

upfield with respect to the spectrum of neat **86**, and that some of the compound **86** remained unincluded. The durene methyl signals show only very small changes in the chemical shifts. The inclusion compound was formed and the durene stopper remained unincluded.

2.7.1 Results

2.7.1.1 Synthesis

The fourth generation rotors **83**, **84**, **85** and the test compound **86** were synthesized as shown in Scheme 2.8.

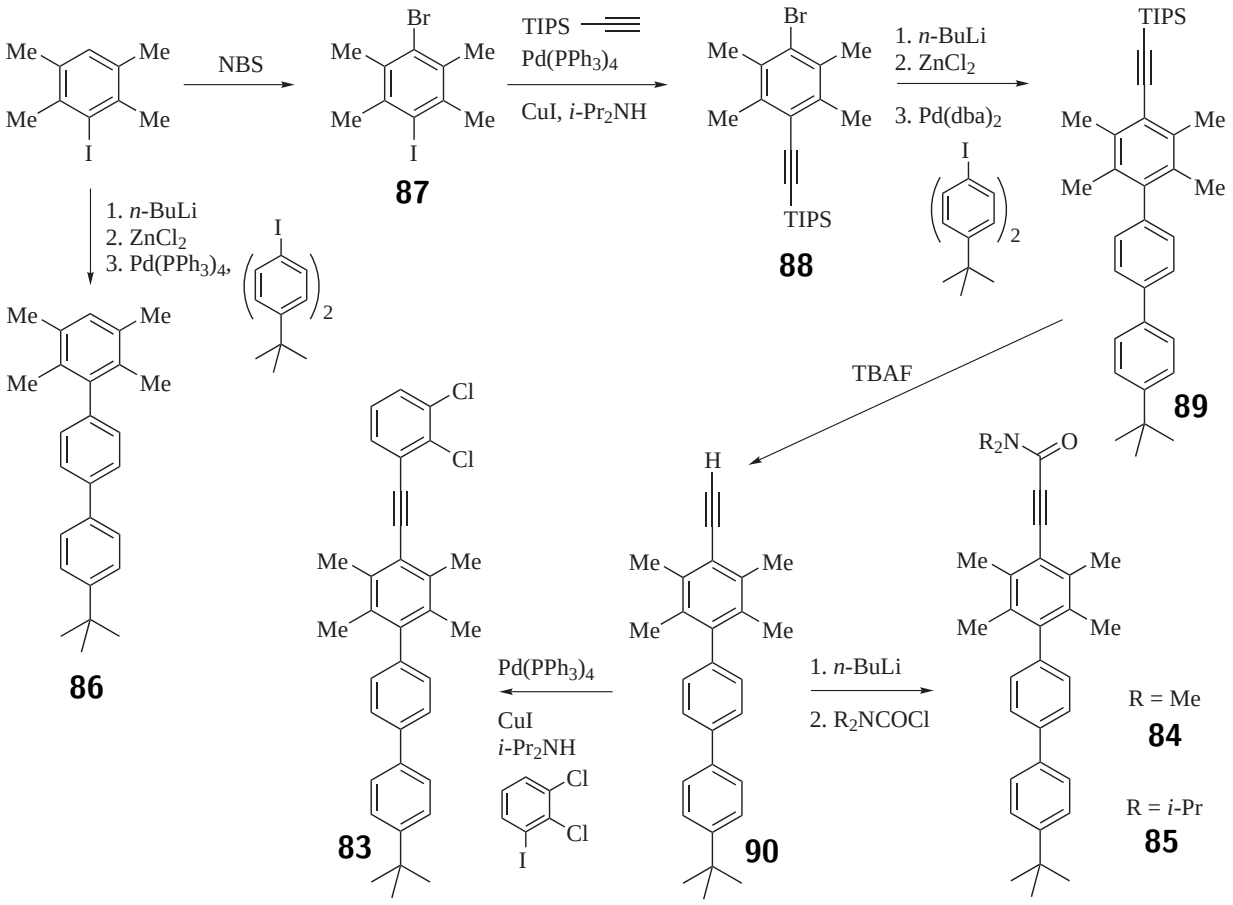

Scheme 2.8: Synthesis of the fourth generation compounds.

The lithiation of 3-iododurene with two equivalents of *t*-BuLi at -78°C, followed by transmetallation with zinc chloride at -78°C and Negishi coupling of the organozinc product

with *p*-*t*-butyl-*p*′-iodobiphenyl at 80 °C gave **86** in 82 % yield.

The bromination of 3-iododurene with NBS at 50 to 60 °C in the dark gave **87** in 93 % yield, and the Sonogashira coupling of the product with triisopropylsilyl acetylene yielded **88** in 85 % yield. The compound **88** was treated with *n*-BuLi at -78°C, the product was trans-metallated with zinc chloride at -78°C, and the resulting organozinc species was used in the Negishi coupling reaction with *p*-*t*-butyl-*p*′-iodobiphenyl to form **89** room temperature using $Pd(dba)_2$ as the catalyst (60 % yield). The use of tetrakis(triphenylphosphino)palladium as the catalyst required higher reaction temperature, and the yield of the desired product **89** was low.

The compound **89** was deprotected with TBAF in 97 % yield. The deprotonation of **90** with *n*-BuLi -78°C and subsequent reaction with an excess of N,N-dimethylcarbamoyl chloride or N,N-diisopropylcarbamoyl chloride yielded the rotors **84** (78 % yield) and **85** (65 % yield), respectively. The rotor **83** was prepared by the Sonogashira coupling of compound **90** with 1,2-dichloro-3-iodobenzene in 91 % yield.

2.7.1.2 NMR Assignments

Rotor 84. The carbon and proton NMR signals in the rotor **84** were assigned using ^{1}H , ^{13}C NMR, ^{1}H -^{1}H gCOSY (Figure 2.73a), ^{1}H -^{13}C gHSQC (Figure 2.73b) and ^{1}H -^{13}C gHMBC (Figure 2.73c).

The proton H_t was assigned based on the chemical shift, multiplicity and integration. The carbon C_t was assigned by its cross-peak with H_t in the gHSQC spectrum. The gHMBC cross-peaks of the proton H_t identify the carbons C_s and C_r. The proton H_p was assigned by its cross-peak with the carbon C_r in gHMBC, and the gHSQC spectrum was used for identification of C_p. The protons H_q were identified by their coupling to the protons H_p in the gCOSY spectrum. The carbons C_o and C_n were assigned by their gHMBC correlations with the protons H_q and H_p, respectively. The cross-peaks of C_o with H_m and C_n with H_l in gHMBC helped to identify the protons H_m and H_l and the carbons C_m and C_l were found

by the inspection of the gHSQC spectrum. The carbons C_k and C_j were assigned by their correlations with the protons H_m and H_l in the gHMBC spectrum.

Table 2.10: Summary of the NMR signal assignments for the rotor **84**.

Atom	^{1}H NMR δ [ppm]	^{13}C NMR δ [ppm]
a	3.07 and 3.34	34.37 and 38.54
b	-	155.28
c	-	89.31
d	-	90.02
e	-	120.22
f	-	132.61 or 137.34
g	2.50	125.90
h	-	132.61 or 137.34
i	1.96	18.19
j	-	143.82
k	-	140.66
l	7.13	129.44
m	7.61	127.08
n	-	139.46
o	-	137.98
p	7.65	126.77
q	7.50	125.90
r	-	150.46
s	-	34.70
t	1.38	31.53

The four-bond correlation of C_k and three-bond correlation of C_j with H_i in gHMBC were used for the indentification of the protons H_i, and the protons H_g were assigned based on their chemical shift and the integration in the ^{1}H NMR spectrum. The carbons C_e and C_d were identified by their cross-peaks with H_g in the gHMBC spectrum, and C_c, C_b, C_a and H_a were assigned based on their chemical shifts. The carbons C_h and C_f could not be identified as they only show correlations to both C_i and C_f. The NMR assignments are summarized in Table 2.10.

Rotor 85. The NMR signals in the rotor **85** were assigned using ^{1}H , ^{13}C NMR, ^{1}H -^{1}H gCOSY (Figure 2.74a), ^{1}H -^{13}C gHSQC (Figure 2.74b), and ^{1}H -^{13}C gHMBC (Figure

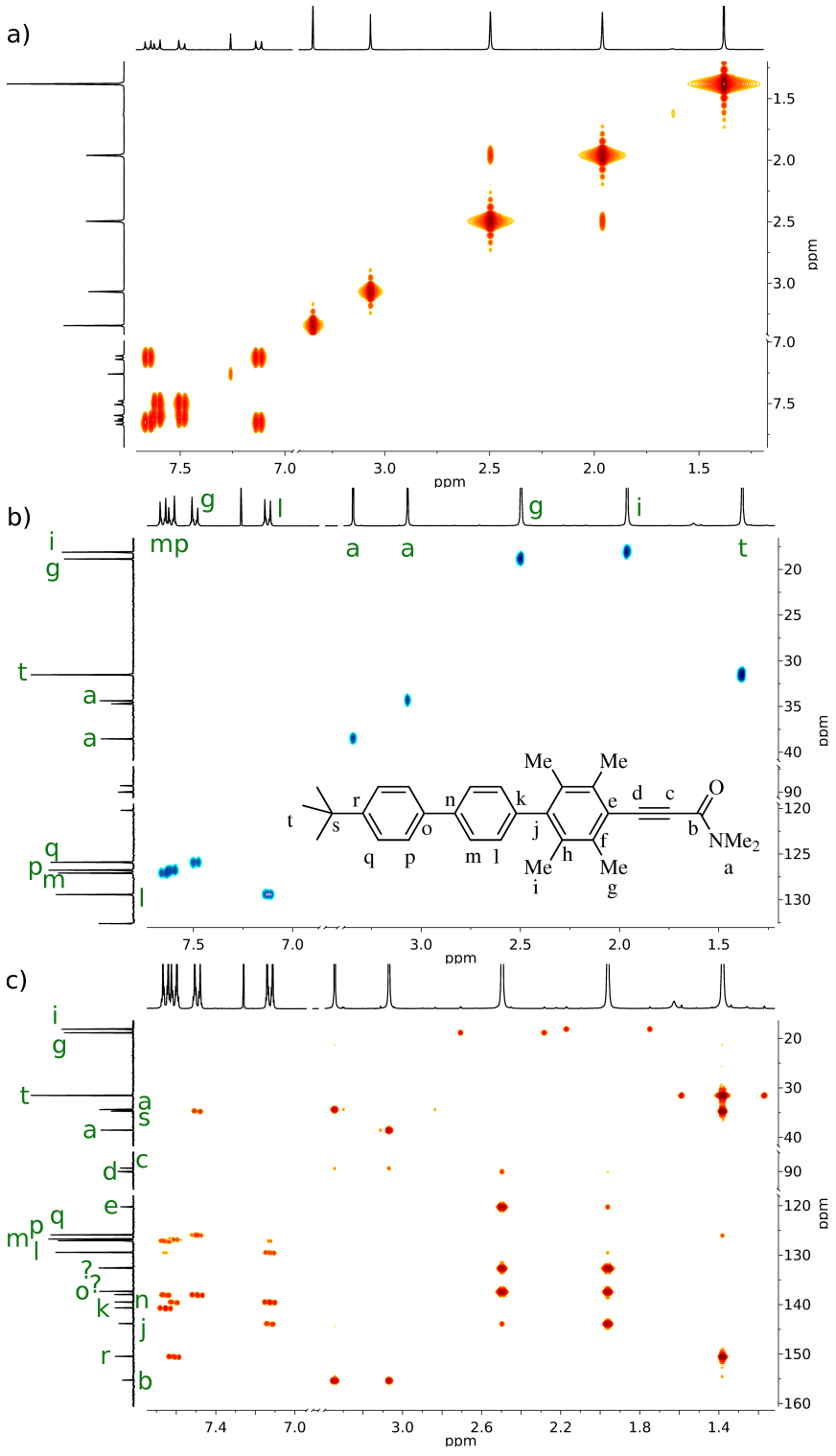

Figure 2.73: NMR assignments for **84**: a) ^{1}H -^{1}H gCOSY, b) ^{1}H -^{13}C gHSQC, c) ^{1}H -^{13}C gHMBC (J = 8 Hz).

2.74c).

The protons H_t were assigned based on their chemical shift, multiplicity and integration. The carbons C_t were assigned based on their cross-peak with H_t in the gHSQC spectrum. The gHMBC cross-peaks of the protons H_t helped to identify the carbons C_s and C_r. The protons H_p were assigned by their cross-peak with the carbon C_r in gHMBC, and the gHSQC spectrum was used for identification of C_p. The protons H_q were identified by their coupling to the protons H_p in the gCOSY spectrum. The carbons C_o and C_n were assigned by their gHMBC correlations with the protons H_q and H_p, respectively.

The cross-peaks of C_o with H_m and C_n with H_l in gHMBC identified the protons H_m and H_l and the carbons C_m and C_l were found with the help of the gHSQC spectrum. The carbons C_k and C_j were assigned by their correlations with the protons H_m and H_l in the gHMBC spectrum. The four-bond correlation of C_k and three-bond correlation of C_j with H_i in gHMBC were used for the indentification of the protons H_i, and the protons H_g were assigned based on their chemical shift and the integration in the ^{1}H NMR spectrum. The carbons C_e and C_d were identified by their cross-peaks with H_g in the gHMBC spectrum, and C_c and C_b were assigned based on their chemical shifts.

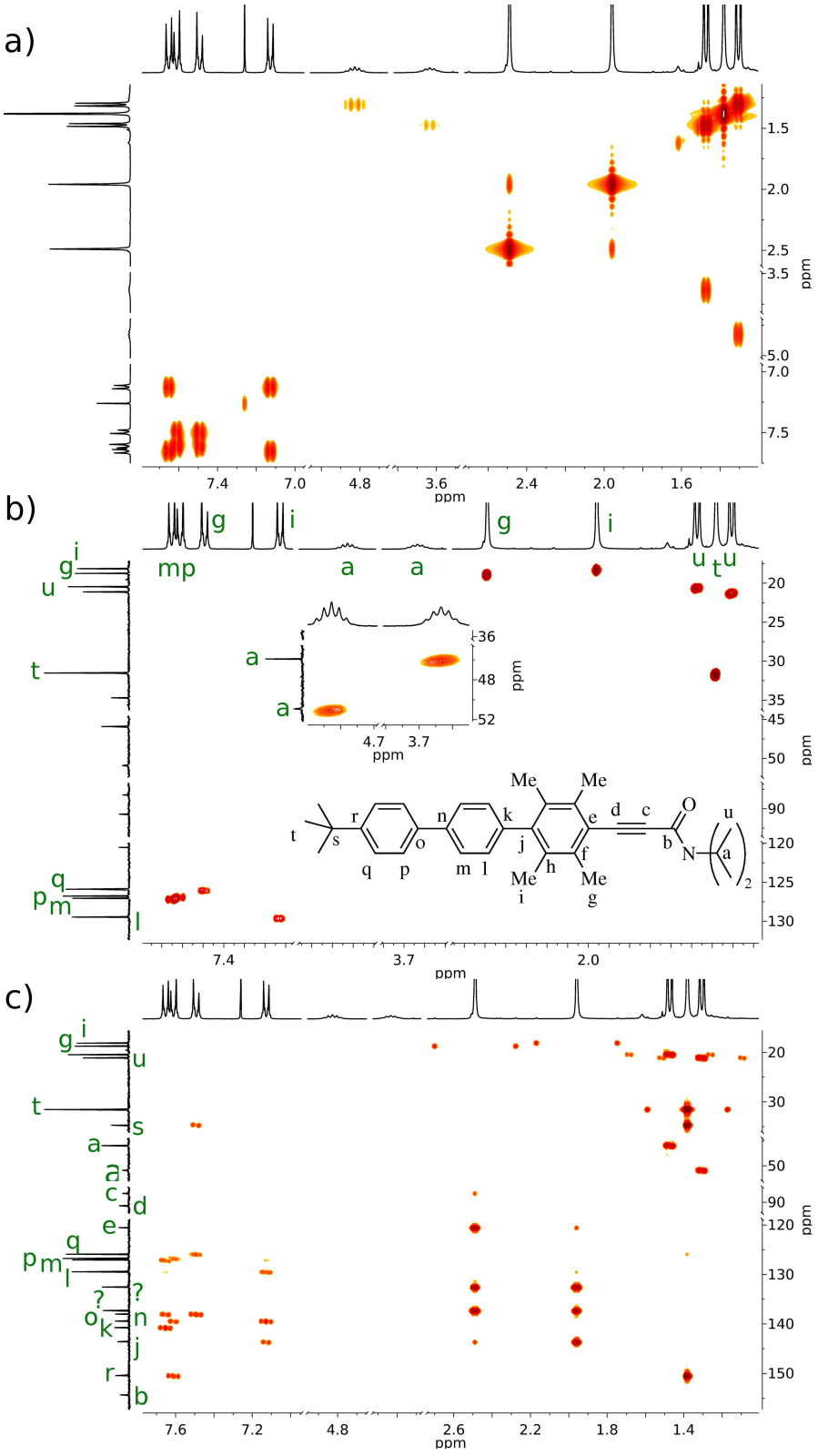

Figure 2.74: NMR assignments for **85**: a) ^{1}H -^{1}H gCOSY, b) ^{1}H -^{13}C gHSQC, c) ^{1}H -^{13}C gHMBC (J = 8 Hz).

The protons H_a and H_u were identified by its chemical shift, integration and the multiplicity, and the carbons C_a and C_u were assigned by their gHSQC cross-peaks with H_a and H_u, respectively. The carbons C_h and C_f could not be identified as they only show correlations to both C_i and C_f. The NMR assignments are summarized in Table 2.11.

Table 2.11: Summary of the NMR signal assignments for the rotor **85**.

Atom	^{1}H NMR δ [ppm]	^{13}C NMR δ [ppm]
a	3.63 and 4.83	45.92 and 50.92
b	-	155.33
c	-	90.70
d	-	88.23
e	-	120.53
f	-	132.54 or 137.29
g	2.49	18.74
h	-	132.54 or 137.29
i	1.96	18.11
j	-	143.60
k	-	140.73
l	7.13	129.47
m	7.61	127.06
n	-	139.42
o	-	138.00
p	7.65	126.77
q	7.49	125.90
r	-	150.44
s	-	34.70
t	1.38	31.53
u	1.31 and 1.47	20.46 and 21.12

2.7.1.3 Solid-State NMR

Rotor 83 and its inclusion behavior. The sample 15%**83**@TPP-d_{12} (15 mol % **83** in TPP-d_{12}) was prepared by the ball milling annealing procedure. Also different methods of preparation were tested such as co-crystallization, melting components together, prolonged ball milling, and annealing at higher temperatures. The different preparation methods resulted in samples with similar solid-state NMR features.

The solid-state ^{13}C CP MAS NMR (5 ms contact time, Figure 2.75a), ^{31}P CP MAS NMR (Figure 2.75b) and ^{31}P SPE MAS NMR (Figure 2.75c) spectra of 15%**83**@TPP-d_{12} were recorded. The 15%**83**@TPP-d_{12} solid-state ^{13}C CP MAS NMR shows no TPP-d_{12} signals and its spectrum matches the spectrum of neat **83**. The solid-state ^{31}P CP MAS NMR spectrum of 15%**83**@TPP-d_{12} shows a weak singlet at 34.0 ppm, and the solid-state ^{31}P SPE MAS NMR spectrum displays three resonances at 33.2 ppm, 36.4 ppm and 39.3 ppm.

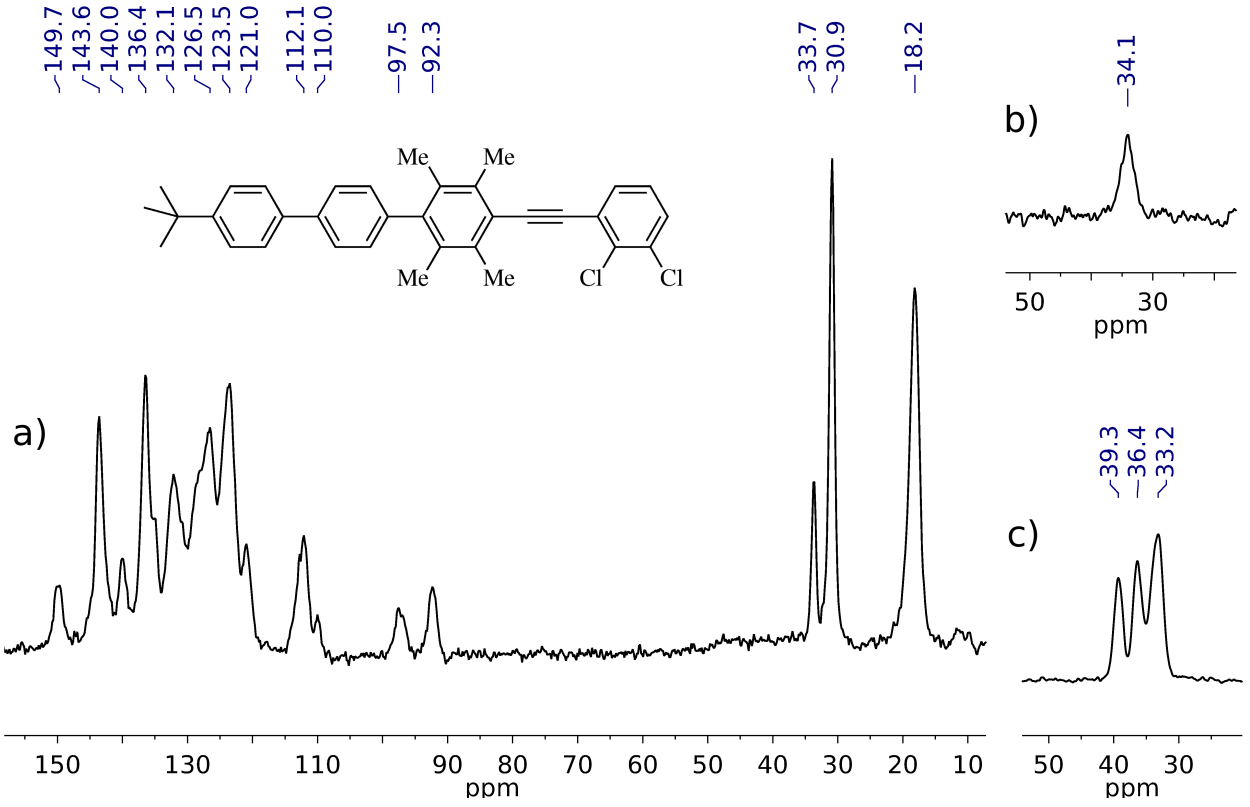

Figure 2.75: Solid-state NMR of 15%**83**@TPP-d_{12} a) ^{13}C CP MAS, b) ^{31}P CP MAS, c) ^{31}P SPE MAS.

Rotor 84 and its inclusion behavior. The inclusion compound 15%**84**@TPP-d_{12} (15 mol % **84** in TPP-d_{12}) was prepared by the ball milling annealing procedure.

The solid-state ^{13}C CP MAS NMR (5 ms contact time, Figure 2.76a), ^{31}P CP MAS NMR (Figure 2.76e), and ^{31}P SPE MAS NMR (Figure 2.76d) spectra of 15%**84**@TPP-d_{12}

were recorded. Both the solid-state ^{31}P CP MAS NMR and SPE MAS NMR of the inclusion compound 15%**84**@TPP-d_{12} show a singlet resonance at 34.1 ppm and 34.2 ppm, respectively.

The solid-state ^{13}C CP MAS NMR spectrum of 15%**84**@TPP-d_{12} displays three intense singlet resonances for the TPP-d_{12} carbons and the carbon signals of the guest rotor **84** have different chemical shifts than the solid-state ^{13}C CP MAS NMR spectrum of neat **84** (Figure 2.76b). The inclusion compound spectrum is not as well resolved as the neat **84** solid-state spectrum. The carbons C_b, C_c, C_d, C_e, C_g, C_i, C_r, C_s and C_t were assigned based on the comparison with **84** solution spectrum (Figure 2.76b). The carbon C_b in the inclusion compound exhibits two signals, both shifted upfield with respect to the solution spectrum, and one upfield, and the other downfield relative to the solid-state spectrum of neat **84**. The carbon C_r displays an upfield change in the chemical shift relative to both solution and the neat **84** solid-state spectrum.

The carbons C_e, C_c and C_d display two peaks each in the inclusion compound spectrum, one set of the signals with the chemical shift similar to the solution spectrum, and one set shifted upfield. The carbons C_a, C_s and C_t partially overlap, but they show components with the chemical shifts similar to the solution spectrum, and signals that are shifted upfield. The carbons C_g and C_i are not resolved, and they exhibit similar chemical shifts as in the solution spectrum. The signal is broader than in the neat **84** spectrum.

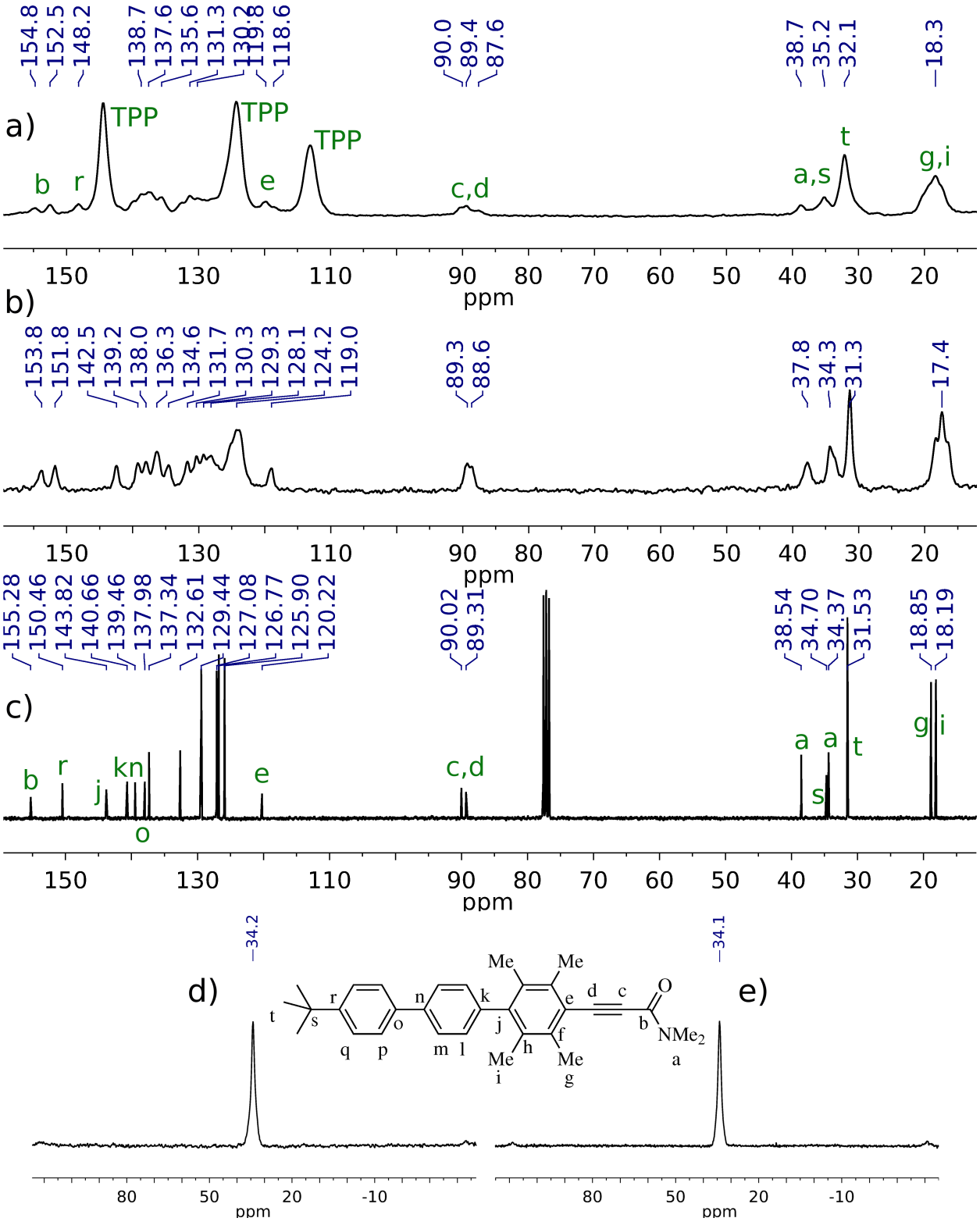

Figure 2.76: ^{13}C NMR spectra of **84** and 15%**84**@TPP-d_{12}: a) 15%**84**@TPP-d_{12} CP MAS, b) neat **84** CP MAS, c) NMR of **84** solution ($CDCl_3$).

Rotor 85 and its inclusion behavior. The inclusion compound 15%**85**@TPP-d_{12} (15 mol % **85** in TPP-d_{12}) was prepared by the ball milling annealing procedure. The solid-state ^{31}P SPE MAS NMR spectrum (Figure 2.77) of 15%**85**@TPP-d_{12} (Figure 2.77) shows a singlet resonance at about 34.0 ppm that partially overlaps with three singlets (39.4 and 36.3 ppm). The solid-state ^{13}C CP MAS NMR spectra of the inclusion compound 15%**85**@TPP-d_{12} (Figure 2.78a) and neat **85** (Figure 2.78b) were recorded using 5 ms contact time. The spectrum of neat **85** is remarkably well resolved and it closely resembles the solution ^{13}C NMR spectrum of **85** (Figure 2.78c).

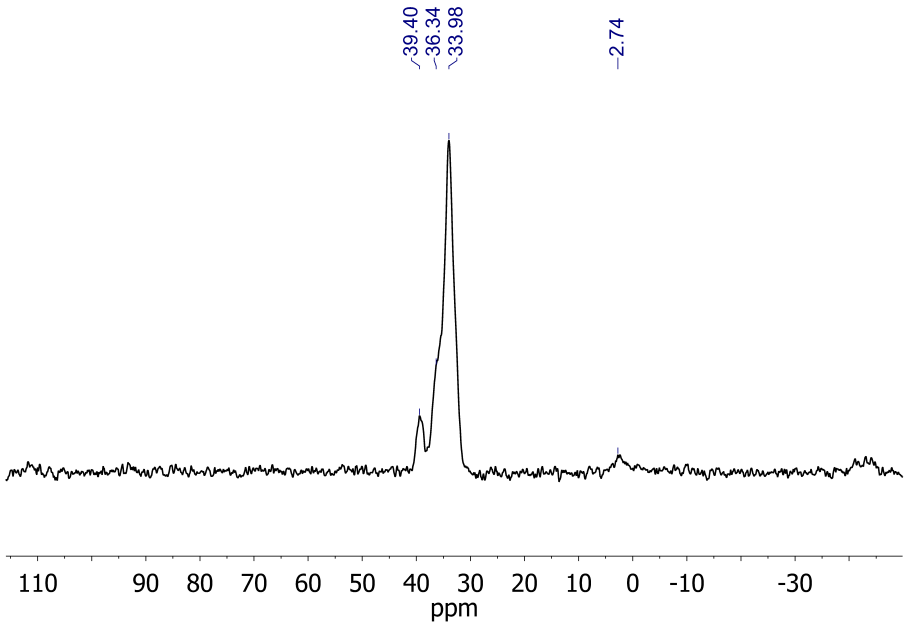

Figure 2.77: Solid-state ^{31}P SPE MAS NMR spectrum of 15%**85**@TPP-d_{12} (small upfield and downfield peaks are spinning sidebands).

The solid-state ^{13}C CP MAS NMR spectrum of 15%**85**@TPP-d_{12} displays three intense singlet resonances for the TPP-d_{12} carbons and the carbon signals of the guest rotor **85** have different chemical shifts than the solid-state ^{13}C CP MAS NMR spectrum of neat **85** (Figure 2.78b). The spectrum is highly heterogeneous, as displayed by the aromatic carbons and especially by the carbons C_a, C_b, C_c, C_d, C_g, C_i and C_u.

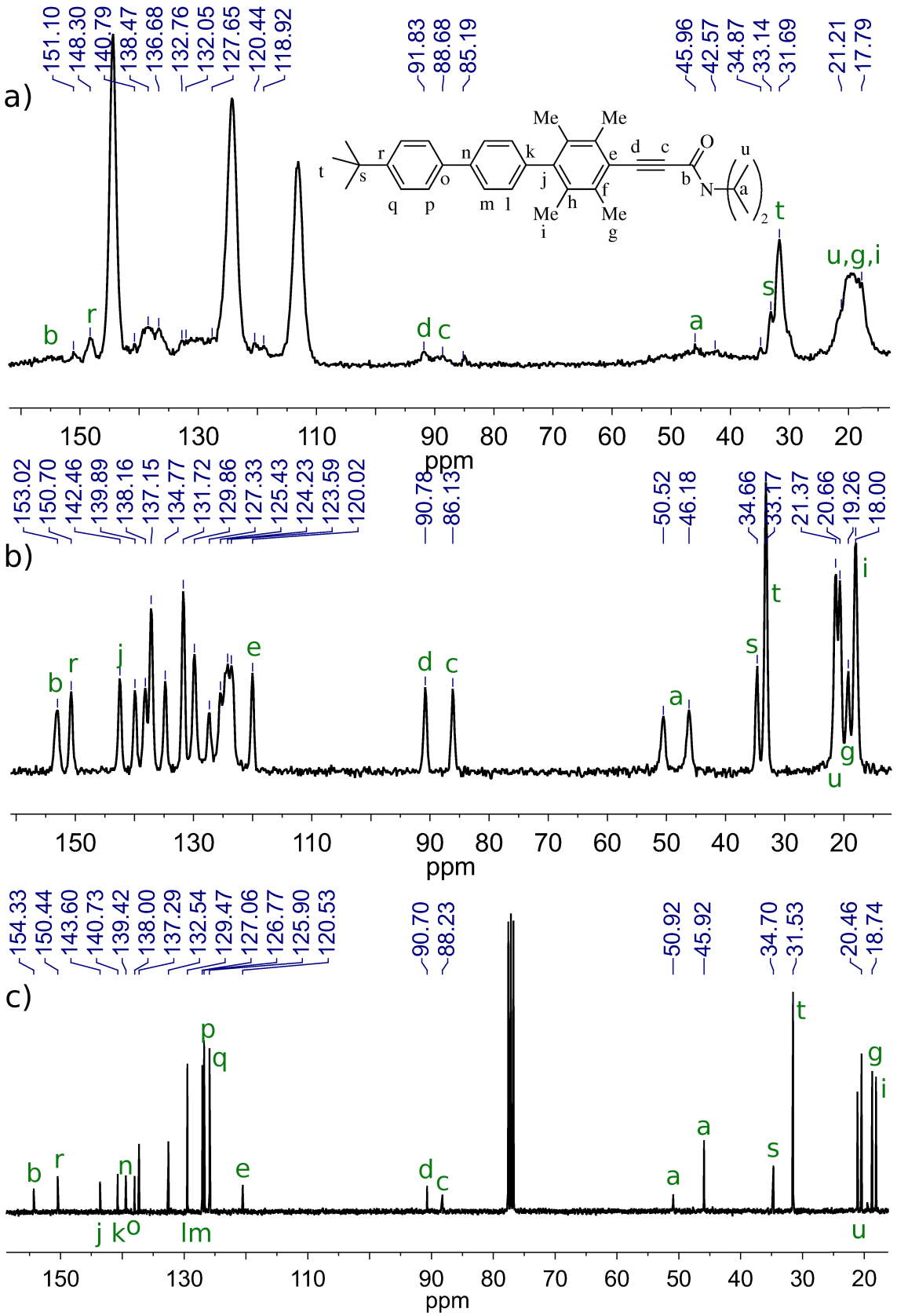

Figure 2.78: ^{13}C NMR spectra of **85** and 15%**85**@TPP-d_{12}: a) 15%**85**@TPP-d_{12} CP MAS, b) neat **85** CP MAS, c) NMR of **85** solution ($CDCl_3$).

The *t*-butyl carbons C_s and C_t both display an upfield change in chemical shift by about 1.5 ppm in the ^{13}C NMR spectrum of the inclusion compound 15%**85**@TPP-d_{12}. The inclusion compound spectrum also shows a small signal with carbon chemical shift close to that of C_s as the neat solid. The signal of carbon C_a in the inclusion compound spectrum is broad and moved upfield relative to the neat solid of **85**. The broad signal of carbon C_d in the inclusion compound spectrum displays about 1 ppm downfield change in chemical shift, while the carbon C_c shows two resolved signals, one moved downfield, the other upfield with respect to the neat solid of **85**. The signals of carbons C_g, C_i and C_u are not resolved in the inclusion compound spectrum, and they do not appear to display large changes in their chemical shifts relative to neat **85**. The carbon C_e gives rise to two signals in the inclusion compound spectrum, one has similar chemical shift as in neat **85**, the other is moved upfield.

Further milling and annealing did not improve the homogeneity of the sample significantly.

2.7.2 Discussion

2.7.2.1 Synthesis

The Negishi coupling used for the synthesis of compound **86** required elevated temperature. When *n*-BuLi was used to generate the organozinc intermediate by the lithiation and transmetallation with zinc chloride, no coupling reaction took place as the *n*-BuBr byproduct alkylated the triphenylphosphine and palladium metal precipitated out of the reaction mixture. The problem was solved by the use of *t*-BuLi in place of *n*-BuLi. The *t*-BuBr formed in the reaction is short lived as it reacts with the second equivalent of *t*-BuLi rapidly at -78°C.

The use of the tetrakis(triphenylphosphino)palladium catalyst in the synthesis of **89** was not successful, as the Negishi coupling with this catalyst required elevated temperature (80°C), and deprotection of the TIPS group took place, followed by unidentified side

reactions, most likely coupling of the deprotected acetylene derivative. Several catalysts ($Pd(PPh_3)_2Cl_2$, $Pd(dba)_2$, $Pd(dba)_2$ + tris(*o*-tolyl)phosphine, $PdCl_2$ + tris(*o*-tolyl)phosphine, $Pd(dppf)Cl_2$) were tested at a model coupling reaction of *p*-*t*-butyl-*p*′-iodobiphenyl with phenyltrimethyltin at room temperature, and $Pd(dba)_2$ has turned out to be a superior catalyst for this reaction.

The yields of rotors **84** and **85** were lower than expected due to presence of substantial amounts of amine hydrochlorides in the commercial N,N-dialkylcarbamoylchlorides that were used without purification.

2.7.2.2 Solid-State NMR

The signal assignment made by comparison of the solid-state ^{13}C NMR spectra of the inclusion compounds with the solution ^{13}C NMR spectra was discussed in previous sections (**??**), and much of the discussion also applies to this section.

Rotor 83 and its inclusion behavior. The absence of the carbon signals of TPP-d_{12} in the solid-state ^{13}C CP MAS NMR spectrum of 15%**83**@TPP-d_{12} (Figure 2.75a), and the fact that the spectrum is identical to the solid-state ^{13}C NMR spectrum of neat **83** are indication that no inclusion compound was formed. The three signals in the 15%**83**@TPP-d_{12} solid-state ^{31}P SPE MAS NMR spectrum confirm that no inclusion compound was formed. The presence of a weak singlet in the solid-state ^{31}P CP MAS NMR spectrum of 15%**83**@TPP-d_{12} is due to a small amount of TPP-d_{12} - water inclusion compound. As none of the usual inclusion compound preparation methods yielded any observable quantities of the inclusion compound, it is likely that the stabilization forces in the neat **83** are greater than in the inclusion compound.

Rotor 84 and its inclusion behavior. The three singlet carbon resonances in the solid-state ^{13}C CP MAS NMR spectrum of 15%**84**@TPP-d_{12} (Figure 2.76a) indicate the presence of TPP-d_{12} in the hexagonal form and the formation of an inclusion compound. This is further confirmed by the ^{31}P solid-state NMR spectra (Figure 2.76d,e).

The two sets of signals for the carbons C_b, C_c, C_d, C_e, C_r, C_s and C_t indicate two modes of insertion, one with the tail down the channel, and the other with the rotator into the channel, and thus formation of two different surface inclusion compounds. As more milling and annealing the inclusion compound 15%**84**@TPP-d_{12} does not change the solid-state NMR spectra significantly, the durene stopper does not insert into the channel. This is also supported by a similar chemical shift of the durene methyls in the inclusion compound and in the **84** solution spectrum. The insertion of the rotator was not expected as the acetylene axle does not provide strong stabilizing interactions with the channel due to the small van der Waals radius of acetylene, and it is undoubtedly favored by faster kinetics of insertion into the channel. Such cases were previously studied in the literature.[71]

Rotor 85 and its inclusion behavior. The presence of the carbon signals of TPP-d_{12} in the solid-state ^{13}C CP MAS NMR spectrum of inclusion compound 15%**85**@TPP-d_{12} (Figure 2.78a) indicate that the sample contains hexagonal TPP-d_{12} with guests inside and thus the inclusion compound was formed. This is also confirmed by the singlet resonance in the solid-state ^{31}P SPE MAS NMR spectrum (Figure 2.77, although the sample also contains monoclinic guest-free TPP-d_{12}.

The upfield changes in the chemical shifts of both *t*-butyl carbons show that the *t*-butyl is inserted into the channel and the small downfield carbon C_s signal indicates the presence of a small amount of unincluded rotor. The inclusion compound is highly heterogeneous. The signal of the carbons C_g, C_i and C_u provides some indication that the durene stopper is not inserted, although better signal separation is necessary to confirm this. Although many carbons display upfield changes in their chemical shift, it is not necessarily an indication of their insertion into the channel. The channel environment imposes quite uniform shielding environment, and if the upfield changes in chemical shifts were caused by the environment of the channel, much sharper signals would be expected. The solid-state ^{13}C NMR spectrum of the inclusion compound 15%**85**@TPP-d_{12} is more consistent with the rotors inserted into different extents and some of the changes in their chemical shifts are due to π-stacking

interactions between them.

The use of smaller loading of the rotor **85** in TPP-d_{12} could lead to more homogeneous inclusion compound.

2.7.3 Conclusions

Four new durene based compounds (**86**, **83**, **84** and **85**) were prepared and their inclusion behavior was studied. The compound **86** formed a surface inclusion compound 20%**86**@TPP-d_{12} as confirmed by solid-state NMR, and showed that the *p*-*t*-butylbiphenyl tail with durene stopper is suitable for preparation of surface inclusion compounds.

The rotor **83** did not form inclusion compound by any usual inclusion compound preparation technique, most likely because of too strong interactions in the crystal of neat **83**.

The rotor **84** formed two types of surface inclusion compounds, one with the tail inserted into the channel, and the other with the rotator inserted into the channel. This case showed the importance of bulky rotators. Even though the N,N-dimethylpropionamide rotator is not expected to have strong stabilizing interactions with the channel, and the insertion with the *p*-*t*-butylbiphenyl tail into the channel should be thermodynamicaly more favorable, the kinetics of the rotor insertion can be more important than the thermodynamics.

The rotor **85** formed a heterogeneous inclusion compound. The solid-state NMR data are consistent with the formation of a surface inclusion compound with partially inserted rotors, which form π-stacking interactions on the surface. Although, the poor signal separation due to high heterogeneity of the sample leaves considerable uncertainty.

Chapter 3

Toward Rotor Arrays Using Self-Assembled Monolayers

3.1 Introduction

3.1.1 Project Overview and Goals

This project explores another novel approach to ordered two-dimensional arrays of artificial dipolar molecular rotors through self-assembly process on a Langmuir-Blodgett water trough.

The target structures are illustrated in Figure 3.1. Each rotor possesses a stand composed of three long *n*-alkane chains terminated by a polar carboxylic acid group. The stand is connected to the rotator either directly (**91**), or via a *p*-phenyleneacetylenyl axle (**92**, **93**).

The carboxylic acid group has affinity for polar media and the rest of the rotor does not. Long *n*-alkanecarboxylic acids are known to self-assemble into organized monolayers on water surface upon compression of the monolayer. The monolayer can then be transferred onto a substrate using the Langmuir-Blodgett technique.[122] The carboxylic acid groups assemble at the water interface and the *n*-alkyl chains tightly pack together, locked in all-anti conformations.

The rotors are expected to assemble in a similar fashion: on the water trough with their carboxylic acid groups on the water surface, with the alkane chains approximately parallel with one another, and with the rotators at the top of the monolayer (Figure 3.2).

The rotors are tripodal as each rotor carries three *n*-alkane carboxylic acid groups. The rotor footprint is therefore approximately trigonal, and it is expected that at the tightest

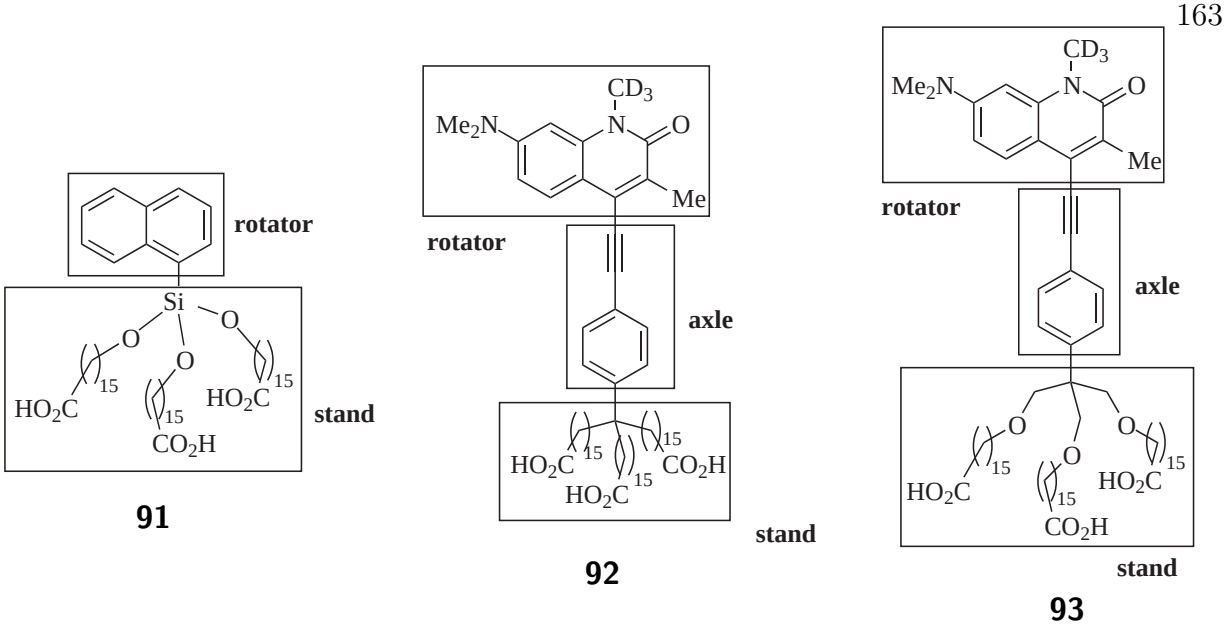

Figure 3.1: Rotor structures.

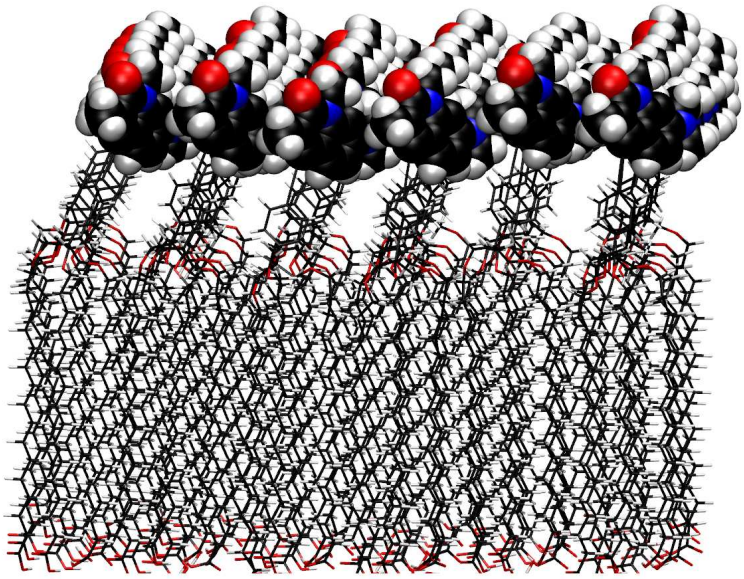

Figure 3.2: Anticipated rotor packing.

packing mode, they should assemble as shown in Figure 3.3, keeping the rotors in trigonal arrangement that should exhibit ferroelectric ordering in its ground state (Section 2.1).

The rotators chosen for the rotors **91**, **92**, and **93** are UV chromophores. The orienta-

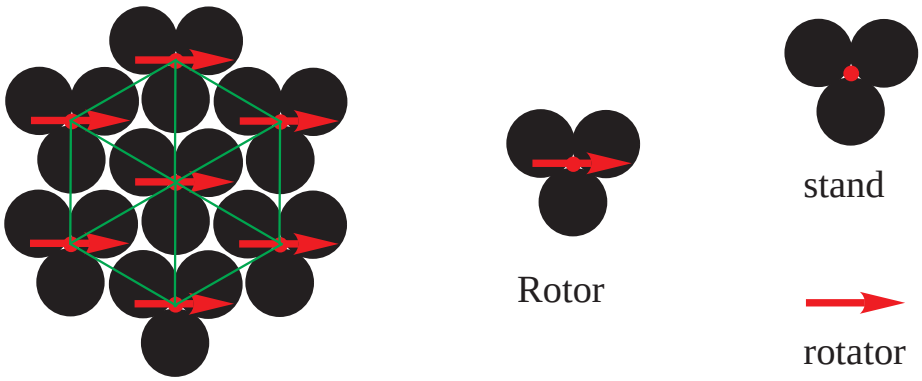

Figure 3.3: The expected rotor assembly on the water surface.

tion of the rotator can be determined from polarized UV-Vis absorption and emission spectra at different monolayer orientations if the directions of the transition dipole moments are determined first. Further information about the structure of the monolayer can be obtained from polarized GATR IR spectroscopy, from elipsometric measurements of the monolayer thickness, as well as from recording the transfer ratios during the process of Langmuir-Blodgett deposition onto a substrate, such as quartz and silicon wafers with native oxide layers.

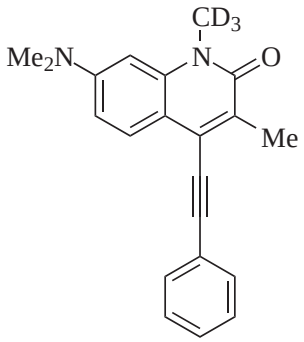

94

Figure 3.4: The chromophore used in the rotors.

The chromophore in rotors **92** and **93** was found by screening a number of potential candidates, and calculating the orientation of the transition dipole moments.[a] The orienta-

[a] Deborah L. Casher, unpublished results.

tion of the transition dipole moment of the lowest energy absorption for the chromophore **94** in compounds **92** and **93** was determined experimentally[123] to be in the axis perpendicular to the axis of rotation which is the most suitable orientation for determination of the rotator orientation. The chromophore has high quantum yield of fluorescence with the transition dipole moment also perpendicular to the axis of rotation (see section 3.1.3 for more details).

3.1.2 Langmuir-Blodgett Films

The surfaces of liquids have excess free energy due to the difference in environments between the liquid-air interface and the bulk liquid.[124] The differences are especially large for solvents forming strong hydrogen bonds, such as water, and they are demonstrated by a high value of the surface tension γ, given by:

$$\gamma = (\partial G/\partial S)_{T,p,n}, \tag{3.1}$$

where G is the free energy, S is the surface area, while the temperature T, ambient pressure p and the composition n are held constant. The high value of water surface tension (73 mN/m at 20°), its availability as well as lack of toxicity and the solvent properties make it by far the most used subphase.

A typical material that forms monolayers on water is amphiphilic, *i.e* it contains both hydrophilic groups and hydrophobic tails, such as long alkanoic acids (more than 13 carbons long), long alkanols, oligophenylenecarboxylic acids or phenols, etc. The monolayer material must be insoluble in the subphase.

The molecules are typically introduced onto the surface of water in a volatile solvent which is then allowed to evaporate, leaving behind a a sparse monolayer. The molecules in the initial monolayer on the sublayer surface are far apart, interact only weakly with each other, and are oriented with the hydrophobic part toward the surface. The monolayer is then compressed, and the surface pressure Π is monitored as a function of the monolayer

surface or mean molecular area. The surface pressure Π for a system in equilibrium is given by:

$$\Pi = \gamma - \gamma_0, \tag{3.2}$$

where γ is the surface tension in the absence of a monolayer and γ_0 is the surface tension with the monolayer at a given compression. The maximum possible monolayer surface pressure γ_0 is the subphase surface tension γ at a given temperature.

A plot showing the dependence of the surface pressure Π on the surface area S at a constant temperature (surface pressure/area isotherm) is an important characteristic of the monolayer. Such plots usually contain several distinct parts (Figure 3.5), classified by Harkins.[125]

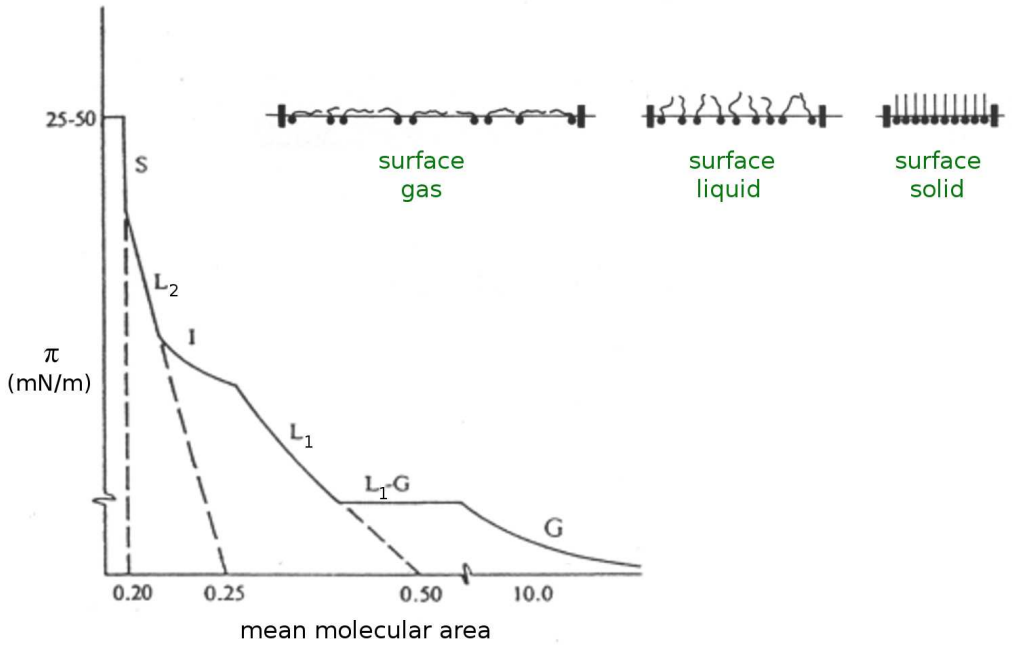

Figure 3.5: Typical surface pressure/area isotherm.

When the molecules are far apart and they do not interact strongly, the surface pressure raises slowly with monolayer compression (Figure 3.5, part G of the plot). The molecules

are in the surface gas state.

When the molecules get into a closer contact, the response of the surface pressure with decreasing surface area becomes larger, as indicated by the steeper section L_2 in the surface pressure/area isotherm. This section corresponds to the surface liquid state.

Upon even closer contact of the molecules, the surface pressure increases greatly with small reductions of the monolayer surface area as indicated by the steepest section, S, in the surface pressure/area isotherm. This section corresponds to the ordered surface solid state. Upon greater compression, the monolayer collapses. The stability of the monolayer against the collapse can be estimated from the equilibrium spreading pressure, which is the surface pressure generated when an excess solid material is put on the trough. At a pressure that is higher than the equilibrium spreading pressure, there is a tendency for the monolayer to aggregate into crystals, although the process is in most instances sufficiently slow that it can be ignored when preparing a monolayer.

Depending on the nature of the monolayer, other parts of the isotherms can often be distinguished: the liquid-expanded state (L_1), the transition of the surface liquid into the liquid-expanded state (L_1-G), and the transition of the liquid-expanded state into the liquid state (I).

The shape of the isotherm is greatly dependent on the temperature (Figure 3.6). For instance, above certain temperature that corresponds to the melting of the surface solid, no surface solid part of the isotherm is observed.

Mixed monolayers with comparable amounts of each component can display two types of behavior: if the components are not miscible, domains of each components exist in the resulting film. If the components are miscible, the resulting films are uniform. The two types of monolayers can best be distinguished by their collapse point characteristic. The uniform monolayer shows a single breakage point, usually different from the ones of the components. A monolayer with inmiscible components shows several breakage points that correspond to breakage points of each neat component films.

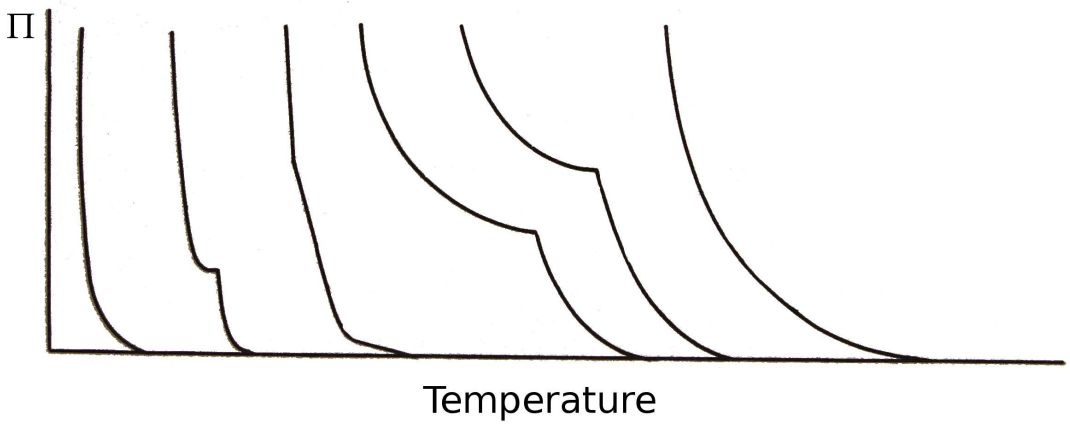

Figure 3.6: Surface pressure/area isotherms versus temperature.

Langmuir-Blodgett deposition. The monolayers can be transferred from the subphase onto a solid substrate using the Langmuir-Blodgett deposition technique: the substrate is first lowered into the subphase, and after the monolayer is formed and compressed, the substrate is slowly withdrawn, while maintaining a constant surface pressure (Figure 3.7).

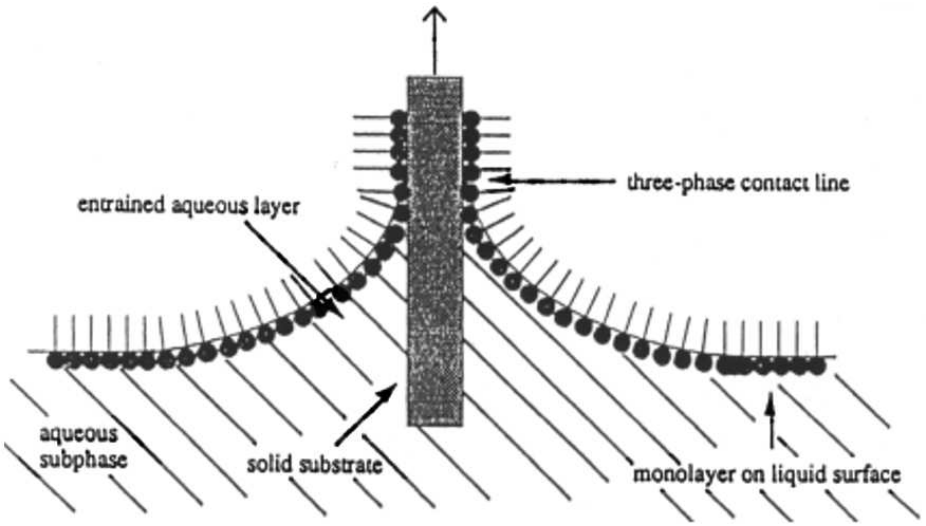

Figure 3.7: Langmuir-Blodgett deposition.

The surface pressures used for the deposition are usually 10 to 40 mN/m. Higher surface pressures usually result in monolayer collapse during the transfer. The collapse of

a monolayer that is normally stable at the given surface pressure is caused by the steric interactions between the chain ends due to bending of the monolayer because of the liquid-substrate meniscus orientation (Figure 3.7). For successful deposition the inequality $-W_{tt} > \gamma$ needs to be satisfied, where W_{tt} is the interaction energy of the tail groups per unit area.

A measure of the quality of the deposition is the transfer ratio. It is defined as the ratio between the surface area removed from the trough and the surface area of the substrate. The transfer ratio should be unity for good deposition, a deviation from this value is a sign of changing molecular orientation during the transfer, insufficient deposition or the collapse of the monolayer.

If the substrate is hydrophilic, the deposition will occur with the hydrophilic ends onto the substrate. It is possible to achieve the opposite orientation and the deposition of multilayers by repeated dips and to control the relative orientations of the hydrophilic ends in the film.[126–135]

The presence of cations and the pH greatly affect the behavior of the monolayer. Cations that form soluble salts (Na^+, K^+) with the alkanoic acid cause formation of micelles that competes with film formation. On the other hand, doubly charged ions (Ca^{2+}, Ba^{2+}, Cd^{2+}) form insoluble soaps with alkanoic acids and they increase the stability of the monolayer. The monolayers of bivalent cations are usually highly organized. Triply charged ions in the subphase (Al^{3+}, Fe^{3+}) form very rigid monolayers with alkanoic acids, and they cannot usually be transferred onto a substrate.

The cations incorporate into the film. The extent of incorporation depends on the subphase pH and the pK_A of the alkanoic acid. At higher pH, the acid is ionized more and more metal cations are incorporated. If the pH is too high, bilayers with the M^{2+} cation are formed (above pH 6.4 for stearic acid with 10^{-4} M Ca^{2+} in the subphase)[136].

The presence of metal ions and the pH also affect the structure of the monolayer and the tilt angle of the acid in the monolayer,[137,138] which is usually between 0° and 40°, as determined by grazing incidence X-ray diffraction,[139,140] polarized FT-IR ATR,[141,142] and

reflection absorption measurements[143,144] of LB films on a wide range of substrates.

3.1.3 Previous Work

The lowest energy UV singlet-singlet absorption band and the emission band of **94** were determined using steady state fluorescence and excitation anisotropy of **94** in a glassy matrix, combined with its IR and UV-vis linear dichroism in stretched polyethylene.[123] The experiments show that the lowest energy UV absorption band and the emission band of of **94** are purely polarized with transition dipoles essentially perpendicular to the triple bond axle of the rotator, while the transition dipole of the second UV band lies very close to the direction of the axle (Figure 3.8).

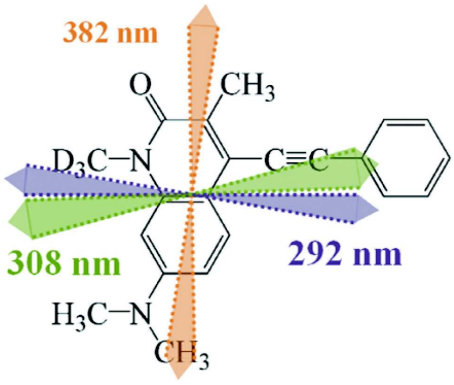

Figure 3.8: Carbostyril chromophore **94** electronic transition dipole moment orientations.[123]

The orientation of the fatty acid chains in the monolayer of rotor **91** was elucidated based on the analysis of the FT-IR GATR spectra of the neat **91** monolayers as well as mixed monolayers with stearic acid.[145] The asymmetric and symmetric carboxylate bands and C-H stretching bands as well as elipsometric thickness measurements were used for the analysis. The results showed the average tilt angle to be around 19° for the alkyl chains.

The orientation of the naphtalene ring in **91** monolayers was determined using FT-IR GATR spectra, UV-vis absorption spectra and steady state fluorescence polarization.[145] The tilting of the rotator from the surface normal was found to be between 55° and 66°.

Evidence for rotor aggregation was found from the red-shifted UV absorption bands relative to the solution. The red-shifted absorption was not observed in **91** films strongly diluted with stearic acid.

3.2 Results

Synthesis of 94. The test chromophore was synthesized according to Scheme 3.1.

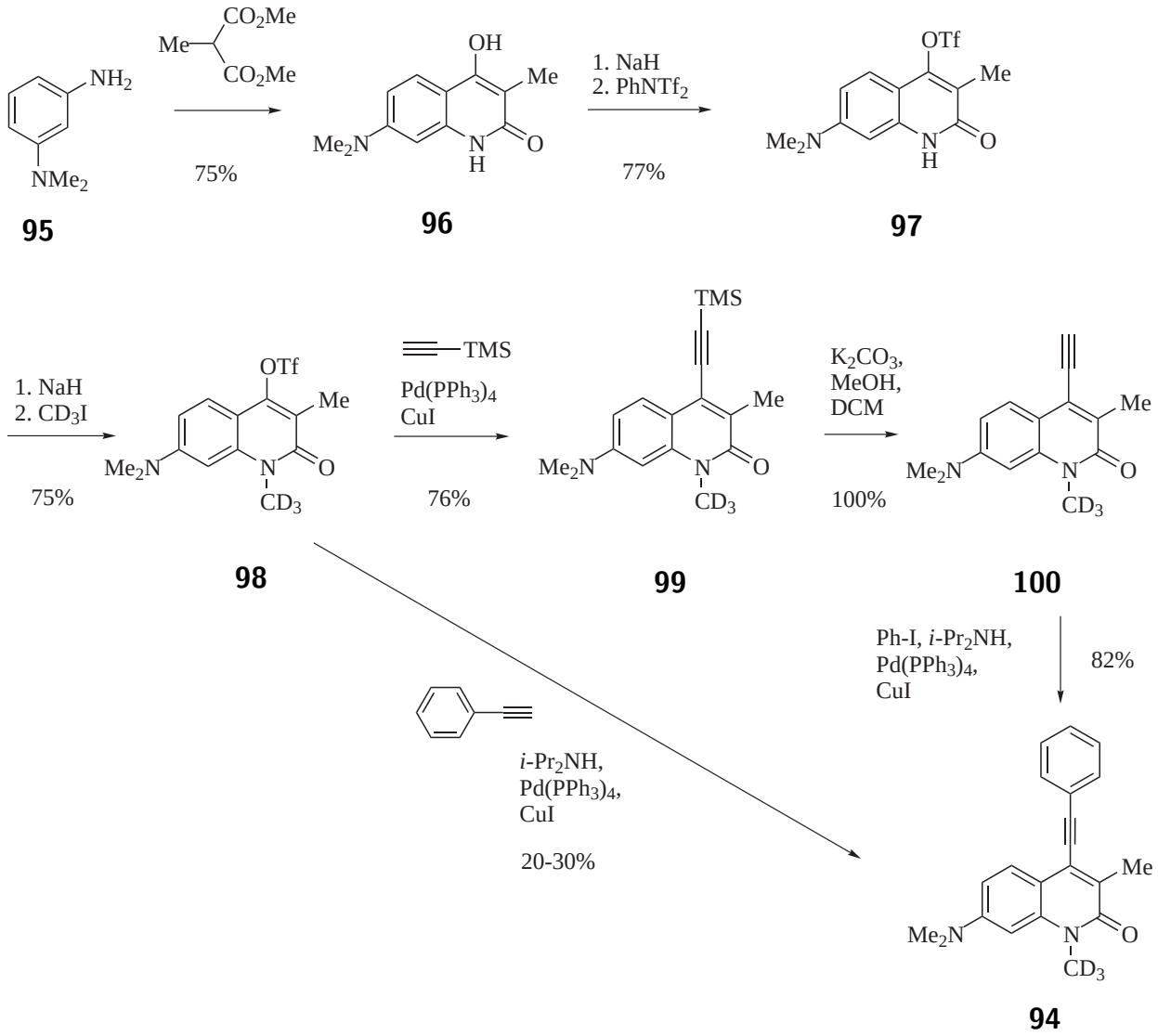

Scheme 3.1: Synthesis of **94**.

The carbostyril derivative **96** was prepared by heating diamine **95** at 200 to 270 °C

according to a known literature procedure in 75% yield.[146]

The deprotonation of **96** with sodium hydride and triflylation with N-phenyltriflimide gave **97** in 77% yield. The compound **97** was then deprotonated with sodium hydride and methylated with methyl-d_3 iodide to yield **98** (75% yield).

The compound **94** can be synthesized directly by Sonogashira coupling of **98** with phenylacetylene, but the yields were low (20 to 30%). On the other hand, Sonogashira coupling of **98** with trimethylsilylacetylene using tetrakis(triphenylphosphino)palladium as a catalyst gave **99** in 76% yield.

The compound **100** was prepared by deprotection of **99** with potassium carbonate in dichloromethane and methanol in quantitative yield.

The compound **94** was synthesized by Sonogashira coupling of **100** with iodobenzene using tetrakis(triphenylphosphino)palladium catalyst (82% yield).

Synthesis of 91. The rotor **91** was synthesized as shown in Scheme 3.2.

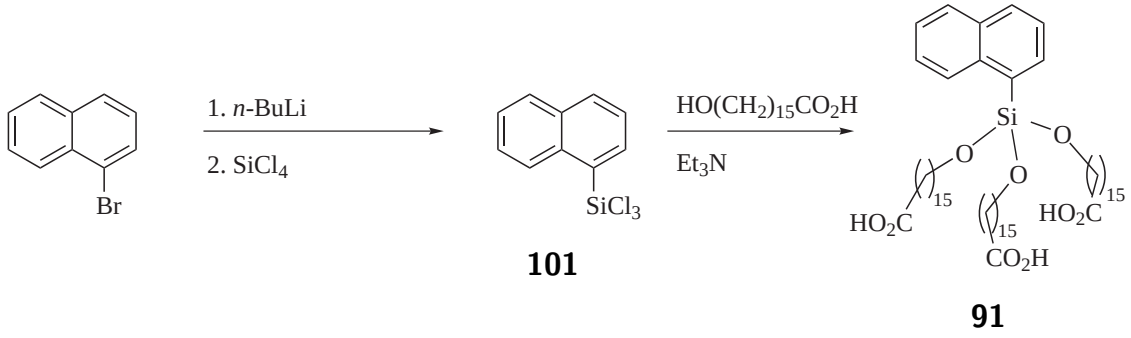

Scheme 3.2: Synthesis of **91**.

The starting 1-bromonaphtalene was lithiated with *n*-BuLi and treated with an excess of silicon tetrachloride to yield **101** which was then reacted with 16-hydroxyhexadecanoic acid in presence of triethylamine to form **91** (40% yield).

Attempted synthesis of 92. The synthesis of the rotor **92** was attempted by a sequence of reactions shown in Scheme 3.3.

The reduction of the carboxylic acid **102** with borane in anhydrous THF yielded **103** (98% yield). The protection of **103** was then performed using methoxymethyl chloride in the presence of diisopropylethylamine (96% yield) or with triisopropylsilyl chloride in the presence of pyridine and DMAP (87% yield).

The lithiation of **104** with *t*-BuLi or magnesiation with metallic magnesium and subsequent reaction of the organometallic compound with phosgene or triphosgene in various solvents (THF, diethyether, *n*-hexane, *n*-octane, *n*-octane/diethyether) gave low yields of the desired product **105** that could not be fully purified.

The deprotection of crude **106** with lithium tetrafluoroborate in boiling acetonitrile for three weeks gave **107** in 30% yield and a mixture of partially MOM-protected products.

The oxidation of **107** with sodium hypochlorite and chlorite with catalytic amounts of TEMPO gave quantitative conversion to **108**. The Friedel-Crafts reaction of **108** gave low yields of **108** which upon halogenation (NBS, NIS in triflic acid, bromine with $FeBr_3$) gave an inseparable mixture of para (major) and meta (minor) products.

Synthesis of 93. The rotor **93** was synthesized as shown in Scheme 3.4.

The bromoacid **102** was transformed into the acid chloride with thionyl chloride and then into the amide by the treatment with excess dimethylamine in dichloromethane (99% yield). The bromoamide **112** was then used in alkylation of the alcoholate from **113**, generated with sodium hydride, to form **114** in 72% yield.

The deprotection of the amide **114** with triflic anhydride and subsequent treatment with methanol[147] yielded **115** (79% yield). The Sonogashira coupling of **115** with trimethylsilylacetylene gave **117** in 67% yield. The deprotection of **117** yielded a quantitative amount of **116** which was then used in the Sonogashira coupling with **97** to prepare **118** in 60% yield.

The compound **118** was alternatively prepared by Sonogashira coupling of **119** with **100** in 82% yield. The iodo derivative **119** was synthesized from **115** by copper catalyzed

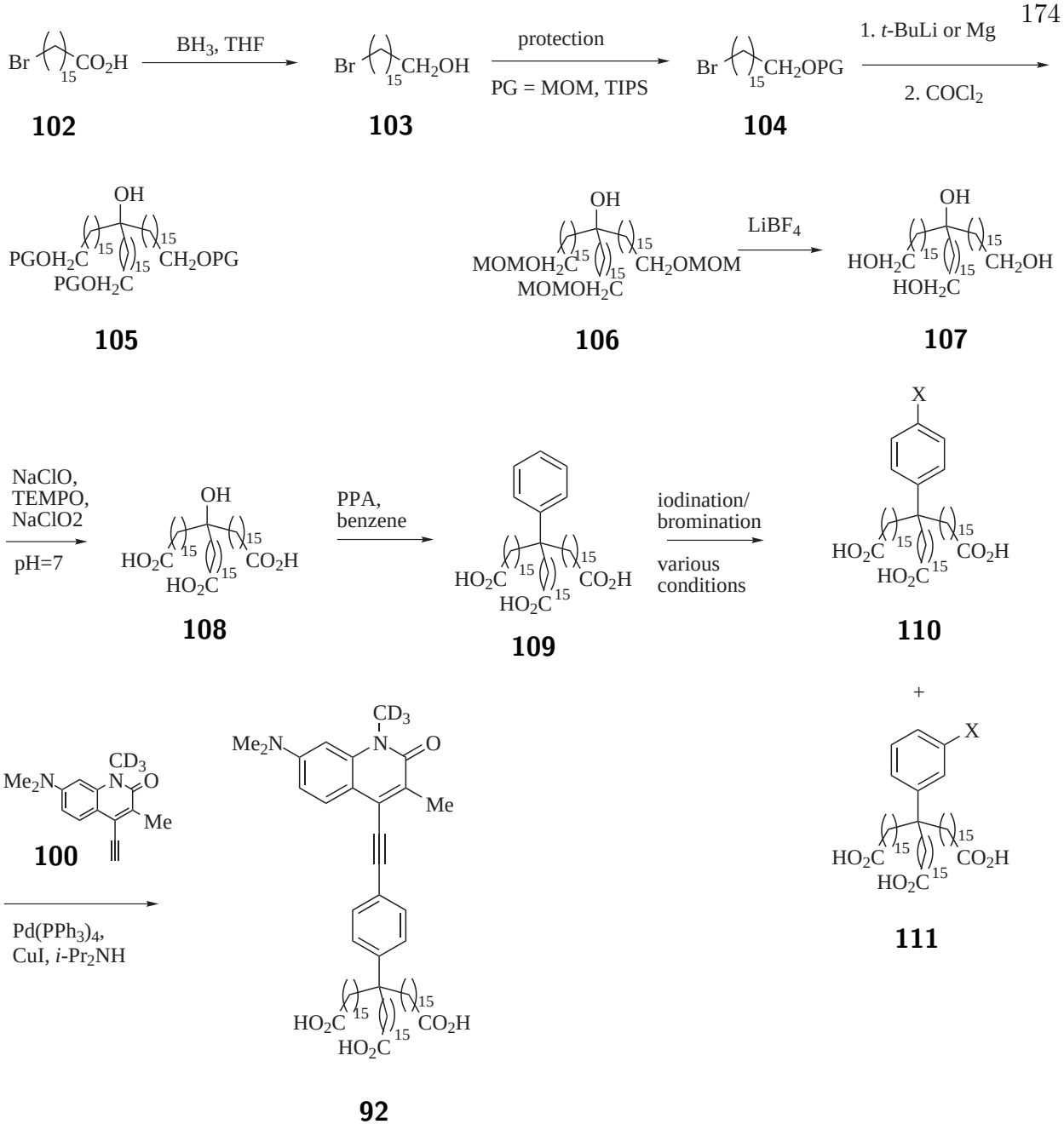

Scheme 3.3: Attempted synthesis of **92**.

Finkelstein reaction[148] in 98% yield.

Calculations. The geometry of a set of 32 rotors **93** was optimized using universal force field and simulated annealing (400 K to 0 K). The monolayer was built from UFF-

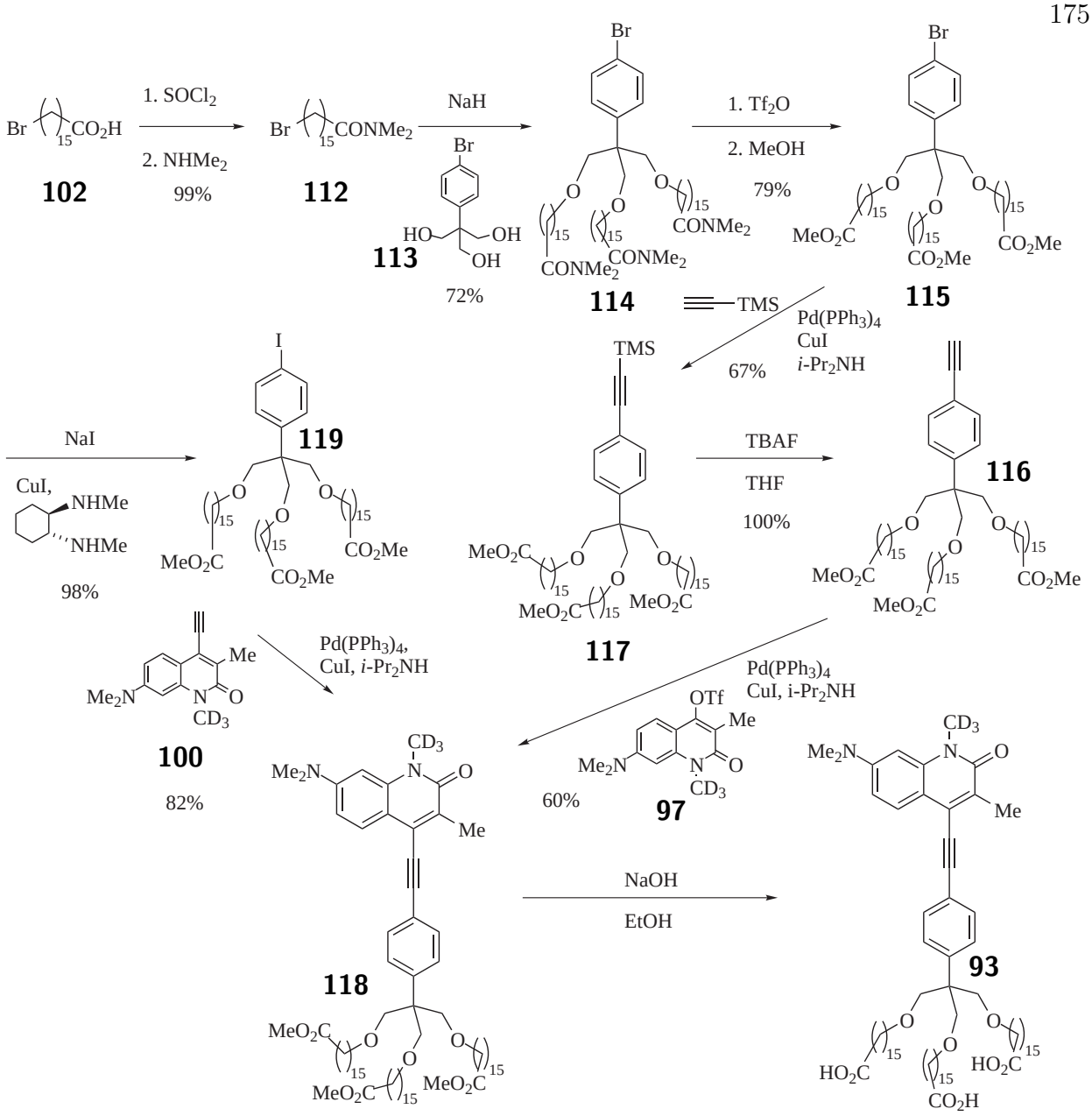

Scheme 3.4: Synthesis of **93**.

optimized molecules **93** and the carboxyl carbons were constrained in the xy plane during the optimization. The optimized geometry is shown in Figure 3.9. The rotors show a mean tilt angle from the surface normal of 33°.

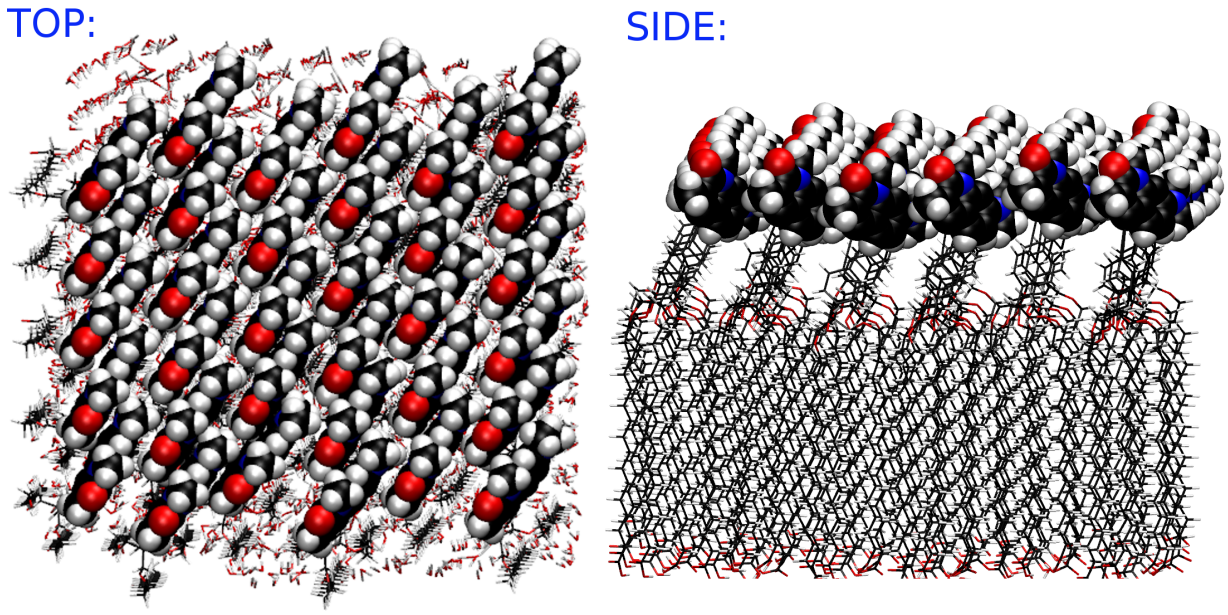

Figure 3.9: Monolayer of **93** optimized by UFF.

3.3 Discussion

Synthesis of 94. The compound **94** was synthesized by a straightforward sequence of reactions (Scheme 3.1). The only somewhat troublesome step was the coupling of **98** with phenylacetylene, which provided only small yields of the product due to low reactivity of both the triflate **97** and the phenylethynylcopper(I) species, and the product was difficult to purify. The desired product **94** was therefore synthesized in three steps: the coupling reaction of **97** with more reactive trimethylsilylethynylcopper(I) proceeds smoothly and gives **99** in a high yield. This was followed by deprotection of the trimethylsilyl group and a coupling reaction with a reactive iodobenzene.

Synthesis of 91. The combination of the carboxylic acid groups and the silyl ethers proved to be unfortunate. The product **91** is sensitive to water and all the work-up had to be done with strict exclusion of moisture. When the reaction mixture with **91** was treated with water, the rotor **91** precipitated out as a sparingly soluble hydrate that underwent slow decomposition - hydrolysis of the silyl ethers catalyzed by the carboxylic acid groups. Water

could not be removed from the hydrate of **91** by conventional drying agents (sodium sulfate, magnesium sulfate, 4 Å molecular sieves) or under reduced pressure. The purification of **91** to remove the triethylammonium chloride side product was achieved by repeated crystallizations from anhydrous acetonitrile.

Attempted synthesis of 92. The lithiation of **104** was troublesome, and it did not proceed at an appreciable rate until close to 0 °C as confirmed by ^{1}H NMR of the reaction mixtures quenched with water. At this temperature, also dehydrobromination to produce **121** was competing with the desired lithiation at an appreciable rate (Scheme 3.5). Various solvents used in the reaction did not help to solve the problem, which was ultimately circumvented by the use of magnesium, which produced **122** in good yields.

The reaction of the organomagnesium compound **122** with phosgene or triphosgene in THF resulted in a mixture of products. Besides the desired compound **105**, products **124** and **125** of the reduction of the ketone **123** with the organomagnesium compound **122**, were formed. Peculiarly, unreacted ketone **123** was always present in the reaction mixture in small quantities, even though the organometallic compound was used in excess. The product **105** could not be obtained pure.

The deprotection of **106** was very slow and it was not complete in three weeks, although the reaction under such conditions usually requires only several hours.[149]

Given the unusual unreactivity of the compounds in the lithiation reactions, reactions of organometallic compounds and in the deprotection of the MOM protecting group, it was thought that there is an underlying reason for these problems. It was hypothesized that the compounds form stable micelles and reversed micelles in the solutions, and the reaction center is locked inside. Thus, the reactions require higher temperatures than is usual for these types of reactions, for the aggregates to dissociate at appreciable rates. At such temperatures, side reactions occur in some instances.

It is believed that this is the reason for the slow lithiation of **104** that occured at

temperature when dehydrobromination significantly competed. As the magnesiation is done in refluxing THF, the use of organomagnesium reagents solved the problem.

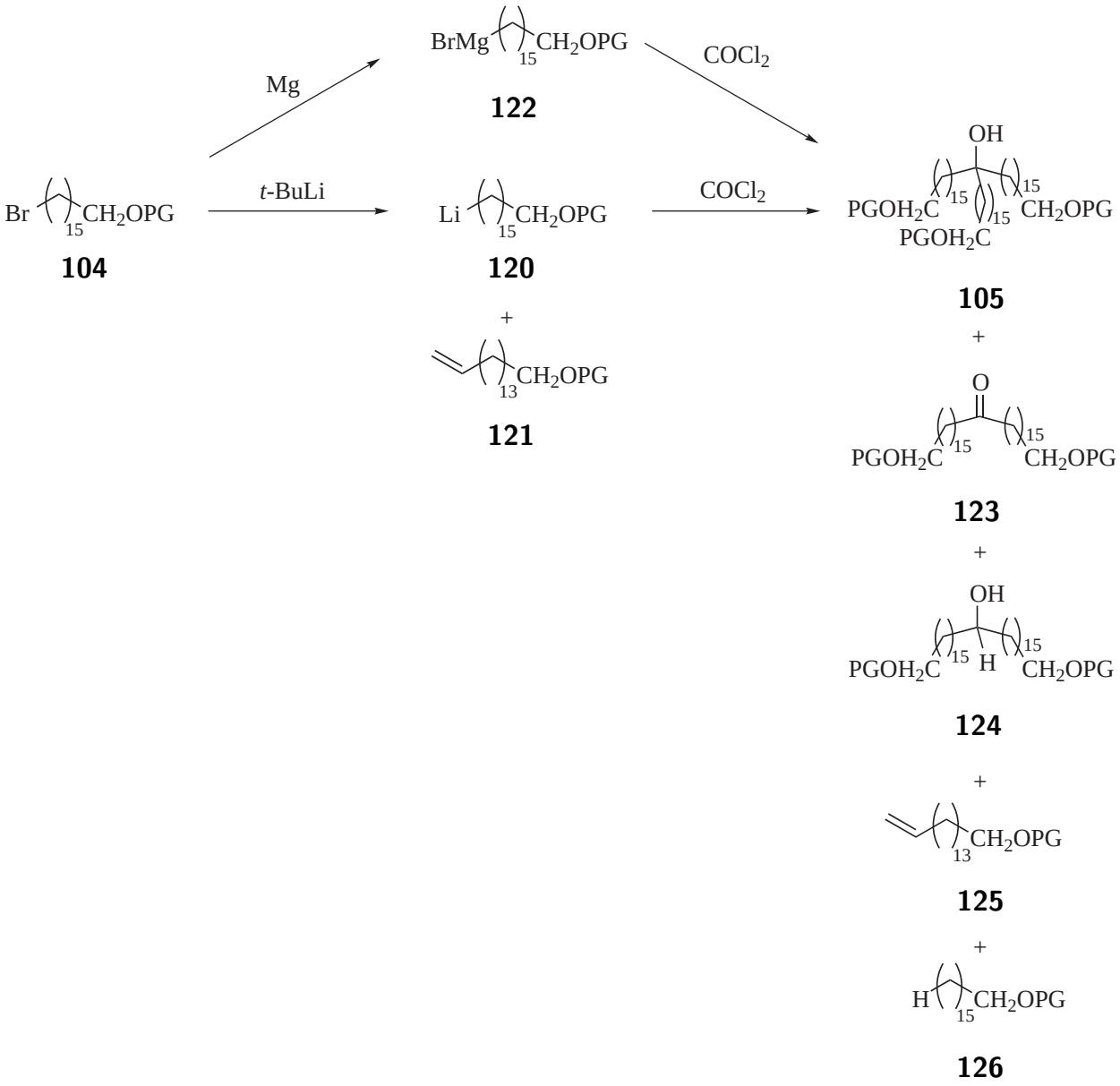

Scheme 3.5: Troublesome steps in synthesis of **92**.

The aggregation hypothesis also explains the troublesome reactions of **120** and **122** with phosgene and the slow deprotection of the methoxymethyl protecting group in **106**.

The use of the bulky TIPS protecting group was an attempt to prevent the formation

of micelles and reversed micelles, but it failed.

In order to circumvent the problem, the design **92** was changed to **93**. The reactions in the synthesis of **93** do not require low temperatures and most of the intermediate products involved in the synthesis of **93** contain polar groups on both ends of the chain. Hence, the formation of micelles and reversed micelles should be less of a problem in this synthesis.

Synthesis of the rotor 93. The alkylation of the triol **113** can also be done with the bromoacid **102** directly, but large quantities on the products from alkylation of the carboxyl group were formed, and the yield of the desired product was low. The alkylation of **113** was also tried with the *t*-butylester of **102** as *t*-alkyl esters are generally more stable to nucleophiles than other esters, but deprotection of the ester and subsequent side reactions took place.

The amide **114** was difficult to deprotect by conventional methods (reflux with mineral acids or with sodium hydroxide in alcohols) and unidentified side reactions also took place. The milder deprotection with potassium *t*-butoxide and water in diethylether[150] was also unsuccessful. The deprotection with trifluoromethanesulfonic anhydride followed by the treatment with methanol went smoothly, and the only detected side products were the partially deprotected compounds.

The direct coupling of **115** with **100** gave poor yields of **118**. When the more reactive trimethylsilylacetylene was used, the reaction proceeded in moderate yield and the compound **118** was synthesized by the deprotection of the trimethylsilyl group in **117** and subsequent Sonogashira coupling with **97**. The exchange of bromine in **115** for iodine yielded **119** in an excellent yield and the compound **119** was reactive enough for the difficult coupling with **100**. The overall yield of the route via compound **119** was the best achieved.

Calculations. The results of calculations suggested that the rotator is tilted with respect to the surface normal (Figure 3.10, right) due to the variation in the C_a-C_b-O-C_c

dihedral angle (C_c is the fatty acid carbon 16; the three dihedral angles are: 111.5°, -120.6° and -179.7°). The angle variation is due to 1,5-hydrogen interactions (Figure 3.10, middle), and to keep the three fatty acid alkyl chains in the optimum distance for attractive van der Waals interactions while also allowing all the fatty acid chain methylenes to be in all-anti conformation.

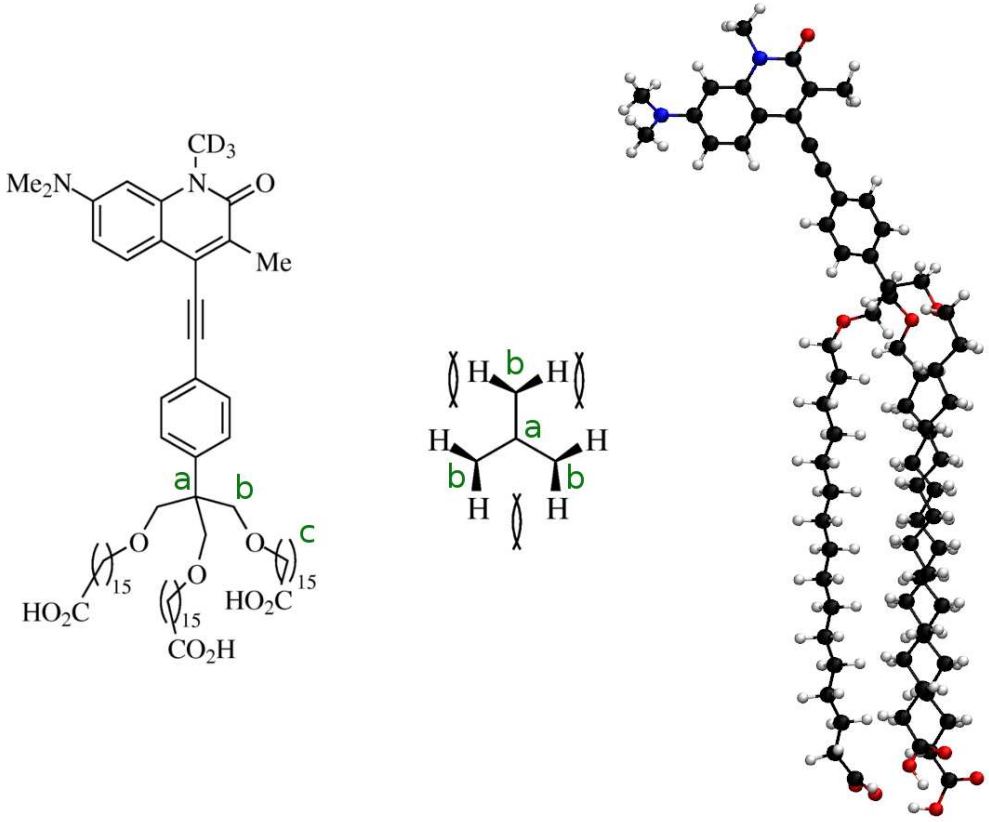

Figure 3.10: Rotor geometry.

The layer preparation can further affect the tilt angle as the conditions of the layer formation (such as ions in the trough) can have effect on the tilt angle of the fatty acid alkyl chain.

3.4 Conclusions

Two new molecular rotors for surface monolayer self-assembly were successfully prepared and the behavior of one of them was predicted and rationalized using molecular modeling.

Chapter 4

Experimental Part

4.1 General Methods

Air-sensitive reactions were carried out under argon, using standard Schlenk techniques: the oven-dried reaction flasks (dried at 200°C for 24 h, allowed to cool in vacuum) were evacuated to a pressure of at least 100 mTorr and filled with dry argon, at least three times. The reactants and the solvents were added with dry needles (filled with argon beforehand) through septa. The reactions flasks were never open to air until the reaction was complete.

When anhydrous solvents were used, they were always freshly distilled from a drying agent. Tetrahydrofuran was distilled from Na/K under argon. Dimethylformamide was distilled from calcium hydride into a flask with freshly activated 3 Å molecular sieves under reduced pressure and degassed by standard freeze-pump-thaw technique (three times). Pyridine, piperidine, diisopropylamine, acetonitrile and dichloromethane were distilled from calcium hydride under argon. Triethylamine was distilled from calcium hydride or from sodium/benzophenone under argon. Benzene and toluene were distilled from sodium under argon. NMR solvents were kept over molecular sieves (except for D_2O).

Cuprous chloride was purchased from Sigma-Aldrich in sealed ampoules and handled in a glove-box. Only cuprous chloride that was white was used in the reactions (greenish color is a sign of oxidation). All the chemicals, except for *p*-carborane (Katchem), were purchased from Sigma-Aldrich, and they were used as received.

Molecular sieves (3 Å and 4 Å) were freshly activated at 500 °C before use and they

were allowed to cool in vacuum.

Potassium bromide for IR spectroscopy was dried at 200 °C for 24 h before use.

IR spectra were recorded with a Nicolet Avatar 360 FT-IR spectrophotometer. UV-Vis spectra were recorded on a Hewlett-Packard 8452A spectrometer. NMR spectra were recorded with an Inova 400, Inova 500 spectrometer or Bruker Avance-III 300 Spectrometer. A Hewlett-Packard 5989B mass spectrophotometer was used to record mass spectra. Elemental analyses were performed by Columbia Analytical Services, Tucson, AZ.

4.2 Synthesis of Compounds from Chapter 2

4.2.1 Synthesis

Synthesis of catechol-d_6. A modified literature procedure was used:[115] a dry high-pressure 500 mL round-bottom Schlenk flask, equipped with a magnetic stir bar, a septum and a hose connector, was charged with catechol (20 g) and 5% Pt/C (4 g). The flask was evacuated and filled with hydrogen three times. After that, deuterium oxide (300 mL) was added through the septum and the resulting mixture was stirred under positive pressure of hydrogen for 5 min The reaction vessel was then closed and it was heated at 120 °C for 48 h behind a blast shield.

The reaction mixture was allowed to cool to about 90 °C and the hot reaction mixture was filtered through a dry glass filter funnel (medium porosity) into a dry 1L round bottom flask. The catalyst was recovered, washed with methanol, dried and reused.

Water was evaporated from the filtrate under reduced pressure and the remaining catechol-d_6 (97 to 98 % deuterium incorporation) was deuterated again by repeating the above procedure with fresh deuterium oxide.

After the second deuteration, the deuterium incorporation was 99.5 to 99.8 %. The product was dissolved in anhydrous dichloromethane (freshly distilled from calcium hydride)

and dried with 4 Å molecular sieves, freshly activated by drying at 500 °C for 24 h. The solvent was evaporated under reduced pressure to yield 19.15 g (91 %) of catechol-d_6 which was used immediately in the next step.

Synthesis of TPP-d_{12}. TPP-d_{12} was synthesized from catechol-d_6 (19.15 g), following the literature procedure for TPP.[82] The crude product was purified by continuous extraction with 1200 mL of anhydrous benzene under argon, using a 1 L Soxhlet extractor insulated with glass wool and aluminum foil. The resulting slurry was concentrated under reduced pressure and the resulting solid was sublimed twice at 200 °C (30 to 70 mTorr) to yield 12 to 16 g (46 to 62 %) of TPP-d_{12} in monoclinic form. The samples were stored in the dark as slow oxidation occurs with air in the presence of light.

Hexagonal TPP-d_{12}/benzene-d_6 inclusion compound was prepared by continuous extraction of monoclinic TPP-d_{12} (5 g) with anhydrous benzene-d_6 (70 mL) under argon and concentrating of the resulting mixture under reduced pressure. The samples were stored in the dark as slow oxidation occurs with air in the presence of light.

Empty hexagonal TPP-d_{12} was used for inclusion compound preparation. Only fresh samples of empty hexagonal TPP-d_{12} (not older than 1 month) were used, as the empty hexagonal form readily absorbs impurities from the atmosphere. The empty hexagonal TPP-d_{12} samples were stored in a flask connected to a diffusion pump at pressures of 10^{-4} to 10^{-5} Torr. The empty hexagonal form can be prepared from the TPP-d_{12}/benzene-d_6 inclusion compound in two different ways. No differences between the samples prepared by the two methods were noticed in inclusion compound preparation.

Method 1: TPP-d_{12}/benzene-d_6 inclusion compound was kept at 10^{-4} to 10^{-5} Torr for 1-2 days, then it was heated at 75 °C at the same pressure for 45 min Samples prepared in this

way contained 10 to 20 % of the monoclinic form.

Method 2: TPP-d_{12}/benzene-d_6 inclusion compound was kept at 10^{-4} to 10^{-5} Torr for 2 to 3 weeks until no change in the weight of the sample could be detected. Samples prepared by this method contained less than 5 % of the monoclinic form.

General procedure for Ulmann coupling with *p*-carborane and its derivatives. A pressure Schlenk flask (25 to 50 mL), equipped with a triply sealed pressure valve, a magnetic stir bar, a septum and a hose connector, was charged with the *p*-carborane derivative (1 mmol, 1.0 equiv or 5 mmol, 5.0 equiv. if *p*-carborane was the starting compound) and with cuprous chloride (1.3 mmol, 1.3 equiv.) in the glove-box. The flask was closed, taken outside the glove-box and connected to the Schlenk line. THF (10 mL) was added through the septum under argon and the resulting mixture was cooled in an acetone/dry ice bath. After 5 min of stirring, *n*-BuLi (1.6 M solution in hexanes, 0.75 mL, 1.2 equiv.) was added dropwise under argon. The reaction mixture was stirred for 15 min at -78 °C and then for 30 min at room temperature. Anhydrous pyridine (1 mL) was added to the mixture and it was stirred until all the cuprous chloride dissolved. The flask was then closed and a solvent trap was connected to it. The trap was evacuated and filled with argon three times. The trap was then evacuated and cooled with liquid nitrogen. Special precaution was taken to seal all the leaks. The reaction mixture was stirred vigorously and slowly opened to the trap. The solvents were removed under reduced pressure and the flask was filled with argon. Afterthat, a suspension/solution of the iodo derivative (1.5 mmol, 1.5 equiv.) in anhydrous DMF (5 to 10 mL) was added under argon. The resulting mixture was heated in a closed vesseel at 120 °C for 24 h and then at 140 to 150 °C for 24 to 48 h. The reation progress was monitored by ^{1}H NMR. After the reaction was complete, the solvents were removed under reduced pressure and the solids were dissolved in dichloromethane (50 to 150 mL), washed with 5% hydrochloric acid (50 mL), with 10% ammonium hydroxide (2 x 50 mL), and with water (50 mL). The organic layer was dried over anhydrous sodium sulfate, filtered

and concentrated under reduced pressure. If *p*-carborane was used in the reaction, it was recovered by sublimation under reduced pressure. The crude product was purified by column chromatography.

Synthesis of 56. A two-necked dry round bottom flask (100 mL), equipped with a magnetic stir bar, septum and a hose connector, was charged with **55** (1.000 g, 2.342 mmol, 1.0 equiv.). The flask was evacuated and filled with argon (three times). Anhydrous THF (25 mL) was added through the septum, and the resulting solution was cooled in an acetone/dry ice bath. After 5 min, 1.6 M *n*-BuLi in hexanes (1.86 mL, 2.980 mmol, 1.2 equiv.) was added to the mixture. The reaction mixture was allowed to warm to room temperature and it was stirred for 30 min After that, *n*-hexadecyl bromide was added (910.0 mg, 2.980 mmol, 1.2 equiv.) and the mixture was allowed to stir overnight (14 h). A few drops of water were added to the mixture and the solvent was then removed under reduced pressure, the residue was dissolved in diethyl ether (50 mL), and the solution was washed with water (20 mL). The organic layer was dried over anhydrous sodium sulfate, filtered and the solvent was removed under reduced pressure. The volatiles were removed by Kugelrohr distillation at 120 °C (50 mTorr) and the residue was purified by column chromatography in hexanes to yield 1.401 g (90 %) of a pure white crystalline product, m.p. (CH_2Cl_2) 79 °C. ^{1}H NMR (300 MHz, $CDCl_3$) δ 7.62 - 7.50 (m, 6H), 7.50 - 7.41 (m, 3H), 7.40 - 7.29 (m, 6H), 3.44 - 1.36 (m , 10H), 1.55 (dd, J = 10.4, 5.8 Hz, 2H), 1.37 - 0.98 (m, 28H), 0.94 - 0.80 (m, 3H). ^{13}C{^{1}H } NMR (75 MHz, $CDCl_3$) δ 137.41 (s), 131.52 (s), 130.18 (s), 127.59 (s), 90.34 (s), 65.64 (s), 39.33 (s), 29.84 (s), 29.83 (s), 29.81 (s), 29.79 (s), 29.74 (s), 29.68 (s), 29.60 (s), 29.51 (s), 29.30 (s), 29.24 (s), 29.1 9 (s), 22.85 (s), 14.29 (s). ^{11}B{^{1}H } NMR (96 MHz, $CDCl_3$) δ -11.33 (s), -12.63 (s). IR (KBr, cm^{-1}): 492, 510, 698, 741, 872, 999, 1030, 1081, 1097, 1105, 1426, 1466, 2603, 2848, 2917, 2950, 3051, 3070. UV-Vis (CH_2Cl_2, nm) λ_{max} (ϵ_{max}): 228 (17000), 261 (1470), 267 (1690), 273 (1470). MS (ESI$^+$): (calcd. for MH$^+$:). Elemental analysis: Calcd. C: 68.96 %, H: 9.32 %, Found: C: 69.32 %, H: 9.42 %.

Synthesis of 57. A round-bottom flask (100 mL) with a magnetic stir bar was charged with **56** (1.2 g, 1.914 mmol, 1.0 equiv.). THF (10 mL), and 1.0 M solution of tetrabutylammonium fluoride in THF (7.6 mL, 7.654 mmol, 4.0 equiv.) were added to the mixture. The mixture was stirred at room temperature for 4 h. The reaction mixture was diluted with diethyl ether (100 mL) and washed with water (3 x 80 mL). The organic layer was dried over anhydrous sodium sulfate, filtered and concentrated under reduced pressure. The product was purified by column chromatography in hexanes to yield 649 mg (92 %) of colorless oil that solidified within several days, m.p. (CH_2Cl_2) 32 °C. ^{1}H NMR (500 MHz, $CDCl_3$) δ 2.83 - 1.50 (m, 11H), 1.61 - 1.55 (m, 2H), 1.34 - 1.02 (m, 28H), 0.88 (t, J = 6.9 Hz, 3H). ^{13}C{^{1}H } NMR (101 MHz, $CDCl_3$) δ 85.18 (s), 58.06 (s), 39.09 (s), 32.09 (s), 29.86 (s), 29.85 (s), 29.83 (s), 29.82 (s), 29.81 (s), 29.76 (s), 29.71 (s), 29.60 (s), 29.53 (s), 29.49 (s), 29.33 (s), 29.23 (s), 22.86 (s), 14.30 (s). ^{11}B{^{1}H } NMR (96 MHz, $CDCl_3$) δ -12.58 (s), -15.18 (s). IR (KBr, cm^{-1}): 673, 715, 727, 799, 907, 1002, 1068, 1128, 1140, 1178, 1260, 1304, 1369, 1375, 1453, 1469, 1723, 1838, 2606, 2848, 2913, 2951, 3067. HRMS (ESI$^-$): 405.4105 (calcd. for MCl$^-$: 405.4099). Elemental analysis: Calcd. C: 58.64 %, H: 12.03 %, Found: C: 58.75 %, H: 11.96 %.

Synthesis of 51. A dry Schlenk flask (25 mL) was equipped with a septum and a magnetic stir bar. It was charged with **57** (200.0 mg, 0.543 mmol, 1.0 equiv.), evacuated and filled with argon (three times). Anhydrous THF (20 mL) was added through the septum and the mixture was cooled in an acetone/dry ice bath. After 5 min, 1.6 M solution of n-BuLi in hexanes (0.41 mL, 0.651 mmol, 1.2 equiv.) was added to the solution which was allowed to warm to room temperature. After 30 min of stirring at room temperature, the mixture was again placed in an acetone/dry ice bath and methyl iodide (154.0 mg, 1.085 mmol, 2.0 equiv.) was added to the mixture. The resulting mixture was allowed to warm to room temperature and it was stirred overnight (16 h). The mixture was quenched with a few drops of water and the solvents were removed under reduced pressure. The solid residues were dissolved in

dichloromethane (100 mL), washed with 5 % hydrochloric acid (20 mL), water (2 x 20 mL) and the organic layer was dried over anhydrous sodium sulfate, filtered and the solvents were removed under reduced pressure. The crude product was filtered through a short column of silica gel to yield 202.0 mg (97 %) of colorless oil that solidified after several days, m.p. (CH_2Cl_2) 32 °C. ^{1}H NMR (500 MHz, $CDCl_3$) δ 2.84 - 1.48 (m, 10H), 1.55 (t, J = 8.1 Hz, 2H), 1.35 - 0.98 (m, 28H), 0.88 (t, J = 7.0 Hz, 3H). ^{13}C{^{1}H } NMR (101 MHz, $CDCl_3$) δ 85.18 (s), 58.06 (s), 39.09 (s), 32.09 (s), 29.86 (s), 29.85 (s), 29.83 (s), 29.82 (s), 29.81 (s), 29.76 (s), 29.71 (s), 29.60 (s), 29.53 (s), 29.49 (s), 29.33 (s), 29.23 (s), 22.86 (s), 14.30 (s). ^{11}B{^{1}H } NMR (96 MHz, $CDCl_3$) δ -12.27 (s). IR (KBr, cm^{-1}): 715, 729, 751, 767, 789, 864, 886, 913, 1001, 1017, 1044, 1066, 1096, 1127, 1163, 1192, 1260, 1298, 1316, 1374, 1383, 1451, 1462, 1471, 1707, 1840, 1863, 1892, 1946, 2015, 2596, 2850, 2922, 2956. HRMS (ESI$^-$): 419.4262 (calcd. for MCl$^-$: 419.4254). Elemental analysis: Calcd. C: 59.63 %, H: 12.12 %, Found: C: 59.59 %, H: 12.13 %.

Synthesis of 52. A dried Schlenk flask (500 mL) was equipped with a septum, a magnetic stir bar and a low temperature thermometer. It was evacuated and filled with argon (three times). Anhydrous THF (140 mL) and 1,2-difluorobenzene (10.00 g, 87.6 mmol, 1.0 equiv.) were added through the septum, and the mixture was cooled in a large acetone/dry ice bath. After 15 min, a cold solution (-78 °C) of 1.6 M *n*-BuLi in hexanes (65.4 mL, 105.2 mmol, 1.2 equiv.) in anhydrous THF (40 mL) was added dropwise. The resulting mixture was stirred for 2.5 h at -78 °C. A solution of iodine (26.70 g, 105.2 mmol, 1.2 equiv.) was added dropwise at such a rate that the temperature of the reaction mixture did not exceed -65 °C. The solution was allowed to warm to room temperature and the solvents were removed under reduced pressure. The remaining liquid was dissolved in diethyl ether (300 mL), and washed with 10 % sodium thiosulfate (2 x 100 mL) until colorless and with water (100 mL). The organic layer was dried over anhydrous sodium sulfate, filtered, and the solvents were removed under reduced pressure. The crude product was distilled under

reduce pressure at 120 °C (2 Torr) to yield 11.82 g (56 %) of colorless liquid that solidified after sitting at room temperature. The ^{1}H NMR spectrum of the product agreed with that reported.[110]

Synthesis of 53. A dried Schlenk flask (25 mL), equipped with a septum and a magnetic stir bar, was charged with **52** (500.0 mg, 2.09 mmol, 1.0 equiv.), tetrakis(triphenylphosphino)palladium (121.0 mg, 0.105 mmol, 5 mol %) and cuprous iodide (20.0 mg, 0.105 mmol, 5 mol %). The flask was evacuated and filled with argon (three times), and anhydrous THF (5 mL), anhydrous triethylamine (1 mL) and trimethylsilylacetylene (0.87 mL, 6.27 mmol, 3.0 equiv.) were added through the septum. The reaction mixture was then stirred at room temperature for 16 h. The mixture was diluted with diethyl ether (100 mL) and it was washd with 5% ammonium hydroxide (50 mL), water (2 x 50 mL), hydrochloric acid (2 x 50 mL) and with water (2 x 50 mL). The organic layer was dried over anhydrous sodium sulfate, filtered and the solvents were removed under reduced pressure. The crude product was purified by flash chromatography in hexanes to yield 433 mg (99 %) of **53** as colorless liquid. ^{1}H NMR (400 MHz, $CDCl_3$) δ 7.20 (ddt, J = 7.5, 5.8, 1.6 Hz, 1H), 7.15 - 7.08 (m, 1H), 7.03 - 6.96 (m, 1H), 0.27 (s, 9H). ^{13}C{^{1}H } NMR (101 MHz, $CDCl_3$) δ 152.26 (dd, J = 77.3, 12.9 Hz), 149.77 (dd, J = 72.0, 12.8 Hz), 128.76 (d, J = 3.4 Hz), 124.04 - 123.85 (m), 117.78 (d, J = 17.3 Hz), 114.14 (d, J = 12.5 Hz), 101.82 (d, J = 3.8 Hz), 96.59 (d, J = 3.9 Hz), -0.10 (s). ^{19}F NMR (376 MHz, $CDCl_3$) δ -135.29 (s), -138.05 (s). IR (KBr, cm^{-1}): 403, 419, 468, 570, 639, 717, 761, 786, 847, 859, 965, 998, 1001, 1013, 1055, 1157, 1218, 1247, 1271, 1294, 1324, 1410, 1470, 1485, 1586, 1621, 2163, 2900, 2961. UV-Vis (CH_2Cl_2, nm) λ_{max} (ϵ_{max}): 287 (490), 278 (640), 258 (7900), 246 (7860). MS (EI): 210.1 (calcd. for M·+: 210.1). Elemental analysis: Calcd. C: 62.82 %, H: 5.75 %, Found: C: 62.94 %, H: 6.01 %.

Synthesis of 58. The general procedure for the Ulmann coupling was followed, starting with 150 mg (0.407 mmol) of **57**, except that tetrakis(triphenylphosphino)palladium catalyst (47 mg, 0.041 mmol, 10 mol %) was used in the coupling. The product was purified by column chromatography in hexanes to yield 153 mg (72 %) of **58** as white crystalline solid, m.p. (CH_2Cl_2) 37 °C. ^{1}H NMR (300 MHz, $CDCl_3$) δ 7.52 - 7.26 (m, J = 40.1, 8.8 Hz, 2H), 6.99 (dd, J = 40.1, 8.8 Hz, 2H), 1.62 - 3.50 (m, 10H), 1.62 (m, 2H), 1.38 - 1.04 (m, 28H), 0.88 (t, J = 6.7 Hz, 3H). ^{13}C{^{1}H } NMR (75 MHz, $CDCl_3$) δ 137.26 (s), 131.25 (s), 129.26 (s), 129.06 (s), 38.10 (s), 32.09 (s), 29.85 (s), 29.84 (s), 29.82 (s), 29.80 (s), 29.75 (s), 29.70 (s), 29.64 (s), 29.58 (s), 29.52 (s), 29.32 (s), 29.24 (s), 22.86 (s), 14.29 (s). ^{11}B{^{1}H } NMR (96 MHz, $CDCl_3$) δ -12.66 (s). IR (KBr, cm^{-1}): 496, 510, 574, 620, 675, 698, 741, 873, 997, 1080, 1097, 1104, 1152, 1428, 1467, 1484, 1586, 1622, 1637, 2602, 2849, 2917, 2940, 2953, 3051, 3072. UV-Vis (CH_2Cl_2, nm) λ_{max} 239 (11020), 231 (11060), 227 (13800). (ϵ_{max}): 236 (1595). Elemental analysis: Calcd. C: 55.05 %, H: 9.05 %, Found: C: 55.14 %, H: 9.26 %.

Synthesis of 50. A dried high-pressure Schlenk flask (25 mL) was equipped with a septum and a magnetic stir bar. It was charged with **58** (140 mg, 0.267 mmol, 1.0 equiv.), **53** (67.4 mg, 0.321 mmol, 1.2 equiv.), tetrakis(triphenylphosphino)palladium (30.8 mg, 0.027 mmol, 10 mol %) and cuprous iodide (10.1 mg, 0.053 mmol, 20 mol %). The flask was evacuated and filled with argon (three times), and degassed 1.0 M solution of TBAF in THF (1 mL), and anhydrous triethylamine (1 mL) were added to the mixture. The Schlenk flask was closed and the reaction mixture was heated at 90 °C for 16 h. The reaction mixture was diluted with diethyl ether (100 mL), washed with 5% ammonium hydroxide (2 x 20 mL), water (2 x 20 mL), 5 % hydrochloric acid (2 x 20 mL) and water (2 x 20 mL). The organic layer was dried over anhydrous sodium sulfate, filtered and the solvents were removed under reduced pressure. The crude product was purified by flash chromatography in pentanes to yield 132.1 mg (85 %) of **50** as white crystalline solid, m.p. (CH_2Cl_2) 90 °C. ^{1}H NMR (300

MHz, $CDCl_3$) δ 7.37 - 7.32 (m, 2H), 7.25 - 6.99 (m, 5H), 1.72 - 1.58 (m, 2H), 3.81 - 1.57 (m, 10H), 1.37 - 1.06 (m, 28H), 0.88 (t, J = 6.7 Hz, 3H). $^{13}C\{^1H\}$ NMR (75 MHz, $CDCl_3$) δ 151.90, 149.80, 137.26, (s), 131.25 (s), 129.26 (s), 129.06 (s), 122.70, 117.70, 114.00, 94.7, 82.8, 82.1, 80.4, 46.4, 38.10 (s), 32.09 (s), 29.85 (s), 29.84 (s), 29.82 (s), 29.80 (s), 29.75 (s), 29.70 (s), 29.64 (s), 29.58 (s), 29.52 (s), 29.32 (s), 29.24 (s), 22.86 (s), 14.29 (s). $^{11}B\{^1H\}$ NMR (96 MHz, $CDCl_3$) δ -12.61 (s). IR (KBr, cm^{-1}): 506, 536, 587, 603, 656, 715, 717, 759, 781, 787, 791, 816, 831, 858, 869, 966, 986, 1021, 1061, 1069, 1170, 1183, 1199, 1226, 1268, 1376, 1402, 1469, 1482, 1512, 1585, 1618, 1786, 1913, 1936, 2222, 2601, 2848, 2869, 2918, 2946, 2955, 3043, 3056, 3088. HRMS (ESI^+): 605.4746 (calcd. for MNa^+: 605.4724). UV-Vis (CH_2Cl_2, nm) λ_{max} (ϵ_{max}): 307 (15510), 297 (10880), 289 (13950), 273 (4330), 258 (1690), 246 (1690). MS (ESI^+): 603.48 (calcd. for MNa^+: 603.48). Elemental analysis: Calcd. C: 66.17 %, 8.68 %, Found: C: 66.34 %, H: 9.02 %.

Synthesis of 70. The general procedure for the Ulmann coupling was followed, starting with 200 mg of **57**. The product was purified by column chromatography in hexanes to yield 257.2 mg (92 %) of **70** as white crystals, m.p. (CH_2Cl_2) 62 °C. ^1H NMR (300 MHz, $CDCl_3$) δ 7.53 (dd, J = 8.4, 1.5 Hz, 1H), 7.36 (dd, J = 7.9, 1.5 Hz, 1H), 7.06 - 6.99 (m, 1H), 3.77 - 1.43 (m, 12H), 1.66 (m, 2H), 1.37 - 1.01 (m, 28H), 0.88 (t, J = 6.7 Hz, 3H). $^{13}C\{^1H\}$ NMR (75 MHz, $CDCl_3$) δ 135.82 (s), 134.27 (s), 131.46 (s), 130.83 (s), 130.80 (s), 126.54 (s), 85.54 (s), 80.02 (s), 38.08 (s), 32.10 (s), 29.87 (s), 29.86 (s), 29.84 (s), 29.83 (s), 29.77 (s), 29.71 (s), 29.63 (s), 29.61 (s), 29.53 (s), 29.34 (s), 29.27 (s), 22.86 (s), 14.29 (s). $^{11}B\{^1H\}$ NMR (96 MHz, $CDCl_3$) δ -12.08 (s), -12.71 (s). IR (KBr, cm^{-1}): 568, 602, 616, 673, 697, 703, 718, 739, 746, 752, 763, 782, 793, 821, 983, 1002, 1054, 1063, 1071, 1123, 1164, 1191, 1376, 1399, 1450, 1456, 1470, 1559, 1580, 1860, 1921, 2585, 2590, 2608, 2641, 2850, 2869, 2918, 2945, 2952, 3067, 3071, 3107. Elemental analysis: Calcd. C: 56.12 %, H: 9.03 %, Found: C: 56.49 %, H: 8.91 %.

Synthesis of 64. A dried high-pressure Schlenk flask (500 mL) with triply sealed teflon valve was equipped with a magnetic stir bar and a septum. It was charged with *p*-*n*-pentylbromobenzene (6.00 g, 26.42 mmol, 1.2 equiv.), evacuated, and filled with argon (three times). Anhydrous THF (80 mL) was added and the solution was cooled in an acetone/dry ice bath. After 5 min, 1.6 M solution of *n*-BuLi in hexanes (16.6 mL, 26.42 mmol, 1.2 equiv.) was added to the solution while stirred. After 10 min, 1.0 M solution of zinc chloride (52.8 mL, 26.42 mmol, 1.2 eqiuv.) was added and the resulting mixture was allowed to warm to room temperature. A suspension of *p*-iodonitrobenzene (5.48 g, 22.01 mmol, 1.0 equiv.) and tetrakis(triphenylphosphino)palladium (763 mg, 0.66 mmol, 3 mol %) in anhydrous THF (20 mL) was added to the mixture. The valve was then closed and the reaction mixture was stirred at room temperature for 48 h. The solvent was removed under reduced pressure and the residue was dissolved in dichloromethane (300 mL). The solution was washed with 10 % hydrochloric acid (2 x 100 mL) and water (2 x 100 mL). The organic layer was dried over anhydrous sodium sulfate, filtered and the solvents were removed under reduced pressure. The crude product was purified by flash chromatography in hexanes and toluene (3/1) to yield 4.969 g (84 %) of **64** as yellow crystals, m.p. (CH_2Cl_2) 46 °C. ^{1}H NMR (400 MHz, $CDCl_3$) δ 8.31 - 8.25 (m, 2H), 7.76 - 7.69 (m, 2H), 7.59 - 7.52 (m, 2H), 7.32 (d, J = 8.3 Hz, 2H), 2.76 - 2.60 (m, 2H), 1.67 (ddd, J = 15.1, 8.3, 4.8 Hz, 2H), 1.43 - 1.30 (m, 4H), 0.97 - 0.87 (m, 3H). ^{13}C{^{1}H } NMR (101 MHz, $CDCl_3$) δ 147.68 (s), 146.89 (s), 144.24 (s), 136.08 (s), 129.34 (s), 127.56 (s), 127.32 (s), 124.18 (s), 35.73 (s), 31.61 (s), 31.20 (s), 22.66 (s), 14.16 (s). IR (KBr, cm^{-1}): 398, 450, 488, 509, 529, 543, 693, 731, 746, 755, 812, 847, 854, 866, 895, 950, 962, 969, 1004, 1023, 1108, 1127, 1176, 1186, 1234, 1250, 1288, 1308, 1339, 1398, 1429, 1454, 1466, 1483, 1513, 1562, 1808, 1917, 1932, 2343, 2858, 2869, 2926, 2954, 2966, 3028, 3077. HRMS (ESI$^+$): 270.1488 (calcd. for MH$^+$: 270.1491). UV-Vis (CH_2Cl_2, nm) λ_{max} (ϵ_{max}): 324 (23700). Elemental analysis: Calcd. C: 75.81 %, H: 7.11 %, N: 5.20 %, Found: C: 75.71 %, H: 7.23 %, N: 5.25 %.

Synthesis of 65. A round bottom flask (500 mL) was charged with **64** (4.80 g, 17.820 mmol, 1.0 equiv.), powdered tin (15.00 g, 126.24 mmol, 7 equiv.), concentrated hydrochloric acid (80 mL), water (80 mL) and ethanol (50 mL). The resulting mixture was refluxed for 6 h. The solvents were removed under reduced pressure, the remaining solid was suspended in water (100 mL), and 10 % sodium carbonate was added to pH=9. The solids were filtered, washed with water, and dried. The product was extracted with boiling ethanol, and the suspension was filtered hot. The solvent was removed under reduced pressure to give 4.024 g (94 %) of white crystalline **65**, m.p. (CH_2Cl_2) 69 °C. ^{1}H NMR (400 MHz, $CDCl_3$) δ 7.47 - 7.43 (m, 2H), 7.43 - 7.38 (m, 2H), 7.23 - 7.18 (m, 2H), 6.78 - 6.72 (m, 2H), 3.70 (s, 2H), 2.68 - 2.55 (m, 2H), 1.70 - 1.58 (m, 2H), 1.40 - 1.28 (m, 4H), 0.96 - 0.84 (m, 3H). ^{13}C{^{1}H } NMR (101 MHz, $CDCl_3$) δ 145.66 (s), 141.16 (s), 138.61 (s), 131.76 (s), 128.85 (s), 127.96 (s), 126.37 (s), 115.48 (s), 35.69 (s), 31.72 (s), 31.40 (s), 22.73 (s), 14.22 (s). IR (KBr, cm^{-1}): 459, 479, 504, 547, 569, 673, 714, 727, 751, 804, 832, 843, 999, 1134, 1177, 1200, 1230, 1273, 1374, 1403, 1429, 1453, 1466, 1500, 1529, 1579, 1606, 1624, 1886, 1900, 2855, 2868, 2922, 2950, 3026, 3198, 3214, 3304, 3384. UV-Vis (CH_2Cl_2, nm) λ_{max} (ϵ_{max}): 280 (41590). MS (ESI$^+$): 240.2 (calcd. for MH$^+$: 240.2). Elemental analysis: Calcd. C: 85.30 %, H: 8.84 %, N: 5.85 %, Found: C: 85.28 %, H: 9.02 %, N: 5.89 %.

Synthesis of 66. A round bottom flask (500 mL) was charged with **65** (3.80 g, 1.0 equiv.), water (160 mL) and concentrated sulfuric acid (30 mL), and the suspension was sonicated for 1 h. The resulting fine suspension was cooled to 0 °C and a solution of sodium nitrite (2.19 g, 31.748 mmol, 2.0 equiv.) in water (30 mL) was added dropwise while the reaction mixture was vigorously stirred. The temperature of the reaction mixture was kept below 5 °C during the addition. After 2 h at 0 to 5 °C a solution of urea (5 g) in water was added dropwise to the reaction mixture while keeping the temperature below 5 °C. Then, the reaction mixture was slowly poured into a hot (80 - 90 °C) solution of potassium iodide (15 g) in water (100 mL), and the mixture was stirred for 1 h. The product was extracted

into diethyl ether (3 x 200 mL), the combined organic layers were washed with 10 % sodium thiosulfate (2 x 100 mL), the organic layer was dried over anhydrous sodium sulfate, filtered, and the solvents were removed under reduced pressure. The crude product was purified by flash chromatography in hexanes and toluene (3/1) to yield 4.652 g (84 %) of **66** as white crystals, m.p. (CH_2Cl_2) 110 °C. ^{1}H NMR (400 MHz, $CDCl_3$) δ 7.82 - 7.74 (m, 2H), 7.54 - 7.47 (m, 2H), 7.39 - 7.33 (m, 2H), 7.33 - 7.27 (m, 2H), 2.78 - 2.64 (m, 2H), 1.77 - 1.64 (m, 2H), 1.47 - 1.33 (m, 4H), 1.03 - 0.91 (m, 3H). ^{13}C{^{1}H } NMR (101 MHz, $CDCl_3$) δ 142.71 (s), 140.71 (s), 137.86 (s), 137.37 (s), 129.07 (s), 128.61 (s), 126.80 (s), 92.77 (s), 35.71 (s), 31.67 (s), 31.29 (s), 22.71 (s), 14.22 (s). IR (KBr, cm^{-1}): 478, 500, 550, 616, 642, 673, 698, 725, 737, 754, 802, 825, 852, 999, 1066, 1110, 1133, 1276, 1376, 1386, 1456, 1466, 1479, 1519, 1550, 1581, 1607, 1644, 1906, 2852, 2866, 2922, 2949, 3026, 3059. UV-Vis (CH_2Cl_2, nm) λ_{max} (ϵ_{max}): 266 (24210). Elemental analysis: Calcd. C: 58.30 %, H: 5.47 %, Found: C: 58.36 %, H: 6.04 %.

Synthesis of 67. The general Ulmann coupling procedure was followed, starting with 800 mg (2.284 mmol) of **66**. The product was purified by column chromatography in hexanes and toluene (3/1) to yield 773.1 mg (92 %) of **67** as white crystals, m.p. (CH_2Cl_2) 79 °C. ^{1}H NMR (300 MHz, $CDCl_3$) δ 7.48 - 7.34 (m, 4H), 7.31 - 7.21 (m, 4H), 2.70 - 2.56 (m, 2H), 3.67 - 1.86 (m, 10H), 1.74 - 1.59 (m, 2H), 1.42 - 1.27 (m, 4H), 1.00 - 0.86 (m, 3H). ^{13}C{^{1}H } NMR (101 MHz, $CDCl_3$) δ 142.66 (s), 141.31 (s), 137.35 (s), 135.63 (s), 128.99 (s), 127.50 (s), 126.96 (s), 126.63 (s), 86.36 (s), 59.85 (s), 35.73 (s), 31.71 (s), 31.29 (s), 22.71 (s), 14.21 (s). ^{11}B{^{1}H } NMR (96 MHz, $CDCl_3$) δ -12.20 (s), -14.89 (s). IR (KBr, cm^{-1}): 505, 548, 582, 693, 721, 726, 737, 749, 768, 786, 801, 846, 896, 912, 939, 1004, 1016, 1022, 1040, 1090, 1124, 1140, 1147, 1193, 1374, 1397, 1429, 1451, 1464, 1501, 1529, 1577, 1906, 2609, 2856, 2866, 2926, 2951, 3027, 3060. UV-Vis (CH_2Cl_2, nm) λ_{max} (ϵ_{max}): 264 (27030). Elemental analysis: Calcd. C: 62.26 %, H: 8.25 %, Found: C: 62.02 %, H: 8.36 %.

Synthesis of 63. The general Ulmann coupling procedure was followed, starting with 200.0 mg (0.546 mmol) of **67**. The prodduct was purified by column chromatography in hexanes and toluene (3/1) to yield 241.7 mg (87 %) of **63** as white crystals, m.p. (CH_2Cl_2) 152 °C. ^{1}H NMR (500 MHz, $CDCl_3$) δ 7.60 (dd, J = 8.4, 1.4 Hz, 1H), 7.48 - 7.37 (m, 5H), 7.32 - 7.28 (m, 2H), 7.25 (t, J = 6.3 Hz, 2H), 7.09 - 7.04 (m, 1H), 2.67 - 2.60 (m, 2H), 3.59 - 2.05 (m, 10H), 1.71 - 1.59 (m, 2H), 1.42 - 1.29 (m, 4H), 0.91 (t, J = 7.0 Hz, 3H). ^{13}C{^{1}H } NMR (101 MHz, $CDCl_3$) δ 142.74 (s), 141.55 (s), 137.32 (s), 135.90 (s), 134.96 (s), 134.19 (s), 131.46 (s), 131.02 (s), 130.69 (s), 129.02 (s), 127.49 (s), 126.98 (s), 126.72 (s), 126.66 (s), 86.60 (s), 81.70 (s), 35.73 (s), 31.70 (s), 31.29 (s), 22.71 (s), 14.20 (s). ^{11}B{^{1}H } NMR (96 MHz, $CDCl_3$) δ -12.25 (s). IR (KBr, cm^{-1}): 462, 488, 514, 548, 593, 607, 660, 698, 738, 758, 790, 805, 848, 861, 871, 901, 933, 1004, 1059, 1069, 1082, 1123, 1164, 1194, 1301, 1347, 1375, 1398, 1421, 1450, 1464, 1493, 1501, 1561, 1578, 1866, 1904, 1931, 1956, 2613, 2852, 2867, 2927, 2951, 3030, 3051, 3088. HRMS (ESI$^+$): 535.2751 (calcd. for MNa^+: 535.2758). UV-Vis (CH_2Cl_2, nm) λ_{max} (ϵ_{max}): 269 (33950). Elemental analysis: Calcd. C: 58.70 %, H: 6.31 %, Found: C: 58.46 %, H: 6.41 %.

Synthesis of 72. The general Ulmann coupling procedure was followed, starting with 150 mg (1.0 equiv.) of *p*-carborane, 1.95 mL (3.0 equiv.) of 1.6 M *n*-BuLi, and with 329.0 mg (4.0 equiv.) of 1,2-dichloro-3-iodobenzene. The product was purified by column chromatography in pentanes and toluene (2/1), and the product was further purified by crystallization from cyclohexane to yield 345.0 mg (76 %) of white crystalline product, m.p. (CH_2Cl_2) 265 °C. ^{1}H NMR (500 MHz, $CDCl_3$) δ 7.56 (dd, J = 8.4, 1.5 Hz, 2H), 7.41 (dd, J = 7.9, 1.5 Hz, 2H), 7.07 (t, J = 8.1 Hz, 2H), 2.10 - 3.70 (m, 10H). ^{13}C{^{1}H } NMR (75 MHz, $CDCl_3$) δ 135.95 (s), 134.02 (s), 131.40 (s), 131.15 (s), 130.53 (s), 126.71 (s), 77.36 (s). ^{11}B{^{1}H } NMR (96 MHz, $CDCl_3$) δ -11.89 (s). IR (KBr, cm^{-1}): 484, 685, 699, 738, 747, 762, 796, 814, 867, 947, 964, 1000, 1040, 1057, 1067, 1080, 1124, 1137, 1166, 1207, 1227, 1245, 1304, 1313, 1348, 1378, 1398, 1448, 1557, 1578, 1604, 1643, 1682, 1700, 1715,

1734, 1874, 1943, 2595, 2607, 2636, 2643, 3060, 3100. HRMS (ESI^-): 469.0680 (calcd. for MCl^-: 469.0695). UV-Vis (CH_2Cl_2, nm) λ_{max} (ϵ_{max}): 241 (15630), 230 (26490). Elemental analysis: Calcd. C: 38.73 %, H: 3.71 %, Found: C: 38.88 %, H: 3.68 %.

Synthesis of 78. The compound **78** was prepared by a modified literature procedure as the original procedure[117] produced large quantities of diiodo derivative that was difficult to remove. A round-bottom flask was charged with *p*-terphenyl (4.60 g, 19.97 mmol, 1.0 equiv.), iodine (2.05 g, 7.98 mmol, 0.4 equiv.), periodic acid (0.91 g, 4.73 mmol, 0.24 equiv.), glacial acetic acid (62 mL), water (12 mL), and concentrated sulfuric acid (1 mL). The resulting mixture was stirred for 12 h at 60 °C, then the temperature was increased gradually to 100 °C within the next 12 h, and the reaction mixture was then stirred for 24 h at 100 °C. The reaction mixture was then cooled to room temperature, and the product was allowed to crystallize overnight (12 h). The product was filtered, washed with water (3 x 100 mL), 5% aqueous sodium thiosulfate (2 x 100 mL), and again with water (2 x 100 mL). The crude product was allowed to dry in the oven at 60 °C, and then it was extracted with boiling toluene (2 x 250 mL), and the suspension was filtered hot. The excess toluene was boiled off until the product started to crystallize. The solution was then allowed to cool to room temperature, and the crystallized product was collected by filtration. Another crystallization from toluene produced 5.70 g (94 %) of pure product (white crystals). The ^{1}H NMR spectrum of the product agreed with that reported.[117]

Synthesis of 77. The general Ulmann coupling procedure was followed, starting with 4.00 g of **78**. The product was purified by chromatography in pentanes and toluene (3/1 to 2/1) on silica gel, and by crystallization from cyclohexane to produce 3.39 g (81 %) of pure white crystalline product, m.p. (CH_2Cl_2) 255 °C. ^{1}H NMR (500 MHz, $CDCl_3$) δ 7.68 - 7.57 (m, 6H), 7.48 - 7.42 (m, 4H), 7.36 (dt, 1H), 7.32 - 7.27 (m, 2H), 3.32 - 1.70 (m, 11H).

$^{13}C\{^{1}H\}$ NMR (75 MHz, $CDCl_3$) δ 140.86 (s), 140.68 (s), 140.64 (s), 138.97 (s), 136.06 (s), 128.97 (s), 127.68 (s), 127.65 (s), 127.58 (s), 127.51 (s), 127.18 (s), 126.73 (s), 86.29 (s), 59.97 (s). $^{11}B\{^{1}H\}$ NMR (96 MHz, $CDCl_3$) δ -12.28 (s), -14.94 (s). IR (KBr, cm^{-1}): 425, 508, 526, 562, 581, 608, 630, 650, 668, 700, 730, 757, 767, 809, 834, 858, 895, 909, 956, 967, 982, 1003, 1038, 1087, 1115, 1139, 1157, 1197, 1207, 1251, 1316, 1356, 1382, 1340, 1414, 1448, 1484, 1505, 1527, 1546, 1570, 1581, 1596, 1684, 1895, 1915, 1949, 1966, 2606, 2837, 2866, 2877, 2918, 2950, 2960, 3030, 3045, 3060, 3075. HRMS (ESI^-): 408.2561 (calcd. for MCl^-: 408.2575). UV-Vis (CH_2Cl_2, nm) λ_{max} (ϵ_{max}): 287 (36180). Elemental analysis: Calcd. C: 64.48 %, H: 6.49 %, Found: C: 64.19 %, H: 6.52 %.

Synthesis of 73. A dry Schlenk flask (25 mL) was equipped with a septum and a magnetic stir bar. It was charged with **77** (200.0 mg, 0.537 mmol, 1.0 equiv.), evacuated and filled with argon (three times). Anhydrous THF (20 mL) was added through the septum, and the mixture was cooled in an acetone/dry ice bath. After 5 min, 1.6 M solution of *n*-BuLi in hexanes (0.40 mL, 0.644 mmol, 1.2 equiv.) was added to the solution which was allowed to warm to room temperature. After 30 min of stirring at room temperature, the mixture was again placed in an acetone/dry ice bath, and methyl iodide (152.3 mg, 1.074 mmol, 2.0 equiv.) was added to the mixture. The resulting mixture was allowed to warm to room temperature, and it was stirred overnight (16 h). The mixture was quenched with a few drops of water, and the solvents were removed under reduced pressure. The solid residues were dissolved in dichloromethane (100 mL), washed with 5 % hydrochloric acid (20 mL), water (2 x 20 mL), and the organic layer was dried over anhydrous sodium sulfate, filtered, and the solvents were removed under reduced pressure. Crystallization from cyclohexane provided 163.7 mg (79 %) of white crystals, m.p. (CH_2Cl_2) 261 °C. ^{1}H NMR (300 MHz, $CDCl_3$) δ 7.68 - 7.55 (m, 6H), 7.48 - 7.41 (m, 4H), 7.39 - 7.32 (m, 1H), 7.28 (dt, J = 7.1, 1.3 Hz, 2H), 1.42-3.5 (m, 10H), 1.48 (s, 3H). $^{13}C\{^{1}H\}$ NMR (75 MHz, $CDCl_3$) δ 140.73 (s), 140.68 (s), 140.59 (s), 139.00 (s), 135.49 (s), 128.96 (s), 127.83 (s), 127.66 (s), 127.56 (s),

127.49 (s), 127.17 (s), 126.70 (s), 79.22 (s), 75.99 (s), 25.83 (s). $^{11}B\{^{1}H\}$ NMR (96 MHz, $CDCl_3$) δ -11.97 (s). IR (KBr, cm^{-1}): 429, 445, 510, 528, 566, 579, 600, 620, 666, 700, 719, 730, 767, 813, 837, 864, 882, 979, 1004, 1032, 1069, 1115, 1133, 1169, 1196, 1253, 1309, 1318, 1331, 1361, 1387, 1396, 1412, 1445, 1482, 1496, 1503, 1526, 1542, 1558, 1568, 1580, 1595, 1953, 2600, 2609, 2873, 2939, 2987, 3027, 3047, 3075, 3085. HRMS (ESI^-): 422.2718 (calcd. for MCl^-: 422.2718). UV-Vis (CH_2Cl_2, nm) λ_{max} (ϵ_{max}): 286 (43980). Elemental analysis: Calcd. C: 65.25 %, H: 6.78 %, Found: C: 64.86 %, H: 7.18 %.

Synthesis of 74. The general Ulmann coupling procedure was followed, starting with 300 mg of **77**. The product was purified by chromatography in pentanes and toluene (3/1 to 2/1) on silica gel to yield 399 mg (96%) of pure product (white crystals), m.p. (CH_2Cl_2) 234 °C. ^{1}H NMR (500 MHz, $CDCl_3$) δ 7.69 - 7.57 (m, 7H), 7.50 - 7.44 (m, 4H), 7.41 (dd, J = 7.9, 1.5 Hz, 1H), 7.38 (d, J = 7.4 Hz, 1H), 7.35 - 7.31 (m, 2H), 7.08 (dt, J = 8.1 Hz, 1H), 3.63 - 1.99 (m, 10H). $^{13}C\{^{1}H\}$ NMR (75 MHz, $CDCl_3$) δ 141.08 (s), 140.69 (s), 140.67 (s), 138.91 (s), 135.93 (s), 135.39 (s), 134.20 (s), 131.48 (s), 131.05 (s), 130.71 (s), 128.98 (s), 127.70 (s), 127.63 (s), 127.60 (s), 127.51 (s), 127.18 (s), 126.82 (s), 126.67 (s), 86.52 (s), 81.80 (s). $^{11}B\{^{1}H\}$ NMR (96 MHz, $CDCl_3$) δ -12.28 (s). IR (KBr, cm^{-1}): 490, 528, 534, 565, 606, 616, 660, 697, 713, 739, 754, 763, 787, 919, 843, 865, 870, 905, 914, 931, 966, 981, 1002, 1015, 1037, 1047, 1061, 1082, 1122, 1132, 1164, 1194, 1204, 1255, 1267, 1314, 1330, 1358, 1397, 1450, 1485, 1504, 1558, 1581, 1594, 1729, 1920, 1950, 1965, 2606, 2663, 2852, 2922, 2955, 3029, 3048, 3055, 3110. HRMS (ESI^-): 552.2105 (calcd. for MCl^-: 552.2083). UV-Vis (CH_2Cl_2, nm) λ_{max} (ϵ_{max}): 290 (46840). Elemental analysis: Calcd. C: 60.34 %, H: 5.06 %, Found: C: 60.13 %, H: 5.17 %.

Synthesis of 79. The general Ulmann coupling procedure was followed, starting with 1.400 g (3.758 mmol, 1.0 equiv.) of **77**, and using 2.832 g (15.032 mmol, 4.0 equiv.) of

2-iodo vinylchloride.[118] The product was purified by column chromatography in pentanes and toluene (3/1 to 2/1), followed by crystallization from cyclohexane to yield 1.240 g (76 %) of pure white crystalline product, m.p. (CH_2Cl_2) 261 °C. ^{1}H NMR (300 MHz, $CDCl_3$) δ 7.69 - 7.54 (m, 6H), 7.50 - 7.41 (m, 4H), 7.37 (dt, J = 9.5, 4.3 Hz, 1H), 7.30 - 7.23 (m, 2H), 6.11 (d, J = 13.3 Hz, 1H), 5.75 (d, J = 13.3 Hz, 1H), 3.66 - 1.47 (m, 10H). ^{13}C{^{1}H } NMR (75 MHz, $CDCl_3$) δ 141.02 (s), 140.69 (s), 140.64 (s), 138.87 (s), 135.36 (s), 130.50 (s), 128.98 (s), 127.69 (s), 127.60 (s), 127.49 (s), 127.17 (s), 126.79 (s), 123.36 (s), 85.25 (s), 82.36 (s). ^{11}B{^{1}H } NMR (96 MHz, $CDCl_3$) δ -12.44 (s). IR (KBr, cm^{-1}): 510, 530, 597, 628, 695, 731, 764, 831, 872, 920, 985, 1003, 1020, 1033, 1041, 1071, 1112, 1123, 1139, 1167, 1207, 1235, 1313, 1351, 1391, 1398, 1412, 1447, 1482, 1504, 1605, 1617, 1643, 2606, 2850, 2920, 3029, 3047. HRMS (ESI^-): 468.2333 (calcd. for MCl^-: 468.2324). UV-Vis (CH_2Cl_2, nm) λ_{max} (ϵ_{max}): 288 (40730). Elemental analysis: Calcd. C: 61.02 %, H: 5.82 %, Found: C: 60.63 %, H: 5.91 %.

Synthesis of 80. A two-necked dry round bottom flask was equipped with a septum, a magnetic stir bar, and a hose connector. It was charged with **79** (470 mg, 1.085 mmol, 1.0 equiv.), evacuated and filled with argon (three times). Anhydrous THF (20 mL) was added, and the mixture was cooled in an acetone/ice bath. A solution of MeLi in diethyl ether (1.6 M, 3.4 mL, 5.425 mmol, 5.0 equiv.) was added dropwise to the mixture which was then allowed to warm to room temperature. The reaction mixture was quenched with water (10 mL) after 2 h. Dichloromethane (100 mL) was added to the mixture, and it was washed with water (2 x 20 mL). The organic layer was dried over anhydrous sodium sulfate, filtered, and the solvents were evaporated under reduced pressure. The product was filtered through a short column of silica gel in cyclohexane to yield 430 mg (100 %) of **80** as white crystals, m.p. (CH_2Cl_2) 227 °C. ^{1}H NMR (500 MHz, $CDCl_3$) δ 7.72 - 7.54 (m, 6H), 7.50 - 7.41 (m, 4H), 7.36 (s, 1H), 7.29 (d, J = 8.6 Hz, 2H), 2.81 (s, 1H), 3.75 - 1.44 (m, 10H). ^{13}C{^{1}H } NMR (75 MHz, $CDCl_3$) δ 141.12 (s), 140.71 (s), 140.62 (s), 138.81 (s), 135.41 (s),

128.98 (s), 127.69 (s), 127.64 (s), 127.60 (s), 127.57 (s), 127.49 (s), 127.17 (s), 126.80 (s), 83.26 (s), 79.59 (s), 68.88 (s), 64.63 (s). $^{11}B\{^{1}H\}$ NMR (96 MHz, $CDCl_3$) δ -12.38 (s). IR (KBr, cm^{-1}): 411, 425, 510, 529, 566, 600, 620, 641, 699, 732, 758, 770, 817, 842, 864, 877, 913, 968, 1002, 1029, 1069, 1115, 1133, 1181, 1195, 1201, 1252, 1277, 1318, 1388, 1397, 1415, 1444, 1481, 1503, 1526, 1539, 1569, 1580, 1596, 2615, 3027, 3047. HRMS (ESI^-): 432.2562 (calcd. for MCl^-: 432.2566). UV-Vis (CH_2Cl_2, nm) λ_{max} (ϵ_{max}): 287 (41120). Elemental analysis: Calcd. C: 66.64 %, H: 6.10 %, Found: C: 66.63 %, H: 6.02 %.

Synthesis of 75. A Schlenk flask (25 mL) was equipped witha a magnetic stir bar and a septum, and it was charged with **80** (200 mg, 0.504 mmol, 1.0 equiv.), 1,2-dichloro-3-iodobenzene (165.1 mg, 0.605 mmol, 1.2 equiv.), tetrakis(triphenylphosphino)palladium (54.5 mg, 0.050 mmol, 10 mol %), and cuprous iodide (19.2 mg, 0.101 mmol, 0.2 equiv.). The flask was evacuated, filled with argon (three times), and anhydrous THF (5 mL) and anhydrous diisopropylamine (0.2 mL) were added through the septum. The resulting mixture was stirred for 24 h at room temperature under argon. The solvents were removed under reduced pressure, the residue was transfered into a separatory funnel with dichloromethane (100 mL), and the organic layer was washed with 10 % ammonium hydroxide (50 mL), water (2 x 50 mL), 5 % hydrochloric acid (50 mL), and water (50 mL). The organic layer was dried over anhydrous sodium sulfate, filtered, and the solvent was removed under reduced pressure. The crude product was purified by column chromatography in pentanes and toluene (3/1 to 2/1) using the dry-load technique. The yield was 250.2 mg (92 %, white crystalline solid), m.p. (CH_2Cl_2) 276 °C. ^{1}H NMR (500 MHz, $CDCl_3$) δ 7.68 - 7.57 (m, 6H), 7.48 - 7.43 (m, 4H), 7.41 (dd, J = 8.1, 1.5 Hz, 1H), 7.37 (dt, J = 7.1, 1.5 Hz, 1H), 7.27 (m, 3H), 7.11 (t, J = 7.9 Hz, 1H), 3.55 - 1.70 (m, 10H). $^{13}C\{^{1}H\}$ NMR (101 MHz, $CDCl_3$) δ 141.12 (s), 140.71 (s), 140.63 (s), 138.83 (s), 135.53 (s), 135.17 (s), 133.49 (s), 131.66 (s), 131.06 (s), 128.98 (s), 127.70 (s), 127.59 (s), 127.50 (s), 127.18 (s), 127.06 (s), 126.81 (s), 123.59 (s), 91.08 (s), 83.39 (s), 76.96 (s), 65.55 (s). $^{11}B\{^{1}H\}$ NMR (96 MHz, $CDCl_3$) δ -12.35 (s). IR (KBr,

cm^{-1}): 486, 530, 552, 563, 577, 597, 620, 691, 702, 727, 737, 753, 766, 776, 815, 832, 842, 863, 886, 905, 963, 980, 1004, 1034, 1048, 1069, 1102, 1113, 1132, 1155, 1198, 1260, 1281, 1317, 1391, 1411, 1448, 1455, 1485, 1504, 1550, 1580, 1600, 2610, 2853, 2921, 3028, 3067. HRMS (ESI^-): 576.2059 (calcd. for MCl^-: 576.2457). UV-Vis (CH_2Cl_2, nm) λ_{max} (ϵ_{max}): 293 (41510), 284 (39750), 268 (36480), 254 (23390). Elemental analysis: Calcd. C: 62.10 %, H: 4.84 %, Found: C: 62.42 %, H: 5.03 %.

Synthesis of 76. A Schlenk flask (25 mL) was equipped with a magnetic stir bar and a septum, and it was charged with **80** (160 mg, 0.403 mmol, 1.0 equiv.), **81** (180.3 mg, 0.605 mmol, 1.5 equiv.), tetrakis(triphenylphosphino)palladium (46.6 mg, 0.040 mmol, 10 mol %), and cuprous iodide (15.3 mg, 0.081 mmol, 0.2 equiv.). The flask was evacuated and filled with argon (three times), and anhydrous THF (5 mL) and anhydrous diisopropylamine (0.2 mL) were added through the septum. The resulting mixture was stirred for 24 h at room temperature under argon. The solvents were removed under reduced pressure, the residue was transfered into a separatory funnel with dichloromethane (100 mL), and the organic layer was washed with 5 % hydrochloric acid (50 mL), and water (50 mL). The organic layer was dried over anhydrous sodium sulfate, filtered, and the solvent was removed under reduced pressure. The crude product was purified by column chromatography in toluene using the dry-load technique. The product was recrystallized from toluene to yield 190.0 mg (83 %, white crystalline solid), m.p. (CH_2Cl_2) 370 °C (decomp.). ^1H NMR (500 MHz, CD_2Cl_2) δ 7.69 - 7.66 (m, 4H), 7.66 - 7.60 (m, 2H), 7.51 - 7.43 (m, 4H), 7.37 (dt, J = 9.2, 4.3 Hz, 1H), 7.31 - 7.26 (m, 2H), 7.09 (s, 1H), 6.25 (s, 1H), 3.35 - 1.97 (m, 10H). $^{13}C\{^1H\}$ NMR (101 MHz, $CDCl_3$) δ 152.94 (s), 151.32 (s), 141.23 (s), 140.75 (s), 140.61 (s), 138.76 (s), 135.37 (s), 128.98 (s), 127.71 (s), 127.62 (s), 127.52 (s), 127.50 (s), 127.17 (s), 126.85 (s), 115.02 (s), 113.94 (s), 113.62 (s), 112.21 (s), 111.49 (s), 107.77 (s), 104.51 (s), 96.80 (s), 84.47 (s), 69.17 (s), 64.14 (s). $^{11}B\{^1H\}$ NMR (96 MHz, $CDCl_3$) δ -12.21 (s). IR (KBr, cm^{-1}): 508, 535, 565, 585, 598, 621, 677, 694, 732, 760, 770, 818, 825, 843, 866, 875, 879, 923, 1003, 1012, 1024,

1043, 1062, 1076, 1119, 1185, 1263, 1320, 1377, 1405, 1415, 1431, 1449, 1469, 1485, 1501, 1595, 1616, 2227, 2617, 2800, 2852, 2919, 3030, 3098. HRMS (ESI^-): 602.2684 (calcd. for MCl^-: 602.2673). UV-Vis (CH_2Cl_2, nm) λ_{max} (ϵ_{max}): 338 (9400), 288 (53260), 256 (65170). Elemental analysis: Calcd. C: 65.71 %, H: 4.62 %, N %, 4.94 %, Found: C: 65.96 %, H: 4.88 %, N: 4.97 %.

Synthesis of 78-d_{13}. A glass vial (5 mL volume) was charged with *p*-terphenyl-d_{14} (250.0 mg, 1.023 mmol, 1.0 equiv.), silver nitrate (700.0 mg, 4.250 mmol, 4.15 equiv.), iodine (1.05 g, 4.132 mmol, 4.0 equiv.), anhydrous acetonitrile (0.2 mL), and a stirrbar. The vial was closed with a lid with a teflon liner, and the resulting paste was shaken vigorously for 12 h. It was then allowed to sit at room temperature for 48 h. The mixture was transfered into a separatory funnel with dichloromethane (100 mL), washed with 10 % ammonium hydroxide (2 x 80 mL), 5 % sodium thiosulfate (2 x 50 mL), and with water (80 mL). The organic layer was dried over anhydrous sodium sulfate, filtered, and the solvents were removed under reduced pressure. The crude product was purified by two Kugelrohr sublimations at 80 °C to 120 °C (50 to 80 mTorr) to yield 245.9 mg (65 %) of pure white crystalline product. NMR (300 MHz, $CDCl_3$) δ 7.81 (s), 7.70 (s), 7.66 (s), 7.48 (s), 7.41 (s), 7.39 (s).

Synthesis of 77-d_{13}. The product was prepared by the same procedure as the non-deuterated version, starting with **78**-d_{13}. Kugelrohr sublimation (140 °C/30 mTorr) was used in place of the crystallization. The yield of the product was 89%. ^{1}H NMR (300 MHz, $CDCl_3$) δ 7.65 (s), 7.63 (s), 7.60 (s), 7.46 (s), 7.45 (s), 7.36 (s), 7.30 (s), 3.68 - 0.75 (m).

Synthesis of 82. The same procedure as for synthesis of non-deuterated **74** was employed, starting with **77**-d_{13}. The yield was 94%. ^{1}H NMR (300 MHz, $CDCl_3$) δ 7.59 (dd, J = 8.4, 1.4 Hz, 1H), 7.41 (dd, J = 7.9, 1.4 Hz, 1H), 7.07 (t, J = 8.1 Hz, 1H), 2.93 (s, 5H),

2.70 (s, 5H).

Synthesis of 86. A dried pressure Schlenk flask (100 mL) was equipped with a magnetic stir bar and filled with argon (three times). Anhydrous THF (5 mL) was added through a septum, and the mixture was cooled in an acetone/dry ice bath. After 5 min, a solution of 1.7 M *t*-BuLi in pentanes (1.34 mL, 2.29 mmol, 2.2 equiv.) was added dropwise. A solution of 3-iododurene (325 mg, 1.249 mmol, 1.2 equiv.) in anhydrous THF (10 mL) was added to the mixture under argon. After 20 min, a 1.0 M solution of zinc chloride in diethyl ether (1.25 mL, 1.249 mmol, 1.2 equiv.) was added and the reaction mixture was allowed to warm to room temperature. A suspension of p-*t*-butyl-*p'*-biphenyl iodide (350 mg, 1.041 mmol, 1.0 equiv.), and tetrakis(triphenylphosphino)palladium (120.3 mg, 0.104 mmol, 10 mol %) in anhydrous toluene (20 mL) was added to the mixture, and it was heated at 100 °C for 20 h in a closed vessel behind a blast shield. The resulting mixture was washed with water (2 x 20 mL), dried over anhydrous sodium sulfate, filtered, and the solvents were removed under reduced pressure. The crude product was purified by gradient flash column chromatography in *n*-pentane and toluene (100 % *n*-pentane to 5/1 *n*-pentane and toluene) to yield 291.7 mg (82 %) of white crystalline **86**, m.p. (CH_2Cl_2) 192 °C. ^{1}H NMR (300 MHz, $CDCl_3$) δ 7.74 - 7.60 (m, 4H), 7.60 - 7.48 (m, 2H), 7.25 - 7.15 (m, 2H), 7.06 (s, 1H), 2.32 (s, 6H), 1.98 (s, 6H), 1.42 (s, 9H). ^{13}C{^{1}H } NMR (75 MHz, $CDCl_3$) δ 150.28 (s), 141.94 (s), 141.26 (s), 139.04 (s), 138.19 (s), 133.68 (s), 132.24 (s), 130.57 (s), 129.86 (s), 126.93 (s), 126.77 (s), 125.86 (s), 34.69 (s), 31.55 (s), 20.37 (s), 17.45 (s). IR (KBr, cm^{-1}): 525, 567, 594, 731, 759, 811, 834, 860, 988, 1002, 1017, 1104, 1112, 1122, 1170, 1270, 1314, 1336, 1360, 1390, 1466, 1498, 2864, 2903, 2919, 2962, 2994, 3027, 3050, 3080. UV-Vis (CH_2Cl_2, nm) λ_{max} (ϵ_{max}): UV-Vis (CH_2Cl_2, nm) λ_{max} (ϵ_{max}): 263 (28590). Elemental analysis: Calcd. C: 91.17 %, H: 8.83 %, Found: C: 90.97 %, H: 8.97 %.

Synthesis of 87. A mixture of 3-iododurene (5.00 g, 19.22 mmol, 1.0 equiv.) and NBS (3.50 g, 19.66 mmol, 1.02 equiv.) in anhydrous acetonitrile (400 mL) was stirred at 55 to 60 °C for 5 days in the dark. The resulting mixture was diluted with water (400 mL), and the precipitate was filtered off. It was then washed with 5 % sodium thiosulfate (200 mL), water (2 x 200 mL), and the crude product was dried. The product was crystallized from acetonitrile to yield 6.07 g (93 %) of white crystals of **87**. The ^{1}H NMR spectrum of the product agreed with that reported.[151]

Synthesis of 88. A dry Schlenk flask (250 mL), equipped with a magnetic stir bar and a septum, was charged with **87** (5.97 g, 17.61 mmol, 1.0 equiv.), tetrakis(triphenylphosphino)palladium (2.04 g, 1.76 mmol, 10 mol %), cuprous iodide (670 mg, 3.58 mmol, 20 mol %). The flask was evacuated and filled with argon (three times). Anhydrous THF (80 mL), triisopropylsilylacetylene (3.5334 g, 19.37 mmol, 1.1 equiv.), and anhydrous diisopropylamine were added through a septum, and the resulting mixture was stirred at room temperature in a large oil-bath for 8 h. The temperature was then increased to 40 °C for 8 more h. The solvents were then removed under reduced pressure, the residue was dissolved in dichloromethane (250 mL), and washed with 5% ammonium hydroxide (100 mL), water (2 x 100 mL), 5 % hydrochloric acid (100 mL), and with water (2 x 100 mL). The organic layer was dried over anhydrous sodium sulfate, filtered, and the solvent was removed under reduced pressure. The crude product was filtered through a short column of silica gel in hexane in order to remove the catalysts, and the yellowish solid residue after solvent removal was purified by Kugelrohr distillation at 160 to 180 °C (30 to 80 mTorr). The yield of the product **88** was 5.86 g (85 %, white crystals), m.p. (CH_2Cl_2) 92 °C. ^{1}H NMR (300 MHz, $CDCl_3$) δ 2.56 (s, 6H), 2.43 (s, 6H), 1.21 (m, 21H). ^{13}C{^{1}H } NMR (75 MHz, $CDCl_3$) δ 137.43 (s), 133.85 (s), 129.69 (s), 123.01 (s), 105.54 (s), 99.15 (s), 21.15 (s), 19.73 (s), 18.88 (s), 11.57 (s). IR (KBr, cm^{-1}): 422, 440, 458, 483, 498, 514, 552, 569, 638, 656, 675, 746, 818, 850, 879, 917, 934, 969, 991, 1015, 1058, 1071, 1080, 1121, 1160, 1157, 1186, 1216, 1228, 1250, 1288, 1298,

1339, 1364, 1366, 1380, 1386, 1421, 1435, 1456, 1460, 1468, 2136, 2722, 2843, 2863, 2887, 2925, 2942, 2954. UV-Vis (CH_2Cl_2, nm) λ_{max} (ϵ_{max}): 303 (1410), 292 (1300), 273 (23160), 262 (23400). Elemental analysis: Calcd. C: 64.10 %, H: 8.45 %, Found: C: 64.11 %, H: 8.57 %.

Synthesis of 89. A dried pressure Schlenk flask (500 mL) with triply sealed teflon valve was equipped with a magnetic stir bar, and charged with **88** (2.00 g, 5.082 mmol, 1.2 equiv.). The flask was evacuated and filled with argon (three times). Anhydrous THF (90 mL) was added through a septum, and the resulting solution was cooled in an acetone/dry ice bath. White precipitate was formed. After that, 1.6 M solution of *n*-BuLi in hexanes (3.18 mL, 5.082 mmol, 1.2 equiv.) was added to the mixture. The mixture was allowed to warm until all the precipitate dissolved, and it was then cooled again in an acetone/dry ice bath. After 5 min, a 1.0 M solution of zinc chloride in THF (5.08 mL, 5.082 equiv.) was added to the reaction mixture. The mixture was allowed to warm to room temperature, and a suspension of *p*-*t*-butylbiphenyl iodide (1.424 g, 4.235 mmol, 1.0 equiv.), and $Pd(dba)_2$ (122 mg, 0.212 mmol, 5 mol %) in anhydrous THF (20 mL) was added through a septum. The reaction flask was closed and it was stirred for 36 to 48 h. The solvents were removed under reduced pressure, the residue was dissolved in dichloromethane (250 mL), and the organic layer was washed with 10 % hydrochloric acid (100 mL), water (2 x 50 mL), 5 % ammonium hydroxide (100 mL), and water (2 x 75 mL). The organic layer was dried over anhydrous sodium sulfate, filtered, and the solvent was removed under reduced pressure. The crude product was filtered through a short column of silica gel in cyclohexane in order to remove the catalysts, and the solvent was evaporated under reduced pressure. The volatile impurities were removed by Kugelrohr sublimation at 180 °C (50 mTorr), and the sublimation residue was purified by gradient flash chromatography (hexanes to hexanes / ethyl acetate 7/1) to yield 1.318 g (60 %) of white crystalline product **89**, m.p. (CH_2Cl_2) 161 °C. ^{1}H NMR (300 MHz, $CDCl_3$) δ 7.74 - 7.60 (m, 4H), 7.58 - 7.45 (m, 2H), 7.16 (m, 2H), 2.55 (s, 6H), 1.99 (s,

6H), 1.41 (s, 9H), 1.21 (m, 21H). $^{13}C\{^{1}H\}$ NMR (75 MHz, $CDCl_3$) δ 150.36 (s), 142.13 (s), 141.12 (s), 139.24 (s), 138.09 (s), 136.43 (s), 132.15 (s), 129.66 (s), 127.00 (s), 126.78 (s), 125.88 (s), 123.11 (s), 106.01 (s), 98.42 (s), 34.69 (s), 31.54 (s), 18.93 (s), 18.79 (s), 18.17 (s), 11.59 (s). IR (KBr, cm^{-1}): 450, 467, 544, 563, 573, 638, 644, 653, 666, 675, 685, 733, 750, 755, 795, 818, 846, 864, 883, 920, 993, 1004, 1013, 1068, 1074, 1111, 1123, 1164, 1203, 1232, 1242, 1270, 1314, 1363, 1381, 1386, 1390, 1421, 1461, 1494, 1500, 1906, 2140, 2195, 2715, 2856, 2890, 2941, 2959, 3003, 3082. UV-Vis (CH_2Cl_2, nm) λ_{max} (ϵ_{max}): 274 (48650), 263 (39570). MS (ESI^+): 545.4 (calcd. for MNa^+: 545.4). Elemental analysis: Calcd. C: 84.99 %, H: 9.64 %, Found: C: 84.92 %, H: 9.78 %.

Synthesis of 90. A solution of **89** (368.0 mg, 0.704 mmol, 1.0 equiv.) and 1.0 M TBAF solution in THF (2.8 mL, 2.815 mmol, 4.0 equiv.) in THF (5 mL) was stirred in a round bottom flask (50 mL) for 8 h. The reaction mixture was diluted with dichloromethane (100 mL), and washed with water (3 x 50 mL). The organic layer was dried over anhydrous sodium sulfate, filtered, and the solvent was removed under reduced pressure. The crude product was purified by gradient flash chromatography in hexanes and ethyl acetate (100 % hexanes to hexanes / ethyl acetate 6/1) to yield 249.5 mg (97 %) of **90** as white crystals, m.p. (CH_2Cl_2) 218 °C. ^{1}H NMR (300 MHz, $CDCl_3$) δ 7.71 - 7.58 (m, 4H), 7.51 (dt, 2H), 7.15 (dt, J = 8.4 Hz, 2H), 3.53 (s, 1H), 2.50 (s, 6H), 1.97 (s, 6H), 1.40 (s, 9H). $^{13}C\{^{1}H\}$ NMR (75 MHz, $CDCl_3$) δ 150.39 (s), 142.49 (s), 140.98 (s), 139.30 (s), 138.07 (s), 136.67 (s), 132.23 (s), 129.62 (s), 127.02 (s), 126.78 (s), 125.89 (s), 121.61 (s), 84.67 (s), 82.79 (s), 34.70 (s), 31.54 (s), 18.62 (s), 18.18 (s). IR (KBr, cm^{-1}): 533, 597, 634, 667, 781, 818, 845, 867, 1004, 1010, 1059, 1114, 1200, 1270, 1362, 1374, 1392, 1420, 1456, 1477, 1499, 1910, 2095, 2867, 2909, 2964, 3030, 3290, 3310. UV-Vis (CH_2Cl_2, nm) λ_{max} (ϵ_{max}): 264 (49030). Elemental analysis: Calcd. C: 91.75 %, H: 8.25 %, Found: C: 91.58 %, H: 8.37 %.

Synthesis of 83. A dried Schlenk flask (25 mL) was charged with **90** (249.0 mg, 0.679 mmol, 1.0 equiv.), 1,2-dichloro-3-iodobenzene (204.0 mg, 0.747 mmol, 1.1 equiv.), tetrakis(triphenylphosphino)palladium (78.4 mg, 0.068 mmol, 10 mol %) and cuprous iodide (25.8 mg, 0.136 mmol, 20 mol %). The flask was evacuated and filled with argon (three times), and anhydrous THF (6 mL) and anhydrous diisopropylamine (1 mL) were added through the septum. The mixture was stirred at 40 °C for 16 h. The solvents were removed under reduced pressure, the residue was dissolved in dichloromethane (100 mL), and the organic layer was washed with 5 % ammonium hydroxide (2 x 30 mL), water (2 x 30 mL), 5 % hydrochloric acid (2 x 30 mL), and water (50 mL). The organic layer was dried over anhydrous sodium sulfate, filtered, and the solvent was removed under reduced pressure. The crude product was purified by gradient flash chromatography in hexanes and ethyl acetate (100 % hexanes to hexanes + ethyl acetate 6/1) to yield 315.6 mg (91 %) of **83** as white crystals, m.p. (CH_2Cl_2) 279 °C. ^{1}H NMR (300 MHz, $CDCl_3$) δ 7.69 - 7.59 (m, 4H), 7.56 - 7.47 (m, 3H), 7.42 (dd, J = 8.1, 1.6 Hz, 1H), 7.24 - 7.17 (m, 1H), 7.17 - 7.13 (m, 2H), 2.58 (s, 6H), 1.99 (s, 6H), 1.39 (s, 9H). ^{13}C{^{1}H } NMR (75 MHz, $CDCl_3$) δ 150.42 (s), 142.93 (s), 140.97 (s), 139.33 (s), 138.06 (s), 136.56 (s), 134.07 (s), 133.47 (s), 132.41 (s), 131.33 (s), 129.79 (s), 129.60 (s), 127.14 (s), 127.04 (s), 126.78 (s), 126.32 (s), 125.90 (s), 121.98 (s), 95.06 (s), 93.44 (s), 34.71 (s), 31.54 (s), 18.80 (s), 18.19 (s). IR (KBr, cm^{-1}): 667, 707, 730, 742, 755, 778, 782, 817, 850, 863, 898, 947, 967, 1003, 1048, 1061, 1108, 1112, 1124, 1153, 1187, 1202, 1231, 1267, 1296, 1318, 1330, 1363, 1378, 1389, 1406, 1457, 1498, 1548, 1577, 1785, 1862, 1904, 1933, 2162, 2201, 2731, 2860, 2941, 2956, 3024, 3058, 3084. UV-Vis (CH_2Cl_2, nm) λ_{max} (ϵ_{max}): 321 (36090), 302 (40080), 260 (24320), 243 (28120). Elemental analysis: Calcd. C: 79.83 %, H: 6.31 %, Found: C: 79.86 %, H: 6.23 %.

Synthesis of 84. A dried three-necked round bottom flask (100 mL) was equipped with a magnetic stir bar, septa, and a hose connector. It was then connected through a cannula to another dried three-necked round bottom flask (250 mL) equipped with a

magnetic stir bar, septa, and a hose connector. The larger flask was placed about 20 cm below the smaller fask. The smaller flask was charged with **90** (250.0 mg, 0.682 mmol and 1.0 equiv.). The larger flask with *N*,*N*-dimethylcarbamoyl chloride (733.0 mg, 6.820 mmol, 10.0 equiv.). The flasks were evacuated and filled with argon (three times). The septa with the cannula were wrapped with teflon tape, parafilm, and kimwipes in order to prevent water from getting into the reaction mixtures when cold liquids are pushed through the cannula. Anhydrous THF (50 mL) was added to the smaller flask and it was cooled in an acetone/dry ice bath. After 5 min, 1.6 M solution of *n*-BuLi in hexanes (0.47 mL, 0.750 mmol, 1.1 equiv.) was added, and the mixture was stirred for 45 min at -78 °C. In the meantime, anhydrous THF (20 mL) was added to the larger flask and the resulting solution was cooled in an acetone/dry ice bath. The solution from the smaller flask was cannulated into the larger flask while the content of the larger flask was stirred well. The smaller flask was rinsed with anhydrous THF (10 mL) twice and the content was cannulated into the larger flask each time. The resulting reaction mixture was allowed to warm to room temperature, and the solvents and unreacted *N*,*N*-dimethylcarbamoyl chloride were removed under reduced pressure (100 °C, 100 mTorr). The solid residue was dissolved in dichloromethane (100 mL), washed with water (2 x 50 mL), the organic layer was dried over anhydrous sodium sulfate, filtered, and the solvent was removed under reduced pressure. The crude product was purified by gradient flash chromatography in hexanes, ethyl acetate and diethyl ether (18/3/1 to 12/2/1) to yield 232.0 mg (78 %) of pure **84** as white crystals, m.p. (CH_2Cl_2) 257 °C. ^{1}H NMR (300 MHz, $CDCl_3$) δ 7.70 - 7.56 (m, 4H), 7.53 - 7.44 (m, 2H), 7.17 - 7.07 (m, 2H), 3.34 (s, 3H), 3.07 (s, 3H), 2.50 (s, 6H), 1.96 (s, 6H), 1.38 (s, 9H). ^{13}C{^{1}H } NMR (75 MHz, $CDCl_3$) δ 155.28 (s), 150.46 (s), 143.82 (s), 140.66 (s), 139.46 (s), 137.98 (s), 137.34 (s), 132.61 (s), 129.44 (s), 127.08 (s), 126.77 (s), 125.90 (s), 120.22 (s), 90.02 (s), 89.31 (s), 38.54 (s), 34.70 (s), 34.37 (s), 31.53 (s), 18.85 (s), 18.11 (s). IR (KBr, cm^{-1}): 534, 565, 575, 605, 727, 814, 866, 921, 973, 1003, 1073, 1113, 1152, 1178, 1263, 1278, 1389, 1405, 1437, 1459, 1498, 1624, 2196, 2868, 2958, 3033. UV-Vis (CH_2Cl_2, nm) λ_{max} (ϵ_{max}): 280 (30300).

MS (ESI^+): 460.3 (calcd. for MNa^+: 460.3). Elemental analysis: Calcd. C: 85.08 %, H: 8.06 %, N %, 3.20 %, Found: C: 84.70 %, H: 8.22 %, N: 3.25 %.

Synthesis of 85. The compound **85** was prepared by the same procedure as **84**, using the same quantities, but using *N*,*N*-diisopropylcarbamoyl chloride (1.116 g, 6.820 mmol, 10.0 equiv.) in place of *N*,*N*-dimethylcarbamoyl chloride. The product was purified by flash chromatography in hexanes and ethyl acetate (6/1) to yield 218.8 mg (65 %) of the product **85** as white crystalline solid, m.p. (CH_2Cl_2) 220 °C. ^{1}H NMR (300 MHz, $CDCl_3$) δ 7.70 - 7.55 (m, 4H), 7.53 - 7.42 (m, 2H), 7.16 - 7.08 (m, 2H), 4.92 - 4.74 (m, 1H), 3.72 - 3.54 (m, 1H), 2.50 (d, J = 5.6 Hz, 6H), 1.96 (s, 6H), 1.47 (d, J = 6.8 Hz, 6H), 1.38 (s, 9H), 1.31 (d, J = 6.8 Hz, 6H). ^{13}C{^{1}H } NMR (75 MHz, $CDCl_3$) δ 154.33 (s), 150.44 (s), 143.60 (s), 140.73 (s), 139.42 (s), 138.00 (s), 137.29 (s), 132.54 (s), 129.47 (s), 127.06 (s), 126.77 (s), 125.90 (s), 120.53 (s), 90.70 (s), 88.23 (s), 50.92 (s), 45.92 (s), 34.70 (s), 31.53 (s), 21.12 (s), 20.45 (s), 18.74 (s), 18.11 (s). IR (KBr, cm^{-1}): 402, 512, 535, 575, 583, 602, 667, 680, 730, 781, 815, 845, 854, 865, 883, 918, 1003, 1040, 1082, 1111, 1134, 1153, 1204, 1216, 1275, 1309, 1335, 1361, 1371, 1376, 1390, 1430, 1458, 1473, 1500, 1628, 1910, 2195, 2608, 2727, 2867, 2901, 2934, 2963, 2998, 3029, 3050, 3086. UV-Vis (CH_2Cl_2, nm) λ_{max} (ϵ_{max}): 278 (29960). MS (ESI^+): 516.4 (calcd. for MNa^+: 516.3). Elemental analysis: Calcd. C: 85.14 %, H: 8.78 %, N %, 2.84 %, Found: C: 84.70 %, H: 8.86 %, N: 2.85 %.

4.2.2 Inclusion Compound Preparation

General procedure. The inclusion compounds were prepared either by grinding or by ball milling with a stainless steel disk (diameter: 6 mm, hight: 3 mm)in a glass vial (15 x 45 mm) wrapped with scotch tape. The vial and the disk were washed with dichloromethane and dried at 200 °C before use.

Ball milling. The host and guest compounds were mixed in the vial with the stainless steel disk, and vial was closed with a lid. The vial was placed in the shaker Vortex Genie 2 (Scientific Industries), and the mixture was shaken at stage 3, vortex scale. The powder was scraped from the walls of the vial every 10 to 15 min in order to ensure proper mixing. **Annealing.** The inclusion compound was annealed in the closed vial at 70 to 75 °C in an oven.

Inclusion compound 51@TPP. Amounts used: **51**: 5.2 mg, TPP: 200 mg. The powders were vigorously ground using an agate mortar and pestle for 30 min.

Inclusion compound 50@TPP. Amounts used: **50**: 12.0, TPP: 180.0 mg. The powders were vigorously ground using an agate mortar and pestle for 30 min.

Inclusion compound of biphenyl in TPP. Amounts used: biphenyl: 3.1 mg, TPP: 180.0 mg. The powders were vigorously ground using an agate mortar and pestle for 30 min.

Inclusion compound 5%63@TPP. Amounts used: **63**: 10.6 TPP: 180.0 mg. The powders were vigorously ground using an agate mortar and pestle for 30 min.

Inclusion compound 15%63@TPP-d_{12}. Amounts used: **63**: 26.8 mg, TPP-d_{12}: 140.0 mg. Ball milling (90 min) was followed by annealing (1 day), ball milling (120 min), and annealing (3 days).

Inclusion compound 10%70@TPP-d_{12}. Amounts used: **70**: 21.7 mg, TPP-d_{12}: 180.0 mg. Ball milling (120 min) was followed by annealing (1 day), ball milling (120 min),

and annealing (3 days).

Inclusion compound 15%70@TPP-d_{12}. Amounts used: **70**: 30.7 mg, TPP-d_{12}: 160.0 mg. Ball milling (120 min) was followed by annealing (1 day), ball milling (120 min), and annealing (3 days).

Inclusion compound 8%70@TPP-d_{12}. Amounts used: **70**: 17.1 mg, TPP-d_{12}: 180.0 mg. Ball milling (120 min) was followed by annealing (1 day), ball milling (120 min), and annealing (3 days).

Inclusion compound of *p*-terphenyl in TPP. Amounts used: *p*-terphenyl: 4.8 mg, TPP: 180.0 mg. Ball milling (120 min) was followed by annealing (1 day).

Inclusion compound of 4-nitro-*p*-terphenyl in TPP. Amounts used: 4-nitro-*p*-terphenyl: 5.7 mg, TPP: 180.0 mg. Ball milling (120 min), was followed by annealing (1 day).

Inclusion compound 15%73@TPP-d_{12}. Amounts used: **73**: 28.9 mg, TPP-d_{12}: 200.0 mg. Ball milling (80 min) was followed by annealing (1 day), ball milling (30 min), and annealing (3 days).

Inclusion compound 15%72@TPP-d_{12}. Amounts used: **72**: 24.3 mg, TPP-d_{12}: 150.0 mg. Ball milling (90 min) was followed by annealing (3 days).

Inclusion compound 15%74@TPP-d_{12}. Amounts used: **74**: 31.0 mg, TPP-d_{12}: 160.0 mg. Ball milling (120 min) was followed by annealing (1 day), ball milling (30 min),

and annealing (3 days).

Inclusion compound 9%82@TPP-d_{12}. Amounts used: **82**: 27.8 mg, TPP-d_{12}: 250.0 mg. Ball milling (90 min) was followed by annealing (1 day), ball milling (45 min), and annealing (3 days).

Inclusion compound het-5%74@TPP-d_{12}. Amounts used: **74**: 14.6 mg, TPP-d_{12}: 250.0 mg. Ball milling (60 min).

Inclusion compound 15%75@TPP-d_{12}. Amounts used: **75**: 36.4 mg, TPP-d_{12}: 180.0 mg. Ball milling (120 min) was followed by annealing (1 day), ball milling (120 min), and annealing (3 days).

Inclusion compound het-22%75@TPP-d_{12}. Amounts used: **75**: 48.6 mg, TPP-d_{12}: 150.0 mg. Ball milling (120 min) was followed by annealing (1 day), ball milling (120 min), and annealing (3 days).

Inclusion compound 15%77@TPP-d_{12}. Amounts used: **77**: 19.5 mg, TPP-d_{12}: 140.0 mg. Ball milling (80 min) was followed by annealing (1 day), ball milling (30 min), and annealing (3 days).

Attempted preparation of the inclusion compound 15%76@TPP-d_{12}. Amounts used: **76**: 33.8 mg, TPP-d_{12}: 160.0 mg. Ball milling (180 min) was followed by annealing (1 day), ball milling (180 min), and annealing (3 days).

Inclusion compound of p,p'-di-t-butylbiphenyl in TPP. Amounts used: p,p'-di-

t-butylbiphenyl: 29.0 mg, TPP: 200.0 mg. Ball milling (120 min) was followed by annealing (3 days).

Attempted preparation of the inclusion compound of hexamethylbenzene in TPP. Amounts used: hexamethylbenzene: 43.0 mg, TPP: 122.0 mg. Ball milling (180 min) was followed by annealing (3 days).

Inclusion compound 20%86@TPP-d_{12}. Amounts used: **86**: 21.8 mg, TPP-d_{12}: 120.0 mg. Ball milling (120 min) was followed by annealing (1 day), ball milling (120 min), and annealing (3 days).

Attempted preparation of the inclusion compound 15%83@TPP-d_{12}. Amounts used: **83**: 38.5 mg, TPP-d_{12}: 201.1 mg. Ball milling (180 min) was followed by annealing (1 day), ball milling (180 min), and annealing (3 days).

Inclusion compound 15%84@TPP-d_{12}. Amounts used: **84**: 27.2 mg, TPP-d_{12}: 166.6 mg. Ball milling (180 min), was followed by annealing (1 day), ball milling (180 min), and annealing (3 days).

Inclusion compound 15%85@TPP-d_{12}. Amounts used: **85**: 30 mg, TPP-d_{12}: 162 mg. Ball milling (8 h) was followed by annealing (1 day), ball milling (8 h), and annealing (3 days).

4.3 Synthesis of Compounds from Chapter 3

Synthesis of 97. A dried three necked round bottom flask, equipped with septa,

magnetic stir bar, and a connection to a Schlenk line was charged with neat sodium hydride (732 mg, 1.2 equiv., 30.5 mmol), and compound **96**[146] (5.554 g, 1.0 equiv., 25.4 mmol) under argon. The reaction flask was immersed in an ice bath, and anhydrous dimethylformamide (110 mL) was added rapidly to the stirred mixture. After the evolution of hydrogen slowed down, the ice bath was removed, and the reaction mixture was stirred at room temperature for additional 45 min After that, the reaction flask was again immersed in an ice bath and N-phenyl-bis(trifluoromethanesulfonimide) (10.896 g, 1.2 equiv., 30.5 mmol) was added. The reaction mixture was left in the ice bath, it was stirred overnight (12 h) at room temperature as the ice melted, and the bath warmed up to ambient temperature. The resulting mixture was quenched with a few drops of water, and it was then slowly poured into stirred diethyl ether (1.5 L). The resulting suspension was washed with water (200 mL), 5 % aqueous sodium hydroxide (200 mL), and brine (200 mL). The solvents were removed under reduced pressure, and the crude product was recrystallized from ethyl acetate to yield 6.420 g (72 %) of white crystals, m.p. (CH_2Cl_2) 253 °C. ^{1}H NMR (300 MHz, $CDCl_3$) δ 11.15 (s, 1H), 7.55 (d, J = 9.1 Hz, 1H), 6.73 (dd, J = 9.1, 2.4 Hz, 1H), 6.44 (d, J = 2.4 Hz, 1H), 3.09 (s, 6H), 2.26 (s, 3H). ^{19}F NMR (282 MHz, $CDCl_3$) δ -72.99 (s). ^{13}C{^{1}H } NMR (75 MHz, DMSO) d 162.43, 151.84, 150.79, 138.93, 121.94, 117.99 (q, J = 320.2 Hz), 115.68, 109.31, 103.70, 95.05, 39.60, 10.67. IR (KBr, cm^{-1}): 499, 588, 596, 669, 692, 726, 747, 756, 789, 821, 880, 922, 980, 1044, 1134, 1151, 1210, 1220, 1243, 1279, 1292, 1347, 1364, 1377, 1391, 1409, 1445, 1488, 1527, 1565, 1629, 1659, 2829, 2867, 2926, 2994, 3093, 3157. UV-Vis (CH_2Cl_2, nm) λ_{max} (ϵ_{max}): 369 (23143), 360 (22012), 305 (4570), 286 (5054), 254 (10465), 229 (38808). MS (ESI$^+$): 373.1 (calcd. for MNa$^+$: 373.0). Elemental analysis: Calcd. C: 44.57 %, H: 3.74 %, N: 8.00 %, Found: C: 44.52 %, H: 3.65 %, N: 7.97 %.

Synthesis of 98. A flame-dried two-necked round bottom flask equipped with a septum was charged with **97** (400 mg, 1.0 equiv., 1.142 mmol), and sodium hydride (32.8 mg, 1.2 equiv., 1.370 mmol). The flask was immersed in an acetone / ice cooling bath (-20

°C) and anhydrous dimethylformamide (10 mL) was added at once. The mixture was stirred under argon, at -20°C for 30 min, and then for 1 h at room temperature. Afterwards, the mixture was recooled to -20 °C and methyl-d_3 iodide (198.5 mg, 1.2 equiv., 1.37 mmol) was added. The reaction mixture was allowed to warm to room temperature, stirred for an additional 4 h, quenched with a few drops of water, diluted with diethyl ether (150 mL), and washed with water (50 mL). The organic layer was dried over anhydrous sodium sulfate and filtered. The solvent was removed under reduced pressure and the crude product was purified by flash chromatography in ethyl acetate to yield 313 mg (75%) of yellowish crystals, m.p. (CH_2Cl_2) 170 °C. ^{1}H NMR (300 MHz, $CDCl_3$) δ 7.60 (d, J = 9.1 Hz, 1H), 6.73 (dd, J = 9.1, 2.4 Hz, 1H), 6.37 (d, J = 2.4 Hz, 1H), 3.11 (s, 6H), 2.25 (s, 3H). ^{19}F NMR (282 MHz, $CDCl_3$) δ -72.98 (s). ^{13}C{^{1}H } NMR (75 MHz, $CDCl_3$) δ 163.56, 152.27, 150.61, 140.34, 123.91, 118.70 (q, J = 118.7 Hz), 116.48, 108.80, 105.85, 94.97, 40.43, 11.89. ^{2}H NMR (61 MHz, $CDCl_3$) δ 3.69 (s). ^{13}C{^{1}H } CP MAS NMR (101 MHz, neat solid) δ 160.88, 151.48, 148.15, 138.90, 121.42, 120.05, 113.82, 109.99, 103.04, 91.82, 39.03, 27.65, 11.35. IR (KBr, cm^{-1}): 505, 594, 620, 667, 694, 747, 815, 868, 946, 965, 1000, 1043, 1140, 1167, 1207, 1228, 1247, 1315, 1347, 1379, 1403, 1489, 1532, 1554, 1605, 1645, 1893, 2081, 2812, 2930, 3108. UV-Vis (CH_2Cl_2, nm) λ_{max} (ϵ_{max}): 370 (24,400), 360 (22,670), 305 (5250), 284 (7160), 231 (42,920). HRMS (ESI$^+$): 368.0969 (calcd. for MH$^+$: 368.0965). Elemental analysis: Calcd. C: 45.77%, H: 4.12%, N: 7.63%, Found, C: 46.02%, H: 3.99%, N: 7.50%.

Synthesis of 99. Compound **98** (300 mg, 1.0 equiv., 0.817 mmol), tetrakis(triphenylphosphino)palladium (94.3 mg, 0.1 equiv., 0.082 mmol), cuprous iodide (31.1 mg, 0.2 equiv., 0.163 mmol), trimethylsilylacetylene (802.0 mg, 10.0 equiv., 8.170 mmol), anhydrous diisopropylamine (0.5 mL), and anhydrous dimethylformamide (6 mL) were combined in a flame-dried Schlenk flask (25 mL) under argon. The reaction mixture was stirred at 120 °C for 24 h under argon. The solvent was removed under reduced pressure and the remaining solid was dissolved in diethyl ether (100 mL). The organic layer was washed with water (2 x

40 mL), dried over anhydrous sodium sulfate, and filtered. The solvent was removed under reduced pressure and the crude product was purified by gradient flash chromatography in a hexanes:ethyl acetate mixture (2:1 to 100% ethyl acetate) to yield 196 mg (76%) of yellow crystalline solid, mp (CH_2Cl_2) 166 °C. ^{1}H NMR (400 MHz, $CDCl_3$) δ 7.79 (d, J = 8.9 Hz, 1H), 6.64 (dd, J = 8.9, 2.2 Hz, 1H), 6.25 (d, J = 2.2 Hz, 1H), 3.04 (s, 6H), 2.37 (s, 3H), 0.32 (s, 9H). ^{2}H NMR (46 MHz, $CDCl_3$) δ 3.67 (s). ^{13}C{^{1}H } NMR (75 MHz, $CDCl_3$) δ 162.77, 151.39, 140.12, 128.35, 127.95, 127.65, 110.89, 108.23, 107.23, 99.90, 95.10, 40.42, 31.00 - 26.96 (m), 16.03, 0.04. IR (KBr, cm^{-1}): 479, 628, 651, 700, 723, 754, 795, 803, 816, 843, 864, 948, 963, 1015, 1030, 1087, 1113, 1165, 1235, 1246, 1308, 1345, 1376, 1399, 1528, 1547, 1580, 1609, 1632, 2140, 2801, 2863, 2911, 2954. UV-Vis (CH_2Cl_2, nm) λ_{max} (ϵ_{max}): 380 (15,560), 262 (27,970), 232 (42,470). HRMS (ESI$^+$): 316.1920 (calcd. for MH$^+$: 316.1919). Elemental analysis: Calcd. C: 68.52%, H: 7.66%, N: 8.88%, Found, C: 68.81%, H: 7.64%, N: 8.60%.

Synthesis of 100. Compound **99** (160 mg) was dissolved in a mixture of dichloromethane (15 mL) and methanol (15 mL) in a round-bottom flask (100 mL). A solution of potassium carbonate (345 mg) in water (30 mL) was added. The reaction mixture was stirred for 4 h at room temperature. Afterwards, it was diluted with diethyl ether (60 mL), and the aqueous layer was separated. The organic layer was dried over anhydrous sodium sulfate and filtered. The solvent was removed under reduced pressure to yield 123 mg (100%) of yellow crystalline product, m.p. (CH_2Cl_2) 171 °C. ^{1}H NMR (300 MHz, $CDCl_3$) δ 7.86 (d, J = 9.0 Hz, 1H), 6.70 (dd, J = 9.0, 2.4 Hz, 1H), 6.35 (d, J = 2.4 Hz, 1H), 3.73 (s, 1H), 3.09 (s, 6H), 2.40 (s, 3H). ^{2}H NMR (46 MHz, $CDCl_3$) δ 3.69 (s). ^{13}C{^{1}H } NMR (101 MHz, $CDCl_3$) δ 162.45, 151.23, 139.93, 128.01, 127.62, 127.36, 110.68, 108.07, 94.84, 88.83, 78.57, 40.29, 30.06 - 27.83 (m), 15.92. IR (KBr, cm^{-1}): 435, 492, 505, 578, 624, 637, 675, 720, 753, 801, 839, 944, 957, 1027, 1059, 1105, 1153, 1169, 1210, 1237, 1266, 1309, 1341, 1370, 1395, 1411, 1432, 1452, 1487, 1522, 1580, 1602, 1629, 1715, 1786, 1882, 2073, 2094, 2124, 2231, 2581,

2798, 2858, 2911, 2989, 3204. UV-Vis (CH_2Cl_2, nm) λ_{max} (ϵ_{max}): 379 (17,470), 294 (4240), 257 (23,850), 232 (45,940). HRMS (ESI^+): 244.1515 (calcd. for MH^+: 244.1523). Elemental analysis: Calcd. C: 74.04%, H: 6.63%, N: 11.51%, Found, C: 74.23%, H: 6.65%, N: 11.66%.

Synthesis of 94. A flame dried Schlenk flask (25 mL) was charged with **100** (140 mg, 1.0 equiv., 0.575 mmol), iodobenzene (141 mg, 1.2 equiv., 0.690 mmol), tetrakis(triphenylphosphino)palladium (66.4 mg, 0.1 equiv., 0.058 mmol), cuprous iodide (21.9 mg, 0.2 equiv., 0.115 mmol), anhydrous tetrahydrofuran (5 mL), and anhydrous diisopropylamine (0.5 mL) under argon. The mixture was stirred at 40 °C under argon for 24 h. The solvent was removed under reduced pressure and the remaining solid was dissolved in diethy ether (100 mL). The organic layer was washed with water (2 x 40 mL), dried over anhydrous sodium sulfate, and filtered. The solvent was removed under reduced pressure and the crude product was purified by gradient flash chromatography in a hexanes:ethyl acetate mixture (2:1 to 100% ethyl acetate) to yield 149 mg (81%) of yellow crystals, mp (CH_2Cl_2) 186 °C. ^{1}H NMR (300 MHz, $CDCl_3$) δ 7.86 (d, J = 8.9 Hz, 1H), 7.66 - 7.57 (m, 2H), 7.44 - 7.34 (m, 3H), 6.64 (dd, J = 8.9, 2.4 Hz, 1H), 6.23 (d, J = 2.4 Hz, 1H), 3.03 (s, 6H), 2.44 (s, 3H). ^{2}H NMR (46 MHz, $CDCl_3$) δ 3.63 (s). ^{13}C{^{1}H } NMR (75 MHz, $CDCl_3$) δ 162.65, 151.28, 140.07, 131.77, 129.06, 128.54, 128.46, 127.79, 126.74, 122.71, 110.84, 108.07, 101.03, 95.03, 84.55, 40.32, 32.26 - 26.61 (m), 16.08. IR (KBr, cm^{-1}): 435, 492, 505, 578, 624, 637, 675, 720, 753, 801, 839, 944, 957, 1027, 1059, 1105, 1153, 1169, 1210, 1237, 1266, 1309, 1341, 1370, 1395, 1411, 1432, 1452, 1487, 1522, 1580, 1602, 1629, 1715, 1786, 1882, 2073, 2094, 2124, 2231, 2581, 2798, 2858, 2911, 2989, 3204. UV-Vis (CH_2Cl_2, nm) λ_{max} (ϵ_{max}): 387 (13,000), 296 (25,320), 283 (25,590), 232 (43,840). HRMS (ESI^+): 320.1839 (calcd. for MH^+: 320.1836). Elemental analysis: C: 78.69%, H: 6.33%, N: 8.62%, calcd.: C: 78.96%, H: 6.31%, N: 8.77%.

Synthesis of 91. A dried Schlenk flask (50 mL), equipped with a septum and magnetic stir bar, was charged with **101**[152] (1.00 g, 3.822 mmol, 1.0 equiv.), and 16-hydroxyhexadecanoic acid (3.124 g, 11.467 mmol, 3.0 equiv.), and it was evacuated and filled with argon (three times). Anhydrous dichloromethane (30 mL), and anhydrous triethylamine (1.161 g, 11.467 mmol, 3.0 equiv.) were added to the mixture, and it was stirred at room temperature for 2 days The reaction mixture was filtered under argon, the filtrate was washed with anhydrous dichloromethane (2 x 20 mL), and the solvent was removed under reduced pressure. The crude product was purified by repeated crystallization from anhydrous acetonitrile to yield 1.485 g (40 %) of white crystals, mp (CH_2Cl_2) 66 °C. ^{1}H NMR (300 MHz, CD2Cl2) δ 8.30 (dd, J = 8.1, 1.6 Hz, 1H), 7.96 (dd, J = 6.8, 1.3 Hz, 1H), 7.94 - 7.89 (m, 1H), 7.87 - 7.82 (m, 1H), 7.54 - 7.43 (m, 3H), 3.80 (t, J = 6.6 Hz, 6H), 2.33 (t, J = 7.4 Hz, 6H), 1.76 - 1.51 (m, 12H), 1.49 - 1.14 (m, 66H). ^{13}C{^{1}H } NMR (75 MHz, CD_2Cl_2) δ 180.07, 137.55, 136.54, 133.80, 131.44, 130.07, 129.23, 129.08, 126.67, 126.10, 125.49, 63.65, 34.43, 33.00, 30.22, 30.19, 30.18, 30.15, 30.10, 29.94, 29.91, 29.75, 29.51, 26.35, 25.23. IR (KBr, cm^{-1}): 718, 774, 796, 832, 912, 948, 987, 1021, 1082, 1093, 1151, 1201, 1218, 1243, 1280, 1297, 1389, 1409, 1432, 1465, 1504, 1705, 2678, 2848, 2918, 3035, 3052. UV-Vis (CH_2Cl_2, nm) λ_{max} (ϵ_{max}): 227 (62500), 264 (4400), 274 (6700), 284 (7900), 296 (5500). MS (ESI$^+$): 991.7 (calcd. for MNa$^+$:991.7). Elemental analysis: Calcd. C: 71.85 %, H: 10.40 %, Found: C: 71.64 %, H: 10.56 %.

Synthesis of 112. A dried round bottom flask (250 mL) was equipped with a magnetic stir bar and a reflux condernser. It was charged with 16-bromohexadecanoic acid (2 g, 5.964 mmol, 1.0 equiv.) and thionyl chloride (10 mL), and the resulting mixture was refluxed for 1 h. The excess thionyl chloride was removed under reduced pressure and the residue was dissolved in anhydrous dichloromethane (80 mL). The mixture was cooled to -20 °C, and a 2.0 M solution of dimethylamine in THF (20 mL, 40.00 mmol, 6.7 equiv.) was added dropwise while the reaction mixture was vigorously stirred. The resulting mixture was stirred

at -20 °C for an hour, and it was then diluted with dichloromethane (100 mL), and washed with water (2 x 50 mL), 5 % hydrochloric acid (2 x 50 mL), and water (50 mL). The organic layer was dried over anhydrous sodium sulfate, filtered, and the solvent was removed under reduced pressure. The product was purified by flash chromatography in hexanes and ethyl acetate to yield 2.136 g (99 %) of **112** as white crystals, m.p. (CH_2Cl_2) 66 °C. ^{1}H NMR (400 MHz, $CDCl_3$) δ 3.35 (t, J = 6.9 Hz, 2H), 2.95 (s, 3H), 2.89 (s, 3H), 2.30 - 2.20 (m, 2H), 1.85 - 1.74 (m, 2H), 1.56 (dd, J = 14.1, 6.9 Hz, 2H), 1.36 (d, J = 7.1 Hz, 2H), 1.20 (m, 20H). ^{13}C{^{1}H } NMR (101 MHz, $CDCl_3$) δ 173.22 (s), 37.32 (s), 35.33 (s), 34.09 (s), 33.43 (s), 32.85 (s), 29.64 (s), 29.53 (s), 29.49 (s), 29.45 (s), 28.78 (s), 28.18 (s), 25.21 (s). IR (KBr, cm^{-1}): 720, 728, 740, 774, 796, 840, 880, 920, 960, 964, 997, 1024, 1047, 1062, 1080, 1112, 1143, 1202, 1221, 1240, 1263, 1282, 1304, 1334, 1362, 1402, 1418, 1433, 1462, 1471, 1495, 1577, 1593, 1605, 1644, 1730, 2849, 2913, 2938, 3033. MS (ESI^+): 384.2 (calcd. for MNa^+: 384.2). Elemental analysis: Calcd. C: 59.66 %, H: 10.01 %, N %, 3.87 %, Found: C: 60.13 %, H: 10.39 %, N: 3.96 %.

Synthesis of 114. A dried Schlenk flask (50 mL) was charged with **113** (811 mg, 3.104 mmol, 1.0 equiv.), sodium hydride (297.9 mg, 12.417 mmol, 5.0 equiv.), and **112** (4.50 g, 12.417 mmol, 4.0 equiv.) The flask was evacuated and filled with argon (three times), placed into an acetone/ice bath, and anhydrous DMF (20 mL) was added rapidly. The reaction mixture was allowed to warm to room temperature, within 1 h, and it was then stirred at room temperature for 16 h, then at 40 °C for 14 h, and at 60 °C for 24 h. The reaction mixture was quenched with a few drops of water, the solvent was removed under reduced pressure, and the residue was dissolved in dichloromethane (200 mL). The solution was washed with water (2 x 50 mL), the organic layer was dried over anhydrous sodium sulfate, filtered, and the solvent was removed under reduced pressure. The product was purified by flash gadient chromatography in ethyl acetate and methanol (19/1 to 9/1) to yield 2.407 g (70 %) of white crystals of **114**, m.p. (CH_2Cl_2) 57 °C. ^{1}H NMR (300 MHz,

$CDCl_3$) δ 7.41 - 7.27 (m, 4H), 3.61 (s, 6H), 3.34 (t, J = 6.5 Hz, 6H), 2.97 (s, 9H), 2.91 (s, 9H), 2.32 - 2.23 (m, 6H), 1.66 - 1.53 (m, 6H), 1.53 - 1.41 (m, 6H), 1.37 - 1.14 (m, 66H). $^{13}C\{^1H\}$ NMR (75 MHz, $CDCl_3$) δ 173.30 (s), 141.76 (s), 130.82 (s), 129.45 (s), 120.16 (s), 72.61 (s), 71.63 (s), 48.05 (s), 37.37 (s), 35.40 (s), 33.51 (s), 29.78 (s), 29.77 (s), 29.74 (s), 29.63 (s), 29.62 (s), 29.57 (s), 29.55 (s), 26.29 (s), 25.28 (s). IR (KBr, cm^{-1}): 470, 512, 582, 607, 615, 657, 716, 740, 751, 762, 816, 842, 899, 935, 950, 968, 1003, 1043, 1060, 1080, 1103, 1120, 1142, 1170, 1187, 1210, 1233, 1267, 1298, 1320, 1357, 1374, 1394, 1407, 1469, 1484, 1490, 1646, 2850, 2970. UV-Vis (CH_2Cl_2, nm) λ_{max} (ϵ_{max}): 228 (12040). MS (ESI^+): 1126.9 (calcd. for MNa^+: 1126.8). Elemental analysis: Calcd. C: 69.53 %, H: 10.76 %, N %, 3.80 %, Found: C: 69.70 %, H: 10.69 %, N: 3.99 %.

Synthesis of 115. A general literature procedure[147] was employed. A dried Schlenk flask (100 mL) equipped with a septum and a magnetic stir bar, was charged with **114** (2.180 g, 1.972 mmol, 1.0 equiv.). The flask was evacuated and filled with argon (three times). Anhydrous dichloromethane (20 mL) was added, the solution was cooled to -20 °C, and triflic anhydride (2.503 g, 8.873 mmol, 4.5 equiv.) and anhydrous pyridine (1.404 g, 17.748 mmol, 9 equiv.) were added. The resulting mixture was stirred at 0 °C for 16 h, and methanol (5 mL) was added. After 8 h, the reaction mixture was allowed to warm to room temperature, and it was diluted with dichloromethane (100 mL), washed with 5 % hydrochloric acid (50 mL), water (50 mL), and saturated aqueous sodium bicarbonate (50 mL). The organic layer was dried over anhydrous sodium sulfate, filtered, and the solvent was removed under reduced pressure. The product was purified by flash chromatography in hexanes and ethyl acetate (2/1) to yield 1.658 g (79 %) of white crystalline product **115**, m.p. (CH_2Cl_2) 56 °C. ^1H NMR (300 MHz, $CDCl_3$) δ 7.35 (m, 4H), 3.65 (s, 9H), 3.63 (s, 6H), 3.35 (t, J = 6.5 Hz, 6H), 2.28 (t, J = 7.5 Hz, 6H), 1.59 (m, 6H), 1.55 - 1.42 (m, 6H), 1.24 (m, 66H). $^{13}C\{^1H\}$ NMR (101 MHz, $CDCl_3$) δ 174.38 (s), 141.73 (s), 130.85 (s), 129.45 (s), 120.19 (s), 72.61 (s), 71.63 (s), 51.51 (s), 48.04 (s), 34.19 (s), 29.80 (s), 29.79 (s), 29.77 (s),

29.72 (s), 29.63 (s), 29.57 (s), 29.38 (s), 29.26 (s), 26.31 (s), 25.05 (s). IR (KBr, cm^{-1}): 666, 704, 720, 741, 756, 780, 821, 883, 970, 990, 1007, 1085, 1105, 1172, 1196, 1217, 1237, 1261, 1279, 1302, 1363, 1378, 1419, 1335, 1466, 1489, 1506, 1519, 1537, 1557, 1575, 1652, 1684, 1698, 1739, 2849, 2917. UV-Vis (CH_2Cl_2, nm) λ_{max} (ϵ_{max}): 228 (19400). MS (ESI^+): 1087.7 (calcd. for MNa^+: 1087.7). Elemental analysis: Calcd. C: 68.70 %, H: 10.30 %, Found: C: 68.93 %, H: 10.32 %.

Synthesis of 119. A general literature procedure[148] was followed: a dried Schlenk flask (25 mL) was charged with **115** (1.00 g, 0.938 mmol, 1.0 equiv.), cuprous iodide (8.9 mg, 0.047 mmol, 5 mol %), dried sodium iodide (1.41 g, 9.377 mmol, 10.0 equiv.), *trans*-*N*,*N*'-dimethyl-1,2-cyclohexanediamine (13.3 mg, 0.094 mmol, 10 mol %), and it was evacuated and filled with argon (three times). Anhydrous dioxane (1 mL) was added, and the reaction mixture was refluxed for 2 days. It was then extracted with dichloromethane (100 mL), washed with 5 % ammonium hydroxide (2 x 20 mL), water (2 x 20 mL), and hydrochloric acid (2 x 20 mL). The organic layer was dried over anhydrous sodium sulfate, filtered, and the solvent was removed under reduced pressure. The crude product was purified by filtration through silica gel in cyclohexane to yield 1.02 g (98 %) of white crystalline product, m.p. (CH_2Cl_2) 56 °C. ^{1}H NMR (300 MHz, $CDCl_3$) δ 7.63 - 7.54 (m, 2H), 7.24 - 7.17 (m, 2H), 3.65 (s, 9H), 3.63 (s, 6H), 3.35 (t, J = 6.5 Hz, 6H), 2.29 (t, J = 7.5 Hz, 6H), 1.67 - 1.56 (m, 6H), 1.55 - 1.43 (m, 6H), 1.25 (m, 66H). ^{13}C{^{1}H } NMR (75 MHz, $CDCl_3$) δ 174.40 (s), 142.51 (s), 136.87 (s), 129.81 (s), 91.90 (s), 72.60 (s), 71.67 (s), 51.52 (s), 48.15 (s), 34.22 (s), 29.82 (s), 29.82 (s), 29.81 (s), 29.79 (s), 29.79 (s), 29.73 (s), 29.65 (s), 29.59 (s), 29.39 (s), 29.28 (s), 26.33 (s), 25.08 (s). IR (KBr, cm^{-1}): 699, 715, 755, 818, 833, 969, 1000, 1037, 1059, 1079, 1102, 1117, 1126, 1151, 1167, 1194, 1216, 1240, 1259, 1280, 1300, 1341, 1354, 1360, 1376, 1395, 1411, 1430, 1471, 1484, 1740, 2850, 2916. UV-Vis (CH_2Cl_2, nm) λ_{max} (ϵ_{max}): 231 (15350). MS (ESI^+): 1135.7 (calcd. for MNa^+: 1135.7). Elemental analysis: Calcd. C: 65.80 %, H: 9.87 %, Found: C: 66.15 %, H: 9.58 %.

Synthesis of 117. A dried Schlenk flask (50 mL) was charged with **119** (500 mg, 0.449 mmol, 1.0 equiv.), tetrakis(triphenylphosphinopalladium (51.8 mg, 0.045 mmol, 10 mol %), and cuprous iodide (17.1 mg, 0.090 mmol, 20 mol %). The flask was evacuated and it was filled with argon (three times). Anhydrous THF (10 mL), anhydrous piperidine (2 mL), and trimethylsilylacetylene (221 mg, 2.245 mmol, 5.0 equiv.) were added, and the reaction mixture was heated at 40 °C for 24 h. The solvents were removed under reduced pressure, the residue was dissolved in dichloromethane (100 mL), and the organic layer was washed with 5 % ammonium hydroxide (2 x 30 mL), water (2 x 30 mL), 5 % hydrochloric acid (2 x 30 mL), and water (50 mL). The organic layer was dried over anhydrous sodium sulfate, filtered, and the solvent was removed under reduced pressure. The crude product was purified by gradient flash chromatography in hexanes and ethyl acetate (19/1 to 8/1) to yield 435 mg (89 %) of white crystalline solid, m.p. (CH_2Cl_2) 30 °C. ^{1}H NMR (300 MHz, $CDCl_3$) δ 7.45 - 7.31 (m, 4H), 3.65 (s, 9H), 3.64 (s, 6H), 3.34 (t, J = 6.5 Hz, 6H), 2.29 (t, J = 7.5 Hz, 6H), 1.68 - 1.55 (m, 6H), 1.55 - 1.42 (m, 6H), 1.38 - 1.17 (m, 66H), 0.22 (s, 9H). ^{13}C{^{1}H } NMR (101 MHz, $CDCl_3$) δ 174.42 (s), 143.47 (s), 131.46 (s), 127.42 (s), 120.80 (s), 105.63 (s), 93.37 (s), 72.63 (s), 71.66 (s), 51.54 (d, J = 4.5 Hz), 48.35 (s), 34.22 (s), 29.82 (s), 29.80 (s), 29.74 (s), 29.67 (s), 29.60 (s), 29.40 (s), 29.28 (s), 26.32 (s), 25.08 (s), 0.16 (s). IR (KBr, cm^{-1}): 720, 760, 842, 862, 988, 1020, 1040, 1103, 1109, 1172, 1196, 1214, 1240, 1248, 1258, 1279, 1293, 1310, 1367, 1382, 1415, 1435, 1453, 1467, 1484, 1740, 2151, 2844, 2913. UV-Vis (CH_2Cl_2, nm) λ_{max} (ϵ_{max}): 283 (1130), 265 (24090), 253 (25020). MS (ESI$^+$): 1105.8 (calcd. for MNa$^+$: 1105.9). Elemental analysis: Calcd. C: 73.15 %, H: 10.97 %, Found: C: 73.46 %, H: 11.34 %.

Synthesis of 116. A round bottom flask (50 mL) was charged with **117** (228 mg, 0.203 mmol, 1.0 equiv.), potassium carbonate (139.9 mg, 1.013 mmol, 5 equiv.), and methanol. The mixture was stirred at room temperature for 12 h. The solvent was removed under reduced pressure, and the product was extracted between diethy ether (100 mL) and water

(3 x 30 mL). The organic layer was dried over anhydrous sodium sulfate, filtered, and the solvent was removed under reduced pressure to yield 202.3 mg (95 %) of white crystals, m.p. (CH_2Cl_2) 35 °C. ^{1}H NMR (400 MHz, $CDCl_3$) δ 3.35 (t, J = 6.9 Hz, 4H), 2.95 (s, 15H), 2.89 (s, 6H), 2.30 - 2.20 (m, 1H), 1.85 - 1.74 (m, 6H), 1.56 (dd, J = 14.1, 6.9 Hz, 6H), 1.36 (d, J = 7.1 Hz, 6H), 1.33 - 1.09 (m, 66H). ^{13}C{^{1}H } NMR (101 MHz, $CDCl_3$) δ 174.46 (s), 143.78 (s), 131.65 (s), 127.57 (s), 119.82 (s), 72.64 (s), 71.68 (s), 51.56 (d, J = 3.8 Hz), 48.38 (s), 34.23 (s), 29.83 (s), 29.81 (s), 29.75 (s), 29.66 (s), 29.61 (s), 29.41 (s), 29.29 (s), 26.33 (s), 25.09 (s). IR (KBr, cm^{-1}): 530, 565, 637, 702, 720, 832, 880, 971, 988, 1015, 1021, 1038, 1073, 1091, 1103, 1114, 1171, 1197, 1215, 1238, 1259, 1279, 1302, 1310, 1368, 1414, 1435, 1464, 1485, 1511, 1740, 2740, 2850, 2911. UV-Vis (CH_2Cl_2, nm) λ_{max} (ϵ_{max}): 282 (3990), 280 (6910), 273 (9266). MS (ESI$^+$): 1033.7 (calcd. for MNa$^+$: 1033.8). Elemental analysis: Calcd. C: 74.80 %, H: 10.96 %, Found: C: 74.87 %, H: 11.08 %.

Synthesis of 118. A dried Schlenk flask (50 mL) was charged with **119** (500 mg, 0.449 mmol, 1.0 equiv.), **100** (131.1 mg, 538.8 mmol, 1.2 equiv.) tetrakis(triphenylphosphino)palladium (51.8 mg, 0.045 mmol, 10 mol %), and cuprous iodide (17.1 mg, 0.090 mmol, 20 mol %). The flask was evacuated and it was filled with argon (three times). Anhydrous THF (10 mL) and anhydrous piperidine (2 mL) were added, and the reaction mixture was heated at 40 °C for 24 h. The solvents were removed under reduced pressure, the residue was dissolved in dichloromethane (100 mL), and the organic layer was washed with 5 % ammonium hydroxide (2 x 30 mL), water (2 x 30 mL), 5 % hydrochloric acid (2 x 30 mL), and water (50 mL). The organic layer was dried over anhydrous sodium sulfate, filtered, and the solvent was removed under reduced pressure. The crude product was purified by gradient flash chromatography in hexanes and ethyl acetate (3/1 to 100 % ethyl acetate) to yield 459.2 (83 %) of yellow solid, m.p. (CH_2Cl_2) 61 °C. ^{1}H NMR (300 MHz, $CDCl_3$) δ 7.93 (d, J = 8.9 Hz, 1H), 7.60 - 7.47 (m, 4H), 6.70 (dd, J = 9.0, 2.4 Hz, 1H), 6.36 (d, J = 2.3 Hz, 1H), 3.70 (s, 6H), 3.65 (s, 9H), 3.39 (t, J = 6.5 Hz, 6H), 3.08 (s, 6H), 2.44 (s, 3H), 2.29 (t,

J = 7.5 Hz, 6H), 1.70 - 1.57 (m, 6H), 1.51 (dd, J = 12.4, 6.7 Hz, 6H), 1.39 - 1.18 (m, 66H). $^{13}C\{^{1}H\}$ NMR (101 MHz, $CDCl_3$) δ 174.46 (s), 162.92 (s), 151.49 (s), 144.24 (s), 140.25 (s), 131.30 (s), 128.92 (s), 128.12 (s), 127.81 (s), 126.86 (s), 120.39 (s), 111.20 (s), 108.26 (s), 101.73 (s), 95.29 (s), 84.06 (s), 72.65 (s), 71.71 (s), 1.56 (s), 48.49 (s), 40.54 (s), 34.23 (s), 29.83 (s), 29.80 (s), 29.74 (s), 29.68 (s), 29.61 (s), 29.60 (s), 29.40 (s), 29.28 (s), 26.35 (s), 25.08 (s), 16.13 (s). ^{2}H NMR (46 MHz, $CDCl_3$) δ 3.70 (s, 3D). IR (KBr, cm^{-1}): 662, 723, 756, 805, 830, 854, 880, 948, 963, 988, 1015, 1029, 1060, 1104, 1153, 1167, 1197, 1216, 1238, 1260, 1280, 1308, 1343, 1375, 1397, 1415, 1437, 1466, 1486, 1510, 1526, 1552, 1604, 1636, 1738, 2075, 2127, 2205, 2850, 2917. UV-Vis (CH_2Cl_2, nm) λ_{max} (ϵ_{max}): 386 (13810), 319 (20390), 301 (27790), 281 (26350), 232 (48980). MS ($MALDI^+$): 1228.8 (calcd. for MH^+: 1229.0). Elemental analysis: Calcd. C: 74.28 %, H: 10.42 %, N %, 2.28 %, Found: C: 74.06 %, H: 10.10 %, N: 2.35 %.

Synthesis of 93. A round bottom flask (50 mL) was charged with **118** (300.0 mg, 0.247 mmol, 1.0 equiv.), potassium hydroxide (1 g), and methanol (20 mL). The resulting suspension was stirred at room temperature for 24 h. It was then diluted with 10 % aqueous ammonium chloride (100 mL) and dichloromethane (500 mL). Acetic acid was added until the organic layer became yellow. The organic layer was extracted with more dichloromethane (2 x 100 mL), and the dichloromethane fractions were combined, dried over anhydrous sodium sulfate, filtered and the solvent was removed under reduced pressure to yield 230.2 mg (79 %) of yellow solid, m.p. (CH_2Cl_2) 200 °C (decomp.). ^{1}H NMR (500 MHz, $CDCl_3$) δ 7.96 (d, J = 8.9 Hz, 1H), 7.60 - 7.49 (m, 4H), 6.74 (dd, J = 8.9, 2.3 Hz, 1H), 6.39 (d, J = 2.0 Hz, 1H), 3.71 (s, 6H), 3.40 (t, J = 6.5 Hz, 6H), 3.10 (s, 6H), 2.46 (s, 3H), 2.35 (t, J = 7.4 Hz, 6H), 1.69 - 1.59 (m, 6H), 1.57 - 1.48 (m, 6H), 1.41 - 1.16 (m, 66H). $^{13}C\{^{1}H\}$ NMR (101 MHz, $CDCl_3$) δ 179.28 (s), 174.52 (s), 163.13 (s), 151.54 (s), 144.25 (s), 140.25 (s), 131.44 (s), 129.03 (s), 128.18 (s), 127.83 (s), 126.87 (s), 120.41 (s), 111.34 (s), 108.36 (s), 101.97 (s), 95.36 (s), 84.06 (s), 72.66 (s), 71.75 (s), 51.60 (s), 48.51 (s), 40.57 (s), 34.25 (s), 29.85 (s),

29.82 (s), 29.76 (s), 29.70 (s), 29.64 (s), 29.62 (s), 29.58 (s), 29.41 (s), 29.30 (s), 26.36 (s), 25.10 (s), 16.15 (s). ^{2}H NMR (46 MHz, $CDCl_3$) δ 3.70 (s, 3D). IR (KBr, cm^{-1}): 720, 755, 804, 829, 948, 962, 1019, 1061, 1105, 1114, 1151, 1168, 1184, 1203, 1233, 1241, 1262, 1284, 1307, 1342, 1377, 1401, 1433, 1466, 1485, 1509, 1526, 1570, 1599, 1627, 1707, 2207, 2848, 2916, 3036, 3089. UV-Vis (CH_2Cl_2, nm) λ_{max} (ϵ_{max}): 385 (8889), 319 (19500), 300 (28800), 281 (27100), 234 (48151). MS (MALDI$^+$): 1186.8 (calcd. for MH$^+$: 1186.9). Elemental analysis: Calcd. C: 73.88 %, H: 10.28 %, N %, 2.36 %, Found: C: 73.77 %, H: 10.24 %, N: 2.24 %.

Bibliography

[1] Feynman, P., Richard; Leighton, B., Robert; Sands, M. *The Feynman Lectures on Physics*, 6th ed.; Addison-Wesley Publishing Company, Reading (Massachusetts), Menlo Park (California), London, Amsterdam, Don Mills (Ontario), Sydney, 1977; Vol. 2.

[2] Hiratsuka, Y.; Miyata, M.; Tada, T.; Uyeda, T. Q. P. *Proc. Natl. Acad. Sci. USA* **2006**, *103*, 13618–13623.

[3] Pijper, D.; Jongejan, M. G. M.; Meetsma, A.; Feringa, B. L. *J. Am. Chem. Soc.* **2008**, *130*, 4541–4552.

[4] Khuong, T.-A. V.; Nuez, J. E.; Godinez, C. E.; Garcia-Garibay, M. A. *Acc. Chem. Res.* **2006**, *39*, 413–422.

[5] Saha, S.; Leung, K.-F.; Nguyen, T.; Stoddart, J.; Zink, J. *Adv. Funct. Mater.* **2007**, *17*, 685–693.

[6] Angelos, S.; Liong, M.; Choi, E.; Zink, J. I. *Chem. Eng. J.* **2008**, *137*, 4 – 13.

[7] Bath, J. N.; Turberfield, A. J. *Nature Nanotech.* **2008**, *2*, 275–284.

[8] Garcia-Garibay, M. A.; Karlen, S. D. *Top. Curr. Chem.* **2005**, 1–49.

[9] Horansky, R. D.; Clarke, L. I.; Winston, E. B.; Price, J. C.; Karlen, S. D.; Jarowski, P. D.; Santillan, R.; Garcia-Garibay, M. A. *Phys. Rev. B* **2006**, *74*, 054306.

[10] Horansky, R. D.; Clarke, L. I.; Price, J. C.; Khuong, T.-A. V.; Jarowski, P. D.; Garcia-Garibay, M. A. *Phys. Rev. B* **2005**, *72*, 014302.

[11] Feynman, R. P. *Eng. Sci.* **1960**, *23*, 22–36.

[12] Michl, J.; Sykes, E. C. H. *ACS Nano* **2009**, *3*, 1042–1048.

[13] Gimzewski, J. K.; Joachim, C.; Schlittler, R. R.; Langlais, V.; Tang, H.; Johannsen, I. *Science* **1998**, *281*, 531–533.

[14] Rao, B. V.; Kwon, K.-Y.; Liu, A.; Bartels, L. **2003**, *119*, 10879–10884.

[15] Browne, W. R.; Feringa, B. L. *Nature Nanotech.*. **2006**, *1*, 25–35.

[16] Weiss, P. S. *Acc. Chem. Res.* **2008**, *41*, 1772–1781.

[17] Comstock, M. J.; Levy, N.; Cho, J.; Berbil-Bautista, L.; Crommie, M. F.; Poulsen, D. A.; Fréchet, J. M. J. **2008**, *92*, 123107.

[18] Kaszynski, P.; Friedli, A. C.; Michl, J. *J. Am. Chem. Soc.* **1992**, *114*, 601–620.

[19] Kottas, G. S.; Clarke, L. I.; Horinek, D.; Michl, J. *Chem. Rev.* **2005**, *105*, 1281–1376.

[20] Zheng, X.; Mulcahy, M. E.; Horinek, D.; Galeotti, F.; Magnera, T. F.; Michl, J. *J. Am. Chem. Soc.* **2004**, *126*, 4540–4542.

[21] Wang, W.; Shi, X.; Jin, M.; Minot, C.; Van Hove, M. A.; Collin, J.-P.; Lin, N. *ACS Nano* **2010**, *4*, 4929–4935.

[22] Tierney, H. L.; Baber, A. E.; Sykes, E. C. H.; Akimov, A.; Kolomeisky, A. B. *J. Phys. Chem. C* **2009**, *113*, 10913–10920.

[23] Forgan, R. S.; Sauvage, J.-P.; Stoddart, J. F. *Chem. Rev.* **2011**, *Article ASAP*, doi: 10.1021/jp2031253.

[24] Caskey, D. C.; Michl, J. *J. Org. Chem.* **2005**, *70*, 5442–5448.

[25] Stang, P. J. *J. Org. Chem.* **2009**, *74*, 2–20.

[26] Karlen, S. D.; Reyes, H.; Taylor, R. E.; Khan, S. I.; Hawthorne, M. F.; Garcia-Garibay, M. A. *Proc. Natl. Acad. Sci.* **2010**, *107*, 14973–14977.

[27] OBrien, Z. J.; Natarajan, A.; Khan, S.; Garcia-Garibay, M. A. *Crys. Growth Des.* **2011**, *11*, 2654–2659.

[28] Wright, R. S.; Vinod, T. K. *Tetrahedron Lett.* **2003**, *44*, 7129 – 7132.

[29] Maly, K. E.; Gagnon, E.; Maris, T.; Wuest, J. D. *J. Am. Chem. Soc.* **2007**, *129*, 4306–4322.

[30] Vergadou, V.; Pistolis, G.; Michaelides, A.; Varvounis, G.; Siskos, M.; Boukos, N.; Skoulika, S. *Crys. Growth Des.* **2006**, *6*, 2486–2492.

[31] Moorthy, J. N.; Natarajan, R.; Venugopalan, P. *J. Org. Chem.* **2005**, *70*, 8568–8571.

[32] Lemouchi, C.; Vogelsberg, C. S.; Zorina, L.; Simonov, S.; Batail, P.; Brown, S.; Garcia-Garibay, M. A. *J. Am. Chem. Soc.* **2011**, *133*, 6371–6379.

[33] Riddell, F. G.; Cameron, K. S.; Holmes, S. A.; Strange, J. H. *J. Am. Chem. Soc.* **1997**, *119*, 7555–7560.

[34] Lunazzi, L.; Mazzanti, A.; Casarini, D.; De Lucchi, O.; Fabris, F. *J. Org. Chem.* **2000**, *65*, 883–888.

[35] Hoatson, G. L.; Vold, R. L. *NMR Basic Princ. Prog.* **1994**, *32*, 1–67.

[36] Cholli, A. L.; Dumais, J. J.; Engel, A. K.; Jelinski, L. W. *Macromolecules* **1984**, *17*, 2399–2404.

[37] Rice, D. M.; Wittebort, R. J.; Griffin, R. G.; Meirovitch, E.; Stimson, E. R.; Meinwald, Y. C.; Freed, J. H.; Scheraga, H. A. *J. Am. Chem. Soc.* **1981**, *103*, 7707–7710.

[38] Rice, D. M.; Meinwald, Y. C.; Scheraga, H. A.; Griffin, R. G. *J. Am. Chem. Soc.* **1987**, *109*, 1636–1640.

[39] Dominguez, Z.; Dang, H.; Strouse, M. J.; Garcia-Garibay, M. A. *J. Am. Chem. Soc.* **2002**, *124*, 2398–2399.

[40] Karlen, S. D.; Garcia-Garibay, M. A. *Chem. Comm.* **2005**, 189–191.

[41] Jarowski, P. D.; Houk, K. N.; Garcia-Garibay, M. A. *J. Am. Chem. Soc.* **2007**, *129*, 3110–3117.

[42] Karlen, S. D.; Khan, S. I.; Garcia-Garibay, M. A. *Mol. Cryst. Liq. Cryst.* **2006**, *456*, 221–230.

[43] Dominguez, Z.; Dang, H.; Strouse, M. J.; Garcia-Garibay, M. A. *J. Am. Chem. Soc.* **2002**, *124*, 7719–7727.

[44] Godinez, C. E.; Zepeda, G.; Garcia-Garibay, M. A. *J. Am. Chem. Soc.* **2002**, *124*, 4701–4707.

[45] Karlen, S. D.; Godinez, C. E.; Garcia-Garibay, M. A. *Org. Lett.* **2006**, *8*, 3417–3420.

[46] OBrien, Z. J.; Karlen, S. D.; Khan, S.; Garcia-Garibay, M. A. *J. Org. Chem.* **2010**, *75*, 2482–2491.

[47] Santillán, R.; Karlen, S. D.; Dang, H.; Garcia-Garibay, M. A. *J. Mex. Chem. Soc.* **2008**, *52*, 125–129.

[48] Dominguez, Z.; Khuong, T.-A. V.; Dang, H.; Sanrame, C. N.; Nuez, J. E.; Garcia-Garibay, M. A. *J. Am. Chem. Soc.* **2003**, *125*, 8827–8837.

[49] Rodriguez-Molina, B.; Ochoa, M. E.; Farfan, N.; Santillan, R.; Garcia-Garibay, M. A. *J. Org. Chem.* **2009**, *74*, 8554–8565.

[50] Horansky, R. D.; Clarke, L. I.; Price, J. C.; Khuong, T.-A. V.; Jarowski, P. D.; Garcia-Garibay, M. A. *Phys. Rev. B* **2005**, *72*, 014302.

[51] Khuong, T.-A. V.; Dang, H.; Jarowski, P. D.; Maverick, E. F.; Garcia-Garibay, M. A. *J. Am. Chem. Soc.* **2007**, *129*, 839–845.

[52] Nuez, J. E.; Khuong, T.-A. V.; Campos, L. M.; Farfn, N.; Dang, H.; Karlen, S. D.; Garcia-Garibay, M. A. *Crys. Growth Des.* **2006**, *6*, 866–873.

[53] Khuong, T.-A. V.; Zepeda, G.; Ruiz, R.; Khan, S. I.; Garcia-Garibay, M. A. *Crys. Growth Des.* **2004**, *4*, 15–18.

[54] Nuez, J. E.; Natarajan, A.; Khan, S. I.; Garcia-Garibay, M. A. *Org. Lett.* **2007**, *9*, 3559–3561.

[55] Gould, S. L.; Rodriguez, R. B.; Garcia-Garibay, M. A. *Tetrahedron* **2008**, *64*, 8336 – 8345.

[56] Khuong, T.-A. V.; Zepeda, G.; Sanrame, C. N.; Dang, H.; Bartberger, M. D.; Houk, K. N.; Garcia-Garibay, M. A. *J. Am. Chem. Soc.* **2004**, *126*, 14778–14786.

[57] Godinez, C. E.; Zepeda, G.; Mortko, C. J.; Dang, H.; Garcia-Garibay, M. A. *J. Org. Chem.* **2004**, *69*, 1652–1662.

[58] Garcia-Garibay, M. A.; Godinez, C. E. *Crys. Growth Des.* **2009**, *9*, 3124–3128.

[59] Karlen, S. D.; Ortiz, R.; Chapman, O. L.; Garcia-Garibay, M. A. *J. Am. Chem. Soc.* **2005**, *127*, 6554–6555.

[60] Karlen, S. D.; Khan, S. I.; Garcia-Garibay, M. A. *Crys. Growth Des.* **2005**, *5*, 53–55.

[61] Kitagawa, S.; Kitaura, R.; Noro, S.-I. *Angew. Chem. Int. Ed.* **2004**, *43*, 2334–2375.

[62] Mellot-Draznieks, C.; Dutour, J.; Frey, G. *Angew. Chem. Int. Ed.* **2004**, *43*, 6290–6296.

[63] Rowsell, J. L. C.; Yaghi, O. M. *Angew. Chem. Int. Ed.* **2005**, *44*, 4670–4679.

[64] Meek, S. T.; Greathouse, J. A.; Allendorf, M. D. *Adv. Mater.* **2011**, *23*, 249–267.

[65] Gould, S. L.; Tranchemontagne, D.; Yaghi, O. M.; Garcia-Garibay, M. A. *J. Am. Chem. Soc.* **2008**, *130*, 3246–3247.

[66] Winston, E. B.; Lowell, P. J.; Vacek, J.; Chocholoušová, J.; Michl, J.; Price, J. C. *Phys. Chem. Chem. Phys.* **2008**, *10*, 5188–5191.

[67] Tafipolsky, M.; Amirjalayer, S.; Schmid, R. *J. Comput. Chem.* **2007**, *28*, 1169–1176.

[68] Horansky, R. D.; F., M. T.; C., P. J.; Michl, J. *Lecture Notes in Physics*; Springer Berlin, 2007; Vol. 711; pp 303–330.

[69] Rozenbaum, V. M. *Sov. Phys.* **1991**, *72*, 1028.

[70] Barbon, A.; Zoleo, A.; Brustolon, M.; Comotti, A.; Sozzani, P. *Inorg. Chim. Act.* **2008**, *361*, 4122 – 4128.

[71] Allcock, H. R.; Siegel, L. A. *J. Am. Chem. Soc.* **1964**, *86*, 5140–5144.

[72] Sozzani, P.; Bracco, S.; Comotti, A.; Ferretti, L.; Simonutti, R. *Angew. Chem. Int. Ed.* **2005**, *44*, 1816–1820.

[73] Hertzsch, T.; Gervais, C.; Hulliger, J.; Jaeckel, B.; Guentay, S.; Bruchertseifer, H.; Neels, A. *Adv. Funct. Mater.* **2006**, *16*, 268–272.

[74] Tonelli, A. E. *Polym. Int.* **1997**, *43*, 295–309.

[75] Wei, M.; Davis, W.; Urban, B.; Song, Y.; Porbeni, F. E.; Wang, X.; White, J. L.; Balik, C. M.; Rusa, C. C.; Fox, J.; Tonelli, A. E. *Macromolecules* **2002**, *35*, 8039–8044.

[76] Hollingsworth, M. D.; Harris, K. D. In *Comprehensive Supramolecular Chemistry*; Atwood, J. L., Davies, J. E., MacNicol, D. D., Voegtle, F., Eds.; Pergamon, Oxford, Vol. 6.

[77] Allcock, H. R. *J. Am. Chem. Soc.* **1964**, *86*, 2591–2595.

[78] Meille, S. V.; Farina, A.; Gallazzi, M. C.; Sozzani, P.; Simonutti, R.; Comotti, A. *Macromolecules* **1995**, *28*, 1893–1902.

[79] Allcock, H. R.; Forgione, P. S.; Valan, K. J. *J. Org. Chem.* **1965**, *30*, 947–949.

[80] Allcock, H. R.; Kugel, R. L. *Inorg. Chem.* **1966**, *5*, 1016–1020.

[81] Allcock, H. R. *J. Am. Chem. Soc.* **1963**, *85*, 4050–4051.

[82] Comotti, A.; Simonutti, R.; Stramare, S.; Sozzani, P. *Nanotechnology* **1999**, *10*, 70–76.

[83] Allcock, H. R.; Levin, M. L.; Whittle, R. R. *Inorg. Chem.* **1986**, *25*, 41–47.

[84] Primrose, A. P.; Parvez, M.; Allcock, H. R. *Macromolecules* **1997**, *30*, 670–672.

[85] Allcock, H. R.; Primrose, A. P.; Sunderland, N. J.; Rheingold, A. L.; Guzei, I. A.; Parvez, M. *Chem. Mater.* **1999**, *11*, 1243–1252.

[86] Brustolon, M.; Barbon, A.; Bortolus, M.; Maniero, A. L.; Sozzani, P.; Comotti, A.; Simonutti, R. *J. Am. Chem. Soc.* **2004**, *126*, 15512–15519.

[87] Sozzani, P.; Comotti, A.; Bracco, S.; Simonutti, R. *Angew. Chem. Int. Ed.* **2004**, *43*, 2792–2797.

[88] Comotti, A.; Simonutti, R.; Catel, G.; Sozzani, P. *Chem. Mater.* **1999**, *11*, 1476–1483.

[89] Sozzani, P.; Comotti, A.; Bracco, S.; Simonutti, R. *Chem. Comm.* **2004**, 768–769.

[90] Allcock, H. R.; Ferrar, W. T.; Levin, M. L. *Macromolecules* **1982**, *15*, 697–703.

[91] Allcock, H. R.; Silverberg, E. N.; Dudley, G. K.; Pucher, S. R. *Macromolecules* **1994**, *27*, 7550–7555.

[92] Khan, A. A.; Bramwell, S. T.; Harris, K. D. M.; Kariuki, B. M.; Truter, M. R. *Chem. Phys. Lett.* **1999**, *307*, 320 – 326.

[93] Sozzani, P.; Comotti, A.; Simonutti, R.; Meersmann, T.; Logan, J.; Pines, A. *Angew. Chem., Int. Ed.* **2000**, *39*, 2695–2698.

[94] Becker, J.; Comotti, A.; Simonutti, R.; Sozzani, P.; Saalwchter, K. *J. Phys. Chem. B* **2005**, *109*, 23285–23294.

[95] Sozzani, P.; Bovey, F. A.; Schilling, F. C. *Macromolecules* **1991**, *24*, 6764–6768.

[96] Meirovitch, E.; Belsky, I.; Vega, S. *J. Phys. Chem.* **1984**, *88*, 1522–1526.

[97] Meirovitch, E. *J. Phys. Chem.* **1984**, *88*, 6411–6414.

[98] Tonelli, A. *NMR Spectroscopy and Polymer Microstructure: The Conformational Connection*; VCH Publishers: Deerfeld Beach, FL, 1988.

[99] Allcock, H. R.; Stein, M. T. *J. Am. Chem. Soc.* **1974**, *96*, 49–52.

[100] Comotti, A.; Gallazzi, M. C.; Simonutti, R.; Sozzani, P. *Chem. Mater.* **1998**, *10*, 3589–3596.

[101] Allcock, H. R.; Allen, R. W.; Bissell, E. C.; Smeltz, L. A.; Teeter, M. *J. Am. Chem. Soc.* **1976**, *98*, 5120–5125.

[102] Kubono, K.; Asaka, N.; Isoda, S.; Kobayashi, T.; Taga, T. *Acta Crystallogr. C* **1994**, *50*, 324–326.

[103] Schubert, U.; Arpac, E.; Glaubitt, W.; Helmerich, A.; Chau, C. *Chem. Mater.* **1992**, *4*, 291–295.

[104] Kubono, K.; Asaka, N.; Isoda, S.; Kobayashi, T.; Taga, T. *Acta Crystallogr. C* **1993**, *49*, 404–406.

[105] Allcock, H. R.; Stein, M. T.; Bissell, E. C. *J. Am. Chem. Soc.* **1974**, *96*, 4795–4800.

[106] Debye, P. *Polar Molecules*; Dover Press, New York, 1929.

[107] Press, W. *Single-Particle Rotations in Molecular Crystals*; Springer-Verlag: Berlin, New York, 1981.

[108] Horansky, R. *PhD thesis, University of Colorado*; University of Colorado, Boulder, 2005.

[109] Landau, L. D.; Lifshitz, E. M. *Statistical Physics: Part 1, 3rd edition*; Butterworth and Heinemann, 1980.

[110] Rausis, T.; Schlosser, M. *Eur. J. Org. Chem.* **2002**, *2002*, 3351–3358.

[111] Herzog, A.; Knobler, C. B.; Hawthorne, M. F.; Maderna, A.; Siebert, W. *J. Org. Chem.* **1999**, *64*, 1045–1048.

[112] Rappe, A. K.; Casewit, C. J.; Colwell, K. S.; Goddard, W. A.; Skiff, W. M. *J. Am. Chem. Soc.* **1992**, *114*, 10024–10035.

[113] Vacek, J.; Michl, J. *New J. Chem.* **1997**, *21*, 1259.

[114] Turbomole V6.0, a development of University of Karlsruhe and Forschungszentrum Karlsruhe GmbH, 1989-2007, TURBOMOLE GmbH, since 2007; available from `http://www.turbomole.com`.

[115] Ito, N.; Esaki, H.; Maesawa, T.; Imamiya, E.; Maegawa, T.; Sajiki, H. *Bull. Chem. Soc. Jpn.* **2008**, *81*, 278–286.

[116] Silverstein, R. M.; Webster, F. X. *Spectrometric Identification of Organic Compounds*, 6th ed.; John Wiley and Sons, New York, 1998.

[117] Unroe, M. R.; Reinhardt, B. A. *Synthesis* **1987**, *11*, 981–986.

[118] Negishi, E.; Okukado, N.; Lovich, S. F.; Luo, F. T. *J. Org. Chem.* **1984**, *49*, 2629–2632.

[119] Kottas, G. S. *PhD thesis, University of Colorado*; University of Colorado, Boulder, 2004.

[120] Ufimtsev, I. S.; Martínez, T. J. *J. Chem. Theory Comput.* **2009**, *5*, 2619–2628.

[121] Harris, K. D. M. *Chem. Soc. Rev.* **1997**, *26*, 279–289.

[122] Barlow, W. A.; Forrester, S. D.; Giles, C. H.; Hann, R. A.; Moebius, D.; Petty, M. C.; Roberts, G. G.; Swart, R. M. In *Langmuir-Blodgett Films*; Roberts, G., Ed.; Plenum Publishing Corporation, New York, 1990.

[123] Casher, D. L.; Kobr, L.; Michl, J. *J. Phys. Chem. A* **2011**, *Article ASAP*, doi: 10.1021/jp2031253.

[124] Gaines, G. L. *Insoluble Monolayers at Liquid-Gas Interfaces*; Wiley Interscience, New York, 1966.

[125] Harkins, W. *The Physical Chemistry of Surface Films*; Reinhold Publishing Corporation, New York, 1952.

[126] Blodgett, K. B. *J. Am. Chem. Soc.* **1935**, *57*, 1007–1022.

[127] Blodgett, K. B.; Langmuir, I. *Phys. Rev.* **1937**, *51*, 964–982.

[128] Peterson, I. L.; Veale, G.; Montgomery, C. M. *J. Colloid Interface Sci.* **1986**, *109*, 527–530.

[129] Fukuda, F.; Nakahara, H.; Kato, T. *J. Colloid Interface Sci.* **1976**, *54*, 430–438.

[130] Nakahara, H.; Fukuda, F. *Thin Solid Films* **1983**, *99*, 45–52.

[131] Kawaguchi, T.; Nakahara, H.; Fukuda, F. *J. Colloid Interface Sci.* **1985**, *104*, 290–293.

[132] Fankuchen, I. *Phys. Rev.* **1938**, *53*, 909.

[133] Harkins, W. D.; Fowkes, F. M. *J. Am. Chem. Soc.* **1938**, *60*, 1511–1512.

[134] Kuhn, H.; Moebius, D. *Angew. Chem. Int. Ed.* **1971**, *10*, 620–637.

[135] Peterson, I. R. *Thin Solid Films* **1985**, *116*, 357–366.

[136] Newman, R. D. *J. Colloid Interface Sci.* **1975**, *53*, 161–171.

[137] Chollet, P. A. *Thin Solid Films* **1978**, *52*, 343–360.

[138] Boudreaux, E. A. *J. Chem. Phys.* **1964**, *40*, 246–247.

[139] Malik, A.; Durbin, M. K.; Richter, A. G.; Huang, K. G.; Dutta, P. *Thin Solid Films* **1996**, *284/285*, 144–146.

[140] Malik, A.; Durbin, M. K.; Richter, A. G.; Huang, K. G.; Dutta, P. *Phys. Rev. B* **1995**, *52*, R11654–R11657.

[141] Ahn, D. J.; Franses, E. I. *J. Phys. Chem.* **1992**, *96*, 9952–9959.

[142] Jang, W.-H.; Miller, J. D. *J. Phys. Chem.* **1995**, *99*, 10272–10279.

[143] Allara, D. L.; Swalen, J. D. *J. Phys. Chem.* **1982**, *86*, 2700–2704.

[144] Kawai, T.; Umemura, J.; Takenaka, T. *Langmuir* **1990**, *6*, 672–676.

[145] Casher, D. L. *PhD thesis, University of Colorado*; University of Colorado, Boulder, 2008.

[146] Nasr, M.; Drach, J. C.; Smith, S. H.; Shipman, C.; Burckhalter, J. H. *J. Med. Chem.* **1988**, *31*, 1347–1351.

[147] Charette, A. B.; Chua, P. *Synlett* **1998**, 163–165.

[148] Klapars, A.; Buchwald, S. L. *J. Am. Chem. Soc.* **2002**, *124*, 14844–14845.

[149] Greene, T. W.; Wuts, P. G. M. *Protective Groups in Organic Synthesis, Third Edition*; John Wiley and Sons, New York, 1999.

[150] Gassman, P. G.; Hodgson, P. K. G.; Balchunis, R. J. *J. Am. Chem. Soc.* **1976**, *98*, 1275–1276.

[151] Hitomi, S.; Haruta, Y. *Bull. Chem. Soc. Jap.* **1973**, *46*, 589–592.

[152] Corriu, R. J. P.; Poirier, M.; Royo, G. *Comptes Rendus de l'Academie des Sciences, Serie II: Mecanique, Physique, Chimie, Sciences de la Terre et de l'Univers* **1990**, *310*, 1337–40.

Appendix A

Appendix

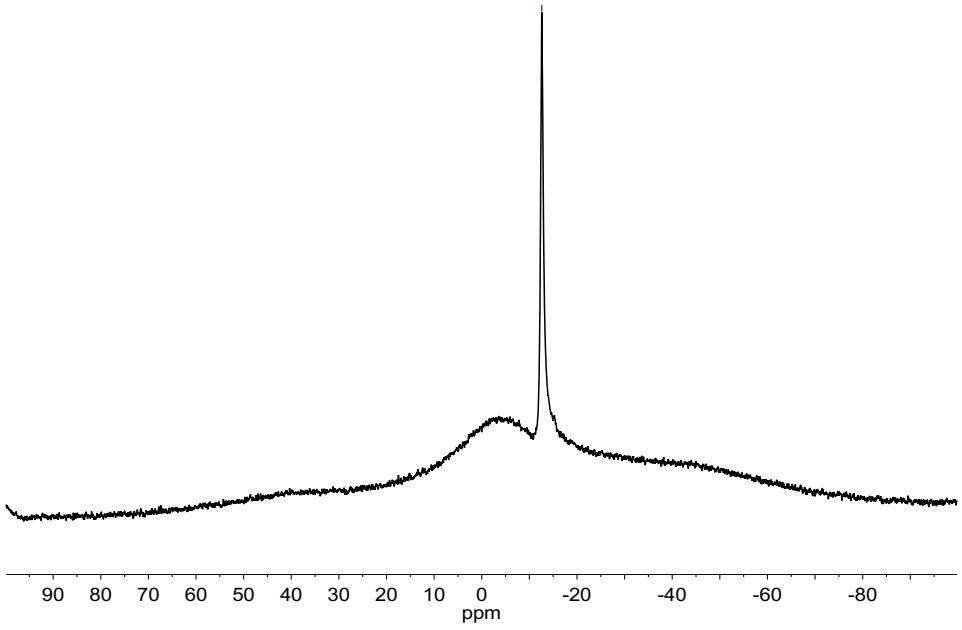

Figure A.1: $^{11}B\{^{1}H\}$ NMR spectrum of **50**.

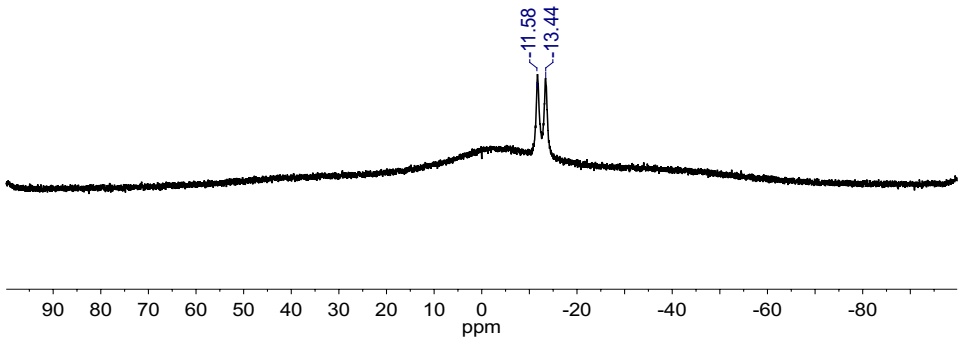

Figure A.2: ^{11}B NMR spectrum of **50**.

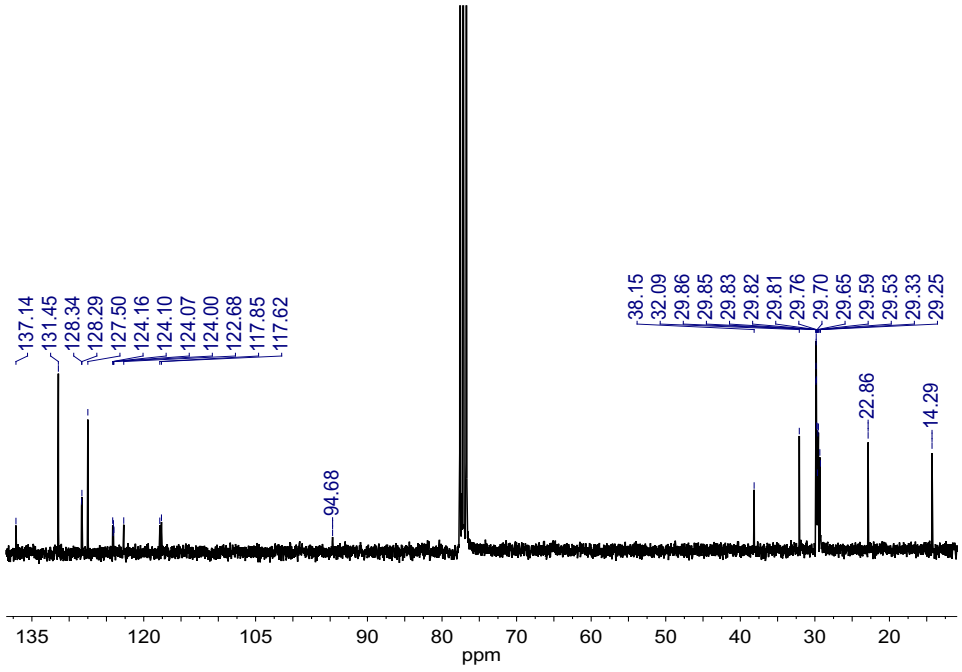

Figure A.3: ^{13}C NMR spectrum of **50**.

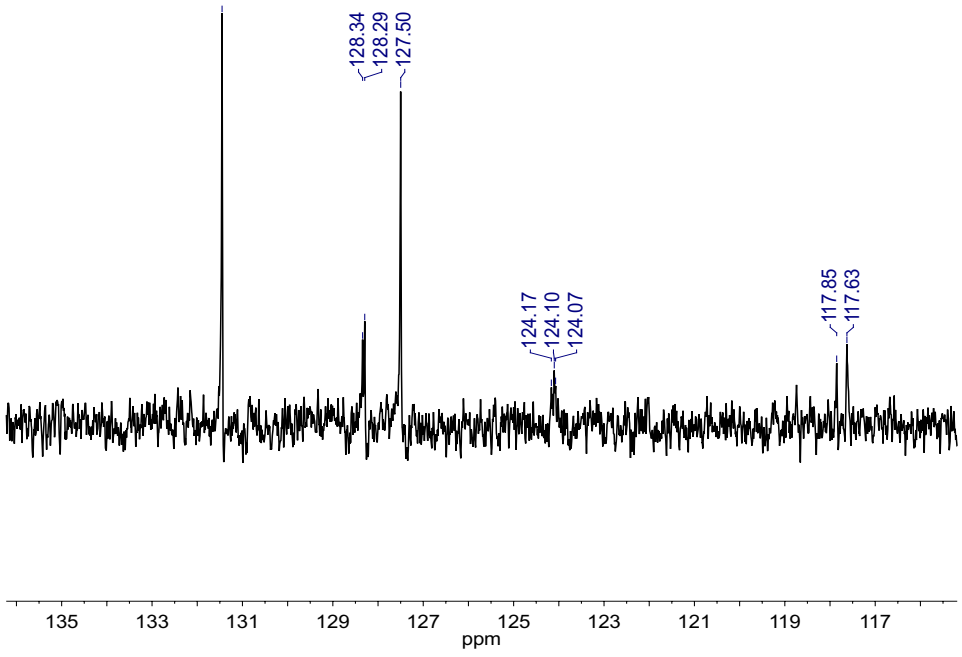

Figure A.4: DEPT-135 NMR spectrum of **50**.

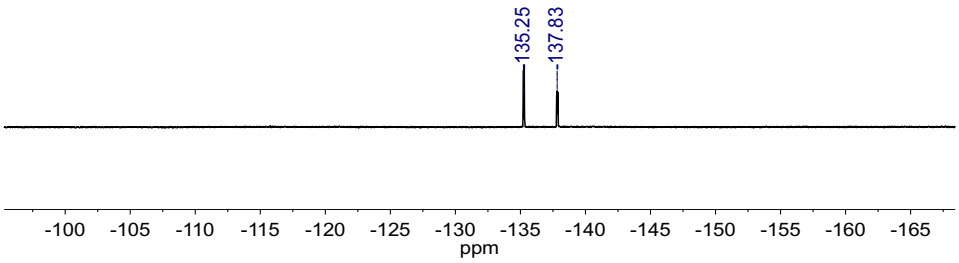

Figure A.5: ^{19}F NMR spectrum of **50**.

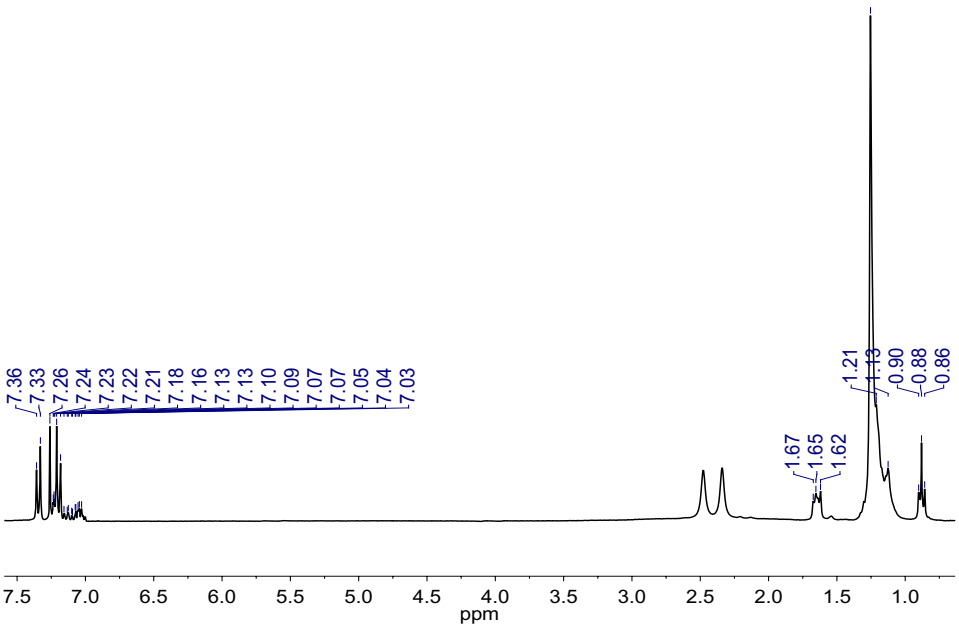

Figure A.6: ^{1}H $\{^{11}$B$\}$ NMR spectrum of **50**.

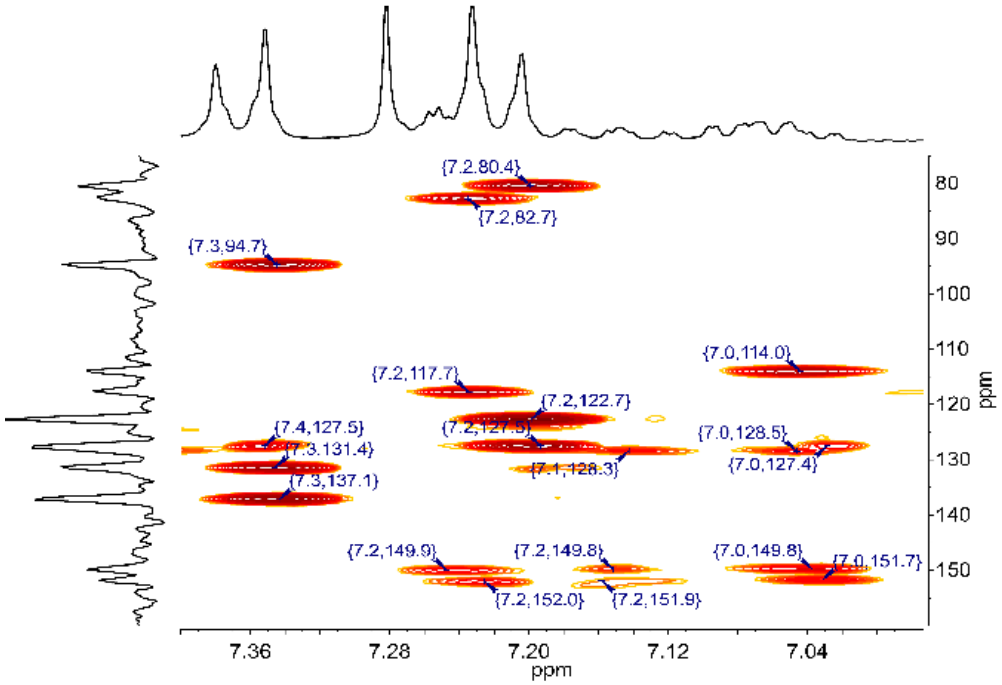

Figure A.7: gHMBC of **50**.

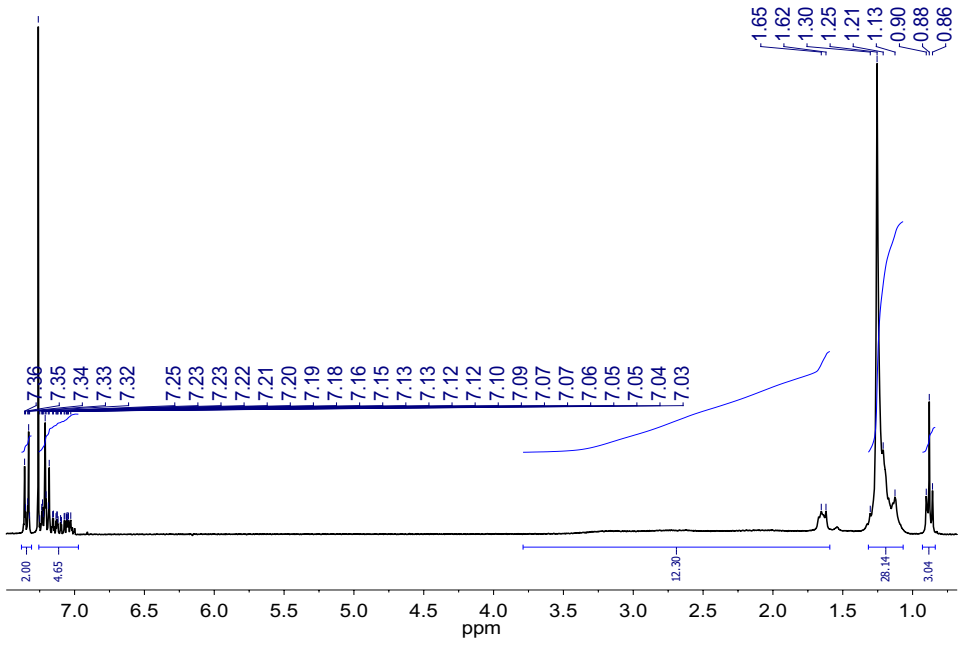

Figure A.8: ^{1}H NMR spectrum of **50**.

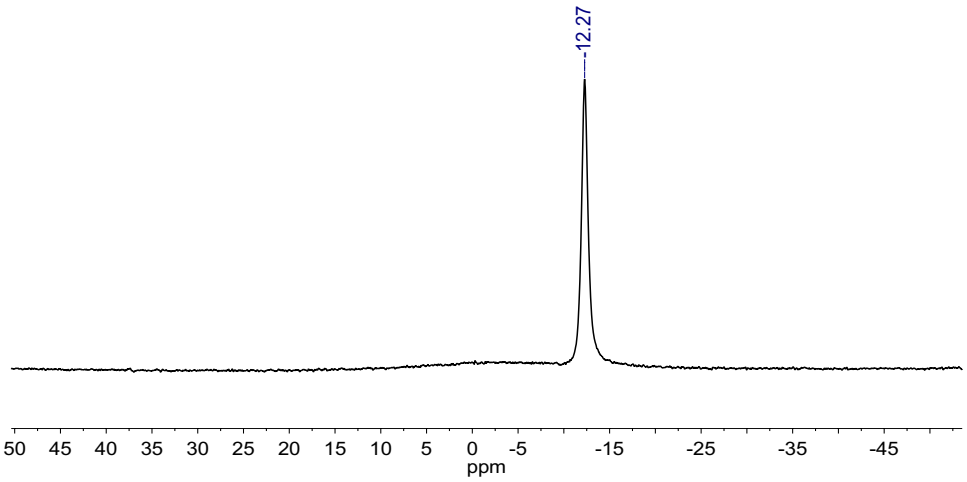

Figure A.9: $^{11}B\{^{1}H\}$ NMR spectrum of **51**.

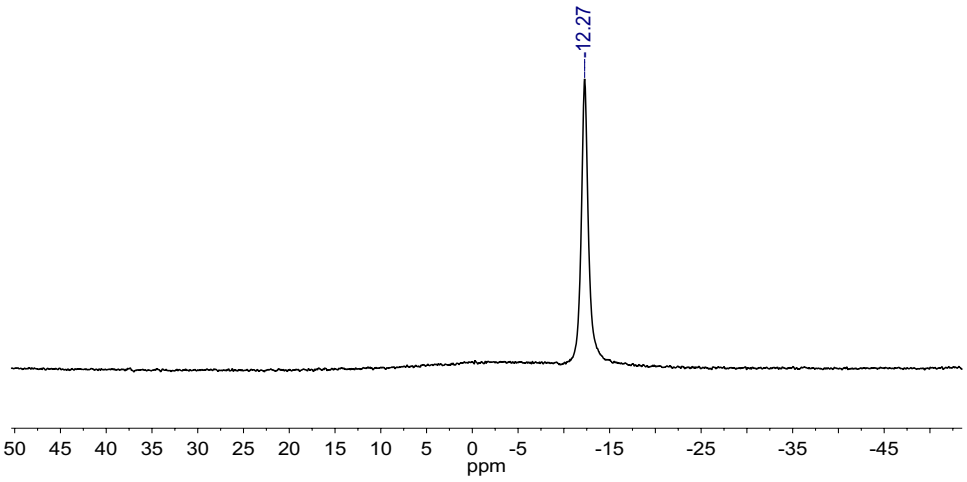

Figure A.10: ^{11}B NMR spectrum of **51**.

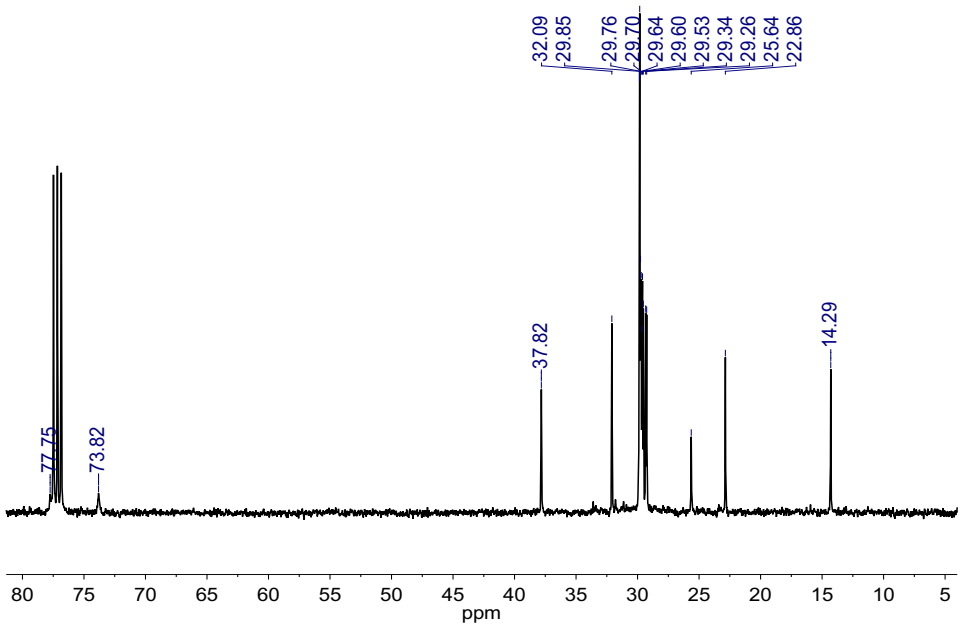

Figure A.11: ^{13}C NMR spectrum of **51**.

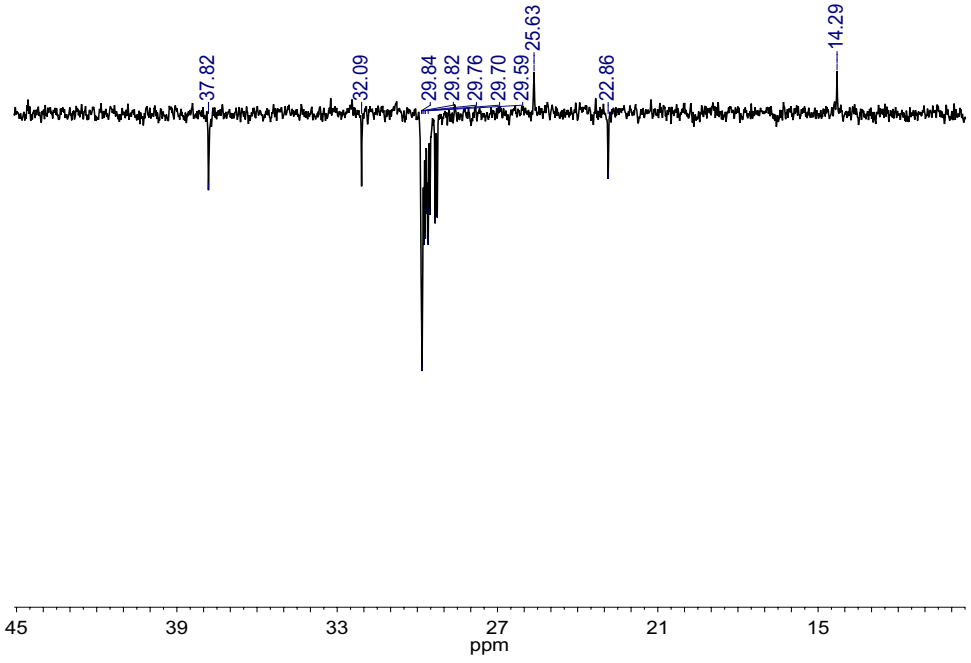

Figure A.12: DEPT-135 NMR spectrum of **51**.

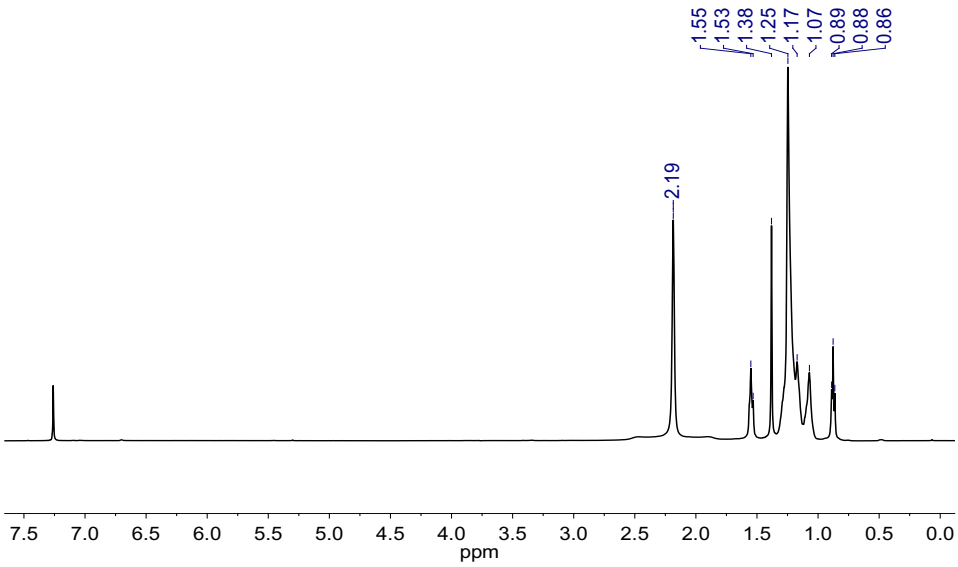

Figure A.13: ^{1}H $\{^{11}$B$\}$ NMR spectrum of **51**.

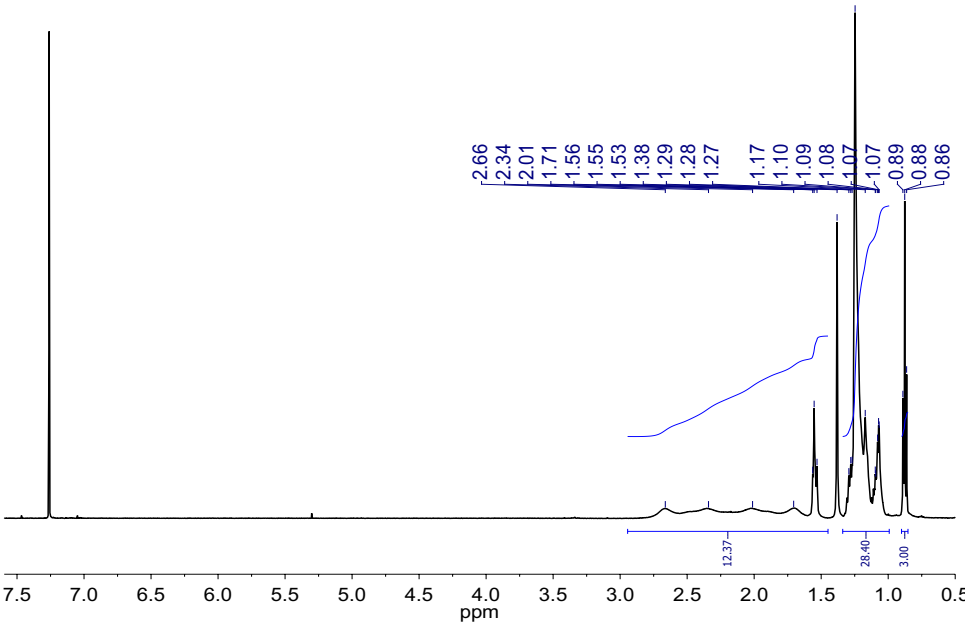

Figure A.14: ^{1}H NMR spectrum of **51**.

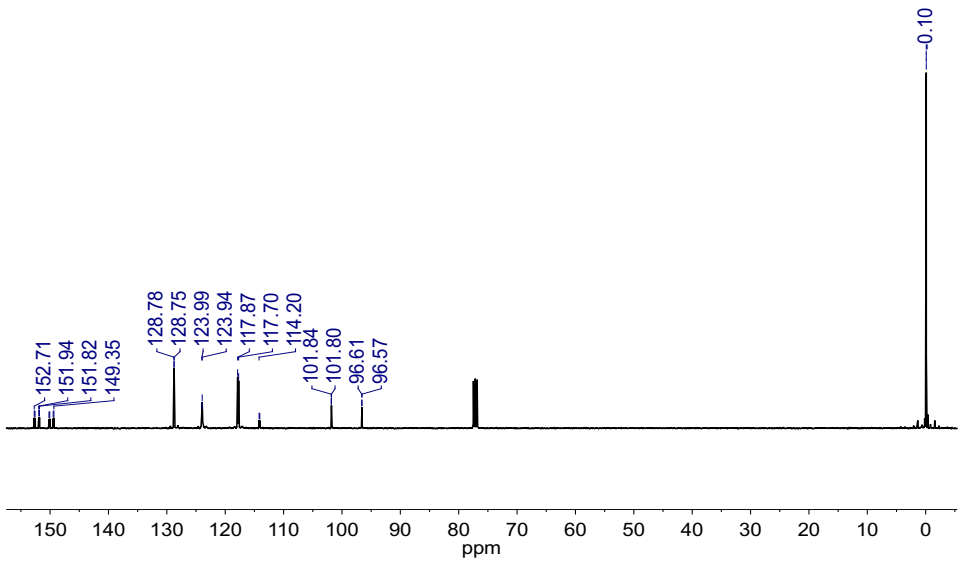

Figure A.15: ^{13}C NMR spectrum of **53**.

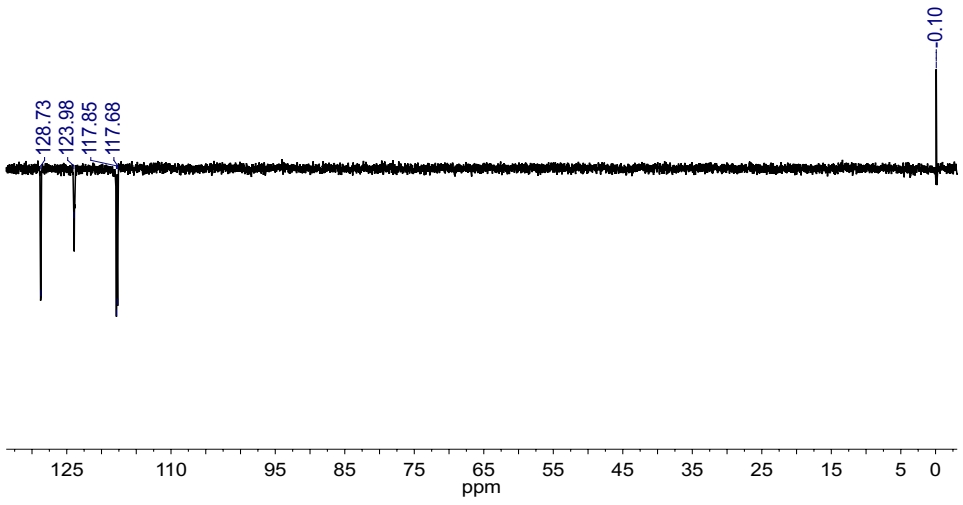

Figure A.16: DEPT-135 NMR spectrum of **53**.

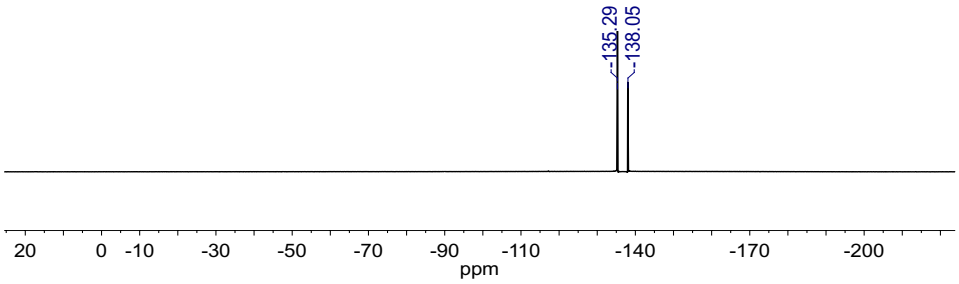

Figure A.17: ^{19}F NMR spectrum of **53**.

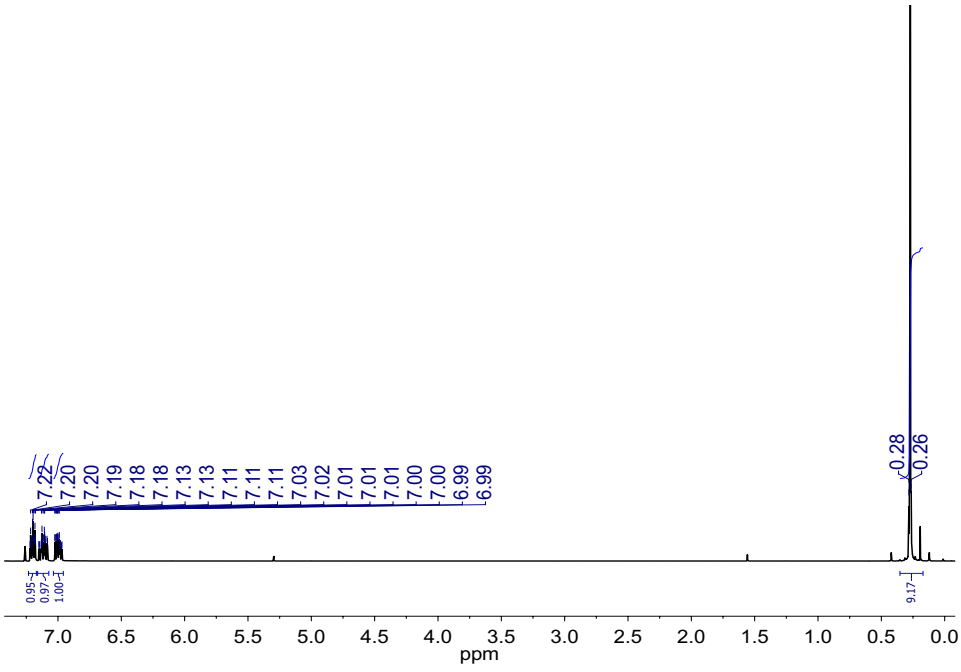

Figure A.18: ^{1}H NMR spectrum of **53**.

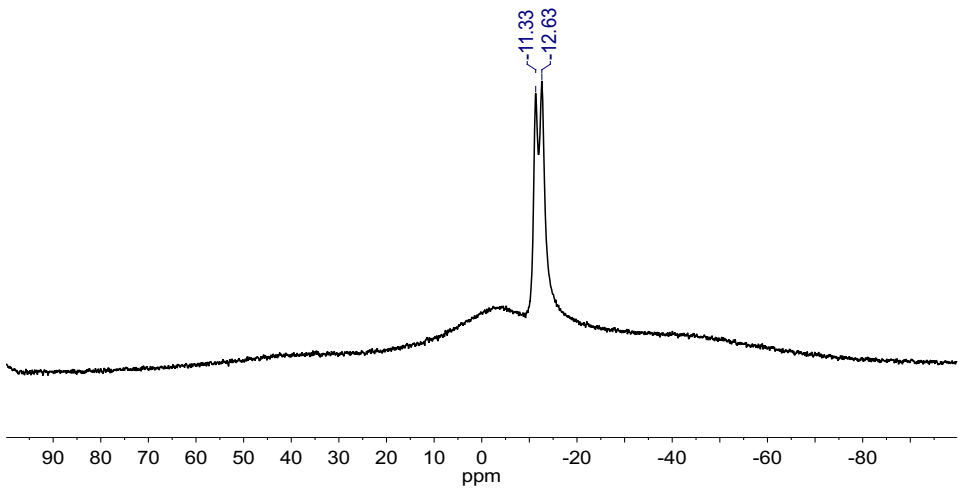

Figure A.19: $^{11}B\{^{1}H\}$ NMR spectrum of **55**.

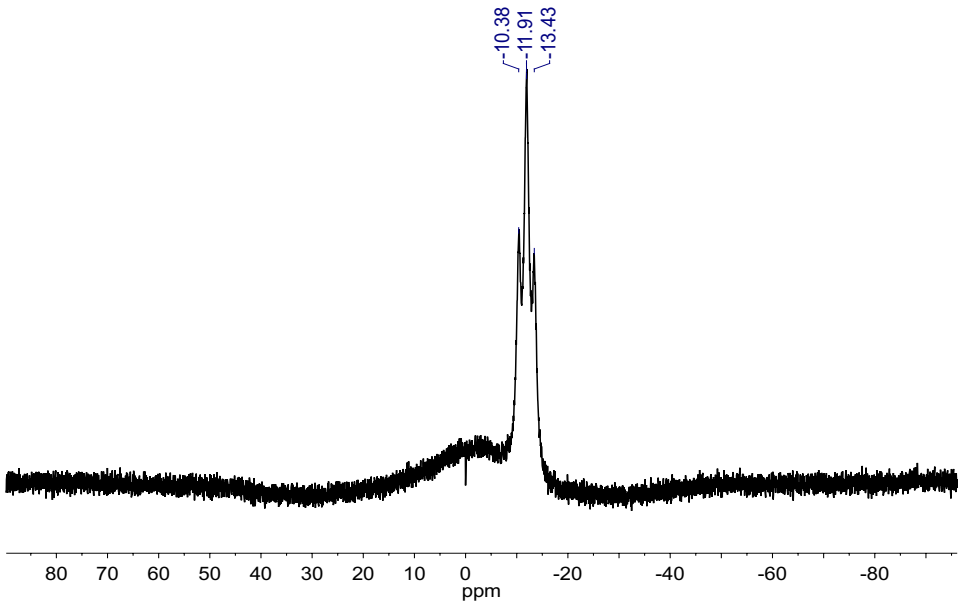

Figure A.20: ^{11}B NMR spectrum of **55**.

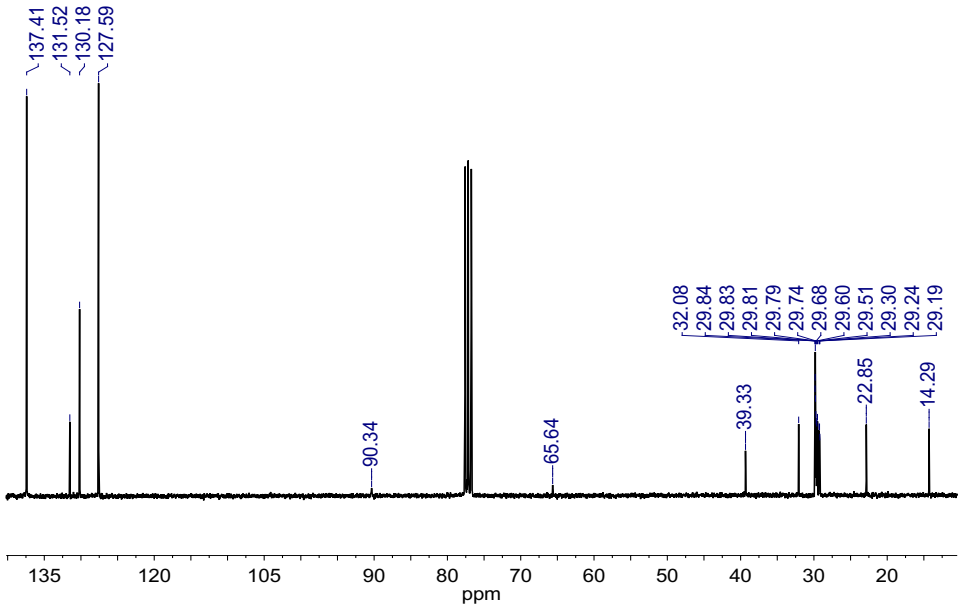

Figure A.21: ^{13}C NMR spectrum of **55**.

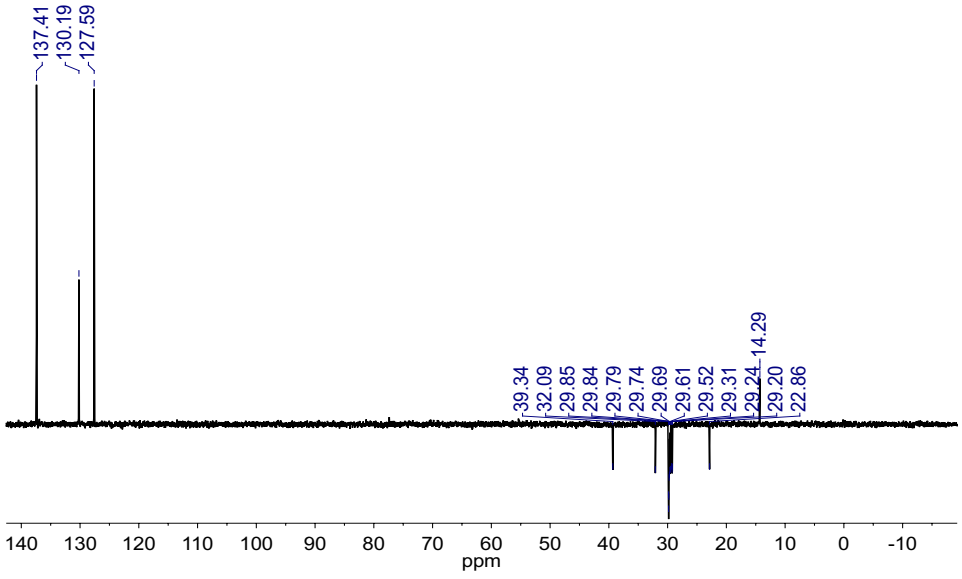

Figure A.22: DEPT-135 NMR spectrum of **55**.

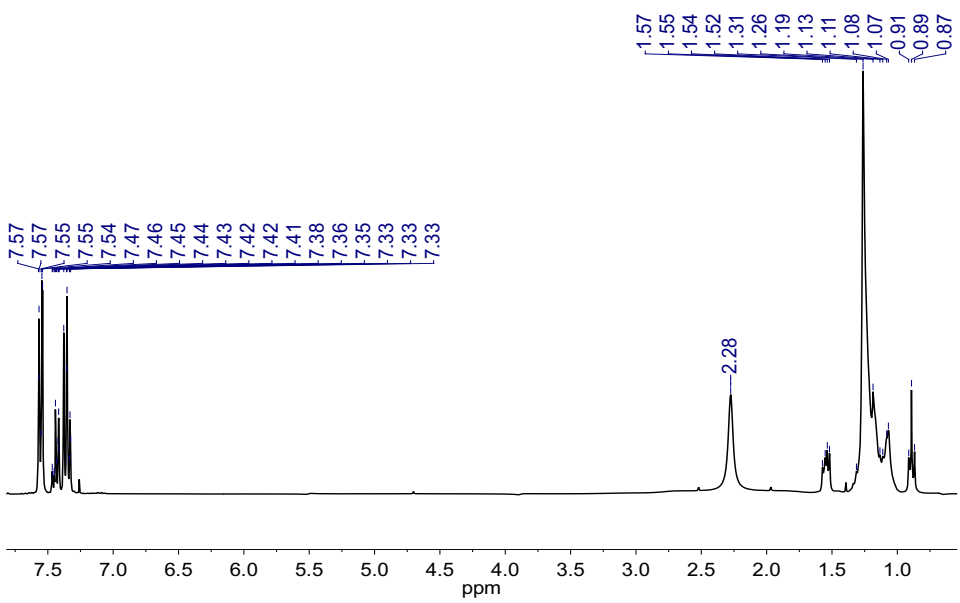

Figure A.23: ^{1}H $\{^{11}$B$\}$ NMR spectrum of **55**.

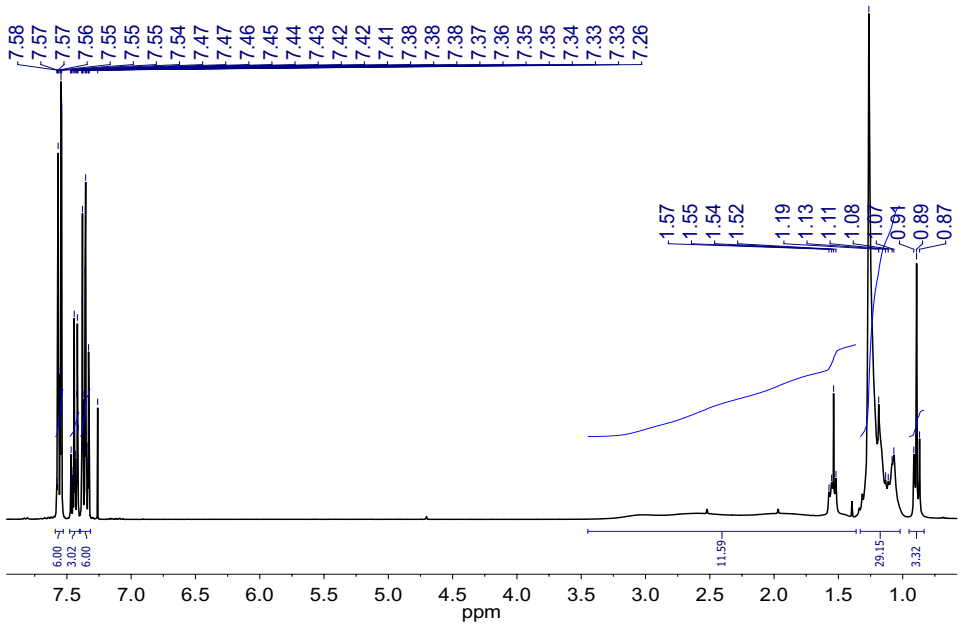

Figure A.24: ^{1}H NMR spectrum of **55**.

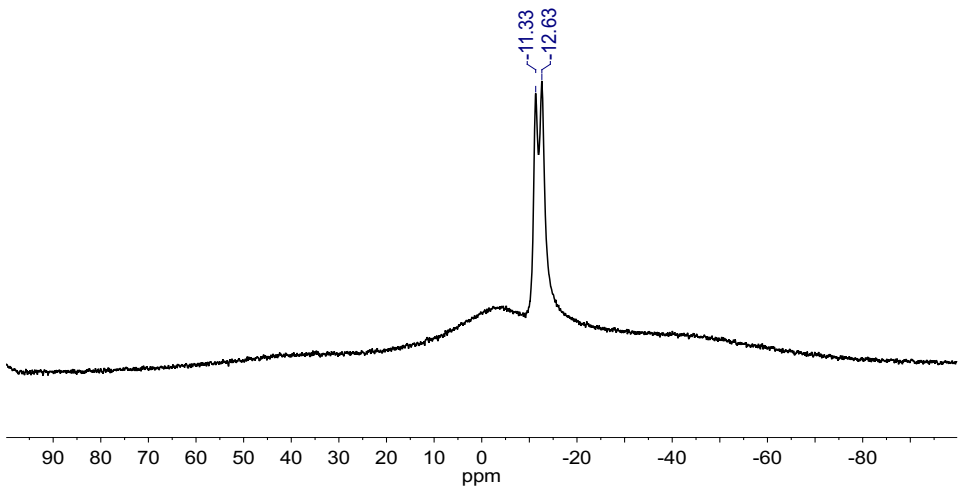

Figure A.25: $^{11}B\{^{1}H\}$ NMR spectrum of **56**.

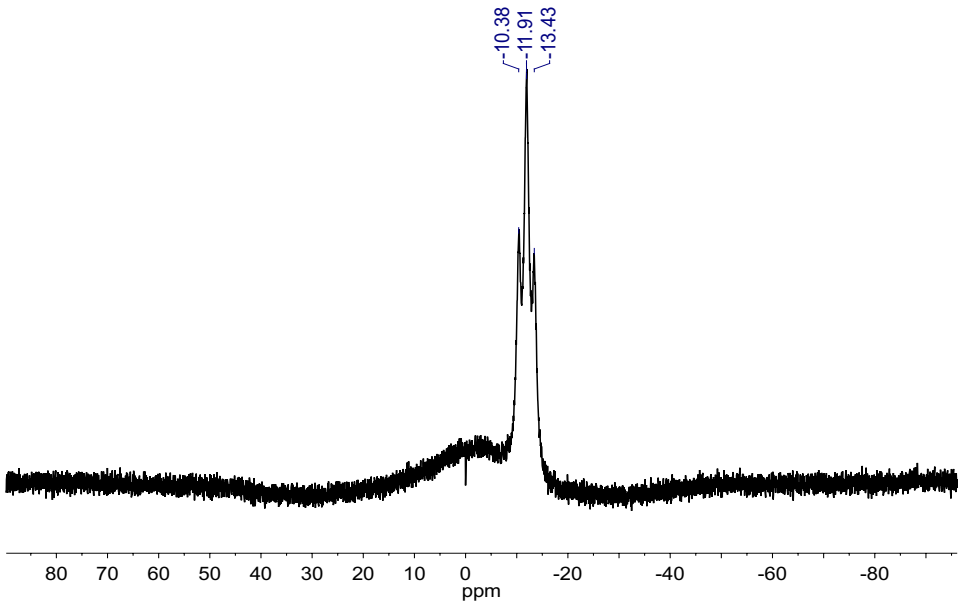

Figure A.26: ^{11}B NMR spectrum of **56**.

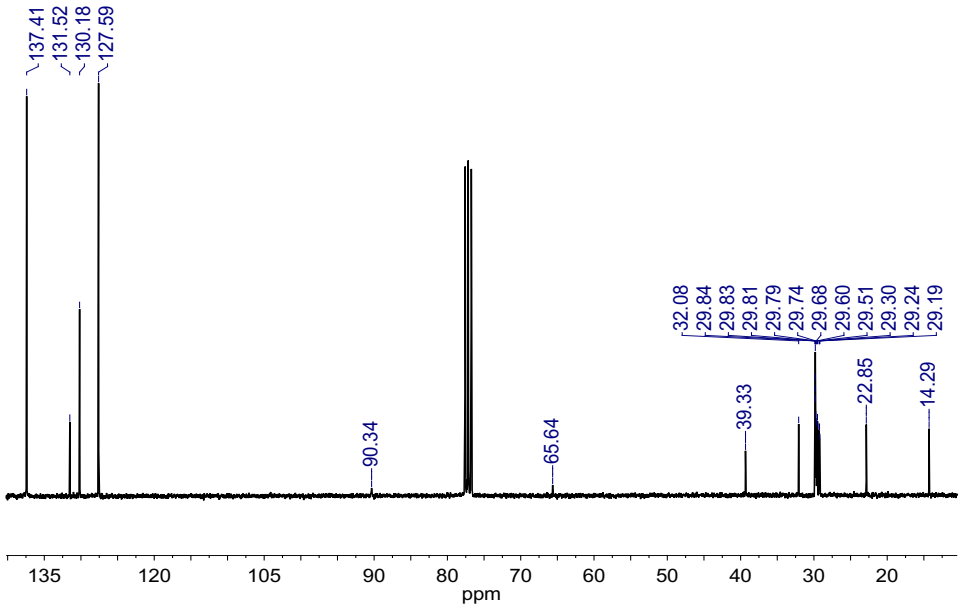

Figure A.27: ^{13}C NMR spectrum of **56**.

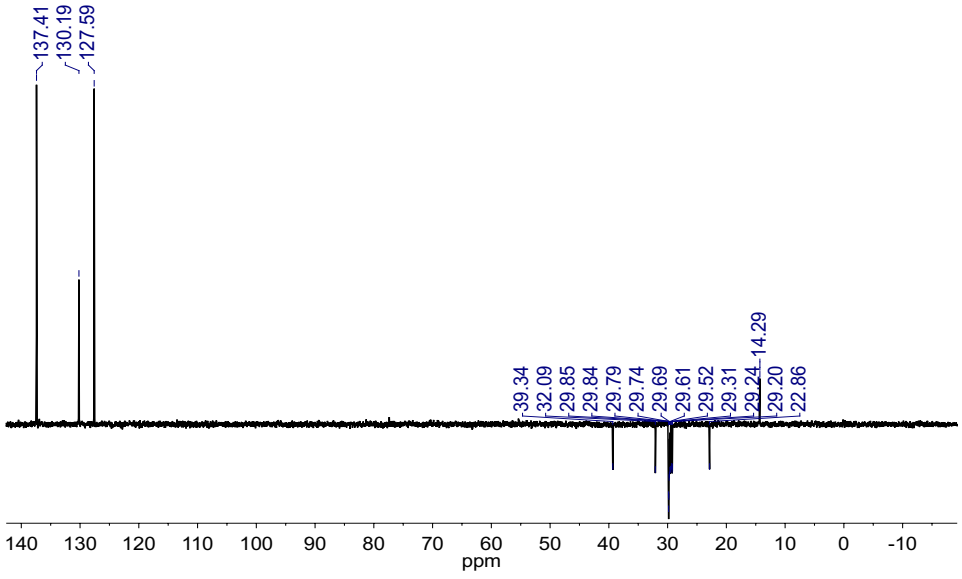

Figure A.28: DEPT-135 NMR spectrum of **56**.

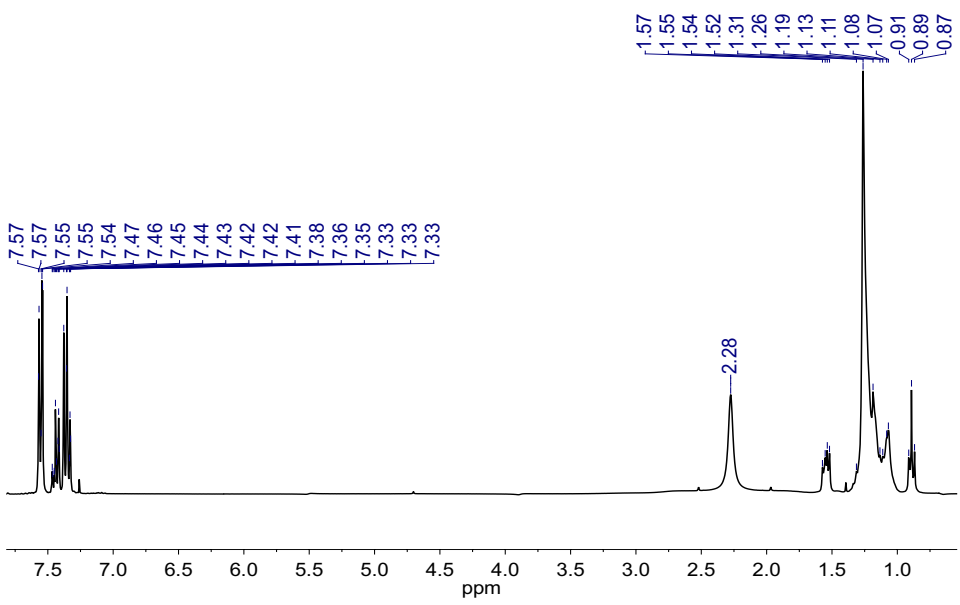

Figure A.29: ^{1}H $\{^{11}$B$\}$ NMR spectrum of **56**.

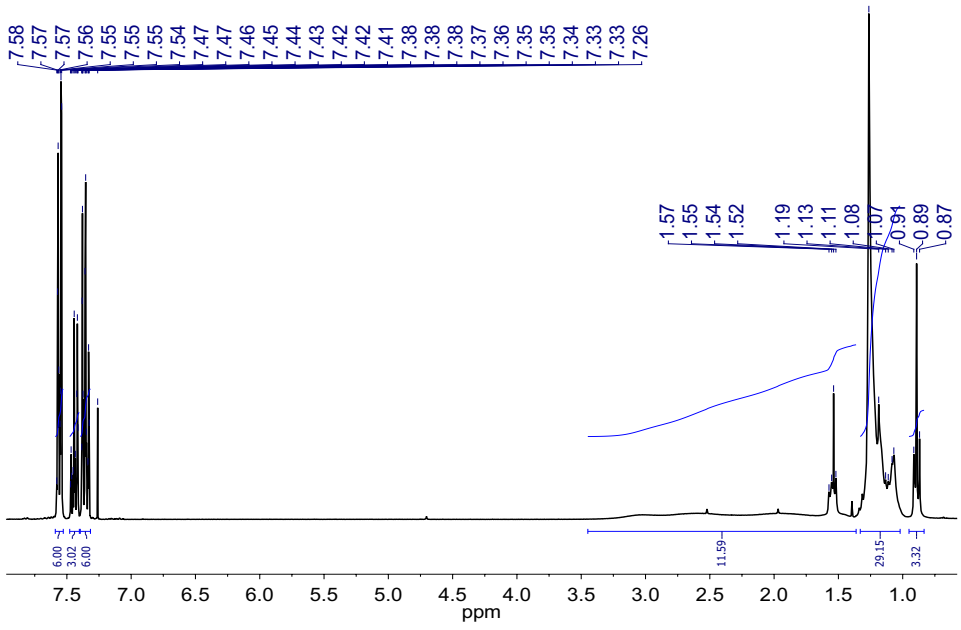

Figure A.30: ^{1}H NMR spectrum of **56**.

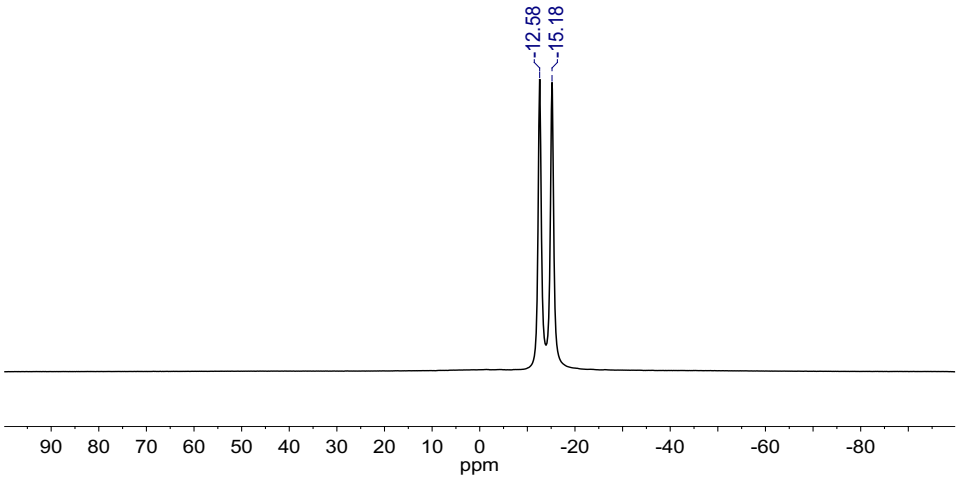

Figure A.31: $^{11}B\{^{1}H\}$ NMR spectrum of **57**.

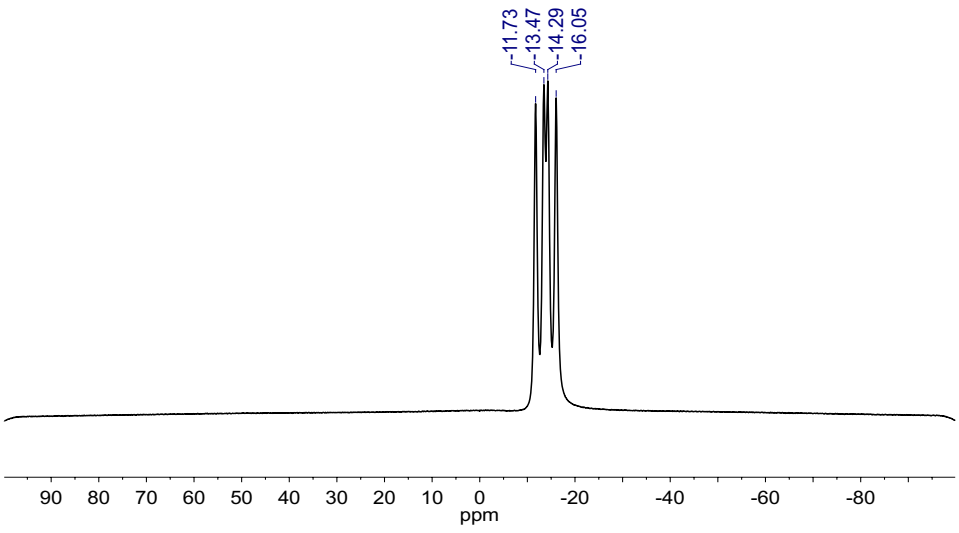

Figure A.32: ^{11}B NMR spectrum of **57**.

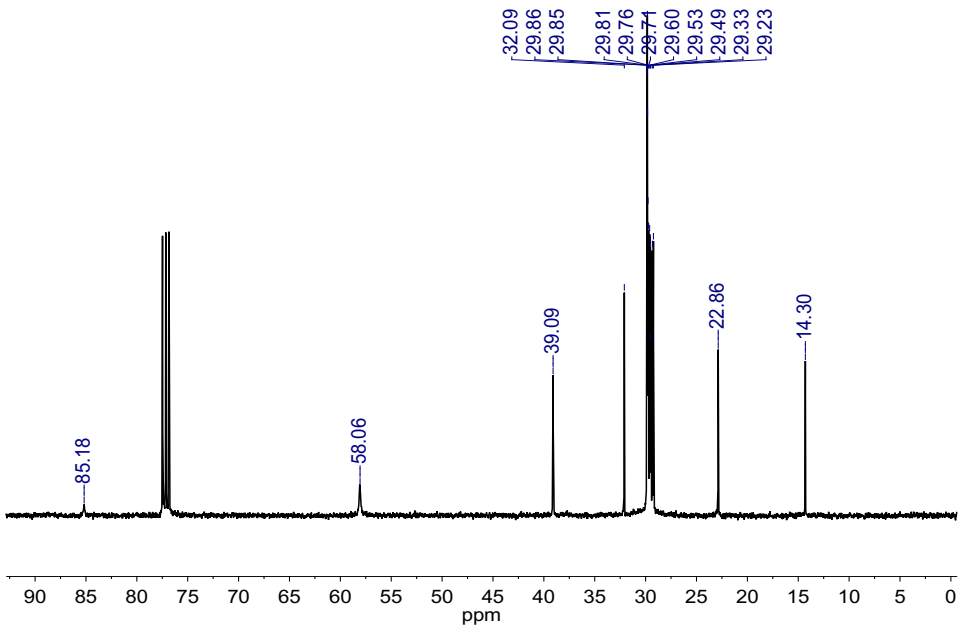

Figure A.33: ^{13}C NMR spectrum of **57**.

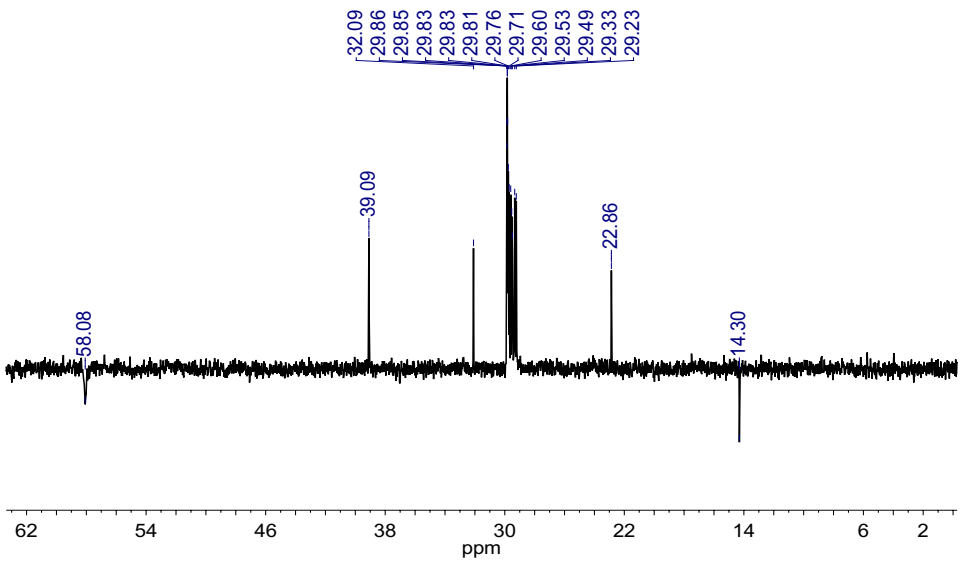

Figure A.34: DEPT-135 NMR spectrum of **57**.

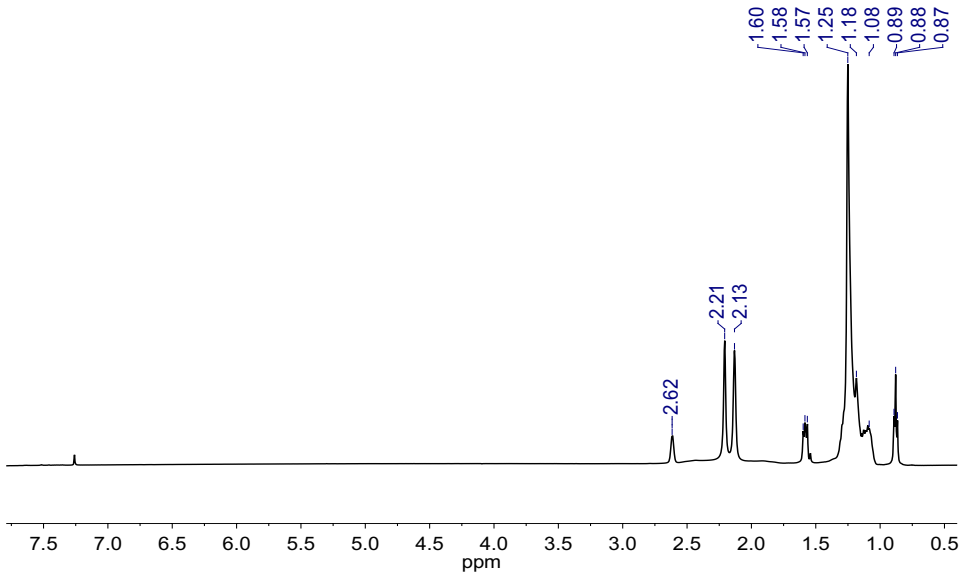

Figure A.35: ^{1}H $\{^{11}$B$\}$ NMR spectrum of **57**.

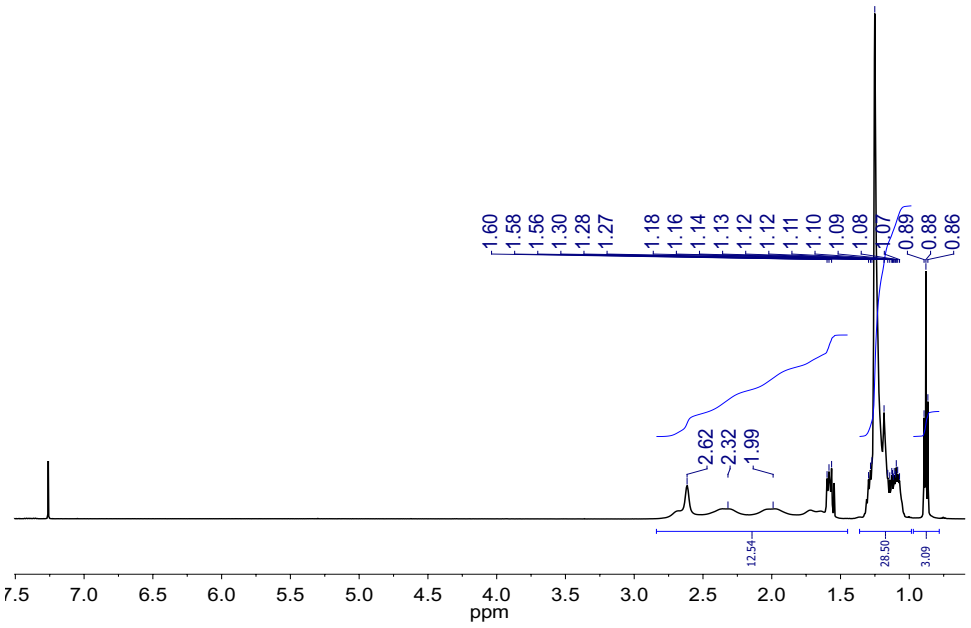

Figure A.36: ^{1}H NMR spectrum of **57**.

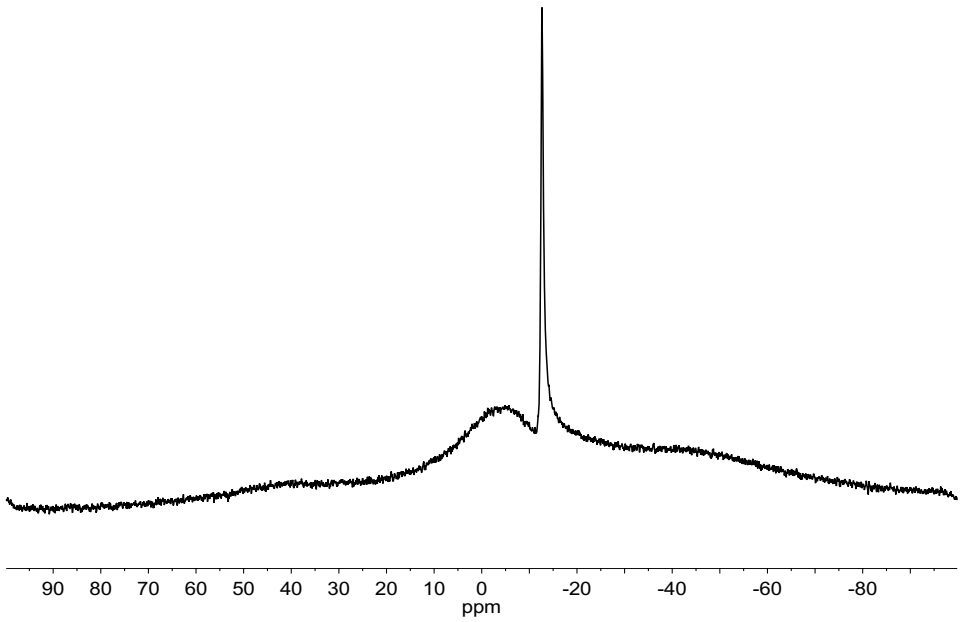

Figure A.37: $^{11}B\{^{1}H\}$ NMR spectrum of **58**.

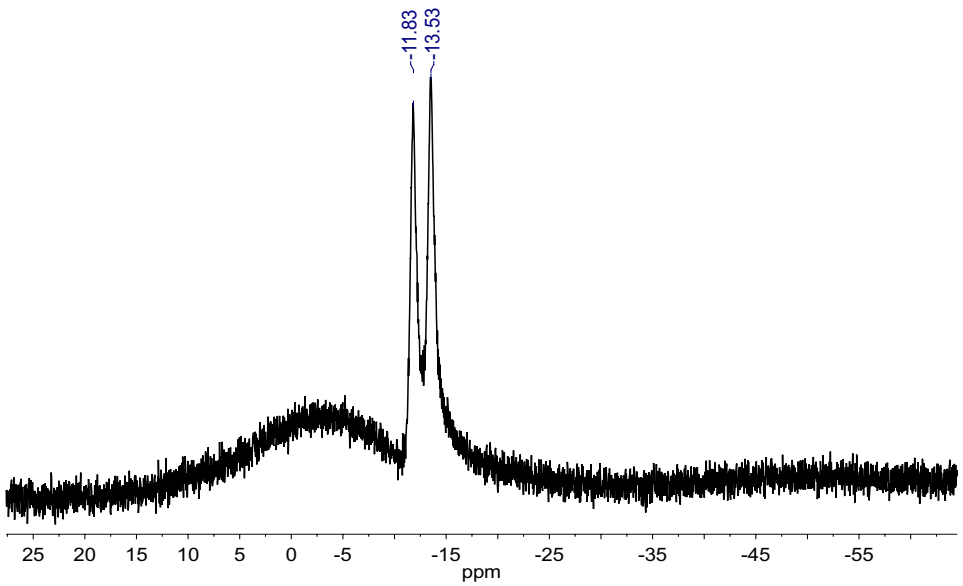

Figure A.38: ^{11}B NMR spectrum of **58**.

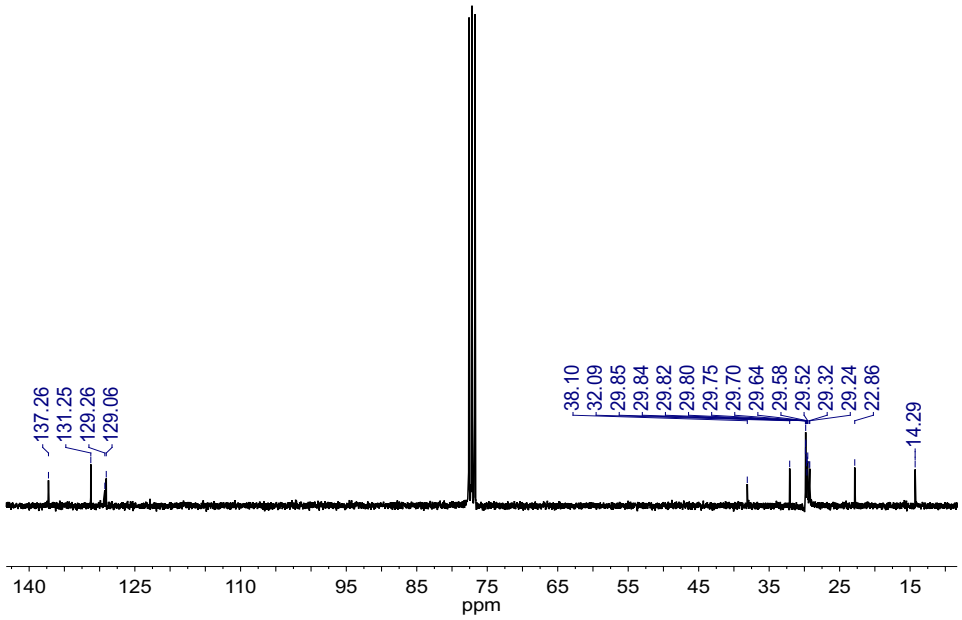

Figure A.39: ^{13}C NMR spectrum of **58**.

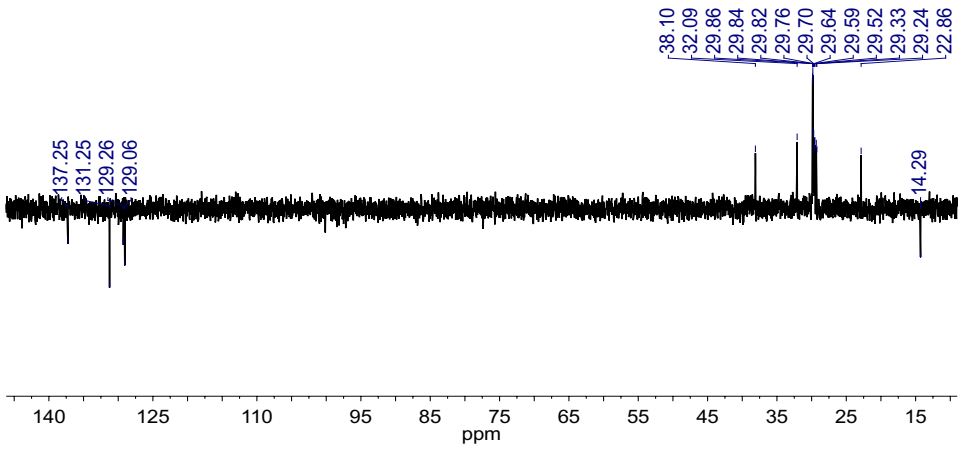

Figure A.40: DEPT-135 NMR spectrum of **58**.

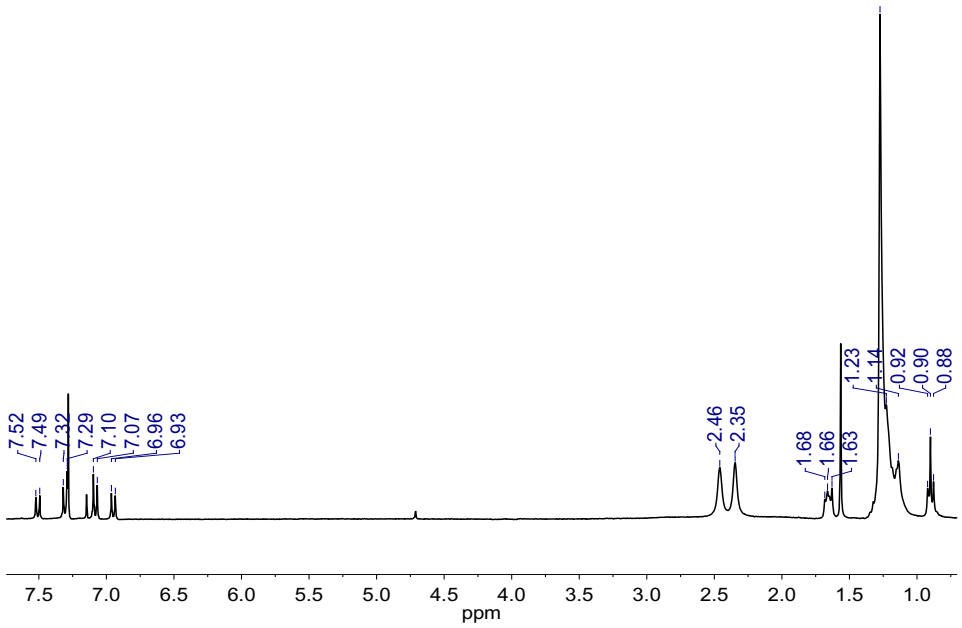

Figure A.41: ^{1}H $\{^{11}$B$\}$ NMR spectrum of **58**.

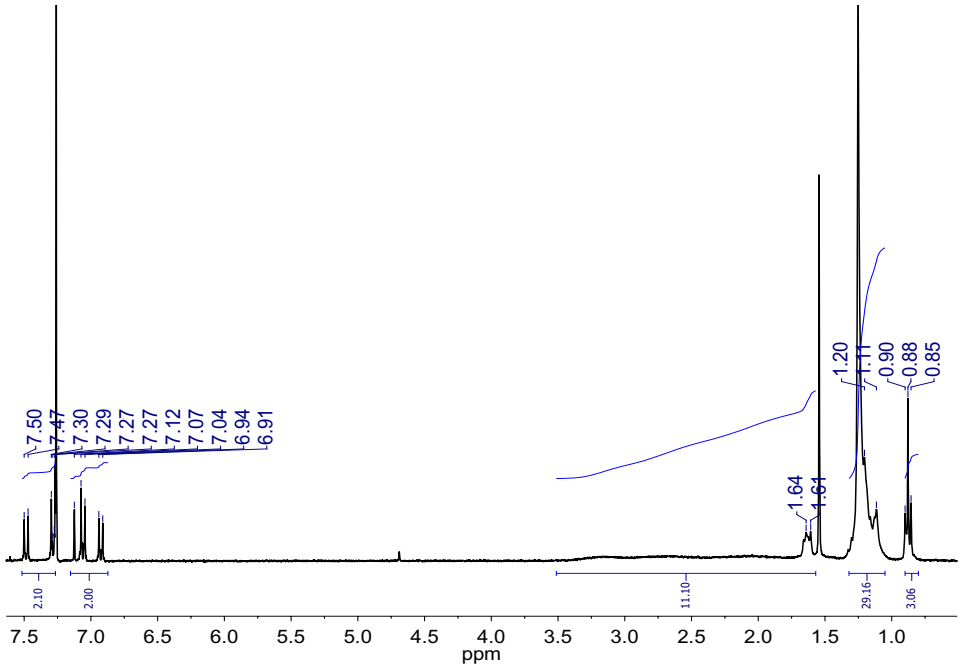

Figure A.42: ^{1}H NMR spectrum of **58**.

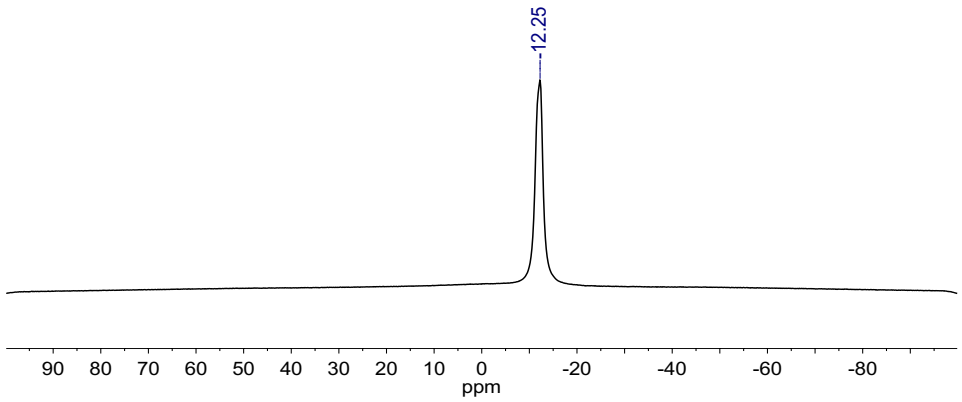

Figure A.43: $^{11}B\{^{1}H\}$ NMR spectrum of **63**.

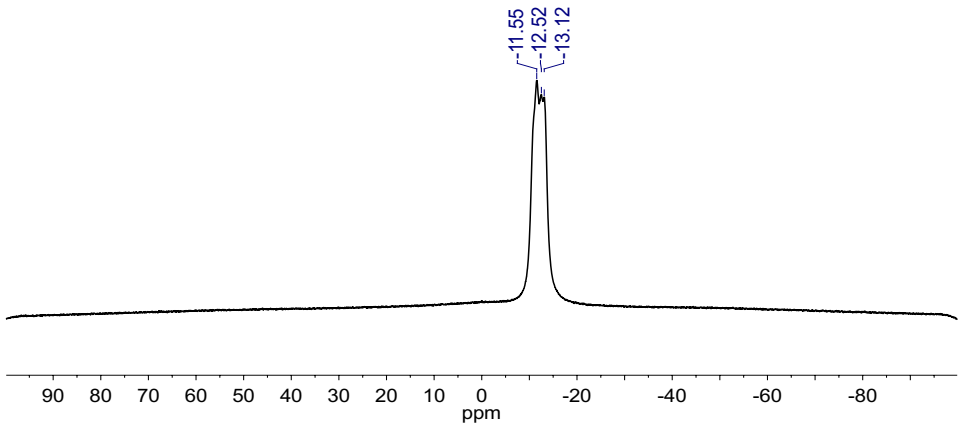

Figure A.44: ^{11}B NMR spectrum of **63**.

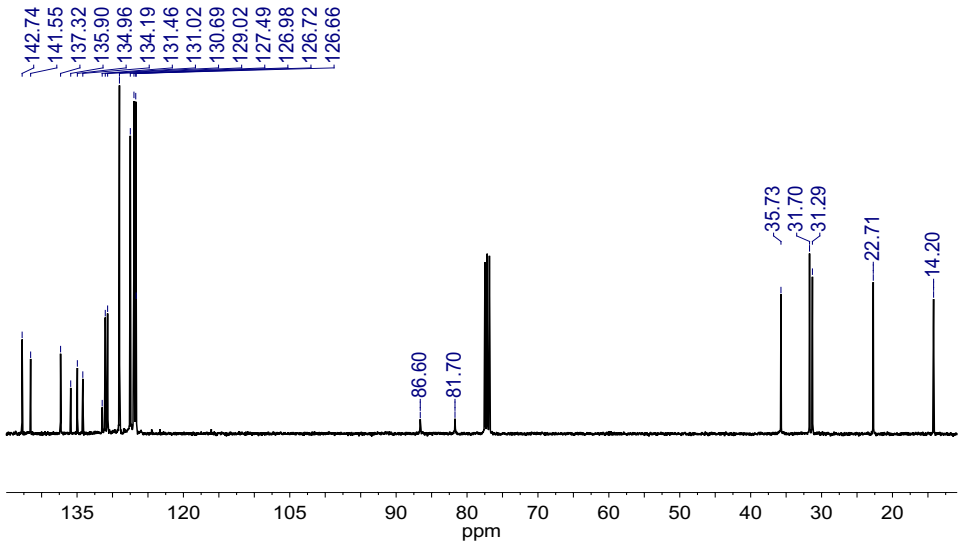

Figure A.45: ^{13}C NMR spectrum of **63**.

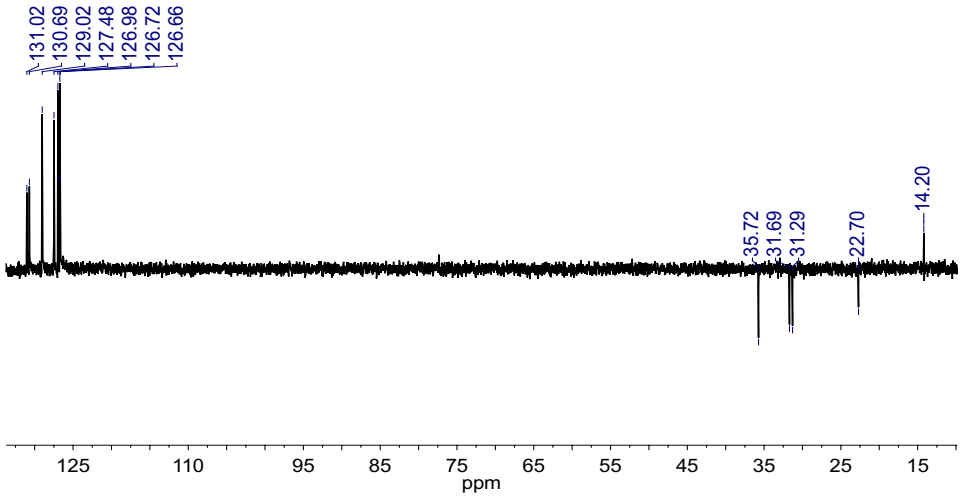

Figure A.46: DEPT-135 NMR spectrum of **63**.

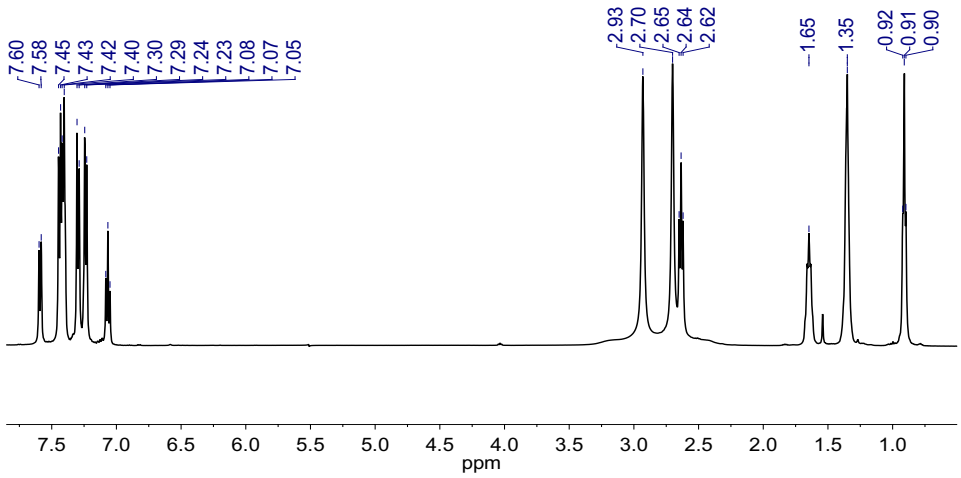

Figure A.47: ^{1}H $\{^{11}$B$\}$ NMR spectrum of **63**.

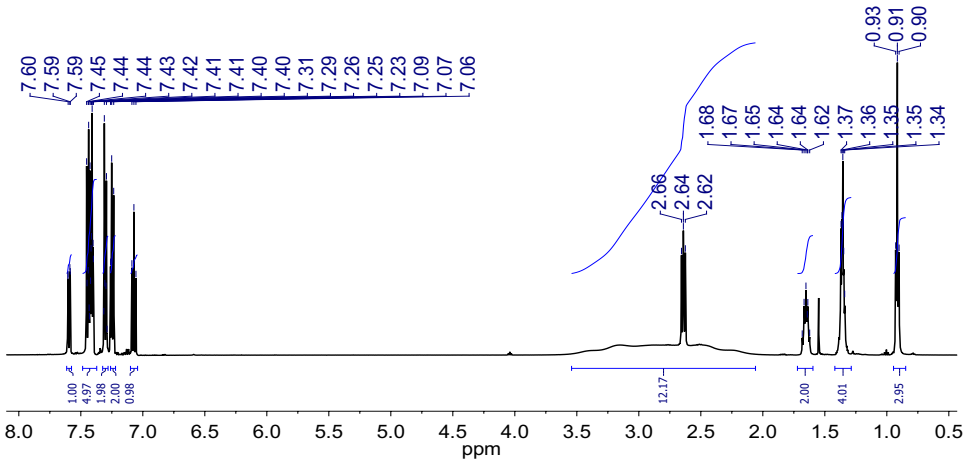

Figure A.48: ^{1}H NMR spectrum of **63**.

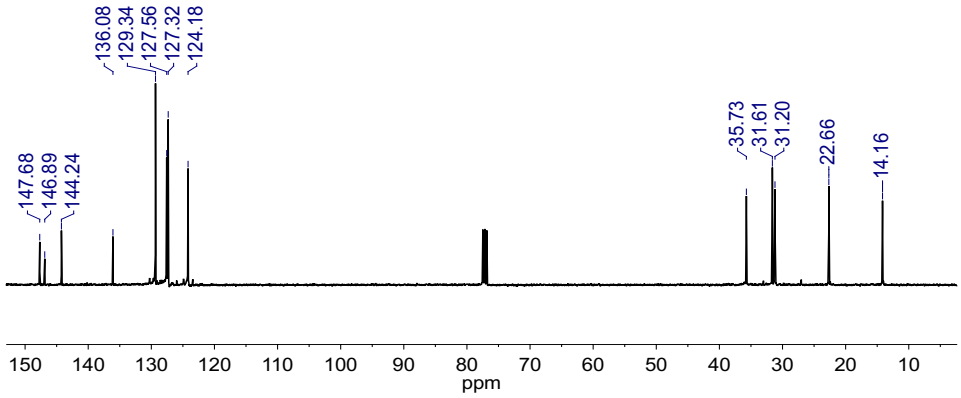

Figure A.49: ^{13}C NMR spectrum of **64**.

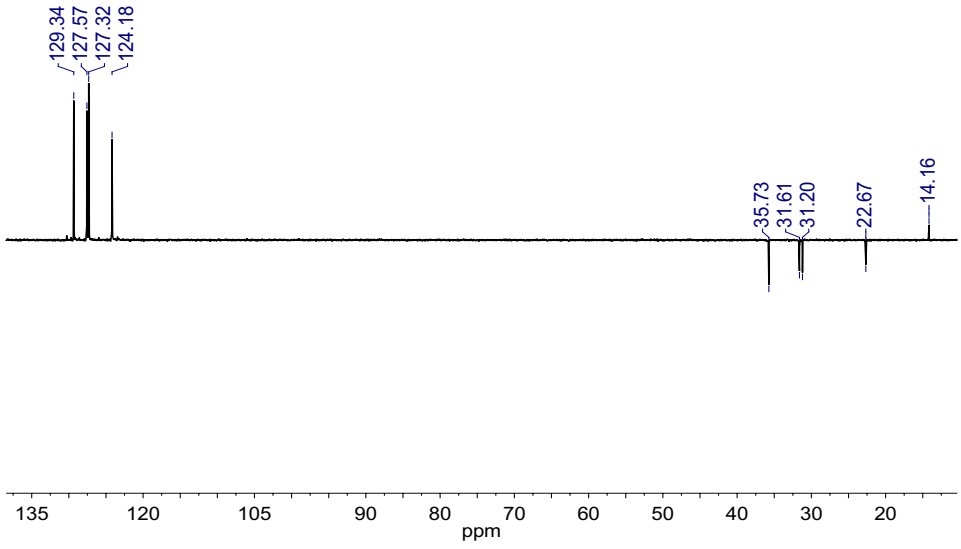

Figure A.50: DEPT-135 NMR spectrum of **64**.

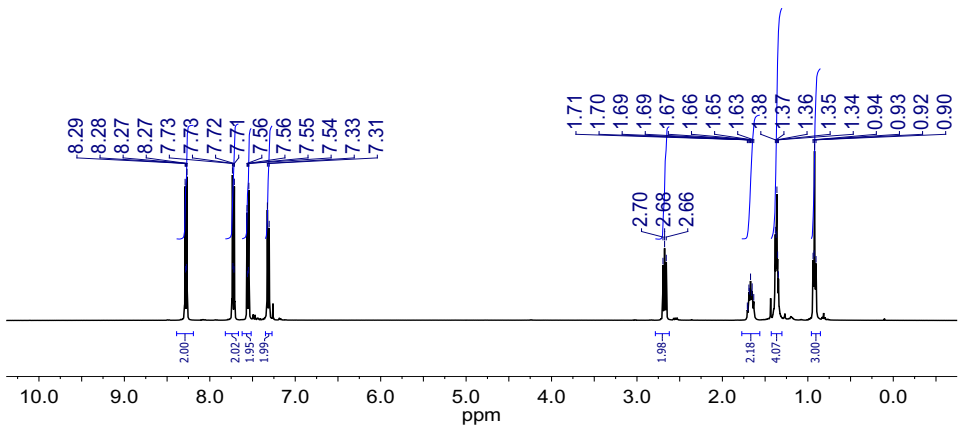

Figure A.51: ^{1}H NMR spectrum of **64**.

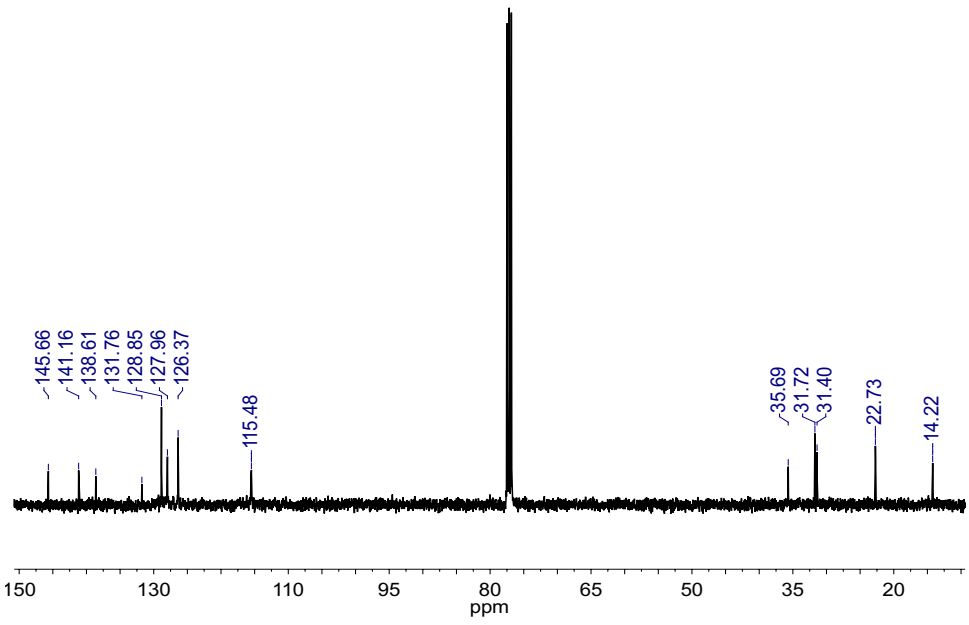

Figure A.52: ^{13}C NMR spectrum of **65**.

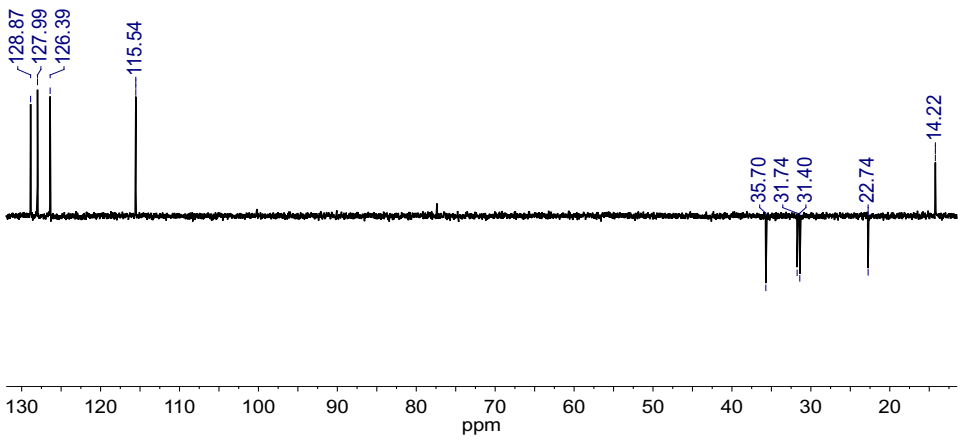

Figure A.53: DEPT-135 NMR spectrum of **65**.

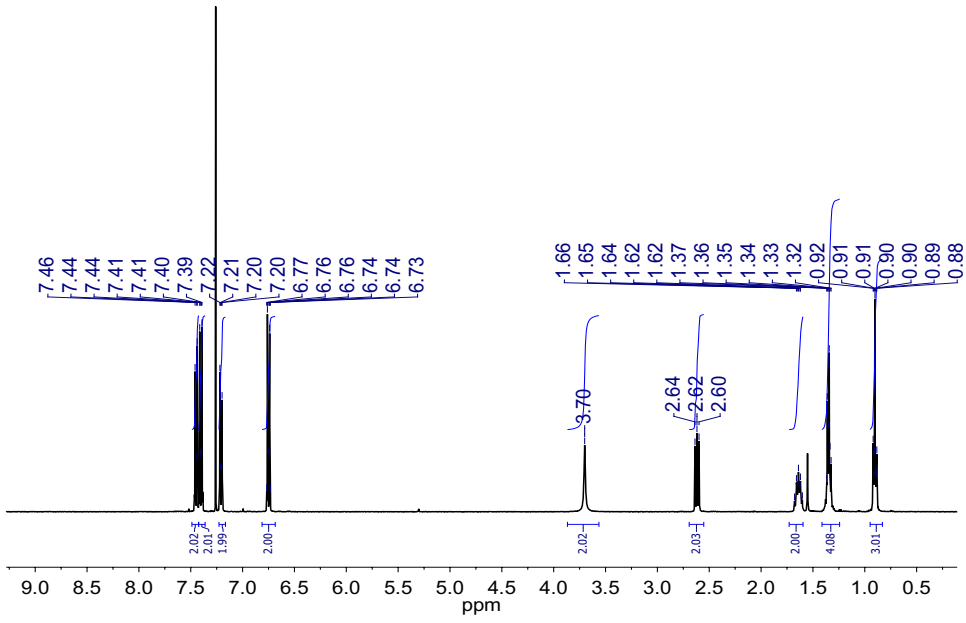

Figure A.54: ^{1}H NMR spectrum of **65**.

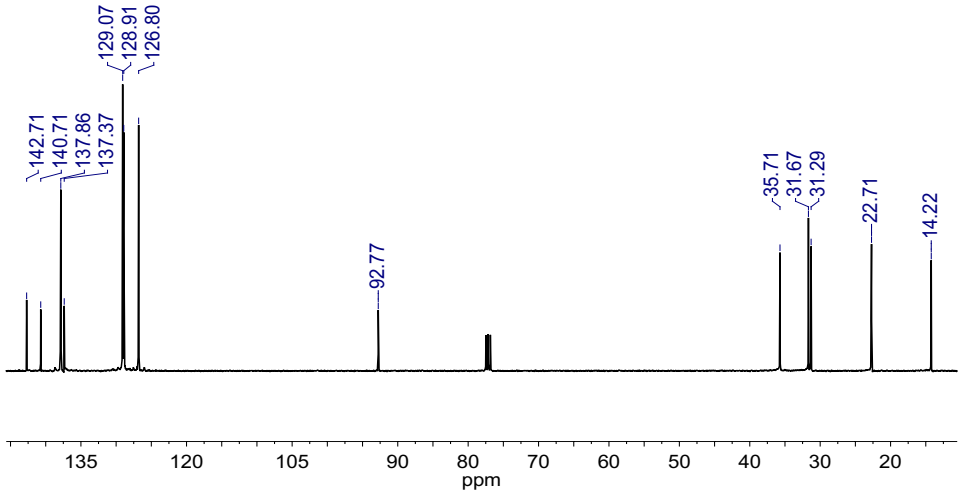

Figure A.55: ^{13}C NMR spectrum of **66**.

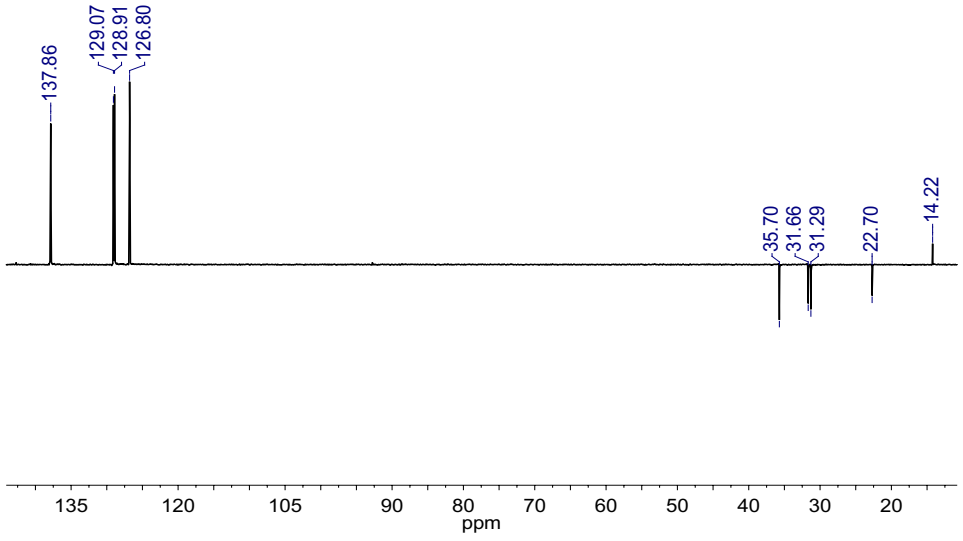

Figure A.56: DEPT-135 NMR spectrum of **66**.

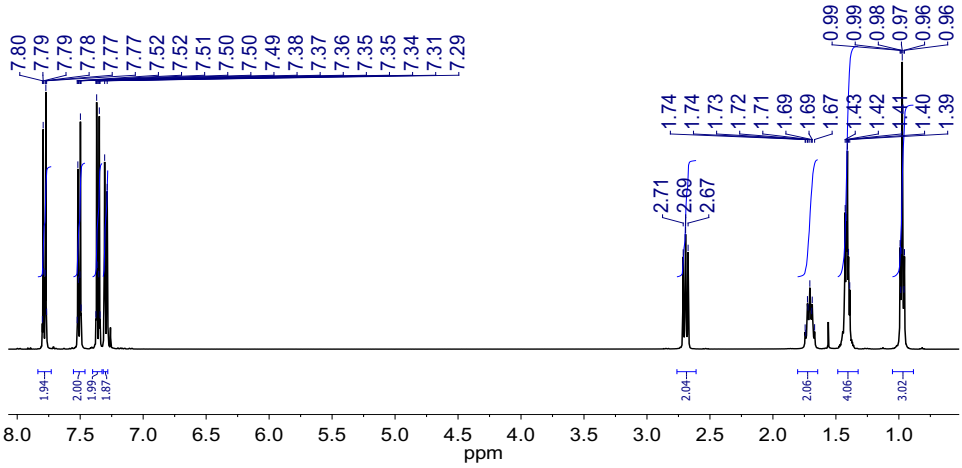

Figure A.57: ^{1}H NMR spectrum of **66**.

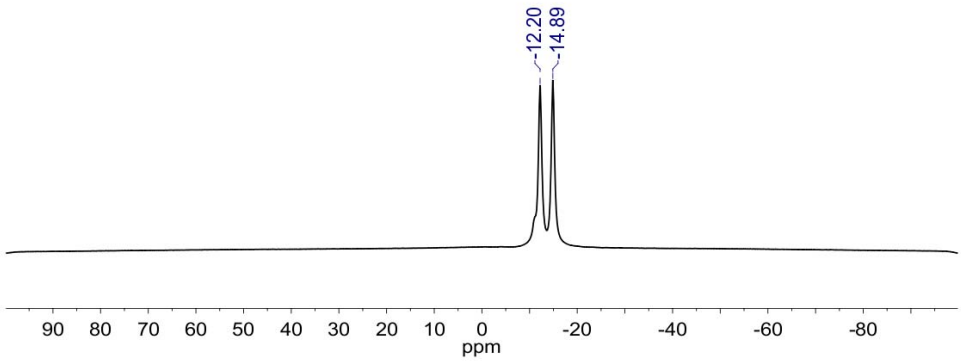

Figure A.58: ^{11}B{^{1}H } NMR spectrum of **67**.

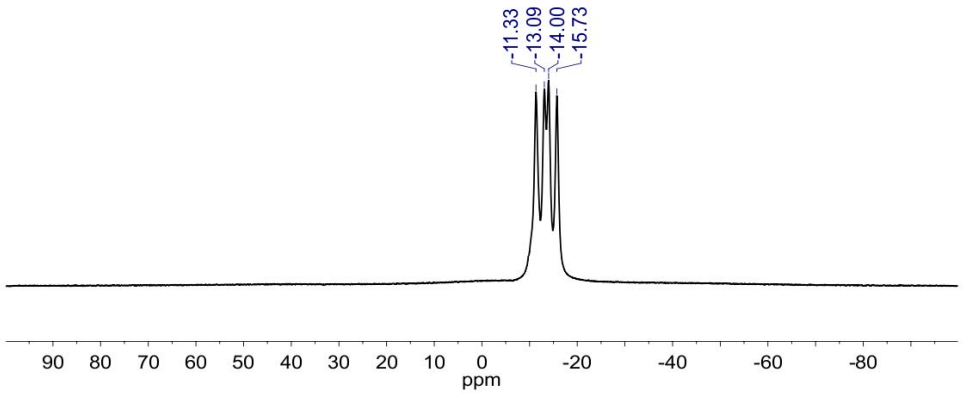

Figure A.59: ^{11}B NMR spectrum of **67**.

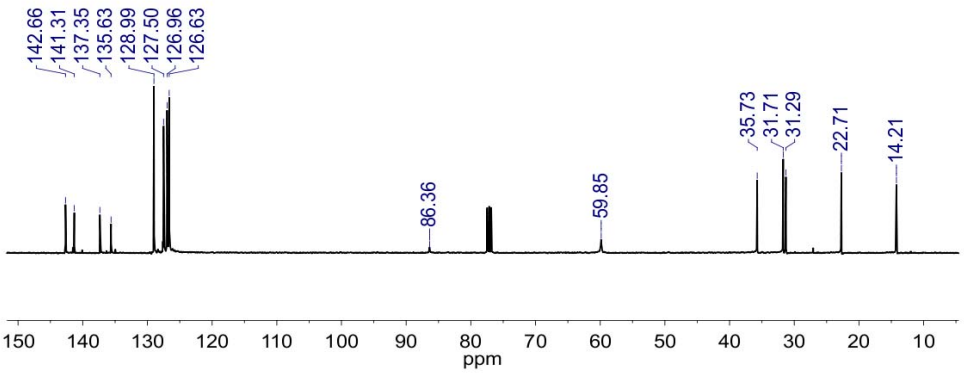

Figure A.60: ^{13}C NMR spectrum of **67**.

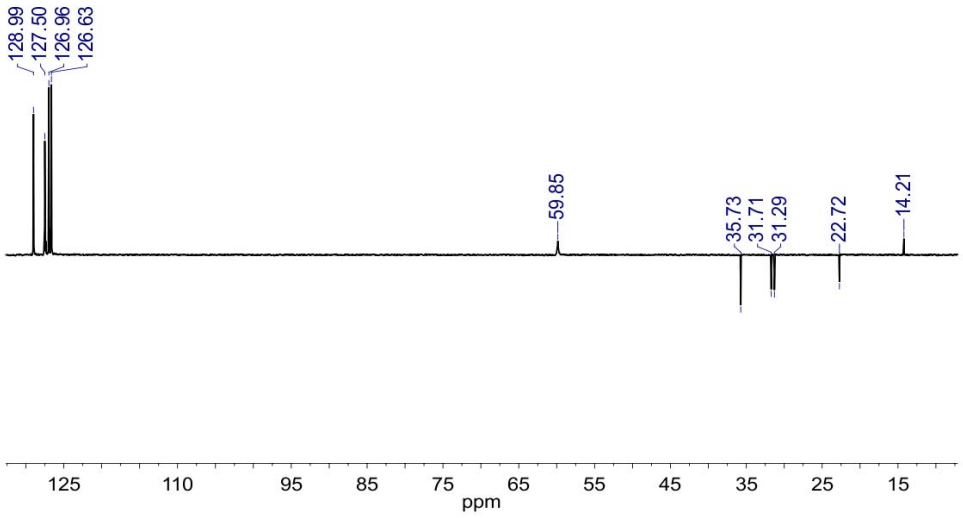

Figure A.61: DEPT-135 NMR spectrum of **67**.

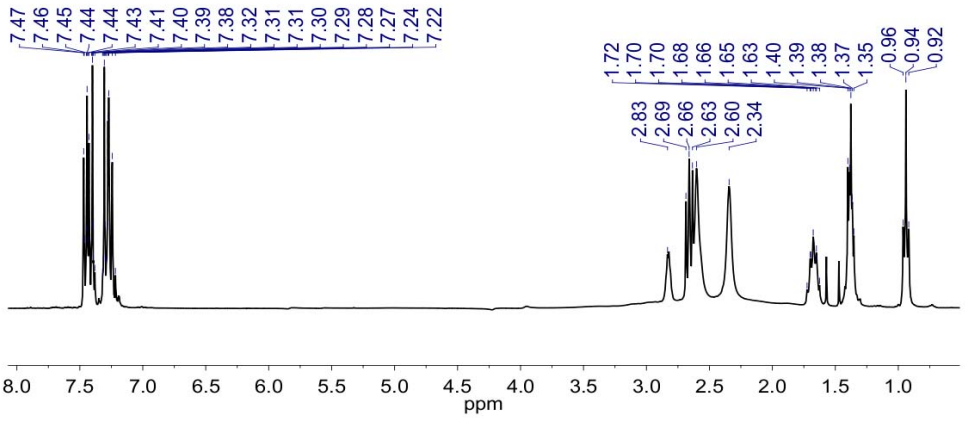

Figure A.62: ^{1}H $\{^{11}$B$\}$ NMR spectrum of **67**.

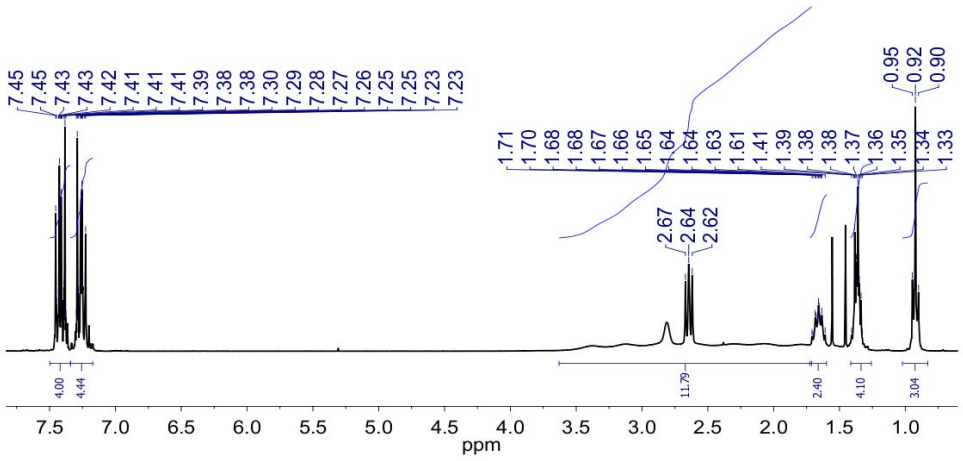

Figure A.63: ^{1}H NMR spectrum of **67**.

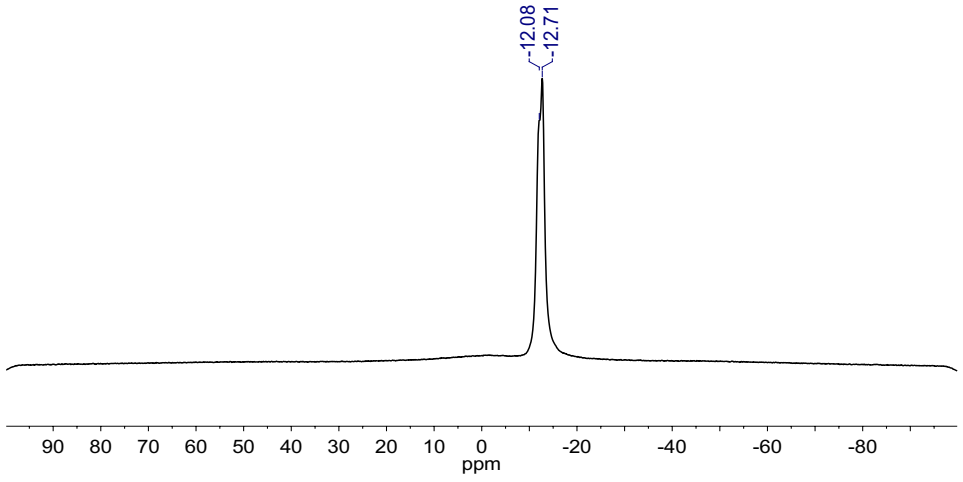

Figure A.64: ^{11}B{^{1}H } NMR spectrum of **70**.

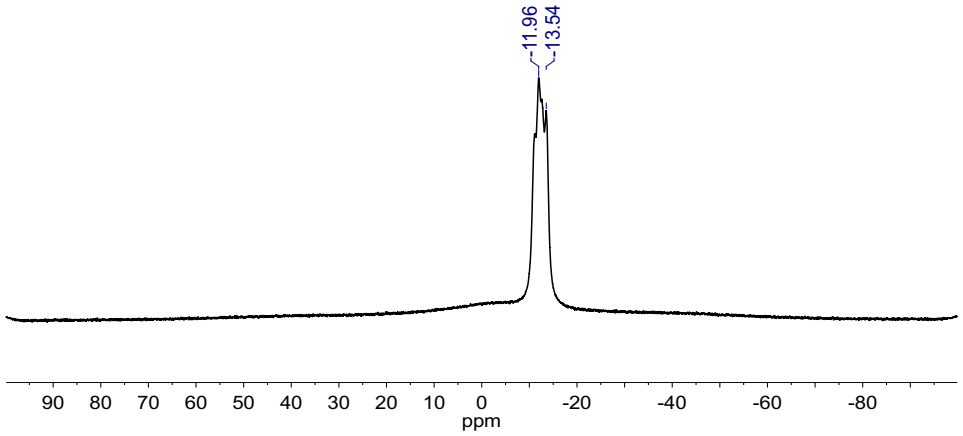

Figure A.65: ^{11}B NMR spectrum of **70**.

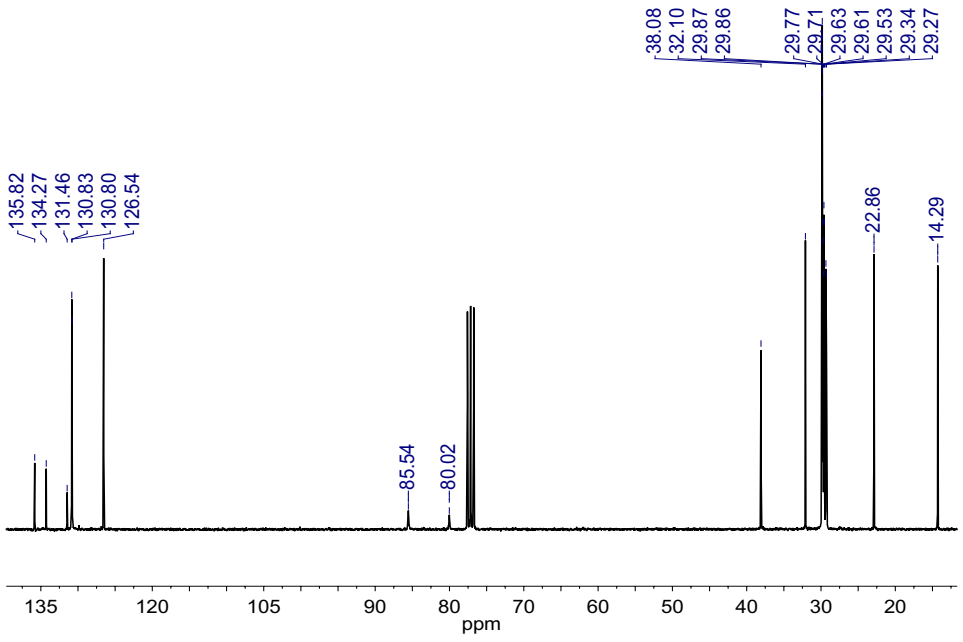

Figure A.66: ^{13}C NMR spectrum of **70**.

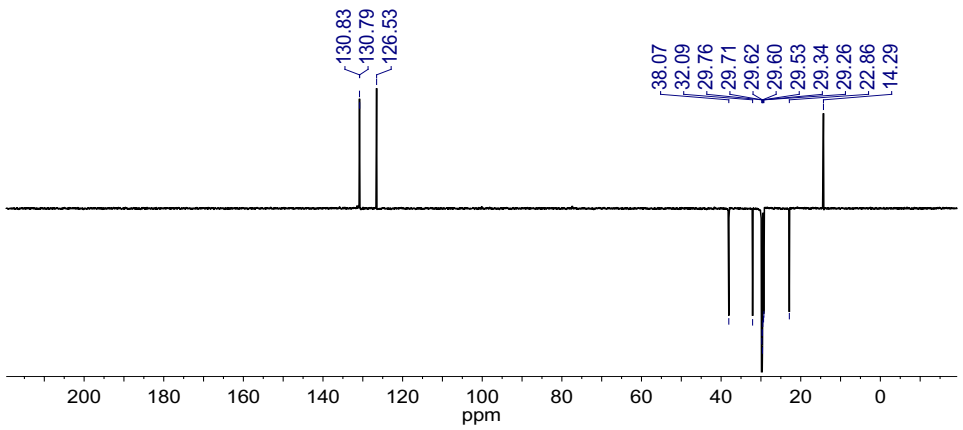

Figure A.67: DEPT-135 NMR spectrum of **70**.

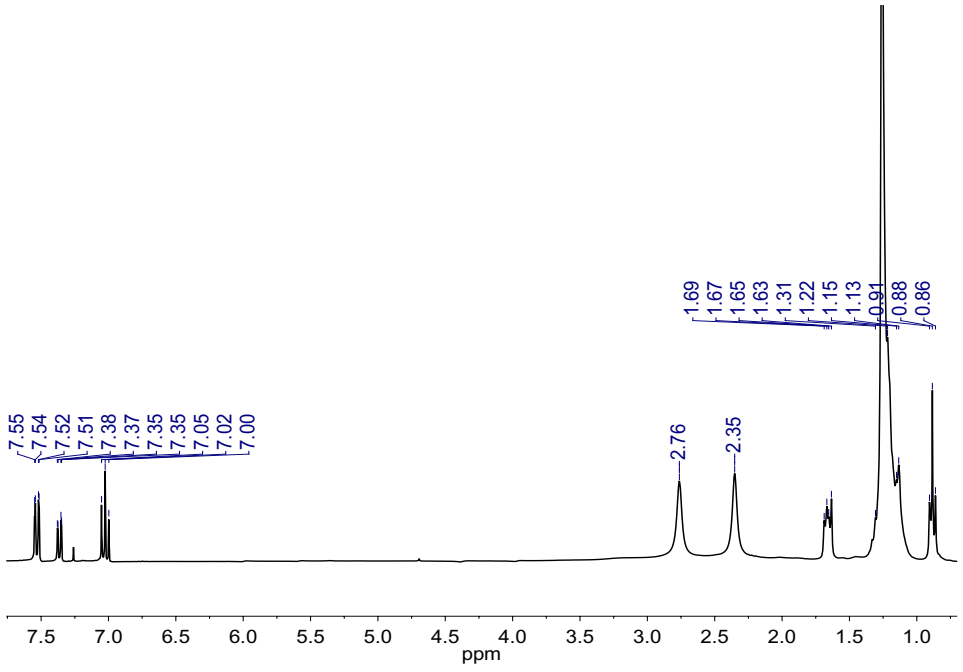

Figure A.68: ^{1}H $\{^{11}$B$\}$ NMR spectrum of **70**.

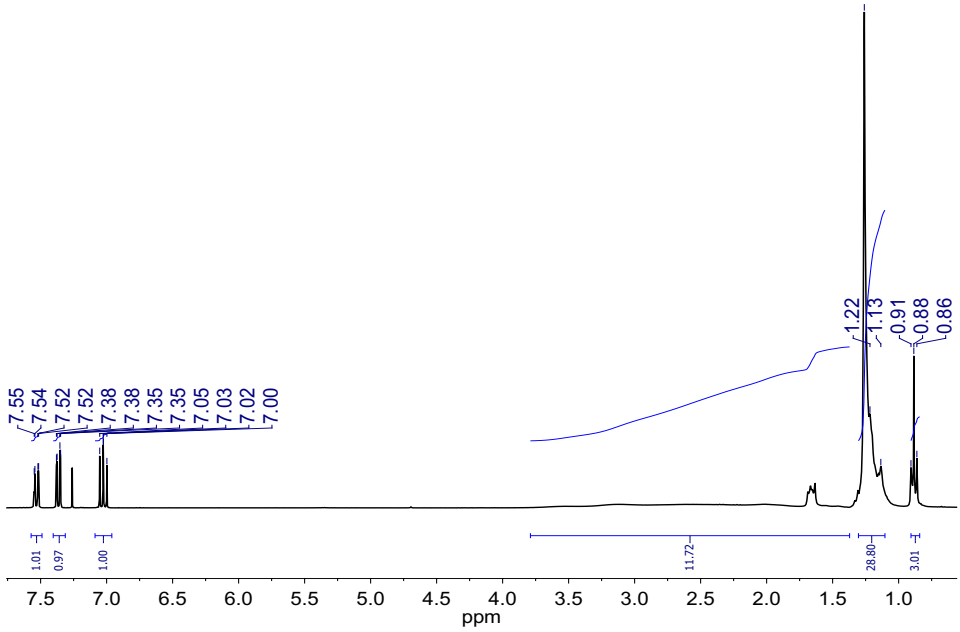

Figure A.69: ^{1}H NMR spectrum of **70**.

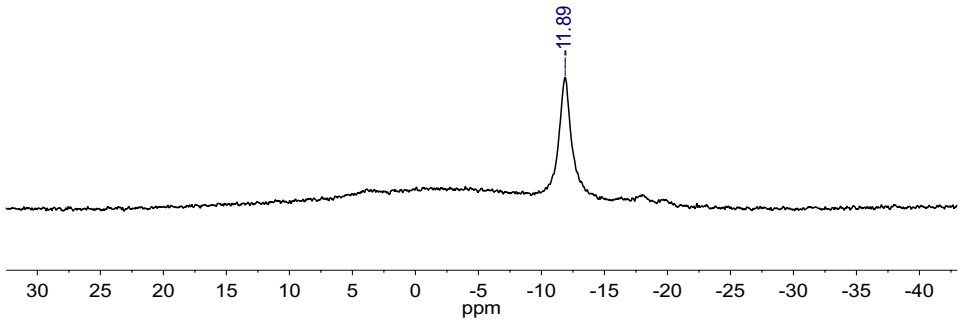

Figure A.70: ^{11}B{^{1}H } NMR spectrum of **72**.

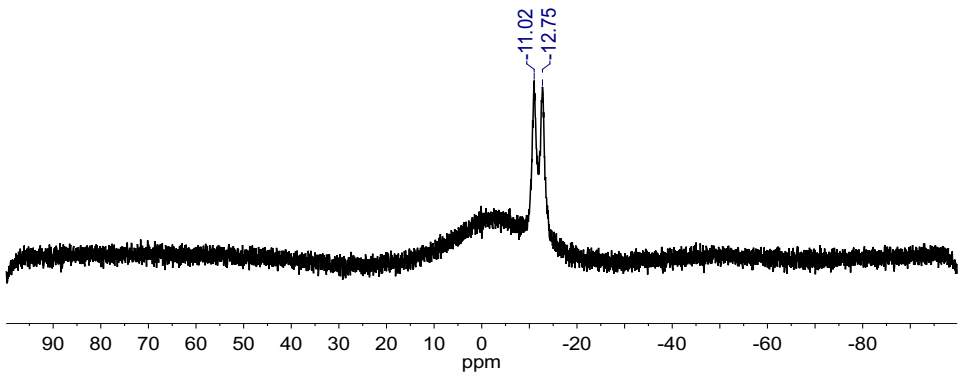

Figure A.71: ^{11}B NMR spectrum of **72**.

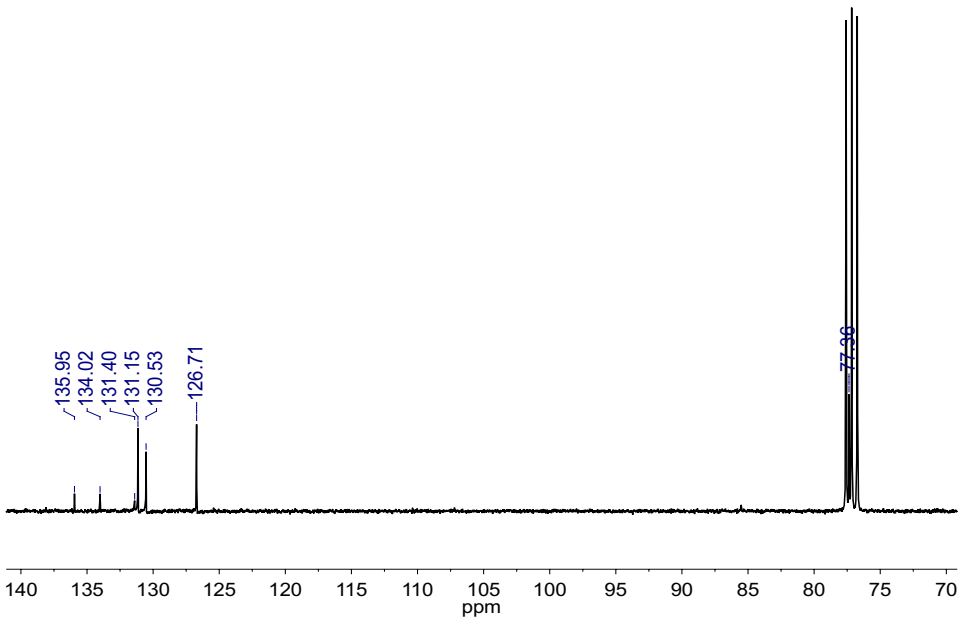

Figure A.72: ^{13}C NMR spectrum of **72**.

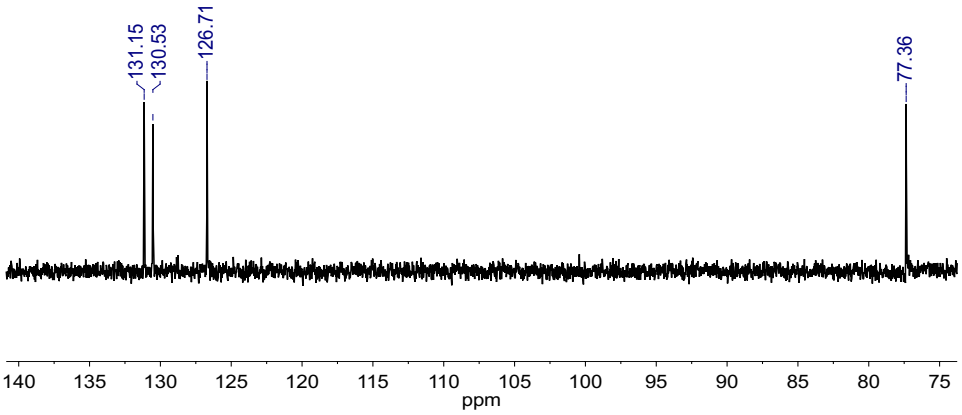

Figure A.73: DEPT-135 NMR spectrum of **72**.

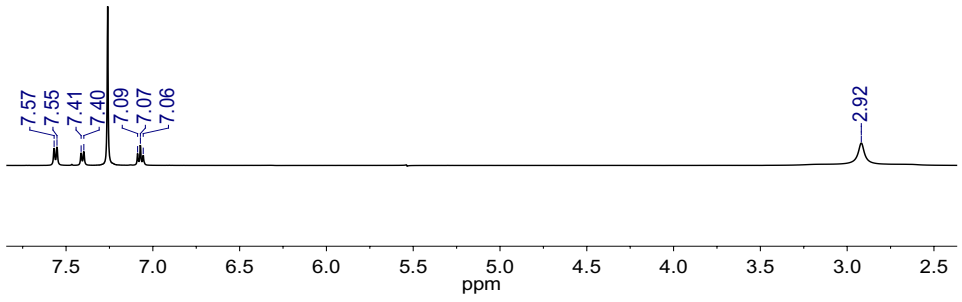

Figure A.74: ^{1}H $\{^{11}$B$\}$ NMR spectrum of **72**.

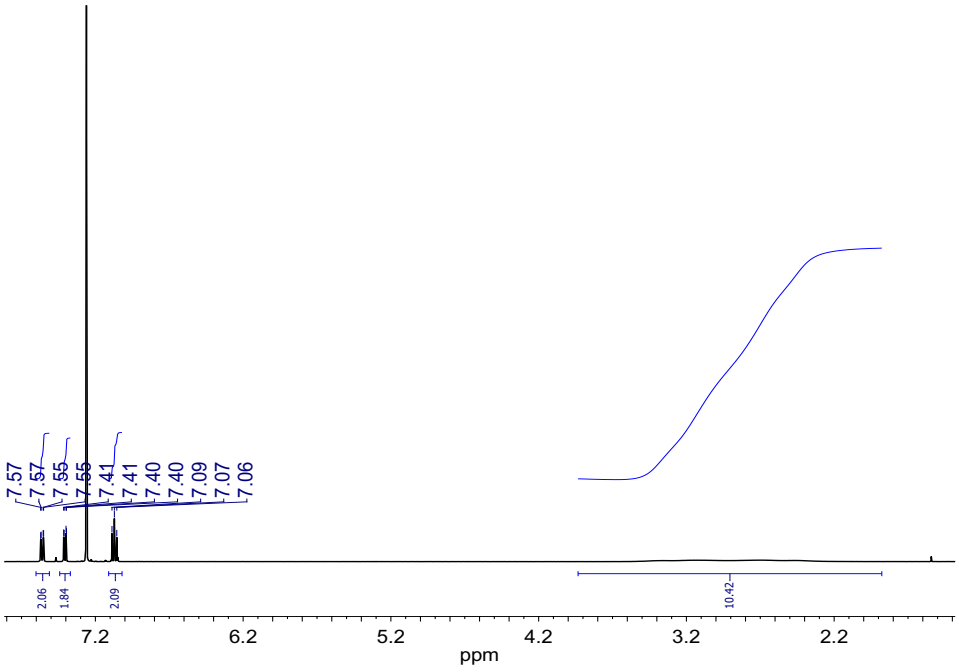

Figure A.75: ^{1}H NMR spectrum of **72**.

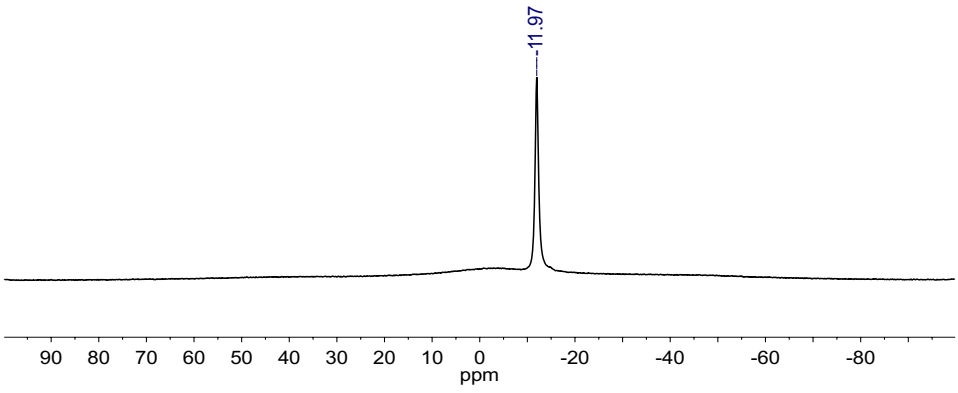

Figure A.76: ^{11}B{^{1}H } NMR spectrum of **73**.

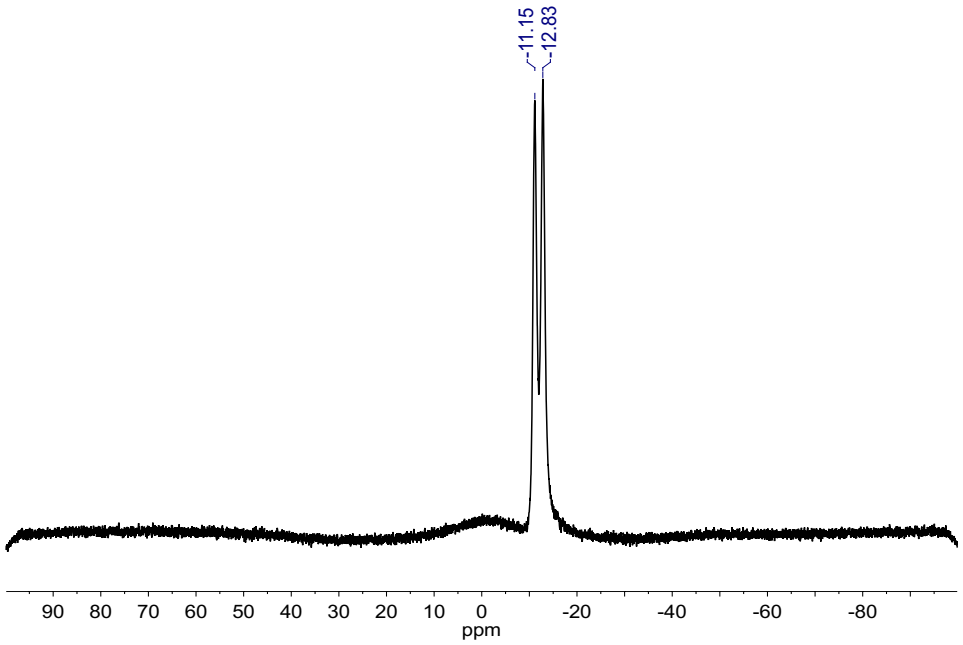

Figure A.77: ^{11}B NMR spectrum of **73**.

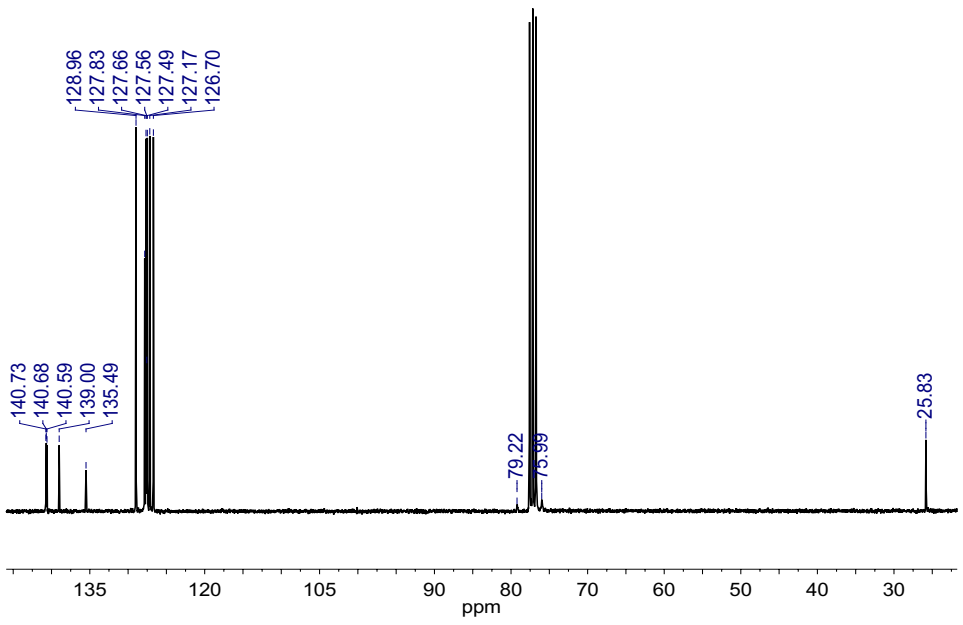

Figure A.78: ^{13}C NMR spectrum of **73**.

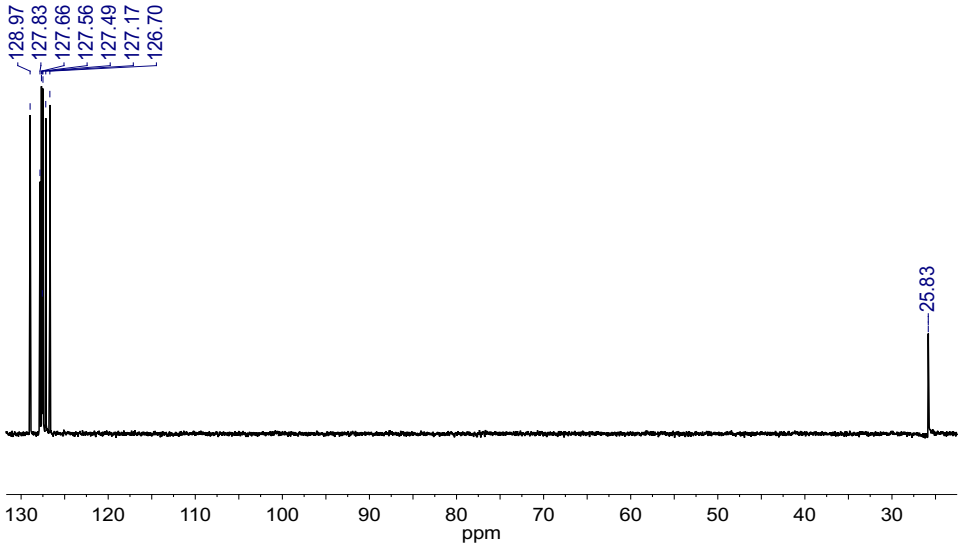

Figure A.79: DEPT-135 NMR spectrum of **73**.

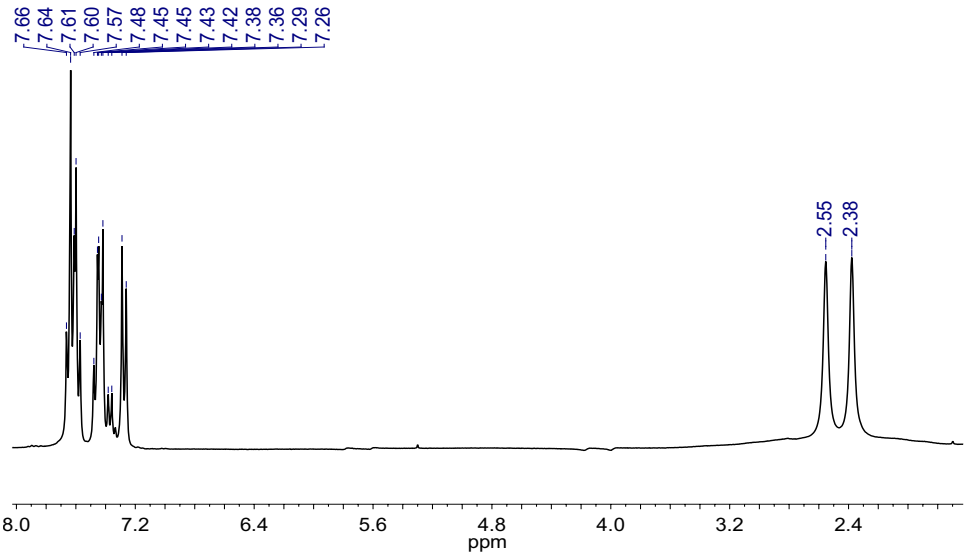

Figure A.80: ^{1}H $\{^{11}$B$\}$ NMR spectrum of **73**.

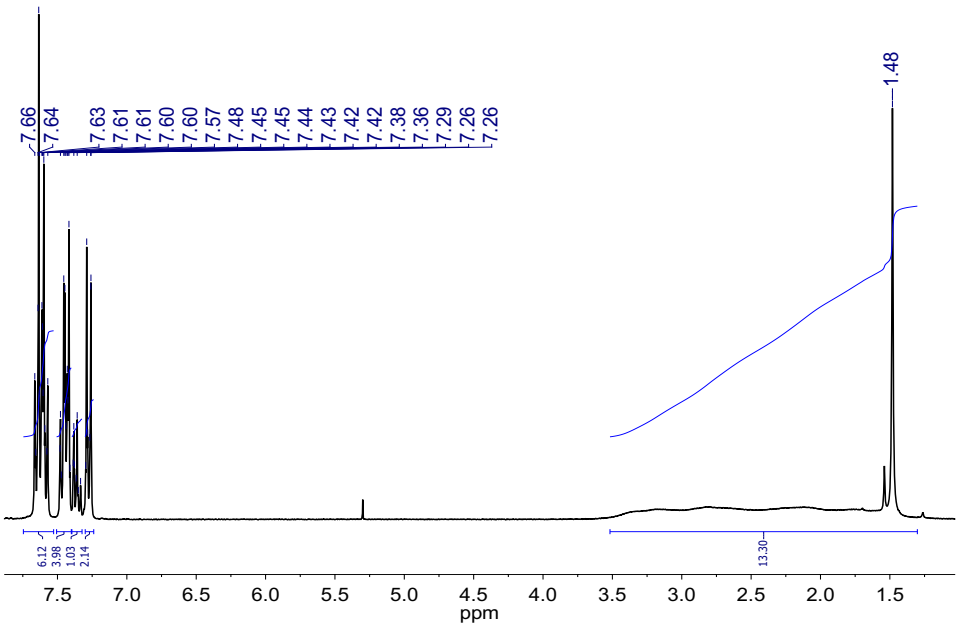

Figure A.81: ^{1}H NMR spectrum of **73**.

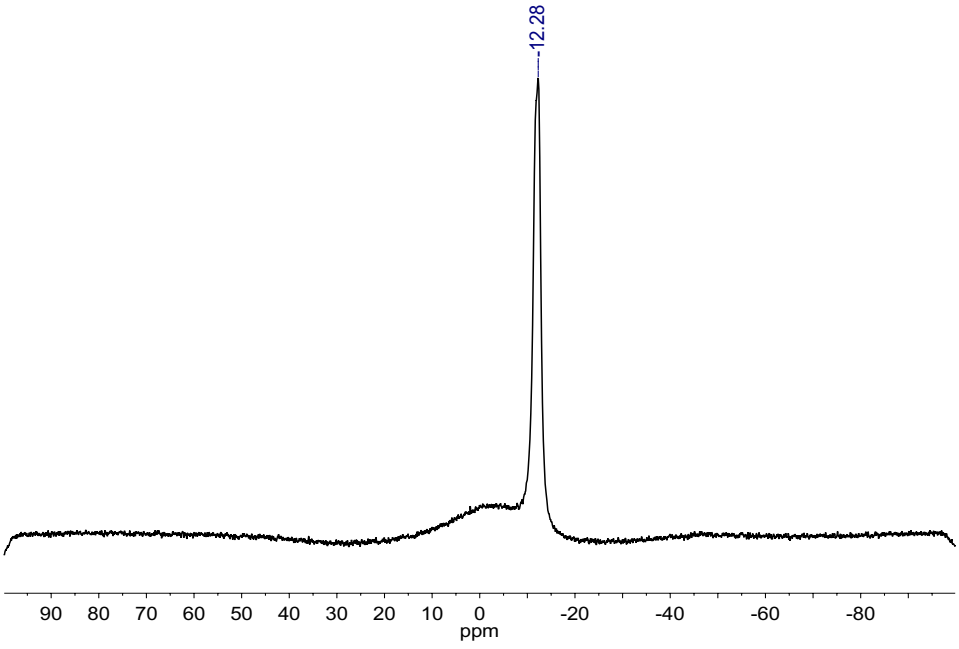

Figure A.82: ^{11}B{^{1}H } NMR spectrum of **74**.

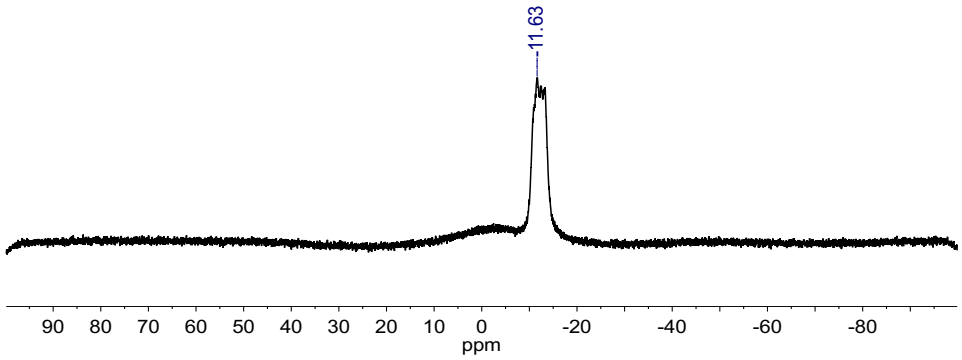

Figure A.83: ^{11}B NMR spectrum of **74**.

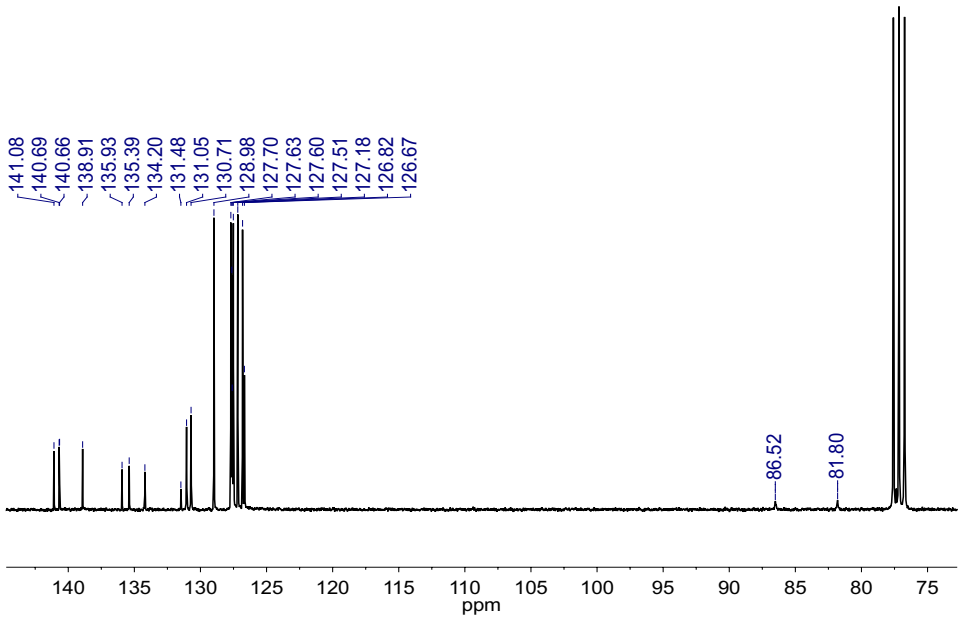

Figure A.84: ^{13}C NMR spectrum of **74**.

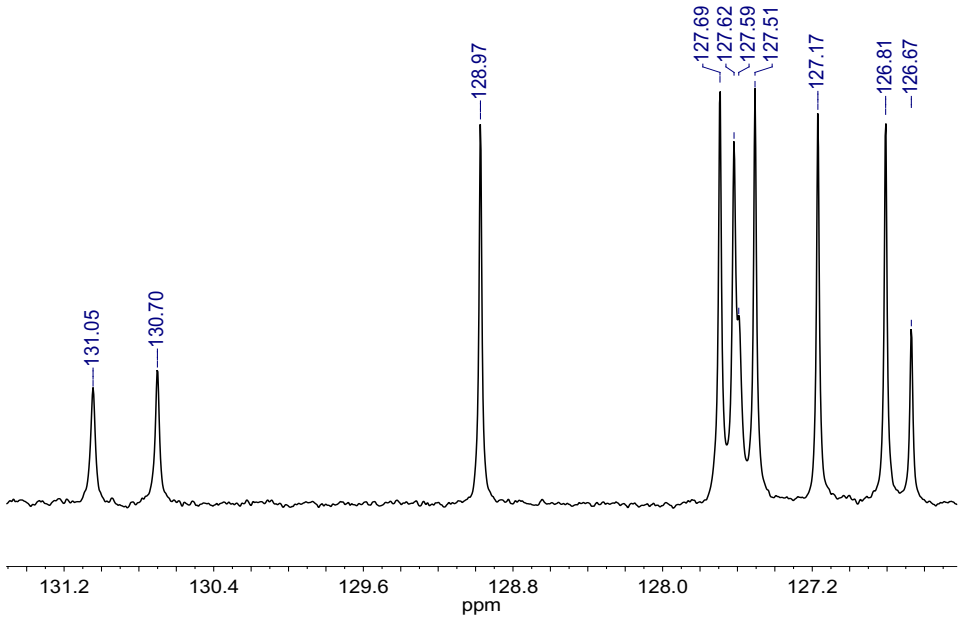

Figure A.85: DEPT-135 NMR spectrum of **74**.

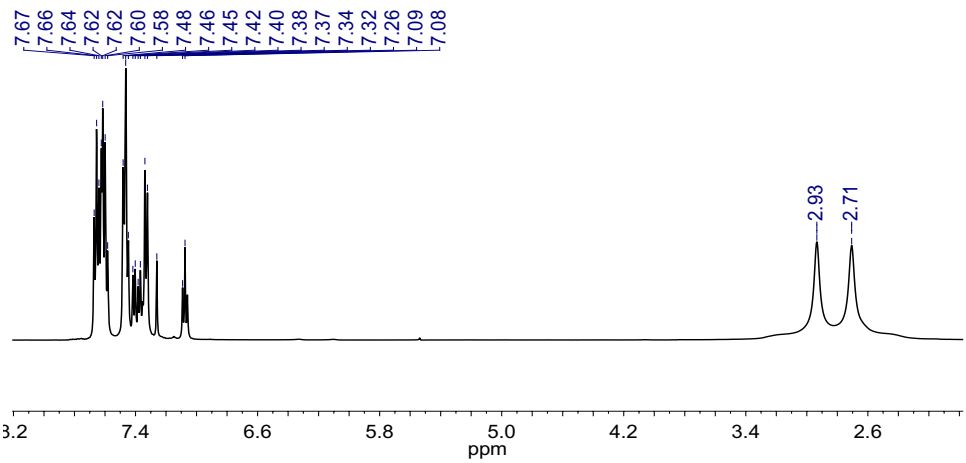

Figure A.86: ^{1}H $\{^{11}$B$\}$ NMR spectrum of **74**.

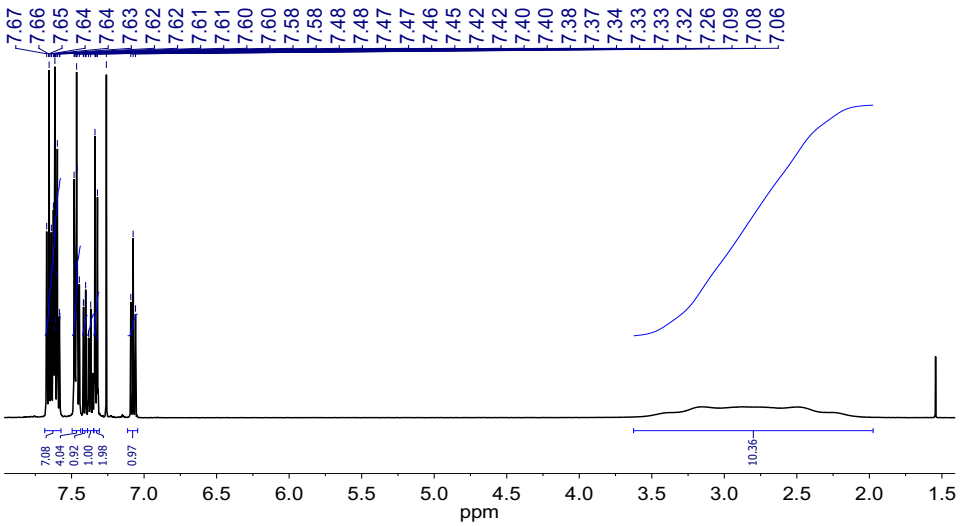

Figure A.87: ^{1}H NMR spectrum of **74**.

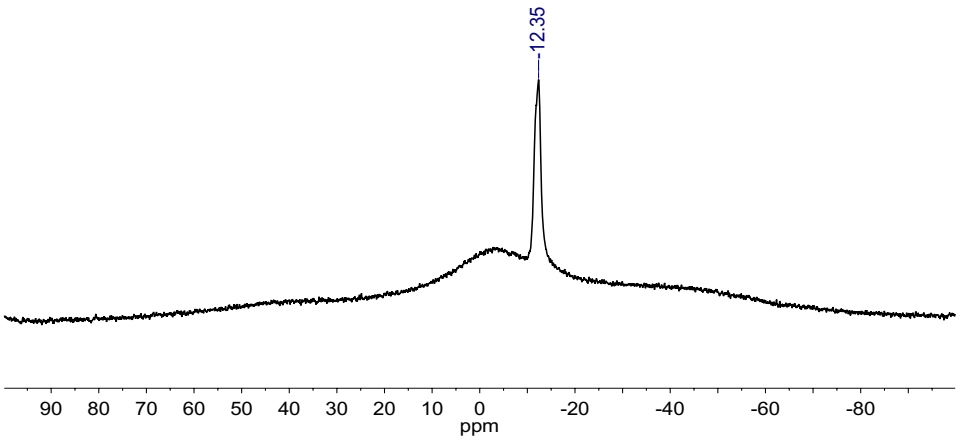

Figure A.88: ^{11}B{^{1}H } NMR spectrum of **75**.

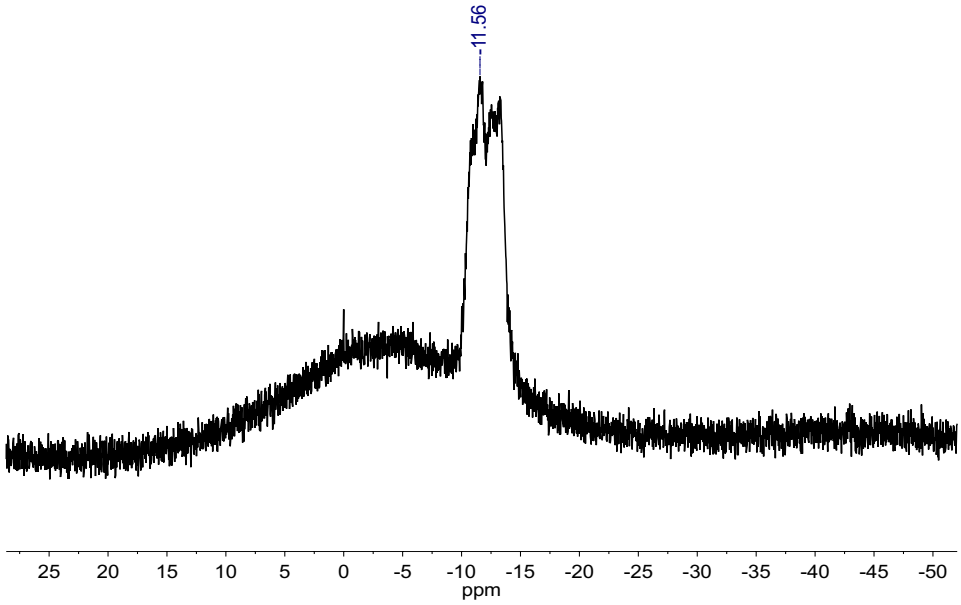

Figure A.89: ^{11}B NMR spectrum of **75**.

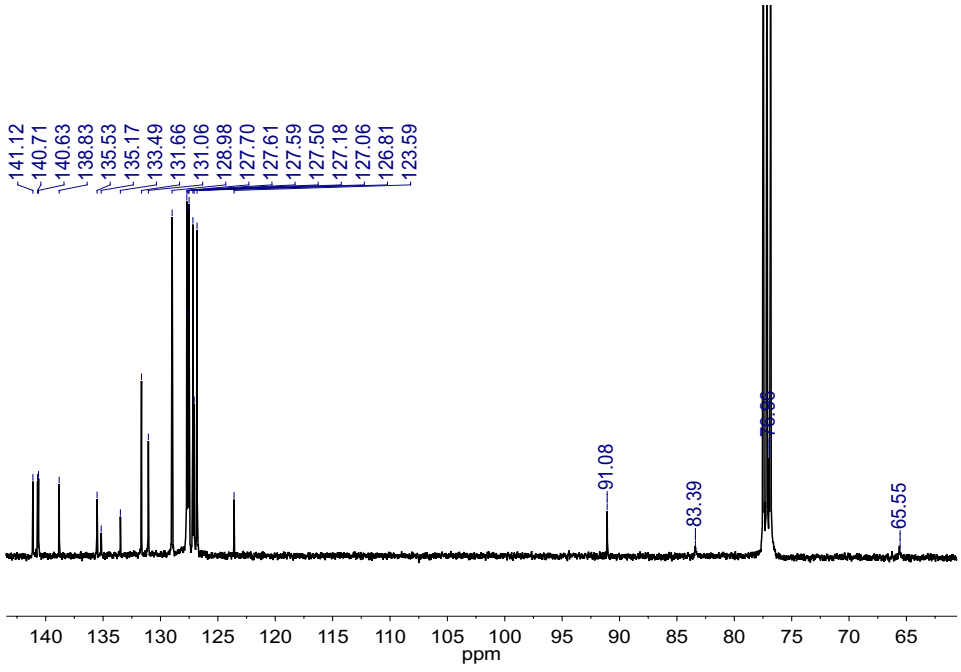

Figure A.90: ^{13}C NMR spectrum of **75**.

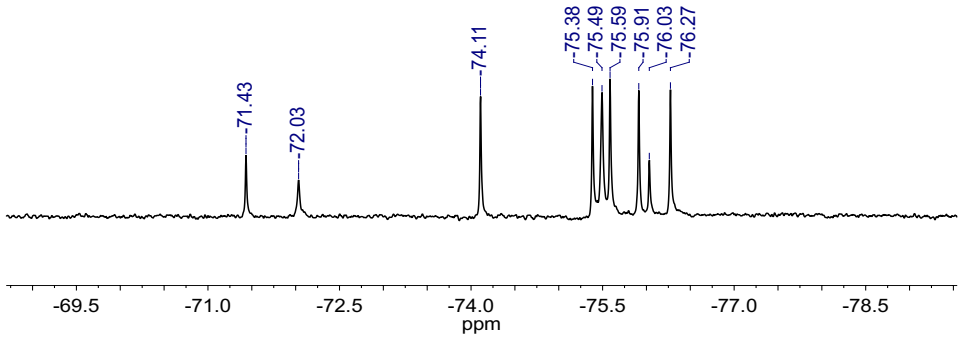

Figure A.91: DEPT-135 NMR spectrum of **75**.

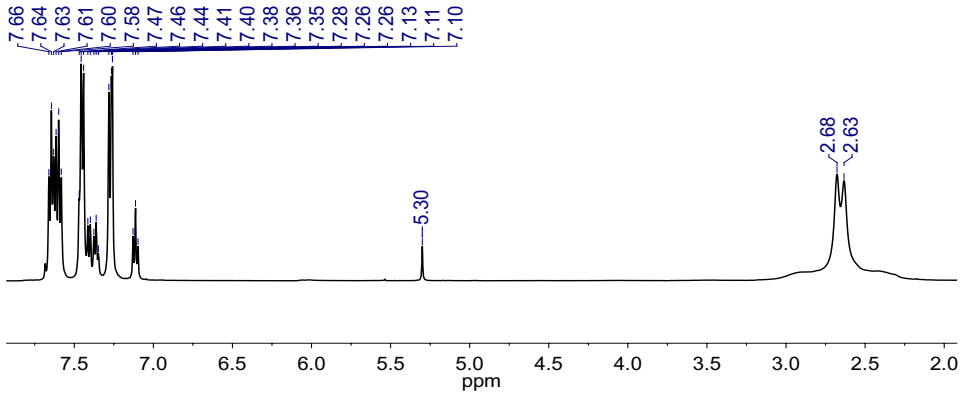

Figure A.92: ^{1}H $\{^{11}$B$\}$ NMR spectrum of **75**.

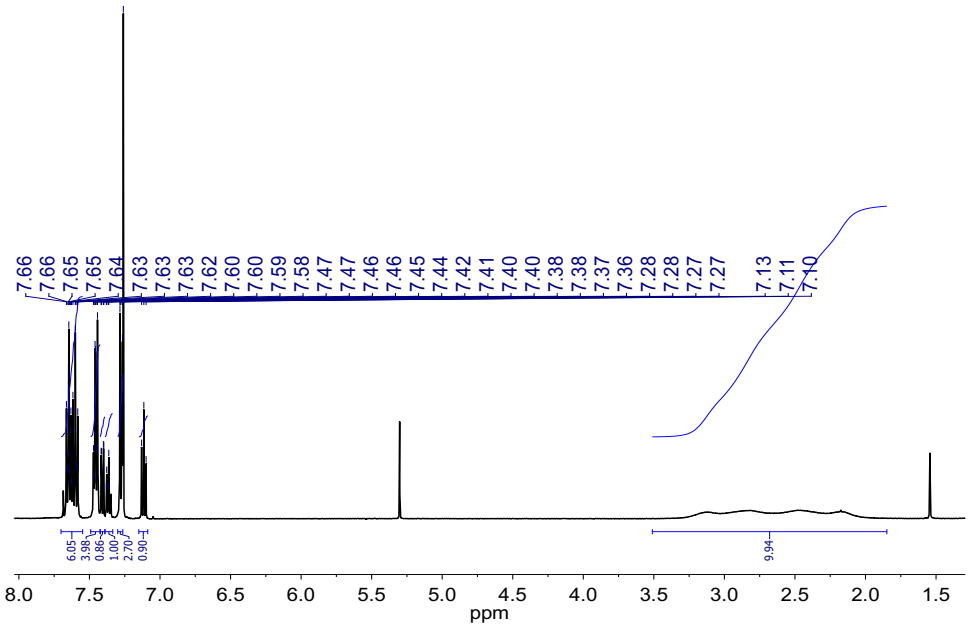

Figure A.93: ^{1}H NMR spectrum of **75**.

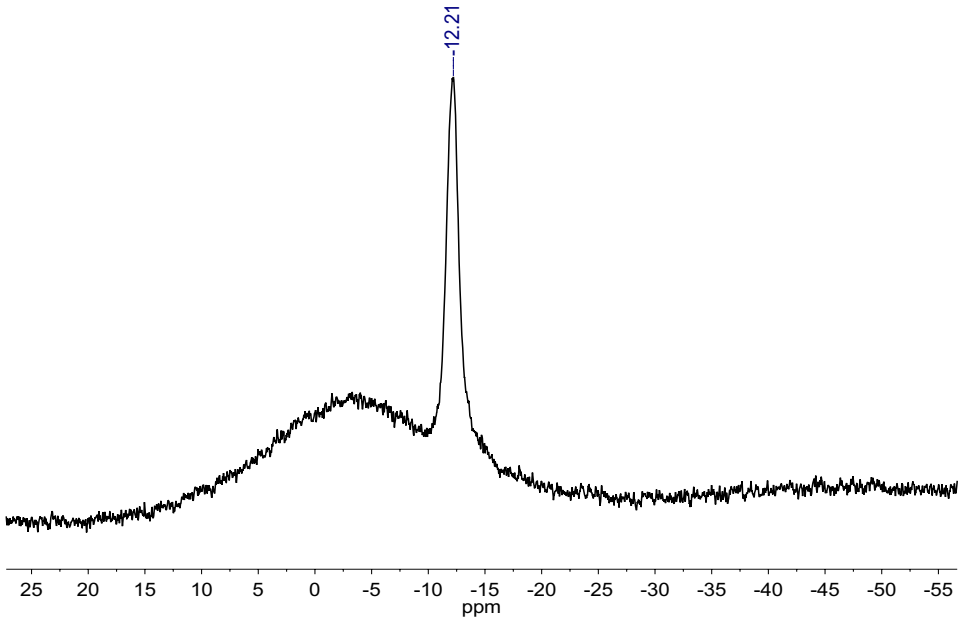

Figure A.94: ^{11}B{^{1}H } NMR spectrum of **76**.

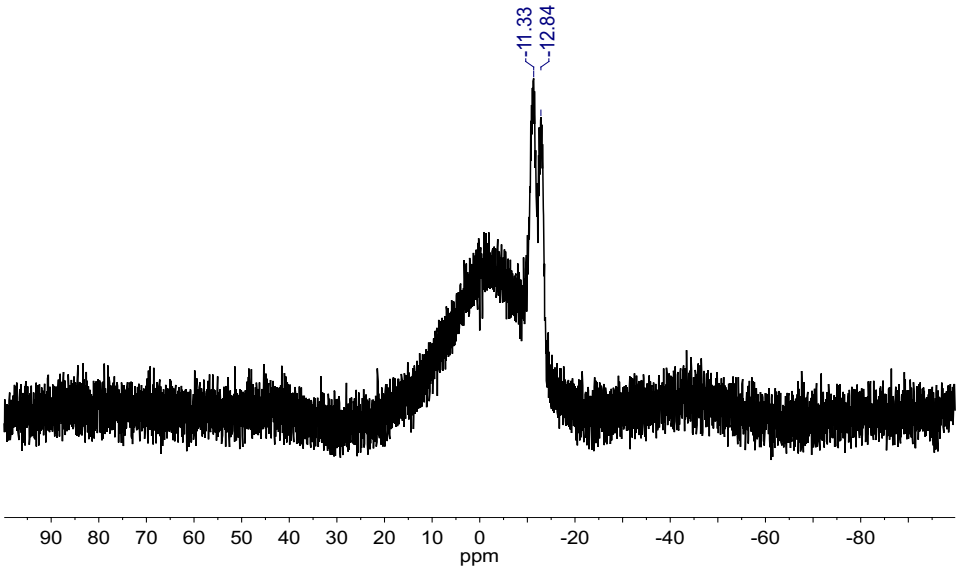

Figure A.95: ^{11}B NMR spectrum of **76**.

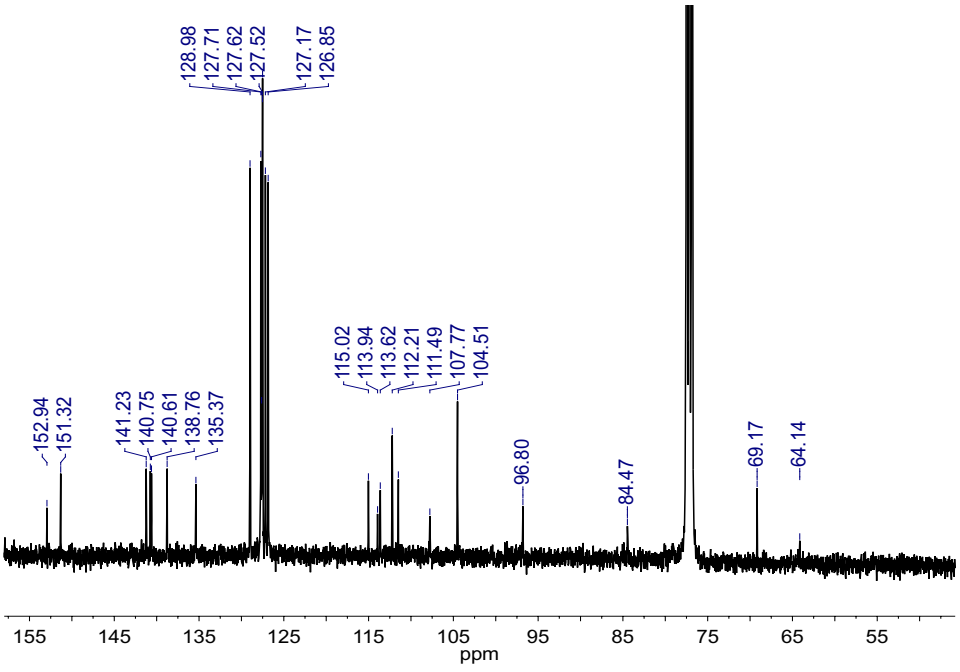

Figure A.96: ^{13}C NMR spectrum of **76**.

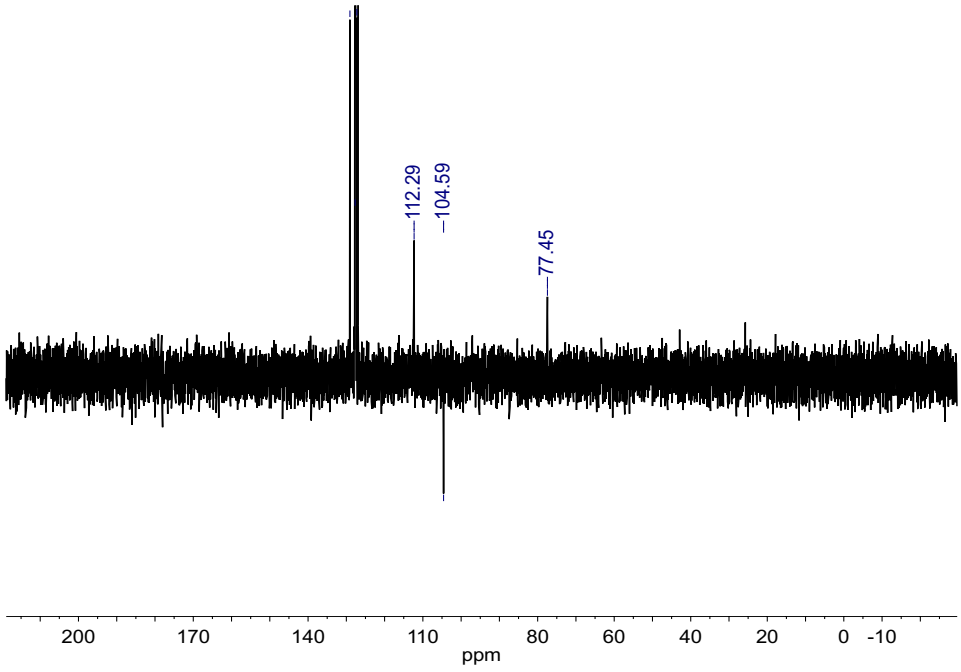

Figure A.97: DEPT-135 NMR spectrum of **76**.

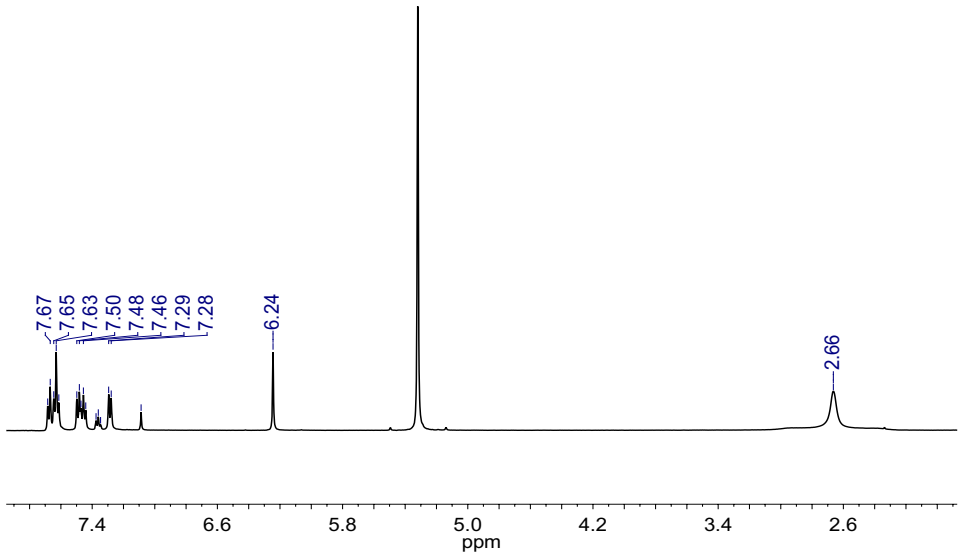

Figure A.98: ^{1}H $\{^{11}$B$\}$ NMR spectrum of **76**.

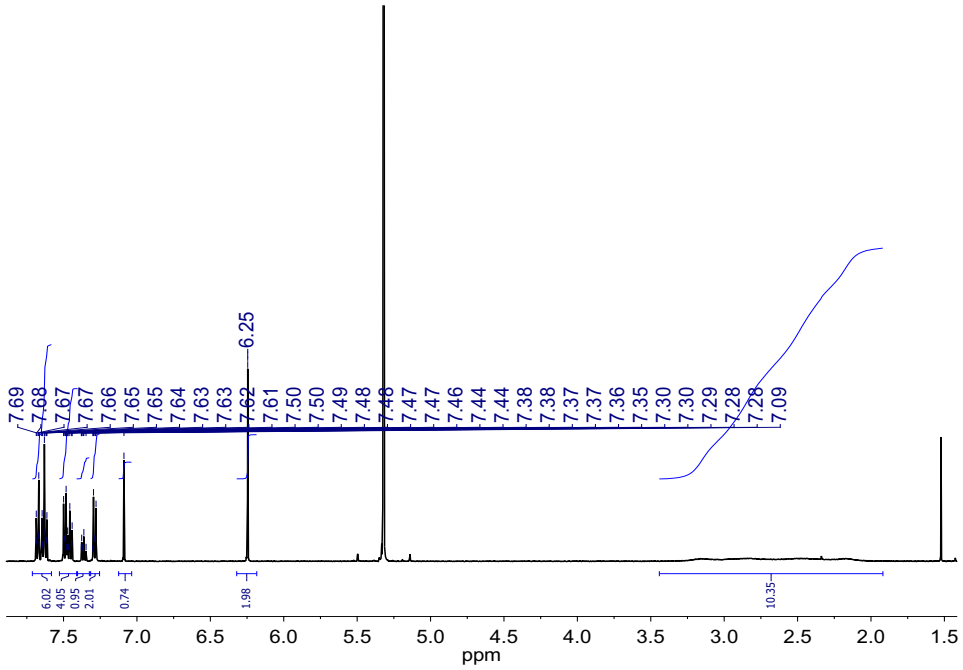

Figure A.99: ^{1}H NMR spectrum of **76**.

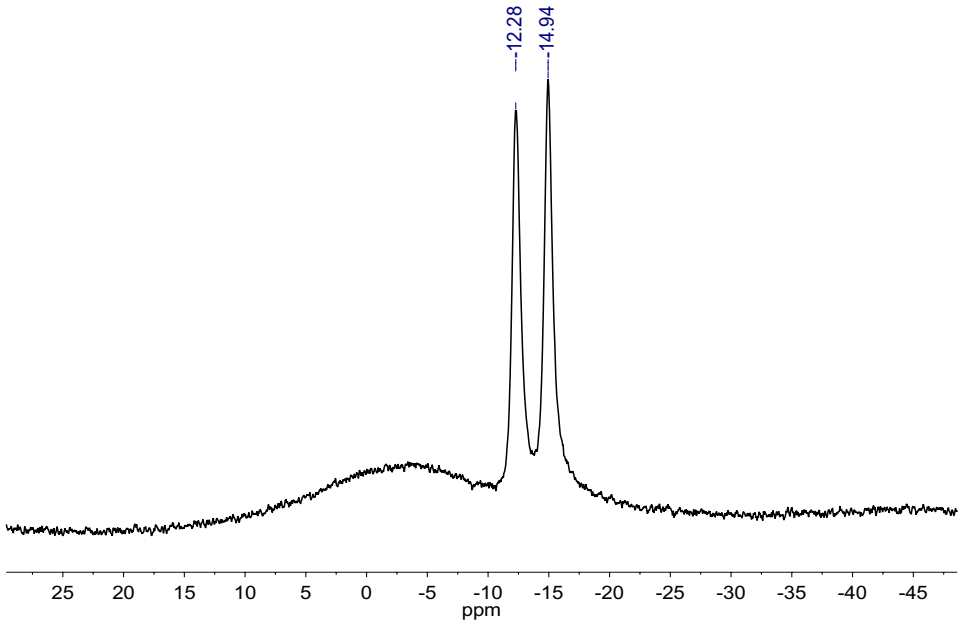

Figure A.100: ^{11}B{^{1}H } NMR spectrum of **77**.

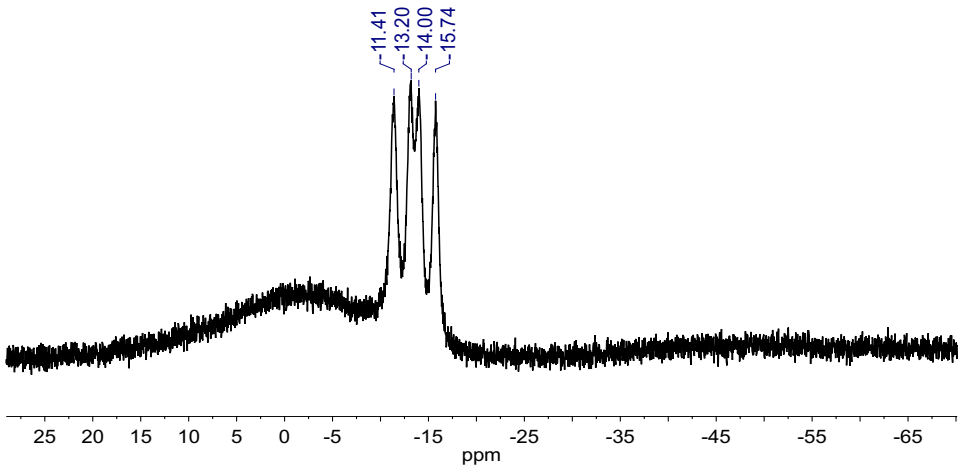

Figure A.101: ^{11}B NMR spectrum of **77**.

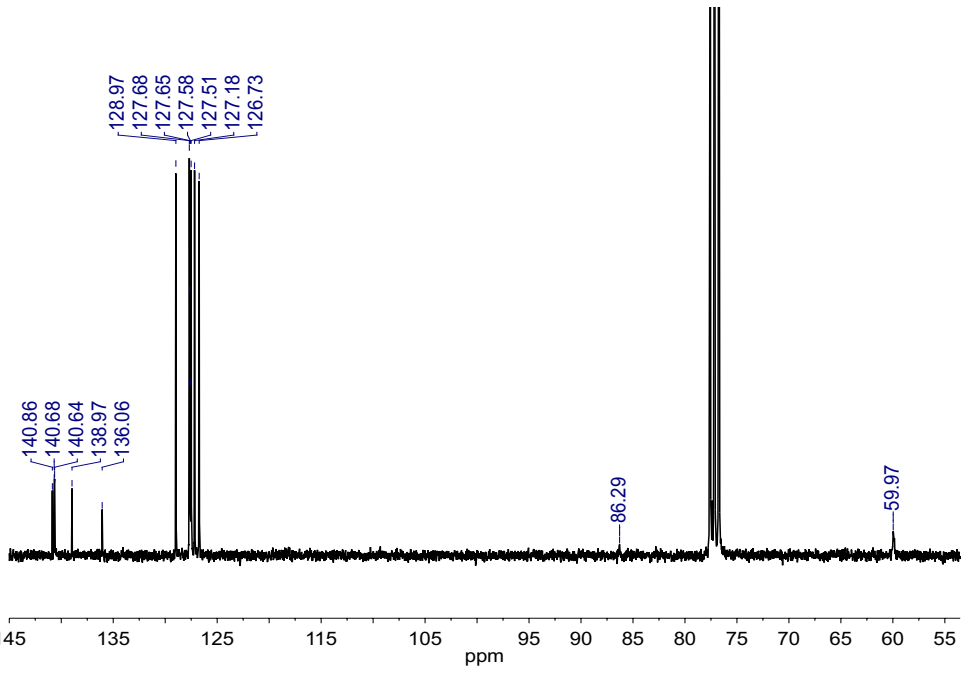

Figure A.102: ^{13}C NMR spectrum of **77**.

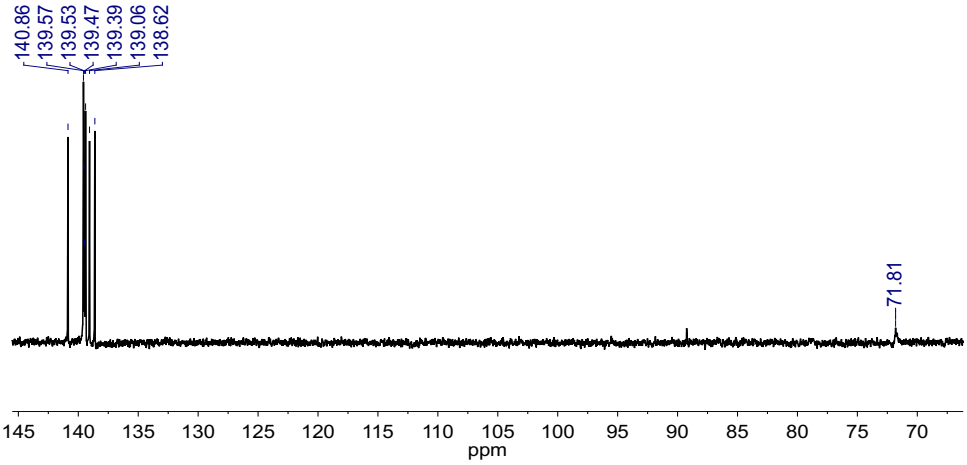

Figure A.103: DEPT-135 NMR spectrum of **77**.

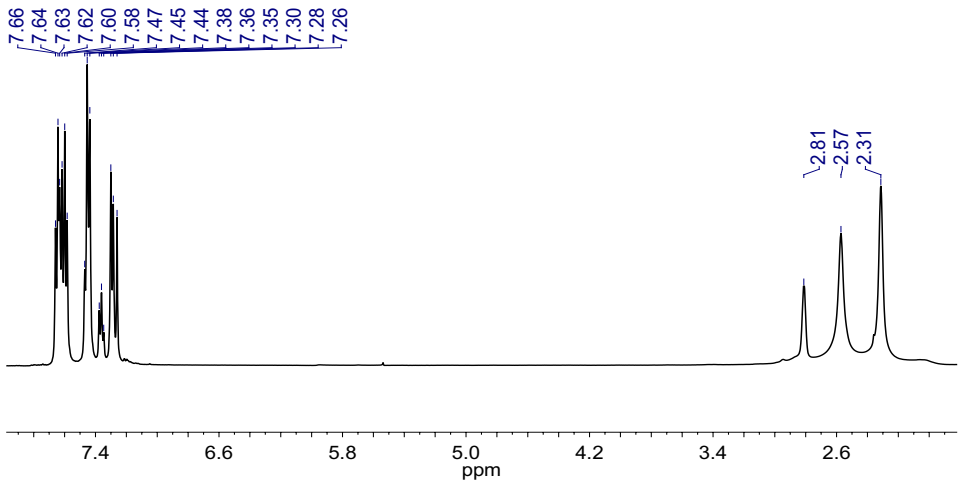

Figure A.104: ^{1}H $\{^{11}$B$\}$ NMR spectrum of **77**.

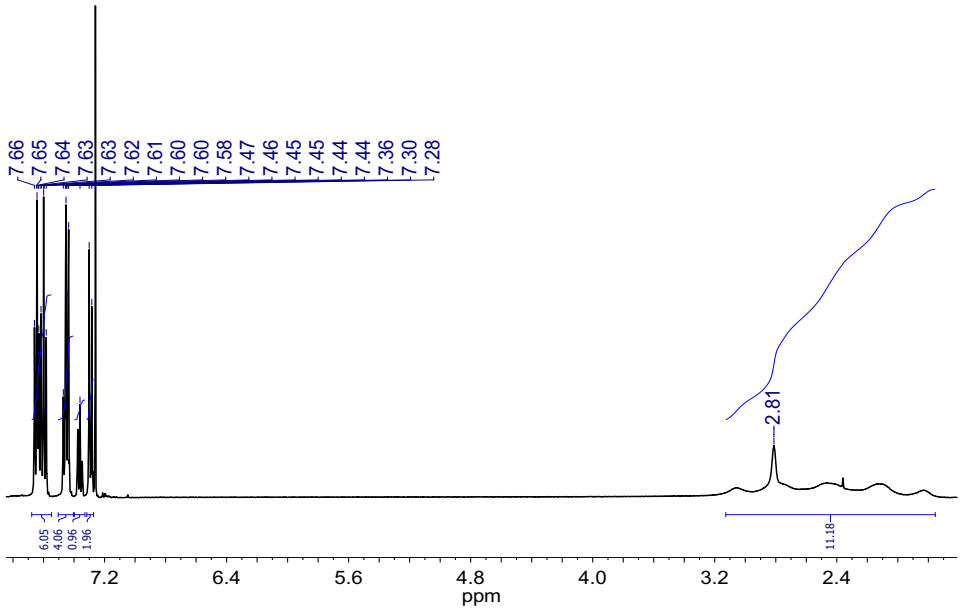

Figure A.105: ^{1}H NMR spectrum of **77**.

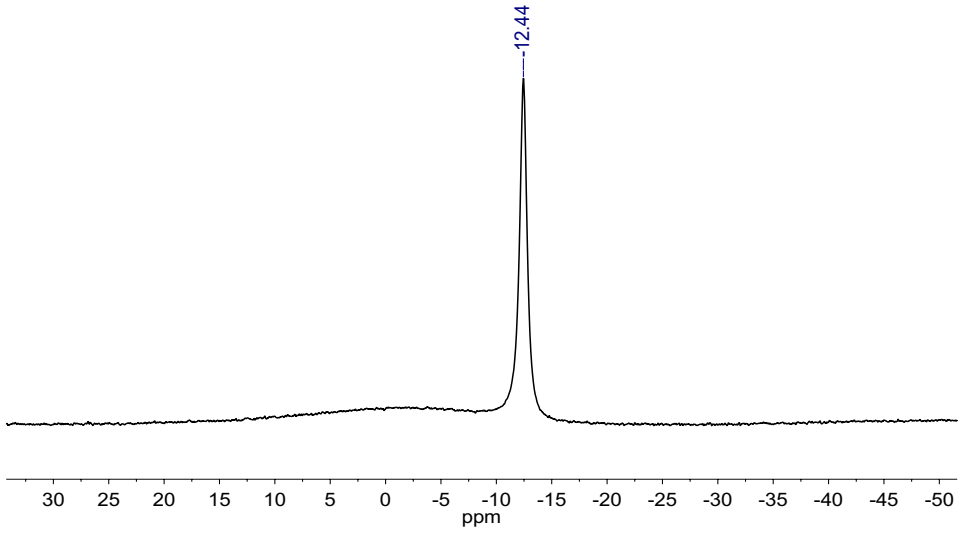

Figure A.106: ^{11}B{^{1}H } NMR spectrum of **79**.

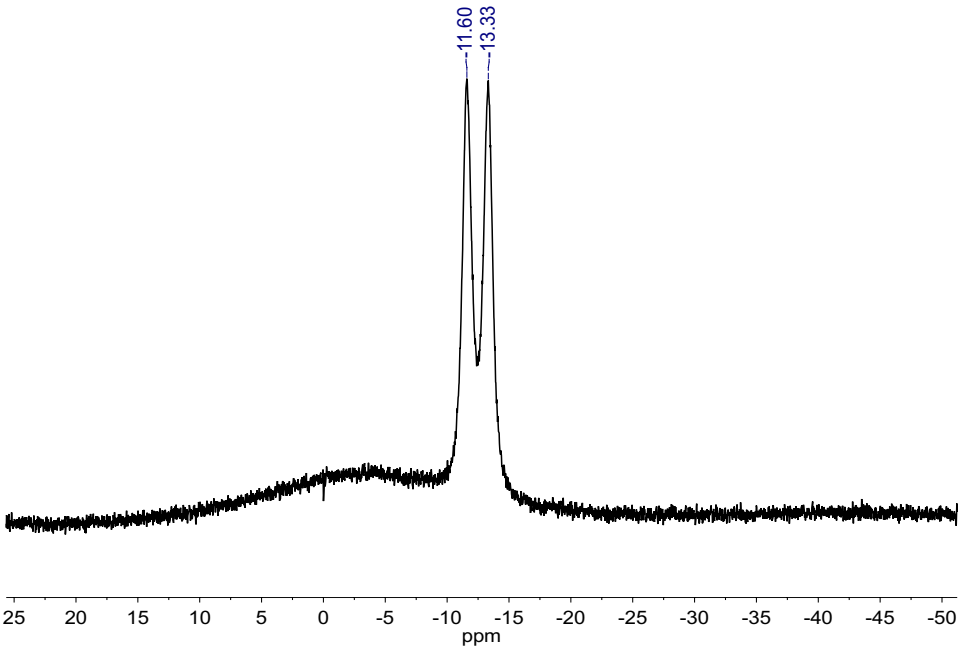

Figure A.107: ^{11}B NMR spectrum of **79**.

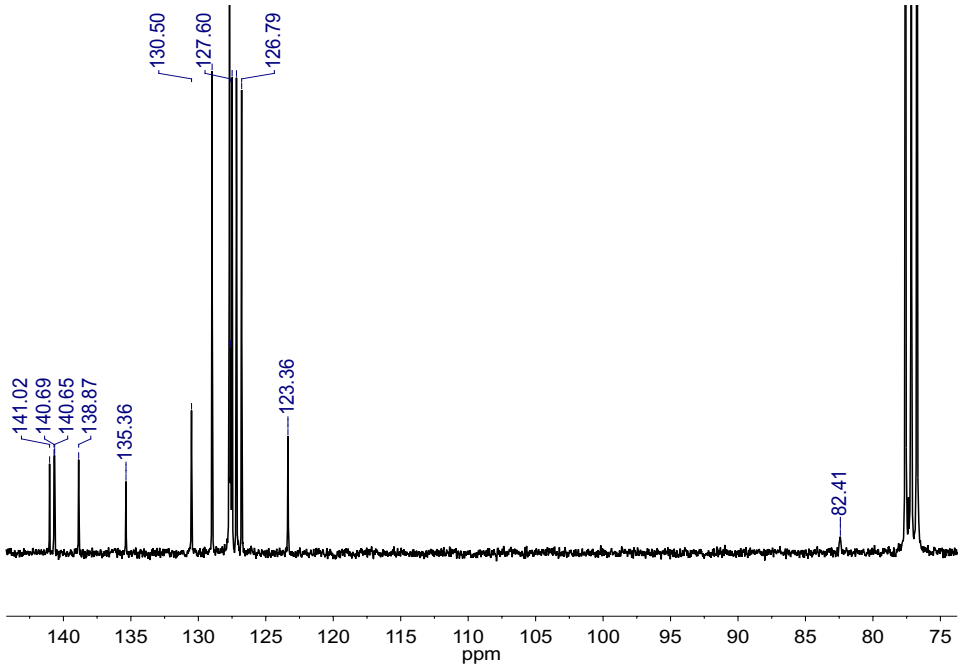

Figure A.108: ^{13}C NMR spectrum of **79**.

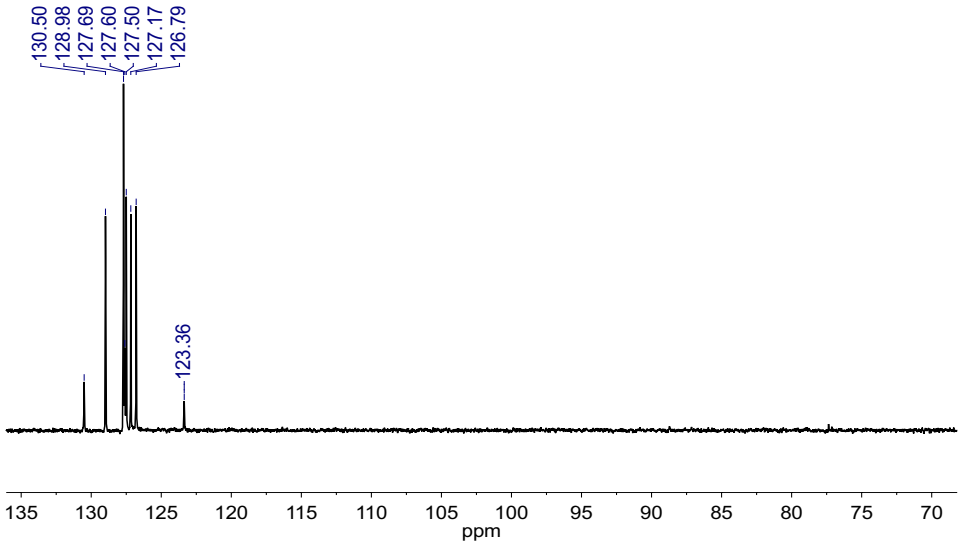

Figure A.109: DEPT-135 NMR spectrum of **79**.

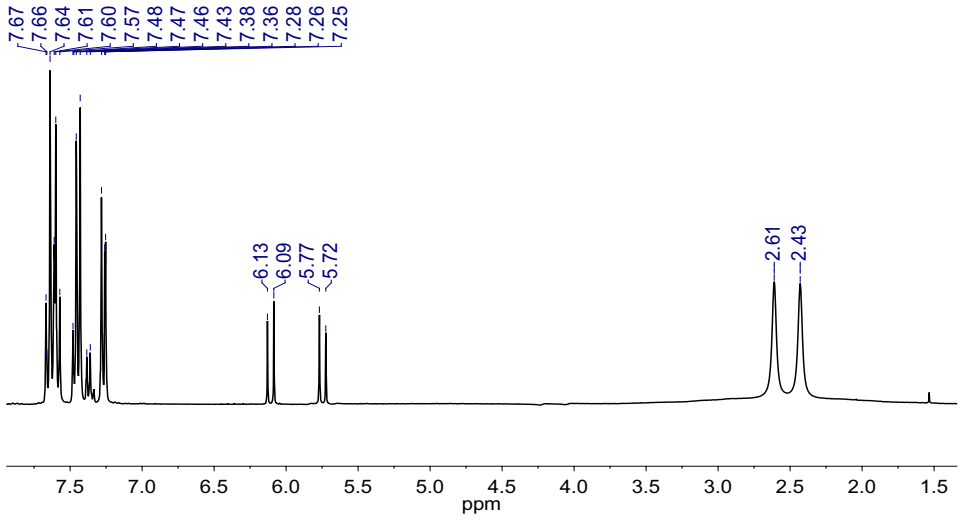

Figure A.110: ^{1}H $\{^{11}$B$\}$ NMR spectrum of **79**.

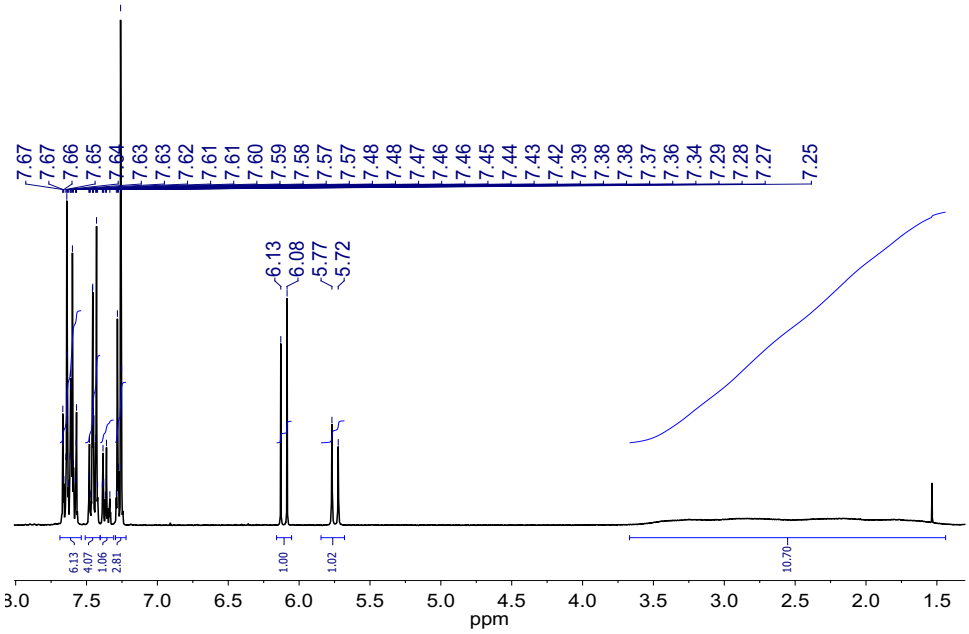

Figure A.111: ^{1}H NMR spectrum of **79**.

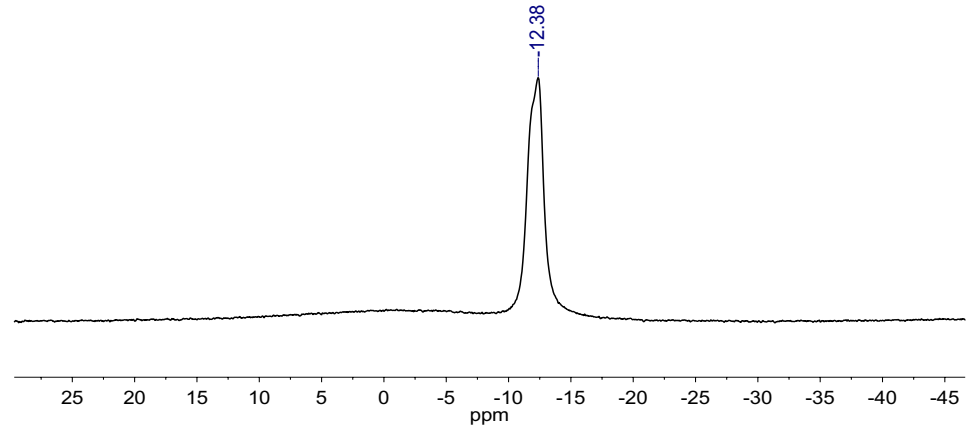

Figure A.112: ^{11}B{^{1}H } NMR spectrum of **80**.

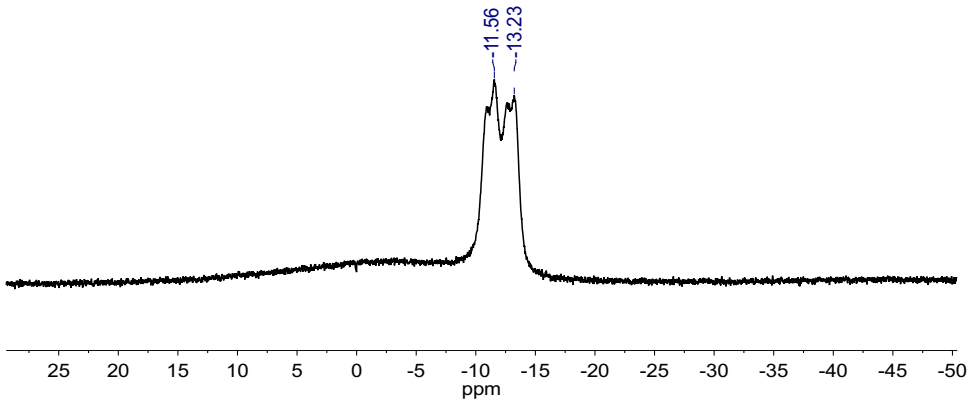

Figure A.113: ^{11}B NMR spectrum of **80**.

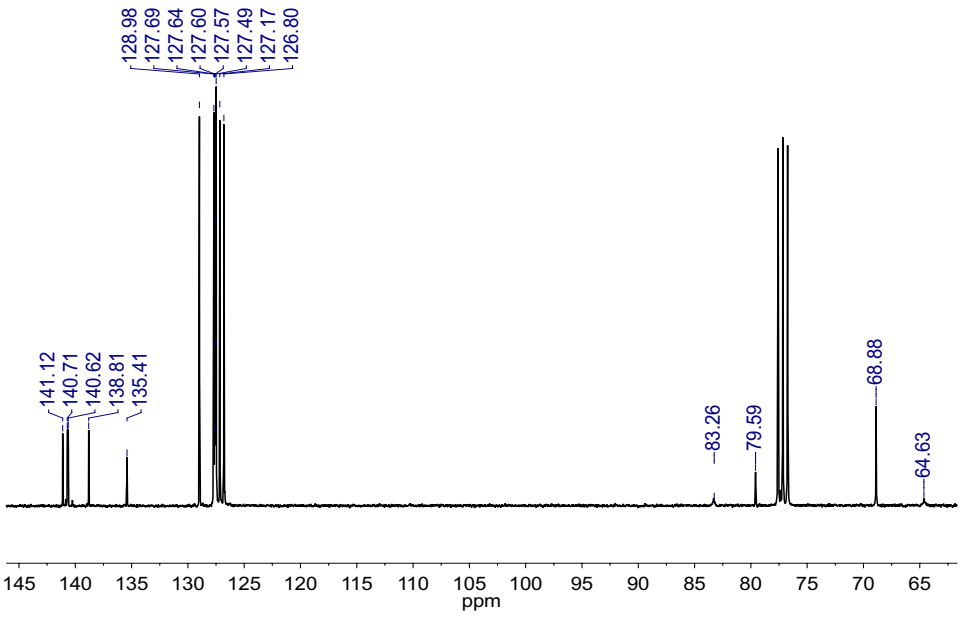

Figure A.114: ^{13}C NMR spectrum of **80**.

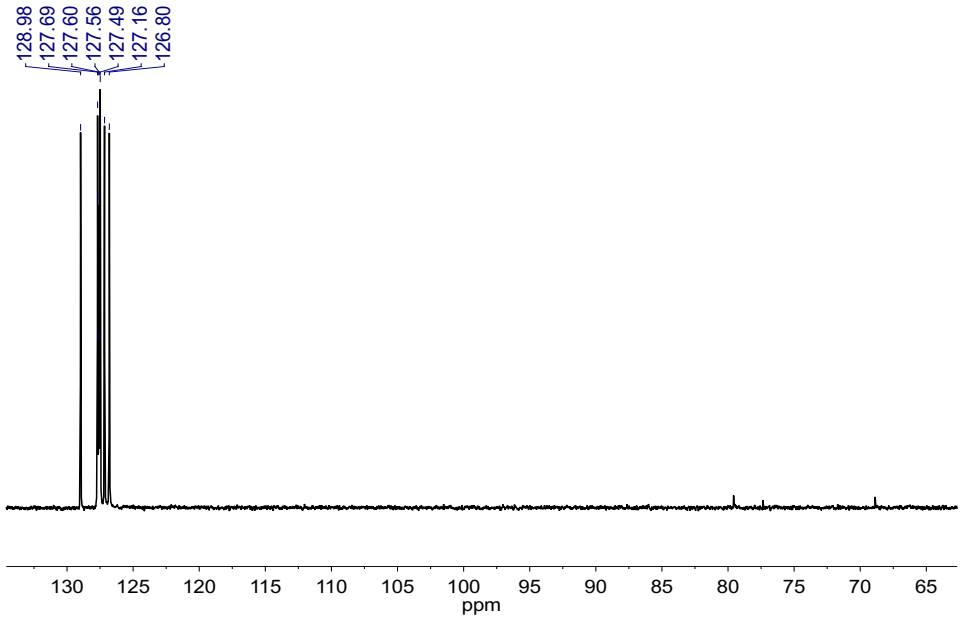

Figure A.115: DEPT-135 NMR spectrum of **80**.

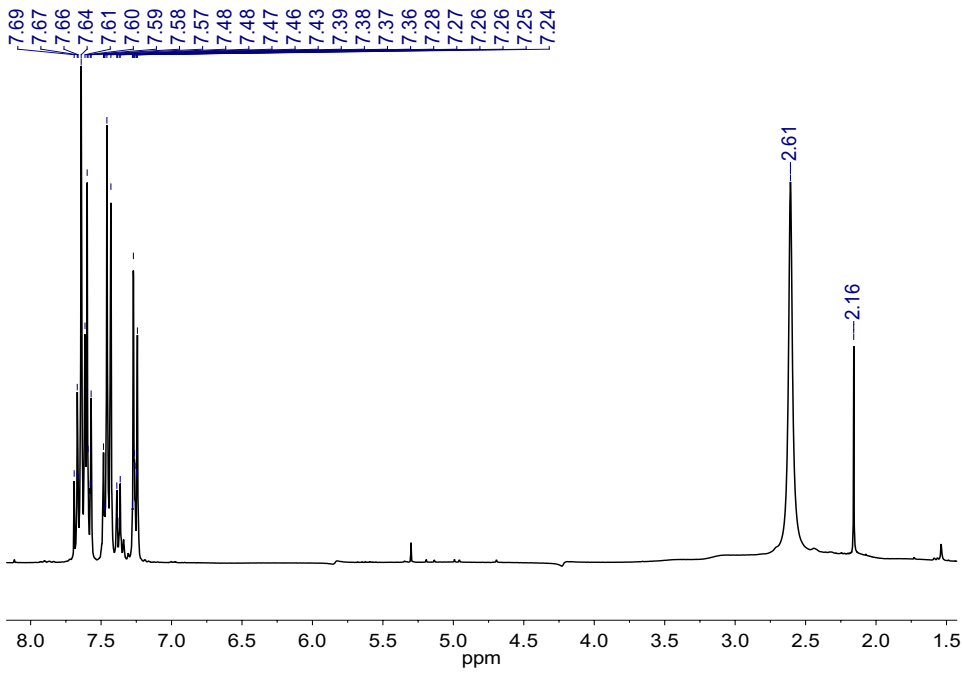

Figure A.116: ^{1}H $\{^{11}$B$\}$ NMR spectrum of **80**.

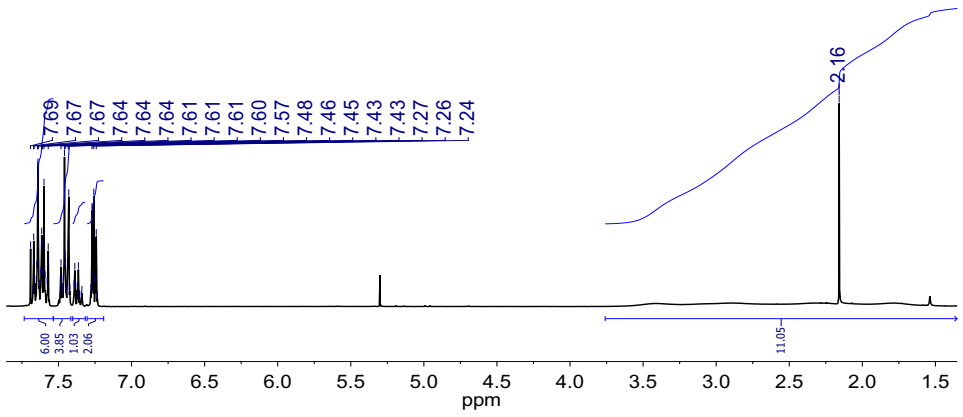

Figure A.117: ^{1}H NMR spectrum of **80**.

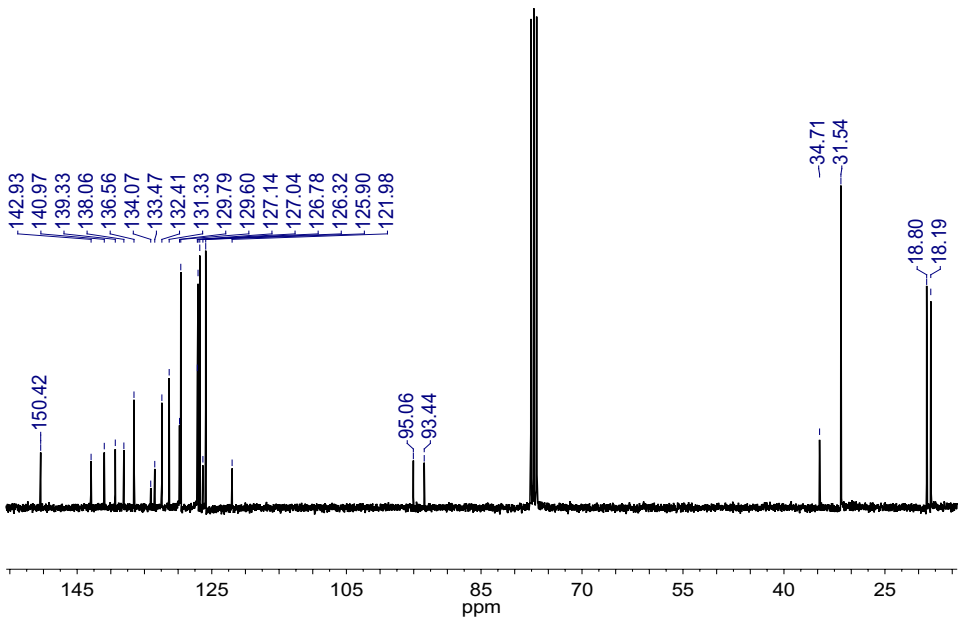

Figure A.118: ^{13}C NMR spectrum of **83**.

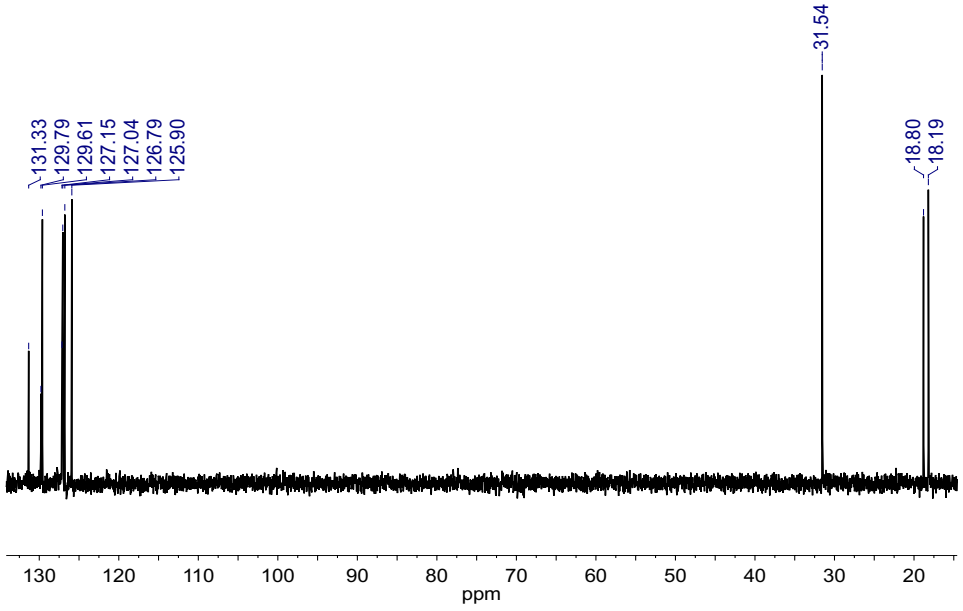

Figure A.119: DEPT-135 NMR spectrum of **83**.

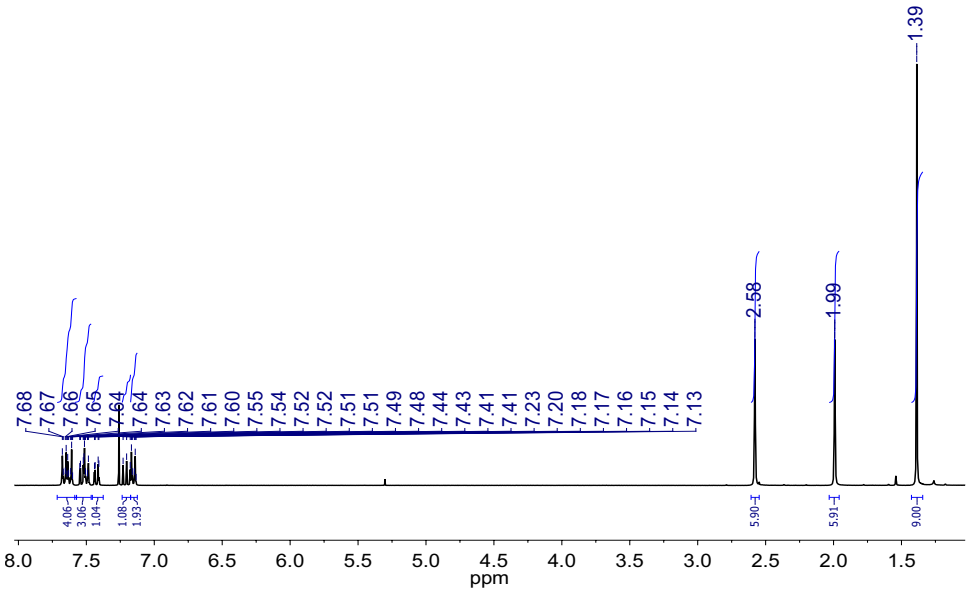

Figure A.120: ^{1}H NMR spectrum of **83**.

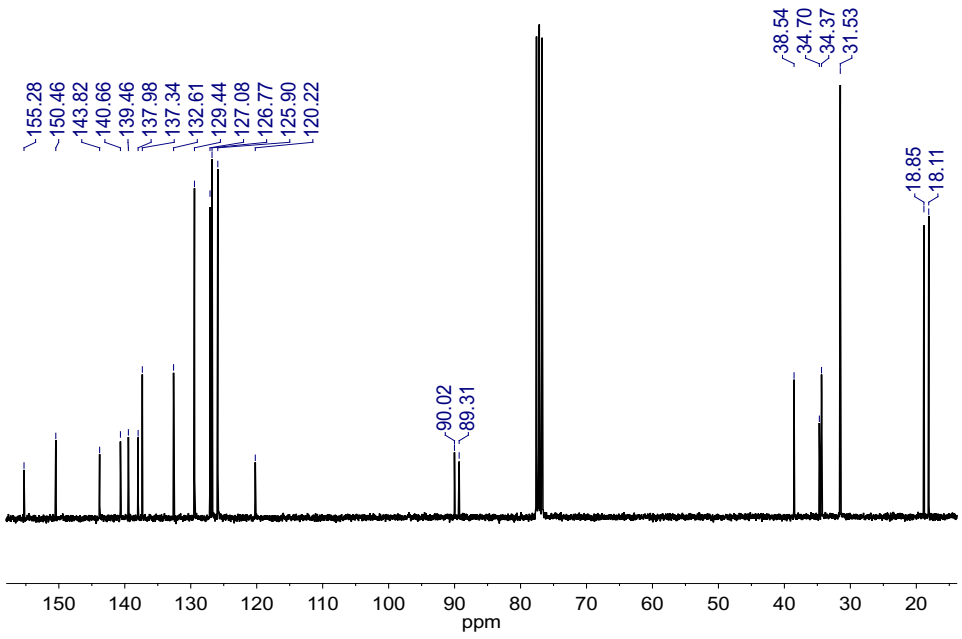

Figure A.121: ^{13}C NMR spectrum of **84**.

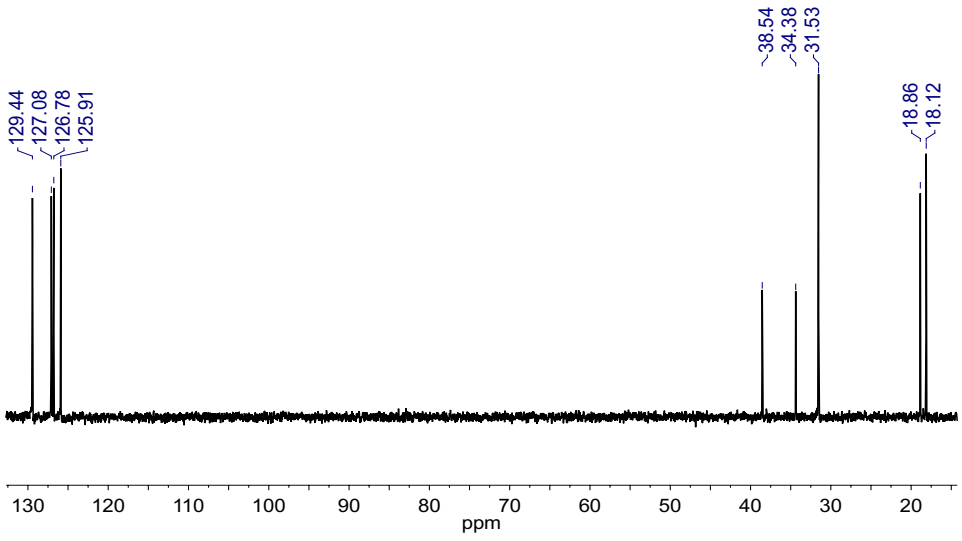

Figure A.122: DEPT-135 NMR spectrum of **84**.

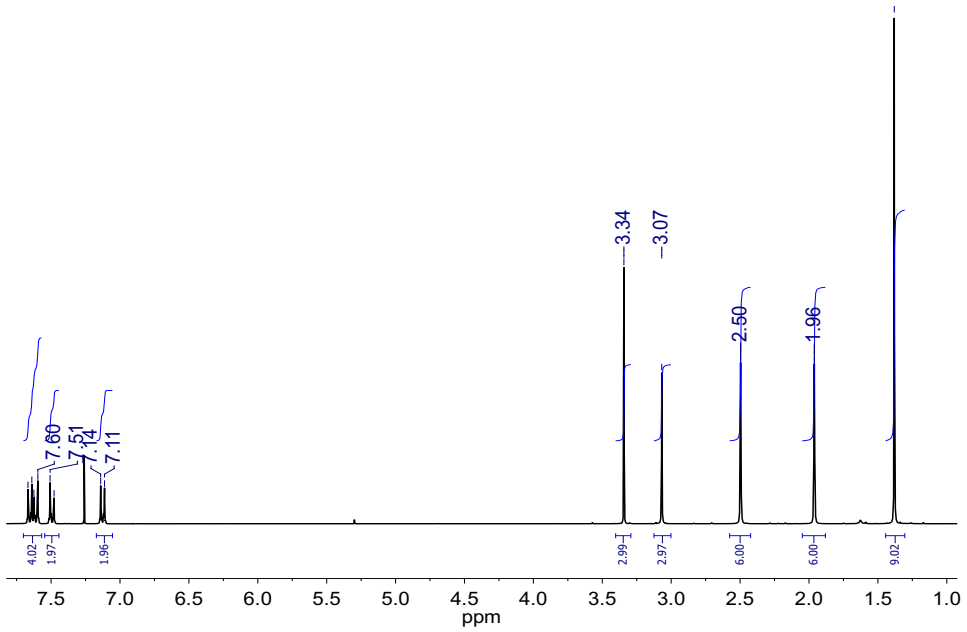

Figure A.123: ^{1}H NMR spectrum of **84**.

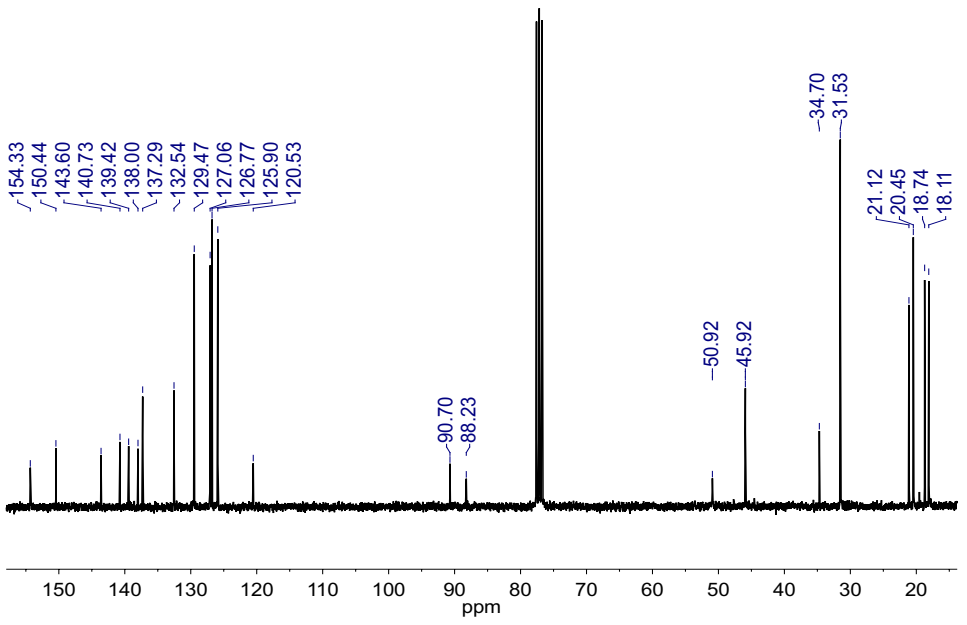

Figure A.124: ^{13}C NMR spectrum of **85**.

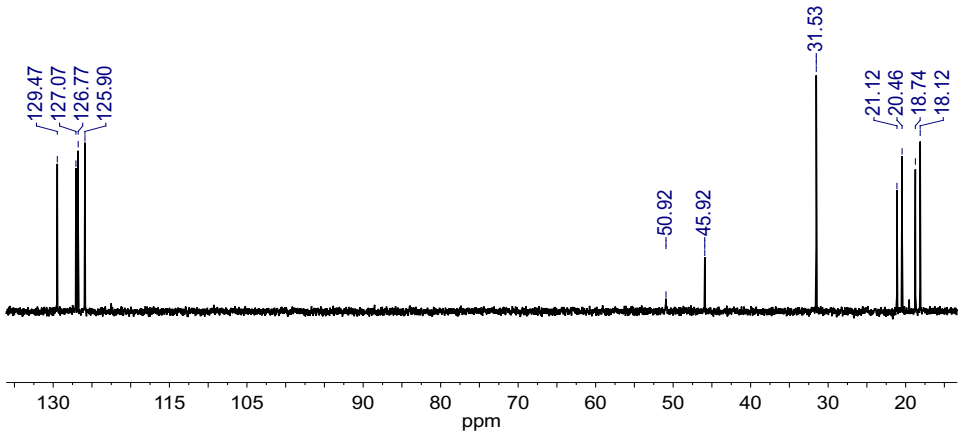

Figure A.125: DEPT-135 NMR spectrum of **85**.

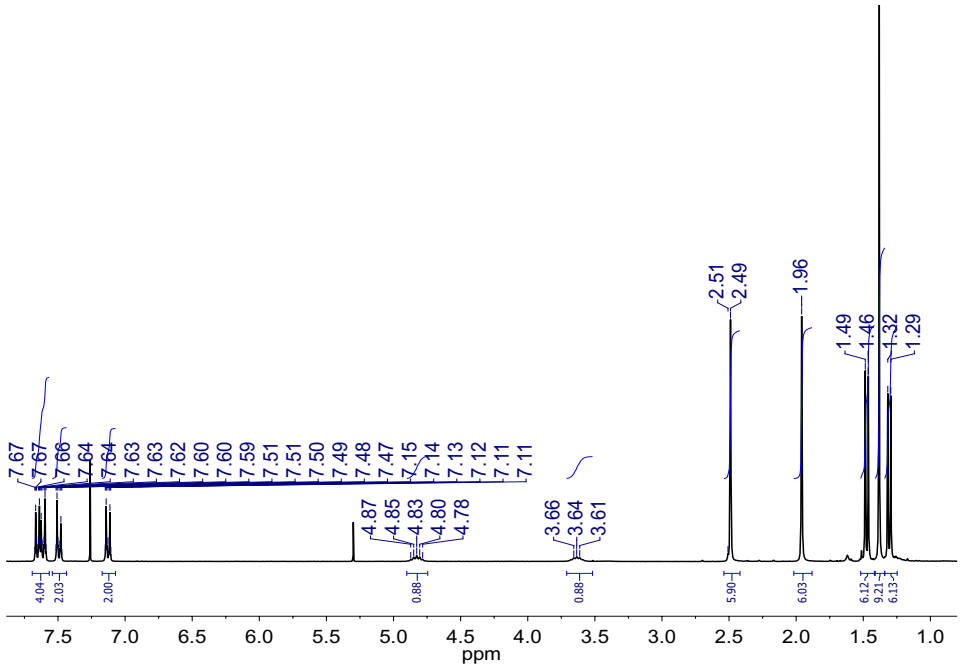

Figure A.126: ^{1}H NMR spectrum of **85**.

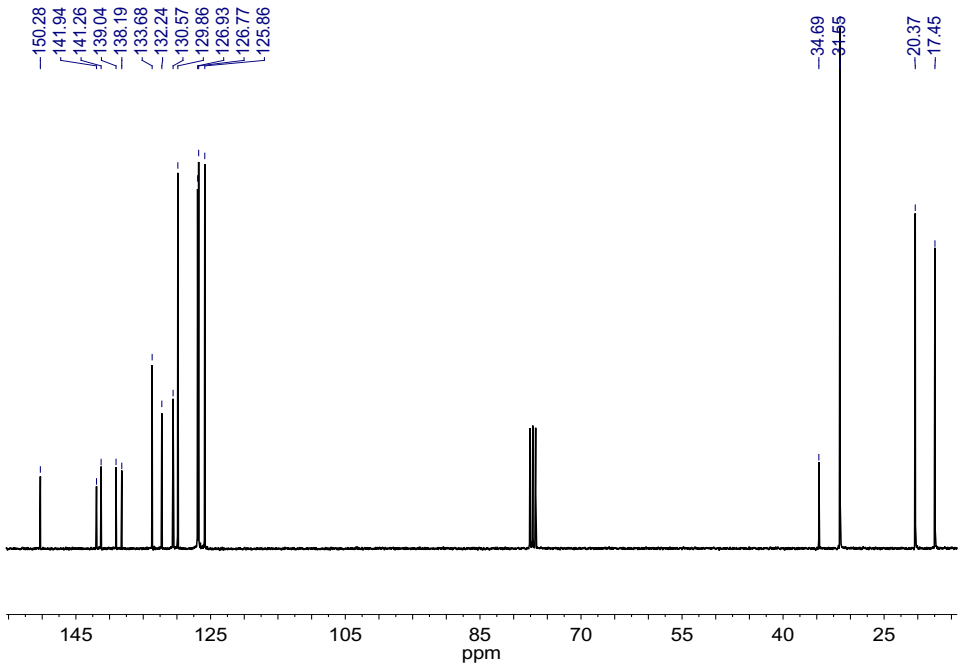

Figure A.127: ^{13}C NMR spectrum of **86**.

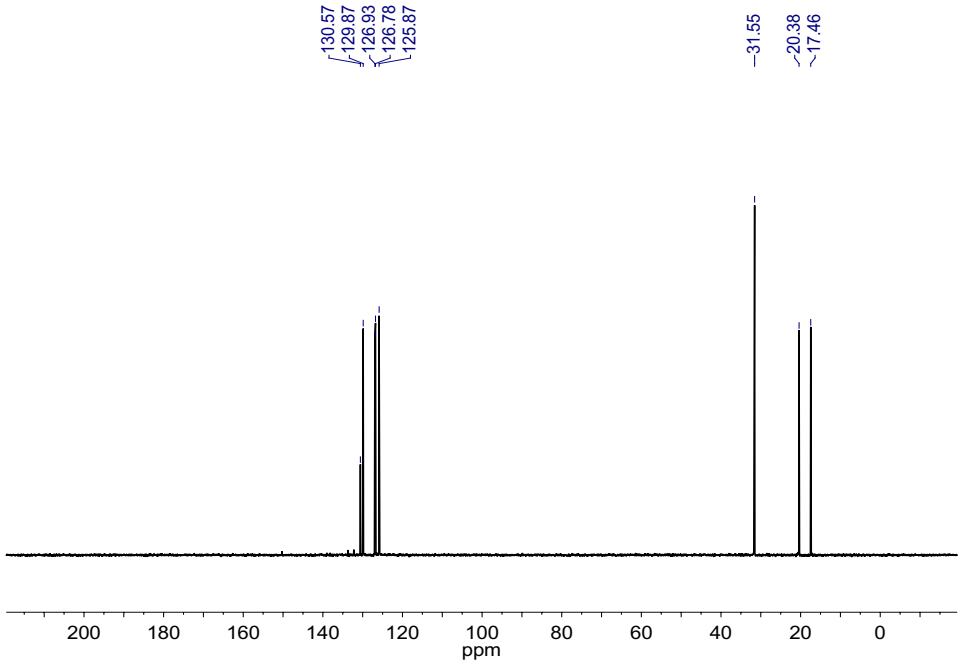

Figure A.128: DEPT-135 NMR spectrum of **86**.

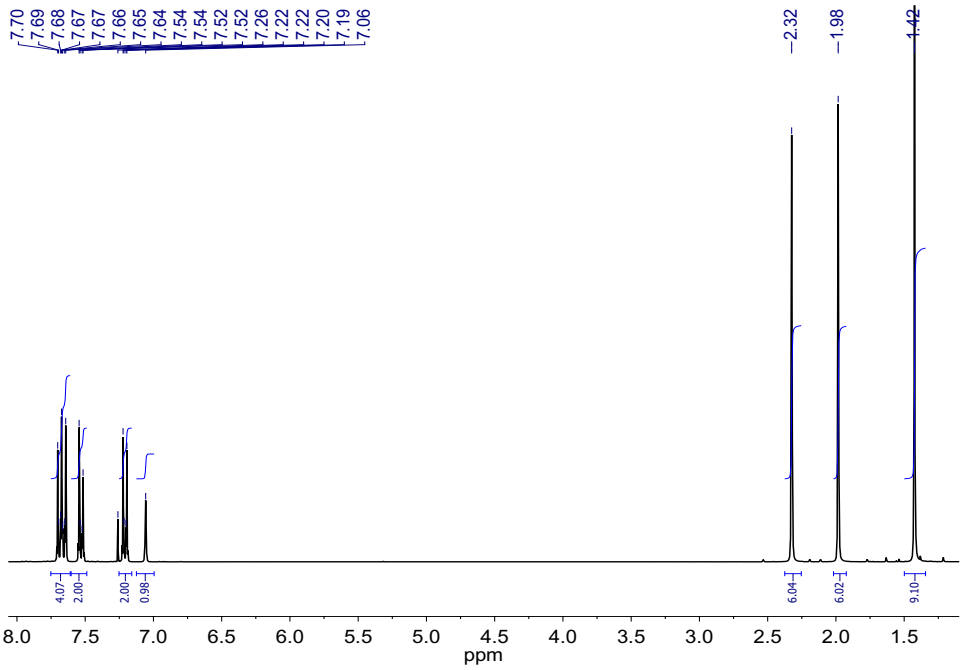

Figure A.129: ^{1}H NMR spectrum of **86**.

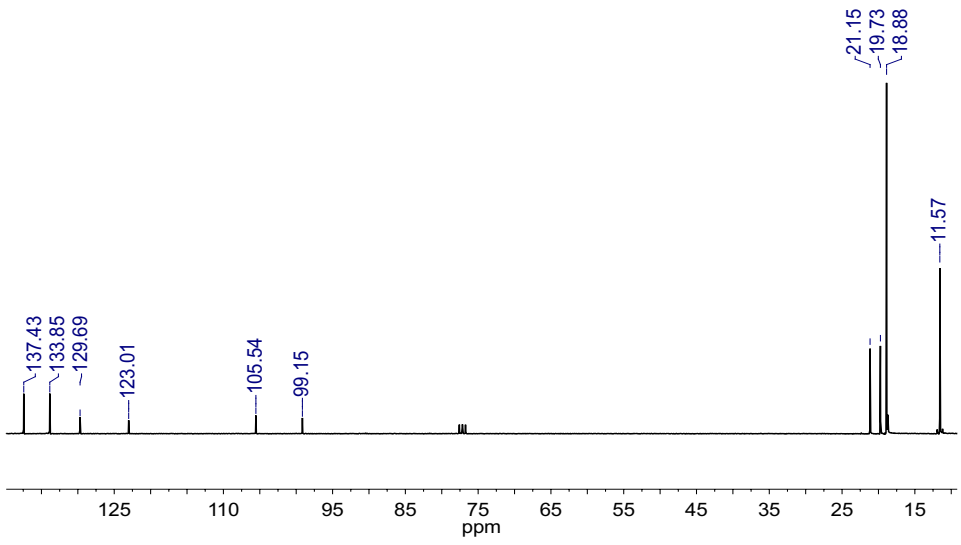

Figure A.130: ^{13}C NMR spectrum of **88**.

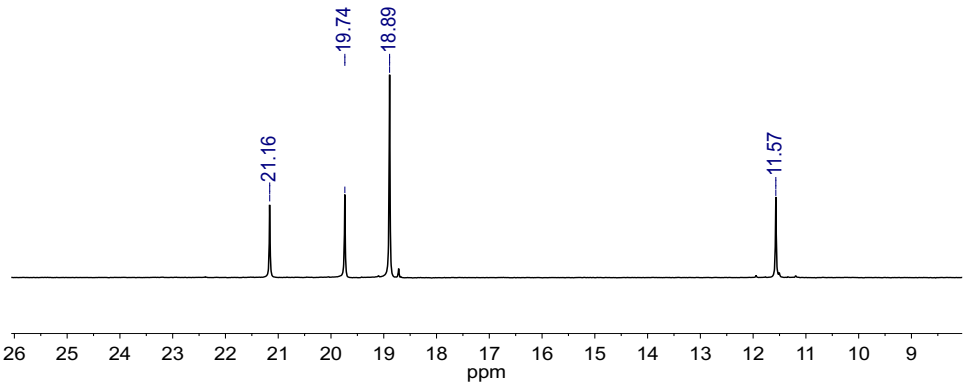

Figure A.131: DEPT-135 NMR spectrum of **88**.

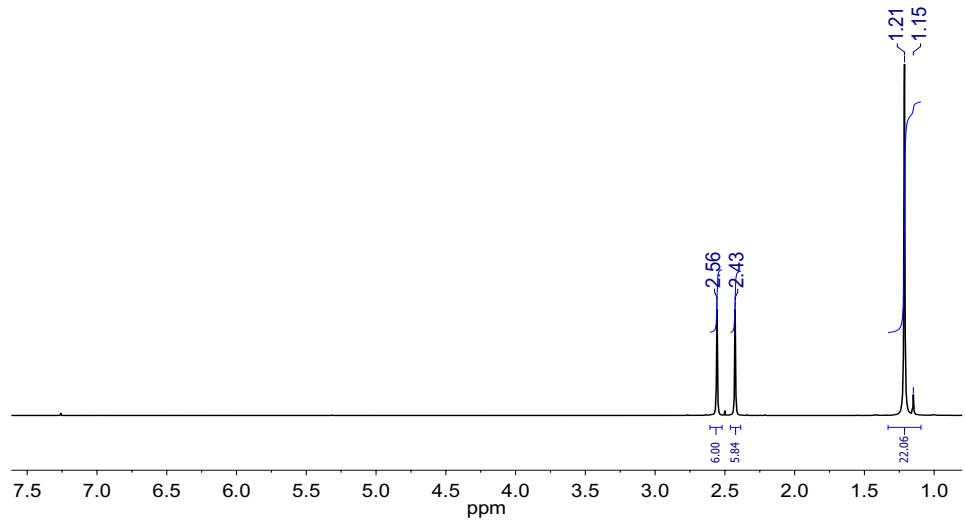

Figure A.132: ^{1}H NMR spectrum of **88**.

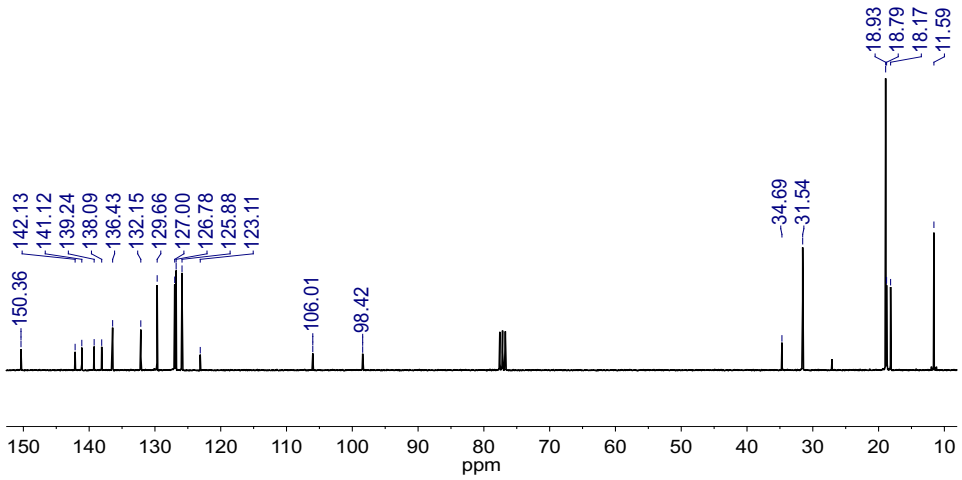

Figure A.133: ^{13}C NMR spectrum of **89**.

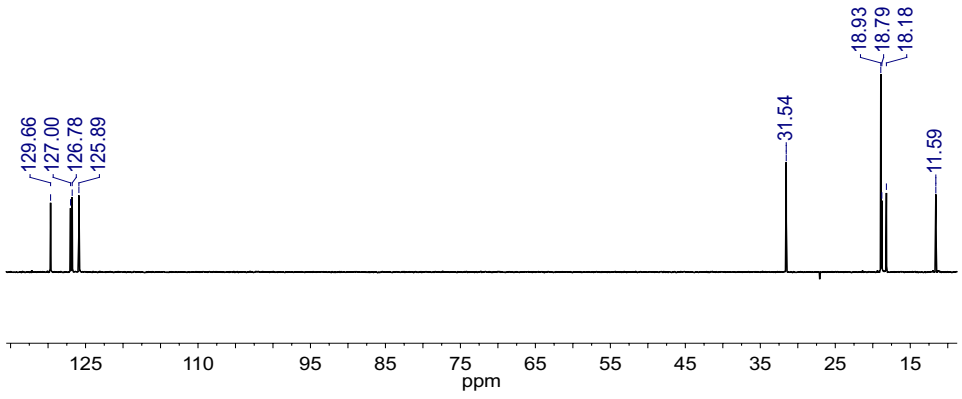

Figure A.134: DEPT-135 NMR spectrum of **89**.

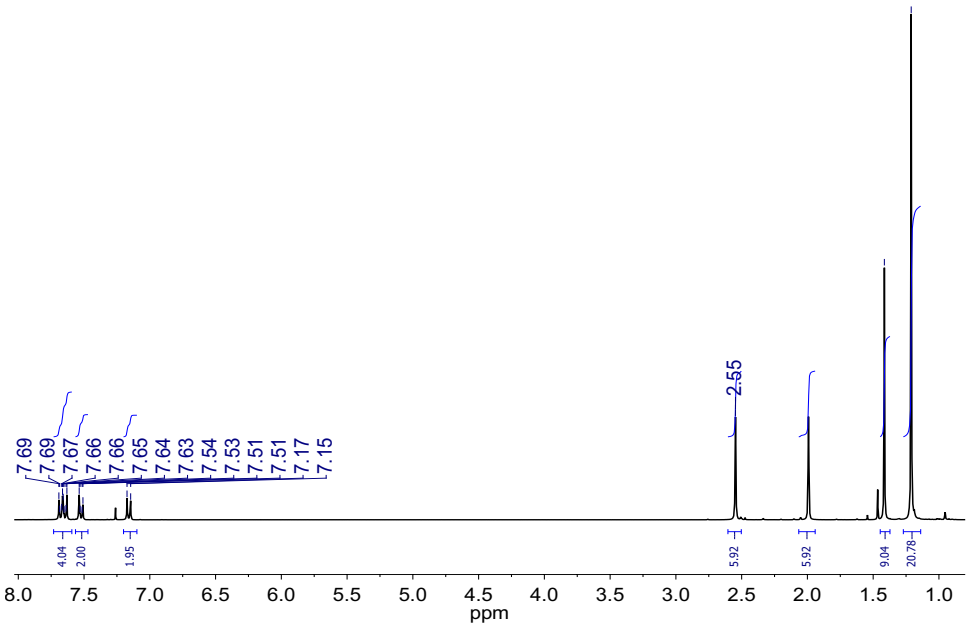

Figure A.135: ^{1}H NMR spectrum of **89**.

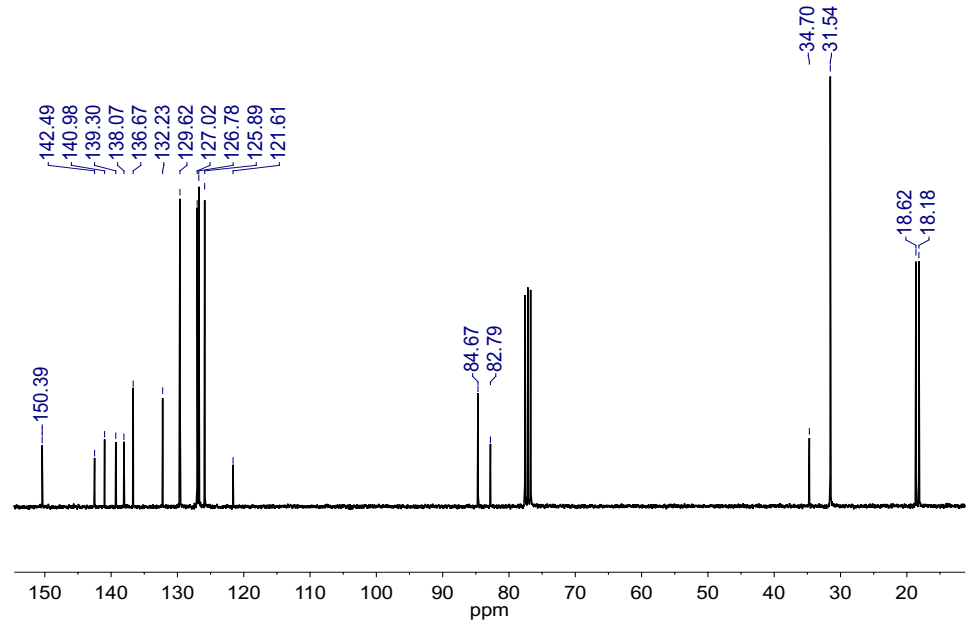

Figure A.136: ^{13}C NMR spectrum of **90**.

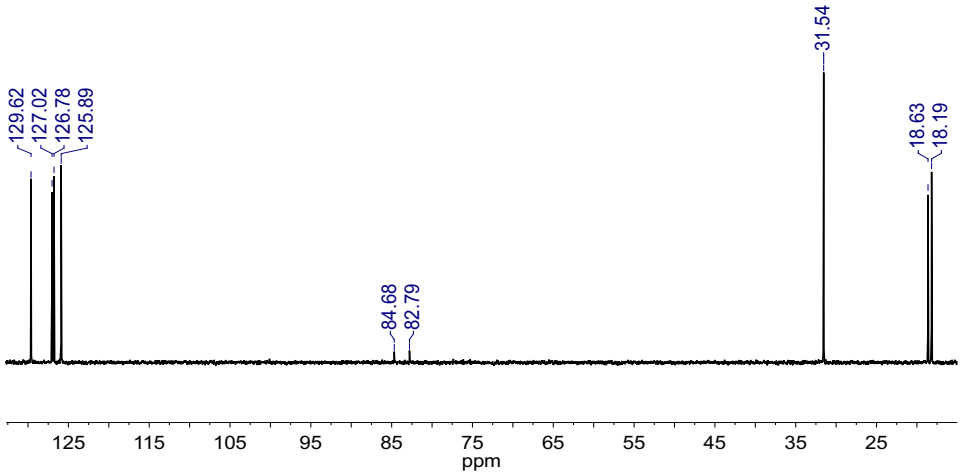

Figure A.137: DEPT-135 NMR spectrum of **90**.

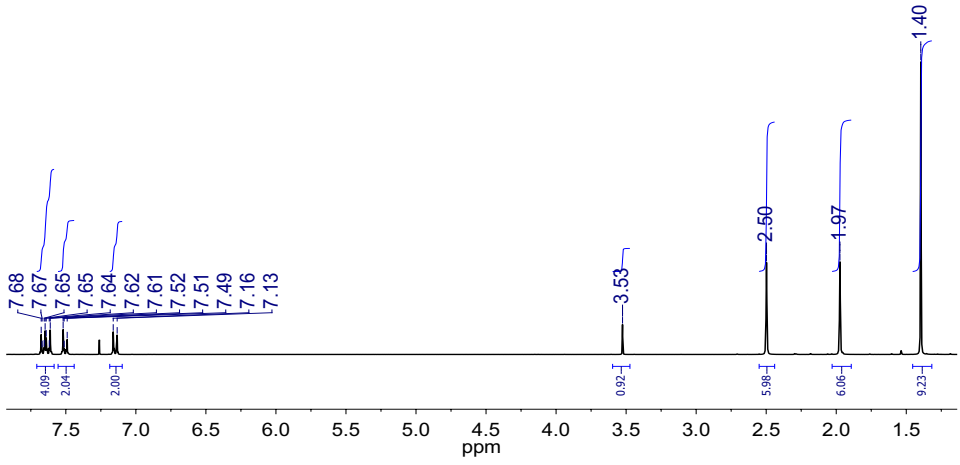

Figure A.138: ^{1}H NMR spectrum of **90**.

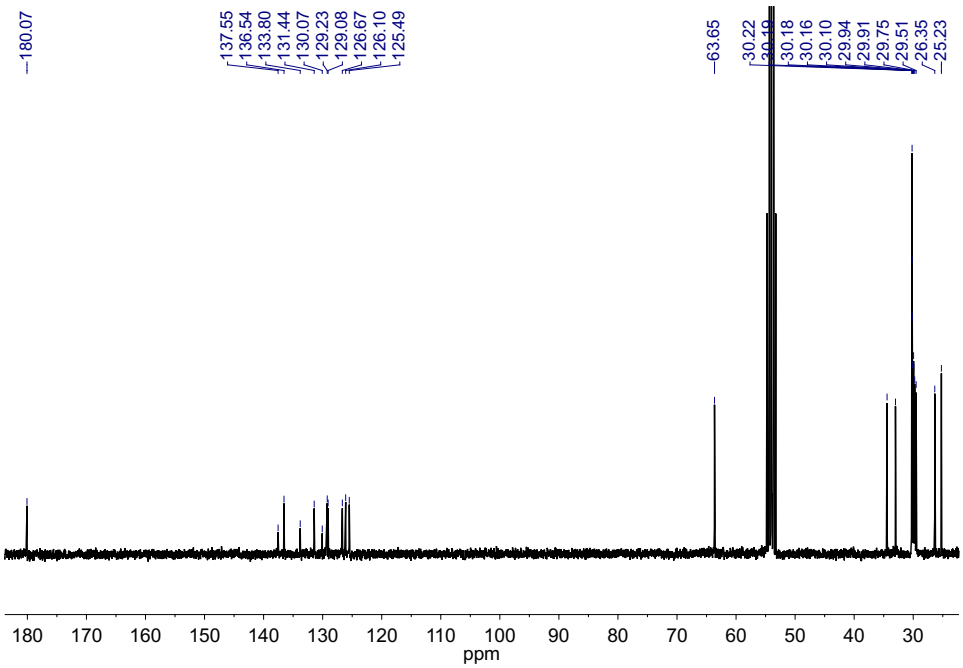

Figure A.139: ^{13}C NMR spectrum of **91**.

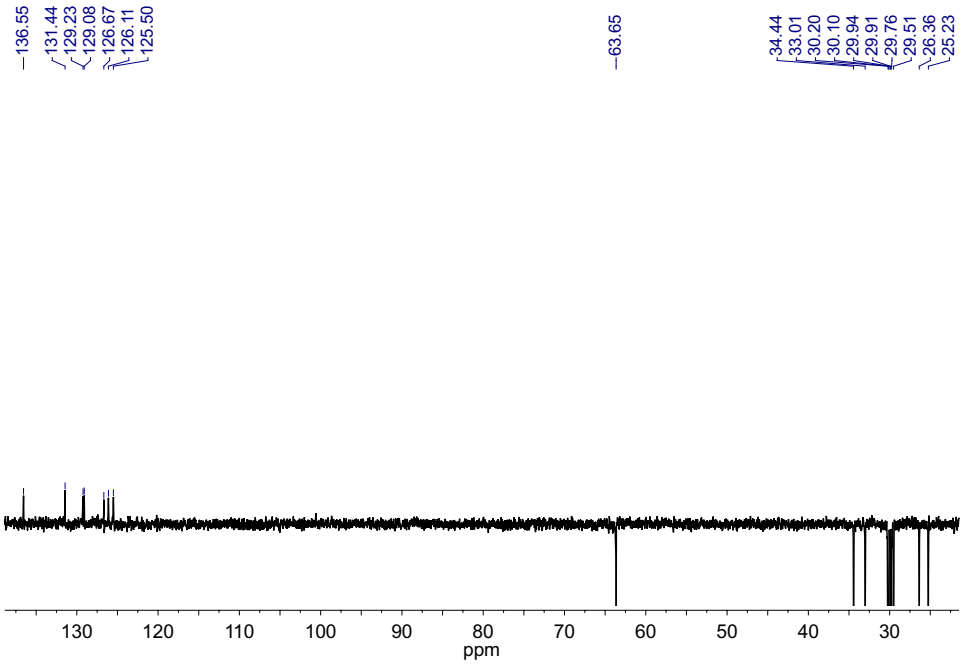

Figure A.140: DEPT-135 NMR spectrum of **91**.

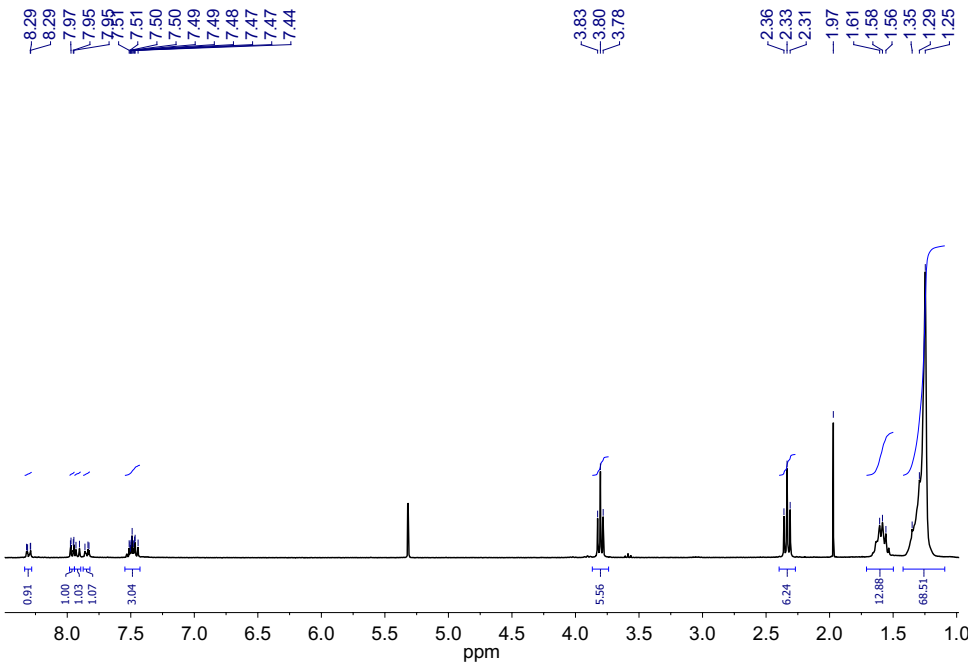

Figure A.141: ^{1}H NMR spectrum of **91**.

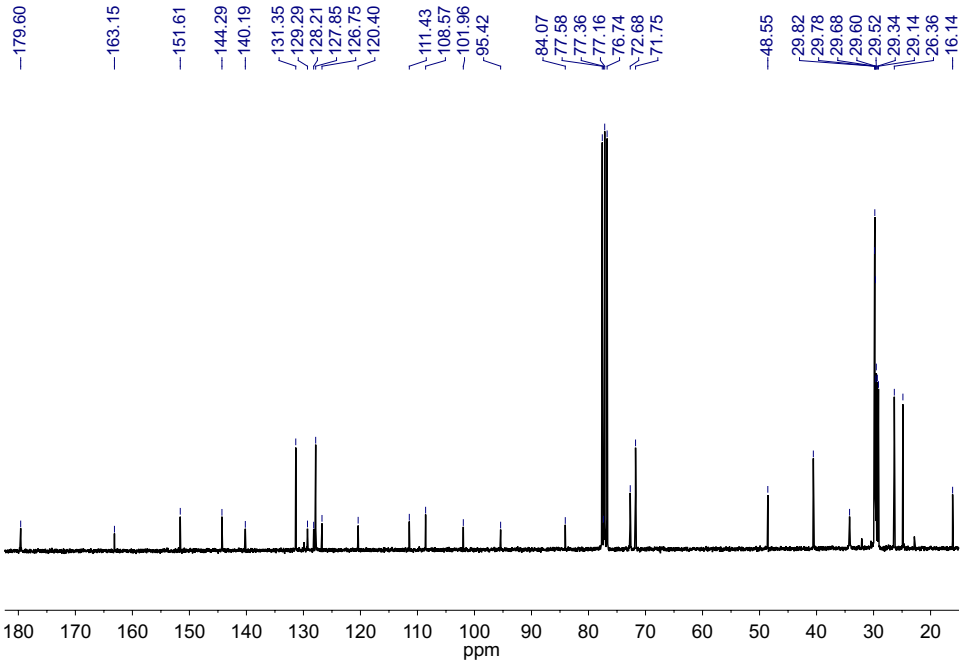

Figure A.142: ^{13}C NMR spectrum of **93**.

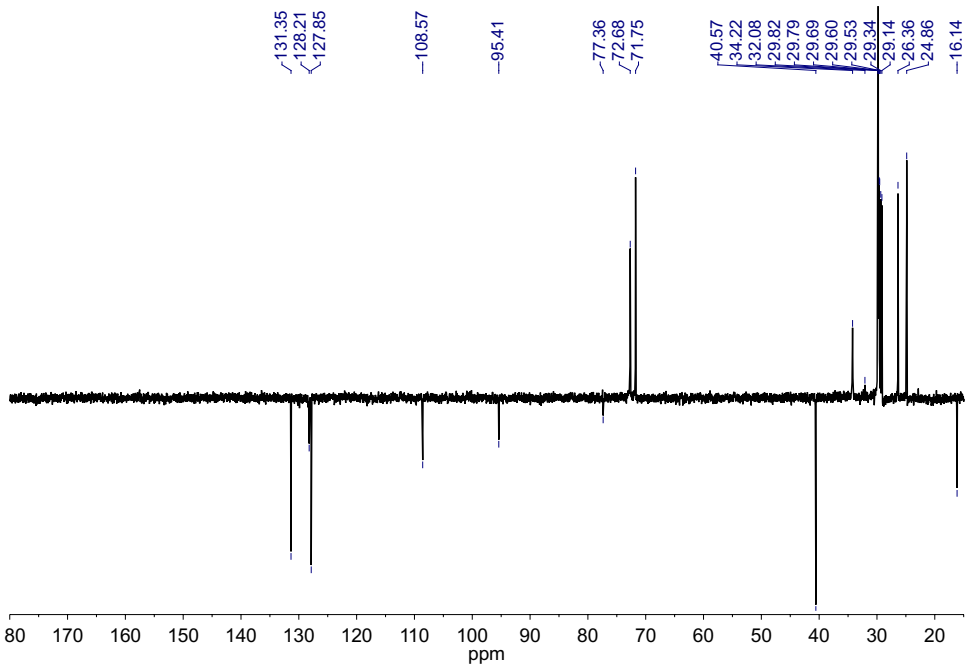

Figure A.143: DEPT-135 NMR spectrum of **93**.

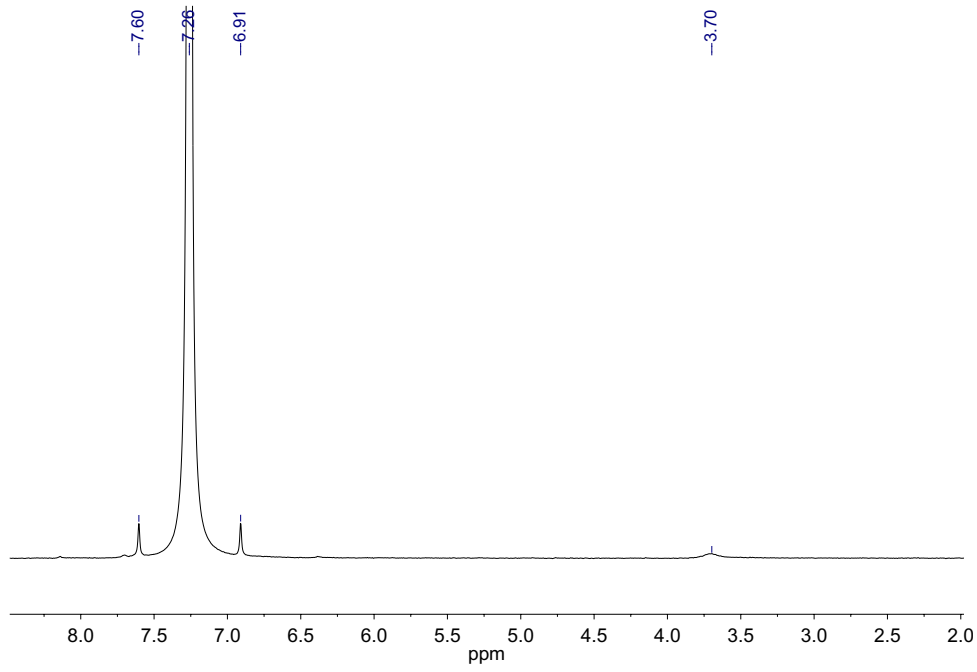

Figure A.144: ^{2}D NMR spectrum of **93**.

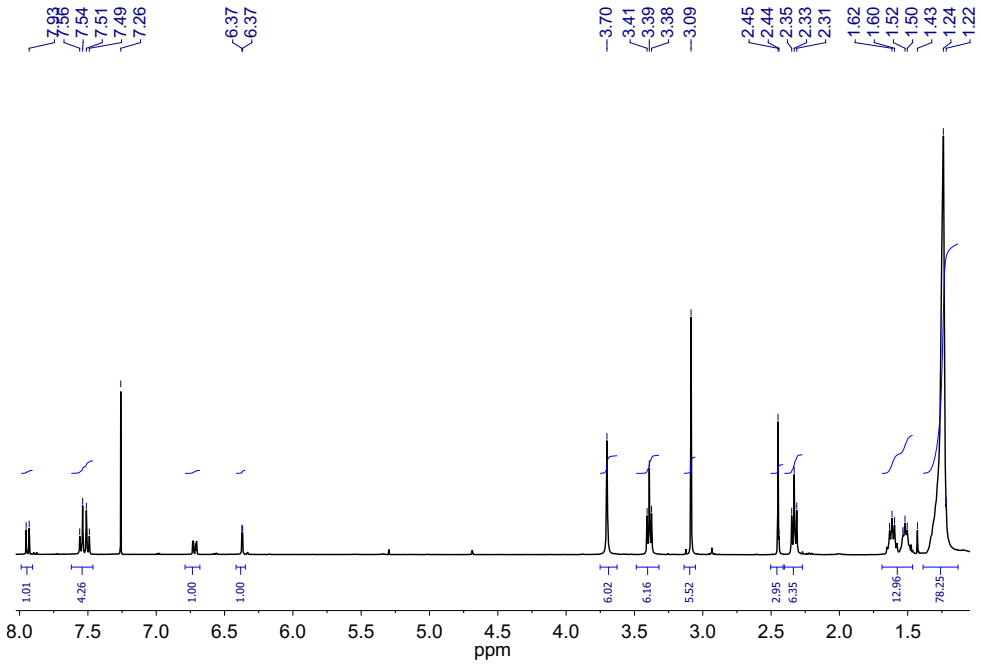

Figure A.145: ^{1}H NMR spectrum of **93**.

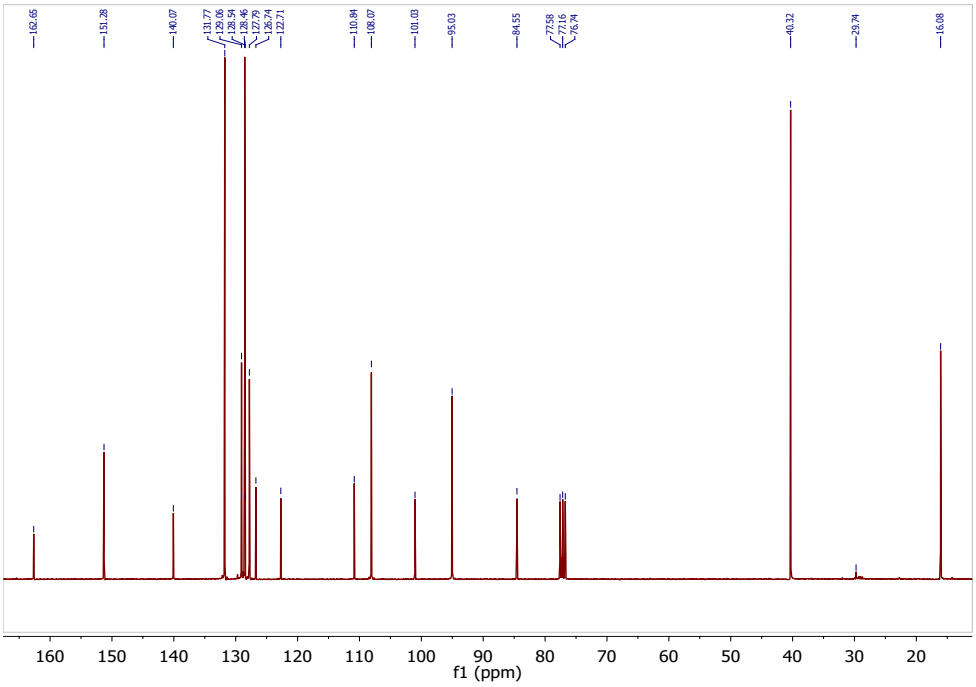

Figure A.146: ^{13}C NMR spectrum of **94**.

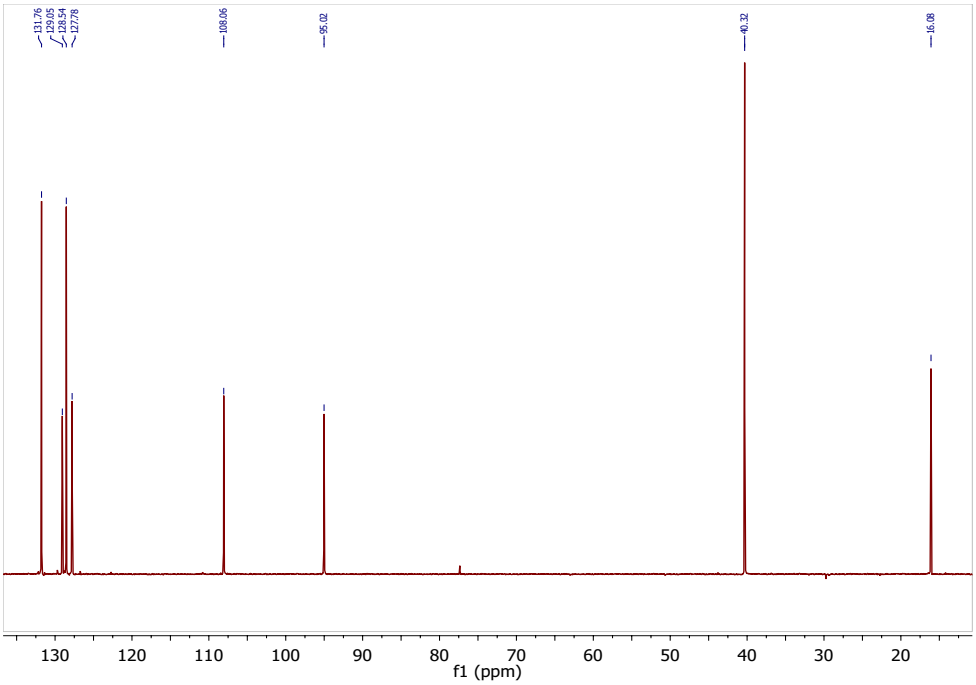

Figure A.147: DEPT-135 NMR spectrum of **94**.

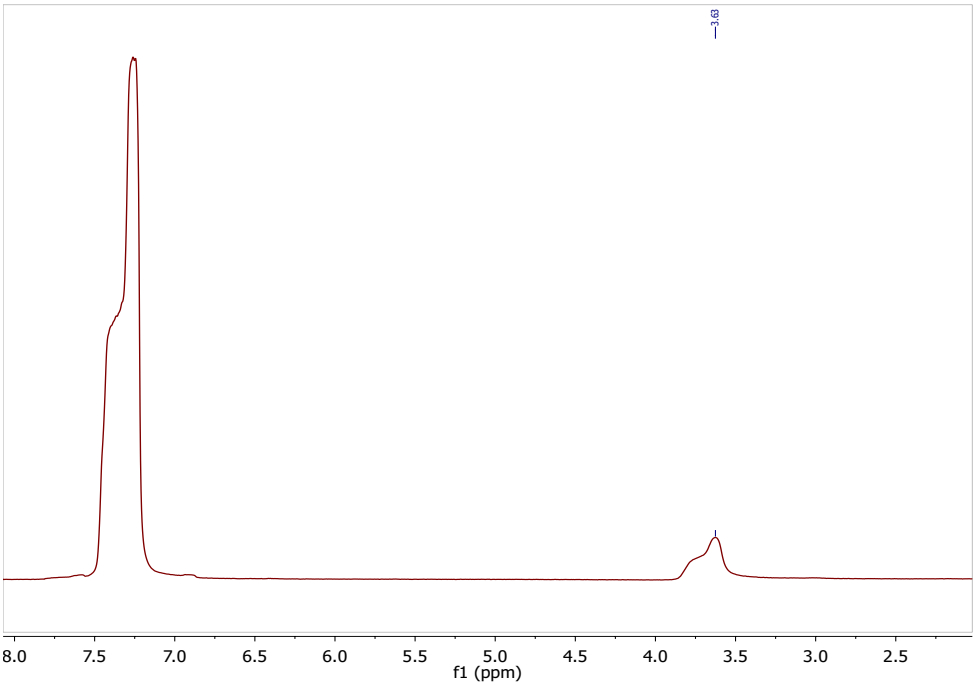

Figure A.148: ^{2}D NMR spectrum of **94**.

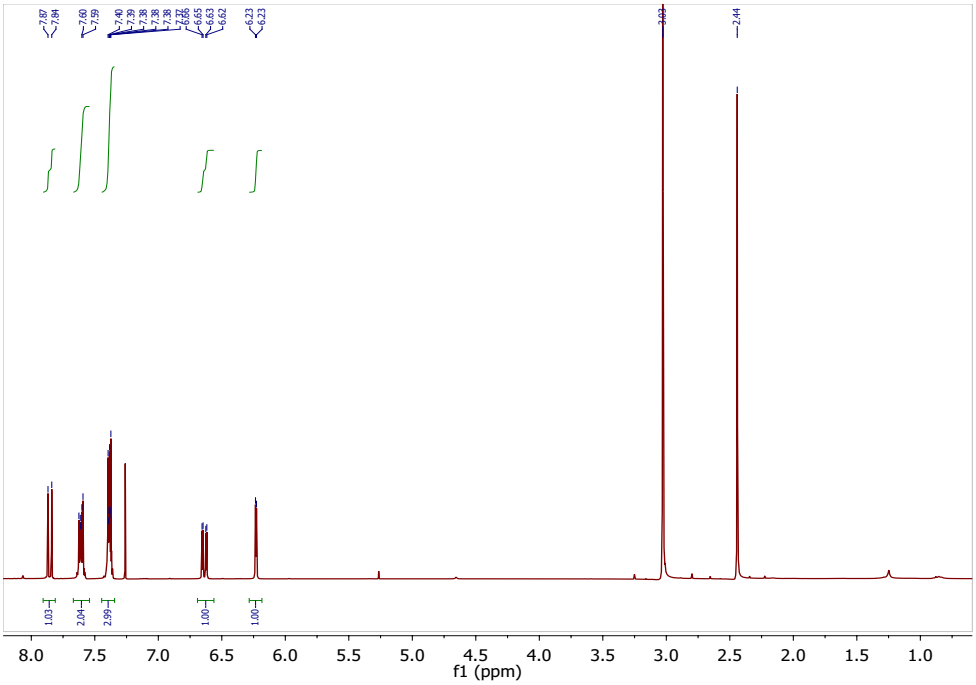

Figure A.149: ^{1}H NMR spectrum of **94**.

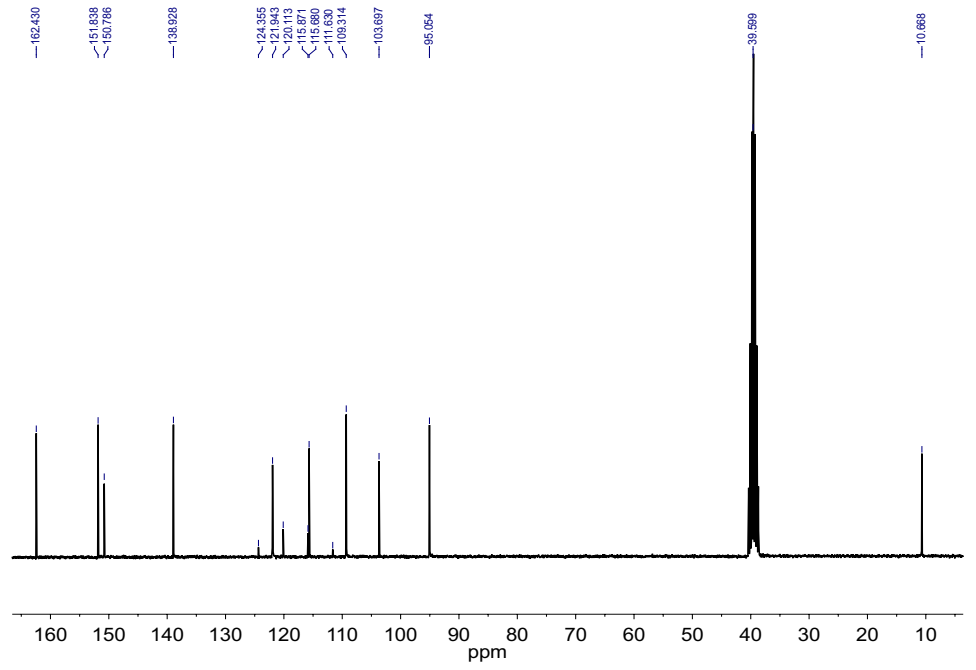

Figure A.150: ^{13}C NMR spectrum of **97**.

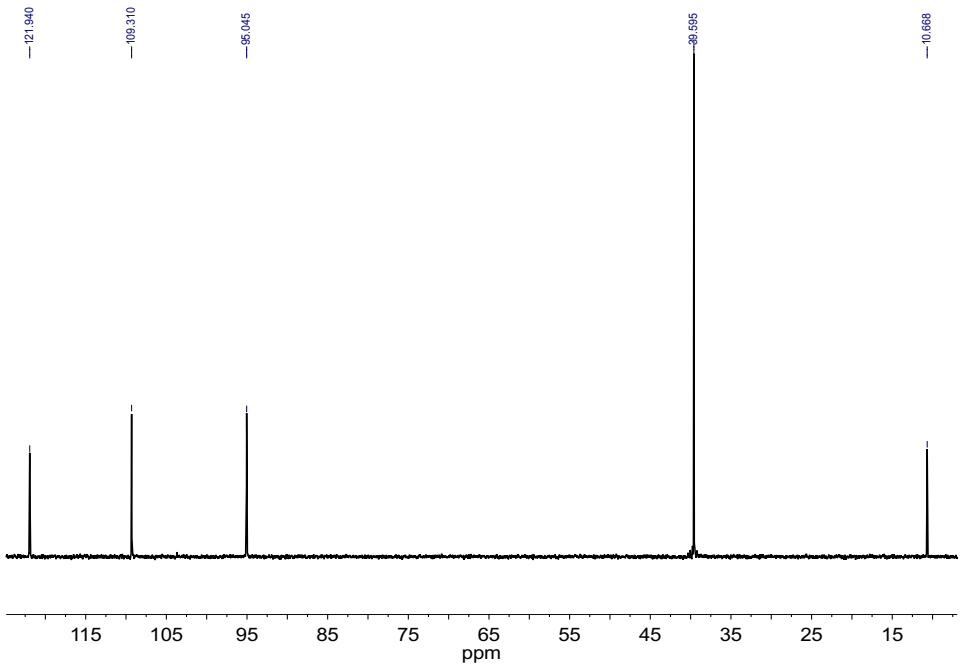

Figure A.151: DEPT-135 NMR spectrum of **97**.

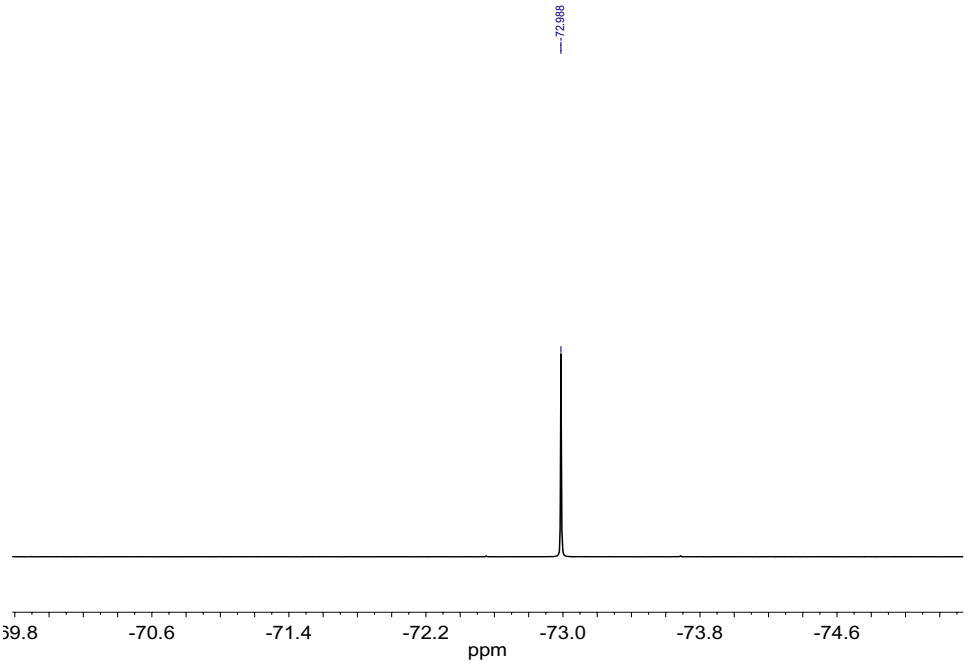

Figure A.152: ^{19}F NMR spectrum of **97**.

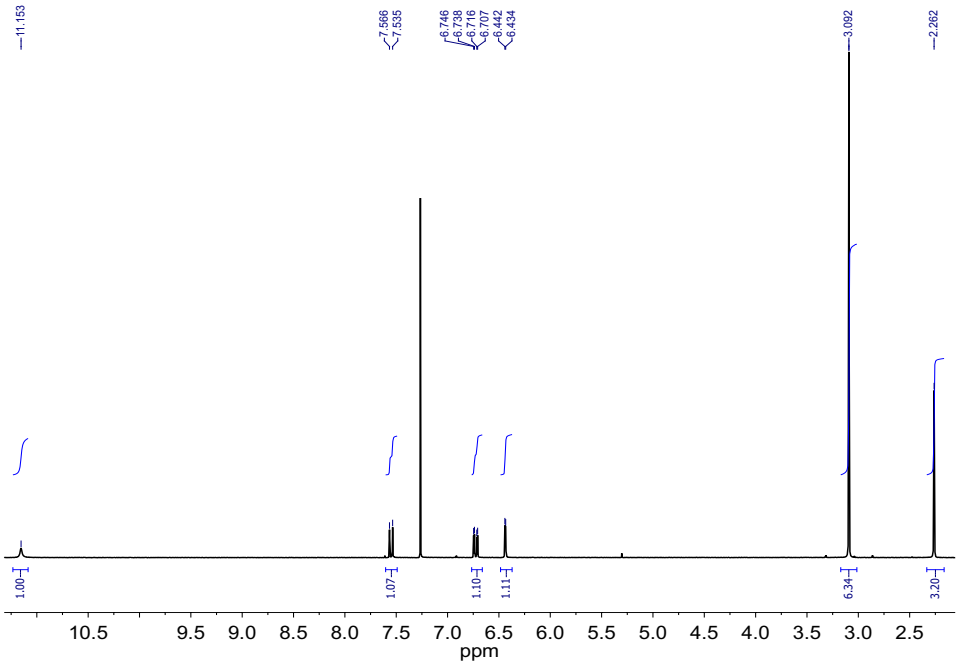

Figure A.153: ^{1}H NMR spectrum of **97**.

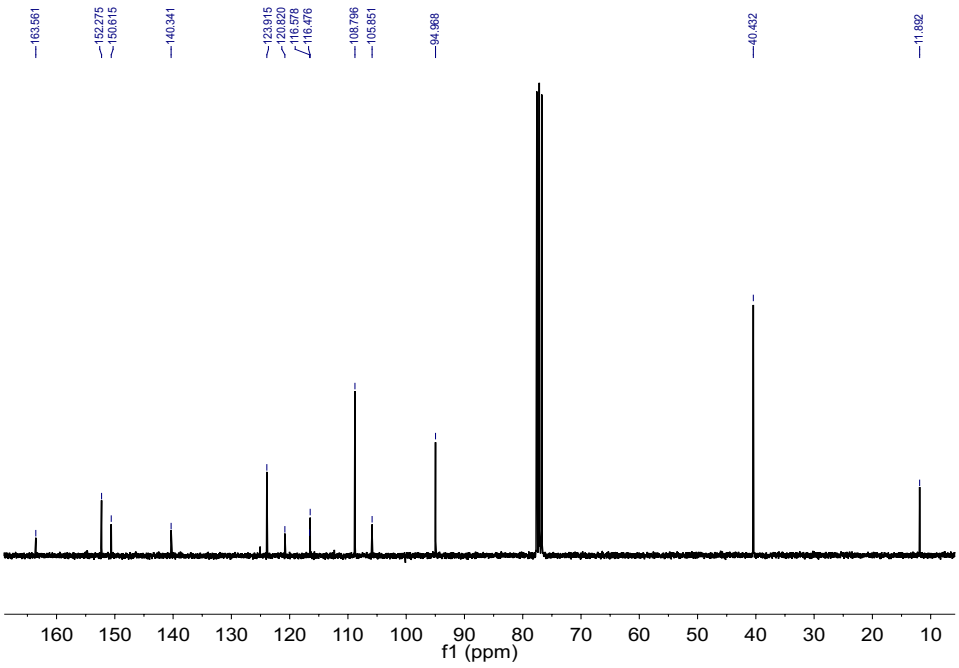

Figure A.154: ^{13}C NMR spectrum of **98**.

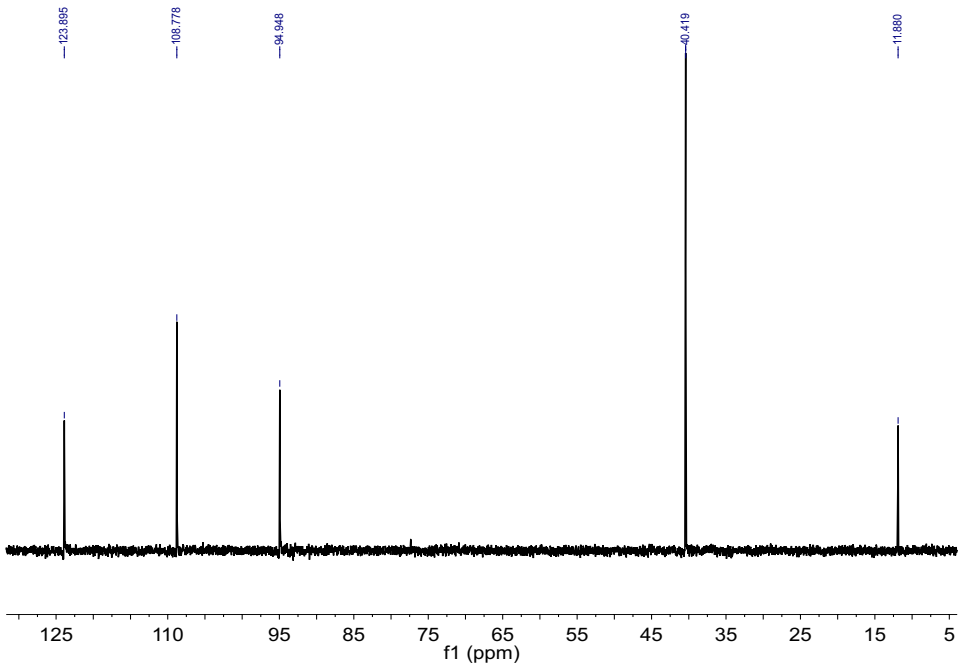

Figure A.155: DEPT-135 NMR spectrum of **98**.

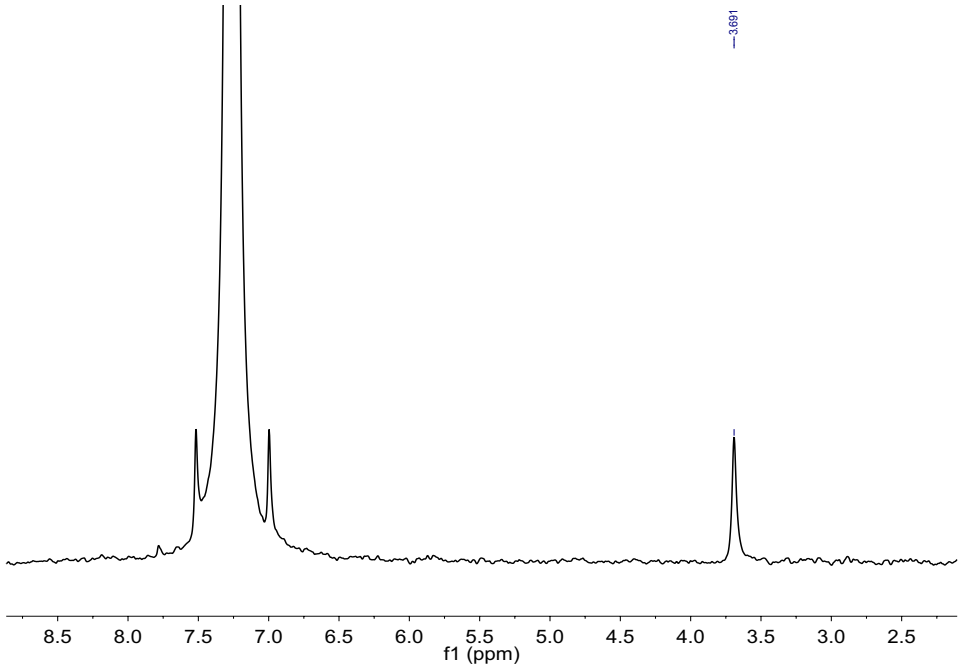

Figure A.156: ^{2}D NMR spectrum of **98**.

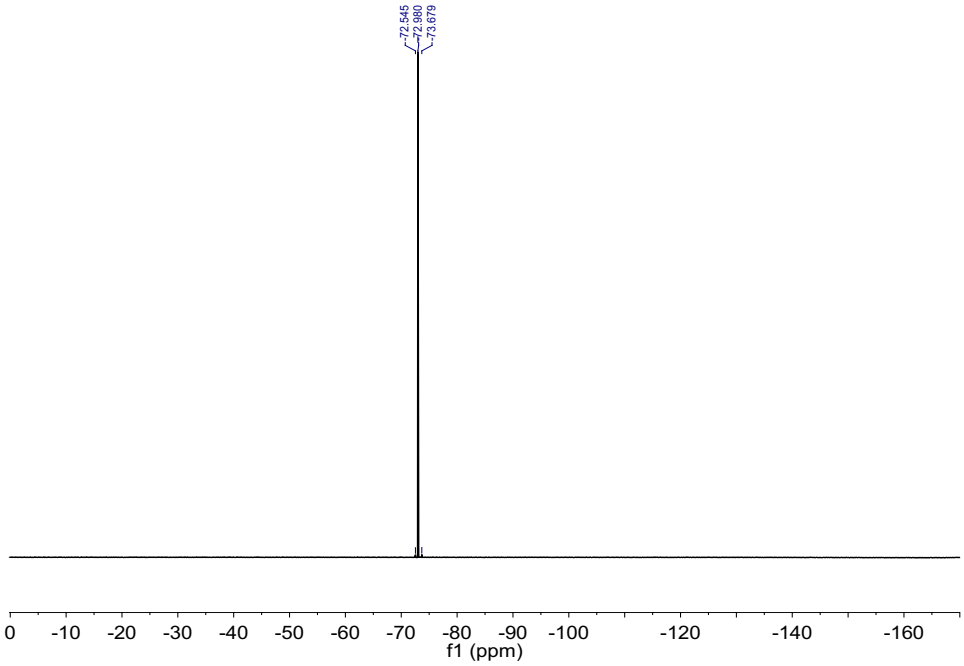

Figure A.157: ^{19}F NMR spectrum of **98**.

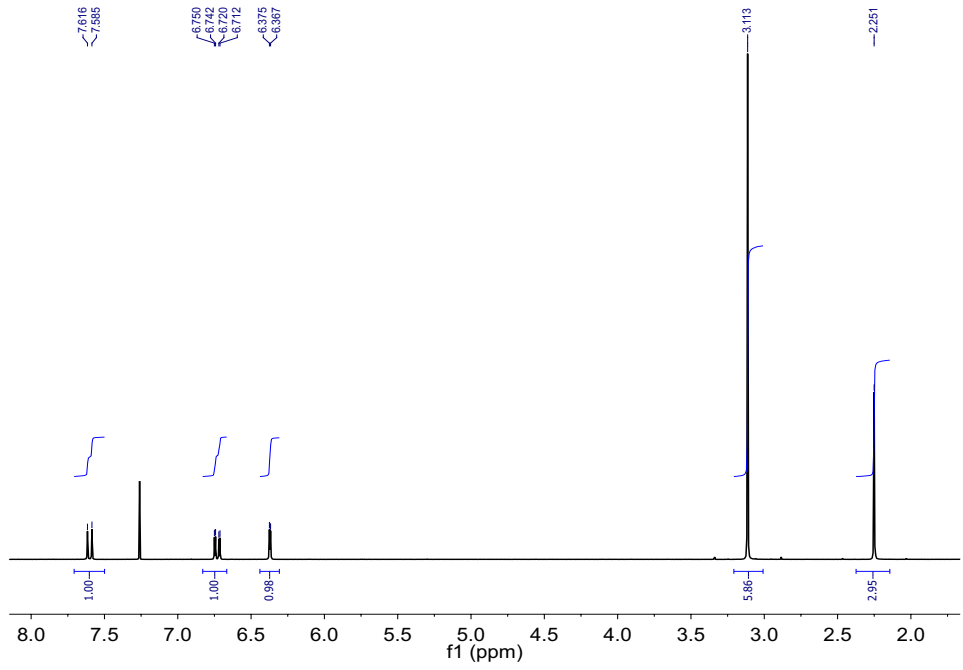

Figure A.158: ^{1}H NMR spectrum of **98**.

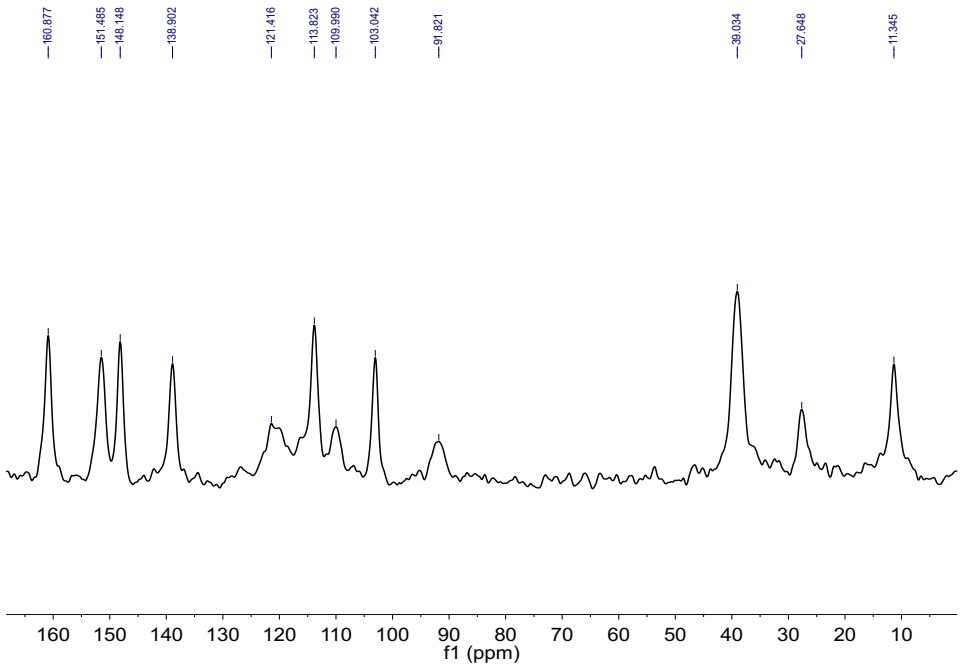

Figure A.159: Solid-state ^{13}C CP MAS NMR spectrum of **98**.

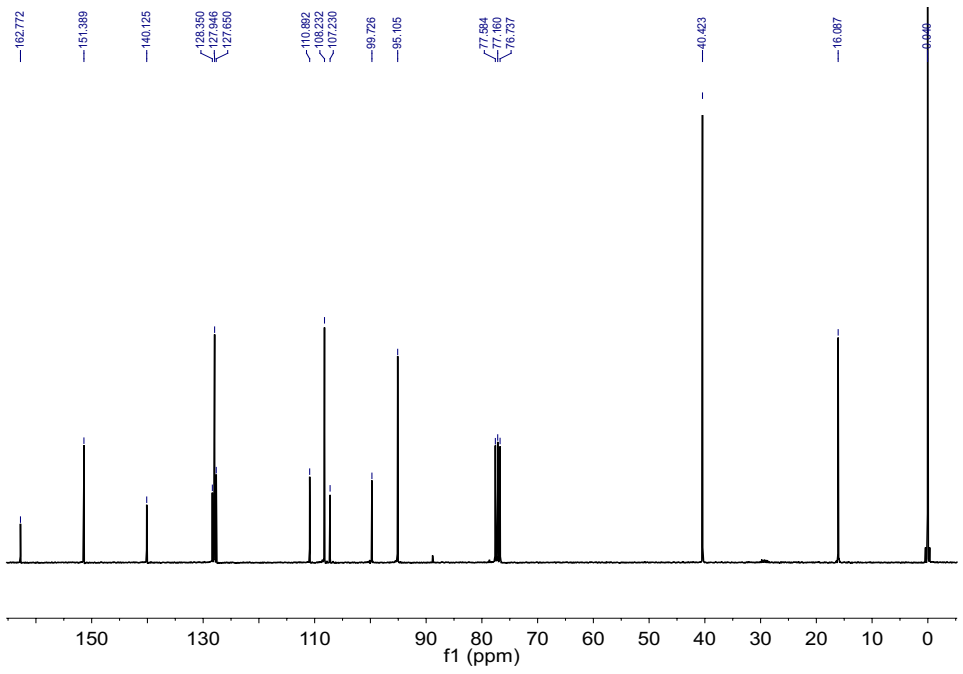

Figure A.160: ^{13}C NMR spectrum of **99**.

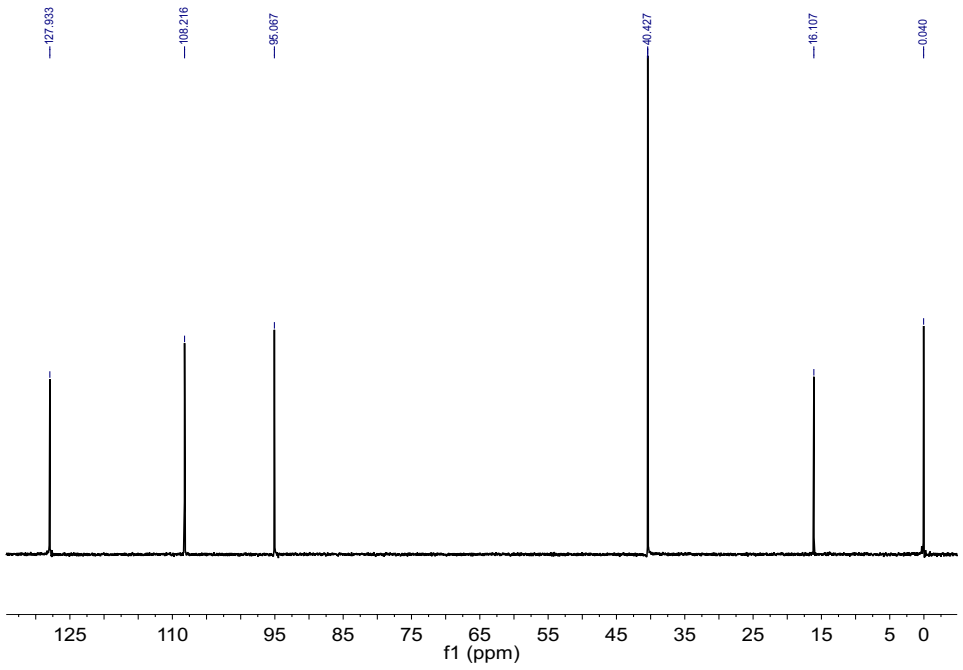

Figure A.161: DEPT-135 NMR spectrum of **99**.

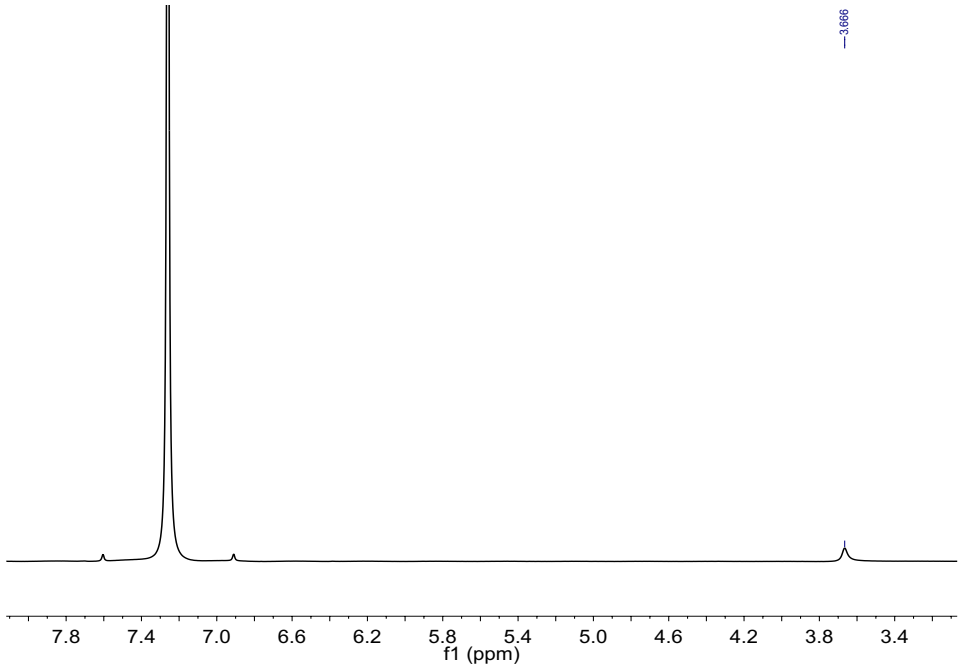

Figure A.162: ^{2}D NMR spectrum of **99**.

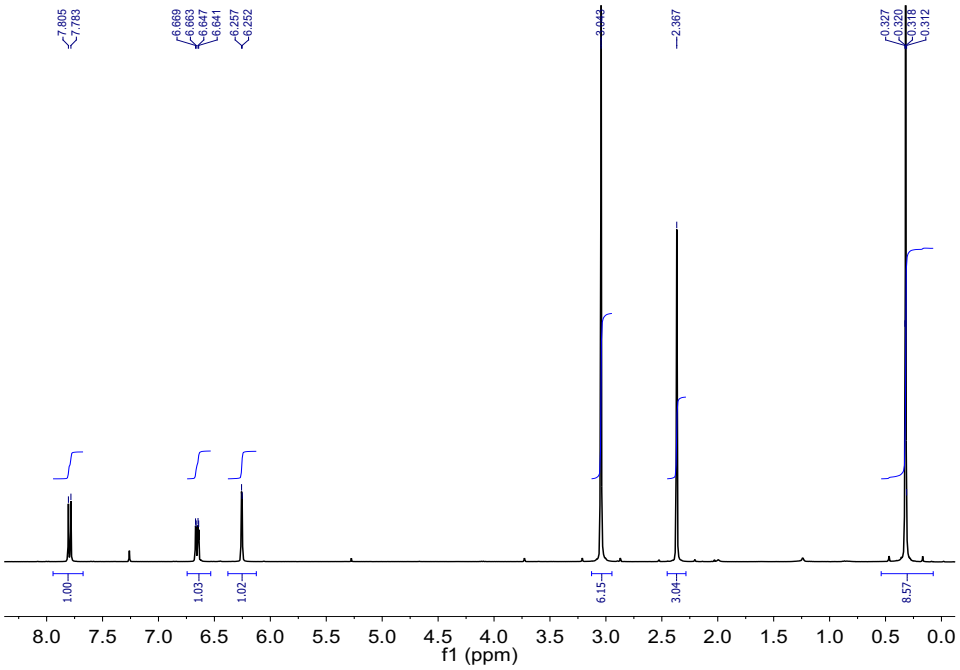

Figure A.163: ^{1}H NMR spectrum of **99**.

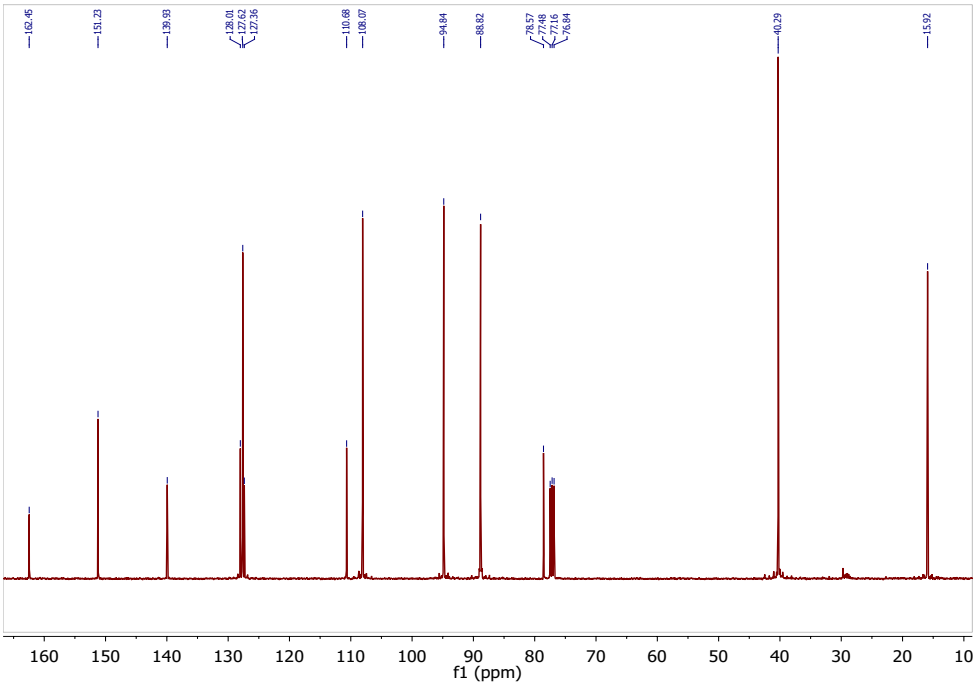

Figure A.164: ^{13}C NMR spectrum of **100**.

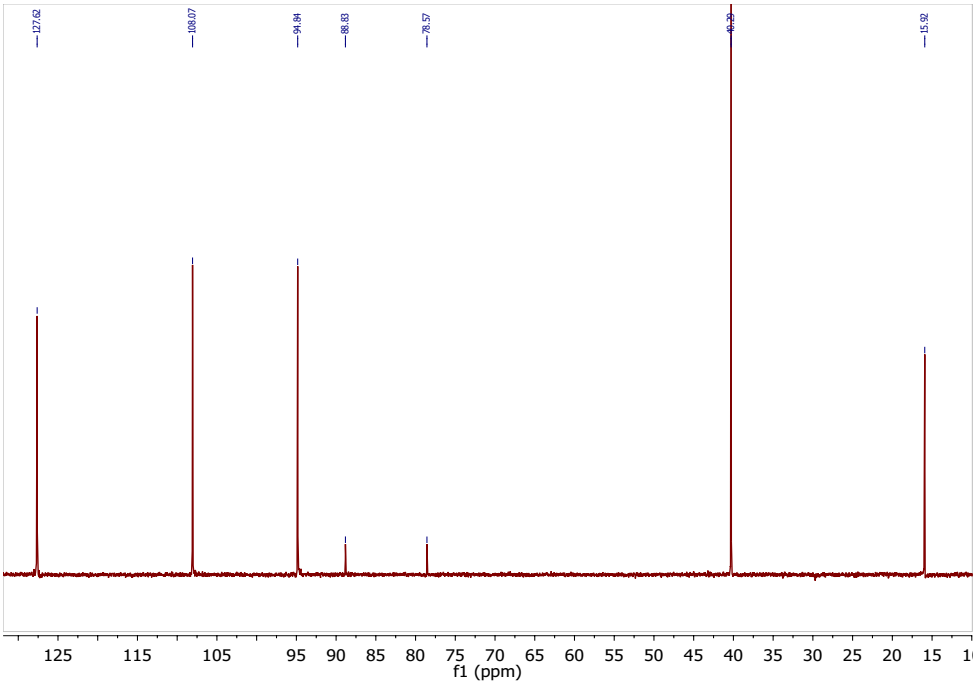

Figure A.165: DEPT-135 NMR spectrum of **100**.

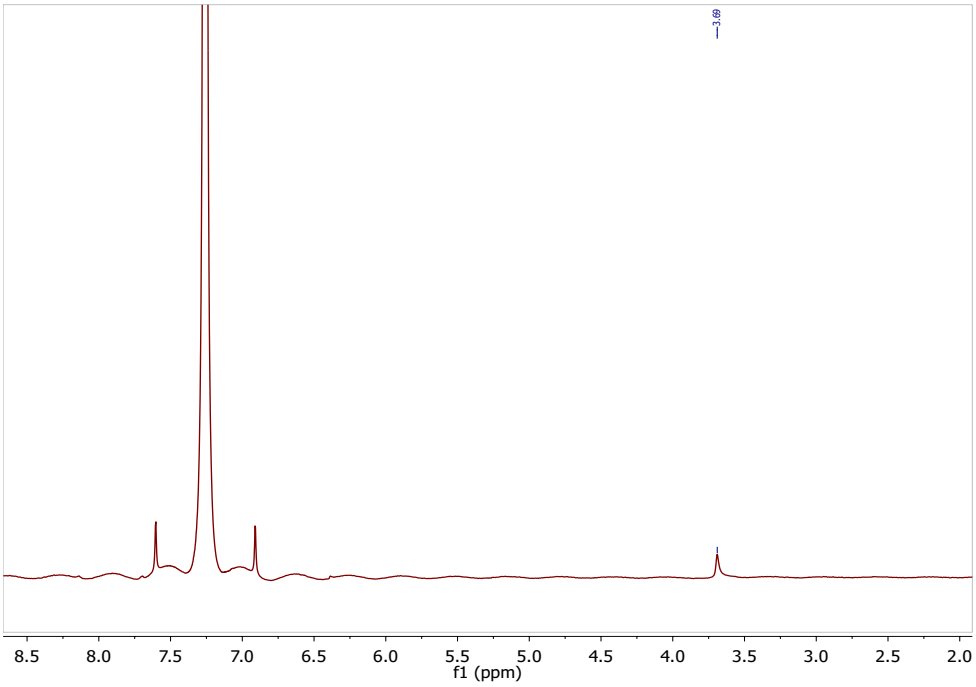

Figure A.166: ^{2}D NMR spectrum of **100**.

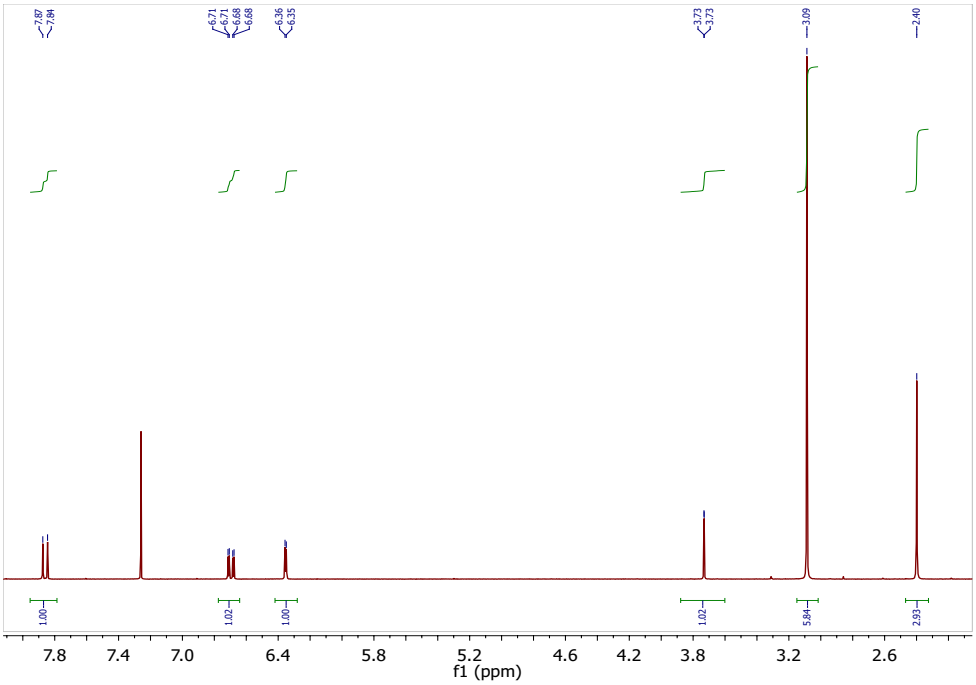

Figure A.167: ^{1}H NMR spectrum of **100**.

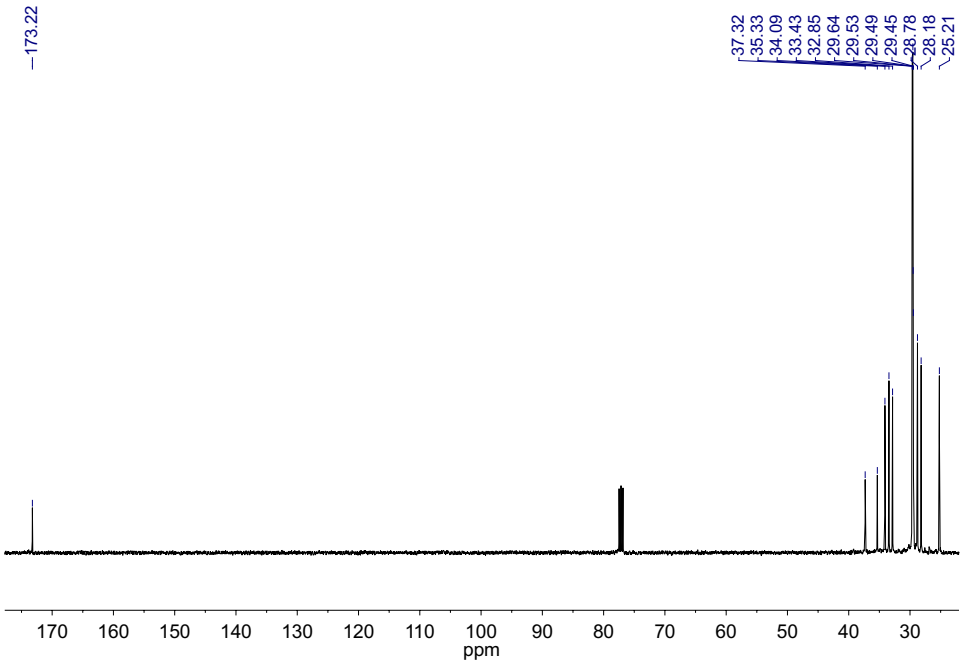

Figure A.168: ^{13}C NMR spectrum of **112**.

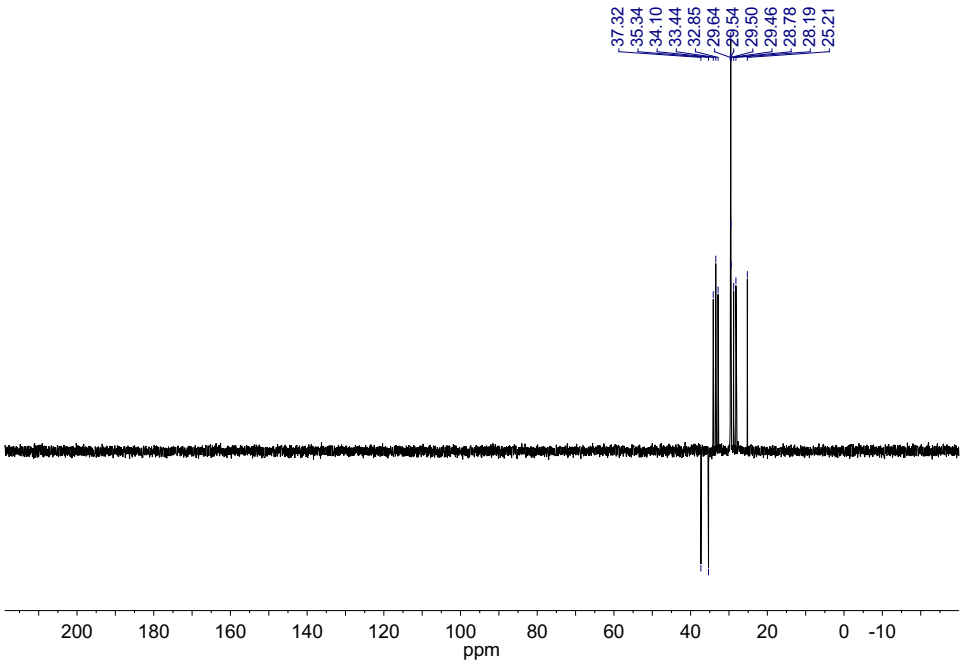

Figure A.169: DEPT-135 NMR spectrum of **112**.

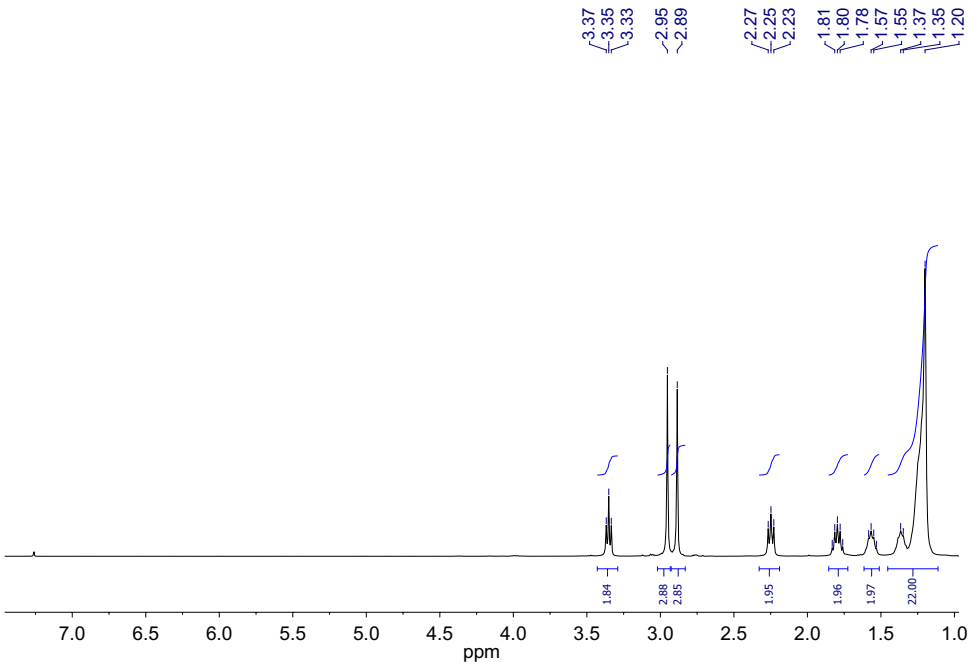

Figure A.170: ^{1}H NMR spectrum of **112**.

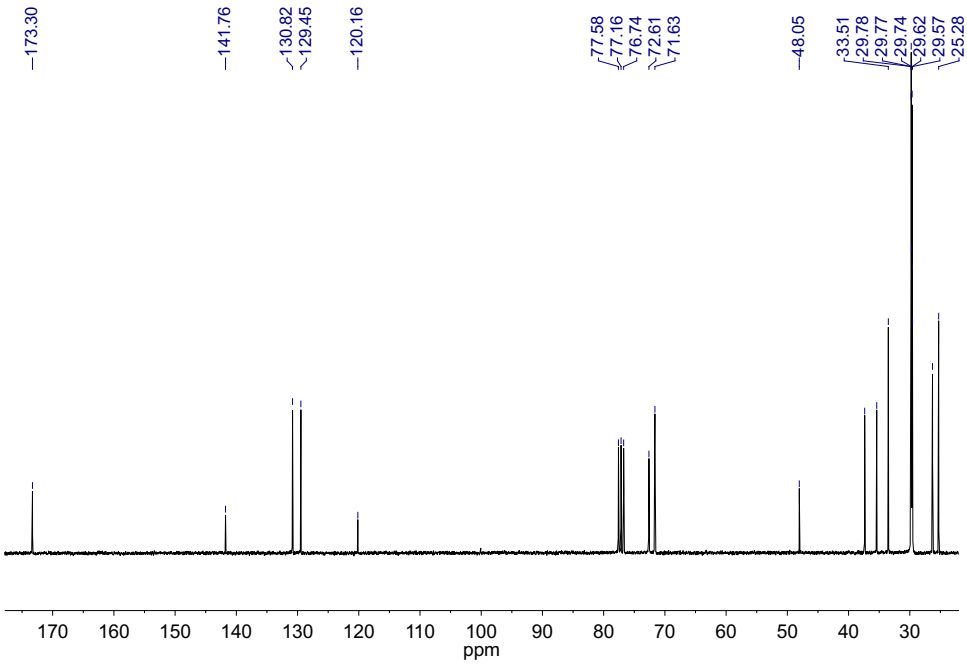

Figure A.171: ^{13}C NMR spectrum of **114**.

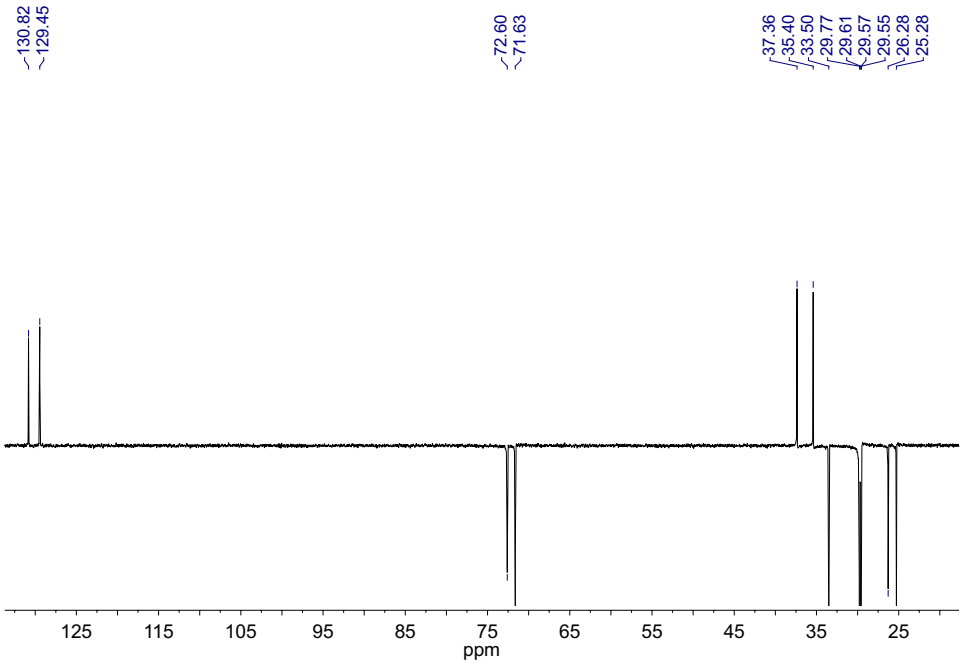

Figure A.172: DEPT-135 NMR spectrum of **114**.

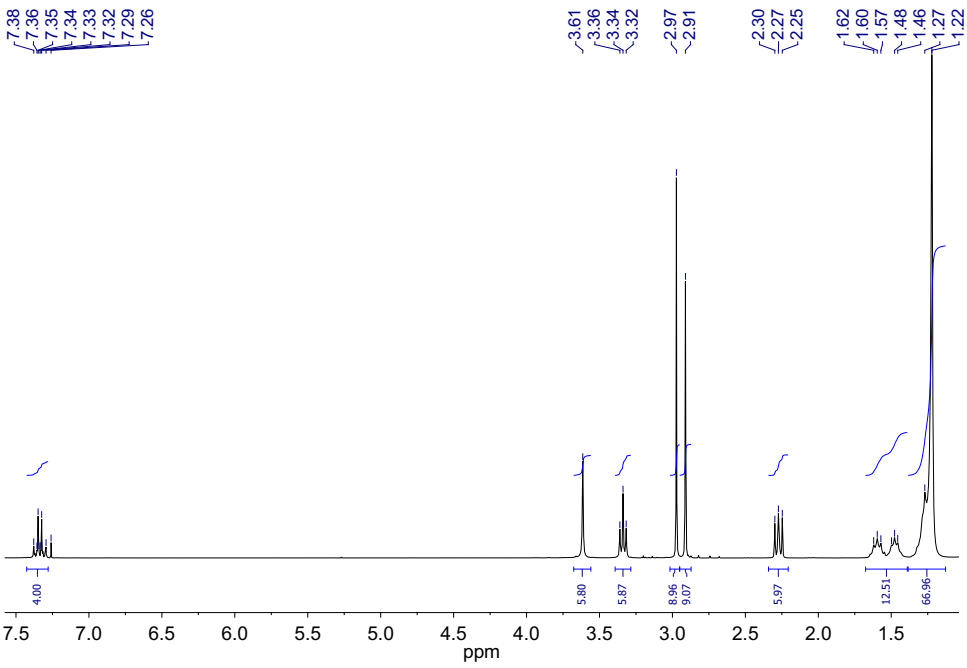

Figure A.173: ^{1}H NMR spectrum of **114**.

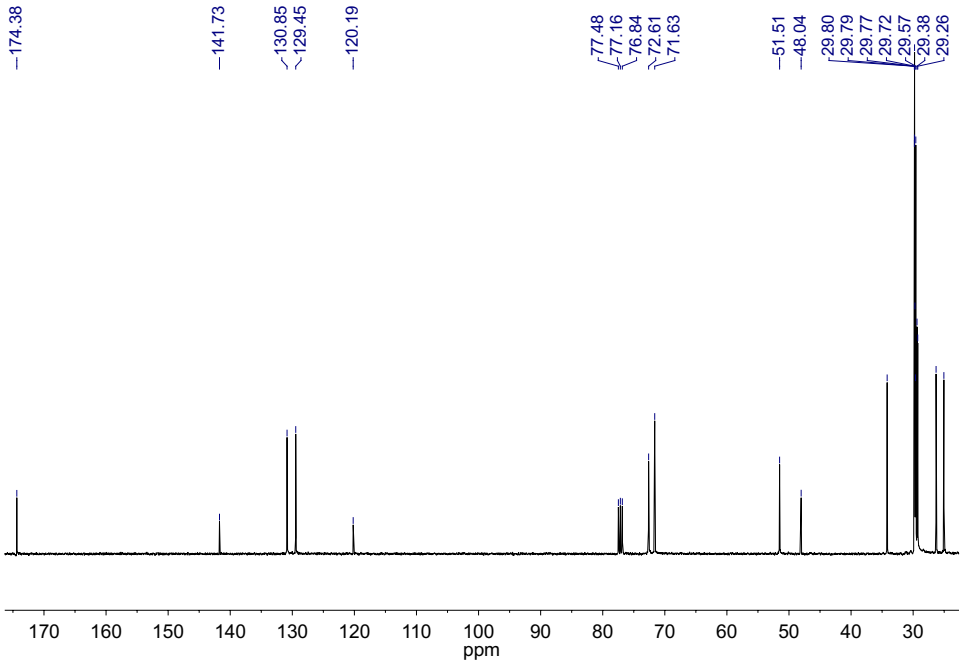

Figure A.174: ^{13}C NMR spectrum of **115**.

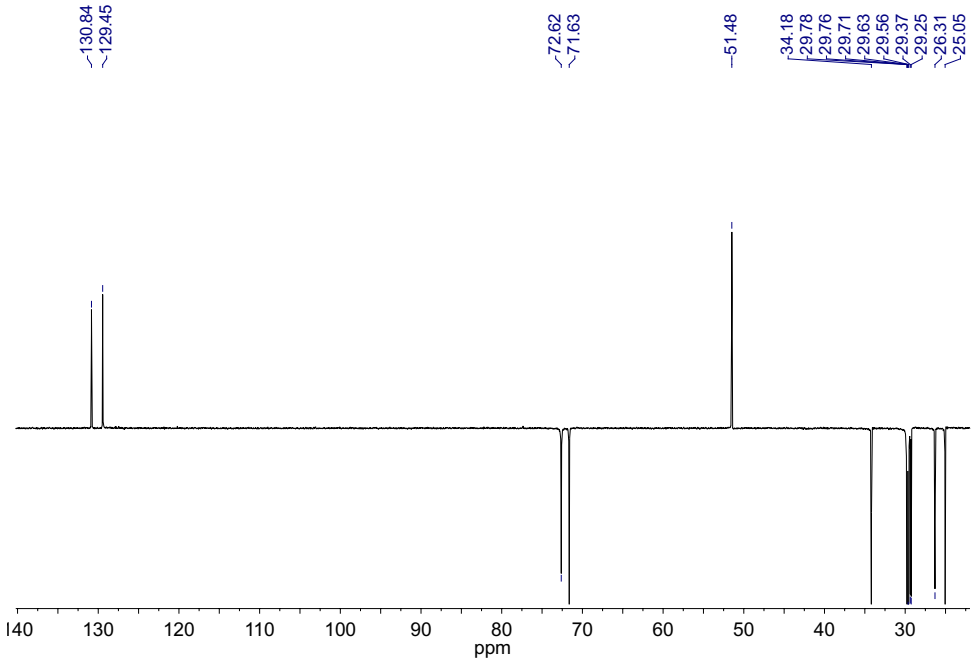

Figure A.175: DEPT-135 NMR spectrum of **115**.

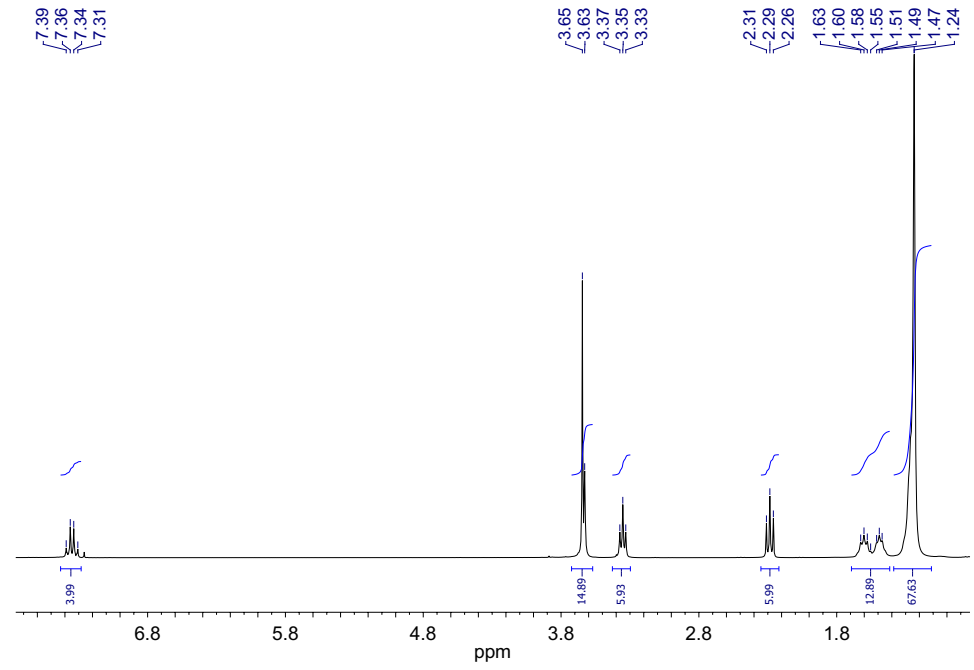

Figure A.176: ^{1}H NMR spectrum of **115**.

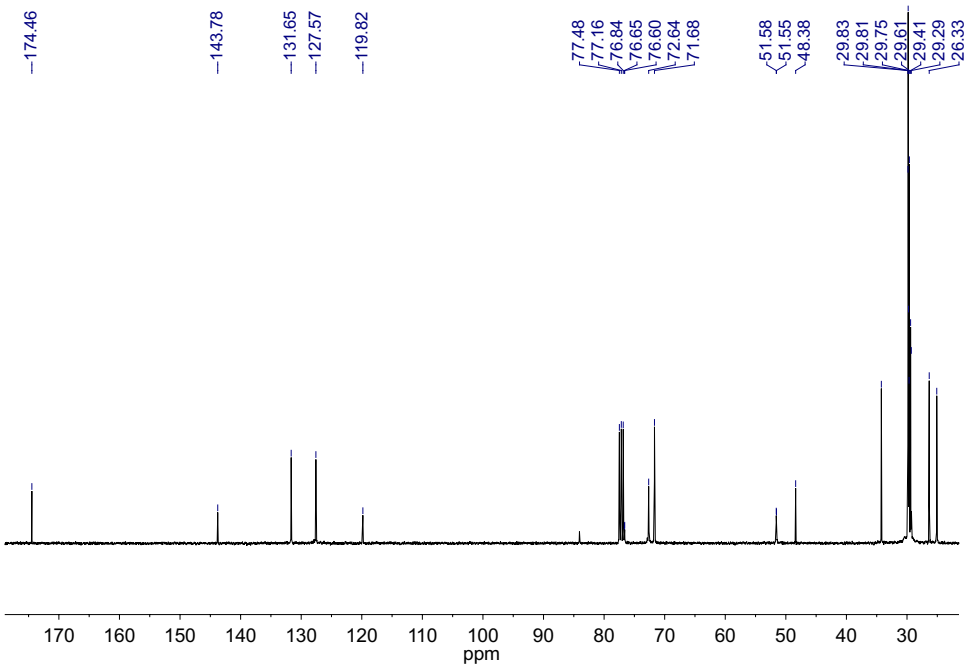

Figure A.177: ^{13}C NMR spectrum of **116**.

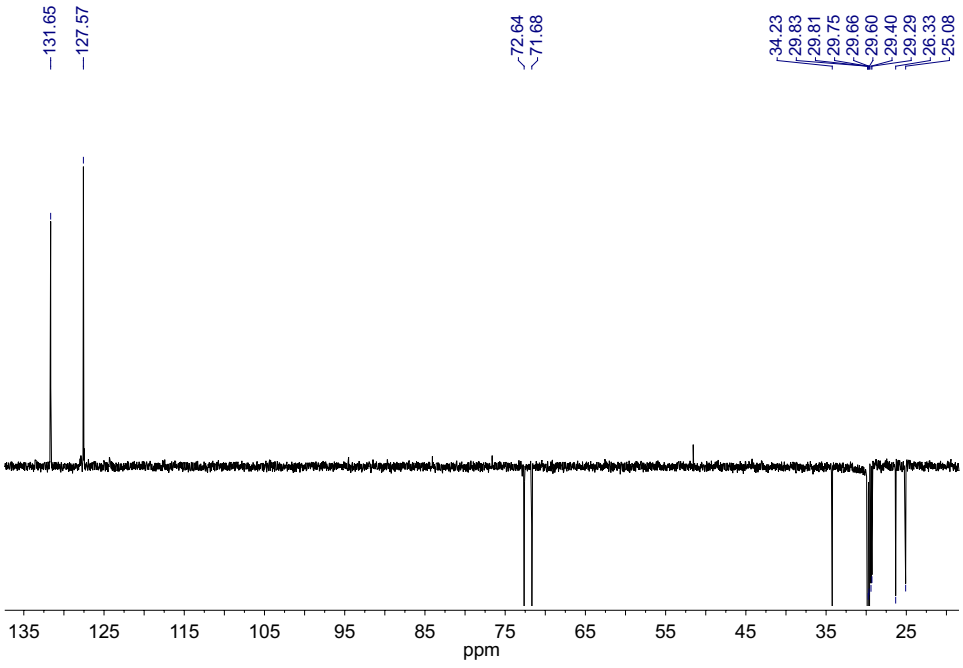

Figure A.178: DEPT-135 NMR spectrum of **116**.

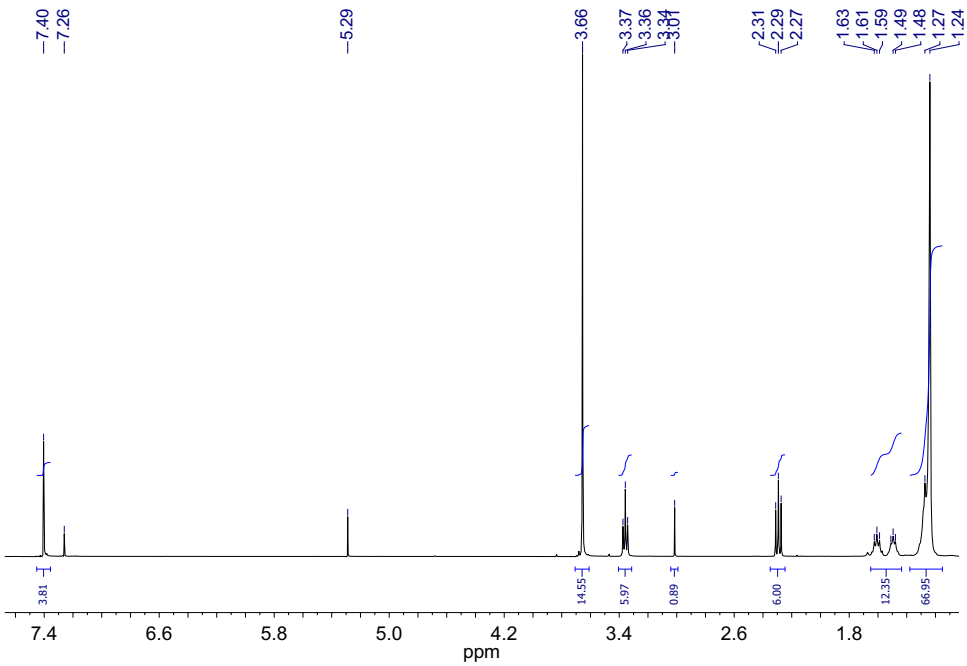

Figure A.179: ^{1}H NMR spectrum of **116**.

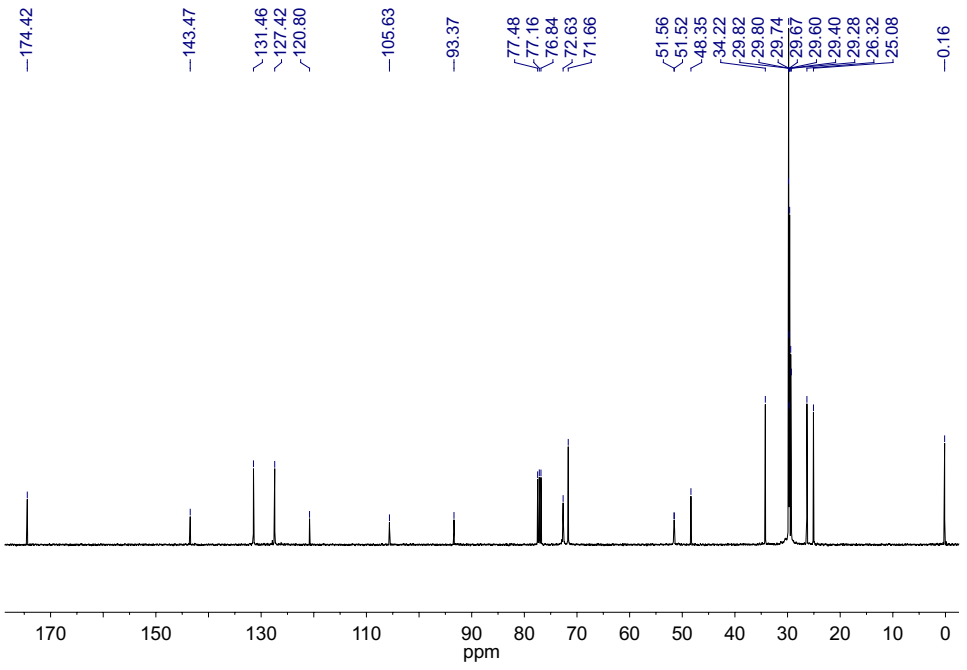

Figure A.180: ^{13}C NMR spectrum of **117**.

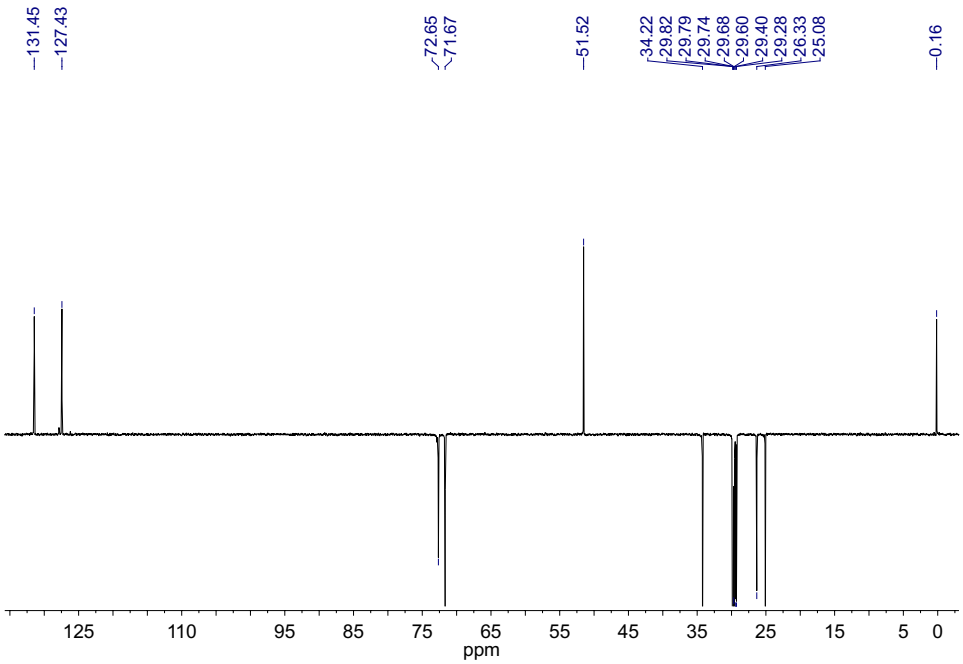

Figure A.181: DEPT-135 NMR spectrum of **117**.

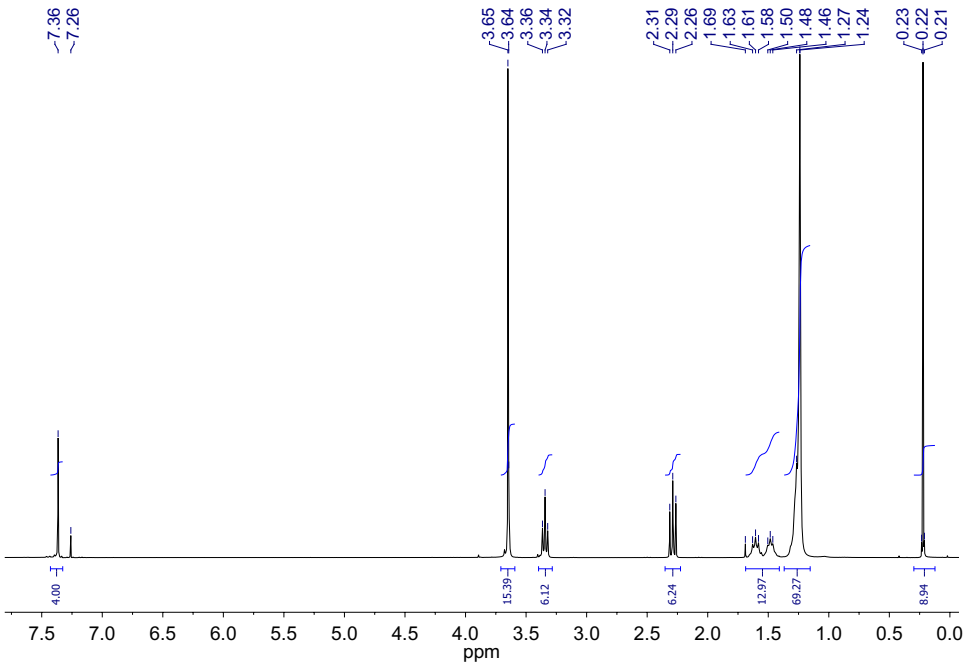

Figure A.182: ^{1}H NMR spectrum of **117**.

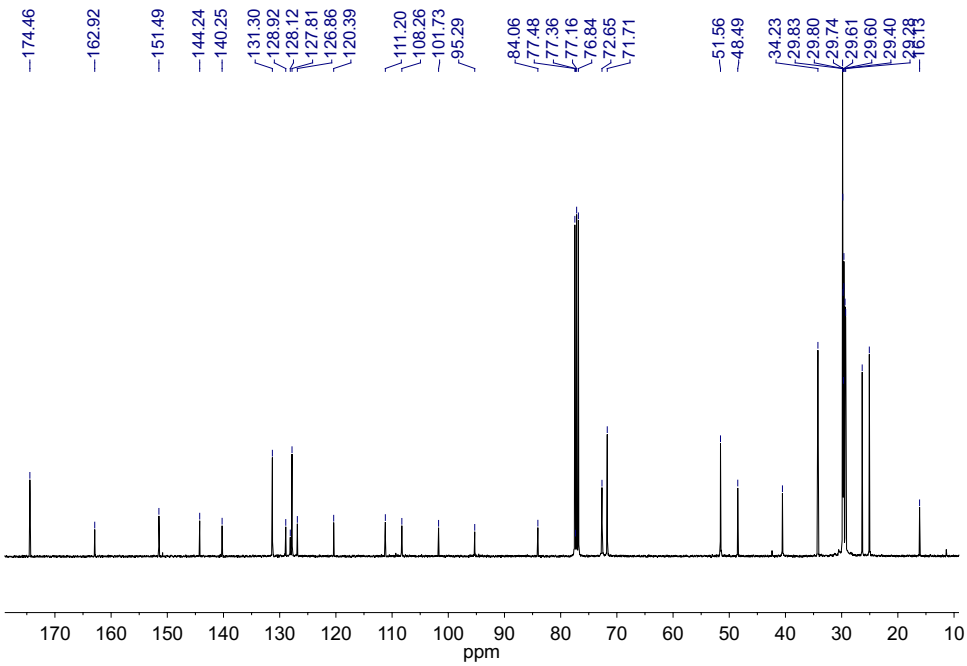

Figure A.183: ^{13}C NMR spectrum of **118**.

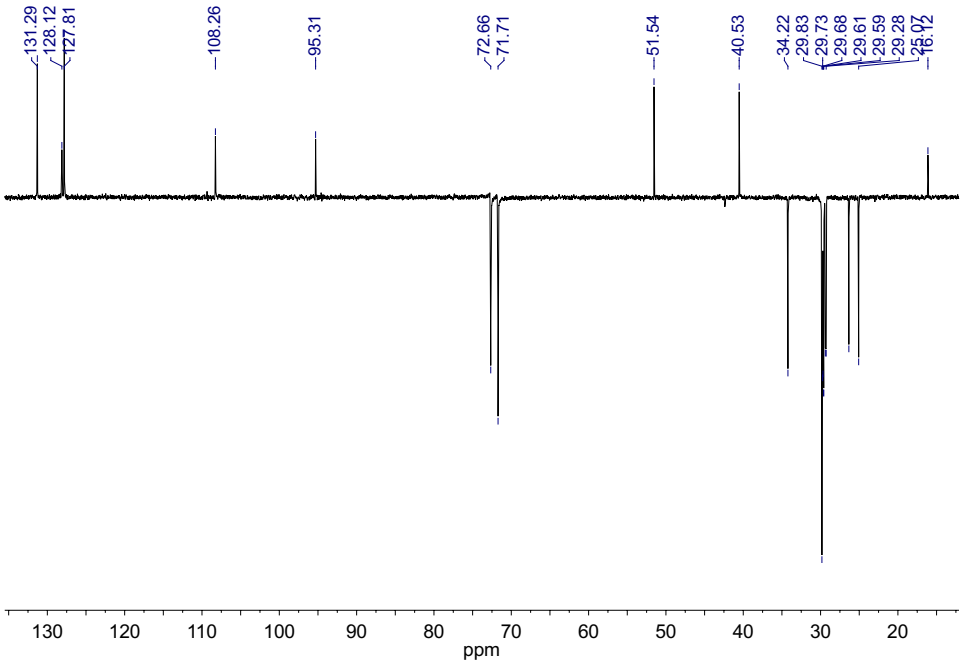

Figure A.184: DEPT-135 NMR spectrum of **118**.

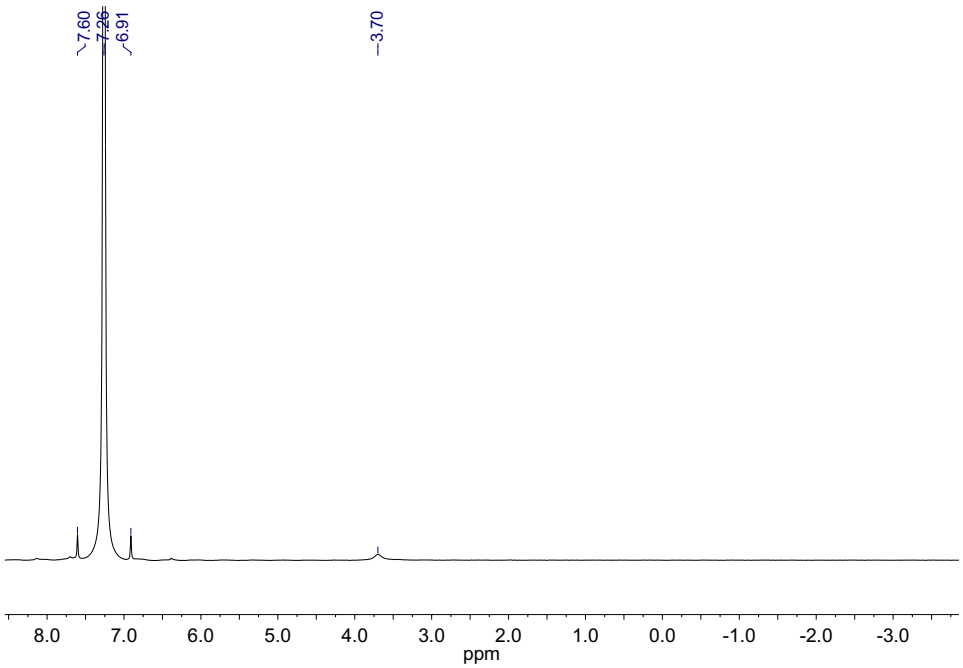

Figure A.185: ^{2}D NMR spectrum of **118**.

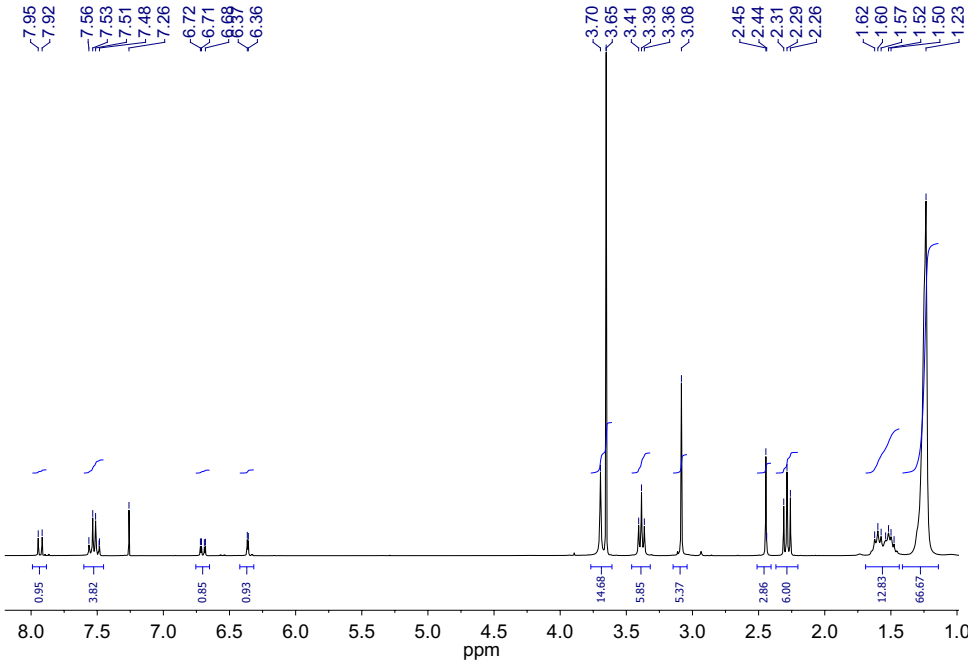

Figure A.186: ^{1}H NMR spectrum of **118**.

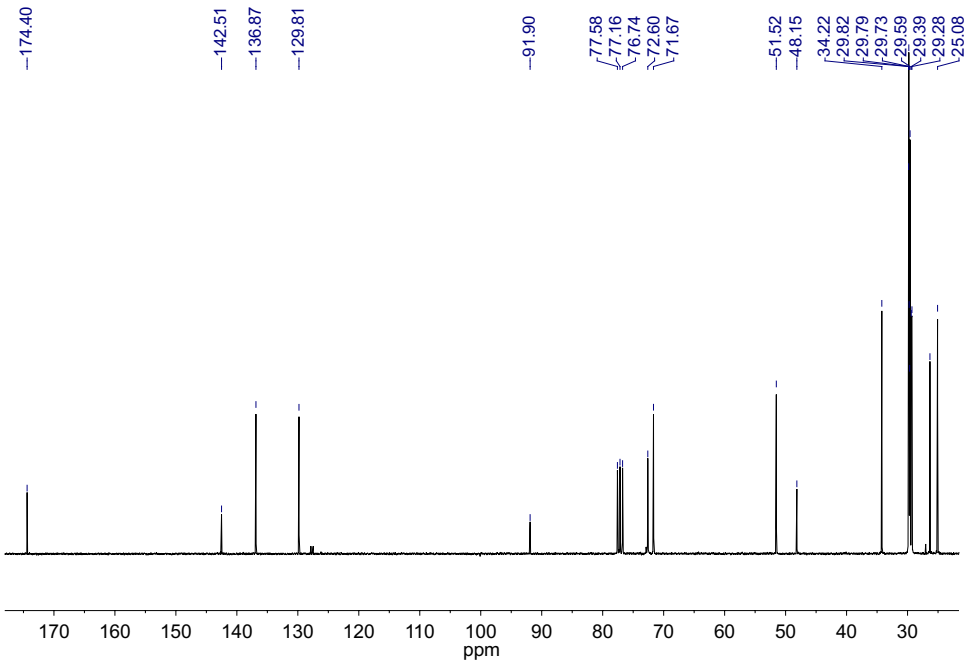

Figure A.187: ^{13}C NMR spectrum of **119**.

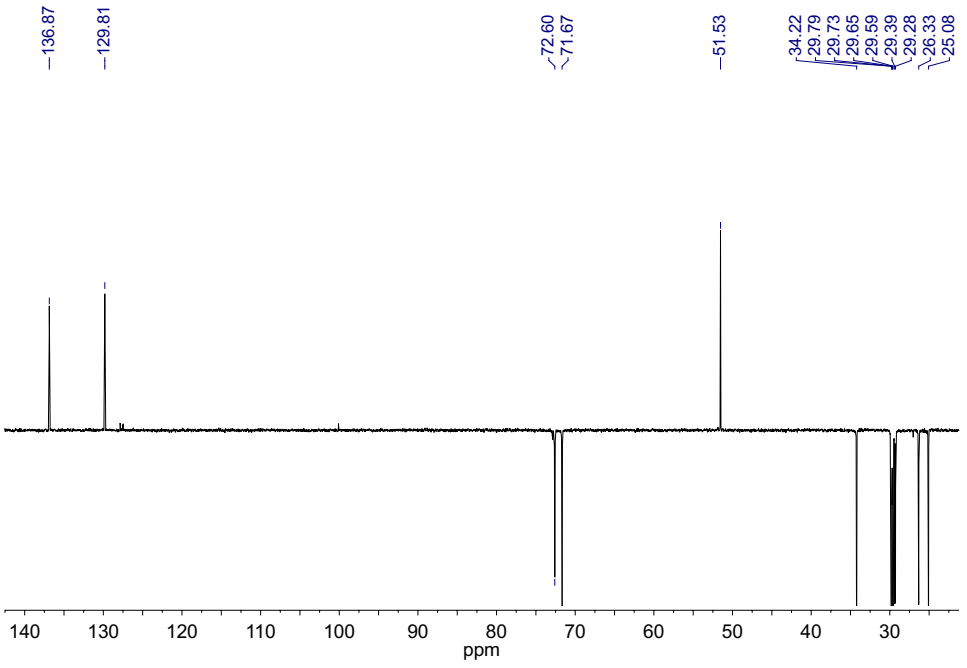

Figure A.188: DEPT-135 NMR spectrum of **119**.

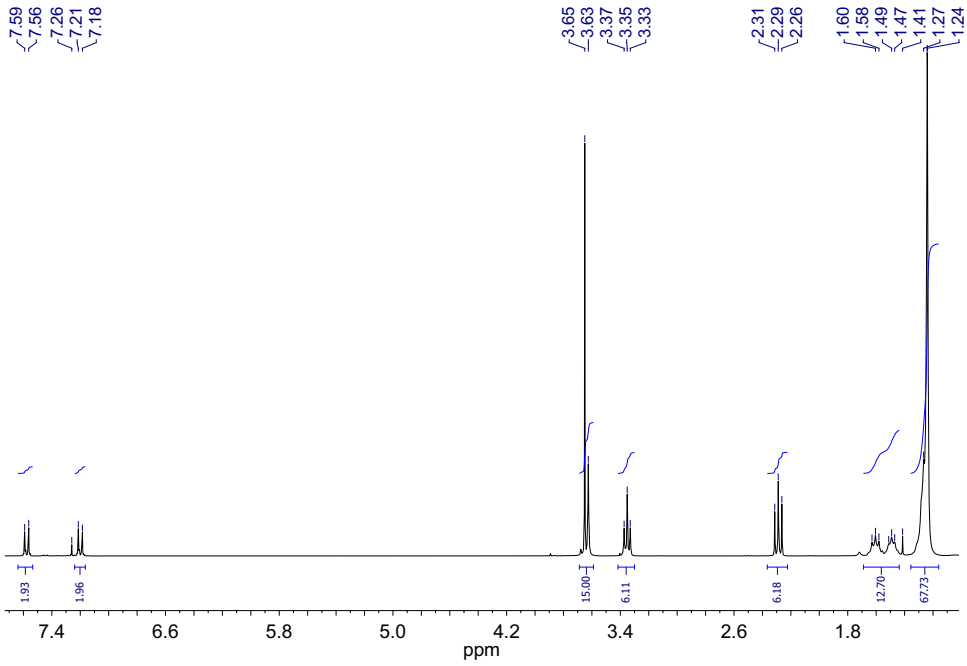

Figure A.189: ^{1}H NMR spectrum of **119**.